

# UNIVERSITÀ DEGLI STUDI DI TRIESTE

---

XXXIV CICLO DEL DOTTORATO DI RICERCA IN CHIMICA

Settore scientifico-disciplinare: CHIM/02

## *Computational spectroscopy of metal clusters: method development and applications*

DOTTORANDO:

**Dott. MEDVES MARCO**

COORDINATORE:

**Prof. ENZO ALESSIO**

SUPERVISORE DI TESI:

**Prof. MAURO STENER**

---

Anno Accademico 2020-2021

# Contents

<b>1 INTRODUCTION.....</b>	<b>3</b>
1.1 Foreword .....	3
1.2 Scope of the Thesis .....	4
1.3 Nanoparticles.....	5
<b>2 THEORY .....</b>	<b>8</b>
2.1 Density functional theory .....	8
2.2 Kohn-Sham approach .....	10
2.3 Exchange-correlation functionals.....	15
2.4 Linear response theory .....	19
2.5 Random phase approximation and TDDFT .....	24
2.6 polTDDFT absorption .....	32
2.7 polTDDFT dichroism.....	38
2.8 Technical remarks .....	42
2.9 Relativistic effects.....	42
<b>3 BIBLIOGRAPHY .....</b>	<b>47</b>
<b>4 RESULTS AND PUBLICATIONS .....</b>	<b>52</b>
4.1 Chiral functionalization of an atomically precise noble metal cluster: insights into the origin of chirality and photoluminescence.....	55
4.1.1 Supporting information.....	69
4.2 Crystal structure of $\text{Au}_{36-x}\text{Ag}_x(\text{SPh-tBu})_{24}$ nanoalloy and the role of Ag doping in excited state coupling.....	104
4.2.1 Supporting information.....	115
4.3 An efficient hybrid scheme for time dependent density functional theory.....	130
4.4 Predictive optical photoabsorption of $\text{Ag}_{24}\text{Au}(\text{DMBT})_{18}^-$ via efficient TDDFT simulations .....	141
4.4.1 Supporting information.....	153

4.5 Plasmonic circular dichroism in chiral gold nanowire dimers.....	160
4.6 Coupling between plasmonic and molecular excitations: TDDFT investigation of an Ag-nanorod/bodipy-dye interaction .....	178
4.6.1 Supporting information.....	203
4.7 Optimization of density fitting auxiliary slater type basis functions for time dependent density functional theory .....	205
<b>5 CONCLUSIONS .....</b>	<b>235</b>

# 1 INTRODUCTION

## 1.1 Foreword

Metal clusters have started to play a major role in material science in the last decades. This is due to the peculiar behaviour showed by the matter at nanosize. Such different behaviours range from typical properties (cohesive energies, ionization potentials, average coordination numbers) up to reactivity (catalysis) and response to external electromagnetic fields (optical behaviours). Moreover matter at nanosize poses interesting questions to interpretative models: it is often hard to describe nanosystem with the paradigms typical of molecules or bulk systems. For such reasons in this field theory and in general computational studies can be very important to rationalize the observed behaviours. In the present study we have focussed on the optical properties of metal clusters, which include standard molecular transitions as well as collective phenomena like plasmons. The necessity to describe plasmons and therefore electron collective motion imposes to go beyond the one-particle (independent particle approximation), considering a linear response model like TDDFT, which offers the computational economy of DFT together the ability to describe collective phenomena. In particular a large part of efforts have been devoted to improve the complex polarizability TDDFT algorithm (POLTDDFT), an efficient method recently developed in the theoretical chemistry group of Trieste University to solve the TDDFT equations for large systems and for a wide energy interval, in order to avoid the limits of more traditional schemes like that due to Casida. In this respect a new scheme called Hybrid Diagonal Approximation (HDA) has allowed to apply hybrid functional in TDDFT calculations of large systems, obtaining excellent match with the experiment. Also in this work the development of a new density fitting basis set, optimized for POLTDDFT, has been carried out, giving to the generic user a valid tool to apply the method to a very wide range of targets. Besides method development, also applications to open fields of cluster science, like Electronic Circular Dichroism (ECD) of chiral metal clusters in collaboration with Thomas Bürgi (Geneve University) as well as very accurate low temperature photoabsorption experiments in collaboration with Flavio Maran (Padua University) have been considered. In the specific field of plasmonics, also the effect of coupling two plasmonic chiral systems on the ECD has been studied, and the underlying coupling mechanism has been identified. The accuracy of the suggested method together with its computational efficiency make POLTDDFT a good candidate for even wider applications, but, more important, the quantitative accuracy obtained makes this method predictive, and therefore a good candidate also for the *in-silico* design of novel materials with requested optical properties.

## 1.2 Scope of the Thesis

In this PhD thesis 3 main objectives were considered. First of all the development of an efficient scheme in order to give quantitative agreement with experimental photoabsorption data. This has been obtained employing the B3LYP functional but introducing an approximation in the exchange-correlation kernel called HDA, which allows to strongly speed up the calculation without losing accuracy. The second objective is to render the POLTDDFT applicable to a wide set of problems. This second objective has been reached by developing a new set of density fitting basis, specifically optimized for POLTDDFT calculations. It is worth noting that both HDA and the new density fitting basis are already available in the latest version of the AMS suite of programs. The third objective is to show that such method can be profitably applied to a wide range of open problems in the field of nanoscience. This has also been reached showing interesting results for the ECD of chiral metal clusters, the photoabsorption study at low temperature and the effect of coupling a pair of chiral metal clusters on the ECD (plasmonic dichroism).

## 1.3 Nanoparticles

As NanoParticles (NPs) we refer to an aggregate of atoms, ions or molecules with dimensions between 1 nm to 100 nm, in this thesis we will be interested in metal clusters. These form a particular class of systems that possess specific properties that are intermediate between those of isolated molecules and those of the solid bulk [1.1-4].

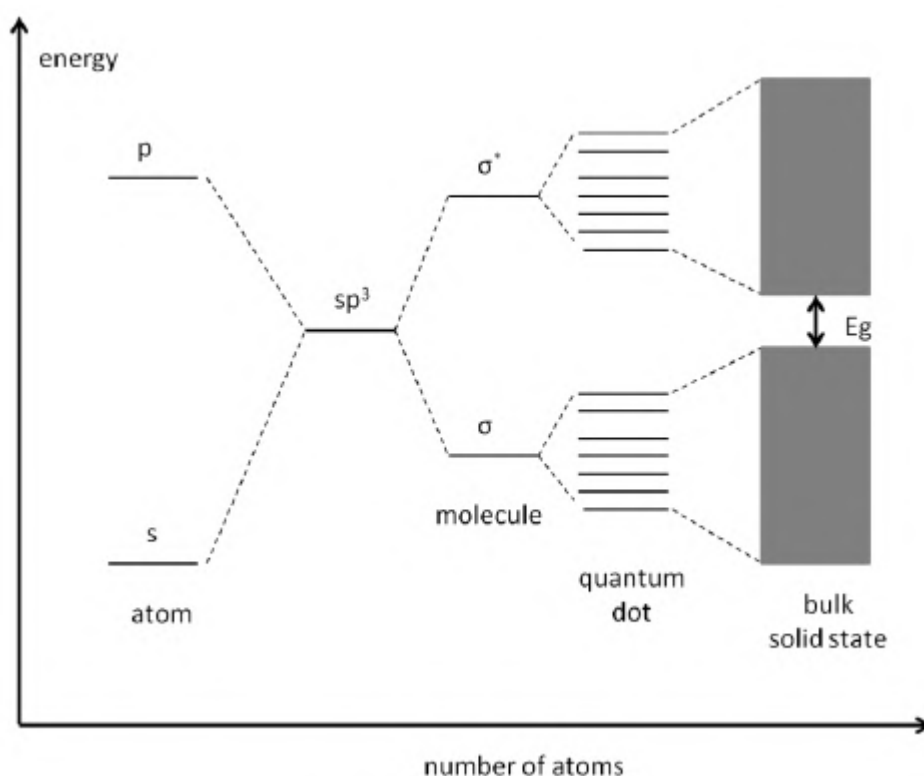


*Figure (1.1.1) Density of states as a function of the size of the system*

These peculiar properties make the NPs real attractive for their possible use in various fields of application.

In particular the interest for the optical properties point of view: LED, for technical applications and energy saving, fluorescent materials, as labelling for diagnosis or lighting, plasmon resonance, for the study of materials or analysis with extremely low limit of detection, photocatalysis, water splitting, solar cells and much more [1.5-8].

In this thesis more attention will be paid to noble metal NPs which are the most studied ones because are used in the medical field. Moreover their synthesis is well known and consolidated, essentially are produced by modification of the original Brust-Schiffrin synthesis. [1.9]

The particular properties of NPs mainly arise from their size-scale, these systems can be produced in various shapes of different sizes such as spheres, rods, plates, prisms, cube, different polyhedral and wires.

Another difference used to classify the metal clusters is the presence or absence of the protective layer, so distinguishing in “naked” (or bare) and protected clusters [1.10-17].

The naked clusters to be studied often require unconventional situations, for example molecular beams or their immobilization in inert matrices (typically insulating media such as silica or alumina), this is because the isolated clusters are very reactive and they have the tendency to aggregate with each other because they tend to minimize their surface. Or, from another point of view, they tend to maximize their average coordination number.

This marked reactivity is also found in non-reactive metals, for example, it is known that solid gold is an inert metal, while its bare clusters are reactive and require passivation to be stable.

Regarding the electronic properties of the metal clusters, there are stability islands linked to the number of valence electrons corresponding to the so-called magic numbers predicted according to the "Jellium" model. This model assumes a diffuse and homogeneous electron gas and the magic numbers correspond to the fully occupied orbitals: 1S, 1P, 1D, 2S, 2P, ... or they correspond to a number of electrons equal to  $2n^2 = 2, 8, 18, 32, 50, \dots$  (note that in the calculation of the electrons those of the eventual ligands must also be included).

Protected clusters are more easily managed with conventional chemical techniques, for example it is possible to work in solution and it has now become quite easy to obtain crystals suitable for structural characterization by X-ray diffraction [1.1].

The protected clusters therefore consist of a metal core covered by an organic monolayer, bound by relatively strong covalent bonds or through weak physisorption (physical adsorption), depending on the type of interaction between metal and binder.

The ligand layer, in addition to the task of passivating and stabilizing the metal, has significant implications on the cluster properties and in particular on the optical ones.

In particular noble metal as gold and silver are commonly protected by thiolates ligands because they bind the metal very strongly. Aliphatic thiols are generally used due to the versatile modification of the tails. For example they can have precursors of reactive groups or contain elements that modify their solubility. In the specific case of gold, aromatic thiols are often used to enhance the plasmon intensity through conjugation with the  $\pi$  electrons (other groups can also give this effect, for example the  $-\text{NO}_2$  substituents), this phenomenon is known as the "plasmon rebirth". [1.18]

The theoretical description of these systems is necessary to understand their properties, because the normal qualitative tools of chemistry, grounded on the valence bond or on the molecular orbital theories, are often insufficient to describe such chemical bonds. This is essentially because the metal-metal interactions, which are characteristic of such systems, require refined models to be described correctly and realistically. Moreover, these quantum effects are what makes these types of compounds and their properties interesting and appealing indeed.

One of the most interesting optical phenomena typical of metal nanoparticles is the Localized Surface Plasmon Resonance (LSPR), that is the electronic collective excitation which is described as oscillation of the electronic density with the formation of an oscillating induced dipole. The fundamental model able to describe a plasmon is based on classical electrodynamics and is the Discrete Dipole Approximation (DDA) [1.19]

It is worth noting that there are clusters, like the nanorods, which are largely anisotropic, since they grow along a specific direction and this will amplify the plasmon in that direction.

The LSPR is particularly interesting for gold and silver NPs because the absorption occurs in the UV-visible range, making it very useful for several applications and studies, for example for SERS [1.20] and single molecule detection [1.21].

The nature of the LSPR is strictly correlated with the cluster shape and size, for example for Ag and Au NPs a general red-shift and enhancement of the plasmonic peak is observed by increasing the size of the cluster [1.22]. This behavior is mainly due to the free motion of the conduction band electrons of the noble metal, independently from the ionic background. The red shift is also an effect of the spillover of the electrons with respect to the cluster surface.

Recently the interest has also shifted towards nanoalloys due to their peculiar properties [1.23-30]

## 2 THEORY

### 2.1 Density functional theory

The DFT [2.1] is a rigorous quantum mechanical theory that employs the electronic density instead of the wavefunction to describe the system. This aspect and its implementation are the basis of its computational efficiency.

The DFT has been known a very fast growing period in the last decades, since its ability to calculate medium and large systems with optimal compromise between accuracy and computational economy. In particular large metallic clusters can't be properly described by the simplest *ab-initio* method such as HF, due to the difficulty of HF to describe metallic systems. Moreover more accurate *ab-initio* schemes beyond HF are too expensive.

A functional is defined as a linear mapping from a vector space into its field of scalars. Specifically in the case of DFT, it is convenient to use an application that associates wavefunction to the space of electronic densities.

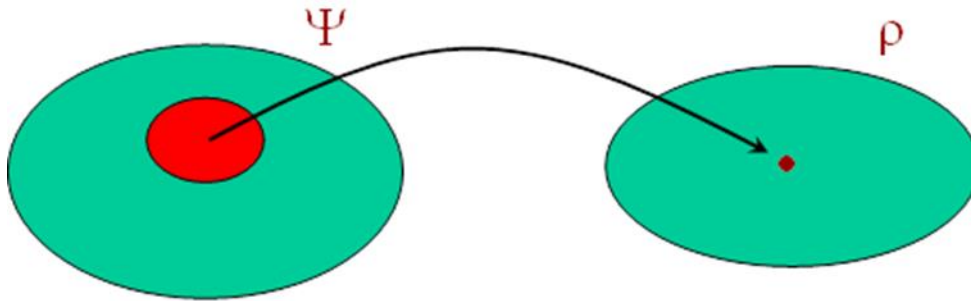


**Figure (2.1.1)** Graphic representation of action an application between  $\Psi$  and  $\rho$

The generic Hamiltonian, in Born-Hoppenheimer approximation regime, for  $N$  interacting electrons in a molecular system is given by the following expression:

$$H = \sum_{i=1}^N \left( -\frac{1}{2} \Delta_i \right) + \sum_{i < j=2}^N \frac{1}{r_{ij}} + \sum_{i=1}^N V_{ext}(\vec{r}_i) = \hat{T} + \hat{V}_{ee} + \hat{V}_{ext} \quad (2.1.1)$$

The first term  $\hat{T}$  is the kinetic energy of the electrons, the second  $\hat{V}_{ee}$  is the exact potential energy between electrons pairs, and the last  $\hat{V}_{ext}$  contains all contribution not considered, or rather, potential due to interactions between nuclei and electrons and other external potentials. However, the potential induced by nuclei is the uppermost and usually the  $\hat{V}_{ext}$  takes the following expression:

$$V_{ext}(\bar{r}_i) = V_{eN} = \sum_{k=1}^{nuclei} \left( -\frac{Z_k}{|\bar{r}_i - \bar{R}_k|} \right) \quad (2.1.2)$$

Now, let's start introducing functional formalism. The first object which includes the first two Hamiltonian terms is  $F[\rho]$ :

$$F[\rho] = \min_{\Psi \rightarrow \rho} \langle \Psi | T + V_{ee} | \Psi \rangle = \langle \Psi_{min} | T + V_{ee} | \Psi_{min} \rangle \quad (2.1.3)$$

This object is written according to the Levy-Lieb formalism and the minimization is done with constrain over the electronic density.

The last term can be written in its classic form:

$$\langle \Psi | V_{ext} | \Psi \rangle = \int \rho(\bar{r}) V_{ext}(\bar{r}) d\bar{r} \quad (2.1.4)$$

It can all be collected in a single functional:

$$E[\rho] = \min_{\Psi \rightarrow \rho} \langle \Psi | T + V_{ee} | \Psi \rangle + \langle \Psi | V_{ext} | \Psi \rangle = F[\rho] + \int \rho(\bar{r}) V_{ext}(\bar{r}) d\bar{r} \quad (2.1.5)$$

Thanks to the variational principle it is possible to prove that the energy associated to any electron density is greater than or equal to that of the ground state:

$$E[\rho] \geq E_{GS} \quad (2.1.6)$$

Is also possible to prove that the energy associated to the electron density of ground state is equal to the energy of ground state:

$$E[\rho_{GS}] = E_{GS} \quad (2.1.7)$$

The coexistence of the previous relations is also a consequence of the theorem of Hohenberg-Kohn, which assures the one-to-one mapping between ground-state density and external potential [2.2].

Lastly there are essentially two methods to address this problem: a direct method for example as in the Thomas-Fermi, that employs the electron density directly as variable, and indirect method, such as Kohn-Sham approach that uses spin-orbitals as variables.

## 2.2 Kohn-Sham approach

The Kohn-Sham approach is an indirect method to solve the DFT equations, which uses a fictitious system of non-interacting electrons ( $V_{ee} = 0$ ) but with the same electronic density of the real one [2.3-4].

To sum up, this approach has only two terms: kinetic energy and a fictitious potential named Kohn-Sham potential ( $V_{KS}$ ).

Therefore, the only variable term is  $V_{KS}$ , which is chosen in order to give the density of the real interacting system.

These assumptions allow to separate this N-electrons Hamiltonian into several mono-electronic Hamiltonians:

$$H_{KS} = \sum_{i=1}^N \left( -\frac{1}{2} \Delta_i \right) + \sum_{i=1}^N V_{KS}(\vec{r}_i) = \sum_{i=1}^N h_{KS}(i) \quad (2.2.1)$$

As a consequence, it is possible to write equations similar to Hartree-Fock ones:

$$h_{KS} \chi_i = \varepsilon_i \chi_i \Rightarrow \left( -\frac{1}{2} \Delta_i + V_{KS} \right) \chi_i = \varepsilon_i \chi_i \quad (2.2.2)$$

These equations can be solved in practice, introducing a basis set, this allows to recast the equations on matrix form similar to the Roothaan equations of Hartree-Fock theory:

$$H_{KS} C = S C E \quad (2.2.3)$$

The spin-orbitals or better the coefficients that determine them, starting from the basis functions, are obtained from the SCF procedure. Such procedure consists of an iterative loop which updates the potential from the orbitals of the last cycle, convergence is obtained when the density variation will go below a specific threshold.

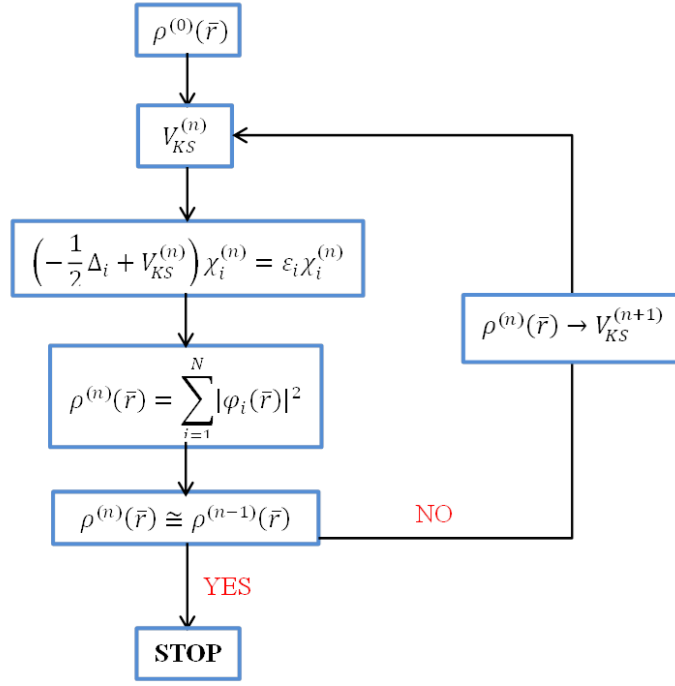


**Figure (2.2.1)** Graphic representation of SCF procedure

Therefore the wavefunction of the non-interacting system is obtained as a single Slater determinant:

$$\Psi_{KS} = \frac{1}{\sqrt{N!}} |\bar{\chi}_1, \bar{\chi}_2, \dots, \bar{\chi}_N\rangle \quad (2.2.4)$$

And the electronic density as from the spatial part:

$$\rho(\bar{r}) = \sum_{i=1}^N \varphi_i^*(\bar{r}) \varphi_i(\bar{r}) = \sum_{i=1}^N |\varphi_i(\bar{r})|^2 \quad (2.2.5)$$

At this point it is possible to write the kinetic energy functional expression in terms of Kohn-Sham orbitals of the non-interacting system:

$$T_0[\rho] = \sum_{i=1}^N \langle \chi_i | -\frac{1}{2} \Delta_i | \chi_i \rangle \quad (2.2.6)$$

$$E_0[\rho] = T_0[\rho] + \int V_{KS}(\vec{r})\rho(\vec{r})d\vec{r} \quad (2.2.7)$$

So the non-interacting kinetic energy written as  $T_0[\rho]$  can be calculated exactly from the KS orbitals, it is worth noting that the only property that the interacting and non-interacting systems share is the density, all the other ones differ, therefore a 0 subscript is conventionally adopted to designate a property relative to the non-interacting system.

At this point the  $V_{KS}$  must be found, for this purpose the equations of interacting and non-interacting system are compared:

$$E_0[\rho] = T_0[\rho] + \int V_{KS}(\vec{r})\rho(\vec{r})d\vec{r} \quad \text{non-interacting} \quad (2.2.8)$$

$$E[\rho] = T[\rho] + V_{ee}[\rho] + \int V_{ext}(\vec{r})\rho(\vec{r})d\vec{r} \quad \text{interacting} \quad (2.2.9)$$

And it is required they have the same density.

In order to simplify this comparison it is possible to rewrite the terms as follows:

$$V_{ee}[\rho] + T[\rho] = T_0[\rho] + J[\rho] + E_{XC}[\rho] \quad (2.2.10)$$

With this choice the  $E_{XC}[\rho]$  is defined as follow:

$$E_{XC}[\rho] = T[\rho] - T_0[\rho] + V_{ee}[\rho] - J[\rho] \quad (2.2.11)$$

This object remains without an explicit expression but can be appropriately modeled depending on the properties of the system to be studied. Useful expressions can be obtained for instance from the uniform and non-uniform electron-gas models.

In this expression two new object are declared: the classical electrostatic interaction ( $J[\rho]$ ) and the exchange-correlation energy ( $E_{XC}[\rho]$ ).

The  $J[\rho]$  is a well defined object and can be calculated exactly, its expression is:

$$J[\rho] = \frac{1}{2} \iint \frac{\rho(\vec{r})\rho(\vec{r}')}{|\vec{r} - \vec{r}'|} d\vec{r}d\vec{r}' \quad (2.2.12)$$

Where it is possible to recognize the classical electrostatic potential:

$$V_{classic}(\vec{r}) = \int \frac{\rho(\vec{r}')}{|\vec{r} - \vec{r}'|} d\vec{r}' \quad (2.2.13)$$

On the other hand, the  $E_{XC}[\rho]$  is unknown but approximate expressions can be derived from models, as already observed.

There are essentially three great families of functionals. Local Density Approximation (LDA) from uniform electron gas, that is used mainly to describe the electronic structure and for geometry optimizations [2.5]. The General Gradient Approximation (GGA) [2.6] from non-uniform electron gas, that is more suitable to describe energies of various processes with better accuracy. Finally hybrid functionals, which include also a part of the non-local HF exchange potential, which makes them computationally more demanding but usually much more accurate. The most popular and widely employed hybrid functional is B3LYP [2.7-9], in general leads to good results for both geometries and energies.

More recently, more elaborate functionals have been suggested as meta- and hyper-GGA [2.10] and double hybrids [2.11]

Finally, accordingly to the variational theorem on the density, we must minimize the  $E[\rho]$  functional in presence of a constraint, namely the total number of electrons as tridimensional integral of electron density over all space:

$$N = \int \rho(\vec{r}) d\vec{r} \quad (2.2.14)$$

This constraint is introduced by the Lagrangian multipliers, whose general form is:

$$\mathcal{L}(x_1, x_2, \dots, x_n, \lambda_1, \lambda_2, \dots, \lambda_m) = f(x_1, x_2, \dots, x_n) + \sum_{k=1}^m \lambda_k g_k(x_1, x_2, \dots, x_n) \quad (2.2.15)$$

Where  $\mathcal{L}$  is the Lagrangian function that contains the original function  $f$  and  $m$  constraints  $g_k$ , these constraints must be written in the form  $g_k = 0$ , while the  $\lambda_k$  correspond to the Lagrangian multipliers.

The condition to find the stationary points is that the gradient of the Lagrangian is equal to null vector ( $0 \in R^{n+m}$ ):

$$\nabla_{x_1, x_2, \dots, x_n, \lambda_1, \lambda_2, \dots, \lambda_m} \mathcal{L}(x_1, x_2, \dots, x_n, \lambda_1, \lambda_2, \dots, \lambda_m) = (0, 0, \dots, 0, 0, 0, \dots, 0) \quad (2.2.16)$$

$$\begin{aligned} \left( \frac{\partial \mathcal{L}}{\partial x_1}, \frac{\partial \mathcal{L}}{\partial x_2}, \dots, \frac{\partial \mathcal{L}}{\partial x_n}, \frac{\partial \mathcal{L}}{\partial \lambda_1}, \frac{\partial \mathcal{L}}{\partial \lambda_2}, \dots, \frac{\partial \mathcal{L}}{\partial \lambda_m} \right) &= \left( \frac{\partial \mathcal{L}}{\partial x_1}, \frac{\partial \mathcal{L}}{\partial x_2}, \dots, \frac{\partial \mathcal{L}}{\partial x_n}, g_1, g_2, \dots, g_m \right) \\ &= (0, 0, \dots, 0, 0, 0, \dots, 0) \end{aligned} \quad (2.2.17)$$

This is equivalent to solve the following system:

$$\begin{cases} \frac{\partial \mathcal{L}}{\partial x_i} = 0 & \forall i = 1, \dots, n \\ g_k = 0 & \forall k = 1, \dots, m \end{cases} \quad (2.2.18)$$

In our case we have only one constrain over the number of electron that must be written in the form:

$$\int_{-\infty}^{+\infty} \rho(\vec{r}) d\vec{r} - N = 0 \quad (2.2.19)$$

It follows that the Lagrangian function will be:

$$\mathcal{L}[\rho] = E[\rho] - \lambda \left( \int \rho(\vec{r}) d\vec{r} - N \right) \quad (2.2.20)$$

The condition to find the minimum (as particular stationary point) is to impose the functional derivative equal to zero:

$$\frac{\delta \mathcal{L}[\rho]}{\delta \rho} = \frac{\delta}{\delta \rho} \left[ E[\rho] - \lambda \left( \int \rho(\vec{r}) d\vec{r} - N \right) \right] = \frac{\delta E[\rho]}{\delta \rho} - \lambda = 0 \quad (2.2.21)$$

At this point, the  $V_{KS}$  is found by comparing the interacting and non-interacting cases:

$$\begin{cases} \frac{\delta \mathcal{L}[\rho]}{\delta \rho} = \frac{\delta E[\rho]}{\delta \rho} - \lambda = \frac{\delta T_0}{\delta \rho} + \frac{\delta J}{\delta \rho} + \frac{\delta E_{XC}}{\delta \rho} + V_{ext}(\vec{r}) - \lambda = 0 & \text{interacting} \\ \frac{\delta \mathcal{L}_0[\rho]}{\delta \rho} = \frac{\delta E_0[\rho]}{\delta \rho} - \lambda = \frac{\delta T_0}{\delta \rho} + V_{KS}(\vec{r}) - \lambda = 0 & \text{non-interacting} \end{cases} \quad (2.2.22)$$

So it follows that the expression for the  $V_{KS}$  will be:

$$V_{KS}(\bar{r}) = \frac{\delta J}{\delta \rho} + \frac{\delta E_{XC}}{\delta \rho} + V_{ext}(\bar{r}) = \int \frac{\rho(\bar{r}')}{|\bar{r} - \bar{r}'|} d\bar{r}' + V_{XC} + V_{ext} \quad (2.2.23)$$

Finally it is possible to write the complete expression of the KS Hamiltonian:

$$\begin{aligned} H_{KS} &= \sum_{i=1}^N \left( -\frac{1}{2} \Delta_i \right) + \sum_{i=1}^N V_{KS}(\bar{r}_i) \\ &= \sum_{i=1}^N \left( -\frac{1}{2} \Delta_i \right) + \sum_{i=1}^N \int \frac{\rho(\bar{r}')}{|\bar{r}_i - \bar{r}'|} d\bar{r}' + \sum_{i=1}^N V_{XC}[\rho(\bar{r}_i)] + \sum_{i=1}^N V_{ext}(\bar{r}_i) \end{aligned} \quad (2.2.24)$$

## 2.3 Exchange-correlation functionals

As already seen in the chapter on the KS approach, the only unknown term in the KS equations is the  $V_{xc}$ .

Therefore this object must be approximated through a model, this operation is not trivial because a universal functional is not available. Moreover, there is still a large number of functionals that are designed for specific purposes.

When we are interested in time-independent properties (or when time dependency is small) we can define a new object named exchange-correlation hole as follows, following Parr-Yang [2.1]:

$$\rho_2(\bar{r}_1, \bar{r}_2) = \frac{1}{2} \rho(\bar{r}_1) \rho(\bar{r}_2) [1 + h_{xc}(\bar{r}_1, \bar{r}_2)] \quad (2.3.1)$$

$$\rho_{xc}(\bar{r}_1, \bar{r}_2) = \rho(\bar{r}_2) h_{xc}(\bar{r}_1, \bar{r}_2) \quad (2.3.2)$$

$$\rho_{xc}(\bar{r}_1, \bar{r}_2) = \frac{2\rho_2(\bar{r}_1, \bar{r}_2)}{\rho(\bar{r}_1)} - \rho(\bar{r}_2) \quad (2.3.3)$$

Where  $h_{xc}(\bar{r}_1, \bar{r}_2)$  is the pair correlation function,  $\rho_{xc}(\bar{r}_1, \bar{r}_2)$  is the exchange-correlation hole and  $\rho_2(\bar{r}_1, \bar{r}_2)$  is the pair density:

$$\rho_2(\bar{r}_1, \bar{r}_2) = \frac{N(N-1)}{2} \int |\Psi(\bar{r}_1, \bar{r}_2, \dots, \bar{r}_N)|^2 d\bar{r}_3 d\bar{r}_4 \dots d\bar{r}_N \quad (2.3.4)$$

$\rho_{xc}(\bar{r}_1, \bar{r}_2)$  represents the difference between the conditioned and unconditioned probability, then in term of correlation function it is possible write:

$$\rho_{xc}(\bar{r}_1, \bar{r}_2) = g(\bar{r}_1, \bar{r}_2) - \rho(\bar{r}_2) \quad (2.3.5)$$

In a system of  $N$  electrons we can imagine  $\rho_2(r_1, r_2)$  as the probability of finding the two electrons in the respective two volume elements neglecting (integrating) over the other  $N-2$  coordinates.

The name and the meaning of  $\rho_{xc}$  is related to its integrals:

$$\int \rho_{xc}(\bar{r}_1, \bar{r}_2) d\bar{r}_2 = \int g(\bar{r}_1, \bar{r}_2) d\bar{r}_2 - \int \rho(\bar{r}_2) d\bar{r}_2 = (N-1) - N = -1 \quad (2.3.6)$$

So it corresponds exactly to the charge of one electron.

In general we can assume that the better one functional approximates the  $\rho_{xc}$  the better is the accuracy.

Now it is possible to rewrite the electron-electron potential inserting the  $h_{xc}$ :

$$\langle V_{ee} \rangle = \frac{1}{2} \left[ \int \frac{\rho(\bar{r}_1)\rho(\bar{r}_2)}{r_{12}} dr_1 dr_2 + \int \frac{\rho(\bar{r}_1)h_{xc}(\bar{r}_1, \bar{r}_2)}{r_{12}} dr_1 dr_2 \right] = J[\rho] + E_{xc}[\rho] \quad (2.3.7)$$

Finally based on spin we can split the  $h_{xc}$  in two part:

$$h_{xc}(\bar{r}_1, \bar{r}_2) = h_x^{s_1=s_2}(\bar{r}_1, \bar{r}_2) + h_c^{s_1, s_2}(\bar{r}_1, \bar{r}_2) \quad (2.3.8)$$

Where the exchange term acts only over electrons that have the same spin instead the correlation term doesn't has spin restriction.

When models are introduced, with the aim to derive explicit expressions for  $E_{xc}$ , it is possible to define a quantity which is the exchange-correlation energy density, which can be further split in the separate exchange and correlation contributions:

$$\varepsilon_{xc} = \varepsilon_x + \varepsilon_c \quad (2.3.9)$$

The oldest and simplest exchange-correlation functional group is the Local Density Approximation (LDA).

The LDA assumes that the electrons are modeled as a uniform gas model, therefore partitioning the space in small volume elements in which the density is considered to be constant.

Then the total  $E_{xc}[\rho]$  is obtained from the integral of the XC energy density  $\varepsilon_{xc}$  at a given density:

$$E_{xc}^{LDA}[\rho(r)] = \int \varepsilon_{xc}^{LDA}[\rho(r)] \rho(r) dr \quad (2.3.10)$$

In this approach both  $\varepsilon_x^{LDA}$  and  $\varepsilon_c^{LDA}$  can be evaluated analytically, in particular the expression of  $\varepsilon_x^{LDA}$  is:

$$\varepsilon_x^{LDA}[\rho(r)] = -\frac{3}{4} \left(\frac{3}{\pi}\right)^{\frac{1}{3}} \int \rho(r)^{\frac{4}{3}} dr \quad (2.3.11)$$

While the expression of  $\varepsilon_c^{LDA}$  is more complex and can be evaluated by a fitting procedure of a set of discrete  $\varepsilon_c^{LDA}$  values calculated by Quantum Monte Carlo approach [2.12].

As already mentioned this method is very simple, however it works surprisingly well in many cases, in particular for geometry and electronic structure and correlated properties such as lattice constants of solids, dipole moments, vibrational frequencies and Fermi surfaces of bulk materials.

The LDA overestimate polarizabilities and underestimate electron affinities and IPs, moreover, KS eigenvalues result to be too low in magnitude, due to the fact that the xc potential does not go to zero correctly as  $-\frac{1}{r}$  at large distances, but exponentially fast.

In particular in this thesis it was used the VWN functional for the geometry optimization.

To overcome the problems of LDA the Generalized Gradient Approximation (GGA) was introduced, that is defined as semi-local approximation because it include the gradient of the density to account the non-homogeneity of the real density.

The GGA use a non-local correction for the exchange energy, this dependency on the gradient of the density has the general form:

$$\varepsilon_x^{GGA}[\rho, \nabla\rho] = -\frac{3}{4} \left(\frac{3}{\pi}\right)^{\frac{1}{3}} \int f(s) \rho(\vec{r})^{\frac{4}{3}} d\vec{r} \quad (2.3.12)$$

Where  $f(s)$  is a function of parameter  $s$ :

$$s = \frac{|\nabla\rho|}{2(3\pi^2)^{\frac{1}{3}}\rho^{\frac{4}{3}}} = \frac{|\nabla\rho|}{2k_F\rho} \quad (2.3.13)$$

Where  $k_F$  is the Fermi wavevector and the function  $f(s)$  must satisfy  $f(0) = 1$  because in homogeneous density case ( $\nabla\rho = 0$ ) the  $\varepsilon_x^{GGA}$  must be equal to  $\varepsilon_x^{LDA}$ .

Typically the GGA functionals do not support the correct asymptotic coulomb decay behavior.

LB94 [2.13], instead, is a model XC potential which supports the asymptotic behavior, such potential has been used in this thesis together BP86 [2.7] and PBE [2.14] for valence photoabsorption and dichroism spectra simulations.

Other popular refinements of GGA are meta-GGA which use higher order derivatives.

Finally other two similar classes can be mentioned, hyper-GGA and generalized random phase approximation, that respectively include the exact exchange energy density and the unoccupied orbitals contributions.

In general the GGA functionals are more accurate for those properties that depend on energies.

The last but very important type of functionals are the hybrid functionals that use a portion of exact non-local Hartree-Fock exchange.

A large number of hybrid functional are available in literature but one of the most used is the B3LYP, which is an example of semi-empirical functional and its expression is:

$$E_{xc}^{B3LYP} = E_x^{LDA} + a_0(E_x^{HF} - E_x^{LDA}) + a_x E_x^{B88} + a_c E_c^{LYP} + (1 - a_c) E_c^{VWN} \quad (2.3.14)$$

Where  $a_0$ ,  $a_x$ ,  $a_c$  are the three parameters which define the potentials, and are approximately equal to 0,2, 0,8, 0,7, respectively.

These types of functionals are very versatile and generally accurate but they may require a larger computational effort due to the HF non-local exchange.

This may become an hard problem for TDDFT calculations, where non-local exchange kernel are extremely computationally demanding, especially when STO basis functions are employed.

In the present thesis it was proposed a new approach named Hybrid Diagonal Approximation (HDA) which employs a simple assumption to reduce drastically the number of HF exchange integrals to calculate without losing accuracy and consequently enormous reduction of computation time.

The HDA is a general approximation for hybrid functionals but in this thesis has been extensively used in combination of B3LYP.

## 2.4 Linear response theory

Both Casida [2.15] and pol-TDDFT [2.16-19] algorithms are specific implementations of the more general Linear Response Theory (LRT) [2.19-20] which hereafter is shortly reviewed.

Starting with the expression of the time-dependent coefficients of final states, they change over time due to a small perturbation:

$$c_n(t) = -i \int_{-\infty}^t \langle \Phi_n^{(0)} | V(t) | \Phi_0^{(0)} \rangle e^{i\omega_{0n}\tau} d\tau \quad (2.4.1)$$

Where, in previous expression,  $\Phi_0^{(0)}$  is the initial state (the ground state),  $\Phi_n^{(0)}$  is the n-th excited state, and  $\omega_{0n} = E_n - E_0$  corresponds to their energy difference. The perturbative potential can be written as follows:

$$V(\vec{r}, t) = A(\vec{r})F(t) \quad (2.4.2)$$

In this expression the potential is separated in a spatial and time-independent part  $A(\vec{r})$  and in a time-dependent one  $F(t)$ .

The  $A(\vec{r})$  represents the spatial shape of perturbation while the  $F(t)$  represents the time-dependent behavior.

Therefore the previous expression for the coefficient of the final states will read:

$$c_n(t) = -i \langle n|A(\bar{r})|0\rangle \int_{-\infty}^t F(\tau) e^{i\omega_{0n}\tau} d\tau \quad (2.4.3)$$

At this point, take a specific time-dependent property of the system indicating with  $B(t)$ , then we measure the difference between the expectation values of the perturbed function and the initial one:

$$\delta\langle B\rangle = \langle B\rangle - \langle B\rangle_0 = \langle \Psi|B|\Psi\rangle - \langle \Psi^{(0)}|B|\Psi^{(0)}\rangle \quad (2.4.4)$$

From the perturbation theory at the first order and neglecting the second order perturbative terms we can write the perturbation of  $B$  as:

$$\delta\langle B\rangle = \langle \Psi^{(0)}|B|\lambda\Psi^{(1)}\rangle + \langle \lambda\Psi^{(1)}|B|\Psi^{(0)}\rangle \quad (2.4.5)$$

Replacing the perturbed eigenfunction with its own expression in term of unperturbed eigenfunctions the result is:

$$\delta\langle B\rangle = \sum_n c_n(t) \langle 0|B|n\rangle e^{i\omega_{0n}t} + \sum_n c_n^*(t) \langle n|B|0\rangle e^{-i\omega_{0n}t} \quad (2.4.6)$$

And inserting the explicit expression of the coefficients we will get:

$$\begin{aligned} \delta\langle B\rangle = & -i \sum_n \langle 0|B|n\rangle e^{-i\omega_{0n}t} \langle n|A|0\rangle \int_{-\infty}^t F(\tau) e^{i\omega_{0n}\tau} d\tau \\ & + i \sum_n \langle n|B|0\rangle e^{i\omega_{0n}t} \langle 0|A|n\rangle \int_{-\infty}^t F(\tau) e^{-i\omega_{0n}\tau} d\tau \end{aligned} \quad (2.4.7)$$

And grouping term by term:

$$\delta\langle B \rangle = i \int_{-\infty}^t \sum_n [\langle n|B|0 \rangle \langle 0|A|n \rangle e^{i\omega_{0n}(t-\tau)} - \langle 0|B|n \rangle \langle n|A|0 \rangle e^{-i\omega_{0n}(t-\tau)}] F(\tau) d\tau \quad (2.4.8)$$

It is convenient to define the linear response function as:

$$R(AB|t-\tau) = i \sum_n [\langle n|B|0 \rangle \langle 0|A|n \rangle e^{i\omega_{0n}(t-\tau)} - \langle 0|B|n \rangle \langle n|A|0 \rangle e^{-i\omega_{0n}(t-\tau)}] \quad (2.4.9)$$

Then it is possible to write in compact form:

$$\delta\langle B(t) \rangle = \int_{-\infty}^t R(AB|t-\tau) F(\tau) d\tau \quad (2.4.10)$$

The linear response function is the variation of  $\langle B \rangle$  at time  $t$  caused by the perturbation  $A$  at time  $\tau$ , notice that this function is defined only for  $(t-\tau) > 0$ , consistently with the principle of causality. Furthermore, this function depends only on the distance of  $t$  and  $\tau$  and not on the two specific values. This dependency is included in  $F(\tau)$ .

It is possible to calculate the effect of the perturbation acting on the observable  $B$ , but it is more practical to work in frequency domain by Fourier transform.

As already mentioned, the dependence on specific times is included in  $F(\tau)$ . Then it is necessary to ensure that the perturbation acts on an unperturbed state, for this purpose an adiabatic switch term  $e^{\varepsilon t}$  is added so that:

$$\lim_{t \rightarrow -\infty} e^{\varepsilon t} = 0 \quad (2.4.11)$$

In this way the perturbation is introduced gradually and it will assume values around unity  $e^{\varepsilon t} \cong 1$  for the times of interest.

The Fourier transform of  $F(t)$  will be:

$$F(t) = e^{\varepsilon t} \frac{1}{2\pi} \int_{-\infty}^{+\infty} f(\omega) e^{-i\omega t} d\omega = \frac{1}{2\pi} \int_{-\infty}^{+\infty} f(\omega) e^{-i(\omega+i\varepsilon)t} d\omega \quad (2.4.12)$$

Therefore, by substitution we will obtain the following expression:

$$\delta\langle B(t)\rangle = \frac{i}{2\pi} \int_{-\infty}^t \int_{-\infty}^{+\infty} f(\omega) e^{-i(\omega+i\varepsilon)\tau} \sum_n [B_{n0}A_{0n}e^{i\omega_{0n}(t-\tau)} - B_{0n}A_{n0}e^{-i\omega_{0n}(t-\tau)}] d\tau d\omega \quad (2.4.12)$$

It is possible to integrate over the  $\tau$  variable in order to have only the frequency dependence:

$$\left\{ \begin{array}{l} \int_{-\infty}^t e^{-i(\omega+i\varepsilon+\omega_{0n})\tau} e^{i\omega_{0n}t} d\tau = e^{i\omega_{0n}t} \frac{e^{-i(\omega+i\varepsilon+\omega_{0n})\tau}}{-i(\omega+i\varepsilon+\omega_{0n})} \Big|_{-\infty}^t = -\frac{e^{-i(\omega+i\varepsilon)t}}{i(\omega+i\varepsilon+\omega_{0n})} \\ \int_{-\infty}^t e^{-i(\omega+i\varepsilon-\omega_{0n})\tau} e^{-i\omega_{0n}t} d\tau = e^{-i\omega_{0n}t} \frac{e^{-i(\omega+i\varepsilon-\omega_{0n})\tau}}{-i(\omega+i\varepsilon-\omega_{0n})} \Big|_{-\infty}^t = -\frac{e^{-i(\omega+i\varepsilon)t}}{i(\omega+i\varepsilon-\omega_{0n})} \end{array} \right. \quad (2.4.13)$$

In the end, we obtain by substitution:

$$\delta\langle B(t)\rangle = \frac{1}{2\pi} \int_{-\infty}^{+\infty} f(\omega) e^{-i(\omega+i\varepsilon)t} \sum_n \left[ \frac{B_{0n}A_{n0}}{\omega+i\varepsilon-\omega_{0n}} - \frac{B_{n0}A_{0n}}{\omega+i\varepsilon+\omega_{0n}} \right] d\omega \quad (2.4.14)$$

The object in the summation is defined as general frequency-dependent (dynamic) polarizability which is indicated as follows:

$$\prod(BA|\omega) = \sum_n \left[ \frac{B_{0n}A_{n0}}{\omega+i\varepsilon-\omega_{0n}} - \frac{B_{n0}A_{0n}}{\omega+i\varepsilon+\omega_{0n}} \right] \quad (2.4.15)$$

This represents the variation of  $B$  induced by  $A$  at frequency  $\omega$ , then we can write the previous integral in compact form:

$$\delta\langle B(t)\rangle = \frac{1}{2\pi} \int_{-\infty}^{+\infty} f(\omega) e^{-i(\omega+i\varepsilon)t} \prod(BA|\omega) d\omega \quad (2.4.16)$$

If the spectral dependency  $f(\omega)$  relative to the perturbation  $A$  is known, we can predict the  $\langle B \rangle$  value at any time.

The polarizability contains two singularities of the first order in the complex plane (simple poles) for  $\omega = -i\varepsilon - \omega_{0n}$  and  $\omega = \omega_{0n} - i\varepsilon$  (the possibility to have null numerator requires a more refined analysis).

Moreover, it is a very interesting case when the perturbation is in resonance with the transition, that is when  $\omega = \omega_{n0}$ :

$$\lim_{\varepsilon \rightarrow 0^+} \prod (BA|\omega_{0n}) \cong \frac{B_{0n}A_{n0}}{i\varepsilon} \quad (2.4.17)$$

This result is extremely useful and is the foundation of the new method pol-TDDFT particularly if we take into account the electric dipoles induced (observable) by the oscillating electric field of the electromagnetic radiation (perturbation). After all we will have an expression linked to the photoabsorption:

$$Im \left[ \lim_{\varepsilon \rightarrow 0^+} \prod (\mu\mu|\omega_{0n}) \right] \cong -\frac{|\langle n|\mu|0 \rangle|^2}{\varepsilon} \quad (2.4.18)$$

Note that we work with an imaginary object and it is proportional to the transition moment and then to the oscillator strength.

Let's make a practical example: we take a monochromatic radiation of frequency  $\omega_0$  from which we can write the perturbative potential as:

$$V(\vec{r}, t) = A(\vec{r})F(t) = A(\vec{r}) \cos(\omega_0 t) \quad (2.4.19)$$

Remembering that the Fourier transform (FT) of cosine function is:

$$\cos(\omega_0 t) \xrightarrow{FT} \pi[\delta(\omega - \omega_0) + \delta(\omega + \omega_0)] \quad (2.4.20)$$

The variation of the expectation value of  $B$  will be:

$$\begin{aligned} \delta\langle B(t) \rangle &= \frac{1}{2\pi} \int_{-\infty}^{+\infty} \pi[\delta(\omega - \omega_0) + \delta(\omega + \omega_0)] e^{-i(\omega+i\varepsilon)t} \prod (BA|\omega) d\omega \\ &= \frac{1}{2} \left[ e^{i(\omega_0-i\varepsilon)t} \prod (BA|-\omega_0) + e^{-i(\omega_0+i\varepsilon)t} \prod (BA|\omega_0) \right] \end{aligned} \quad (2.4.21)$$

## 2.5 Random phase approximation and TDDFT

The rigorous foundation of TDDFT is provided by the Runge-Gross theorem which is an extension of the Hohenberg-Kohn theorem to the case of time-dependent external potential [2.21]. Therefore it ensures that also in this case the density is unique (at any time) when the expression of external potential is known (applies vice versa, the connection is injective). Finally, the van Leeuwen theorem ensures that the density found is correct.

In this thesis a new method to solve the TDDFT equations is proposed, for this reason is useful to show the connection between TDDFT and linear response theory.

Let's start from the first order perturbation theory, the first order perturbation can be written as:

$$H^{(1)}(\vec{r}, t) = A_{\omega} e^{-i\omega t} + A_{-\omega} e^{i\omega t} \quad (2.5.1)$$

So the time dependent Schrödinger equation will be:

$$\begin{aligned} & [H^{(0)} + \lambda(A_{\omega} e^{-i\omega t} + A_{-\omega} e^{i\omega t})][\Psi_0^{(0)} e^{-iE_0 t} \\ & \quad + \lambda(\Psi_0^{(1,-)} e^{-i(E_0+\omega)t} + \Psi_0^{(1,+)} e^{-i(E_0-\omega)t})] \\ & = i \frac{\partial}{\partial t} [\Psi_0^{(0)} e^{-iE_0 t} + \lambda(\Psi_0^{(1,-)} e^{-i(E_0+\omega)t} + \Psi_0^{(1,+)} e^{-i(E_0-\omega)t})] \end{aligned} \quad (2.5.2)$$

Where it is assumed that the perturbed wavefunction has only two components in time,  $e^{-i(E_0+\omega)t}$  is associated with  $\Psi_0^{(1,-)}$  and  $e^{-i(E_0-\omega)t}$  with  $\Psi_0^{(1,+)}$ .

The first order terms can be grouped according to their time behaviors:

$$\begin{aligned} & e^{-i(E_0+\omega)t} [H^{(0)} \Psi_0^{(1,-)} + A_{\omega} \Psi_0^{(0)} - (E_0 + \omega) \Psi_0^{(1,-)}] \\ & \quad + e^{-i(E_0-\omega)t} [H^{(0)} \Psi_0^{(1,+)} + A_{-\omega} \Psi_0^{(0)} - (E_0 - \omega) \Psi_0^{(1,+)}] = 0 \end{aligned} \quad (2.5.3)$$

Such expression is null and it is a linear combination of two time dependent linear independent functions, therefore their coefficients must be zero. The coefficients correspond to the square brackets.

Now we proceed with the implementation of this theory taking our unperturbed Hamiltonian as the Fock operator and our wavefunction relative to the ground state as the occupied orbitals.

The perturbation of wavefunction must preserve the orthonormality condition over the occupied orbitals:

$$\langle \delta\varphi_i | \varphi_j \rangle + \langle \varphi_i | \delta\varphi_j \rangle = 0 \quad (2.5.4)$$

Each term is equal to zero. This means that the perturbed function is orthogonal to all the occupied orbitals and therefore it must be a linear combination of virtual orbitals:

$$\delta\varphi_i = \sum_b^{virt} c_{ib} |\varphi_b\rangle \quad (2.5.5)$$

Now it is possible to substitute the two perturbed wavefunctions with properly linear combination of virtual orbitals:

$$\varphi_i^{(1,-)} = \sum_b^{virt} X_{ib} \varphi_b \quad (2.5.6)$$

$$\varphi_i^{(1,+)} = \sum_b^{virt} Y_{ib}^* \varphi_b \quad (2.5.7)$$

As a consequence, the expressions of the two first order terms will be:

$$\sum_b^{virt} X_{ib} F |\varphi_b\rangle + A_{\omega} |\varphi_i\rangle - (\varepsilon_i + \omega) \sum_b^{virt} X_{ib} |\varphi_b\rangle = 0 \quad (2.5.8)$$

$$\sum_b^{virt} Y_{ib}^* F |\varphi_b\rangle + A_{-\omega} |\varphi_i\rangle - (\varepsilon_i - \omega) \sum_b^{virt} Y_{ib}^* |\varphi_b\rangle = 0 \quad (2.5.9)$$

Then we can close the brackets with scalar product of another virtual orbital (bra):

$$\sum_b^{virt} \langle \varphi_a | F | \varphi_b \rangle X_{ib} + \langle \varphi_a | A_\omega | \varphi_i \rangle - (\varepsilon_i + \omega) \sum_b^{virt} X_{ib} \langle \varphi_a | \varphi_b \rangle = 0 \quad (2.5.10)$$

$$\sum_b^{virt} \langle \varphi_a | F | \varphi_b \rangle Y_{ib}^* + \langle \varphi_a | A_{-\omega} | \varphi_i \rangle - (\varepsilon_i - \omega) \sum_b^{virt} Y_{ib}^* \langle \varphi_a | \varphi_b \rangle = 0 \quad (2.5.11)$$

Remembering that  $\langle \varphi_a | F | \varphi_b \rangle = \varepsilon_b \delta_{ab}$  and that the virtual orbitals are orthonormal, we can collapse the two sums of both equations in only one term:

$$(\varepsilon_a - \varepsilon_i - \omega) X_{ia} + \langle \varphi_a | A_\omega | \varphi_i \rangle = 0 \quad (2.5.12)$$

$$(\varepsilon_a - \varepsilon_i + \omega) Y_{ib}^* + \langle \varphi_a | A_{-\omega} | \varphi_i \rangle = 0 \quad (2.5.13)$$

To be consistent with the literature, we consider the complex conjugate of the second equation and so our expressions will be:

$$(\varepsilon_a - \varepsilon_i - \omega) X_{ia} + \langle \varphi_a | A_\omega | \varphi_i \rangle = 0 \quad (2.5.14)$$

$$(\varepsilon_a - \varepsilon_i + \omega) Y_{ib} + \langle \varphi_i | A_\omega | \varphi_a \rangle = 0 \quad (2.5.15)$$

However, the perturbation modifies the orbitals and then also the Fock operator. As a consequence, we must evaluate this variation in order to calculate the term  $\langle \varphi_a | A_\omega | \varphi_i \rangle$  and to do this we use the first order perturbed Fock operator  $F^{(1)}$  defined as:

$$F^{(1)} = \sum_j^{occ} \langle \delta \varphi_j | | \varphi_j \rangle + \langle \varphi_j | | \delta \varphi_j \rangle \quad (2.5.16)$$

Therefore, the matrix elements are:

$$\langle \varphi_a | F^{(1)} | \varphi_i \rangle = \sum_j^{occ} \langle \varphi_a \delta \varphi_j | | \varphi_i \varphi_j \rangle + \langle \varphi_a \varphi_j | | \varphi_i \delta \varphi_j \rangle \quad (2.5.17)$$

We can substitute the expression of perturbed  $\varphi_j$  with the corresponding linear combination of virtual orbitals:

$$\begin{aligned} \langle \varphi_a | F^{(1)} | \varphi_i \rangle &= \sum_j^{occ} \sum_b^{virt} e^{-i\omega t} (Y_{jb} \langle \varphi_a \varphi_b | | \varphi_i \varphi_j \rangle + X_{jb} \langle \varphi_a \varphi_j | | \varphi_i \varphi_b \rangle) \\ &+ \sum_j^{occ} \sum_b^{virt} e^{i\omega t} (X_{jb}^* \langle \varphi_a \varphi_b | | \varphi_i \varphi_j \rangle + Y_{jb}^* \langle \varphi_a \varphi_j | | \varphi_i \varphi_b \rangle) \end{aligned} \quad (2.5.18)$$

From this expression derives that:

$$\langle \varphi_a | A_\omega | \varphi_i \rangle = \langle \varphi_a | z | \varphi_i \rangle + \sum_j^{occ} \sum_b^{virt} X_{jb} \langle \varphi_a \varphi_j | | \varphi_i \varphi_b \rangle + Y_{jb} \langle \varphi_a \varphi_b | | \varphi_i \varphi_j \rangle \quad (2.5.19)$$

Now the  $X$  and  $Y$  coefficients are unknown and  $z$  is the electric dipole operator.

However, we have all terms of both coupled equations which can be rewritten as follows:

$$(\varepsilon_a - \varepsilon_i - \omega) X_{ia} + \sum_j^{occ} \sum_b^{virt} X_{jb} \langle \varphi_a \varphi_j | | \varphi_i \varphi_b \rangle + Y_{jb} \langle \varphi_a \varphi_b | | \varphi_i \varphi_j \rangle = -\langle \varphi_a | z | \varphi_i \rangle \quad (2.5.20)$$

$$(\varepsilon_a - \varepsilon_i + \omega) Y_{ia} + \sum_j^{occ} \sum_b^{virt} Y_{jb} \langle \varphi_i \varphi_b | | \varphi_a \varphi_j \rangle + X_{jb} \langle \varphi_i \varphi_j | | \varphi_a \varphi_b \rangle = -\langle \varphi_i | z | \varphi_a \rangle \quad (2.5.21)$$

Or in matrix form:

$$\begin{pmatrix} A & B \\ B^* & A^* \end{pmatrix} \begin{pmatrix} X \\ Y \end{pmatrix} - \omega \begin{pmatrix} 1 & 0 \\ 0 & -1 \end{pmatrix} \begin{pmatrix} X \\ Y \end{pmatrix} = \begin{pmatrix} -V \\ -V^* \end{pmatrix} \quad (2.5.22)$$

Where the two submatrices (the other two are simply the complex conjugate ones) have the following matrix elements:

$$A_{ia,jb} = \delta_{ij}\delta_{ab}(\varepsilon_a - \varepsilon_i) + \langle \varphi_a \varphi_j \| \varphi_i \varphi_b \rangle \quad (2.5.23)$$

$$B_{ia,jb} = \langle \varphi_a \varphi_b \| \varphi_i \varphi_j \rangle \quad (2.5.24)$$

By solving this matrix problem it is possible to obtain the coefficient  $X$  and  $Y$  for a given  $\omega$ . In particular when the frequency is in resonance with the transition we formally have the values that goes to infinite.

Now it is possible to observe that this object is connected with polarizability. First we consider the variation of the electric dipole as our observable:

$$\delta B = \sum_i^{occ} \langle \delta \varphi_i | B | \varphi_i \rangle + \langle \varphi_i | B | \delta \varphi_i \rangle = \sum_i^{occ} \langle \delta \varphi_i | z | \varphi_i \rangle + \langle \varphi_i | z | \delta \varphi_i \rangle \quad (2.5.25)$$

Carrying on with the usual substitution of perturbed orbitals, which is the linear combination of virtual orbitals, we get:

$$\begin{aligned} \delta B = & \sum_i^{occ} \sum_a^{virt} e^{-i\omega t} (Y_{ia} \langle \varphi_a | z | \varphi_i \rangle + X_{ia} \langle \varphi_i | z | \varphi_a \rangle) \\ & + \sum_i^{occ} \sum_a^{virt} e^{i\omega t} (X_{ia}^* \langle \varphi_a | z | \varphi_i \rangle + Y_{ia}^* \langle \varphi_i | z | \varphi_a \rangle) \end{aligned} \quad (2.5.26)$$

And by comparison with the expression of polarizability we obtain:

$$\prod (BA_\omega | \omega) = \sum_i^{occ} \sum_a^{virt} Y_{ia} \langle \varphi_a | z | \varphi_i \rangle + X_{ia} \langle \varphi_i | z | \varphi_a \rangle \quad (2.5.27)$$

Therefore  $\delta B$  goes to infinite (absorption) when  $X$  and  $Y$  are the solutions of the pseudo-eigenvalues equations:

$$\begin{pmatrix} A & B \\ B^* & A^* \end{pmatrix} \begin{pmatrix} X \\ Y \end{pmatrix} = \omega \begin{pmatrix} 1 & 0 \\ 0 & -1 \end{pmatrix} \begin{pmatrix} X \\ Y \end{pmatrix} \quad (2.5.28)$$

This formulation is well known as the Random Phase Approximation (RPA), which can be simplified with some more hypothesis and approximations:

- 1) If the molecular orbitals are real,  $A^* = A$  and  $B^* = B$
- 2) It is possible to neglect the  $B$  matrix, such approximation is known as the Tamm Dancoff Approximation (TDA) [2.22]

Then we obtain the more common eigenvalues equation:

$$AX = \omega X \quad (2.5.29)$$

The substitution of Fock operator with the KS Hamiltonian leads to the TDDFT equations, which differ from RPA only for one bielectronic term in the submatrices and the presence of exchange-correlation potential in the KS formulation:

$$A_{ia,jb} = \delta_{ij}\delta_{ab}(\varepsilon_a - \varepsilon_i) + \langle \varphi_a \varphi_j || \varphi_i \varphi_b \rangle = \begin{cases} RPA \Rightarrow \delta_{ij}\delta_{ab}(\varepsilon_a - \varepsilon_i) + \langle \varphi_a \varphi_j | \varphi_i \varphi_b \rangle - \langle \varphi_a \varphi_j | \varphi_b \varphi_i \rangle \\ TDDFT \Rightarrow \delta_{ij}\delta_{ab}(\varepsilon_a - \varepsilon_i) + \langle \varphi_a \varphi_j | \varphi_i \varphi_b \rangle - \langle \varphi_a \varphi_j | K_{xc} | \varphi_i \varphi_b \rangle \end{cases} \quad (2.5.30)$$

$$B_{ia,jb} = \langle \varphi_a \varphi_b || \varphi_i \varphi_j \rangle = \begin{cases} RPA \Rightarrow \langle \varphi_a \varphi_b | \varphi_i \varphi_j \rangle - \langle \varphi_a \varphi_b | \varphi_j \varphi_i \rangle \\ TDDFT \Rightarrow \langle \varphi_a \varphi_b | \varphi_i \varphi_j \rangle - \langle \varphi_a \varphi_b | K_{xc} | \varphi_i \varphi_j \rangle \end{cases} \quad (2.5.31)$$

Assuming both  $A$  and  $B$  are real matrices, the RPA matrix problem will become:

$$\begin{cases} AX + BY - \omega X = -V \\ BX + AY + \omega Y = -V \end{cases} \quad (2.5.32)$$

Subtracting the second equation from the first one we obtain:

$$(A - B)(X - Y) = \omega(X + Y) \Rightarrow (X - Y) = \omega(A - B)^{-1}(X + Y) \quad (2.5.33)$$

Such expression is quite interesting for TDDFT, since only in that case the  $(A - B)$  matrix is diagonal, this is not true in RPA.

And from this follows that:

$$[(A + B) - \omega^2(A - B)^{-1}](X + Y) = -2V \quad (2.5.34)$$

Now is common to define the diagonal  $(A - B)^{-1}$  matrix as  $\varepsilon^{-1}$  and finally write the Casida formulation of TDDFT as follows:

$$\Omega F = \omega^2 F \quad (2.5.35)$$

Where it is defined  $\Omega = \varepsilon^{-\frac{1}{2}}(A + B)\varepsilon^{\frac{1}{2}}$  and  $F = \varepsilon^{-\frac{1}{2}}(X + Y)$ .

This eigenvalues problem can be transformed in the following expression:

$$(\Omega - \omega^2)^{-1} = F_{n0} \left( \frac{1}{\omega_{n0}^2 - \omega^2} \right) F_{n0}^+ \quad (2.5.36)$$

Considering the variation of our observable  $B$  we obtain:

$$\delta B = V^+(X + Y) = V^+ \varepsilon^{\frac{1}{2}} F = V^+ \varepsilon^{\frac{1}{2}} (-2) F_{n0} \left( \frac{1}{\omega_{n0}^2 - \omega^2} \right) F_{n0}^+ \varepsilon^{\frac{1}{2}} V \quad (2.5.37)$$

When the resonant condition is considered we can simplify the expression as follows:

$$\delta B \cong -\frac{2 \left| V^+ \varepsilon^{\frac{1}{2}} F_{n0} \right|^2}{\omega_{n0}^2 - \omega^2} \cong -\frac{\cancel{2} \left| V^+ \varepsilon^{\frac{1}{2}} F_{n0} \right|^2}{(\omega_{n0} - \omega) \cancel{2} \omega} = \frac{\left| V^+ \varepsilon^{\frac{1}{2}} F_{n0} \right|^2}{(\omega - \omega_{n0}) \omega} \quad (2.5.38)$$

For replacement of  $\left| V^+ \varepsilon^{\frac{1}{2}} F_{n0} \right|^2$  with  $\omega |\langle n|z|0 \rangle|^2$  (is the same for the other two dipoles) we obtain:

$$\delta B \cong \frac{|\langle n|z|0 \rangle|^2}{\omega - \omega_{n0}} \quad (2.5.39)$$

Then, to solve the TDDFT equations with the Casida formulation it is necessary diagonalize the  $\Omega$  matrix which has the following matrix elements:

$$\Omega_{ia\sigma,jb\tau} = \delta_{\sigma\tau}\delta_{ij}\delta_{ab}(\varepsilon_a - \varepsilon_i)^2 + 2\sqrt{\varepsilon_a - \varepsilon_i}K_{ia\sigma,jb\tau}\sqrt{\varepsilon_b - \varepsilon_j} \quad (2.5.40)$$

Where  $K_{ia\sigma,jb\tau}$  is the so called coupling matrix and it contains Exchange-Correlation kernel, in Adiabatic Local Density Approximation (ALDA) we will have:

$$K_{ia\sigma,jb\tau} = \int \int \varphi_{i\sigma}(\vec{r}) \varphi_{a\sigma}(\vec{r}) \left[ \frac{1}{\vec{r} - \vec{r}'} + f_{xc}^{ALDA}(\vec{r})\delta(\vec{r} - \vec{r}') \right] \varphi_{j\tau}(\vec{r}') \varphi_{b\tau}(\vec{r}') d\vec{r}' d\vec{r} \quad (2.5.41)$$

Starting from the eigenvectors  $F_{n0}$  corresponding to the eigenvalues  $\omega_{n0}$ , it is possible extract the intensities as follows:

$$\begin{aligned} f_{n0} &= \frac{2}{3} \omega (|\langle n|x|0\rangle|^2 + |\langle n|y|0\rangle|^2 + |\langle n|z|0\rangle|^2) \\ &= \frac{2}{3} \left( x^+ \varepsilon^{\frac{1}{2}} F_{n0} + y^+ \varepsilon^{\frac{1}{2}} F_{n0} + z^+ \varepsilon^{\frac{1}{2}} F_{n0} \right) \end{aligned} \quad (2.5.42)$$

Until now the spin coordinate hasn't been discussed; in this approach the spin contribution is simplified because spin flip is not allowed.

The  $\Omega$  matrix can conveniently take into account also for the spin value of the electrons involved in the transitions:

- 1)  $\sigma$  is the spin state of  $i$  and  $a$  orbitals
- 2)  $\tau$  is the spin state of  $j$  and  $b$  orbitals

and it is possible to adapt the kernel in order to distinguish, for closed shell systems, between singlet-singlet and singlet-triplet transitions.

In practice, the eigenvalues and eigenvectors of the  $\Omega$  matrix are extracted with the Davidson algorithm that is a very efficient method to extract the lowest roots of the excitation spectrum. However, when a large number of eigenvalues are required this procedure may become numerically unstable.

To overcome these problems the theoretical chemistry group of Trieste has developed the pol-TDDFT that is an alternative and very efficient method to solve the TDDFT equations.

## 2.6 polTDDFT absorption

The Casida method is robust and very efficient method, however it requires the use of very large matrices (of the order of  $N_{occ} * N_{virt}$ ) that must be diagonalized with the Davidson's iterative algorithm.

Unfortunately the Davidson's algorithm is able to extract only "few" low energy eigenvalues, beyond which it becomes unstable and may give numerically deteriorated results.

This problem is important in the case of metallic clusters because in this case the eigenvalues are very dense (high number of eigenvalues for small energy range), in particular when plasmonic phenomena are under study.

To overcome these problems the theoretical chemistry group of Trieste has developed an alternative and very efficient method to solve the TDDFT equations named polTDDFT [2.11].

The polTDDFT method is actually present in the commercial ADF code (Amsterdam Density Functional) which is itself embedded the AMS driver (Amsterdam Modeling Suite).

This new method uses the polarizability tensor and the LR-TDDFT (linear response TDDFT) to reduce drastically the size of the matrices to be diagonalized therefore it is extremely faster but above all it makes it possible to calculate the absorption and dichroism spectra of large systems up to the required excitation energy.

In particular the polTDDFT is based on the extraction of the imaginary part of the frequency-dependent dynamic polarizability, derived from the time evolution of electron density as a first order perturbation.

Let's start by giving the expression of the absorption spectrum  $\sigma(\omega)$ , this will be calculated point by point starting from the imaginary part of the dynamic polarizability  $\alpha(\omega)$ :

$$\sigma(\omega) = \frac{4\pi\omega}{c} \text{Im}[\alpha(\omega)] \quad (2.6.1)$$

Important note is that  $\omega \in \mathbb{C}$ , and in particular we can write:

$$\omega = \omega_r + i\omega_i \quad (2.6.2)$$

Where the real part  $\omega_r$  is the part relating to the frequency of the photon (energy) while the imaginary part  $\omega_i$  represents the line enlargement that naturally arises from the uncertainty between lifetime and energy of the excited states.

In term of oscillator strength we can write:

$$f(\omega_r) = \frac{2\omega_i\omega_r}{3} \text{Im}[\alpha(\omega)] \quad (2.6.3)$$

The last expression [2.11] is useful to compare the intrinsically smoothed polTDDFT results with respect to discrete lines calculations (like Casida) broadened by lorentzian functions with Half Width Half Maximum (HWHM) =  $\omega_i$ .

$$f(\omega) = \sum_{i=1}^N \frac{\eta^2 f_i}{(\omega - \omega_i)^2 + \eta^2} \quad (2.6.4)$$

Where  $\eta^2$  factor guarantees that the maximum of the Lorentzian for  $\omega = \omega_i$  corresponds to the value of  $f_i$  when only one line is present.

Starting from the definition we can write the diagonal elements of polarizability tensor as follows:

$$\alpha_{zz}(\omega) = \int \rho_z^{(1)}(\omega, \vec{r}) z d\vec{r}$$

Where  $\alpha_{zz}$  is the  $z$ -th diagonal element of the polarizability tensor while  $\rho_z^{(1)}(\omega, \vec{r})$  is the component to which applied the Fourier transform returns the time-dependent first-order correction of the electronic density induced by the external electromagnetic field time dependent (incident radiation).

From now on we will take as an example only the  $z$  component but the same considerations will apply to the other two directions  $x, y$ .

In particular we use the average trace of the tensor:

$$\alpha(\omega) = \frac{1}{3} \sum_{i=1}^3 \alpha_{ii} \quad (2.6.5)$$

Where the index  $i$  runs on the three components  $x, y$  and  $z$ . An important observation is that the trace of the tensor is invariant with respect to the chosen coordinate system and therefore does not require the diagonalization or choice of the principal axes.

At this point our unknown term is the  $\rho_z^{(1)}(\omega, \vec{r})$  that can be calculated starting from the Kohn-Sham dielectric susceptibility  $\chi_{KS}(\omega, \vec{r}, \vec{r}')$ , which is referred to a non-interacting electron system, under the influence of an effective perturbative potential  $V_{SCF}^Z(\omega, \vec{r})$  sum of the external potential, the coulomb and exchange-correlation terms.

In practice, the following system must be solved:

$$\left\{ \begin{array}{l} \rho_z^{(1)}(\omega, \bar{r}) = \int \chi_{KS}(\omega, \bar{r}, \bar{r}') V_{SCF}^z(\omega, \bar{r}') d\bar{r}' \\ V_{SCF}^z(\omega, \bar{r}) = V_{EXT}^z(\omega, \bar{r}) + \int \frac{\rho_z^{(1)}(\omega, \bar{r}')}{|\bar{r} - \bar{r}'|} d\bar{r}' + \left. \frac{\partial V_{XC}}{\partial \rho} \right|_{\rho_0} \rho_z^{(1)}(\omega, \bar{r}) \end{array} \right. \quad (2.6.6)$$

The last expression contains the ALDA approximation (Adiabatic Local Density Approximation) [2.23-24] which implies that exchange-correlation kernel is local in time and space.

Rewriting in the form of operators we obtain:

$$\left\{ \begin{array}{l} \rho_z^{(1)} = \chi_{KS} V_{SCF}^z \\ V_{SCF}^z = V_{EXT}^z + K \rho_z^{(1)} \end{array} \right. \quad (2.6.7)$$

Where  $K$  contains the Coulomb and the exchange-correlation kernels:

$$K(\bar{r}, \bar{r}') = K_C(\bar{r}, \bar{r}') + K_{XC}(\bar{r}, \bar{r}') = \frac{1}{|\bar{r} - \bar{r}'|} + \delta(r - r') \left. \frac{\partial V_{XC}}{\partial \rho} \right|_{\rho_0} \quad (2.6.8)$$

Given the linearity of the operators, the system of equations can be reworked as follows:

$$\left\{ \begin{array}{l} \rho_z^{(1)} = \chi_{KS} V_{SCF}^z \\ V_{SCF}^z = V_{EXT}^z + K \rho_z^{(1)} \end{array} \right. \Rightarrow \left\{ \begin{array}{l} V_{SCF}^z = (\chi_{KS})^{-1} \rho_z^{(1)} \\ V_{SCF}^z = V_{EXT}^z + K \rho_z^{(1)} \end{array} \right. \Rightarrow (\chi_{KS})^{-1} \rho_z^{(1)} = V_{EXT}^z + K \rho_z^{(1)} \Rightarrow \quad (2.6.9)$$

$$\rho_z^{(1)} - \chi_{KS} K \rho_z^{(1)} = \chi_{KS} V_{EXT}^z \Rightarrow (1 - \chi_{KS} K) \rho_z^{(1)} = \chi_{KS} V_{EXT}^z \quad (2.6.10)$$

To solve this matrix problem is convenient to expand the induced density as a linear combination of fitting function  $\{f_\mu\}$  frequency independent:

$$\rho_z^{(1)}(\omega, \bar{r}) = \sum_{\mu} f_{\mu}(\bar{r}) b_{\mu}(\omega) \quad (2.6.11)$$

Then by simple substitution:

$$\sum_{\mu} \left( |f_{\mu}\rangle - \chi_{KS} K |f_{\mu}\rangle \right) b_{\mu}(\omega) = \chi_{KS} V_{EXT}^z \quad (2.6.12)$$

and taking the scalar product we obtain:

$$\sum_{\mu} \left( \langle f_{\nu} | f_{\mu} \rangle - \langle f_{\nu} | K \chi_{KS} | f_{\mu} \rangle \right) b_{\mu}(\omega) = \langle f_{\nu} | \chi_{KS} V_{EXT}^z \rangle \quad (2.6.13)$$

In terms of element of matrices:

$$\sum_{\mu} \left( S_{\nu\mu} - M_{\nu\mu}(\omega) \right) b_{\mu}(\omega) = d_{\nu}(\omega) \quad (2.6.14)$$

Writing the non-homogeneous system in compact matrix form we obtain:

$$[S - M(\omega)]b = d \quad (2.6.15)$$

Where  $S$  is the overlap matrix of the fitting functions,  $b$  is the unknown vector of the frequency-dependent expansion coefficients and  $d$  is the known frequency-dependent vector and its expression is:

$$d_{\nu} = \langle f_{\nu} | \chi_{KS} | z \rangle \quad (2.6.16)$$

Where we have written  $V_{EXT}^z = z$ , that is the  $z$ -th component of the external oscillating dipole.

The matrix  $M(\omega)$  turns out to be a frequency-dependent matrix which should be calculated for each wavelength, this problem is computationally impossible to deal with and requires an approximation.

The innovation of the polTDDFT method concerns precisely this aspect, the frequency-dependent matrix  $M(\omega, \bar{r}, \bar{r}')$  is expressed as a linear combination of a set of matrices  $\{G^k\}$  frequency-independent and frequency-dependent expansion coefficients  $s_k(\omega)$ :

$$M(\omega) = \sum_k s_k(\omega) G^k \quad (2.6.17)$$

Therefore the matrix  $M(\omega)$  is built by varying the coefficients  $s_k(\omega)$  once the set of matrices has been constructed, this calculation is extremely fast and applicable for any frequency.

To justify this approximation, the expression of dielectric susceptibility must be considered:

$$\begin{aligned}\chi_{KS}(\omega, \vec{r}, \vec{r}') &= \sum_i^{\text{occ}} \sum_a^{\text{virt}} \varphi_i(\vec{r}) \varphi_a(\vec{r}) \frac{4\varepsilon_{ia}}{\omega^2 - \varepsilon_{ia}^2} \varphi_i(\vec{r}') \varphi_a(\vec{r}') \\ &= \sum_i^{\text{occ}} \sum_a^{\text{virt}} \theta_{ia}(\vec{r}) \lambda_{ia}(\omega) \theta_{ia}(\vec{r}')\end{aligned}\quad (2.6.18)$$

Where  $\varepsilon_{ia} = \varepsilon_a - \varepsilon_i$  has been defined and the only frequency dependent object is  $\lambda_{ia}(\omega)$ , this is taken as "almost constant", this approximation is legitimate and is due to the fact that the  $\varepsilon_{ia}$  are close to each other, that is when the density of excitation energies at zero order is high.

Let us consider to divide the scale of excitation energies into  $P$  ordered intervals  $I_k$ , that is  $\{E_k\}_{k=1,2,\dots,P+1}$  which graphically translates into the following scheme:

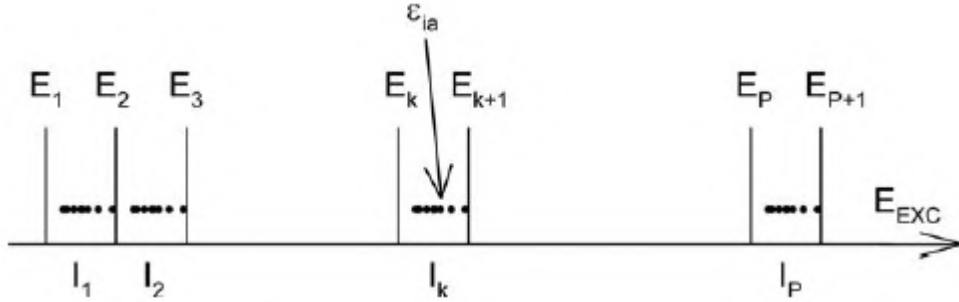


Figure (2.6.1) Graphic representation of energy grid

Note that the minimum corresponds to the  $\varepsilon_{HOMO} - \varepsilon_{LUMO}$ , given the density of the excitation energies, one can approximate the energies as an arithmetic average as a good approximation:

$$\bar{E}_i = \frac{E_i + E_{i+1}}{2}\quad (2.6.19)$$

With this in mind, the double summation can be rewritten by extracting the part containing the excitation energies from the internal one:

$$\begin{aligned}\chi_{KS}(\omega, \vec{r}, \vec{r}') &= \sum_i^{\text{occ}} \sum_a^{\text{virt}} \theta_{ia}(\vec{r}) \lambda_{ia}(\omega) \theta_{ia}(\vec{r}') = \sum_{k=1}^P \frac{4\bar{E}_k}{\omega^2 - \bar{E}_k^2} \sum_{\varepsilon_{ia} \in I_k} \theta_{ia}(\vec{r}) \theta_{ia}(\vec{r}') \\ &= \sum_{k=1}^P s_k(\omega) \tilde{G}^k(\vec{r}, \vec{r}')\end{aligned}\quad (2.6.20)$$

So the part of the frequencies and the space part have been separated.

Generally we are interested only in the lower part of the spectrum so we can define a cutoff energy and from this the series is truncated.

Therefore, the matrix  $M(\omega)$  can be effectively constructed using the following expression:

$$\begin{aligned} M_{\mu\nu}(\omega) &= \langle f_\nu | \chi_{KS} K | f_\mu \rangle = \sum_{k=1}^{max} \langle f_\nu | s_k(\omega) \tilde{G}^k(\bar{r}, \bar{r}') K | f_\mu \rangle \\ &= \sum_{k=1}^{max} s_k(\omega) \sum_{\varepsilon_{ia} \in I_k} \langle f_\nu | \theta_{ia}(\bar{r}) \rangle \langle \theta_{ia}(\bar{r}') | K | f_\mu \rangle = \sum_{k=1}^{max} s_k(\omega) G_{\nu\mu}^k \end{aligned} \quad (2.6.21)$$

Therefore the  $s_k(\omega)$  coefficients are determinates from the following expression:

$$s_k(\omega) = \frac{4\bar{E}_k}{\omega^2 - \bar{E}_k^2} \quad (2.6.22)$$

Note that the  $G_{\nu\mu}^k$  matrix can be conveniently separated in other two submatrices:

$$G_{\nu\mu}^k = \sum_{\varepsilon_{ia} \in I_k} \langle f_\nu | \theta_{ia}(\bar{r}) \rangle \langle \theta_{ia}(\bar{r}') | K | f_\mu \rangle = \sum_{\varepsilon_{ia} \in I_k} A_{\nu, \varepsilon_{ia}}^k B_{\varepsilon_{ia}, \mu}^k \quad (2.6.23)$$

Corresponding to:

$$A_{\nu, \varepsilon_{ia}}^k = \langle f_\nu | \theta_{ia}(\bar{r}) \rangle \quad (2.6.24)$$

$$B_{\varepsilon_{ia}, \mu}^k = \langle \theta_{ia}(\bar{r}') | \frac{1}{|\bar{r} - \bar{r}'|} | f_\mu \rangle + \langle \theta_{ia}(\bar{r}') | (r - r') \frac{\delta V_{XC}}{\delta \rho} \Big|_{\rho_0} | f_\mu \rangle \quad (2.6.25)$$

Similar expressions can be derived for the elements of the  $d$  vector which appears in the non-homogeneous system [2.11].

So now we have all elements for determinate the unknown vector  $b(\omega)$  of the equation  $[S - M]b = d$  and with this explicitly determine the induced density:

$$\rho_z^{(1)}(\omega, \bar{r}) = \sum_{\mu} f_{\mu}(\bar{r}) b_{\mu}(\omega) \quad (2.6.26)$$

Finally we can calculate the dynamic polarizability:

$$\alpha_{zz}(\omega) = \int \rho_z^{(1)}(\omega, \bar{r}) z d\bar{r} = \sum_{\mu} b_{\mu}(\omega) \int f_{\mu}(\bar{r}) z d\bar{r} \quad (2.6.27)$$

From whose imaginary part the spectrum will be extracted.

A more accurate expression to evaluate the spectrum can be obtained with the Modified Sternheimer Approach and is described in ref. [2.11].

## 2.7 polTDDFT dichroism

The method described in the previous chapter can also be easily extended in order to calculate the Electronic Circular Dichroism (ECD) spectrum [2.13]. It should be noted that in the following discussion the dependence on the current density in the exchange-correlation functionals will be ignored.

Let's start by giving the definition of circular dichroism, it is defined by the difference between the absorption of left and right circularly polarized light:

$$CD = A_L - A_R \quad (2.7.1)$$

Where  $A_L$  and  $A_R$  are respectively the absorption of light describing a left-handed helix and the absorption of light describing a right-handed helix.

If we now admit that the radiation propagates along the  $x$  direction, we can write that:

$$CD = 2\gamma Im[\langle 0|\mu_y|n\rangle\langle n|m_y|0\rangle + \langle 0|\mu_z|n\rangle\langle n|m_z|0\rangle] \quad (2.7.2)$$

Where  $\mu_i$  and  $m_i$  are respectively the  $i$ -th electric dipole component and the magnetic one (orthogonal to the direction of propagation) and  $\gamma$  is a constant.

It must be considered that the molecules in solutions are subject to free rotation, therefore it will be necessary to take into account an average of all possible orientations:

$$CD = \frac{4}{3}\gamma Im[\langle 0|\mu|n\rangle\langle n|m|0\rangle] \quad (2.7.3)$$

This expression is known as the Rosenfeld equation, in terms of rotatory strength it can be written [2.h]:

$$R_{0n} = Im[\langle 0|\mu|n\rangle\langle n|m|0\rangle] \quad (2.7.4)$$

And this is the object that will be calculated, to do this it is convenient to examine the expression of the dipole induced by electromagnetic radiation:

$$\mu_i^{(1)} = \sum_j \alpha_{ij} \mathcal{C}_j - \sum_j \frac{\beta_{ij}}{c} \frac{\partial B_j}{\partial t} \quad (2.7.5)$$

Where as usual we define  $\alpha$  the polarizability tensor,  $\mathcal{C}$  the electric field and  $B$  the magnetic field while a new object has been introduced, the optical rotation tensor  $\beta$ , which is shown to be correlated to the rotatory strength through the following formula:

$$\beta = \frac{1}{3} \sum_{i=1}^3 \beta_{ii} = \frac{2}{3} c \sum_{n \neq 0} \frac{R_{0n}}{\omega_{n0}^2 - \omega^2} \quad (2.7.6)$$

Note that as already done for the polarizability, only the trace of the tensor has taken into account.

Therefore the object to be calculated will be the matrix  $\beta$ , it will derive from the electric dipole induced by the external oscillating magnetic field, therefore considering only the component  $z$ , a perturbed time-dependent Hamiltonian can be written in a completely analogous way to what done in the chapter on polarizability:

$$H^{(1)}(t) = -\bar{m} \cdot \bar{B} = -m_z B_z \cos(\omega t) = -\frac{1}{2} (m_z e^{i\omega t} + m_z^+ e^{-i\omega t}) B_z \quad (2.7.7)$$

Using the linear response theory we can rewrite the dipoles induced (polarization) by the perturbation (incident radiation) in the following way:

$$\prod(\mu_z m_z | \omega) = \lim_{\varepsilon \rightarrow 0^+} \sum_{n \neq 0} \left( \frac{\langle 0 | \mu_z | n \rangle \langle n | m_z | 0 \rangle}{\omega - \omega_{n0} + i\varepsilon} - \frac{\langle 0 | m_z | n \rangle \langle n | \mu_z | 0 \rangle}{\omega + \omega_{n0} + i\varepsilon} \right) \quad (2.7.8)$$

Where  $\varepsilon$  is the term of adiabatic switch.

Note that this result has been obtained through the Fourier transform (which is generally done in association with the use of linear response theory) and we have passed from the time domain to that of frequencies, in order to simplify the expression.

If we assume real wavefunctions we can recast the magnetic dipole matrix element as follows, in the first step the hermiticity is used, in the second one the fact that the operator is purely imaginary:

$$\langle 0 | m_z | n \rangle = \langle n | m_z | 0 \rangle^* = -\langle n | m_z | 0 \rangle \quad (2.7.9)$$

Where the real wave functions have been assumed, remembering that the electric dipole operator is Hermitian, it will be written that:

$$\prod(\mu_z m_z | \omega) = \lim_{\varepsilon \rightarrow 0^+} \sum_{n \neq 0} \langle 0 | \mu_z | n \rangle \langle n | m_z | 0 \rangle \left( \frac{1}{\omega - \omega_{n0} + i\varepsilon} + \frac{1}{\omega + \omega_{n0} + i\varepsilon} \right) \quad (2.7.10)$$

Then we have:

$$\prod(\mu_z m_z | \omega) = - \int \rho_z^{(1)}(\omega, \bar{r}) z d\bar{r} \quad (2.7.11)$$

However, this is a formal result because it is not possible to carry out the summation over all excited states, however the non-interacting Kohn-Sham method can be used, for which the expression of the induced density is obtained as a perturbation due to the magnetic field:

$$\begin{aligned} \rho_z^{(1)}(\omega, \bar{r}) = & \sum_i^{\text{occ}} \sum_a^{\text{virt}} \varphi_i \varphi_a \langle a | m_z | i \rangle \left( \frac{1}{\omega - \omega_{ai} + i\varepsilon} + \frac{1}{\omega + \omega_{ai} + i\varepsilon} \right) \\ & + \int \chi_{KS}(\omega, \bar{r}, \bar{r}') V_{z,ind}(\omega, \bar{r}') d\bar{r}' \end{aligned} \quad (2.7.12)$$

In this expression the potential induced by the induced density is defined as:

$$V_{z,ind}(\omega, \bar{r}) = \int \frac{\rho_t^{(1)}(\omega, \bar{r}')}{|\bar{r} - \bar{r}'|} d\bar{r}' + \left. \frac{\partial V_{XC}}{\partial \rho} \right|_{\rho_0} \rho_t^{(1)}(\omega, \bar{r}) \quad (2.7.13)$$

In a completely similar way to what was done for absorption, the induced density is expanded as a linear combination:

$$\rho_z^{(1)}(\omega, \bar{r}) = \sum_{\mu} f_{\mu}(\bar{r}) q_{\mu}(\omega) \quad (2.7.14)$$

Where by simple substitution a matrix problem similar to the one faced in the case of absorption is obtained:

$$[S - M(\omega)]q = g \quad (2.7.15)$$

The only new object compared to the previous chapter is the vector  $g$ , whose expression is:

$$g_{\mu} = \sum_{k=1}^{\max} t_k(\omega) \sum_{\varepsilon_{ia} \in I_k} A_{\mu,ia}^k(\bar{r}, \bar{r}') \langle i | m_z | a \rangle \quad (2.7.16)$$

Then the expression of the coefficient frequency-dependent is:

$$t_k(\omega) = \frac{1}{\omega - \omega_{ai} + i\varepsilon} + \frac{1}{\omega + \omega_{ai} + i\varepsilon} \quad (2.7.17)$$

So it can be seen that once the absorption spectrum (the objects contained in this method) has been calculated it is completely inexpensive to expand the calculation to the dichroism spectrum, since the only object not yet calculated is the column vector  $g$ .

At this point we have all the necessary elements to have the spectrum of dichroism, to have a practical expression it will be necessary to rework some expressions, in particular:

$$\begin{cases} \mu_i^{(1)} = \sum_j \alpha_{ij} C_j - \sum_j \frac{\beta_{ij}}{c} \frac{\partial B_j}{\partial t} \\ \prod (\mu_i m_i | \omega) = - \int \rho_i^{(1)}(\omega, \bar{r}) i d\bar{r} \end{cases} \quad (2.7.18)$$

Taking for example the component z we obtain,:

$$-\frac{\beta_{zz}}{c} \frac{\partial B_z}{\partial t} = \frac{1}{2} \left( \prod (\mu_i m_i | \omega) e^{-i\omega t} + \prod (\mu_i m_i | -\omega) e^{i\omega t} \right) \quad (2.7.19)$$

So if we admit that we have a monochromatic radiation of pulsation  $\omega$  we can easily write the equation that describes the trend of the magnetic field over time:

$$B_z(t) = B_z \cos(\omega t) = B_z \left( \frac{e^{-i\omega t} + e^{i\omega t}}{2} \right) \quad (2.7.20)$$

Therefore its derivative will be:

$$\frac{\partial B_z(t)}{\partial t} = B_z \left( \frac{-i\omega e^{-i\omega t} + i\omega e^{i\omega t}}{2} \right) \quad (2.7.21)$$

Then by substitution:

$$\beta_{zz} = -\frac{ic}{\omega} \prod (\mu_i m_i | \omega) \quad (2.7.22)$$

Also in this case it is seen that in resonance case this object is a pole and the strength of the rotator will be extracted from the residue, in particular we will have that:

$$\beta_{zz} = -\frac{ic}{\omega} \frac{\langle 0 | \mu_z | n \rangle \langle n | m_z | 0 \rangle}{i\varepsilon} \quad (2.7.23)$$

Therefore, considering the average over all orientations and considering closed-shell molecules (only the singlet-singlet transition) we obtain:

$$\beta = -\frac{2icR_{0n}}{3\omega\varepsilon} \quad (2.7.24)$$

And by reordering, we finally get the strength of the rotator:

$$R_{0n} = \frac{3\omega\varepsilon}{2c} \text{Im}[\beta(\omega)] \quad (2.7.25)$$

## 2.8 Technical remarks

In this section some purely technical but extremely important strengths are briefly presented. These aspects are not explicitly mentioned by the articles produced and contribute to making the polTDDFT the method of choice for the calculation of large systems in a very flexible way both on small and large calculators.

A short list of these of these technical remarks follows:

- One of the fundamental differences from the Casida method (and from most of the calculation codes) is the possibility of fragmenting the computation at the  $A^k$  submatrix level (see section 2.6 and 2.7). This allows you to choose the amount of usable memory, the time estimate and therefore to choose a time limit according to the walltime imposed by the policy of the calculator used. It is also possible to perform a restart which makes the exploration of various numerical choices extremely fast.
- polTDDFT and new innovation are perfectly integrated in ADF code, thus consider symmetry as Wigner–Eckart theorem then this reduce computational effort and the time consuming.
- All new feature are optimally parallelized at MPI level, in both symmetrical and non-symmetrical cases.
- New HDA contains a special indexing that allows to switch between Casida and polTDDFT and vice-versa by calculating the necessary integrals only once (see the relative article). Also in this case it is possible choose how many integrals must be calculated and restart from this point. in this case a very precise estimate of the time required occurs.
- All tests (not shown in this thesis) confirm that HDA is completely general and can be used with extreme precision even in other time dependent calculation (for example core spectra), with various hybrid functionals (other than B3LYP), different bases, etc.
- Preliminary test suggest that the new fitting functions are very robust and can also be transferred to other bases and functionalities with excellent results, including: SZ, DZ, DZP, TZP, BP86, LB94, PBE, HDA, all with and without approximation.
- Finally, large number of analysis tool are present: TCM, ICM, fragment analysis and other graphic representation.

## 2.9 Relativistic effects

In some circumstances the relativistic effects become important and they may have a large number of different implications [2.26-28].

These effects arise when we work with objects that move at speed “near” to the speed of light ( $c$ ).

In chemistry this situation occurs when heavy elements are considered because the electrons belonging to the inner orbitals, and in particular the 1s ones, have an average speed comparable to  $c$ .

By the way, the relativistic treatment is also required when high accuracy is needed in simulation.

In the relativistic theory there is a fundamental relation between mass and velocity:

$$m(m_0, v) = \frac{m_0}{\sqrt{1 - \left(\frac{v}{c}\right)^2}} \quad (2.9.1)$$

Where  $m(m_0, v)$  is the effective mass that is function of velocity of the particle  $v$  and its rest mass  $m_0$ .

The consequence of previous expression is that when the speed increases also the effective mass increases with the implication that a particle cannot exceed (or to equal) the speed of light.

From the chemistry point of view the increase in mass affects the shape of atomic orbitals and more precisely a contraction of orbitals is observed, for example we can examine how the Bohr radius changes:

$$a_0 = \frac{4\pi\epsilon_0\hbar^2}{me^2} \quad (2.9.2)$$

Although only deep core orbitals are directly affected by relativistic effects, also the higher orbitals show a contraction, as an indirect consequence of the orthogonality among the orbitals. Moreover, the contraction of s orbitals improves the nuclear shielding, therefore the orbitals with higher angular momentum are destabilized.

Now a brief summary of the most salient relativistic effect is here considered:

- Bond length and structure: the non-relativistic calculations overestimate the bond length, for example in the case of AuH and Au<sub>2</sub> this effect is of the order of 0.2-0.3Å.

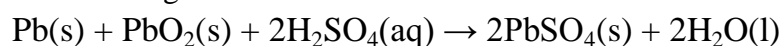
The metallophilic interaction is the tendency of heavy metals to “polymerize”, and in particular Au has a great tendency in fact often it refers to the specific term of aurophilicity.

The flat structure of the small gold clusters (in contrast to the 3D arrangement of the Ag clusters) seems to be linked to relativistic effects and in particular to the

strong 5d-6s hybridization, on the other hand contrary the Spin-Orbit interaction (SO) favors three dimensional structures for anions around  $\text{Au}_{12}^-$ .

- Anomalies of reactivity and physical properties: the end of the third period of transition metal is strongly affected by the relativistic effects. Hg is the only liquid metal at room temperature ( $\cong 360^\circ\text{C}$  lower melting point than Cd) and together Au and Pt are unexpectedly chemically inert (in particular Au and Pt are essentially unreactive) due to the strong contraction of 6s orbital.

Regarding the following electrochemical reaction:



The calculated electromotive force at non-relativistic level returns 0,39V but the relativistic simulation returns the value of 2,13V (close to the experimental value of 2,107V), this is mainly due to of high energy of Pb(IV) compounds (PbO<sub>2</sub> is rare example of neutral Pb(IV) stable compound) that is caused of the loss of high stable 6s electrons, we can say that “our car starts thanks to relativity”.

Finally the well known lanthanide contraction gives special properties and gives very similar reactivity to all elements of this group.

Essentially relativistic phenomena are the topological insulators in which an insulating compound, such as  $\text{Bi}_x\text{Sb}_{1-x}$  or  $\text{Bi}_2\text{Se}_3$ , has metallic surface states created by SO coupling.

Similar SO effects may arise in the Mott insulator transition.

- Spin-orbit: As concerns the Spin-Orbit (SO) coupling, electronic excitations starting from a non-s core orbital generate doubly-split states.

This splitting typically complicate the interpretation of the spectrum, for example, in Ti 2p core spectrum of  $\text{TiCl}_4$  the calculated SO value is more than 5eV, while for S 2p in  $\text{SO}_2$  is 1.3eV, so the two spectral patterns, respectively associated to  $L_3$  ( $2p_{3/2}$ ) and  $L_2$  ( $2p_{1/2}$ ) edges, strongly overlap and the consequent assignment of the calculated peaks is rather complicated.

- Spectroscopic anomalies: the most famous “relativistic color effect” is that of Au, the non-relativistic calculation predict the color of Au similar to Ag with absorption in UV region, in contrast the relativistic contraction of 6s orbital and 5d expansion narrow the gap resulting in a strong transition in visible region.

A similar effect is observed in  $\text{PbCl}_6^{2-}$  where the starting excitation orbitals have strong ligand character but the LUMO is prevalent 6s character.

In the case of  $\text{Pb(NO}_2)_2$  the color is attributed to a singlet-triplet transition of the nitrite induced by the SO coupling of the Pb center.

At non-relativistic level triplet-singlet decay (phosphorescence) is forbidden but the SO coupling makes this process possible, therefore it is common to find phosphorescent materials doped with heavy elements, such as the case of Eu or Dy in  $\text{Sr(AlO}_2)_2$ .

The quantum mechanical theoretical description including the relativistic effects has been developed by Dirac who suggested the Dirac equation, which consists in the extension of the Schrödinger equation to the relativistic case:

$$\hat{H}_D \Psi(\vec{r}, t) = i\hbar \frac{\partial \Psi(\vec{r}, t)}{\partial t} \quad (2.9.3)$$

Where the new Dirac Hamiltonian is composed of four components:

$$\hat{H}_D = c\alpha \cdot p + m_0 c^2 \beta \quad (2.9.4)$$

Where  $p$  is the usual moment operator:

$$p = -i\hbar \nabla \quad (2.9.5)$$

$\beta$  is a traceless 4x4 diagonal matrix:

$$\beta = \begin{pmatrix} 1_2 & 0 \\ 0 & -1_2 \end{pmatrix} \quad (2.9.6)$$

With the form of the elements are:

$$1_2 = \begin{pmatrix} 1 & 0 \\ 0 & 1 \end{pmatrix} \quad 0 = \begin{pmatrix} 0 & 0 \\ 0 & 0 \end{pmatrix} \quad (2.9.7)$$

$\alpha$  is a vector  $\alpha = (\alpha_x, \alpha_y, \alpha_z)$  where the three components are traceless 4x4 diagonal matrix of the type:

$$\alpha_i = \begin{pmatrix} 0 & \sigma_i \\ \sigma_i & 0 \end{pmatrix} \quad (2.9.8)$$

Where  $\sigma_i$  are the Pauli spin matrices, which they have the form:

$$\sigma_x = \begin{pmatrix} 0 & 1 \\ 1 & 0 \end{pmatrix} \quad \sigma_y = \begin{pmatrix} 0 & -i \\ i & 0 \end{pmatrix} \quad \sigma_z = \begin{pmatrix} 1 & 0 \\ 0 & -1 \end{pmatrix} \quad (2.9.9)$$

Note that also the wavefunction is more complex, because we must consider the two possible spin of the electrons, and then we must consider the four component spinor:

$$\Psi(\vec{r}, t) = \begin{pmatrix} \varphi_\alpha(\vec{r}, t) \\ \varphi_\beta(\vec{r}, t) \\ \xi_\alpha(\vec{r}, t) \\ \xi_\beta(\vec{r}, t) \end{pmatrix} \quad (2.9.10)$$

Where  $\alpha$  and  $\beta$  refer to spin up and down respectively,  $\varphi$  and  $\xi$  are the so-called large and small components. Now, introducing a potential  $V$  in the Hamiltonian we have:

$$\hat{H} = \hat{H}_D + V = c\alpha \cdot p + m_0c^2\beta + V \quad (2.9.11)$$

And then:

$$(E - c\alpha \cdot p - m_0c^2\beta - V)\Psi(\vec{r}, t) = 0 \quad (2.9.12)$$

The treatment of this Hamiltonian poses some formal problems, for example the solution furnishes also eigenvalues with negative energy since the equation is not bound from below, therefore at the theoretical level the variational principle is no longer granted as the solutions do not have a minimum.

Moreover this Hamiltonian requires special basis functions and its four-components nature makes it computationally very expensive.

In practice it is possible to avoid the solution of the Dirac equation, for example by means of the Douglass-Kroll (DK) transformation [2.29] it is possible, with very good approximation, to decouple the large and the small components reducing the scheme from a four-components to a two-components one. Moreover, if also the Spin Orbit (SO) coupling is neglected, a one-component relativistic formulation is obtained, known also as Scalar Relativistic (SR).

In the present thesis we always employed the Zero Order Regular Approximation (ZORA) [2.30] scheme to introduce relativistic effects. The SO coupling has been always neglected, so all the calculations have been performed at the SR-ZORA level of theory.

### 3 BIBLIOGRAPHY

- [1.1] Tatsuya Tsukuda, Hannu Hakkinen; “*Protected metal cluster: from fundamentals to applications*”; Elsevier; 9 (2016); ISBN 978-0-08-100086-1
- [1.2] Chakraborty I., Pradeep T.; “*Atomically Precise Clusters of Noble Metals: Emerging Link between Atoms and Nanoparticles*”; Chem. Rev.; 117 (2017) 8208–8271
- [1.3] Jin R., Zeng C., Zhou M., Chen Y.; “*Atomically Precise Colloidal Metal Nanoclusters and Nanoparticles: Fundamentals and Opportunities*”; Chem. Rev.; 116 (2016) 10346–10413
- [1.4] Krishnadas K. R., Baksi A., Ghosh A., Natarajan G., Pradeep T.; “*Structure-Conserving Spontaneous Transformations between Nanoparticles*”; Nat. Commun.; 7 (2016) 13447
- [1.5] Z. Zhong, D. Wang, Y. Cui, M. W. Bockrath, C. M. Lieber; “*Nanowire Crossbar Arrays as Address Decoders for Integrated Nanosystems*”; Science; 5649 (2003) 1377–1379
- [1.6] C. Murphy and N. Jana; “*Controlling the aspect ratio of inorganic nanorods and nanowires*”; Advanced Materials; 1 (2002) 80–82
- [1.7] V. Rodrigues, T. Fuhrer, and D. Ugarte; “*Signature of atomic structure in the quantum conductance of gold nanowires*”; Phys. Rev. Lett.; 85 (2000) 4124–4127
- [1.8] A. Kunzmann, B. Andersson, T. Thurnherr, H. Krug, A. Scheynius, and B. Fadeel; “*Toxicology of engineered nanomaterials: Focus on biocompatibility, biodistribution and biodegradation*”; Biochim Biophys Acta; 1810 (2010) 361-373.
- [1.9] M. Brust, M. Walker, D. Bethell, D. J. Schiffrin, R. Whyman; “*Synthesis of thiol-derivatised gold nanoparticles in a two-phase Liquid–Liquid system*”; J. Chem. Soc. Chem Commun.; (1994) 801-802
- [1.10] Ricca Rahman Nasaruddin, Tiankai Chen, Ning Yan, Jianping Xie; “*Roles of thiolate ligands in the synthesis, properties and catalytic application of gold nanoclusters*”; Coordination Chemistry Reviews; 368 (2018) 60–79
- [1.11] Wang G. Guo, R. Kalyuzhny, G. Choi, J.-P. Murray, R. W.; “*NIR Luminescence Intensities Increase Linearly with Proportion of Polar Thiolate Ligands in Protecting Monolayers of Au<sub>38</sub> and Au<sub>140</sub> Quantum Dots*”; J. Phys. Chem. B; 110 (2006) 20282–20289
- [1.12] Wu Z., Jin R.; “*On the Ligand’s Role in the Fluorescence of Gold Nanoclusters*”; Nano Lett.; 10 (2010) 2568–2573

- [1.13] Wang Y., Wan X.-K., Ren L., Su H., Li G., Malola S., Lin S., Tang Z., Häkkinen H., Teo B. K., et al.; “*Atomically Precise Alkynyl-Protected Metal Nanoclusters as a Model Catalyst: Observation of Promoting Effect of Surface Ligands on Catalysis by Metal Nanoparticles*”; J. Am. Chem. Soc.; 138 (2016) 3278–3281
- [1.14] Rambukwella M., Chang L., Ravishanker A., Fortunelli A., Stener M., Dass A.; “*Au<sub>36</sub>(SePh)<sub>24</sub> Nanomolecules: Synthesis, Optical Spectroscopy and Theoretical Analysis*”; Phys. Chem. Chem. Phys.; 20 (2018) 13255–13262
- [1.15] Bootharaju M. S., Chang H., Deng G., Malola S., Baek W., Häkkinen H., Zheng N., Hyeon T.; “*Cd<sub>12</sub>Ag<sub>32</sub>(SePh)<sub>36</sub>: Non-Noble Metal Doped Silver Nanoclusters*”; J. Am. Chem. Soc.; 141 (2019) 8422–8425
- [1.16] Shichibu Y., Negishi Y., Watanabe T., Chaki N. K., Kawaguchi H., Tsukuda T.; “*Biicosahedral Gold Clusters [Au<sub>25</sub>(PPh<sub>3</sub>)<sub>10</sub>(SCnH<sub>2n+1</sub>)<sub>5</sub>Cl<sub>2</sub>]<sup>2+</sup> (n = 2–18): A Stepping Stone to Cluster-Assembled Materials*”; J. Phys. Chem. C; 111 (2007) 7845–7847
- [1.17] Jiang D., Whetten R. L.; “*Magnetic Doping of a Thiolated-Gold Superatom: First-Principles Density Functional Theory Calculations*”; Phys. Rev. B; 80 (2009) 115402
- [1.18] L. Sementa, G. Barcaro, A. Dass, M. Stener, A. Fortunelli; “*Designing Ligand-Enhanced Optical Adsorption of Thiolated Gold NanoClusters*”; Chem. Comm.; 51 (2015) 7935 – 7938
- [1.19] Howard DeVoe; “*Optical Properties of Molecular Aggregates. I. Classical Model of Electronic Absorption and Refraction*”; J. Chem. Phys.; 41 (1964) 393
- [1.20] Gergo Peter Szekeres; Janina Kneipp; “*SERS Probing of Proteins in Gold Nanoparticle Agglomerates*”; 7 (2019) 1-10
- [1.21] Xuxing Lu, Gang Ye, Deep Punj, Ryan C. Chiechi, Michel Orrit; “*Quantum Yield Limits for the Detection of Single-Molecule Fluorescence Enhancement by a Gold Nanorod*”; ACS Photonics; 9 (2020) 2498–2505
- [1.22] A. Liebsch; “*Surface-plasmon dispersion and size dependence of Mie resonance: Silver versus simple metals*”; Phys. Rev. B; 48 (1993) 11317 –11328
- [1.23] Kwak K., Choi W., Tang Q., Kim M., Lee Y., Jiang D.; “*Molecule-like PtAu<sub>24</sub>(SC<sub>6</sub>H<sub>13</sub>)<sub>18</sub> Nanocluster as an Electrocatalyst for Hydrogen Production*”; Nat. Commun.; (2017) 14723
- [1.24] Hossain S., Ono T., Yoshioka M., Hu G., Hosoi M., Chen Z., Nair L. V., Niihori Y., Kurashige W., Jiang D., et al.; “*Thiolate-Protected Trimetallic Au<sub>~20</sub>Ag<sub>~4</sub>Pd and Au<sub>~20</sub>Ag<sub>~4</sub>Pt Alloy Clusters with Controlled Chemical Composition and Metal Positions*”; J. Phys. Chem. Lett.; 9 (2018) 2590–2594
- [1.25] Hossain S., Niihori Y., Nair L. V., Kumar B., Kurashige W., Negishi Y.; “*Alloy Clusters: Precise Synthesis and Mixing Effects*”; Acc. Chem. Res.; 51 (2018) 3114–3124

- [1.26] Wang S., Li Q., Kang X., Zhu M.; “*Customizing the Structure Composition and Properties of Alloy Nanoclusters by Metal Exchange*”; *Acc. Chem. Res.*; 51 (2018) 2784–2792
- [1.27] Jiang D., Whetten R. L.; “*Magnetic Doping of a Thiolated-Gold Superatom: First-Principles Density Functional Theory Calculations*”; *Phys. Rev. B*; 80 (2009) 115402
- [1.28] Choi W., Hu G., Kwak K., Kim M., Jiang D.-e., Choi J.-P., Lee D.; “*Effects of Metal-Doping on Hydrogen Evolution Reaction Catalyzed by MAu<sub>24</sub> and M<sub>2</sub>Au<sub>36</sub> Nanoclusters (M = Pt Pd)*”; *ACS Appl. Mater. Interfaces*; 10 (2018) 44645–44653
- [1.29] Pelton M., Tang Y., Bakr O. M., Stellacci F.; “*Long-Lived Charge-Separated States in Ligand-Stabilized Silver Clusters*”; *J. Am. Chem. Soc.*; 134 (2012) 11856–11859
- [1.30] Soldan G., Aljuhani M. A., Bootharaju M. S., AbdulHalim L. G., Parida M. R., Emwas A.-H., Mohammed O. F., Bakr O. M.; “*Gold Doping of Silver Nanoclusters: A 26-Fold Enhancement in the Luminescence Quantum Yield*”; *Angew. Chem. Int. Ed.*; 55 (2016) 5749–5753
- [2.1] Robert G. Parr and Yang Weitao; “*Density-Functional Theory of Atoms and Molecules*”; Oxford University Press; (1989) ISBN-13: 978-0195092769
- [2.2] P. Hohenberg and W. Kohn; “*Inhomogeneous Electron Gas*”; *Phys. Rev.*; 136 (1964) B864
- [2.3] W. Kohn and L. J. Sham; “*Self-Consistent Equations Including Exchange and Correlation Effects*”; *Phys. Rev.*; 140 (1965) A1133
- [2.4] Wolfram Koch, Max C. Holthausen; “*A Chemist's Guide to Density Functional Theory*”; Wiley; (2001) ISBN 9783527600045
- [2.5] S. H. Vosko, L. Wilk, M. Nusair; “*Accurate spin-dependent electron liquid correlation energies for local spin density calculations: a critical analysis*”; *Can. J. Phys.*; 58 (1980) 1200-1211
- [2.6] J. P. Perdew; “*Density-functional approximation for the correlation energy of the inhomogeneous electron gas*”; *Phys. Rev.*; 33 (1986) 8822-8824
- [2.7] A. D. Becke; “*Density-functional exchange-energy approximation with correct asymptotic behavior*”; *Phys. Rev.*; 38 (1988) 3098-3100
- [2.8] A. D. Becke; “*Density-functional thermochemistry. III. The role of exact exchange*”; *J. Chem. Phys.*; 98 (1993) 5648-5652
- [2.9] C. Lee, W. Yang, and R. G. Parr; “*Development of the Colic-Salvetti correlation-energy formula into a functional of the electron density*”; *Phys. Rev.*; 37 (1988) 785-789

- [2.10] Perdew John P., Staroverov Viktor N., Tao Jianmin, Scuseria Gustavo E.; “*Density functional with full exact exchange, balanced nonlocality of correlation, and constraint satisfaction*”; Phys. Rev. A.; 78 (2008) 1-13
- [2.11] Stefan Grimme; “*Double-hybrid density functional theory for excited electronic states of molecules*”; J. Chem. Phys.; 127 (2007) 154116-154134
- [2.12] D. M. Ceperley and B. J. Alder; “*Ground State of the Electron Gas by a Stochastic Method*”; Phys. Rev. Lett.; 45 (1980) 566-569
- [2.13] R. van Leeuwen and E. J. Baerends; “*Exchange-correlation potential with correct asymptotic behavior*”; Phys. Rev. A; 49 (1994) 2421-2431
- [2.14] John P. Perdew, Kieron Burke, and Matthias Ernzerhof; “*Generalized Gradient Approximation Made Simple*”; Phys. Rev. Lett.; 78 (1996) 3865-3868
- [2.15] M. E. Casida; “*Recent Advances in Density-Functional Methods*”; Delano P. Chong World Scientific; 1 (1995); ISBN 9810224427
- [2.16] Oscar Baseggio, Giovanna Fronzoni, Mauro Stener; “*A New Time Dependent Density Functional Algorithm For Large Systems And Plasmons In Metal Clusters*”; J. Chem. Phys.; 143 (2015), 024106
- [2.17] Oscar Baseggio, Martina De Vetta, Giovanna Fronzoni, Mauro Stener, Alessandro Fortunelli; “*A new Time Dependent Density Functional Method for molecular plasmonics: formalism, implementation and the Au144(SH)60 case study*”; Int. J. Quantum Chem.; 116 (2016), 1603 – 1611
- [2.18] Baseggio Oscar, Toffoli Daniele, Fronzoni Giovanna, Stener Mauro, Sementa Luca, Fortunelli Alessandro; “*Extension of the Time Dependent Density Functional complex polarizability algorithm to circular dichroism: implementation and applications to Ag8 and Au38(SC2H4C6H5)24*”; J. Phys. Chem. C; 120 (2016), 24335 – 24345
- [2.19] R. McWeeny; “*Methods of Molecular Quantum Mechanics*”; Academic Press; 1 (1989); ISBN 9780124865501
- [2.20] G. Diercksen and R. McWeeny; “*Self-Consistent Perturbation Theory. I. General Formulation and Some Applications*”; J. Chem. Phys.; 44 (1966) 3554-3560
- [2.21] Erich Runge, E. K. U. Gross; “*Density-Functional Theory for Time-Dependent Systems*”; Phys. Rev. Lett.; 52 (1984) 997–1000
- [2.22] Chunping Hu, Osamu Sugino, Kazuyuki Watanabe; “*Performance of Tamm-Dancoff approximation on nonadiabatic couplings by time-dependent density functional theory*”; J. Chem. Phys.; 140 (2014) 054106
- [2.23] E. K. U. Gross and W. Kohn; “*Time-dependent density-functional theory*”; Quantum. Chem.; 21 (1990) 255-291

[2.24] E. K. U. Gross and Walter Kohn; “*Local density-functional theory of frequency-dependent linear response*”; Phys. Rev. Lett.; 57 (1986) 2850-2852

[2.25] L. Rosenfeld; “*Quantenmechanische Theorie der natürlichen optischen Aktivität von Flüssigkeiten und Gasen*”; Zeitschrift für Physik; 52 (1929) 161–174

[2.26] Pekka Pyykko; “*Relativistic effects in structural chemistry*”; Chem. Rev.; 88 (1988) 563–594

[2.27] Pekka Pyykko and Jean Paul Desclaux; “*Relativity and the periodic system of elements*”; Acc. Chem. Res.; 12 (1979) 276–281

[2.28] Pekka Pyykko; “*The Physics behind Chemistry and the Periodic*”; Chem. Rev.; 112 (2012) 371–384

[2.29] M. Douglas, N. M. Kroll; “*Quantum electrodynamical corrections to the fine structure of helium*”; Ann. Phys.; 82 (1974) 89-155

[2.30] E. van Lenthe, E. J. Baerends, J. G. Snijders; “*Relativistic regular two-component Hamiltonians*”; J. Chem. Phys.; 99 (1993) 4597

## 4 RESULTS AND PUBLICATIONS

1) K. R. Krishnadas, L. Sementa, **M. Medves**, A. Fortunelli, M. Stener, A. Fürstenberg, G. Longhi, T. Burgi; “Chiral functionalization of an atomically precise noble metal cluster: insights into the origin of chirality and photoluminescence”; ACS NANO; 14 (2020); 9687–9700

For this article M. Medves did all the TDDFT calculations, the following analysis (ICM, TCM, electronic structure, fragment analysis, orbital visualization and transition composition) partial construction of convincing structures by relaxation of geometry at the LDA-DFT level and wrote the first version of the results and computational method sections of the paper. This article demonstrates that chiroptical spectroscopic techniques such as circular dichroism and circularly polarized luminescence represent useful tools to understand the nature of electronic transitions in ligand-protected metal clusters and the importance of theoretical simulation in explaining that chiral properties arise not only from chiral ligands but also from metal-sulfur staples.

2) Naga Arjun Sakthivel, Mauro Stener, Luca Sementa, **Marco Medves**, Guda Ramakrishna, Alessandro Fortunelli, Allen G. Oliver, Amala Dass; “Crystal structure of  $\text{Au}_{36-x}\text{Ag}_x(\text{SPh-tBu})_{24}$  nanoalloy and the role of Ag doping in excited state coupling”; J. Phys. Chem. C; 123 (2019); 29484–29494

For this article M. Medves did all the TDDFT calculations, the following analysis (ICM, TCM, electronic structure, fragment analysis, orbital visualization and transition composition) and wrote the first version of the results and computational method sections of the paper. This article shows how crucial it is to understand the correct arrangement of metals in nano alloys. To corroborate the structural hypotheses it is crucial to use fast but also accurate spectroscopic simulations like polTDDFT.

3) **M. Medves**, L. Sementa, D. Toffoli, G. Fronzoni, A. Fortunelli, M. Stener; “An efficient hybrid scheme for time dependent density functional theory”; J. Chem. Phys. 152 (2020); 184104

For this article M. Medves did the implementation of the method and integrated it into the ADF code present in the AMS package, did all the following calculations and wrote the first version of the theory, results and computational method sections of the paper. This article provides a very fast, accurate and robust method to use hybrid functionals (not only B3LYP discussed in this work) in time-dependent calculations. HDA is also a general approximation, which thanks to its representation as super operator, makes it very easy to implement it in other codes of chemistry and physics.

4) **Marco Medves**, Luca Sementa, Daniele Toffoli, Giovanna Fronzoni, Kumaranchira Ramankutty Krishnadas, Flavio Maran, Thomas Bürgi, Alessandro Fortunelli, Mauro Stener; “Predictive optical photoabsorption of  $[\text{Ag}_{24}\text{Au}(\text{DMBT})_{18}]^-$  via efficient TDDFT simulations”; *J. Chem. Phys.* 155 (2021); 084103

For this article M. Medves did all the TDDFT calculations, the following analysis (ICM, TCM, electronic structure, fragment analysis, orbital visualization and transition composition) and wrote the first version of the results and computational method sections of the paper. This article shows the great importance in the choice of the functional (also depending on the energy range and therefore on the transitions involved), the limits of the Casida method were further demonstrated, overcome with that of the polTDDFT. This is the first article where HDA approximation was used giving really accurate results (in the entire energetic range of the experimental spectrum), especially when compared to low temperature spectra.

5) Daniele Toffoli, **Marco Medves**, Giovanna Fronzoni, Emanuele Coccia, Mauro Stener, Luca Sementa, Alessandro Fortunelli; “Plasmonic circular dichroism in chiral gold nanowire dimers”; *Molecules*; 27(2022); 93

For this article M. Medves did some calculations and relative analysis, provided technical support (especially the parallelization part) wrote part of the first version of the computational method sections of the paper. This article aims to explore the destructive, constructive and structural interactions related to nanostructures with a strong plasmonic character. In particular the interest is aimed at the part of circular dichroism, the use of analysis tools such as ICM and TCM turns out to be fundamental in the rationalization of destructive or constructive couplings by evaluating their energy and intensity.

6) **Marco Medves**, Daniele Toffoli, Mauro Stener, Luca Sementa, Alessandro Fortunelli; “Coupling between plasmonic and molecular excitations: TDDFT investigation of an ag-nanorod/bodipy-dye interaction”; *J. Phys. Chem. A*; accepted

For this article M. Medves did all the TDDFT calculations, the following analysis (ICM, TCM, electronic structure, fragment analysis, orbital visualization and transition composition) and wrote the first version of the results and computational method sections of the paper. This article provides an example of coupling between a plasmon and a fluorescent organic compound, this is a starting point for the theoretical design of new sensors, radiation sources (also circularly polarized) and a deeper understanding of the coupling trend as the distance varies.

7) **Marco Medves**, Giovanna Fronzoni, Mauro Stener; “Optimization of density fitting auxiliary slater type basis functions for time dependent density functional theory”; *Journal of Computational Chemistry*; accepted

For this article M. Medves did the implementation of the method, suggested many procedures for basis optimization and pruning, did all the following calculations as well as the relative analysis and wrote the first version of the theory, results and computational

method sections of the paper. This article is rather technical but real important in having a great diffusion of the polTDDFT to a wide audience of users, as it provides small but very accurate as well as general bases. This work required the development of an “automatic” code written in various programming languages: shell scripting for use/modify environmental variables and interaction with AMS and monitoring, Python for high-level operation such as file/object-oriented one and resource management, Fortran for brute force calculation and parallelization, finally Visual Basic for Application for post-processing and specific graphics for data visualization. We were inspired by some typical concepts of Machine Learning (ML) with particular attention to memory management and an impressive number of calculations to perform with calculators of different design (many processors & limited walltime like CINECA’s supercomputer or few processors & large walltime) so one of the main differences with the ML is the ability to restart. Fundamental was the introduction of a new descriptor alternative to the well-known cosine of similarity, this descriptor turns out to be an effective statistical tool for fields of application very different from theoretical chemistry. The code is not implemented in AMS but very easy to use and flexible.

# Chiral Functionalization of an Atomically Precise Noble Metal Cluster: Insights into the Origin of Chirality and Photoluminescence

Kumaranchira Ramankutty Krishnadas,\* Luca Sementa, Marco Medves, Alessandro Fortunelli, Mauro Stener,\* Alexandre Fürstenberg, Giovanna Longhi, and Thomas Bürgi\*

Cite This: *ACS Nano* 2020, 14, 9687–9700

Read Online

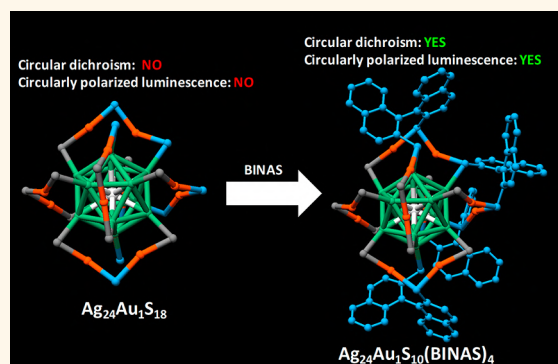
ACCESS |

Metrics & More

Article Recommendations

Supporting Information

**ABSTRACT:** We probe the origin of photoluminescence of an atomically precise noble metal cluster,  $\text{Ag}_{24}\text{Au}_1(\text{DMBT})_{18}$  (DMBT = 2,4-dimethylbenzenethiolate), and the origin of chirality in its chirally functionalized derivatives,  $\text{Ag}_{24}\text{Au}_1(\text{R/S-BINAS})_x(\text{DMBT})_{18-2x}$ , with  $x = 1-7$  (R/S-BINAS = R/S-1,1'-[binaphthalene]-2,2'-dithiol), using chiroptical spectroscopic measurements and density functional theory (DFT) calculations. Combination of chiroptical and luminescence spectroscopies to understand the nature of electronic transitions has not been applied to such molecule-like metal clusters. In order to impart chirality to the achiral  $\text{Ag}_{24}\text{Au}_1(\text{DMBT})_{18}$  cluster, the chiral ligand, R/S-BINAS, was incorporated into it. A series of clusters,  $\text{Ag}_{24}\text{Au}_1(\text{R/S-BINAS})_x(\text{DMBT})_{18-2x}$ , with  $x = 1-7$ , were synthesized. We demonstrate that the low-energy electronic transitions undergo an unexpected achiral to chiral and back to achiral transition from pure  $\text{Ag}_{24}\text{Au}_1(\text{DMBT})_{18}$  to  $\text{Ag}_{24}\text{Au}_1(\text{R/S-BINAS})_x(\text{DMBT})_{18-2x}$  by increasing the number of BINAS ligands. The UV/vis, luminescence, circular dichroism, and circularly polarized luminescence spectroscopic measurements, in conjunction with DFT calculations, suggest that the photoluminescence in  $\text{Ag}_{24}\text{Au}_1(\text{DMBT})_{18}$  and its chirally functionalized derivatives originates from the transitions involving the whole  $\text{Ag}_{24}\text{Au}_1\text{S}_{18}$  framework and not merely from the icosahedral  $\text{Ag}_{12}\text{Au}_1$  core. These results suggest that the chiroptical signatures and photoluminescence in these cluster systems cannot be solely attributed to any one of the structural components, that is, the metal core or the protecting metal–ligand oligomeric units, but rather to their interaction and that the ligand shell plays a crucial role. Our work demonstrates that chiroptical spectroscopic techniques such as circular dichroism and circularly polarized luminescence represent useful tools to understand the nature of electronic transitions in ligand-protected metal clusters and that this approach can be utilized for gaining deeper insights into the structure–property relationships of the electronic transitions of such molecule-like clusters.



**KEYWORDS:** metal clusters, chirality, circular dichroism, circularly polarized luminescence, gold clusters, alloy clusters

Atomically precise, thiolate-protected noble metal clusters such as  $\text{Au}_{102}(\text{SR})_{44}$ ,<sup>1</sup>  $\text{Au}_{25}(\text{SR})_{18}$ ,<sup>2,3</sup>  $\text{Au}_{38}(\text{SR})_{24}$ ,<sup>4-6</sup> and  $\text{Ag}_{44}(\text{SR})_{30}$ ,<sup>7-9</sup> wherein –SR is an alkyl or aryl thiolate, are a unique class of nanoparticles<sup>10,11</sup> exhibiting molecule-like properties in their composition, structure, and chemical reactivity.<sup>12</sup> Many of these clusters consist of an inner core containing a precise number of metal atoms protected by a precise number of metal–ligand oligomeric units. For example,  $\text{Au}_{25}(\text{SR})_{18}$  consists of an inner  $\text{Au}_{13}$  icosahedron and six  $\text{Au}_2(\text{SR})_3$  units.<sup>2,3</sup> These clusters possess well-defined optical absorption bands which are assigned to discrete transitions between their quantized electronic energy levels.<sup>13-15</sup> An important manifestation of their molecule-like electronic structure is photoluminescence,

which has been useful for practical applications.<sup>16</sup> The origin of photoluminescence and various electronic relaxation pathways of such clusters in terms of the role of their inner cores, ligands, and the metal–ligand interface has been investigated.<sup>17-21</sup> Processes such as ligand to metal charge transfer (LMCT) have been proposed to be at the root of luminescence in some of these

Received: February 10, 2020

Accepted: July 16, 2020

Published: July 16, 2020



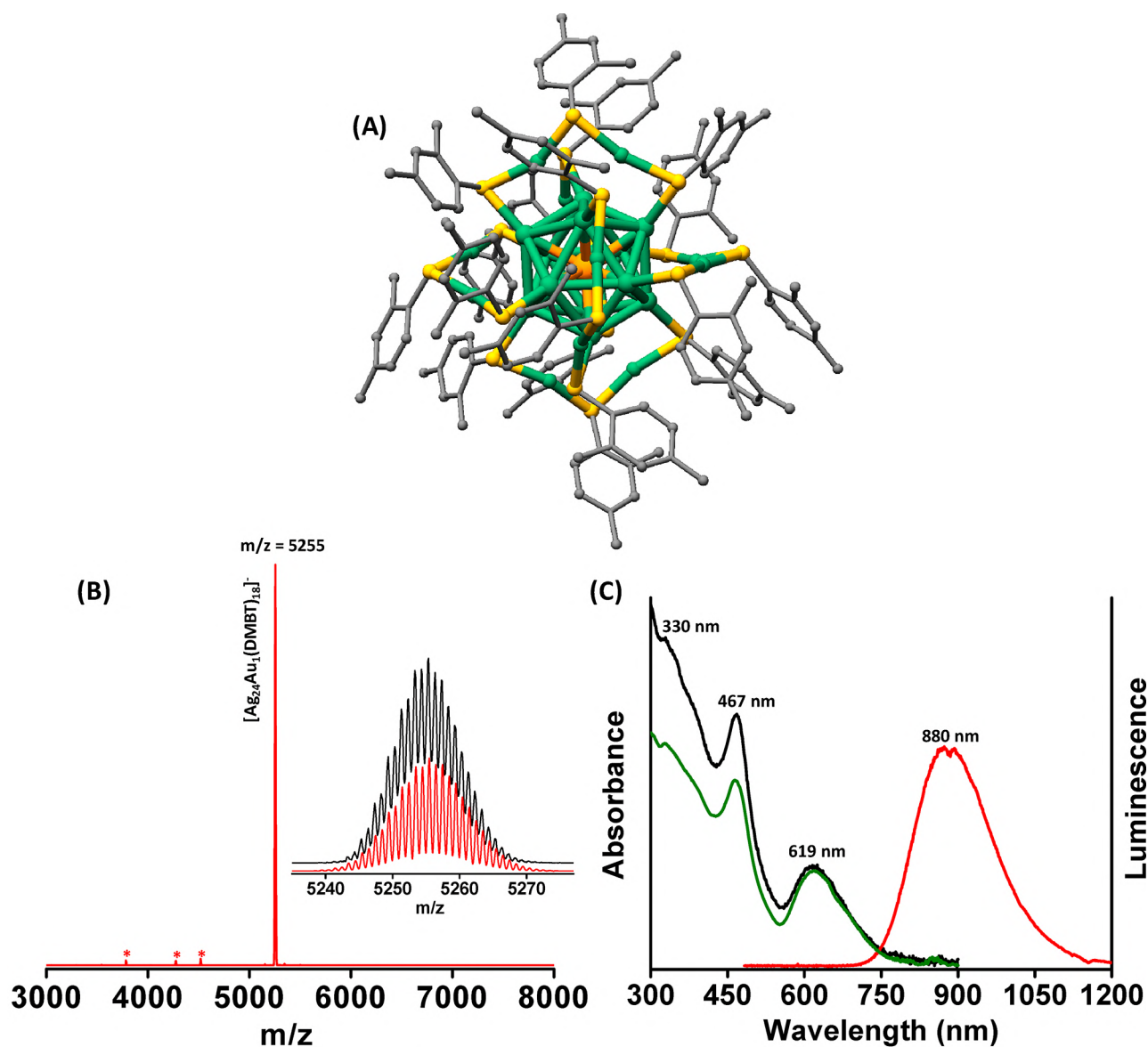


**Figure 1.** Schematic of the crystal structure (A), negative ion mode ESI MS spectrum (B), UV/vis absorption (black trace), excitation (green trace), and emission spectra (red trace) (C) of  $\text{Ag}_{24}\text{Au}_1(\text{DMBT})_{18}$ . Inset of (B) shows the theoretical (red) and experimental (black) isotopic distribution corresponding to the formula,  $\text{Ag}_{24}\text{Au}_1(\text{DMBT})_{18}$ . The features labeled with \* in (B) are due to typical fragments of the molecular ion,  $[\text{Ag}_{24}\text{Au}_1(\text{DMBT})_{18}]^-$ , due to sequential losses of (Ag-DMBT) units (see Figure S1). Characteristic peak positions are marked in (B) and (C). Color codes of atoms in (A): silver (green), gold (orange), sulfur (yellow), and carbon (gray). The H atoms are omitted for clarity. The structure in (A) was created using the coordinates reported in ref 18. The dip at around 880 nm in the emission spectra shown in (C) is due to an artifact from the monochromator response.

clusters.<sup>22</sup> Recently, Jin *et al.* showed that the metal core is mostly involved in the photoluminescence in a series of structurally related gold clusters.<sup>23</sup> However, in spite of being atomically precise in their compositions and possessing well-defined geometric and electronic structures, a detailed understanding of structure–property correlations of photoluminescence in these molecule-like clusters remains elusive.<sup>23</sup>

Circular dichroism (CD) and circularly polarized luminescence (CPL) spectroscopies are essential tools for probing the nature and the origin of the chirality in various systems. The former technique measures the difference in the absorbance of left and right circularly polarized light by a chiral molecule, whereas the latter measures the difference in the intensity of emission of left and right circularly polarized light. Therefore, these two techniques are complementary to each other,

providing information about the chirality of the ground and the excited electronic (emissive) states of molecules, respectively.<sup>24–26</sup> In atomically precise, ligand-protected noble metal clusters, the origin of chirality has been attributed to the chirality of the ligands,<sup>27–30</sup> the chiral arrangement of achiral ligands on the cluster surface,<sup>1,6</sup> and to the inherently chiral inner metal cores.<sup>31,32</sup> Furthermore, discrete electronic absorption bands in some of these clusters, ( $\text{Au}_{25}(\text{SR})_{18}$ , for example),<sup>13</sup> were assigned to the transitions involving inner cores and outer metal–ligand oligomeric units. Bearing in mind that the chirality and electronic absorption bands could be correlated with the structural features of these clusters, a combined CD and CPL investigation, in conjunction with density functional theory (DFT) calculations, is extremely helpful to unravel the origin of chiroptical signatures and photoluminescence in atomically

precise, structurally well-defined, molecule-like noble metal clusters. Such an approach, combining chiroptical and luminescence spectroscopies toward understanding the nature of electronic transitions have been used mostly for organic molecules,<sup>33–35</sup> and to the best of our knowledge, this method has not been applied to such molecule-like ligand-protected noble metal clusters.  $\text{Ag}_{24}\text{Au}_1(\text{DMBT})_{18}$  (DMBT = 2,4-dimethylbenzenethiolate) is an ideal system, in this regard, owing to its well-defined composition and its precisely known crystal structure.<sup>36</sup> Most importantly, this cluster exhibits intense photoluminescence.  $\text{Ag}_{24}\text{Au}_1(\text{DMBT})_{18}$  possesses a symmetric, achiral  $\text{Ag}_{12}\text{Au}_1$  icosahedral core protected by six  $\text{Ag}_2(\text{DMBT})_3$  units and is structurally analogous to the well-known  $\text{M}_{25}(\text{SR})_{18}$  ( $\text{M} = \text{Au}, \text{Ag}$ ) clusters (see Figure 1A).<sup>36</sup> Recent experimental investigations suggested that the photoluminescence in  $\text{Ag}_{24}\text{Au}_1(\text{DMBT})_{18}$  could be due to the charge transfer processes involving the ligands.<sup>18</sup> In contrast, theoretical calculations by Aikens *et al.* suggest that the photoluminescence in  $\text{M}_{25}(\text{SR})_{18}$  ( $\text{M} = \text{Au}, \text{Ag}$ ) is due to the transitions involving the icosahedral core-based superatomic orbitals and that the ligand-based orbitals are not involved in these transitions.<sup>19</sup> Hence, the origin of photoluminescence in these clusters remains ambiguous.

Here, we investigate the origin of chiroptical signatures and photoluminescence of  $\text{Ag}_{24}\text{Au}_1(\text{DMBT})_{18}$  and its chiral derivatives using chiroptical spectroscopic measurements and DFT calculations. In order to impart chirality to the achiral  $\text{Ag}_{24}\text{Au}_1(\text{DMBT})_{18}$  cluster, a chiral ligand,  $R/S$ -1,1'-[binaphthalene]-2,2'-dithiol ( $R/S$ -BINAS) was incorporated into it. Electrospray ionization mass spectroscopic (ESI MS) measurements showed that the overall composition of the cluster remains unaltered after the incorporation of the BINAS ligand. A series of clusters,  $\text{Ag}_{24}\text{Au}_1(\text{R/S-BINAS})_x(\text{DMBT})_{18-2x}$  with  $x = 1-7$ , were synthesized. Ultraviolet/visible (UV/vis) absorption and CD spectroscopic measurements showed systematic changes in the lower-energy electronic transitions of  $\text{Ag}_{24}\text{Au}_1(\text{R/S-BINAS})_x(\text{DMBT})_{18-2x}$  as a function of the number of BINAS ligands. The CD spectroscopic measurements revealed that the incorporation of BINAS induced chiroptical signatures in the cluster and, in particular, that the low-energy electronic absorption bands undergo an unexpected achiral to chiral and back to achiral transition from pure  $\text{Ag}_{24}\text{Au}_1(\text{DMBT})_{18}$  to  $\text{Ag}_{24}\text{Au}_1(\text{R/S-BINAS})_x(\text{DMBT})_{18-2x}$  by increasing the number of incorporated BINAS ligands in them. Luminescence spectra of  $\text{Ag}_{24}\text{Au}_1(\text{R/S-BINAS})_x(\text{DMBT})_{18-2x}$  clusters are red-shifted with regard to that of  $\text{Ag}_{24}\text{Au}_1(\text{DMBT})_{18}$ ; furthermore, these clusters exhibit weak CPL activity, providing further insights into the nature of the excited states that are responsible for the photoluminescence. Our analysis of the trends in the UV/vis, CD, luminescence and CPL spectroscopic changes, in conjunction with DFT calculations indicates that the photoluminescence in  $\text{Ag}_{24}\text{Au}_1(\text{DMBT})_{18}$  and its chirally functionalized derivatives originate from transitions involving the whole  $\text{Ag}_{24}\text{Au}_1\text{S}_{18}$  framework, not merely from the icosahedral  $\text{Ag}_{12}\text{Au}_1$  core. Therefore, these results indicate that the photoluminescence in these cluster systems cannot be solely attributed to any one of the structural components, such as the metal core or the protecting metal–ligand oligomeric units. Our work also shows that, as in the case of common molecules, chiroptical spectroscopic techniques are a potential experimental tool for understanding the nature of electronic transitions in molecule-like ligand-protected metal clusters.

## RESULTS AND DISCUSSION

**Synthesis and Characterization of  $[\text{Ag}_{24}\text{Au}_1(\text{R/S-BINAS})_x(\text{DMBT})_{18-2x}][\text{PPh}_4]$ .** A schematic picture of the crystal structure of  $\text{Ag}_{24}\text{Au}_1(\text{DMBT})_{18}$  is shown in Figure 1A.<sup>36</sup> The negative ion mode ESI mass spectrum of  $[\text{Ag}_{24}\text{Au}_1(\text{DMBT})_{18}][\text{PPh}_4]$  (Figure 1B) shows an expected band at  $m/z$  5255. The features labeled with \* are due to typical fragments of the molecular ion,  $[\text{Ag}_{24}\text{Au}_1(\text{DMBT})_{18}]^-$ , due to sequential losses of ( $\text{Ag}$ -DMBT) units, as presented in the Supporting Information (Figure S1). The theoretical and experimental isotope patterns, shown in the inset of Figure 1B, further confirm this assignment. Figure 1C shows the UV/vis absorption (black trace) and luminescence excitation (green trace) and emission (red trace) bands of  $\text{Ag}_{24}\text{Au}_1(\text{DMBT})_{18}$ . Hence, the mass spectrometric and spectroscopic measurements presented above confirm the purity and the identity of this cluster.

Incorporation of the chiral ligand,  $R/S$ -BINAS, into  $\text{Ag}_{24}\text{Au}_1(\text{DMBT})_{18}$  has been carried out using the method described in the Experimental Section. Figure 2A–D shows the ESI mass spectra of the clusters obtained after the reaction of  $\text{Ag}_{24}\text{Au}_1(\text{DMBT})_{18}$  with  $R$ -BINAS at various  $\text{Ag}_{24}\text{Au}_1(\text{DMBT})_{18}$ /BINAS molar ratios.

Figure 2A shows that the parent cluster,  $\text{Ag}_{24}\text{Au}_1(\text{DMBT})_{18}$  (see the feature corresponding to  $x = 0$ ), is also present along with a series of bands, separated by 42 Da, at the higher  $m/z$  region. The mass separation of 42 Da corresponds to the loss of two DMBT ligands and incorporation of a BINAS ligand (*i.e.*,  $M_{\text{BINAS}}(316) - 2 \times M_{\text{DMBT}}(2 \times 137) = 42$ ). Therefore, a general molecular formula,  $\text{Ag}_{24}\text{Au}_1(\text{R/S-BINAS})_x(\text{DMBT})_{18-2x}$  ( $x =$  number of BINAS ligands), is given to the BINAS-incorporated clusters synthesized. The good agreement between theoretical and experimental isotope patterns of one of the features that corresponds to  $x = 3$  in Figure 2A, which is due to  $\text{Ag}_{24}\text{Au}_1(\text{BINAS})_3(\text{DMBT})_{12}$  presented in Figure S2, further confirms the incorporation of the BINAS ligand into  $\text{Ag}_{24}\text{Au}_1(\text{DMBT})_{18}$ . Furthermore, note that the separation between the features in the experimental isotopic pattern is 1 Da, indicating that these clusters bear single negative charge, as in the case of  $[\text{Ag}_{24}\text{Au}_1(\text{DMBT})_{18}]^-$ . Figures 2A–D shows that groups of clusters containing 0–3, 2–5, 3–5, and 4–7 BINAS ligands can be synthesized by increasing the concentration of BINAS in the reaction mixture. These four groups of clusters will be referred to as groups I, II, III, and IV, respectively in the following discussion for convenience. Group IV is the mixture containing the maximum number of BINAS ligands, as shown in Figures 2D and S3D. Further increase of the concentration of the BINAS ligand did not result in the incorporation of more than seven BINAS ligands; however, clusters of different nuclearities which do not correspond to the general formula,  $\text{Ag}_{24}\text{Au}_1(\text{R-BINAS})_x(\text{DMBT})_{18-2x}$  were formed at higher concentrations of BINAS, as presented in Figure 2D. Mass spectra of the clusters synthesized with  $S$ -BINAS, such as  $\text{Ag}_{24}\text{Au}_1(\text{S-BINAS})_x(\text{DMBT})_{18-2x}$ , at similar  $\text{Ag}_{24}\text{Au}_1(\text{DMBT})_{18}$ /BINAS molar ratios are presented in Figure S3, which further confirms the incorporation of BINAS.

Note that there were no mass spectral features observed which correspond to the clusters formed by the loss of a single DMBT ligand and incorporation of a single BINAS ligand. The features corresponding to such clusters should appear at a mass separation of 179 Da (*i.e.*,  $M_{\text{BINAS}}(316) - M_{\text{DMBT}}(137) = 179$ ); however, such features have not been detected in our measurements. Therefore, the mass spectrometric measure-

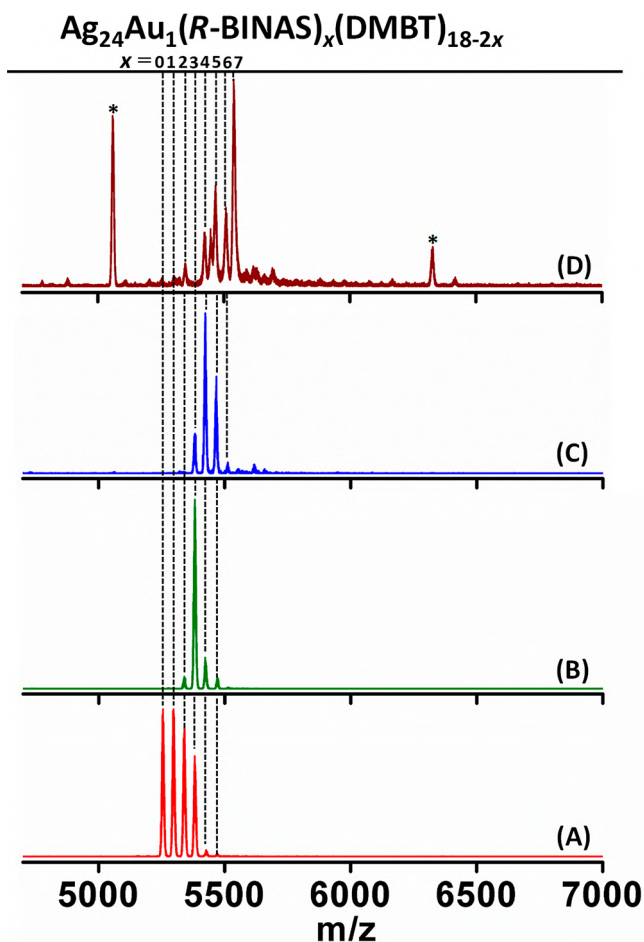


**Figure 2.** Negative ion mode ESI mass spectra of  $\text{Ag}_{24}\text{Au}_1(\text{R-BINAS})_x(\text{DMBT})_{18-2x}$  group of clusters I (A), II (B), III (C), and IV (D) synthesized at various  $\text{Ag}_{24}\text{Au}_1(\text{DMBT})_{18}/\text{BINAS}$  molar ratios. The features (labeled with \*) which do not correspond to the general formula,  $\text{Ag}_{24}\text{Au}_1(\text{R-BINAS})_x(\text{DMBT})_{18-2x}$ , were also observed in (D), which could be due to decomposition or the core transformation of the  $\text{Ag}_{24}\text{Au}_1(\text{R-BINAS})_x(\text{DMBT})_{18-2x}$  resulting from the use of a slightly higher concentration of R-BINAS in the reaction.

ments presented above confirm that one BINAS replaces two DMBT on the clusters. It is known that the BINAS acts as a bidentate ligand to structurally analogous clusters such as  $\text{Au}_{25}(\text{SR})_{18}$  and  $\text{Au}_{24}\text{Pd}(\text{SR})_{18}$ .<sup>37,38</sup> For example, in the case of  $\text{Au}_{24}\text{Pd}(\text{SR})_{18}$ , a single BINAS binds with two Au atoms; that is, one of the two sulfur atoms of BINAS occupies the terminal position of an  $\text{Au}_2(\text{SR})_3$  staple, and the other sulfur atom occupies the bridging position of the adjacent  $\text{Au}_2(\text{SR})_3$  staple of the cluster. Considering the structural similarity of  $\text{Au}_{24}\text{Pd}(\text{SR})_{18}$  and on the basis of the mass spectrometric measurements presented above, we assume that the BINAS ligand binds to  $\text{Ag}_{24}\text{Au}_1(\text{DMBT})_{18}$  in a similar fashion. The bidentate mode of binding was further confirmed by experiments with another dithiolate ligand, namely, 1,1'-biphenyldithiol (BPT), which are presented in Figures S4 and S5. Therefore, mass spectrometric measurements unambiguously confirm the incorporation of the BINAS ligand into  $\text{Ag}_{24}\text{Au}_1(\text{DMBT})_{18}$  without altering the overall composition, that is, the total number of metal atoms and sulfur atoms and the charge state. This is surprising, considering the fact that DMBT is the only ligand known so far to protect the  $\text{Ag}_{25}$  and  $\text{Ag}_{24}\text{Au}_1$  cores.

**UV/vis Absorption Measurements.** UV/vis absorption spectroscopic measurements showed systematic changes in the low-energy band, at 619 nm, of  $\text{Ag}_{24}\text{Au}_1(\text{DMBT})_{18}$  as a function of the number of BINAS ligands incorporated. Figure 3 shows the UV/vis absorption spectra of groups I–IV. These measurements reveal that for I (i.e.,  $\text{Ag}_{24}\text{Au}_1(\text{R-BINAS})_x(\text{DMBT})_{18-2x}$  containing smaller numbers of BINAS i.e.,  $x = 0–3$ ) the spectral bands (see trace a in Figure 3) are similar to those of  $\text{Ag}_{24}\text{Au}_1(\text{DMBT})_{18}$  (see inset of Figure 3), except for some broadening of the band at around 619 nm. However, as the number of incorporated BINAS ligands increases, this band changes significantly. At higher concentration of BINAS (see traces b and c in Figure 3),  $\text{Ag}_{24}\text{Au}_1(\text{R-BINAS})_x(\text{DMBT})_{18-2x}$  exhibits a significantly broadened band with multiple features at around 590 and 664 nm, compared to the single band at around 619 nm for  $\text{Ag}_{24}\text{Au}_1(\text{DMBT})_{18}$ . However, note that the shapes and the peak positions of the bands at higher energies remain almost unchanged irrespective of the number of BINAS ligands incorporated. In particular, the band at 467 nm for the  $\text{Ag}_{24}\text{Au}_1(\text{DMBT})_{18}$  is almost unchanged. However, the hump at  $\sim 380$  nm and a weak shoulder at  $\sim 330$  nm in parent  $\text{Ag}_{24}\text{Au}_1(\text{DMBT})_{18}$  disappeared and a weak hump/shoulder at  $\sim 362$  nm appeared when BINAS was incorporated. It is interesting to note that for group IV (i.e., the  $\text{Ag}_{24}\text{Au}_1(\text{R-S-BINAS})_x(\text{DMBT})_{18-2x}$  clusters containing 4–7 ligands; see mass spectra Figures 2D and S3D), a single weak absorption band, at around 590 nm, was observed in the low-energy side of the spectrum (see trace d in Figure 3) in contrast to that in groups II and III (see traces b and c in Figure 3), wherein two bands were observed. UV/vis spectra of  $\text{Ag}_{24}\text{Au}_1(\text{S-BINAS})_x(\text{DMBT})_{18-2x}$  synthesized at similar  $\text{Ag}_{24}\text{Au}_1(\text{DMBT})_{18}/\text{BINAS}$  molar ratios are shown in Figure S6, which further support this trend. We observed similar changes in the UV/vis absorption bands (Figures S7 and S8) in the experiments with BPT ligand, as well. Hence, the UV/vis absorption spectroscopic measurements confirm that, as the number of dithiolate ligands on the cluster increases, the low-energy transitions are significantly altered; however, the higher energy transitions remains almost unaffected. This implies that the binaphthyl tail groups of the BINAS ligands do not significantly alter the nature of the molecular orbitals associated with higher energy transitions.

The crystal structure of  $\text{Ag}_{24}\text{Au}_1(\text{DMBT})_{18}$  shows that this cluster consists of an icosahedral  $\text{Ag}_{12}\text{Au}_1$  core protected by six  $\text{Ag}_2(\text{DMBT})_3$  staple motifs,<sup>36</sup> which is similar to the structural framework of well-known  $\text{Au}_{25}(\text{SR})_{18}$ .<sup>2,3</sup> Previous DFT calculations<sup>19</sup> suggested that the lowest-energy UV/vis absorption band of  $\text{Ag}_{24}\text{Au}_1(\text{SH})_{18}$ , at around 619 nm, is due to the HOMO–LUMO electronic transition involving the superatomic orbitals derived predominantly from the metal atoms of the  $\text{Ag}_{12}\text{Au}_1$  core (see however a more refined analysis below) in contrast with the charge transfer mechanism involving ligands.<sup>18</sup> The bands at higher energies have been assigned to transitions involving the orbitals with larger contributions from the ligands.<sup>19</sup> However, the clusters used in our experiments contain aromatic thiols whose interaction with the metal core is quite different with respect to the SH ligands which were used in the previous calculations. For this reason, the present calculations (see below) will furnish a different and more realistic description of the electronic structure as well as of the assignment of the most relevant optical transitions.

The incorporation of larger numbers of BINAS could lower the symmetry of the  $\text{Ag}_{24}\text{Au}_1\text{S}_{18}$  framework, which might be the

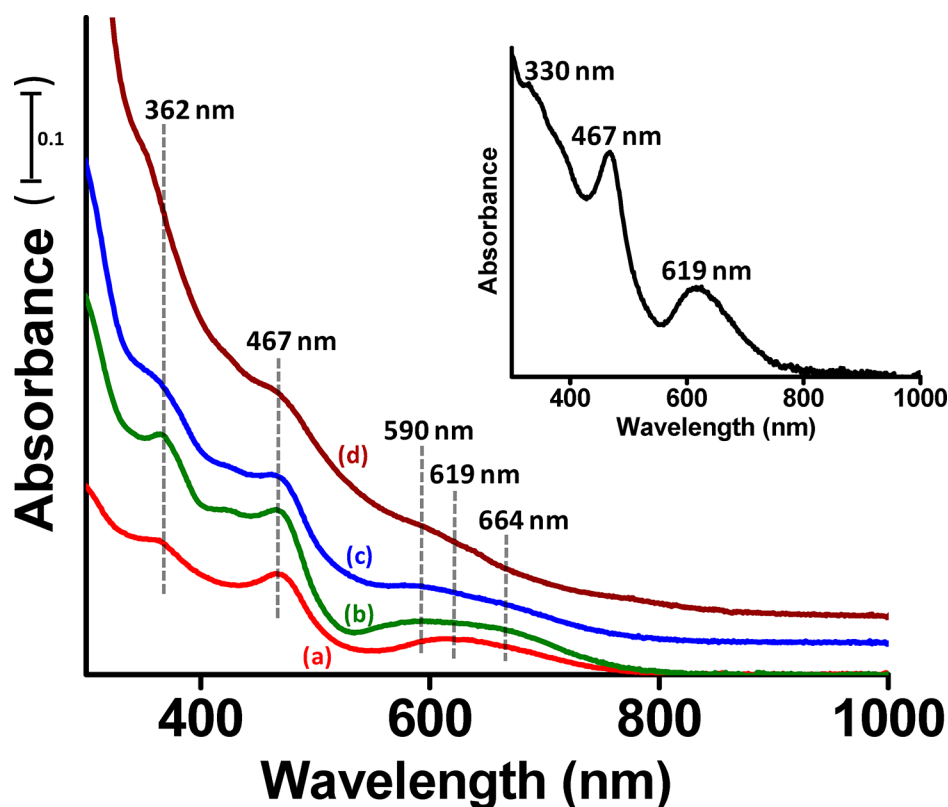


Figure 3. The UV/vis absorption spectra of  $\text{Ag}_{24}\text{Au}_1(\text{R-BINAS})_x(\text{DMBT})_{18-2x}$  group of clusters I (a), II (b), III (c), and IV (d). Inset shows the UV/vis spectrum of  $\text{Ag}_{24}\text{Au}_1(\text{DMBT})_{18}$  for comparison. Traces (b), (c) and (d) have been shifted upward for sake of clarity.

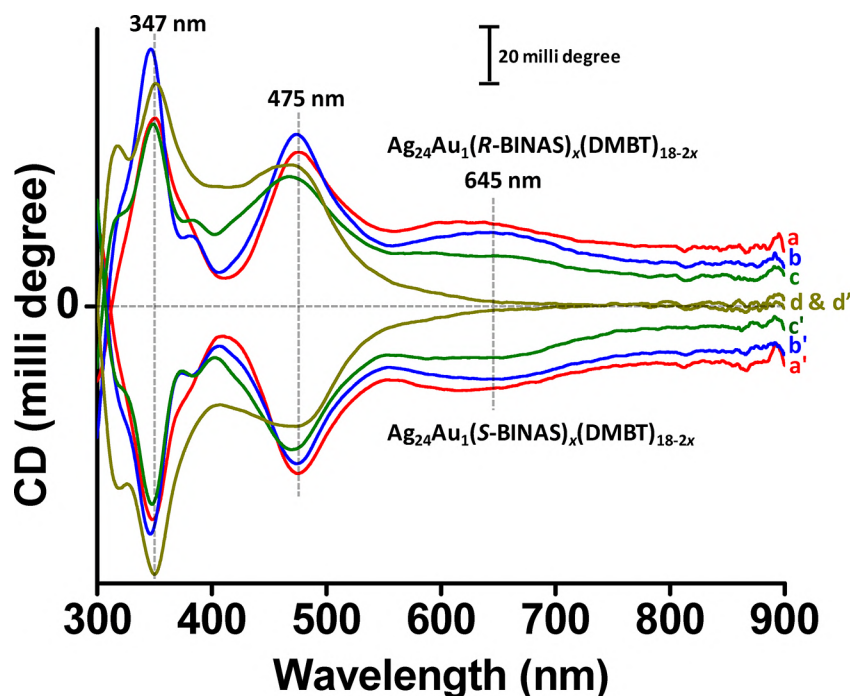


Figure 4. CD spectra of  $\text{Ag}_{24}\text{Au}_1(\text{R/S-BINAS})_x(\text{DMBT})_{18-2x}$  groups of clusters I (a and a'), II (b and b'), III (c and c'), and IV (d and d'). Traces a–d and a'–d' correspond to the  $\text{Ag}_{24}\text{Au}_1(\text{BINAS})_x(\text{DMBT})_{18-2x}$  clusters containing R- and S-BINAS, respectively. Traces a–c (and a'–c') have been shifted upward (downward) for the sake of clarity.

reason for the changes in the low-energy UV/vis absorption bands. Apart from any ligand-induced structural distortions, the peak shifts and the changes in the shape of the UV/vis absorption bands can also occur due to the conjugation of the  $\pi$

electrons of the aromatic tail groups (*i.e.*, binaphthyl and biphenyl in BINAS and BPT, respectively). In order to test this, we attempted to incorporate aliphatic dithiols such as 1,3-propanedithiol and 1,4-butanedithiol (wherein the aromatic tail

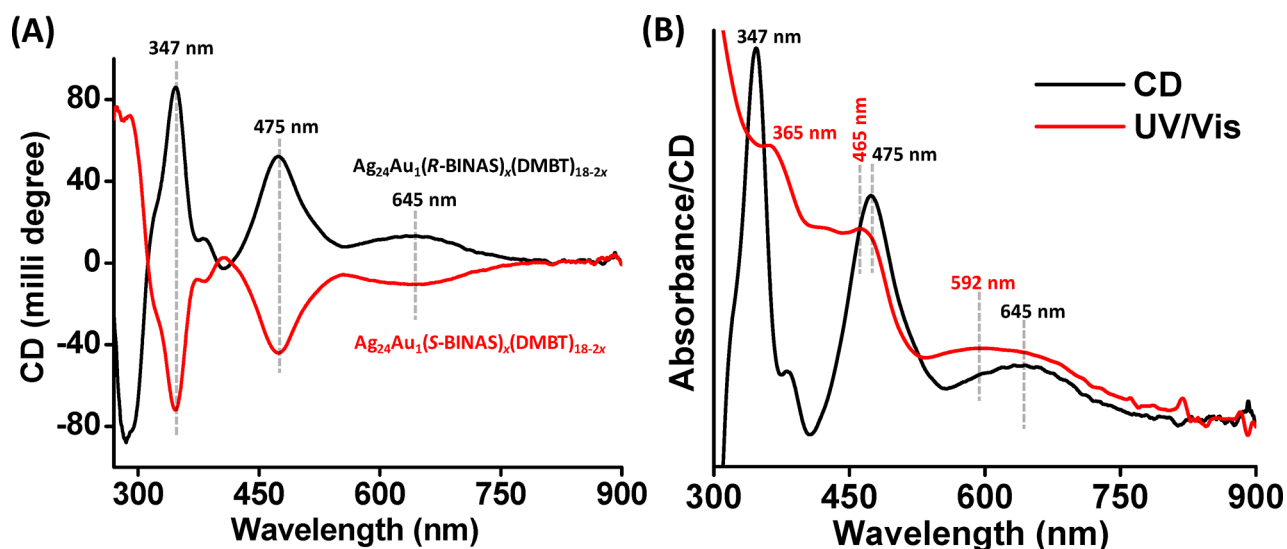


Figure 5. CD spectra (A) and a comparison of the CD and the UV/vis absorption spectra (B) of  $\text{Ag}_{24}\text{Au}_1(\text{R/S-BINAS})_x(\text{DMBT})_{18-2x}$  group II.

groups are absent); however, the reactions of  $\text{Ag}_{24}\text{Au}_1(\text{DMBT})_{18}$  clusters with these aliphatic dithiols resulted in decomposition of the cluster, and no ligand exchange was observed, in contrary to a previously reported experiment with structurally analogous  $\text{Au}_{25}(\text{SR})_{18}$ .<sup>39</sup> Therefore, the above experiments show that the changes in the UV/vis absorption spectra of  $\text{Ag}_{24}\text{Au}_1(\text{DMBT})_{18}$  clusters induced by dithiolate ligands could be either due to structural distortions due to the bidentate binding mode or due to the conjugation of the  $\pi$  electrons of the ligand's tail groups. Results of the DFT calculations (see below for the details) show that structural distortions to the  $\text{Ag}_{24}\text{Au}_1\text{S}_{18}$  framework indeed occur due to the incorporation of BINAS ligands.

**Circular Dichroism of  $\text{Ag}_{24}\text{Au}_1(\text{R/S-BINAS})_x(\text{DMBT})_{18-2x}$ : Chiral to Achiral Transition in Low-Energy Excitations.** CD spectroscopy provides information about the excited electronic state manifold in relation to the ground state of a chiral molecule.<sup>24,26</sup> As mentioned previously,  $\text{Ag}_{24}\text{Au}_1(\text{SR})_{18}$  has a symmetric structure consisting of an icosahedral  $\text{Ag}_{12}\text{Au}_1$  core and six  $\text{Ag}_2(\text{SR})_3$  staple motifs,<sup>36</sup> and hence, this cluster is achiral. However, in order to test whether the incorporation of the chiral dithiolate ligand, BINAS, induces any chiroptical signatures, CD measurements were carried out. The CD spectra of groups I–IV, presented in Figure 4, reveal that these clusters exhibit distinct CD bands at around 347, 475, and 645 nm with exact mirror image relationships for the clusters containing R-BINAS and S-BINAS ligands. Control experiments with pure BINAS ligand and Ag-BINAS complexes (see Figures S9 and S10) confirm that the observed CD bands are due to the dissolved clusters and not due to any impurities such as free ligands or metal–ligand complexes.

Note that group IV (see traces d and d' in Figure 4) do not show any CD band at 645 nm, whereas groups I–III exhibit this band. The mirror image relationship is more clearly presented for group II in Figure 5A. In order to correlate the UV/vis and the CD spectral bands, a comparison of the UV/vis and CD spectra of group II is presented in Figure 5B. It is evident from Figure 5B that the strong CD band at around 475 nm coincides with the UV/vis absorption band at around 465 nm. The CD spectra of pairs of groups I, III, and IV presented separately in Figures S11–S13 further support this observation.

The band at around 467 nm in the  $\text{Ag}_{24}\text{Au}_1(\text{DMBT})_{18}$  has been assigned to the transitions involving the molecular orbitals derived from the metal atoms and ligands.<sup>19</sup> The coincidence of these CD and UV/vis absorption bands at 475 and 465 nm, respectively, shows that the incorporation of the chiral BINAS ligands induces chirality to the staple motifs of these clusters. Similar induction of chirality has been observed in clusters such as  $\text{Au}_{25}(\text{SR})_{18}$ <sup>37</sup> and  $\text{Au}_{38}(\text{SR})_{24}$ .<sup>40</sup> Furthermore, the fact that peak maxima of the bands at higher energies in UV/vis and CD spectra remain unchanged irrespective of the number of BINAS ligands incorporated indicates that the nature of the tail groups of the ligands, that is, 2,4-dimethylphenyl (in DMBT) versus binaphthyl (in BINAS), does not alter the net energy gaps between the molecular orbitals involved in these electronic transitions and is confirmed by present calculations (see peaks at 473–484 nm in Figure 7, left panel).

More interestingly, we observed a weak, broad CD band at around 645 nm (see Figures 4 and 5) that coincides with one of the UV/vis bands (see Figure 5B). A comparison of the UV/vis and CD traces in Figure 5B further shows that even though there are two bands at 590 and 664 nm in the UV/vis spectrum (in Figure 3), the corresponding CD spectrum shows only a single band at 645 nm. However, the CD measurements show that parent  $\text{Ag}_{24}\text{Au}_1(\text{DMBT})_{18}$ , which was originally achiral, becomes chiral after functionalization with BINAS. For  $\text{Ag}_{24}\text{Au}_1(\text{R/S-BINAS})_x(\text{DMBT})_{18-2x}$  clusters containing 4–7 BINAS ligands (*i.e.*, for group IV), there are no CD bands observed at lower energies (see Figures 4 and S13) that correspond to its distinct UV/vis band at around 590 nm (see Figures 3 and S6) showing that when a large number of ligands is present the low-energy excitations lose their chiral character.

Note that even though the  $\text{Ag}_{24}\text{Au}_1(\text{R/S-BINAS})_x(\text{DMBT})_{18-2x}$  clusters with  $x = 4$  and 5 are commonly present in groups III and IV, there is no CD band at around 600 nm for the latter. In order to understand this, we synthesized a new group of  $\text{Ag}_{24}\text{Au}_1(\text{R-BINAS})_x(\text{DMBT})_{18-2x}$  clusters with  $x = 3-5$  (referred to as group V), wherein the cluster with  $x = 5$  is the most abundant species. No CD band at low energies at around 645 nm was observed for group V, though there is a distinct band at around 600 nm in the UV/vis spectrum, as in the case of group IV (see Figures S14 and S15). Note that groups III and V contain clusters with the same composition although at

different relative abundances. The most abundant cluster in III is the one with  $x = 4$ , and that in V is the one with  $x = 5$ . This experiment clearly shows that this low-energy CD band in  $\text{Ag}_{24}\text{Au}_1(\text{R/S-BINAS})_x(\text{DMBT})_{18-2x}$  clusters appears only for clusters with  $x = 1-4$ : when  $x > 4$ , these clusters do not show any CD features at low energies. Therefore, the absence of this CD band at around 600 nm in groups IV and V, in spite of its presence of clusters with  $x = 4$  in it, could be because of their lower concentrations in IV and V compared to that in III. A probable reason for the absence of this CD band for groups IV and V is provided below in light of the DFT calculations.

**DFT Calculations on  $\text{Ag}_{24}\text{Au}_1(\text{R/S-BINAS})_x(\text{DMBT})_{18-2x}$**   
In order to gain better insight into the origin of the experimentally observed electronic absorption and CD bands of  $\text{Ag}_{24}\text{Au}_1(\text{R/S-BINAS})_x(\text{DMBT})_{18-2x}$  clusters, DFT calculations were performed. Note that irrespective of the  $\text{Ag}_{24}\text{Au}_1(\text{DMBT})_{18}$ /BINAS molar ratios used in the synthesis, a mixture of  $\text{Ag}_{24}\text{Au}_1(\text{R/S-BINAS})_x(\text{DMBT})_{18-2x}$  clusters was formed. Furthermore, considering the structural similarity of  $\text{Ag}_{24}\text{Au}_1(\text{DMBT})_{18}$  with  $\text{Au}_{25}(\text{SR})_{18}$  and  $\text{Au}_{24}\text{Pd}(\text{SR})_{18}$ ,<sup>2,3,36,38</sup> we assume that the BINAS ligand in  $\text{Ag}_{24}\text{Au}_1(\text{R/S-BINAS})_x(\text{DMBT})_{18-2x}$  exists in a bidentate fashion, binding two adjacent  $\text{Ag}_2(\text{SR})_3$  staple motifs (see Figure 6).

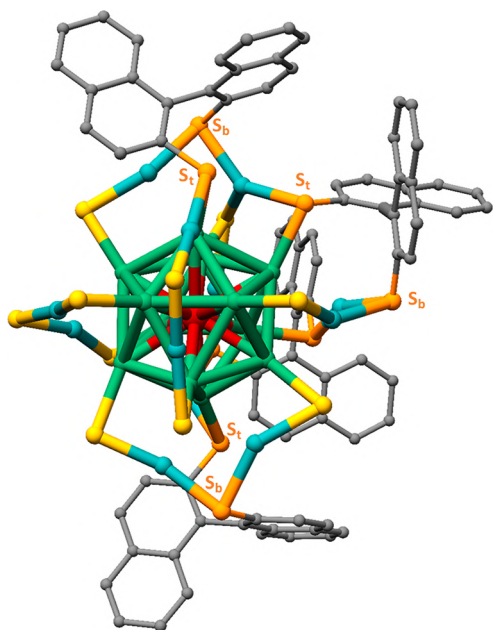


**Figure 6.** DFT/local density approximation fully relaxed geometry of “best 1” isomer of the  $[\text{Ag}_{24}\text{Au}_1(\text{S-BINAS})_4(\text{DMBT})_{10}]^-$ . The DMBT ligands and the hydrogen atoms are omitted for clarity. Atom colors: Ag atoms in the  $\text{Ag}_2\text{S}_3$  staples (cyan), in  $\text{Ag}_{12}\text{Au}_1$  icosahedron (green), Au atom in center of the icosahedron (red), S atoms of DMBT ligands (yellow) and that of BINAS ligands (orange), carbon atoms (black). Some of the bridging and terminal S atom locations (labeled  $\text{S}_b$  and  $\text{S}_a$ , respectively) are marked to show the nature of the binding of BINAS ligands.

The introduction of the new ligand (*i.e.*, BINAS) onto  $\text{Ag}_{24}\text{Au}_1(\text{DMBT})_{18}$  generates a large number of structural isomers because there are various unique binding sites (*i.e.*, pairs of S atom locations in adjacent staples; see Figure 6) for the new ligand. For a single BINAS ligand, that is, for  $\text{Ag}_{24}\text{Au}_1(\text{R/S-BINAS})_1(\text{DMBT})_{16}$ , there is only one unique binding site available, and hence, no isomers exist. However, for  $x = 2$  and  $x =$

3, the number of unique binding sites increases, and hence, the number of structural isomers increases to six and seven, respectively.<sup>38</sup> As it would be computationally very demanding to perform computations on all of the isomers of  $\text{Ag}_{24}\text{Au}_1(\text{R/S-BINAS})_x(\text{DMBT})_{18-2x}$  generated for each value of  $x$ , we focused our computational analysis on a specific composition of  $\text{Ag}_{24}\text{Au}_1(\text{R/S-BINAS})_x(\text{DMBT})_{18-2x}$ , namely, the  $[\text{Ag}_{24}\text{Au}_1(\text{S-BINAS})_4(\text{DMBT})_{10}]^-$  cluster anion. The cluster,  $\text{Ag}_{24}\text{Au}_1(\text{S-BINAS})_4(\text{DMBT})_{10}$ , has been chosen for simulations primarily because this cluster is present in all of the four groups (I-IV) in various abundances (although the mass spectral intensity of this cluster is low in group I, Figure 2A), and hence, it would fairly represent groups I-IV.

Structural models of  $[\text{Ag}_{24}\text{Au}_1(\text{S-BINAS})_4(\text{DMBT})_{10}]^-$  were generated as follows. Starting from the reported experimental single-crystal X-ray coordinates of the  $\text{Ag}_{24}\text{Au}_1(\text{DMBT})_{18}$  cluster anion,<sup>36</sup> we replaced four pairs of DMBT ligands with 4 S-BINAS ligands *via* a systematic docking procedure. We first identified all of the possible pairs of S atoms suitable to host a S-BINAS ligand on the  $\text{Ag}_{24}\text{Au}_1\text{S}_{18}$  framework as those belonging to two neighboring S-Ag-S-Ag-S staples and lying at a distance not larger than a chosen cut off of 4.5 Å (of the order of the equilibrium distance between S atoms in the BINAS ligand). We then generated an ensemble of  $[\text{Ag}_{24}\text{Au}_1(\text{S-BINAS})_4(\text{DMBT})_{10}]^-$  isomers by docking the 4 S-BINAS ligands onto the previously identified S atom pairs and completing the rest of the ligand shell with 10 DMBT ligands. It turned out that 42 isomer structures were generated *via* this docking procedure. Note that we did not take into account the cluster symmetry in the structure generation. These structures were then subjected to local relaxations with the internal  $\text{Ag}_{12}\text{Au}_1$  core kept frozen and the rest of the coordinates fully optimized. Two of the isomeric structural models thus produced were found to be almost isoenergetic and more stable than the others by few tenths of electronvolts and were, therefore, selected for further study (energies and coordinates of all isomer structural models are reported in the Table S3): hereafter, these two most stable isomers are referred to as “best 1” and “best 2” geometries. Optical absorption spectra were simulated on these final optimized geometries *via* real time time-dependent density functional theory (TDDFT) and complex polarizability algorithm<sup>41,42</sup> approaches.

In Figure 7, the absorption and CD spectra of  $[\text{Ag}_{24}\text{Au}_1(\text{S-BINAS})_4(\text{DMBT})_{10}]^-$  are reported, which are calculated at the TDDFT/LB94/TZV level for “best 1” and “best 2” geometries (reported in Table S4), fully optimized at the local density approximation (LDA) level. As presented previously (see Figures 3 and 4), incorporation of BINAS ligands most significantly alters the low-energy UV/vis and CD bands (*i.e.*, 619 nm and at 632 nm, respectively) of  $\text{Ag}_{24}\text{Au}_1(\text{DMBT})_{18}$ , whereas the bands at higher energies are less affected. DFT calculations also reveal a similar trend as shown in Figure 7 (left panel) when comparing  $[\text{Ag}_{24}\text{Au}_1(\text{S-BINAS})_4(\text{DMBT})_{10}]^-$  with  $[\text{Ag}_{24}\text{Au}_1(\text{DMBT})_{18}]^-$ . The calculated absorption profiles of the two geometries (“best 1” and “best 2”) show some differences, suggesting that structural differences between isomers play a role in photoabsorption. It is worth noting that the bands calculated at 473 nm (for “best 1”) and 484 nm (for “best 2”) are in nice agreement with the experimental counterpart at 467 nm (see Figure 3) and the one at 356 nm present only in “best 1”, which is in nice agreement with the experimental band at 362 nm (see Figure 3). The matching between theory and experiment is less precise at low energy: the

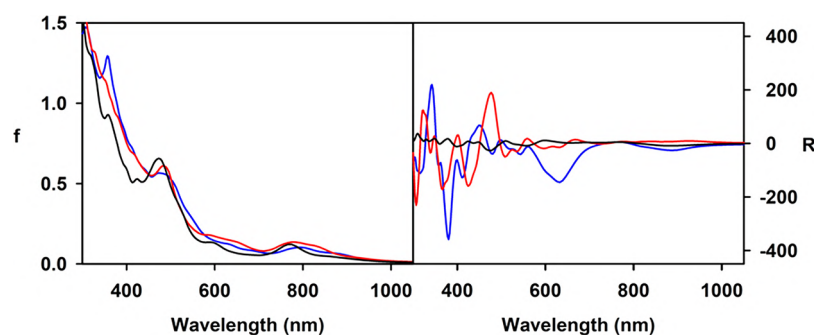


**Figure 7.** Photoabsorption oscillator strength ( $f$ , left panel) and circular dichroism rotatory strength ( $R$ , right panel) calculated at the TDDFT/LB94/TZV level for the geometries “best 1” (blue) and “best 2” (red) of the  $[\text{Ag}_{24}\text{Au}_1(\text{S-BINAS})_4(\text{DMBT})_{10}]^-$  cluster anion; see text for details. The spectra for the  $[\text{Ag}_{24}\text{Au}_1(\text{DMBT})_{18}]^-$  cluster anion (black lines) are also shown for comparison.

bands at 795 nm (for “best 1”) and at 775 nm (for “best 2”) do not have an experimental counterpart. We argue that the employed LB94 xc-potential underestimates the energy position of these bands (as it occurs with this xc-functional) that are thus missing as distinct bands in the experiment, probably hidden in the long wavelength spectral tail of the experimental bands which appear at around 619 nm. More accurate xc-functionals (such as hybrid ones), presently not implemented with the complex polarizability algorithm, on experimentally derived geometries would be needed to achieve a good agreement between theory and experiment also at low energies.<sup>43</sup> Interestingly, from the analysis of the CD spectra in Figure 7 (right panel), it is clear that the calculated bands at 795 and 775 nm are not detected in CD-simulated spectra; that is, they have a very low rotatory strength. Considering that the LB94 spectra are qualitatively correct in terms of spectral bands,<sup>43</sup> we use them as an acceptable compromise. To further support this strategy, we tried to employ the B3LYP functional<sup>44</sup> with the conventional Casida approach; however, due to the computational cost of the nonlocal exchange, it has been possible to extract only very few discrete excitations, so the calculated spectrum does not cover the spectral region below 500 nm. Instead, we have been able to calculate the whole photoabsorption spectrum at the B3LYP level by means of the very recent hybrid diagonal approximation approach,<sup>45</sup> and the results are presented in Figure S16. Interestingly, the band predicted by LB94 at around 800 nm is blue-shifted and reduced in intensity and appears as a weak shoulder (around 745 nm) of a stronger peak whose maximum lies at 653 nm. This comparison shows that the description of the low-energy part of the spectrum is improved if a hybrid xc-functional is employed, corroborating our hypothesis to ascribe the disagreement between theory and experiment at 800 nm to deficiencies of the LB94 xc-potential. Experimentally derived geometries would be needed to perfect the agreement between theory and experiment.<sup>43</sup> The other features at lower wavelengths are less sensitive to the choice of the xc-functional.

In contrast with photoabsorption, the TDDFT-simulated CD spectra shown in Figure 7 (right panel) are rather sensitive to the difference in geometries of “best 1” and “best 2”. The comparison with experiment is not straightforward for this property; however, we can say that, at least qualitatively, most of the experimental bands are reproduced by theory in the “best 1” structure. The experimental CD profile of the *S* enantiomers of groups I–IV (Figure 4) is characterized by a broad negative minimum at 645 nm, followed by two other negative minima at 475 and 347 nm, further followed by a sudden change of sign of

the CD, which becomes positive below 300 nm. In the TDDFT-simulated CD profile of “best 1”, we find a broad negative minimum at 632 nm, followed by two additional minima at 480 and 380 nm and then a sudden change of sign of the CD which becomes positive below 352 nm. The comparison is rather satisfactory in terms of peak positions, albeit less quantitative in terms of intensity. The disagreement between theory and experiment may also be ascribed to the conformational degrees of freedom of the ligands, which are not accounted for in the present simulations and have important consequences on the CD intensity.<sup>46</sup>

It is interesting to note that the UV/vis absorption band at 795 nm in “best 1” does not have a counterpart in its calculated CD spectrum. This can be explained *via* an individual component maps of rotatory strength (ICM-RS) analysis (see ref 47). It represents the most sophisticated tool of chiroptical response and is reported for  $[\text{Ag}_{24}\text{Au}_1(\text{S-BINAS})_4(\text{DMBT})_{10}]^-$  (“best 1” configuration) in Figures S17 and S18, which shows that all three magnetic dipole contributions to the CD spectrum of “best 1” are nonzero but they nearly cancel each other to give an almost zero chiroptical response. Moreover, a molecular orbital (MO) analysis of this cluster shows that the ICM-RS plots have contributions from several different excited configurations. Table S1, reporting the analysis of the transition density matrix of the excitation at 795 nm in terms one-electron excited configurations (occupied-virtual pairs), provides more detail. The largest contribution (30%) is given by the HOMO–2  $\rightarrow$  LUMO configuration, mixed with 25% of the HOMO–1  $\rightarrow$  LUMO+1 and 11% of the HOMO–2  $\rightarrow$  LUMO+1 ones. Such excited configurations are shown as vertical arrows in Figure 8, where the MO energy levels are reported together with a Mulliken analysis of Ag, Au, S, and C+H contributions. As reported in Table S1 and in Figure 8, the occupied orbitals playing a role in the transition at 795 nm are contributed mainly by S 3p and Ag 5s atomic functions involved in the Ag–S staple chemical bonds, whereas the virtual orbitals are mainly contributed by Ag 5s. 3D plots of these molecular orbitals reported in Figure S19 confirm their nature: whereas HOMO–1 and HOMO–2 appear to be localized near the Ag–S bonds, LUMO and LUMO+1 are much more delocalized over the metal atoms, extending on the metal core, as well. This suggests that the low rotational strength at 795 nm may be due to cancellation effects among occupied virtual pairs, with the same virtual orbitals delocalized over the less chiral metallic core of the cluster, whereas chirality is mainly induced by staples.

It is interesting to investigate also the nature of the CD band calculated at 632 nm for “best 1” geometry. An analysis in terms

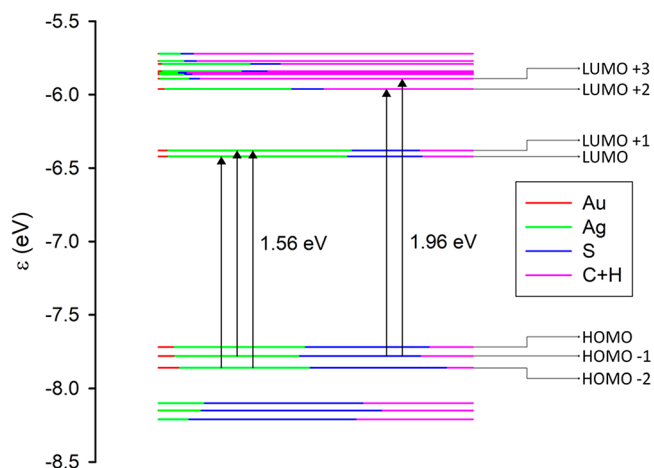


**Figure 8.** Molecular orbital (energy levels) diagram showing the leading contributions to the two lowest transitions at 1.56 eV (795 nm) and 1.96 eV (632 nm) for the geometry “best 1” of the  $[\text{Ag}_{24}\text{Au}_1(\text{S-BINAS})_4(\text{DMBT})_{10}]^-$  cluster anion. Orbital character in terms of Mulliken analysis of Ag, Au, S, and C+H contributions is given in terms of colors of the level, according to the inset legend. HOMO and LUMO are at  $-7.60$  and  $-6.33$  eV, respectively.

of excited configurations for this transition is reported in Table S1, whereas the involved orbitals are the ones reported in Figure S19. In this case, the involved virtual orbitals are LUMO+2 and LUMO+3, which contain a dominant ligand contribution (see the strong participation of the BINAS  $\pi$  orbitals; see Table S1 and Figure S19), while concomitantly the CD rotational strength is much more pronounced with respect to the transition calculated at 795 nm, where the ligand contribution is much smaller. This suggests that the CD signal at 632 nm in calculated spectra (see Figure 7, right panel), that we claim corresponds to the broad experimental band centered at 645 nm (see Figures 4 and 5), is generated by the asymmetry of the  $\text{Ag}_{24}\text{Au}_1\text{S}_{18}$  framework induced by the ligands. For completeness, we report in Table S1 also the analysis of the features calculated for the “best 1” structure at 2.54 eV (488 nm) and 2.72 eV (356 nm), which correspond to the experimental bands at 475 and 347 nm, respectively. Unfortunately, these transitions are strongly mixed, so their assignment is not straightforward. However, from the orbitals involved, it can be seen that they are both mainly contributed by the ligands (S 3p and C 2p) with a minor contribution of the metal atoms. A more comprehensive description can be extracted from the ICM-OS plots reported in Figure S18. The strongly mixed character is corroborated by the “spots” on the reference straight line, indicating mixing of almost degenerate configurations. The minor role of the off-diagonal spots rules out plasmonic behavior, as can be expected due to the too small size of the cluster.

Further simulations on the “best 1” structure were conducted to elucidate the origin of chirality. In detail, a  $[\text{Ag}_{24}\text{Au}_1(\text{SCH}_3)_{18}]^-$  model structure was generated from “best 1” geometry of the  $[\text{Ag}_{24}\text{Au}_1(\text{S-BINAS})_4(\text{DMBT})_{10}]^-$  anion by transforming its BINAS and DMBT ligands into thiomethyl residues and relaxing the geometry, first keeping the  $\text{Ag}_{24}\text{Au}_1\text{S}_{18}$  core frozen and using DFT/PBE-D3 with CP2K code and then fully relaxing the resulting model using DFT/LDA with ADF code (the final structure is named “best 1-CH<sub>3</sub>”). Any residual chiral response of this model structure must be related to a desymmetrization of the  $\text{Ag}_{24}\text{Au}_1\text{S}_{18}$  framework of the parent  $\text{Ag}_{24}\text{Au}_1(\text{DMBT})_{18}^-$  induced by the replacement of

DMBT with BINAS ligands, significant enough to survive as a local energy minimum even after the transformation into thiomethyl ligands. The TDDFT-simulated CD spectrum of “best 1-CH<sub>3</sub>” is reported in Figure 9 and compared with that of

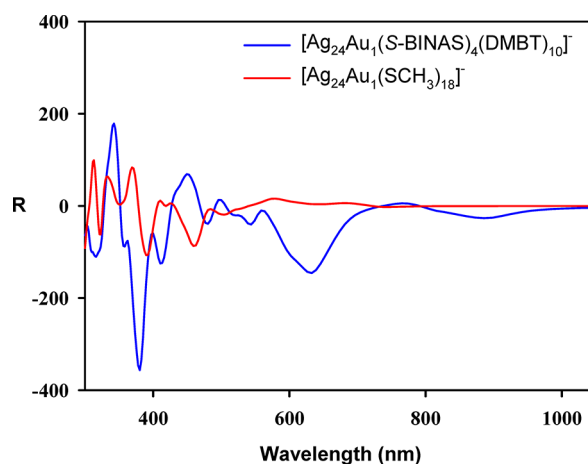


**Figure 9.** Circular dichroism rotatory strength ( $R$ ) calculated at the TDDFT level for the  $[\text{Ag}_{24}\text{Au}_1(\text{S-BINAS})_4(\text{DMBT})_{10}]^-$  cluster anion (geometry “best 1”) and a  $[\text{Ag}_{24}\text{Au}_1(\text{SCH}_3)_{18}]^-$  model structure derived from the “best 1” by transforming the BINAS and DMBT ligands into thiomethyl residues; see text for details.

the “best 1” structure. A residual, although much damped, CD activity for “best 1-CH<sub>3</sub>” is apparent, with values of rotator strength ( $R$ ) ranging between  $-50$  and  $+60$ . This finding suggests that the chiral desymmetrization due to the BINAS ligands partially transfers into the staple units but leaves the icosahedral metal core almost unaffected, as visualized in Figure S20, where we compare the  $\text{Ag}_{24}\text{Au}_1\text{S}_{18}$  skeletons of the geometries: “best 1-CH<sub>3</sub>” with the experimental structure of  $[\text{Ag}_{24}\text{Au}_1(\text{DMBT})_{18}]^-$ . Note that the TDDFT-simulated rotatory strength of a  $[\text{Ag}_{24}\text{Au}_1(\text{DMBT})_{18}]^-$  model structure calculated following the same protocol as used for  $[\text{Ag}_{24}\text{Au}_1(\text{S-BINAS})_4(\text{DMBT})_{10}]^-$  is negligible (as shown in Figure S21), confirming the achiral nature of the starting compound. We conclude that the CD of the  $[\text{Ag}_{24}\text{Au}_1(\text{S-BINAS})_4(\text{DMBT})_{10}]^-$  at 632 nm is not directly due to chiral BINAS ligands, but the chiral ligands induce a structural lowering of the symmetry of the  $\text{Ag}_{24}\text{Au}_1\text{S}_{18}$  framework, mainly in the staple units. The ligand’s tail groups also contribute significantly to the intensity of these CD bands.

DFT calculations predict the presence of a CD band at 632 nm, which is assigned to the experimental band at 645 nm for groups I–III. As shown in Figure S20, the  $\text{Ag}_{24}\text{Au}_1\text{S}_{18}$  skeleton of the “best 1-CH<sub>3</sub>” geometry of  $\text{Ag}_{24}\text{Au}_1(\text{S-BINAS})_4(\text{DMBT})_{10}$  exhibits structural distortions compared to that in the experimental structure of  $[\text{Ag}_{24}\text{Au}_1(\text{DMBT})_{18}]^-$ . The  $\text{Ag}_{24}\text{Au}_1(\text{R/S-BINAS})_x(\text{DMBT})_{18-2x}$  clusters with  $x = 5-7$  are more uniformly surrounded by the BINAS ligands, and the distortions by these uniformly arranged ligands could result in a more symmetric  $\text{Ag}_{24}\text{Au}_1\text{S}_{18}$  skeleton compared to that in the clusters with  $x = 1-4$  in I–III. This could result in the absence of this CD band at low energies. The absence of this band in group IV, in spite of the presence of clusters with  $x = 4$  in it, could be because of their lower concentrations in IV compared to that in III. Although the clusters with  $x = 4$  exhibit a CD band at 645 nm, it could be invisible due to the low concentration of these clusters compared to the other two clusters with  $x = 5-7$  which

do not show any such CD band. Therefore, we think that the absence of the CD band at 645 nm for IV could be due to the different relative concentrations of these two different types of clusters.

**Luminescence and Circularly Polarized Luminescence Measurements.** Figure 10 shows the photoluminescence

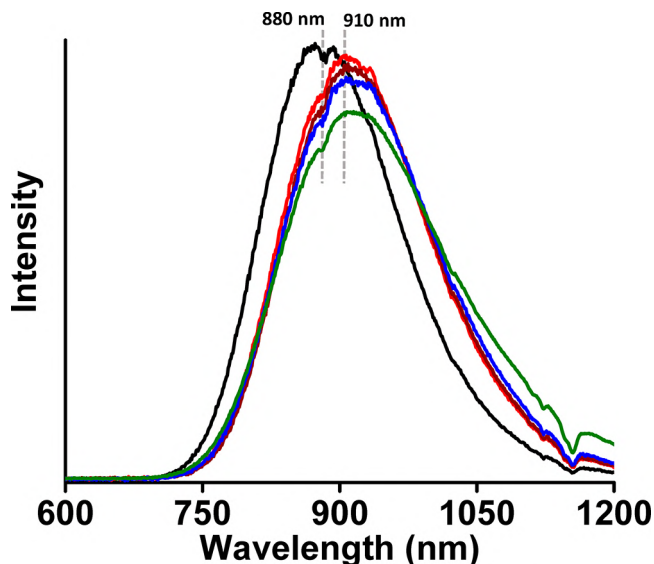


**Figure 10.** Luminescence spectra of  $\text{Ag}_{24}\text{Au}_1(\text{DMBT})_{18}$  (black) and  $\text{Ag}_{24}\text{Au}_1(\text{R-BINAS})_x(\text{DMBT})_{18-2x}$  group of clusters I (red), II (wine red), III (blue), and IV (green) collected at excitation wavelength of 467 nm.

spectra of  $\text{Ag}_{24}\text{Au}_1(\text{DMBT})_{18}$  and  $\text{Ag}_{24}\text{Au}_1(\text{R-BINAS})_x(\text{DMBT})_{18-2x}$  group of clusters I–IV. The excitation spectra of groups II and III are presented in Figures S22 and S23, respectively. The emission spectra of the parent  $\text{Ag}_{24}\text{Au}_1(\text{DMBT})_{18}$  and group II clusters collected at various excitation wavelengths are presented in the Figures S24 and S25, which shows that the nature of the emission band does not depend on the excitation wavelength. The emission maximum of groups I–IV undergoes a red shift of  $\sim 30$  nm with regard to that of  $\text{Ag}_{24}\text{Au}_1(\text{DMBT})_{18}$ . The red shift of the luminescence was further confirmed with clusters containing another bidentate ligand, namely, BPT, as presented in Figures S26 and S27.

The observed red shift in the emission bands of I–IV could either be due to the change in the ligand's tail group, that is, from 2,4-dimethylbenzyl to binaphthyl (through the extended conjugation of  $\pi$  electrons) or due to the structural distortion of the  $\text{Ag}_{24}\text{Au}_1\text{S}_{18}$  framework due to the bidentate mode of binding, as discussed previously. DFT calculations on  $\text{Ag}_{24}\text{Au}_1(\text{S-BINAS})_4(\text{DMBT})_{10}$  reveal that there is structural distortion on the  $\text{Ag}_{24}\text{Au}_1\text{S}_{18}$  framework. However, we note that the red shift of photoluminescence for the BPT-containing clusters ( $\sim 15$  nm) is less and almost half compared to that of BINAS-containing clusters ( $\sim 30$  nm), even though both the ligands are bidentate in nature. Furthermore, it is interesting to note that the red shift for the clusters containing 5–7 BPT ligands (see Figures S5 and S26) is less compared to that for the clusters with 4–7 BINAS ligands (see Figures 2D, S3D, and 10). However, there is no gradual increase in the red shift for these clusters as a function of the number of BINAS and BPT ligands in them. This can be due to the fact that all of the binaphthyl or biphenyl tail groups may not be able to adopt a favorable

(planar) arrangement on clusters. Hence, an increasing conjugation of the  $\pi$  electrons (resulting in an increased red shift) with increasing number of BINAS or BPT ligands may not be possible. These observations suggest that the conjugation effects indeed play a role in the observed red shift of the luminescence; however, the conjugation alone cannot be the reason for the red shift of absorption and emission bands and that both of these effects are contributing to the observed changes in the absorption and emission features of BINAS-containing clusters. As the cluster  $\text{Ag}_{24}\text{Au}_1(\text{S-BINAS})_4(\text{DMBT})_{10}$  represents the  $\text{Ag}_{24}\text{Au}_1(\text{R/S-BINAS})_x(\text{DMBT})_{18-2x}$  clusters in general, as mentioned previously, and DFT calculations show the involvement of binaphthyl groups in the MOs (see Table S1 and Figure S19) associated with the low-energy transitions, we think that the changes in absorption and emission bands could be due to the incorporation of the BINAS ligands and associated effects mentioned above. However, it is difficult to disentangle the contributions of the structural distortion and conjugation in greater detail from the present study.

The CD spectroscopic measurements presented above reveal that the incorporation of BINAS induces chiroptical signatures in these clusters. Therefore, it is worthwhile to check whether this induced chirality has any effect on the luminescence of these clusters. In order to test this, we carried out CPL spectroscopy on groups I–IV. Our measurements show that even though there are well-defined signatures in the CD spectra, these clusters exhibit very weak CPL activity, as shown in Figures S28 and S29. Due to the weak signal, averaged spectra are presented for each sample. Due to instrumental limitations, the fluorescence maximum could not be reached, so we can just say that within the observed range one may estimate a value of  $1.5 \times 10^{-4}$  for the  $g_{\text{lum}}$  ratio, whereas  $g_{\text{abs}}$  for the lowest-energy band is about  $5\text{--}8 \times 10^{-4}$ . We note that the clusters with R-BINAS and S-BINAS exhibit positive and negative CPL bands, respectively, which is in accordance with the signs of their CD bands (see Figures 4 and 5). Furthermore, we note that the group IV (i.e.,  $\text{Ag}_{24}\text{Au}_1(\text{R/S-BINAS})_x(\text{DMBT})_{18-2x}$  clusters with 4–7 BINAS ligands) do not exhibit any CPL bands within our detection limit (see Supplementary Note 1): this sample exhibits distinct UV/vis and CD bands at 475 and 347 nm (see Figure 3, traces d and d' in Figure 4 and Figure S13) but no CD signal at 645 nm (in the same experimental conditions of the other samples). A further discussion on the origin of luminescence in these clusters is presented in the next section in light of DFT calculations.

**Discussion on the Origin of Chiroptical Features and Photoluminescence in  $\text{Ag}_{24}\text{Au}_1(\text{SR})_{18}$  and  $\text{Ag}_{24}\text{Au}_1(\text{S-BINAS})_4(\text{DMBT})_{10}$ .** The  $\text{Ag}_{24}\text{Au}_1(\text{SR})_{18}$  is structurally analogous to  $\text{Au}_{25}(\text{SR})_{18}$  and  $\text{Ag}_{25}(\text{SR})_{18}$ . These clusters share common structural features, that is, an  $\text{M}_{13}$  icosahedral core and six  $\text{M}_2(\text{SR})_3$  staple motifs ( $\text{M} = \text{Ag}/\text{Au}$ ).<sup>2,3,36,48</sup> All three clusters (anions) are superatoms<sup>49,50</sup> with eight free valence electrons contributed from the metal atoms of their icosahedral cores and an overall negative charge. Considering the electronic absorption spectra, previous theoretical calculations suggest that the low-energy absorption band of these clusters (at  $\sim 690$  nm for  $\text{Au}_{25}(\text{SR})_{18}$ ,  $\sim 680$  nm for  $\text{Ag}_{25}(\text{SR})_{18}$ , and  $\sim 619$  nm for  $\text{Ag}_{24}\text{Au}_1(\text{SR})_{18}$ ) originates from the intraband transitions involving superatomic orbitals derived from the metal atoms of their  $\text{M}_{13}$  icosahedral core.<sup>13,19</sup> The electronic absorption bands at higher energies are due to various transitions involving the molecular orbitals with significant contributions from the

sulfur atoms and the tail groups of their ligands.<sup>19</sup> However, there are contradicting conclusions on the nature of the transitions responsible for their photoluminescence. As mentioned previously, experiments suggest that the photoluminescence in  $\text{Ag}_{24}\text{Au}_1(\text{DMBT})_{18}$  is due to the charge transfer processes involving the ligands,<sup>18</sup> whereas theoretical calculations by Aikens *et al.* suggest that the photoluminescence in  $\text{M}_{25}(\text{SR})_{18}$  ( $\text{M} = \text{Ag}/\text{Au}$ ) clusters is due to the transitions involving the icosahedral core-based superatomic orbitals and that the contribution of the ligands and the metal atoms in the staple motifs is not significant in these transitions.<sup>19</sup> We solve this discrepancy by noting that the orbital analysis in that work was limited to SH groups, instead of DMBT ligands, whose aromatic ligands are expected to behave quite differently with respect to the much simpler SH, due to coupling *via* conjugation between the ligand and the metal core.<sup>51</sup> Based on our experimental observations and DFT calculations presented above, we now discuss the nature of the electronic transitions responsible for the photoluminescence of  $\text{Ag}_{24}\text{Au}_1(\text{DMBT})_{18}$  and  $\text{Ag}_{24}\text{Au}_1(\text{R/S-BINAS})_x(\text{DMBT})_{18-2x}$  clusters.

UV/vis spectra show that the absorption band at around 619 nm for  $\text{Ag}_{24}\text{Au}_1(\text{DMBT})_{18}$  undergoes systematic changes with increasing number of incorporated BINAS ligands. The group of clusters I, II, and III exhibit strong absorption bands in the UV/vis spectra and corresponding CD bands (see Figures 3, 4, and S6). Similarly, the luminescence maximum of groups I–IV is red-shifted with regard to that of  $\text{Ag}_{24}\text{Au}_1(\text{DMBT})_{18}$ . Interestingly, even though the group IV  $\text{Ag}_{24}\text{Au}_1(\text{R-BINAS})_x(\text{DMBT})_{18-2x}$  clusters with 4–7 BINAS ligands exhibit a band in the UV/vis spectra at around 590 nm (Figure 3), this sample does not have the corresponding CD band (*i.e.*, there is no band in traces d and d' at low energies, corresponding to the ones at 645 nm for groups I–III; see Figure 4). Paralleling the UV/vis and the CD responses, no CPL was observed for this sample (see Supplementary Note 1), whereas weak CPL was observed for the other three  $\text{Ag}_{24}\text{Au}_1(\text{R-BINAS})_x(\text{DMBT})_{18-2x}$  clusters containing lower numbers of BINAS ligands.

In order to understand the origin of luminescence and CPL in  $\text{Ag}_{24}\text{Au}_1(\text{R/S-BINAS})_x(\text{DMBT})_{18-2x}$  clusters, the nature of molecular orbitals (in terms of the contributions of the metal atoms, in the cores and the staples, and ligands) involved in these transitions are to be considered. The MO diagram, based on the calculations on the model system,  $[\text{Ag}_{24}\text{Au}_1(\text{S-BINAS})_4(\text{DMBT})_{10}]^-$ , shows the leading contributions to the two lowest transitions at 795 nm (1.56 eV) and 632 nm (1.96 eV) for the geometry “best 1”, as shown in Figure 8. The DFT calculations show that the calculated CD band at around 632 nm is due to HOMO–1  $\rightarrow$  LUMO+2 and LUMO+3 transitions. Furthermore, the analysis of the molecular orbitals (see Figure 8, Figure S19, and Table S1) shows that the occupied molecular orbital (*i.e.*, HOMO–1) for this transition is mostly localized on the metal–ligand staple motifs (with noticeable Ag and S contributions), and the excited MOs (*i.e.*, LUMO+2 and LUMO+3) are mostly localized on the ligand's carbon atoms, giving an appreciable CD signal. However, this level of DFT predicts low-energy bands (estimated to lie around 795 nm by our TDDFT but arguably in the tail of the 632 nm at the experimental level), associated with HOMO–1, HOMO–2  $\rightarrow$  LUMO, LUMO+1 transitions, which are dark in the CD spectrum. For the photoluminescence and CPL activity, we can then argue that they should be assigned to an excitation transfer from the 632 nm band to its neighboring low-energy excited states (LUMO/LUMO+1, those calculated by TDDFT around 795 nm), which

should become the leading decay channel in luminescence and CPL. This suggests that the luminescence and CPL activity of  $\text{Ag}_{24}\text{Au}_1(\text{R/S-BINAS})_x(\text{DMBT})_{18-2x}$  clusters could arise from these low-lying excited states (LUMO and LUMO+1) where the contribution of the ligand's tail groups (C and H atoms) is lower compared to that in the higher excited states (LUMO+2 and LUMO+3) (see Figure 8). However, the contributions from of the whole ligand (all of the atoms, S, C, and H) are important, as indicated by the red shift in the luminescence maximum when the DMBT ligands are exchanged with BPT and BINAS ligand which have larger aromatic tail groups. The red shift could be due to the fact that corresponding molecular orbitals have lower energies in BPT and BINAS compared to that in DMBT. The nature of the LUMO and LUMO+1 also explains the low values of circularly polarized luminescence, as chiral bands are lost in the evolution of these excited states in which electrons reside in the less chiral  $\text{Ag}_{24}\text{Au}_1\text{S}_{18}$  framework of the cluster. As the CD response of the bands predicted at 795 nm is very weak, we expect a very low CPL signal, in agreement with experiment. This assignment is strongly corroborated by the red shift of  $\approx 30$  nm in the calculated photoabsorption band at 795 nm in going from  $\text{Ag}_{24}\text{Au}_1(\text{DMBT})_{18}$  to  $\text{Ag}_{24}\text{Au}_1(\text{R/S-BINAS})_x(\text{DMBT})_{18-2x}$  (see Figure 7, left panel), which matches a corresponding red shift as measured in the experimental photoluminescence spectra. In Table S2, an analysis of the calculated spectral bands at 765 and 590 nm of the parent, achiral cluster,  $\text{Ag}_{24}\text{Au}_1(\text{DMBT})_{18}$  is shown with the orbitals involved (see Figure S30). Their nature is similar as found in the  $[\text{Ag}_{24}\text{Au}_1(\text{S-BINAS})_4(\text{DMBT})_{10}]^-$  cluster, and the only difference is the absence of the ligand's aromatic ring participation at the 590 nm transition. Therefore, theoretical results and the correlations between the observed UV/vis, CD, luminescence, and CPL bands of groups I–IV with that of the  $\text{Ag}_{24}\text{Au}_1(\text{DMBT})_{18}$  confirm that the luminescence in these clusters occurs due to the transitions involving the whole  $\text{Ag}_{24}\text{Au}_1\text{S}_{18}$  framework and not merely from the icosahedral  $\text{Ag}_{12}\text{Au}_1$  core.

## CONCLUSIONS

In summary, we presented an experimental approach utilizing chiroptical spectroscopic techniques to probe the origin of electronic transitions responsible for the photoluminescence of an atomically precise noble metal cluster, namely,  $\text{Ag}_{24}\text{Au}_1(\text{DMBT})_{18}$ , and chiroptical responses in its chirally functionalized derivatives. To the best of our knowledge, a combination of the chiroptical and luminescence spectroscopies to understand the nature of electronic transitions has not been applied in such molecule-like metal clusters. In order to enable the use of chiroptical techniques, a chiral ligand, *R/S*-1,1'-[binaphthalene]-2,2'-dithiol (*R/S*-BINAS) was incorporated into  $\text{Ag}_{24}\text{Au}_1(\text{DMBT})_{18}$ , and a series of clusters of the general formula  $\text{Ag}_{24}\text{Au}_1(\text{R/S-BINAS})_x(\text{DMBT})_{18-2x}$ , with  $x = 1-7$ , were synthesized without altering the overall structure and composition. The effect of BINAS on the UV/vis, CD, luminescence, and CPL bands of these clusters was systematically analyzed, which reveals an unexpected transition of the low-energy electronic excitations from achiral to chiral and back to achiral from  $\text{Ag}_{24}\text{Au}_1(\text{DMBT})_{18}$  to  $\text{Ag}_{24}\text{Au}_1(\text{R/S-BINAS})_x(\text{DMBT})_{18-2x}$  by increasing the number of incorporated BINAS ligands. Our chiroptical spectroscopic measurements, in conjunction with DFT calculations, suggest that the photoluminescence in  $\text{Ag}_{24}\text{Au}_1(\text{DMBT})_{18}$  and its chirally functionalized derivatives originates from the transitions involving the

whole  $\text{Ag}_{24}\text{Au}_1\text{S}_{18}$  framework and not merely from the icosahedral  $\text{Ag}_{12}\text{Au}_1$  core, with an important contribution of conjugation effects with aromatic tails of the ligands.<sup>51</sup> These results show that the photoluminescence in these cluster systems cannot be solely attributed to any one of the structural components, that is, the metal core or the protecting metal–ligand oligomeric units, but rather to their interaction and that the ligand shell plays a crucial role.<sup>52</sup> Our work demonstrates that chiroptical spectroscopic techniques such as circular dichroism and circularly polarized luminescence represent useful tools to understand the nature of electronic transitions in ligand-protected metal clusters and that this approach can be utilized for gaining deeper insights into the structure–property relationships of the electronic transitions of such molecule-like cluster systems.

## EXPERIMENTAL SECTION

**Materials Used.** Silver nitrate ( $\text{AgNO}_3$ ), 2,4-dimethylbenzene thiol (DMBT), tetraphenylphosphonium bromide ( $\text{PPh}_4\text{Br}$ ), and sodium borohydride ( $\text{NaBH}_4$ ) were purchased from Sigma-Aldrich. Chloro-(triphenylphosphine)gold(I) ( $\text{AuClPPh}_3$ ) was purchased from Acros Chemicals. All solvents used, dichloromethane (DCM), methanol, etc., were of analytical grade and used without further purification. 1,1'-[binaphthalene]-2,2'-dithiol (BINAS) and 1,1'-biphenyldithiol (BPT) were synthesized by adopting the method reported previously.<sup>53–55</sup> Bio Beads SX-1 (Bio-Rad) for column size-exclusion chromatography was purchased from Bio-Rad Companies, USA.

**Instrumentation.** Ultraviolet–visible spectra were recorded on a Varian Cary 50 spectrophotometer using a quartz cuvette with a 10 mm path length. CD spectra were recorded on a JASCO J-815SE CD spectrometer using a quartz cuvette with a 2 mm path length. All CD and UV/vis measurements were carried out using DCM as the solvent.

Electrospray ionization mass spectra were measured on a QSTAR pulsar *i* (AB Sciex) using a quadrupole and time-of-flight analyzers. The spectra were measured in the mass range of  $m/z$  500–12,000 in the negative ion mode. Further details of the instrumental parameters used for the measurements are provided in the Supporting Information.

Emission spectra were measured on a Fluorolog-3 fluorescence spectrometer (Horiba JobinYvon) equipped with a liquid nitrogen-cooled NIR photomultiplier tube with an extended detection capability in the visible region (RS509-73, Hamamatsu). The measurements were carried out using a quartz cuvette with a 1 cm path length. DCM was used as solvent for all of the measurements. All of the emission spectra were collected at an excitation wavelength of 467 nm (unless otherwise stated) with an excitation monochromator slit of 5 nm and an emission slit of 2 nm.

Circularly polarized luminescence spectra were measured using a home-built spectrometer (allowing to simultaneously record also fluorescence spectra).<sup>56</sup> DCM was used as solvent for all of the measurements. The same solutions employed for CD measurements were used in a 10 mm  $\times$  2 mm fluorescence quartz cell. Excitation radiation (470 nm wavelength) was brought to the sample through an optical fiber from a Jasco FP8200 fluorimeter. Thirty scans were accumulated for each spectrum, with the following conditions: incident bandwidth of 20 nm, emission band pass of approximately 10 nm, and scan speed of 0.5 nm/s. The signal is very noisy due both to low fluorescence of samples and to low sensitivity of the instrument in the spectroscopic region of interest; for this reason, the spectra are plotted after an “adjacent average” over 100 points (data pitch 0.25 nm). The original spectra are reported in Figure S29.

**Synthesis of  $[\text{Ag}_{24}\text{Au}_1(\text{DMBT})_{18}][\text{PPh}_4]$ .**  $[\text{Ag}_{24}\text{Au}_1(\text{DMBT})_{18}][\text{PPh}_4]$  was synthesized by the reaction of  $[\text{Ag}_{25}(\text{DMBT})_{18}][\text{PPh}_4]$  with  $\text{AuClPPh}_3$  by adopting a reported procedure<sup>36</sup> with slight modifications.  $[\text{Ag}_{25}(\text{DMBT})_{18}][\text{PPh}_4]$  was synthesized by adopting a reported procedure.<sup>48</sup> To synthesize  $[\text{Ag}_{24}\text{Au}_1(\text{DMBT})_{18}][\text{PPh}_4]$ , 16 mg of  $[\text{Ag}_{25}(\text{DMBT})_{18}][\text{PPh}_4]$  was dissolved in 5 mL of DCM. Two hundred microliters of  $\text{AuClPPh}_3$  solution (4.2 mg in 500  $\mu\text{L}$  of DCM) was then added to it. The reaction mixture was gently shaken by hand

and kept undisturbed for about 2 h. The color of the solution changed from dark brown to dark green during this time interval, indicating the formation of  $[\text{Ag}_{24}\text{Au}_1(\text{DMBT})_{18}][\text{PPh}_4]$ . Formation of the alloy cluster was confirmed using UV/vis spectroscopy. The reaction mixture was then centrifuged at a speed of  $\sim 10000$  rpm for about ten minutes in order to remove any insoluble materials formed ( $\text{AgCl}$ , for example) and the supernatant DCM solution was collected and dried using a rotary evaporator. Then the reaction mixture was passed through a size exclusion chromatographic column using DCM as the eluting solvent. The pure  $[\text{Ag}_{24}\text{Au}_1(\text{DMBT})_{18}][\text{PPh}_4]$  thus obtained was dried using rotary evaporation.

**Synthesis of  $[\text{Ag}_{24}\text{Au}_1(\text{R/S-BINAS})_x(\text{DMBT})_{18-2x}][\text{PPh}_4]$ .** These clusters were synthesized through a ligand exchange reaction of  $[\text{Ag}_{24}\text{Au}_1(\text{DMBT})_{18}][\text{PPh}_4]$  with R/S-BINAS. The number of BINAS ligands incorporated (*i.e.*,  $x$ ) in the general molecular formula,  $[\text{Ag}_{24}\text{Au}_1(\text{R/S-BINAS})_x(\text{DMBT})_{18-2x}]$  is controlled by varying the  $\text{Ag}_{24}\text{Au}_1(\text{DMBT})_{18}/\text{BINAS}$  molar ratios. The groups of  $[\text{Ag}_{24}\text{Au}_1(\text{R/S-BINAS})_x(\text{DMBT})_{18-2x}]$  clusters with varying numbers of BINAS in them, I ( $x = 0-3$ ), II ( $x = 2-5$ ), and III ( $x = 3-5$ ), were synthesized at  $\text{Ag}_{24}\text{Au}_1(\text{DMBT})_{18}/\text{BINAS}$  molar ratios of 0.5:1.0, 0.25:1.0, and 0.1:1.0, respectively. The  $[\text{Ag}_{24}\text{Au}_1(\text{S-BINAS})_x(\text{DMBT})_{18-2x}]$  clusters of group IV ( $x = 4-7$ ) were synthesized at a  $\text{Ag}_{24}\text{Au}_1(\text{DMBT})_{18}/\text{S-BINAS}$  molar ratio of 0.01:1.0. The  $[\text{Ag}_{24}\text{Au}_1(\text{R-BINAS})_x(\text{DMBT})_{18-2x}]$  of group IV was synthesized by furthering the ligand exchange of the corresponding group II, wherein  $x = 2-5$ . For the synthesis of  $[\text{Ag}_{24}\text{Au}_1(\text{R/S-BINAS})_x(\text{DMBT})_{18-2x}]$  typically,  $\sim 2.5$  mg of  $[\text{Ag}_{24}\text{Au}_1(\text{DMBT})_{18}][\text{PPh}_4]$  was dissolved in 1 mL of DCM. Then, various volumes of R/S-BINAS solution (2 mg in 100  $\mu\text{L}$  of DCM) was added to it. The mixture was then shaken gently by hand and kept undisturbed for about 1.5 h at room temperature. The reaction mixture was then purified by size exclusion chromatography using DCM as the eluting solvent.

**Synthesis of  $[\text{Ag}_{24}\text{Au}_1(\text{BPT})_x(\text{DMBT})_{18-2x}][\text{PPh}_4]$ .** These clusters were synthesized through a ligand exchange reaction of  $[\text{Ag}_{24}\text{Au}_1(\text{DMBT})_{18}][\text{PPh}_4]$  with BPT. Typically, 2.0 mg of  $[\text{Ag}_{24}\text{Au}_1(\text{DMBT})_{18}][\text{PPh}_4]$  was dissolved in 1 mL of DCM. Then, various volumes of BPT solution (2 mg of BPT in 100  $\mu\text{L}$  of DCM) were added to it. The mixture was then shaken gently by hand and kept undisturbed for about 1 h at room temperature. The reaction mixture was then purified by size exclusion chromatography using DCM as the eluting solvent.

## ASSOCIATED CONTENT

### Supporting Information

The Supporting Information is available free of charge at <https://pubs.acs.org/doi/10.1021/acsnano.0c01183>.

Parameters used for ESI MS measurements, computational details, additional mass spectrometry data, UV/vis spectroscopy data, CD, luminescence, CPL data, additional DFT results, energies and coordinates of  $\text{Ag}_{24}\text{Au}_1(\text{DMBT})_{18}$ , all isomer structural models from the docking study (PDF)

## AUTHOR INFORMATION

### Corresponding Authors

**Thomas Bürgi** – Département de Chimie Physique, Université de Genève, 1211 Geneva 4, Switzerland; [orcid.org/0000-0003-0906-082X](https://orcid.org/0000-0003-0906-082X); Email: [thomas.buergi@unige.ch](mailto:thomas.buergi@unige.ch)

**Kumaranchira Ramankutty Krishnadas** – Département de Chimie Physique, Université de Genève, 1211 Geneva 4, Switzerland; Email: [krishnadas.kumaranchiraramankutty@unige.ch](mailto:krishnadas.kumaranchiraramankutty@unige.ch)

**Mauro Stener** – Dipartimento di Scienze Chimiche e Farmaceutiche, Università degli Studi di Trieste, 34127 Trieste, Italy; [orcid.org/0000-0003-3700-7903](https://orcid.org/0000-0003-3700-7903); Email: [stener@units.it](mailto:stener@units.it)

## Authors

Luca Sementa – CNR-ICCOM & IPCF, Consiglio Nazionale delle Ricerche, 56124 Pisa, Italy

Marco Medves – Dipartimento di Scienze Chimiche e Farmaceutiche, Università degli Studi di Trieste, 34127 Trieste, Italy

Alessandro Fortunelli – CNR-ICCOM & IPCF, Consiglio Nazionale delle Ricerche, 56124 Pisa, Italy; [orcid.org/0000-0001-5337-4450](https://orcid.org/0000-0001-5337-4450)

Alexandre Fürstenberg – Département de Chimie Analytique et Minérale, Université de Genève, 1211 Geneva 4, Switzerland; [orcid.org/0000-0002-6227-3122](https://orcid.org/0000-0002-6227-3122)

Giovanna Longhi – Dipartimento di Medicina Molecolare e Traslazionale, Università di Brescia, 25123 Brescia, Italy; [orcid.org/0000-0002-0011-5946](https://orcid.org/0000-0002-0011-5946)

Complete contact information is available at:

<https://pubs.acs.org/10.1021/acsnano.0c01183>

## Notes

The authors declare no competing financial interest.

## ACKNOWLEDGMENTS

Financial support from the University of Geneva and the Swiss National Science Foundation (Grant No. 200020\_172511) is kindly acknowledged. We also acknowledge the support from the MZ 2.0 mass spectrometry core facility at the Faculty of Sciences, University of Geneva. This work was supported by Stiftung Beneficentia and by Finanziamento per la Ricerca di Ateneo (FRA) of the Università degli Studi di Trieste. Computational resources from the Cineca Supercomputing Center is gratefully acknowledged (Project CHROMPC). We thank Dr. Arnulf Rosspeintner for fruitful discussions.

## REFERENCES

- (1) Jadzinsky, P. D.; Calero, G.; Ackerson, C. J.; Bushnell, D. A.; Kornberg, R. D. Structure of a Thiol Monolayer-Protected Gold Nanoparticle at 1.1 Å Resolution. *Science* **2007**, *318*, 430–433.
- (2) Akola, J.; Walter, M.; Whetten, R. L.; Häkkinen, H.; Grönbeck, H. On the Structure of Thiolate-Protected Au<sub>25</sub>. *J. Am. Chem. Soc.* **2008**, *130*, 3756–3757.
- (3) Heaven, M. W.; Dass, A.; White, P. S.; Holt, K. M.; Murray, R. W. Crystal Structure of the Gold Nanoparticle [N(C<sub>8</sub>H<sub>17</sub>)<sub>4</sub>]-[Au<sub>25</sub>(SCH<sub>2</sub>CH<sub>2</sub>Ph)<sub>18</sub>]. *J. Am. Chem. Soc.* **2008**, *130*, 3754–3755.
- (4) Lopez-Acevedo, O.; Tsunoyama, H.; Tsukuda, T.; Häkkinen, H.; Aikens, C. M. Chirality and Electronic Structure of the Thiolate-Protected Au<sub>38</sub> Nanocluster. *J. Am. Chem. Soc.* **2010**, *132*, 8210–8218.
- (5) Qian, H.; Eckenhoff, W. T.; Zhu, Y.; Pintauer, T.; Jin, R. Total Structure Determination of Thiolate-Protected Au<sub>38</sub> Nanoparticles. *J. Am. Chem. Soc.* **2010**, *132*, 8280–8281.
- (6) Dolamic, I.; Knoppe, S.; Dass, A.; Bürgi, T. First Enantioseparation and Circular Dichroism Spectra of Au<sub>38</sub> Clusters Protected by Achiral Ligands. *Nat. Commun.* **2012**, *3*, 798.
- (7) Desireddy, A.; Conn, B. E.; Guo, J.; Yoon, B.; Barnett, R. N.; Monahan, B. M.; Kirschbaum, K.; Griffith, W. P.; Whetten, R. L.; Landman, U.; Bigioni, T. P. Ultrastable Silver Nanoparticles. *Nature* **2013**, *501*, 399–402.
- (8) Yang, H.; Wang, Y.; Huang, H.; Gell, L.; Lehtovaara, L.; Malola, S.; Häkkinen, H.; Zheng, N. All-Thiol-Stabilized Ag<sub>44</sub> And Au<sub>12</sub>Ag<sub>32</sub> Nanoparticles with Single-Crystal Structures. *Nat. Commun.* **2013**, *4*, 2422.
- (9) Harkness, K. M.; Tang, Y.; Dass, A.; Pan, J.; Kothalawala, N.; Reddy, V. J.; Cliffl, D. E.; Demeler, B.; Stellacci, F.; Bakr, O. M.; McLean, J. A. Ag<sub>44</sub>(SR)<sub>30</sub><sup>4-</sup>: A Silver-Thiolate Superatom Complex. *Nanoscale* **2012**, *4*, 4269–4274.

(10) Chakraborty, I.; Pradeep, T. Atomically Precise Clusters of Noble Metals: Emerging Link between Atoms and Nanoparticles. *Chem. Rev.* **2017**, *117*, 8208–8271.

(11) Jin, R.; Zeng, C.; Zhou, M.; Chen, Y. Atomically Precise Colloidal Metal Nanoclusters and Nanoparticles: Fundamentals and Opportunities. *Chem. Rev.* **2016**, *116*, 10346–10413.

(12) Krishnadas, K. R.; Baksi, A.; Ghosh, A.; Natarajan, G.; Pradeep, T. Structure-Conserving Spontaneous Transformations between Nanoparticles. *Nat. Commun.* **2016**, *7*, 13447.

(13) Zhu, M.; Aikens, C. M.; Hollander, F. J.; Schatz, G. C.; Jin, R. Correlating the Crystal Structure of a Thiol-Protected Au<sub>25</sub> Cluster and Optical Properties. *J. Am. Chem. Soc.* **2008**, *130*, 5883–5885.

(14) Aikens, C. M. Origin of Discrete Optical Absorption Spectra of M<sub>25</sub>(SH)<sub>18</sub><sup>-</sup> Nanoparticles (M = Au, Ag). *J. Phys. Chem. C* **2008**, *112*, 19797–19800.

(15) Fernando, A.; Weerawardene, K. L. D. M.; Karimova, N. V.; Aikens, C. M. Quantum Mechanical Studies of Large Metal, Metal Oxide, and Metal Chalcogenide Nanoparticles and Clusters. *Chem. Rev.* **2015**, *115*, 6112–6216.

(16) Xie, J.; Zheng, Y.; Ying, J. Y. Highly Selective and Ultrasensitive Detection of Hg<sup>2+</sup>-Based on Fluorescence Quenching of Au Nanoclusters by Hg<sup>2+</sup>-Au<sup>+</sup> Interactions. *Chem. Commun.* **2010**, *46*, 961–963.

(17) Wu, Z.; Jin, R. On the Ligand's Role in the Fluorescence of Gold Nanoclusters. *Nano Lett.* **2010**, *10*, 2568–2573.

(18) Liu, X.; Yuan, J.; Yao, C.; Chen, J.; Li, L.; Bao, X.; Yang, J.; Wu, Z. Crystal and Solution Photoluminescence of MAg<sub>24</sub>(SR)<sub>18</sub> (M = Ag/Pd/Pt/Au) Nanoclusters and Some Implications for the Photoluminescence Mechanisms. *J. Phys. Chem. C* **2017**, *121*, 13848–13853.

(19) Weerawardene, K. L. D. M.; Aikens, C. M. Origin of Photoluminescence of Ag<sub>25</sub>(SR)<sub>18</sub><sup>-</sup> Nanoparticles: Ligand and Doping Effect. *J. Phys. Chem. C* **2018**, *122*, 2440–2447.

(20) Mustalahti, M.; Myllyperkiö, P.; Malola, S.; Lahtinen, T.; Salorinne, K.; Koivisto, J.; Häkkinen, H.; Pettersson, M. Molecule-Like Photodynamics of Au<sub>102</sub>(pMBA)<sub>44</sub> Nanocluster. *ACS Nano* **2015**, *9*, 2328–2335.

(21) Mustalahti, S.; Myllyperkiö, P.; Lahtinen, T.; Salorinne, K.; Malola, S.; Koivisto, J.; Häkkinen, H.; Pettersson, M. Ultrafast Electronic Relaxation and Vibrational Cooling Dynamics of Au<sub>144</sub>(SC<sub>2</sub>H<sub>4</sub>Ph)<sub>60</sub> Nanocluster Probed by Transient Mid-IR Spectroscopy. *J. Phys. Chem. C* **2014**, *118*, 18233–18239.

(22) Green, T. D.; Yi, C.; Zeng, C.; Jin, R.; McGill, S.; Knappenberger, K. L., Jr. Temperature-Dependent Photoluminescence of Structurally-Precise Quantum-Confined Au<sub>25</sub>(SC<sub>8</sub>H<sub>9</sub>)<sub>18</sub> and Au<sub>38</sub>(SC<sub>12</sub>H<sub>25</sub>)<sub>24</sub> Metal Nanoparticles. *J. Phys. Chem. A* **2014**, *118*, 10611–10621.

(23) Li, Q.; Zhou, M.; So, W. Y.; Huang, J.; Li, M.; Kauffman, D. R.; Cotlet, M.; Higaki, T.; Peteanu, L. A.; Shao, Z.; Jin, R. A Monocuboctahedral Series of Gold Nanoclusters: Photoluminescence Origin, Large Enhancement, Wide Tunability, and Structure-Property Correlation. *J. Am. Chem. Soc.* **2019**, *141*, 5314–5325.

(24) Riehl, J. P.; Richardson, F. S. Circularly Polarized Luminescence Spectroscopy. *Chem. Rev.* **1986**, *86*, 1–16.

(25) Kumar, J.; Nakashima, T.; Kawai, T. Circularly Polarized Luminescence in Chiral Molecules and Supramolecular Assemblies. *J. Phys. Chem. Lett.* **2015**, *6*, 3445–3452.

(26) Longhi, G.; Castiglioni, E.; Koshoubu, J.; Mazzeo, G.; Abbate, S. Circularly Polarized Luminescence: A Review of Experimental and Theoretical Aspects. *Chirality* **2016**, *28*, 696–707.

(27) Schaaff, T. G.; Whetten, R. L. Giant Gold-Glutathione Cluster Compounds: Intense Optical Activity in Metal-Based Transitions. *J. Phys. Chem. B* **2000**, *104*, 2630–2641.

(28) Zhu, M.; Qian, H.; Meng, X.; Jin, S.; Wu, Z.; Jin, R. Chiral Au<sub>25</sub>Nanospheres and Nanorods: Synthesis and Insight into the Origin of Chirality. *Nano Lett.* **2011**, *11*, 3963–3969.

(29) Sanchez-Castillo, A.; Noguez, C.; Garzon, I. L. On the Origin of the Optical Activity Displayed by Chiral-Ligand-Protected Metallic Nanoclusters. *J. Am. Chem. Soc.* **2010**, *132*, 1504–1505.

(30) Noguez, C.; Garzon, I. L. Optically Active Metal Nanoparticles. *Chem. Soc. Rev.* **2009**, *38*, 757–771.

- (31) Zeng, C.; Chen, C.; Liu, C.; Nobusada, K.; Rosi, N. L.; Jin, R. Gold Tetrahedra Coil Up: Kekulé-Like and Double Helical Superstructures. *Sci. Adv.* **2015**, *1*, No. e1500425.
- (32) Pelayo, J. J.; Whetten, R. L.; Garzon, I. L. Geometric Quantification of Chirality in Ligand-Protected Metal Clusters. *J. Phys. Chem. C* **2015**, *119*, 28666–28678.
- (33) Tanaka, H.; Kato, Y.; Fujiki, M.; Inoue, Y.; Mori, T. Combined Experimental and Theoretical Study on Circular Dichroism and Circularly Polarized Luminescence of Configurationally Robust D<sub>3</sub>-Symmetric Triple Pentahelicene. *J. Phys. Chem. A* **2018**, *122*, 7378–7384.
- (34) Longhi, G.; Castiglioni, E.; Abbate, S.; Lebon, F.; Lightner, D. A. Experimental and Calculated CPL Spectra and Related Spectroscopic Data of Camphor and Other Simple Chiral Bicyclic Ketones. *Chirality* **2013**, *25*, 589–599.
- (35) Mori, T. Frontiers of Circularly Polarized Luminescence Chemistry of Isolated Small Organic Molecules. *Circularly Polarized Luminescence of Isolated Small Organic Molecules*, 1st ed.; Springer: Singapore, 2020; pp 1–10.
- (36) Bootharaju, M. S.; Joshi, C. P.; Parida, M. R.; Mohammed, O. F.; Bakr, O. M. Templated Atom-Precise Galvanic Synthesis and Structure Elucidation of a [Ag<sub>24</sub>Au(SR)<sub>18</sub>]<sup>-</sup> Nanocluster. *Angew. Chem.* **2016**, *128*, 934–938.
- (37) Knoppe, S.; Bürgi, T. The Fate of Au<sub>25</sub>(SR)<sub>18</sub> Clusters upon Ligand Exchange with Binaphthyl-Dithiol: Interstaple Binding vs Decomposition. *Phys. Chem. Chem. Phys.* **2013**, *15*, 15816–15820.
- (38) Sels, A.; Barrabés, N.; Knoppe, S.; Bürgi, T. Isolation of Atomically Precise Mixed Ligand Shell PdAu<sub>24</sub> Clusters. *Nanoscale* **2016**, *8*, 11130–11135.
- (39) Jupally, V. R.; Kota, R.; Dornshuld, E. V.; Mattern, D. L.; Tschumper, G. S.; Jiang, D.-e.; Dass, A. Interstaple Dithiol Cross-Linking in Au<sub>25</sub>(SR)<sub>18</sub> Nanomolecules: A Combined Mass Spectrometric and Computational Study. *J. Am. Chem. Soc.* **2011**, *133*, 20258–20266.
- (40) Molina, B.; Sánchez-Castillo, A.; Knoppe, S.; Garzón, I. L.; Bürgi, T.; Tlahuice-Flores, A. Structures and Chiroptical Properties of the BINAS-Monosubstituted Au<sub>38</sub>(SCH<sub>3</sub>)<sub>24</sub> Cluster. *Nanoscale* **2013**, *5*, 10956–10962.
- (41) Baseggio, O.; Fronzoni, G.; Stener, M. A New Time Dependent Density Functional Algorithm for Large Systems and Plasmons in Metal Clusters. *J. Chem. Phys.* **2015**, *143*, 024106.
- (42) Baseggio, O.; Toffoli, D.; Fronzoni, G.; Stener, M.; Sementa, L.; Fortunelli, A. Extension of the Time Dependent Density Functional Complex Polarizability Algorithm to Circular Dichroism: Implementation and Applications to Ag<sub>8</sub> and Au<sub>38</sub>(SC<sub>2</sub>H<sub>4</sub>C<sub>6</sub>H<sub>5</sub>)<sub>24</sub>. *J. Phys. Chem. C* **2016**, *120*, 24335–24345.
- (43) Baseggio, O.; De Vetta, M.; Fronzoni, G.; Toffoli, D.; Stener, M.; Sementa, L.; Fortunelli, A. Time-Dependent Density-Functional Study of the Photoabsorption Spectrum of Au<sub>25</sub>(SC<sub>2</sub>H<sub>4</sub>C<sub>6</sub>H<sub>5</sub>)<sub>18</sub> Anion: Validation of the Computational Protocol. *Int. J. Quantum Chem.* **2018**, *118*, No. e25769.
- (44) Becke, A. D. Density-Functional Thermochemistry. III. The Role of Exact Exchange. *J. Chem. Phys.* **1993**, *98*, 5648–5652.
- (45) Medves, M.; Sementa, L.; Toffoli, D.; Fronzoni, G.; Fortunelli, A.; Stener, M. An Efficient Hybrid Scheme for Time Dependent Density Functional Theory. *J. Chem. Phys.* **2020**, *152*, 184104.
- (46) Toffoli, D.; Baseggio, O.; Fronzoni, G.; Stener, M.; Fortunelli, A.; Sementa, L. Pd Doping, Conformational, and Charge Effects on the Dichroic Response of a Monolayer Protected Au<sub>38</sub>(SR)<sub>24</sub> Nanocluster. *Phys. Chem. Chem. Phys.* **2019**, *21*, 3585–3596.
- (47) Chang, L.; Baseggio, O.; Sementa, L.; Cheng, D.; Fronzoni, G.; Toffoli, D.; Aprà, E.; Stener, M.; Fortunelli, A. Individual Component Map of Rotatory Strength and Rotatory Strength Density Plots as Analysis Tools of Circular Dichroism Spectra of Complex Systems. *J. Chem. Theory Comput.* **2018**, *14*, 3703–3714.
- (48) Joshi, C. P.; Bootharaju, M. S.; Alhilaly, M. J.; Bakr, O. M. [Ag<sub>25</sub>(SR)<sub>18</sub>]<sup>-</sup>: The “Golden” Silver Nanoparticle. *J. Am. Chem. Soc.* **2015**, *137*, 11578–11581.
- (49) Walter, M.; Akola, J.; Lopez-Acevedo, O.; Jadzinsky, P. D.; Calero, G.; Ackerson, C. J.; Whetten, R. L.; Grönbeck, H.; Häkkinen, H. A Unified View of Ligand-Protected Gold Clusters as Superatom Complexes. *Proc. Natl. Acad. Sci. U. S. A.* **2008**, *105*, 9157–9162.
- (50) Häkkinen, H. Atomic and Electronic Structure of Gold Clusters: Understanding Flakes, Cages and Superatoms from Simple Concepts. *Chem. Soc. Rev.* **2008**, *37*, 1847–1859.
- (51) Sementa, L.; Barcaro, G.; Dass, A.; Stener, M.; Fortunelli, A. Designing Ligand-Enhanced Optical Absorption of Thiolated Gold Nanoclusters. *Chem. Commun.* **2015**, *51*, 7935–7938.
- (52) Rambukwella, M.; Sakthivel, N. A.; Delcamp, J. H.; Sementa, L.; Fortunelli, A.; Dass, A. Ligand Structure Determines Nanoparticles’ Atomic Structure, Metal-Ligand Interface and Properties. *Front. Chem.* **2018**, *6*, 330.
- (53) Fabbri, D.; Delogu, G.; De Lucchi, O. Preparation of Enantiomerically Pure 1,1'-Binaphthalene-2,2'-Diol and 1,1'-Binaphthalene-2,2'-Dithiol. *J. Org. Chem.* **1993**, *58*, 1748–1750.
- (54) He, H.; Chen, L.-Y.; Wong, W.-Y.; Chan, W.-H.; Lee, A. W. M. Practical Synthetic Approach to Chiral Sulfonylimides (CSIs) - Chiral Brønsted Acids for Organocatalysis. *Eur. J. Org. Chem.* **2010**, *2010*, 4181–4184.
- (55) Knoppe, S.; Azoulay, R.; Dass, A.; Bürgi, T. *In Situ* Reaction Monitoring Reveals a Diastereoselective Ligand Exchange Reaction between the Intrinsically Chiral Au<sub>38</sub>(SR)<sub>24</sub> and Chiral Thiols. *J. Am. Chem. Soc.* **2012**, *134*, 20302–20305.
- (56) Castiglioni, E.; Abbate, S.; Longhi, G. Revisiting with Updated Hardware an Old Spectroscopic Technique: Circularly Polarized Luminescence. *Appl. Spectrosc.* **2010**, *64*, 1416–1419.

## Supporting Information for the paper:

### Chiral Functionalization of an Atomically Precise Noble Metal Cluster: Insights into the Origin of Chirality and Photoluminescence

*Kumaranchira Ramankutty Krishnadas*<sup>\*a</sup>, *Luca Sementa*<sup>b</sup>, *Marco Medves*<sup>c</sup>, *Alessandro Fortunelli*,<sup>b</sup> *Mauro Stener*,<sup>\*c</sup> *Alexandre Fürstenberg*,<sup>d</sup> *Giovanna Longhi*,<sup>e</sup> *Thomas Bürgi*<sup>\*a</sup>

<sup>a</sup>Département de Chimie Physique, Université de Genève, 30 Quai Ernest-Ansermet, 1211 Genève 4, Switzerland

<sup>b</sup>CNR-ICCOM & IPCF, Consiglio Nazionale delle Ricerche, Via Giuseppe Moruzzi 1, Pisa, Italy.

<sup>c</sup>Dipartimento di Scienze Chimiche e Farmaceutiche, Università degli Studi di Trieste, Via Giorgieri 1, 34127 Trieste, Italy.

<sup>d</sup>Département de Chimie Analytique et Minérale, Université de Genève

30 Quai Ernest-Ansermet, 1211 Geneva 4, Switzerland.

<sup>e</sup>Dipartimento di Medicina Molecolare e Traslazionale, Università di Brescia, Viale Europa 11, 25123, Brescia, Italy.

#### Parameters used for ESI MS measurements

The sample solubilized in dichloromethane was analyzed by electrospray high resolution mass spectrometry (ESI HRMS) with the general instrumental parameters:

nano ESI voltage: 1900 kV (negative),

Curtain gas (N<sub>2</sub>): 20 psi,

Declustering and focusing lenses: DP = -110 V, DP2 = -20 V, FP = -250 V

Mass range: m/z 500 – 12'000 (accumulation time = 1s) with external TOF calibration (Agilent)

Bin:1 (automatic signal smoothing)

Data processing software: PeakView 2.2 (AB Sciex)

#### Computational Details

Density-functional theory (DFT) calculations of BINAS docking and thio-methyl models were conducted using the CP2K package.<sup>1</sup> Geometry optimizations were performed at the DFT/PBE level<sup>2</sup> plus Grimme-D3 dispersion terms.<sup>3</sup> In the DFT-PBE simulations, based on the hybrid Gaussian/Plane-Wave scheme (GPW)<sup>4</sup> as implemented in CP2K, double-zeta-valence-plus

polarization DZVP basis sets<sup>5</sup> plus GTH pseudopotentials<sup>6</sup> were used to represent the DFT Kohn–Sham orbitals, while the cut-off for the auxiliary plane wave representation of the density was set to 300 Ry. The so generated geometries were then fully optimized (no constraints) using the ADF package,<sup>7</sup> the Local Density Approximation (ALDA),<sup>8</sup> and a basis set of Slater Type Orbitals (STO) included in the ADF database of triple-zeta polarized (TZP) quality.

Chiroptical spectra were simulated using time-dependent DFT (TDDFT) *via* a complex polarizability algorithm,<sup>9, 10</sup> the ADF package,<sup>7</sup> and the LB94 exchange-correlation potential,<sup>11</sup> while the exchange-correlation kernel in the TDDFT part was approximated according to the Adiabatic LDA (ALDA).<sup>12</sup> A STO basis set of TZP quality was employed, which has proven to provide fully converged results.<sup>13</sup> The Zero Order Regular Approximation (ZORA)<sup>13</sup> was employed to include relativistic effects, which are important for heavy elements such as gold. The imaginary frequency employed to introduce finite lifetime of the excited state was fixed to 0.075 eV.

TDDFT/LB94 spectra were also analysed in terms of Individual Component Maps of Rotatory Strength (ICM.-RS) plots, as proposed in Ref. 14. These plots illustrate the contribution to the Rotatory Strength from the single-particle excitations in the (virtual/occupied) Molecular Orbital plane for an excited state at a given energy and in a given Cartesian direction, see Ref. 14 for a detailed discussion of the approach.

## Supporting Information 1

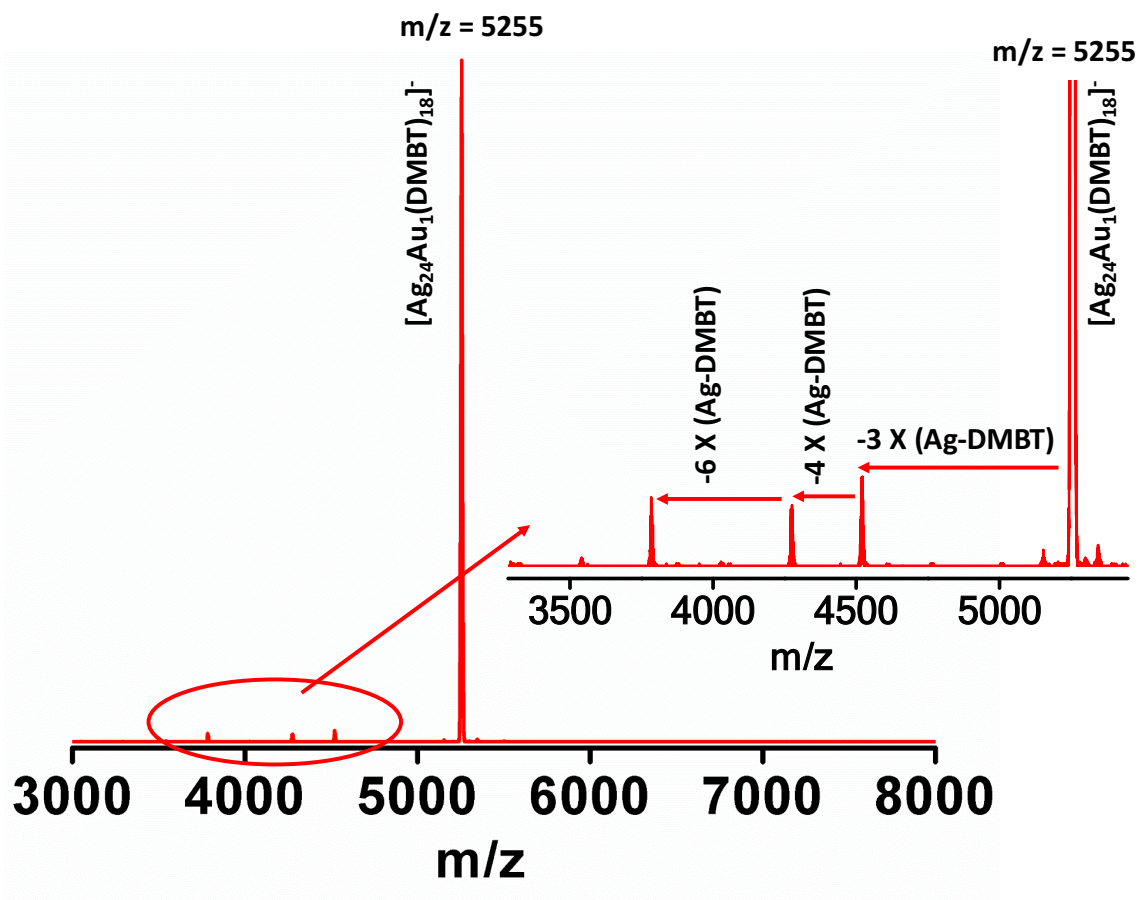


**Figure S1.** ESI MS spectrum of  $[\text{Ag}_{24}\text{Au}_1(\text{DMBT})_{18}][\text{PPh}_4]$  showing the molecular anion,  $[\text{Ag}_{24}\text{Au}_1(\text{DMBT})_{18}]^-$ , and its typical fragmentation pattern as shown in the inset.

## Supporting Information 2

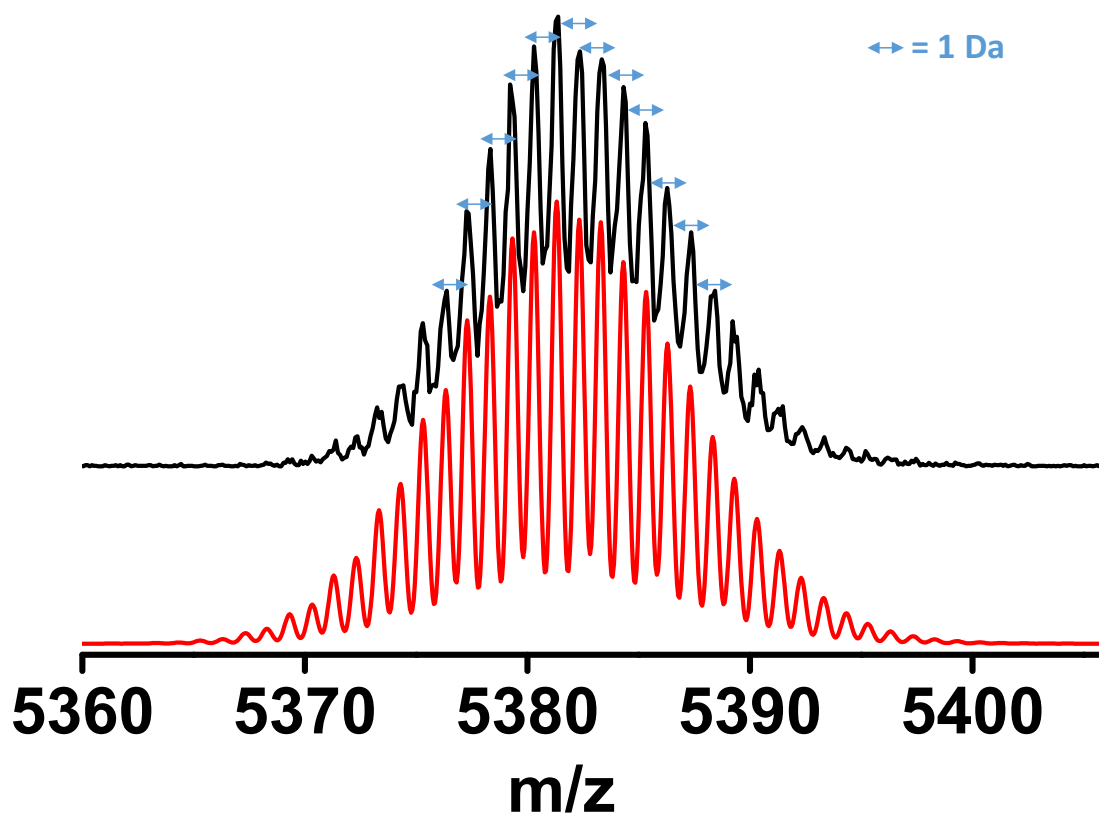


**Figure S2.** Negative ion ESI MS spectra showing the theoretical (red trace) and experimental (black trace) isotope patterns of  $\text{Ag}_{24}\text{Au}_1(\text{BINAS})_3(\text{DMBT})_{12}$ .

Supporting Information 3

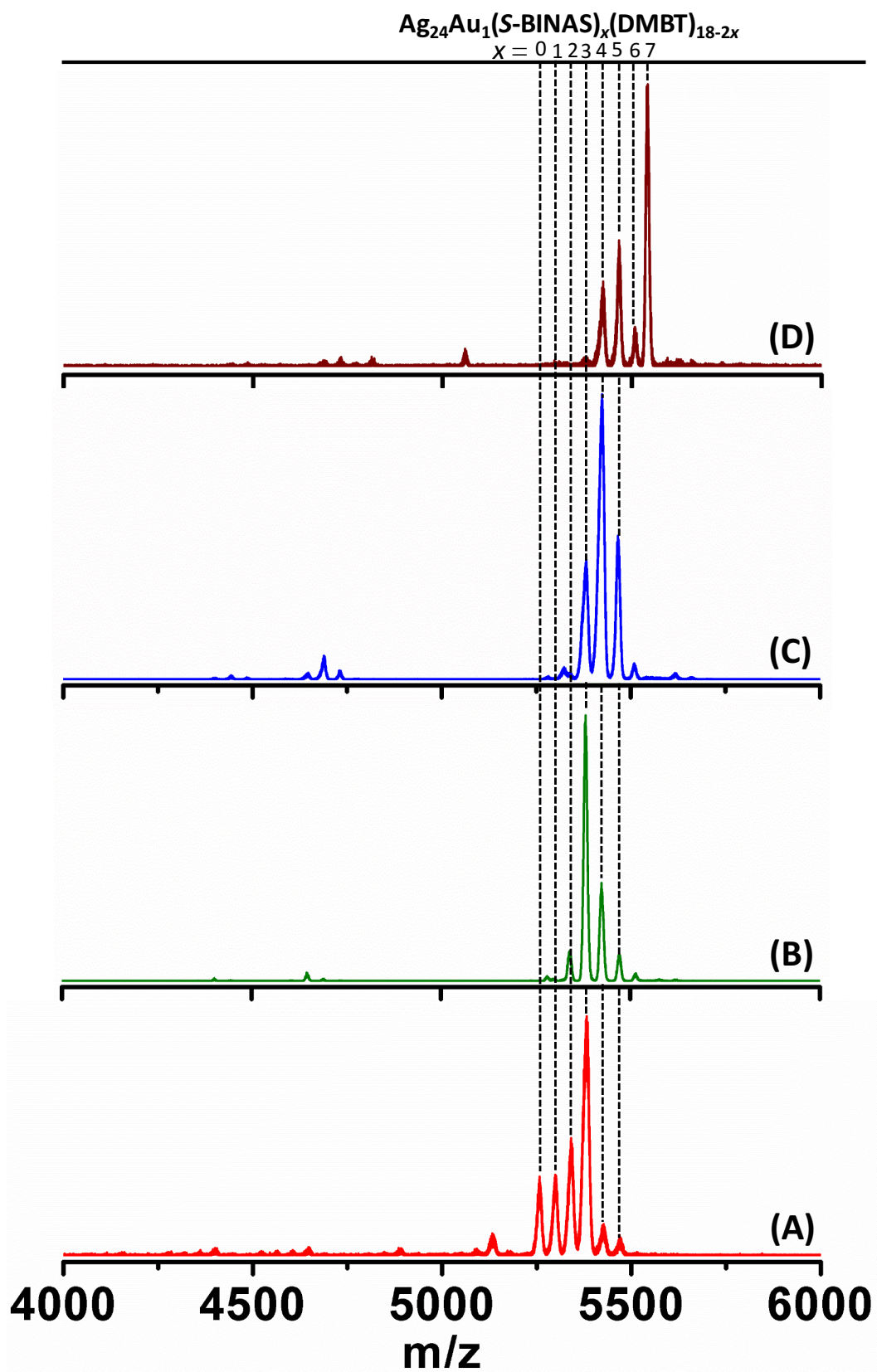


**Figure S3.** Negative ion ESI MS spectra of  $\text{Ag}_{24}\text{Au}_1(\text{S-BINAS})_x(\text{DMBT})_{18-2x}$  groups **I** (A), **II** (B), **III** (C) and **IV** (D) synthesized at various  $\text{Ag}_{24}\text{Au}_1(\text{DMBT})_{18}:\text{BINAS}$  molar ratios.

#### Supporting Information 4

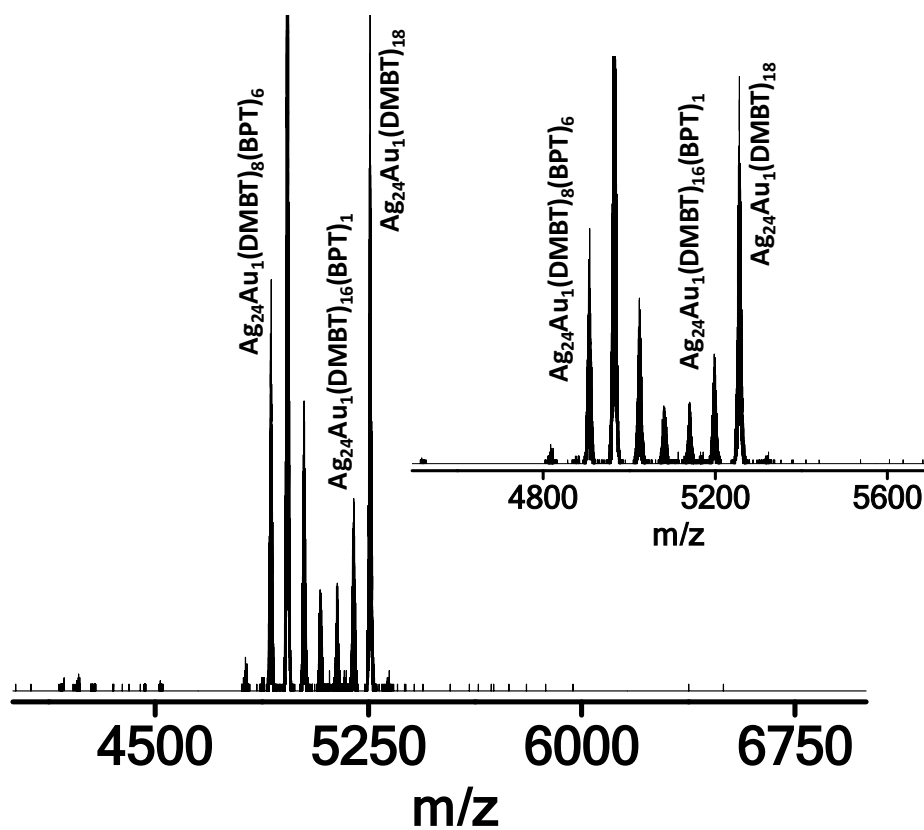


**Figure S4.** Negative ion ESI MS spectra of  $\text{Ag}_{24}\text{Au}_1(\text{BPT})_x(\text{DMBT})_{18-2x}$  clusters synthesized at  $\text{Ag}_{24}\text{Au}_1(\text{DMBT})_{18}:\text{BPT}$  molar ratio of 0.3:1.0. The inset shows a zoomed in view of the features.

## Supporting Information 5

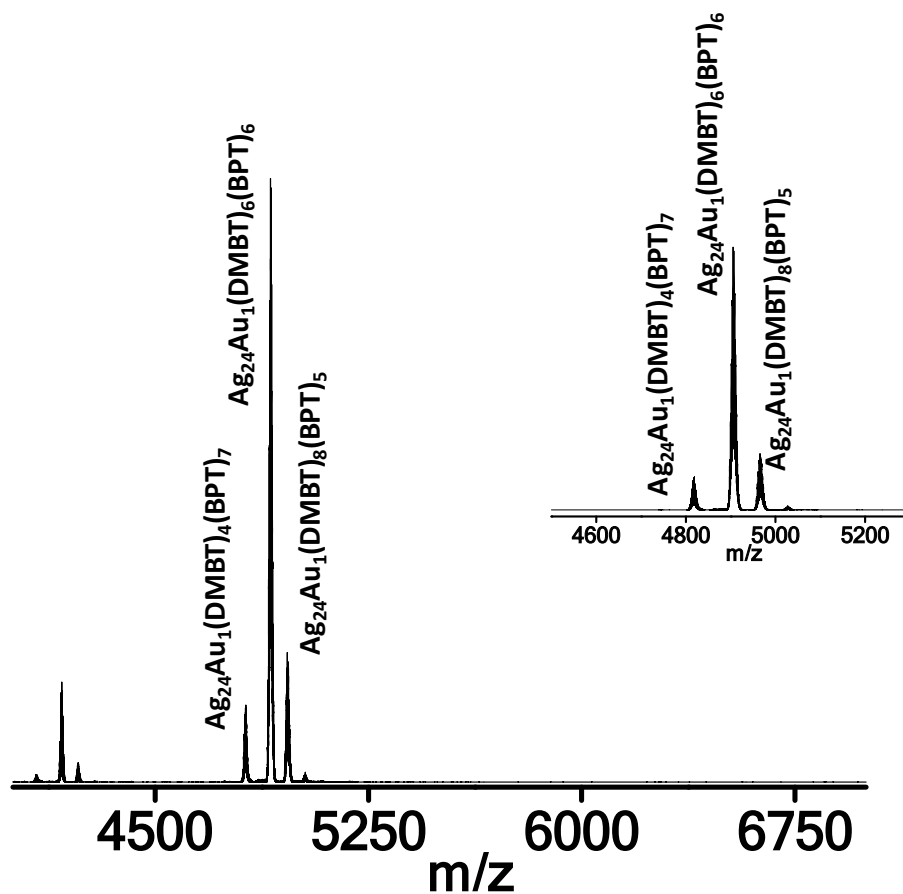


**Figure S5.** Negative ion ESI MS spectra of  $\text{Ag}_{24}\text{Au}_1(\text{BPT})_x(\text{DMBT})_{18-2x}$  clusters synthesized at  $\text{Ag}_{24}\text{Au}_1(\text{DMBT})_{18}:\text{BPT}$  molar ratio of 0.2:1.0. The features at below  $m/z$  4500 are due to the fragments (as presented in Figure S1) of the molecular ion features which are labeled. Inset shows a zoomed in view of the molecular ion region of these clusters.

## Supporting Information 6

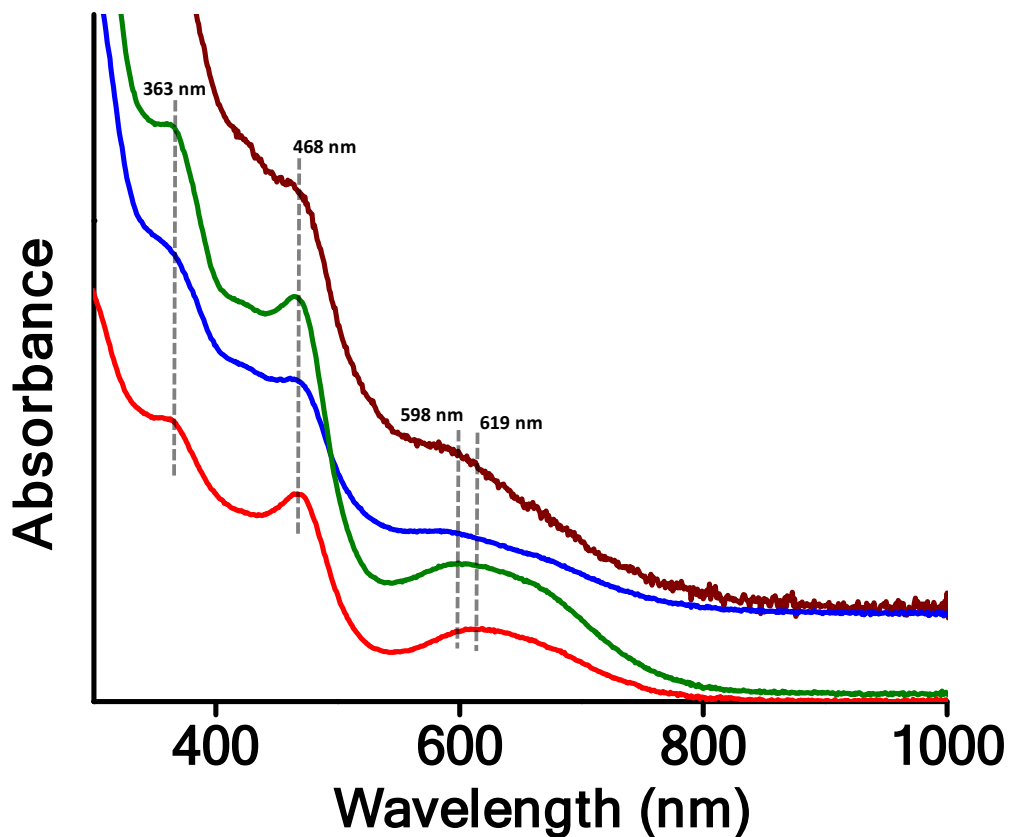


**Figure S6.** UV/Vis absorption spectra of  $\text{Ag}_{24}\text{Au}_1(\text{S-BINAS})_x(\text{DMBT})_{18-2x}$  group of clusters **I** (red trace), **II** (green trace), **III** (blue trace) and **IV** (wine red trace) synthesized at various  $\text{Ag}_{24}\text{Au}_1(\text{DMBT})_{18}:\text{BINAS}$  molar ratios. The mass spectra of these samples are presented in Figure S3.

## Supporting Information 7

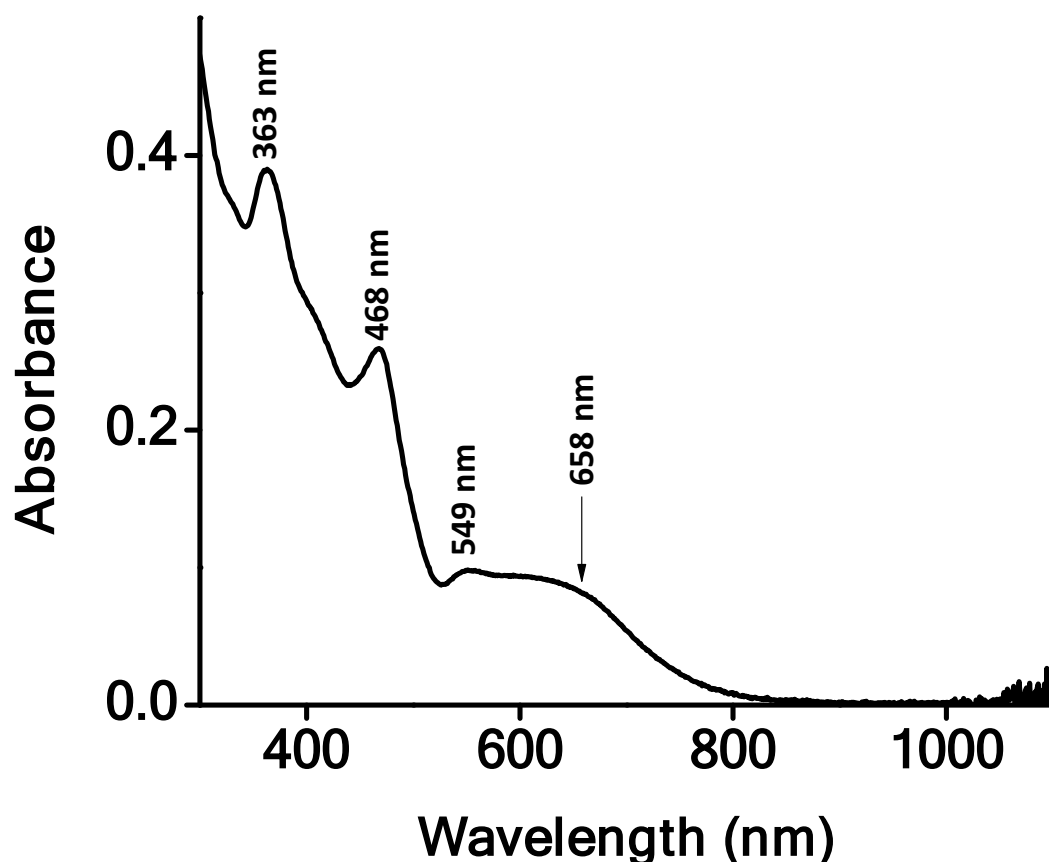


**Figure S7.** UV/Vis absorption spectra of Ag<sub>24</sub>Au<sub>1</sub>(BPT)<sub>x</sub>(DMBT)<sub>18-2x</sub> clusters synthesized at Ag<sub>24</sub>Au<sub>1</sub>(DMBT)<sub>18</sub>:BPT molar ratio of 0.3:1.0.

## Supporting Information 8

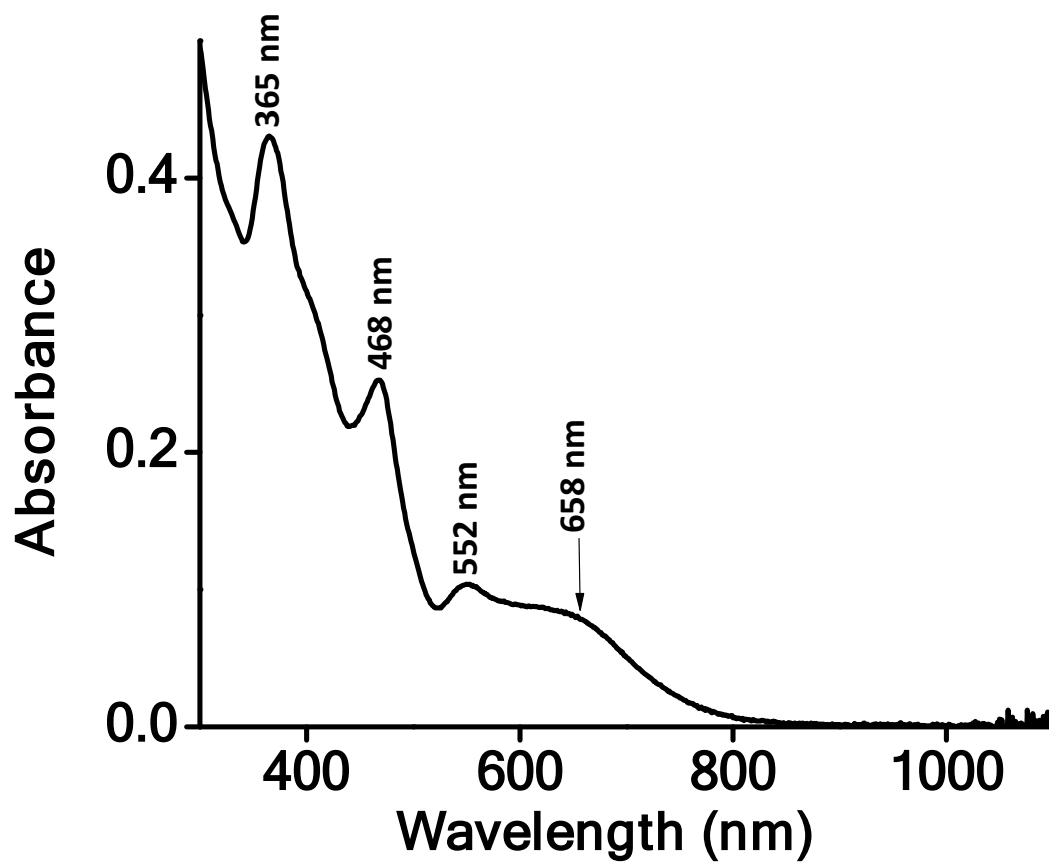


**Figure S8.** UV/Vis absorption spectra of Ag<sub>24</sub>Au<sub>1</sub>(BPT)<sub>x</sub>(DMBT)<sub>18-2x</sub> clusters synthesized at Ag<sub>24</sub>Au<sub>1</sub>(DMBT)<sub>18</sub>:BPT molar ratio of 0.2:1.0.

## Supporting Information 9

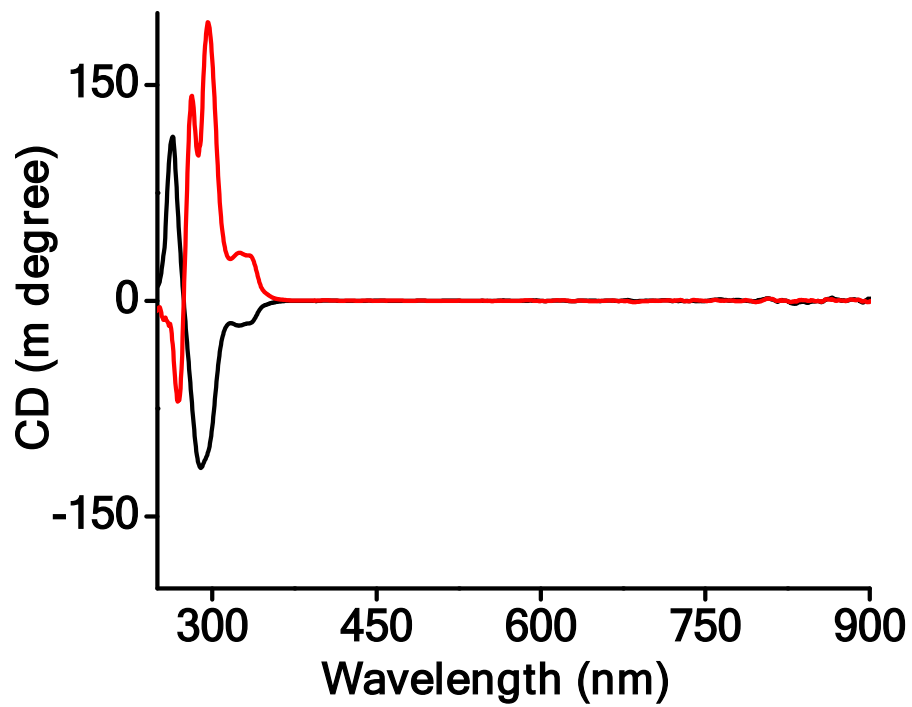


**Figure S9.** CD spectra of *R*-BINAS (red) and *S*-BINAS (black) measured in DCM.

Supporting Information 10

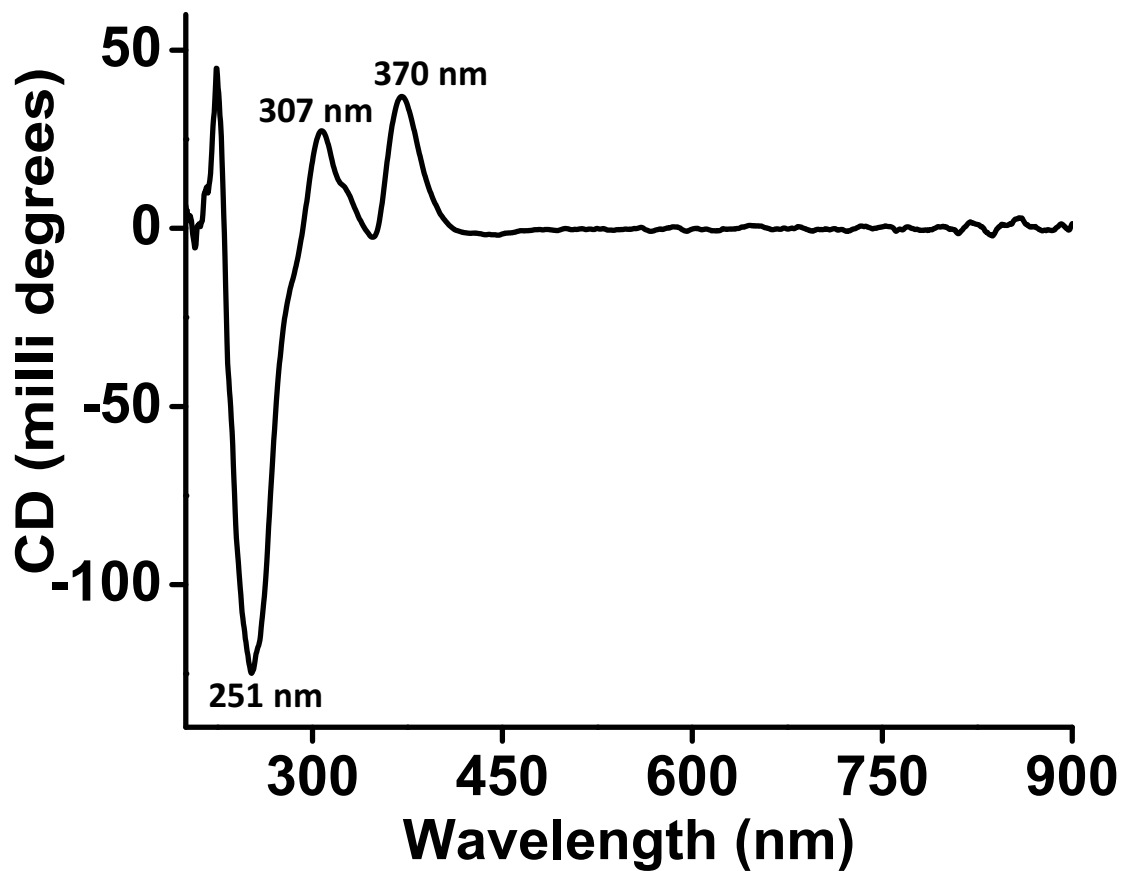
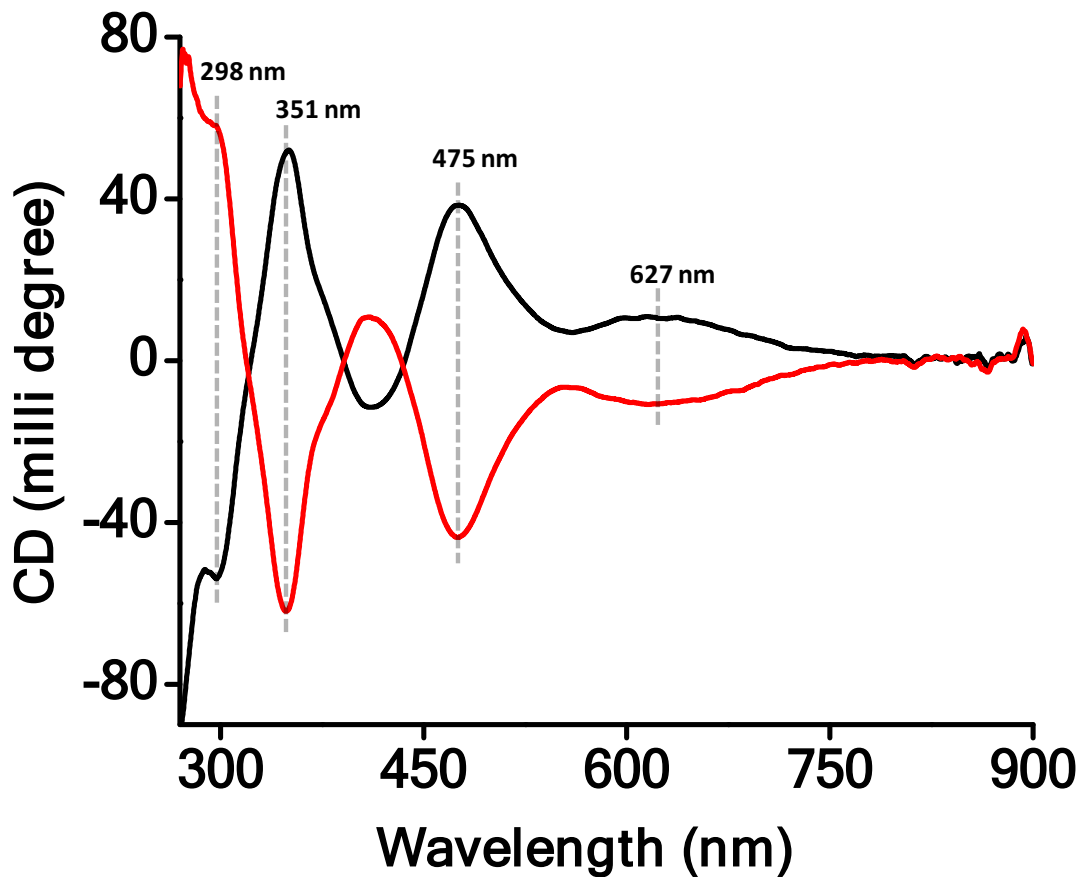


Figure S10. CD spectra of Ag-(*R*-BINAS) complex dispersed in DCM.

## Supporting Information 11



**Figure S11.** CD spectra of  $\text{Ag}_{24}\text{Au}_1(\text{R/S-BINAS})_x(\text{DMBT})_{18-2x}$  group I. Black and red traces correspond to clusters containing *R*- and *S*-BINAS, respectively. The mass spectra of these samples are presented in Figures 2A and S3A.

## Supporting Information 12

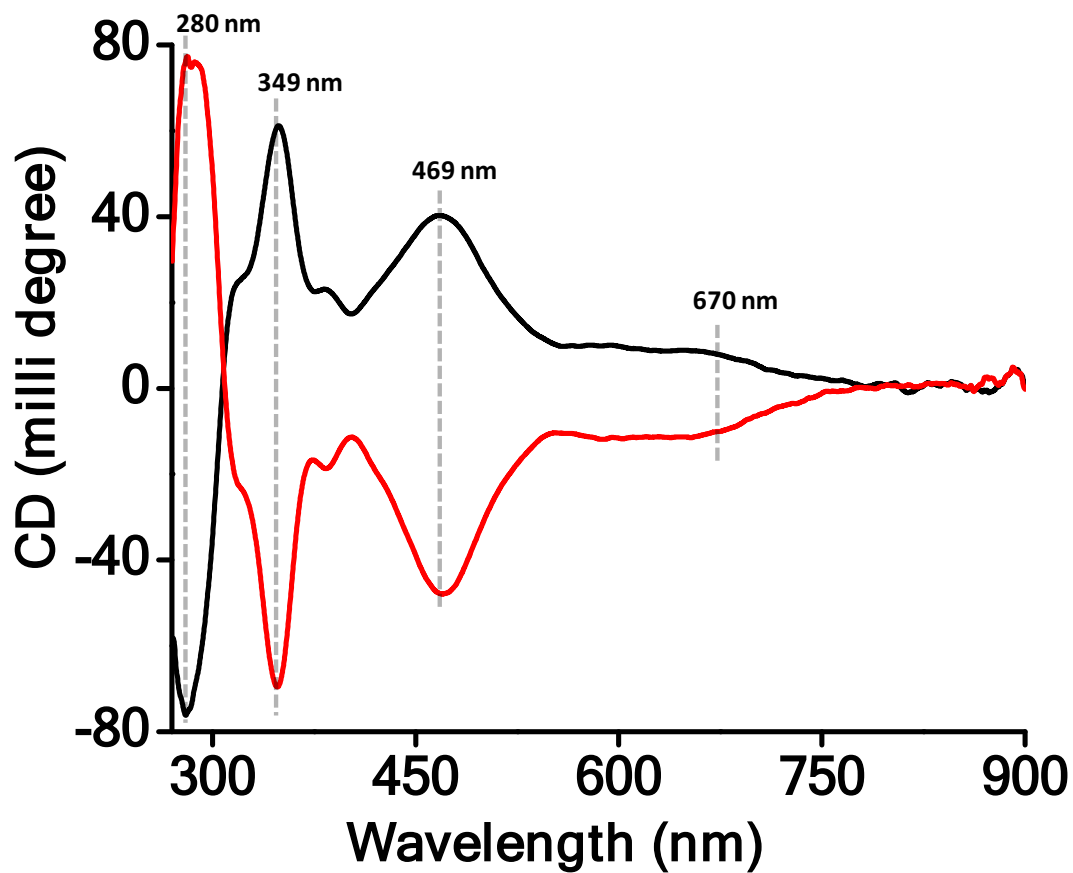


**Figure S12.** CD spectra of Ag<sub>24</sub>Au<sub>1</sub>(*R/S*-BINAS)<sub>*x*</sub>(DMBT)<sub>18-2*x*</sub> group III. Black and red traces correspond to clusters containing *R*- and *S*-BINAS, respectively. The mass spectra of these samples are presented in Figures 2C and S3C.

### Supporting Information 13

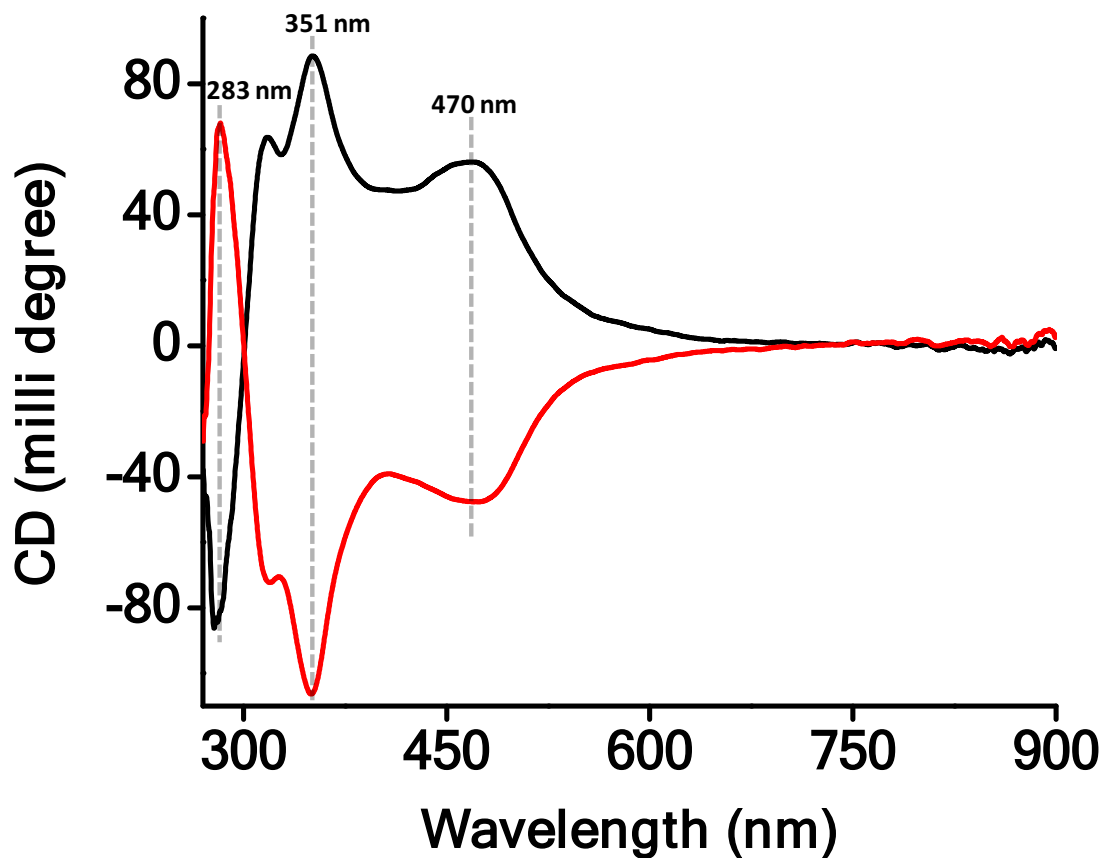


**Figure S13.** CD spectra of Ag<sub>24</sub>Au<sub>1</sub>(R/S-BINAS)<sub>x</sub>(DMBT)<sub>18-2x</sub> group IV. Black and red traces correspond to clusters containing *R*- and *S*-BINAS, respectively. The mass spectra of these samples are presented in Figures 2D and S3D.

Supporting Information 14

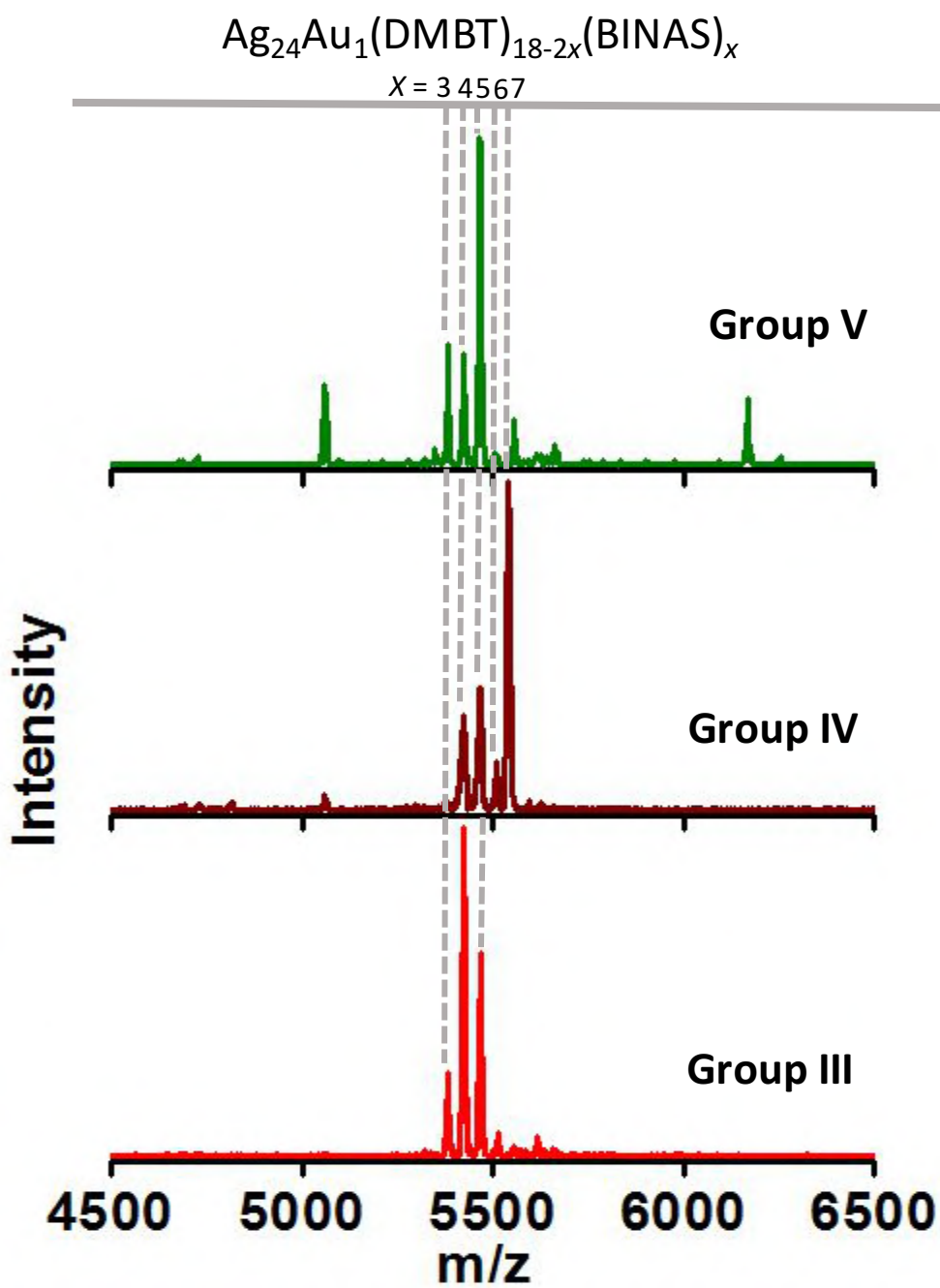
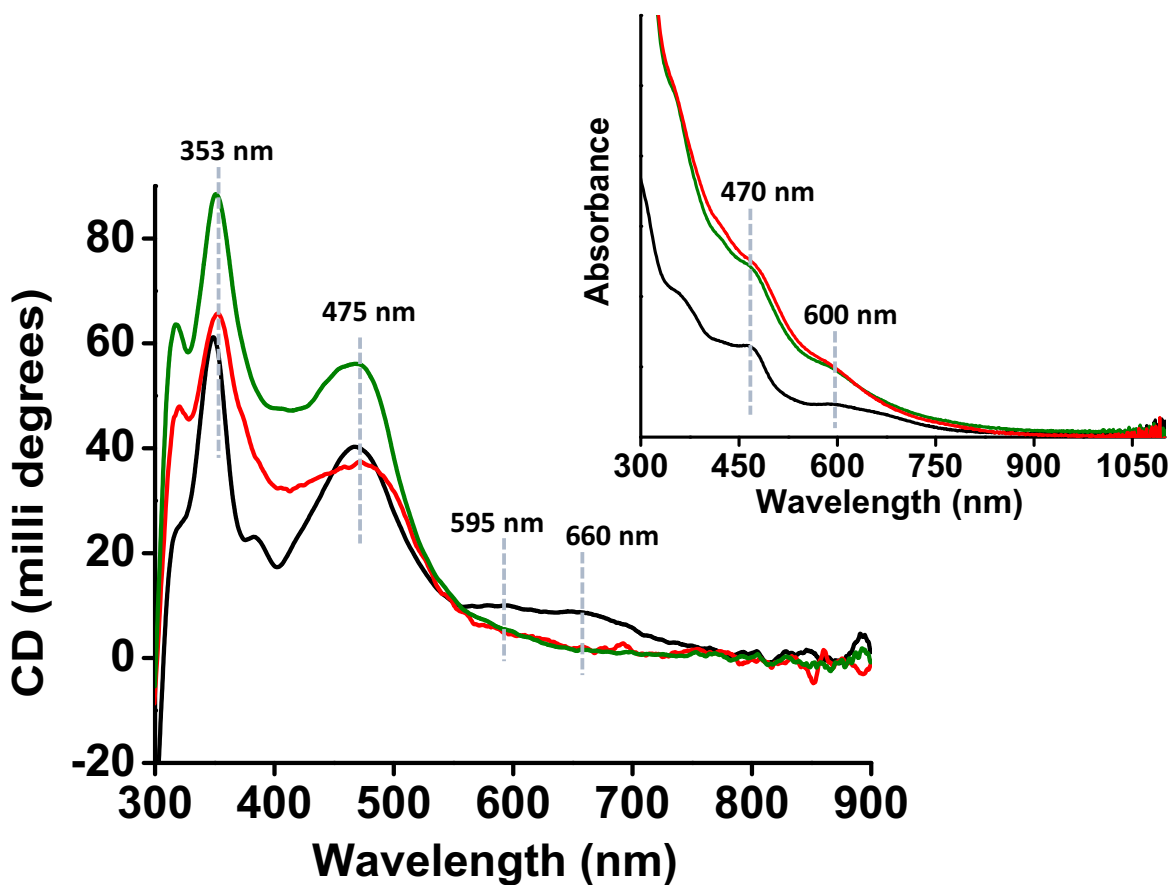


Figure S14. Negative ion mode ESI mass spectra of groups III, IV and V.

Supporting Information 15



**Figure S15.** CD spectra of Ag<sub>24</sub>Au<sub>1</sub>(R-BINAS)<sub>x</sub>(DMBT)<sub>18-2x</sub> groups **III** (black), **IV** (green) and **V** (red) and their UV/Vis absorption spectra in the inset.

### Supporting Information 16

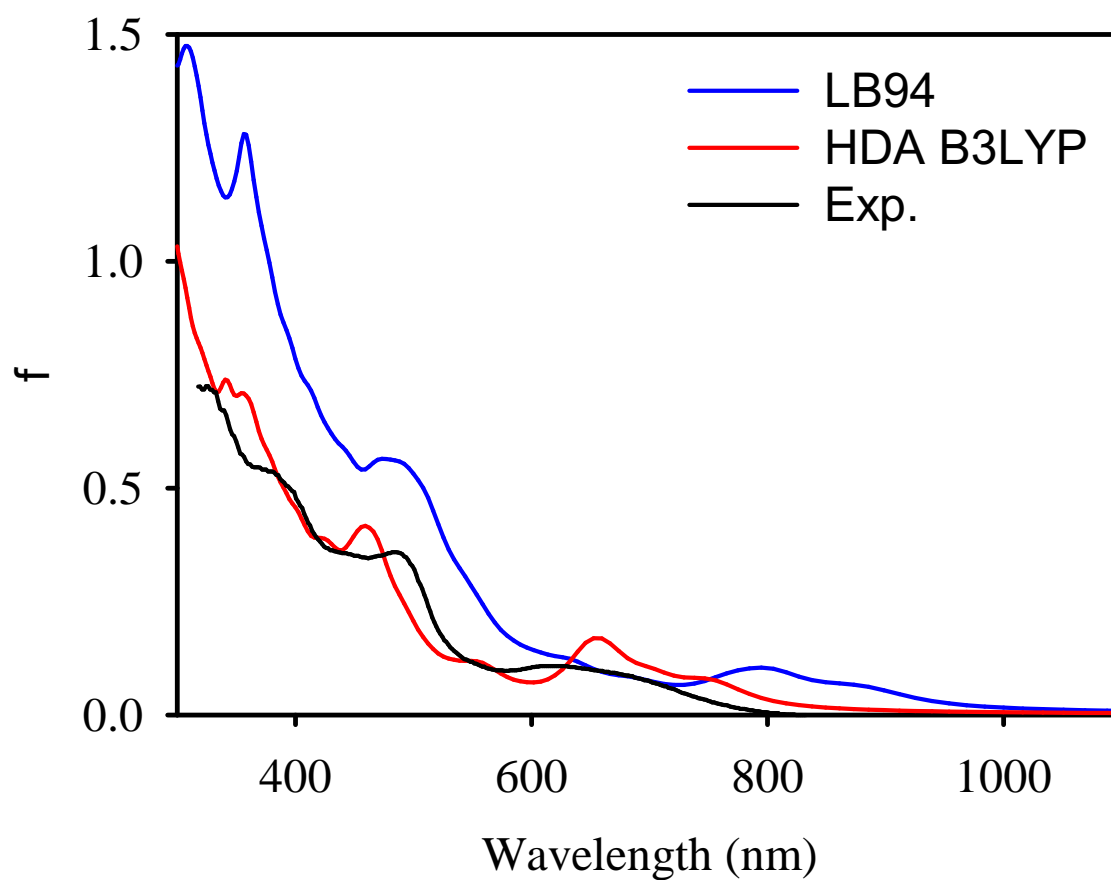


**Figure S16.** Oscillator strength ( $f$ ) calculated at the TDDFT level with LB94 and HDA - B3LYP functionals for the  $[\text{Ag}_{24}\text{Au}_1(\text{DMBT})_{10}(\text{S-BINAS})_4]^-$  cluster anion (for the geometry “best1”). Experimental data (present work) are reported with arbitrary normalization.

## Supporting Information 17

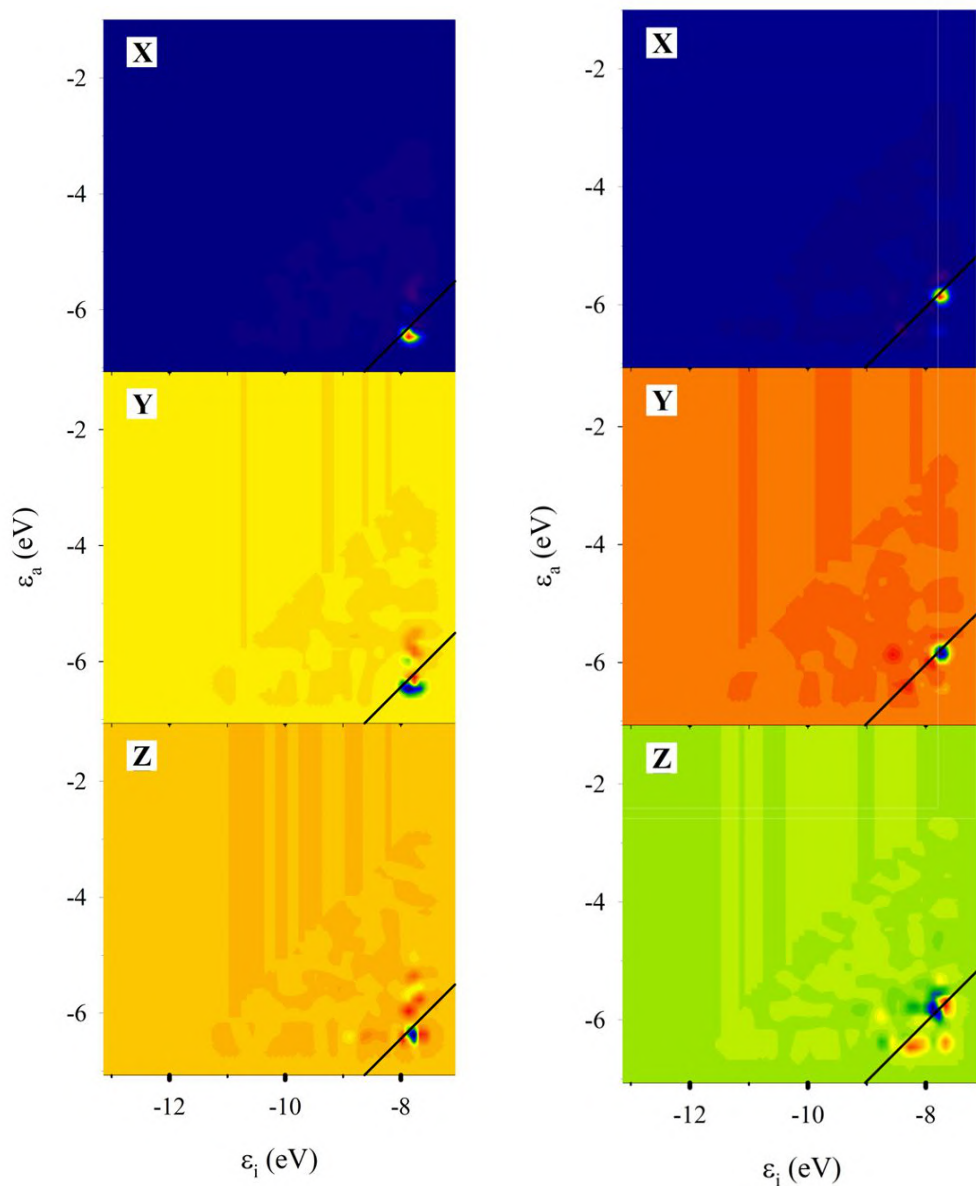


**Figure S17.** ICM-RS plots calculated at the TDDFT level for the excited state at 1.56 eV (795 nm) (left) and at 1.96 eV (632 nm) (right) of the  $[\text{Ag}_{24}\text{Au}_1(\text{DMBT})_{10}(\text{S-BINAS})_4]^-$  cluster anion (for the geometry “best1”). All three electric dipole Cartesian components are shown, see text for details.

## Supporting Information 18

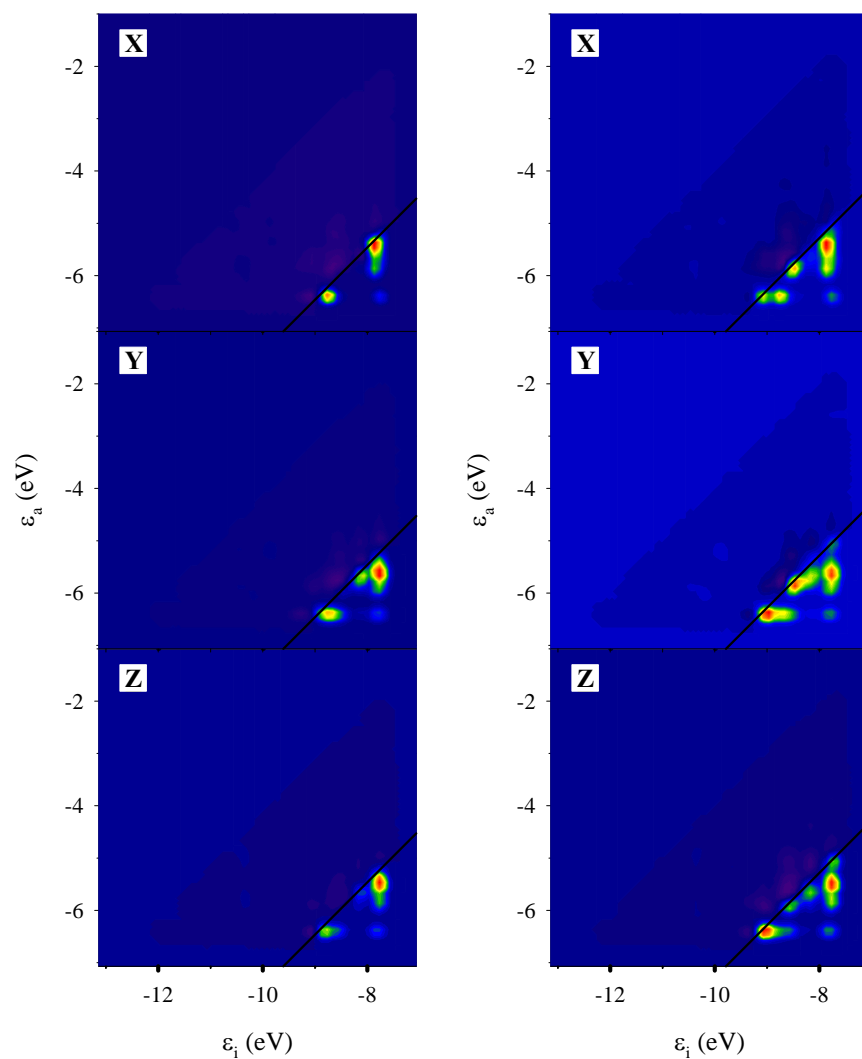


**Figure S18.** ICM-OS plots calculated at the TDDFT level for the excited state at 2.54 eV (488 nm) (left) and at 2.72 eV (356 nm) (right) of the  $[\text{Ag}_{24}\text{Au}_1(\text{DMBT})_{10}(\text{S-BINAS})_4]^-$  cluster anion (for the geometry “best1”). All three electric dipole Cartesian components are shown, see text for details.

## Supporting Information 19

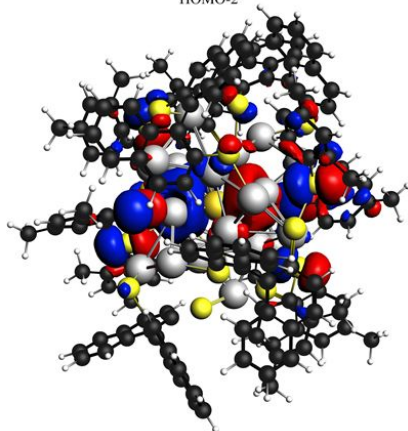
**Table S1.** Analysis of the TDDFT/LB94/TZP excitation of  $[\text{Ag}_{24}\text{Au}_1(\text{S-BINAS})_4(\text{DMBT})_{10}]^-$  at 1.56 eV (795 nm), 1.96 eV (632 nm), 2.54 (488 nm), 2.72 (356) for the “best1” geometry.

$E_{\text{exc}}$ (eV / nm)	$f$	excited state composition
1.56 / 795	0.103	30% HOMO-2 → LUMO 25% HOMO-1 → LUMO+1 11% HOMO-2 → LUMO+1
1.96 / 632	0.123	13% HOMO-1 → LUMO+2 10% HOMO-1 → LUMO+3
2.54 / 488	0.233	7% HOMO-2 → LUMO+14 6% HOMO-1 → LUMO+14 5% HOMO-3 → LUMO+11 3% HOMO-19 → LUMO+1 3% HOMO-2 → LUMO+12 3% HOMO-21 → LUMO 2% HOMO-20 → LUMO 2% HOMO-17 → LUMO+1 2% HOMO-21 → LUMO+1 2% HOMO-1 → LUMO+15 2% HOMO-19 → LUMO 1% HOMO → LUMO+13 1% HOMO-22 → LUMO+1 1% HOMO-5 → LUMO+11 1% HOMO-20 → LUMO+1
2.72 / 356	0.438	3% HOMO-2 → LUMO+14 3% HOMO-24 → LUMO+1 2% HOMO-23 → LUMO 2% HOMO-26 → LUMO 2% HOMO → LUMO+23 2% HOMO-1 → LUMO+19 1% HOMO-27 → LUMO 1% HOMO-2 → LUMO+18 1% HOMO-7 → LUMO+7 1% HOMO-25 → LUMO 1% HOMO-6 → LUMO+8 1% HOMO-6 → LUMO+8 1% HOMO-26 → LUMO+1 1% HOMO-12 → LUMO+2 1% HOMO-24 → LUMO 1% HOMO-25 → LUMO+1
<b>Molecular Orbital energies (eV)</b>		<b>Molecular Orbital composition</b>

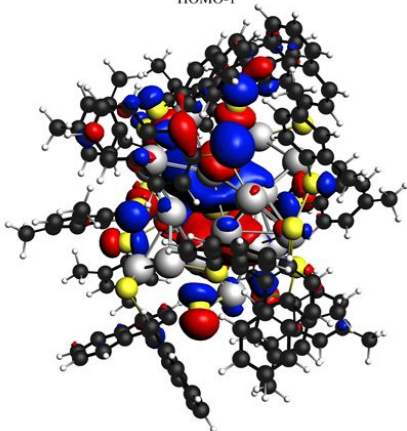
-9.113	HOMO-27 = 38% 3p S, 13% 2p C
-9.084	HOMO-26 = 41% 3p S, 3% 5s Ag
-9.024	HOMO-25 = 28% 3p S, 4% 5s Ag, 3% 2p C
-9.020	HOMO-24 = 29% 3p S, 13% 2p C, 4% 5s Ag
-8.999	HOMO-23 = 33% 3p S, 3% 2p C, 7% 5s Ag, 2% 7s Au, 1% 4d Ag
-8.923	HOMO-22 = 29% 3p S, 8% 2p C, 4% 5s Ag, 2% 7s Au
-8.907	HOMO-21 = 38% 3p S, 6% 2p C, 3% 5s Ag
-8.816	HOMO-20 = 51% 3p S, 3% 2p C
-8.788	HOMO-19 = 38% 3p S, 4% 5s Ag, 2% 2p C
-8.724	HOMO-17 = 38% 3p S, 5% 2p C, 4% 5s Ag
-8.605	HOMO-12 = 33% 3p S, 12% 2p C, 1% 5s Ag
-8.427	HOMO-7 = 42% 3p S, 8% 2p C, 2% 5s Ag
-8.278	HOMO-6 = 50% 3p S, 8% 2p C, 2% 4d Ag
-8.205	HOMO-5 = 52% 3p S, 24% 2p C, 1% 5p Ag
-8.098	HOMO-3 = 48% 3p S, 19% 2p C, 4% 4d Ag, 2% 5s Ag, 1% 5p Ag
-7.864	HOMO-2 = 37% 3p S, 26% 5s Ag, 6% 6p Au, 2% 5p Ag
-7.784	HOMO-1 = 32% 3p S, 23% 5s Ag, 5% 6p Au, 3% 5p Ag, 2% 2p C
-6.419	LUMO = 33% 5s Ag, 12% 3p S, 9% 5p Ag
-6.383	LUMO+1 = 30% 5s Ag, 11% 3p S, 9% 5p Ag
-5.956	LUMO+2 = 21% 2p C, 13% 5s Ag, 9% 5p Ag, 3% 3p S
-5.892	LUMO+3 = 62% 2p C
-5.785	LUMO+7 = 22% 2p C, 5% 5s Ag, 1% 5p Ag, 1% 3p
-5.769	LUMO+8 = 65% 2p C
-5.636	LUMO+11 = 63% 2p C, 1% 5s Ag
-5.567	LUMO+12 = 19% 5s Ag, 12% 5p Ag, 7% 3p S, 3% 2p C
-5.522	LUMO+13 = 13% 2p C, 11% 5s Ag, 4% 7s Au, 2% 3p S, 1% 6s Ag, 1% 5p Ag
-5.395	LUMO+14 = 17% 2p C, 11% 5s Ag, 5% 7s Au, 2% 5p Ag, 1% 3p S
-5.360	LUMO+15 = 22% 2p C, 11% 5s Ag, 3% 5p Ag, 1% 6s Ag, 1% 3p S
-5.174	LUMO+18 = 52% 2p C, 1% 5s Ag, 1% 3p S
-5.118	LUMO+19 = 51% 2p C
-4.970	LUMO+23 = 36% 2p, 1% 5s Ag

## Supporting Information 20

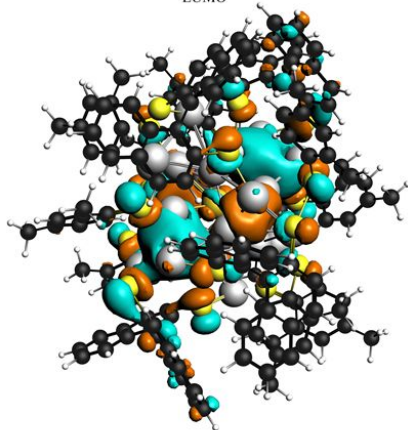
HOMO-2



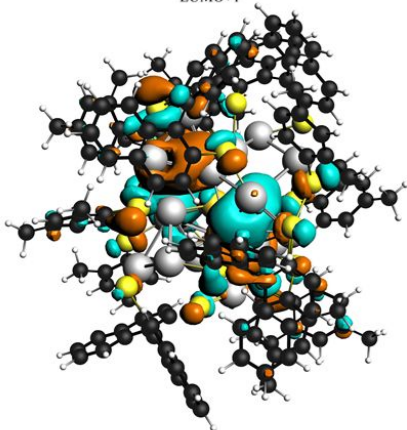
HOMO-1



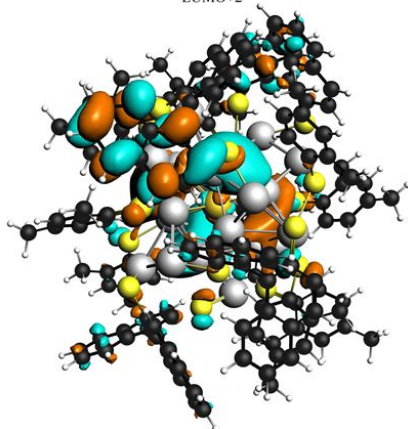
LUMO



LUMO+1



LUMO+2



LUMO+3

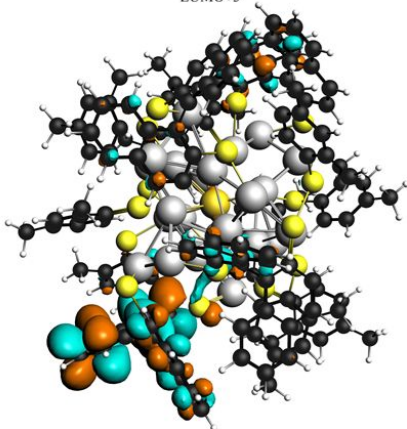


**Figure S19.** Plots of the Molecular orbitals mostly involved in the excited state at 1.56 eV (795 nm) and at 1.96 eV (632 nm) of the  $[\text{Ag}_{24}\text{Au}_1(\text{DMBT})_{10}(\text{S-BINAS})_4]^-$  cluster anion (geometry “best1”), see Table S1 and text for details. Isosurfaces are drawn at  $0.015 \text{ e}/\text{\AA}^{3/2}$ .

### Supporting Information 21

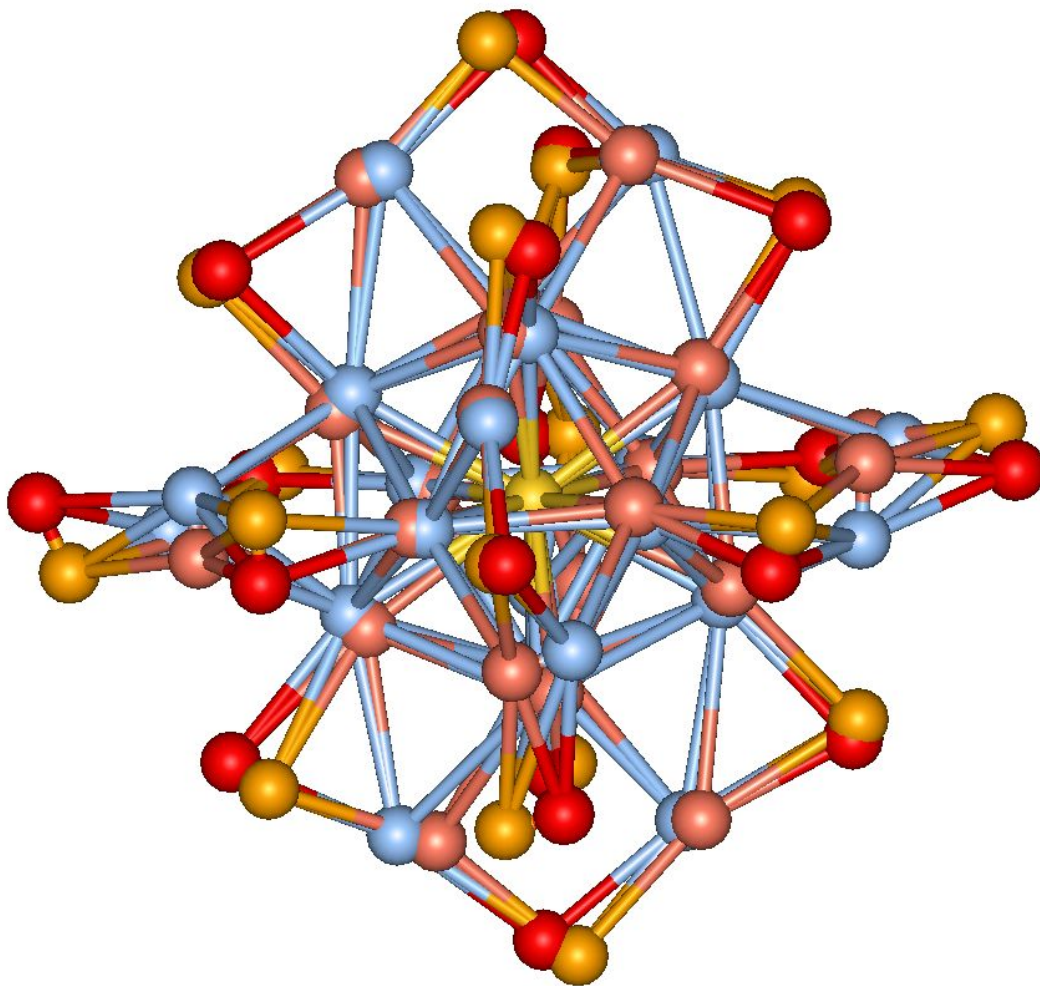


**Figure S20.** Depiction of the  $\text{Ag}_{24}\text{AuS}_{18}$  skeletons from the geometries: “best1CH<sub>3</sub>” and the experimental structure of  $[\text{Ag}_{24}\text{Au}_1(\text{DMBT})_{18}]^-$  (see main text for more details). Color convention: Ag, S atoms of the experimental (symmetric) structure in light blue and red, respectively; Ag, S atoms of the “best1CH<sub>3</sub>” (dissymmetric) structure in pink and orange, respectively. Due to the graphics software, some fictitious bonds among neighboring atoms pertaining to the two different structures are also present.

## Supporting Information 22

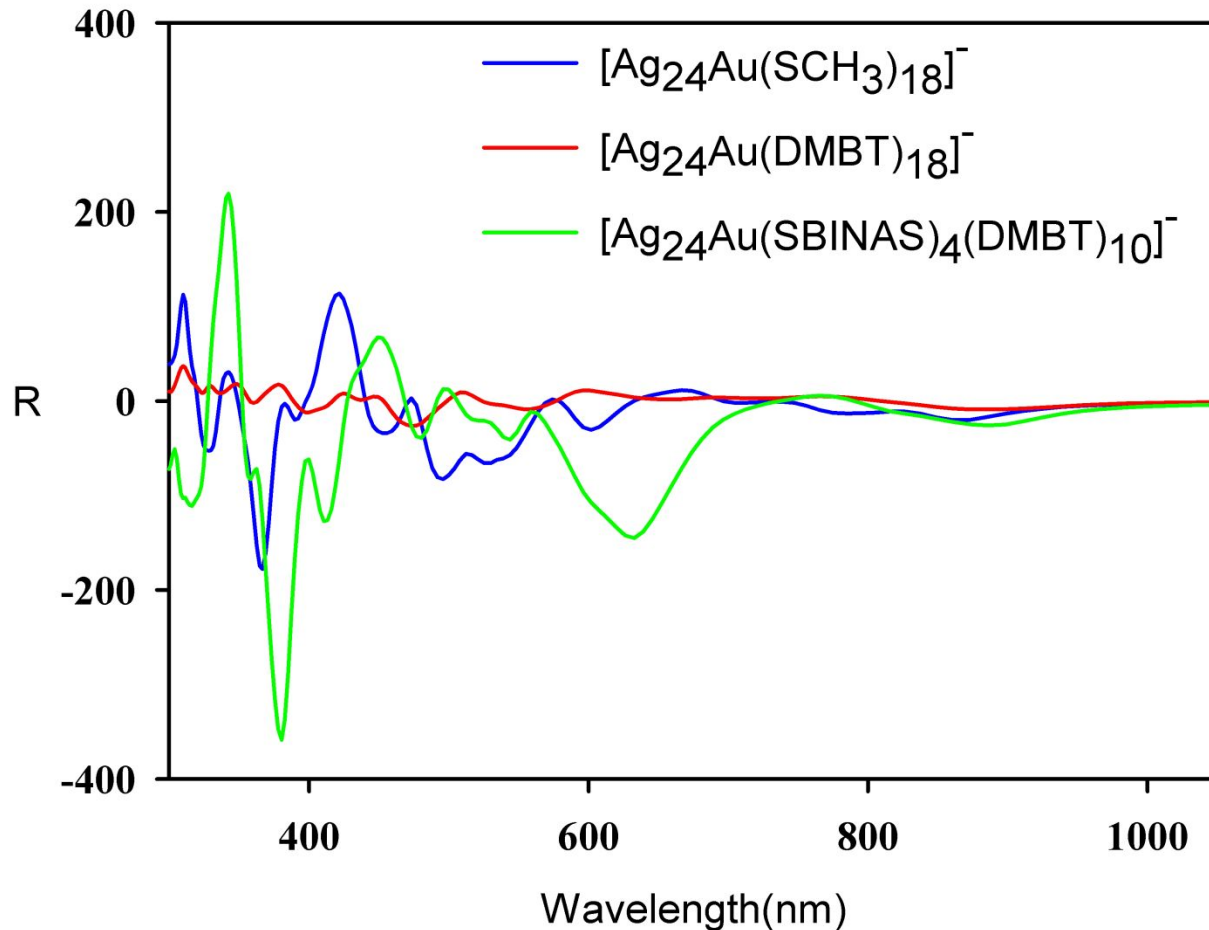


**Figure S21.** Circular dichroism rotational strength (R) calculated at the TDDFT level for the [Ag<sub>24</sub>Au<sub>1</sub>(S-BINAS)<sub>4</sub>(DMBT)<sub>10</sub>]<sup>-</sup> cluster anion (geometry “best1), for the [Ag<sub>24</sub>Au(SCH<sub>3</sub>)<sub>18</sub>]<sup>-</sup> model structure derived from the previous one by transforming the BINAS and DMBT ligands into thio-methyl residues, and for the experimental structure of [Ag<sub>24</sub>Au<sub>1</sub>(DMBT)<sub>18</sub>]<sup>-</sup>. See text for details.

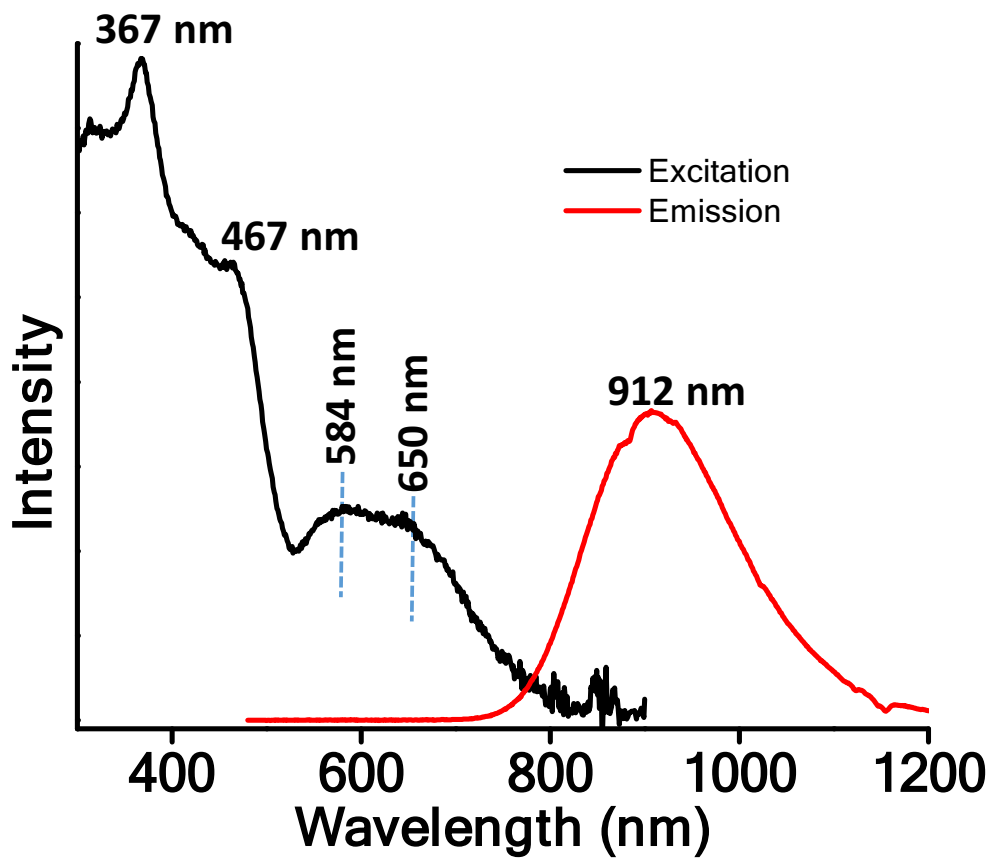


**Figure S22.** Excitation and emission spectra of  $\text{Ag}_{24}\text{Au}_1(\text{R-BINAS})_x(\text{DMBT})_{18-2x}$  group II.

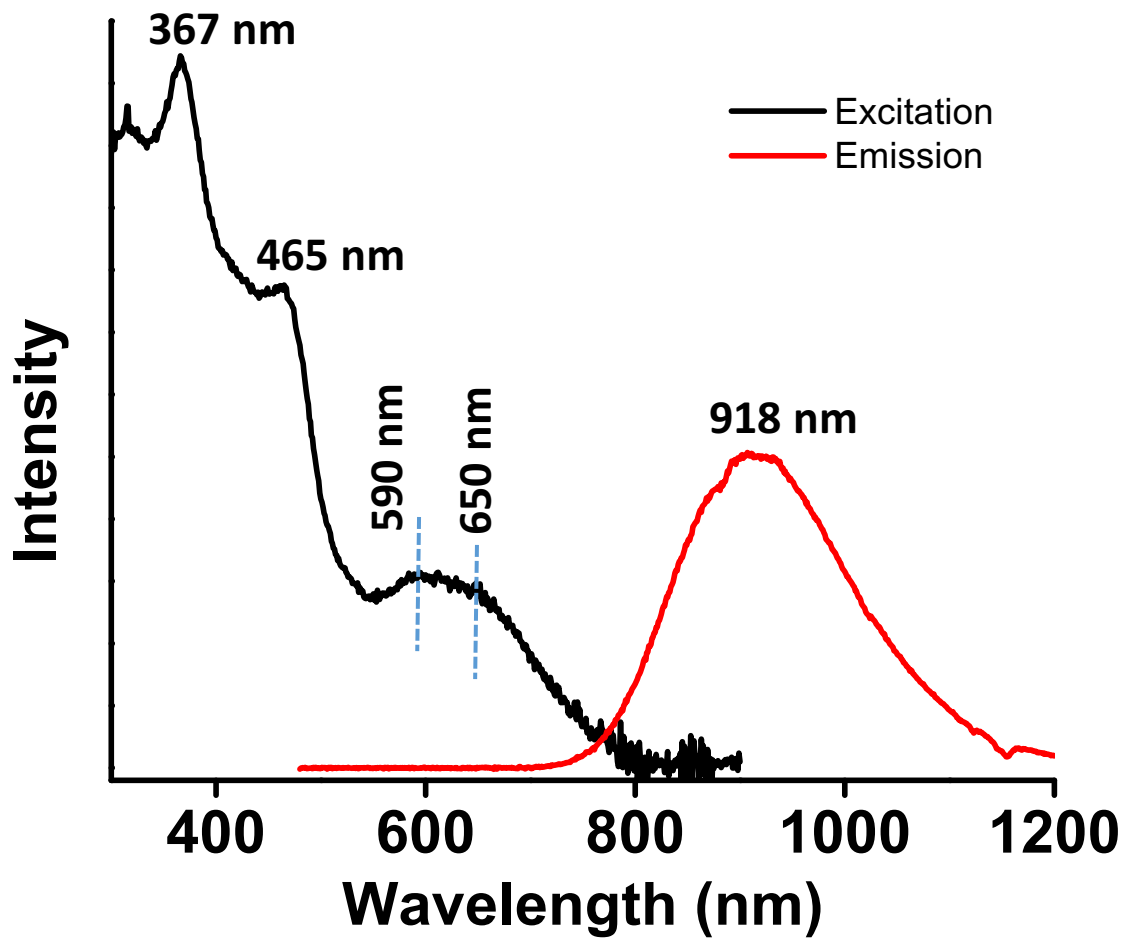
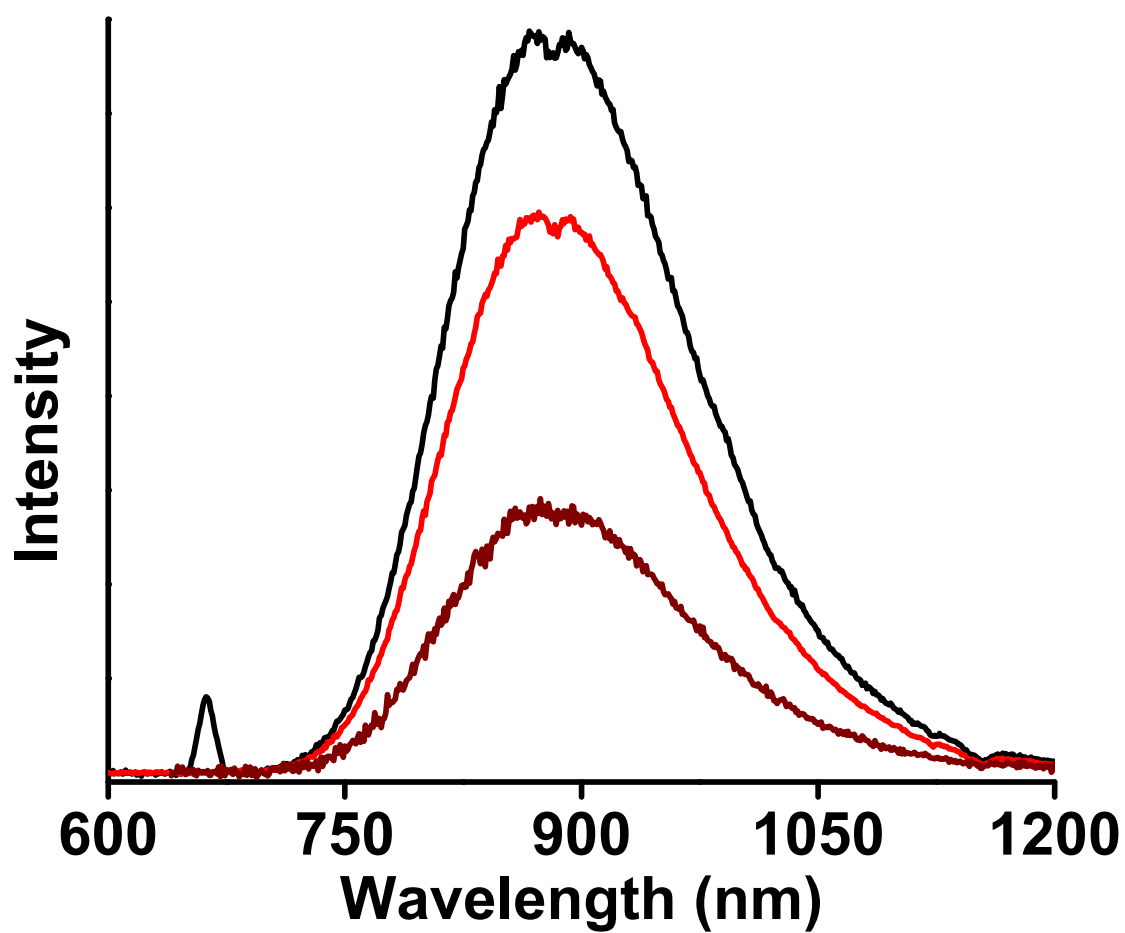
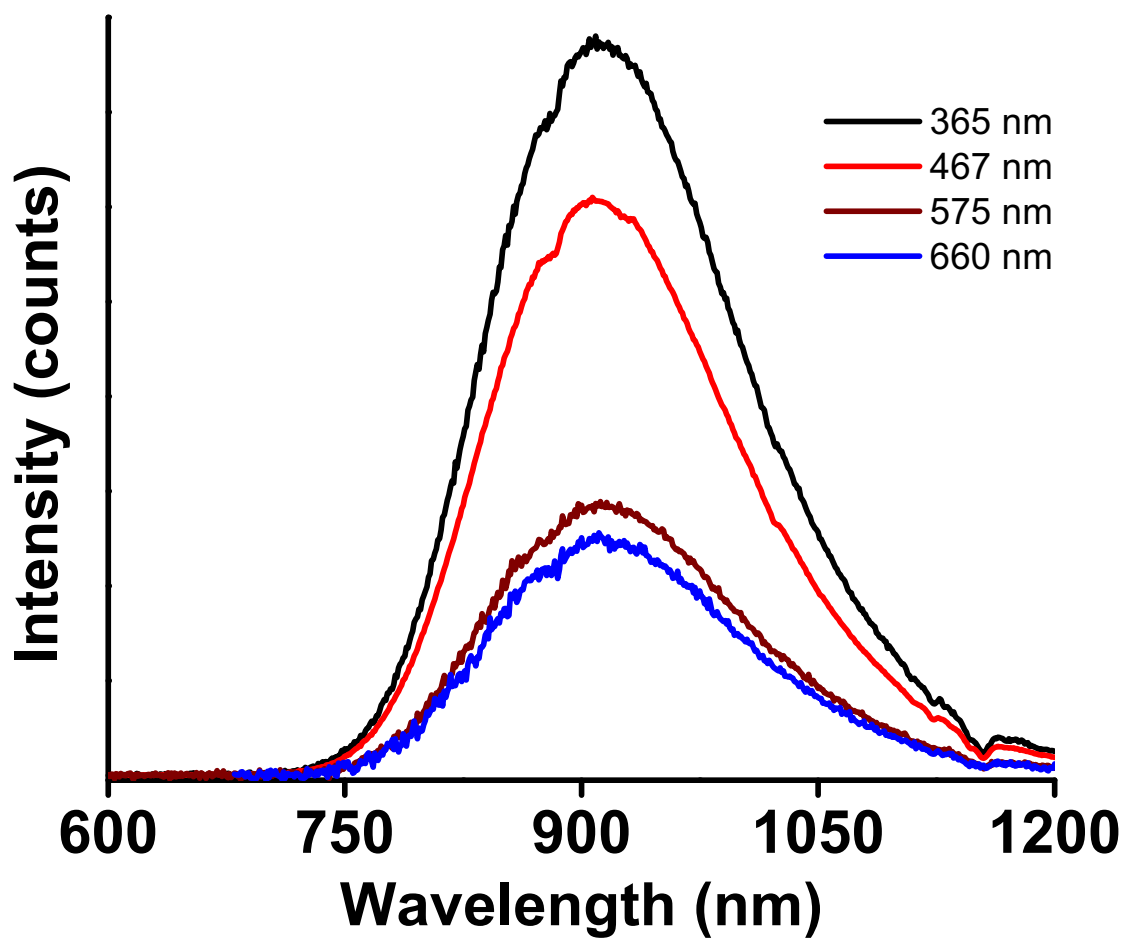


Figure S23. Excitation and emission spectra of  $\text{Ag}_{24}\text{Au}_1(\text{R-BINAS})_x(\text{DMBT})_{18-2x}$  group III.



**Figure S24.** Emission spectra of  $\text{Ag}_{24}\text{Au}_1(\text{DMBT})_{18}$  collected at excitation wavelengths of 330 nm (black), 467 nm (red) and 619 nm (wine red).



**Figure S25.** Emission spectra of  $\text{Ag}_{24}\text{Au}_1(\text{R/S-BINAS})_x(\text{DMBT})_{18-2x}$  group II collected at various excitation wavelengths.

Supporting Information 27

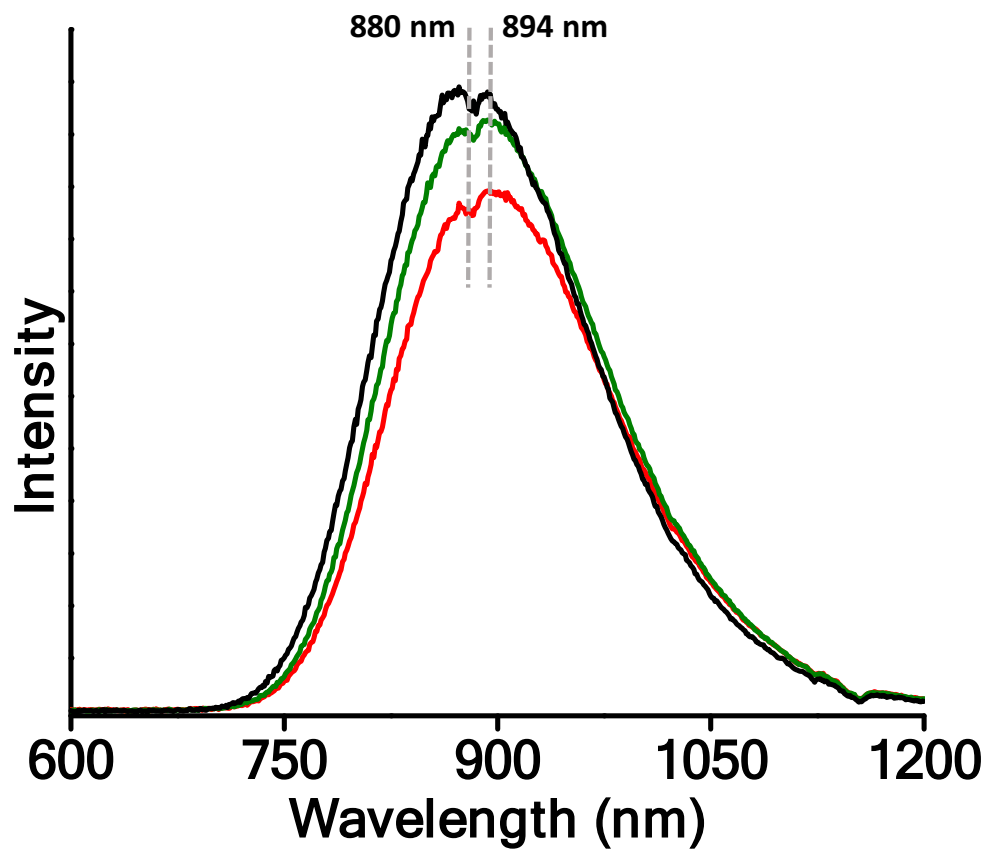


**Figure S26.** Emission spectra of Ag<sub>24</sub>Au<sub>1</sub>(DMBT)<sub>18</sub> (black trace) Ag<sub>24</sub>Au<sub>1</sub>(BPT)<sub>x</sub>(DMBT)<sub>18-2x</sub> clusters synthesized at Ag<sub>24</sub>Au<sub>1</sub>(DMBT)<sub>18</sub>:BPT molar ratios of 0.3:1.0 (red trace) and 0.2:1.0 (green trace).

Supporting Information 28

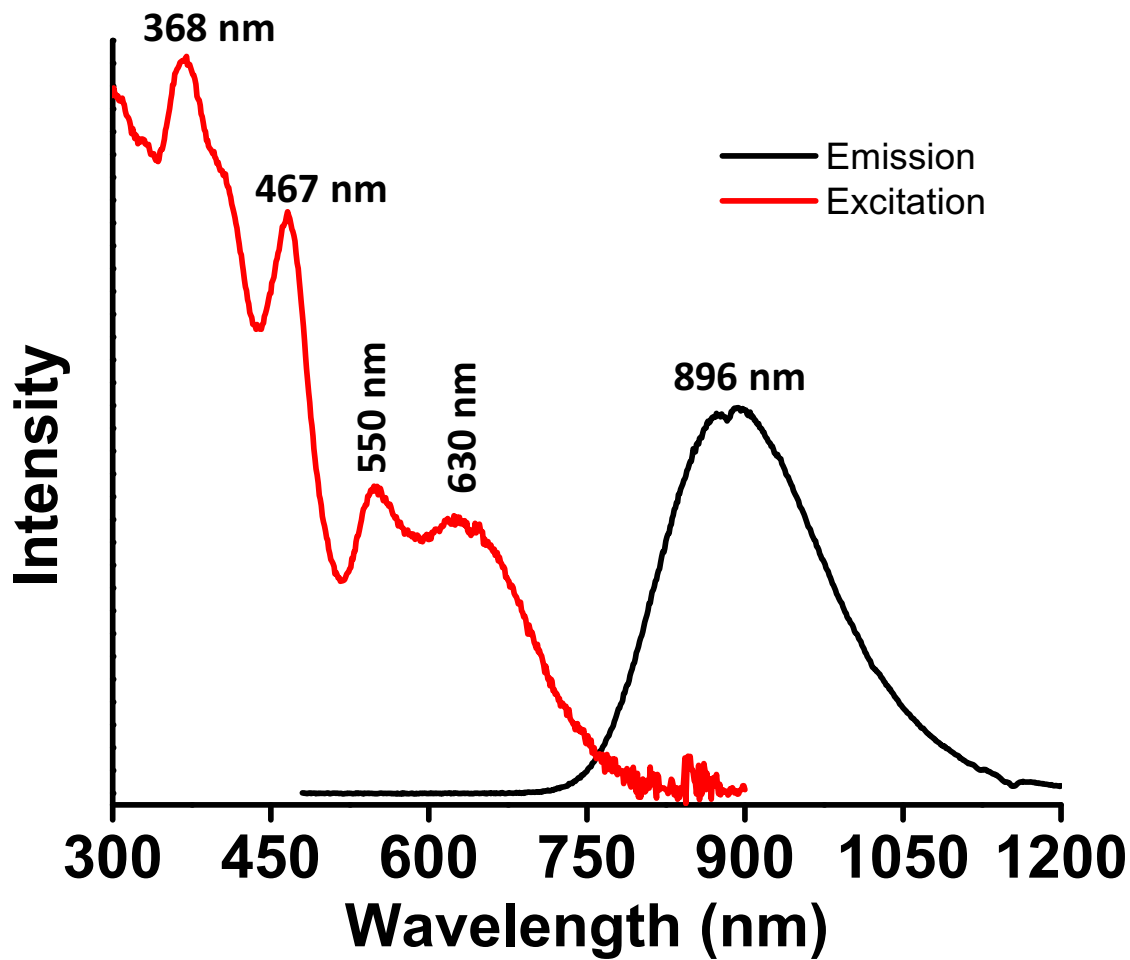


**Figure S27.** Excitation and emission spectra of  $\text{Ag}_{24}\text{Au}_1(\text{BPT})_x(\text{DMBT})_{18-2x}$  clusters synthesized at  $\text{Ag}_{24}\text{Au}_1(\text{DMBT})_{18}:\text{BPT}$  molar ratio of 0.2:1.0.

## Supporting Information 29

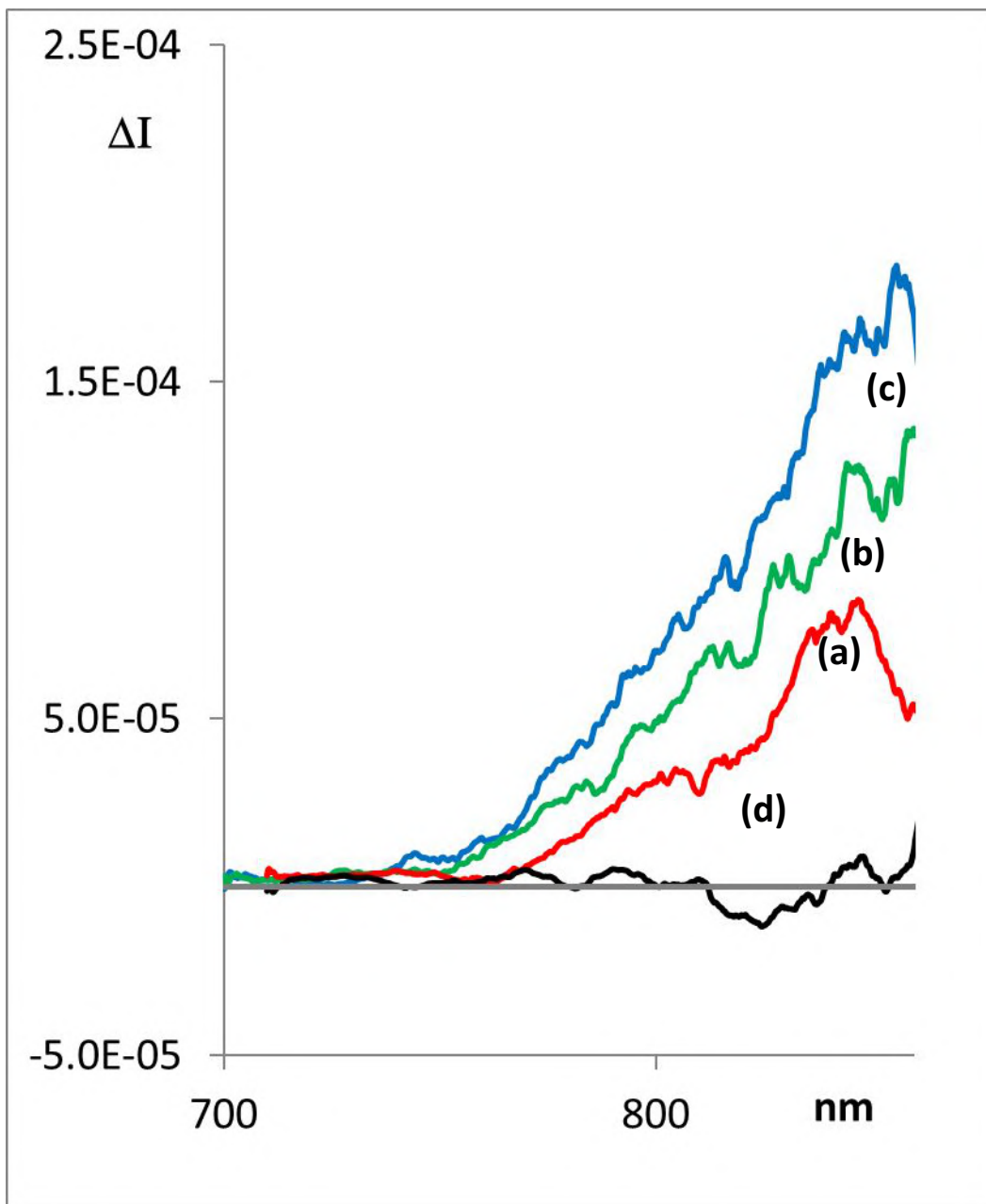


**Figure S28.** CPL spectra (semi-difference between *R* and *S*) of  $\text{Ag}_{24}\text{Au}_1(\text{R/S-BINAS})_x(\text{DMBT})_{18-2x}$  group of clusters **I** (a), **II** (b) and **III**(c). Trace (d) correspond to the achiral cluster,  $\text{Ag}_{24}\text{Au}_1(\text{DMBT})_{18}$ . Traces are rescaled after normalization of the corresponding fluorescence spectra. Plots are obtained after an “adjacent average” over 100 points (data pitch 0.25 nm). The original spectra are reported in the Figure S29.

### Supporting Information 30

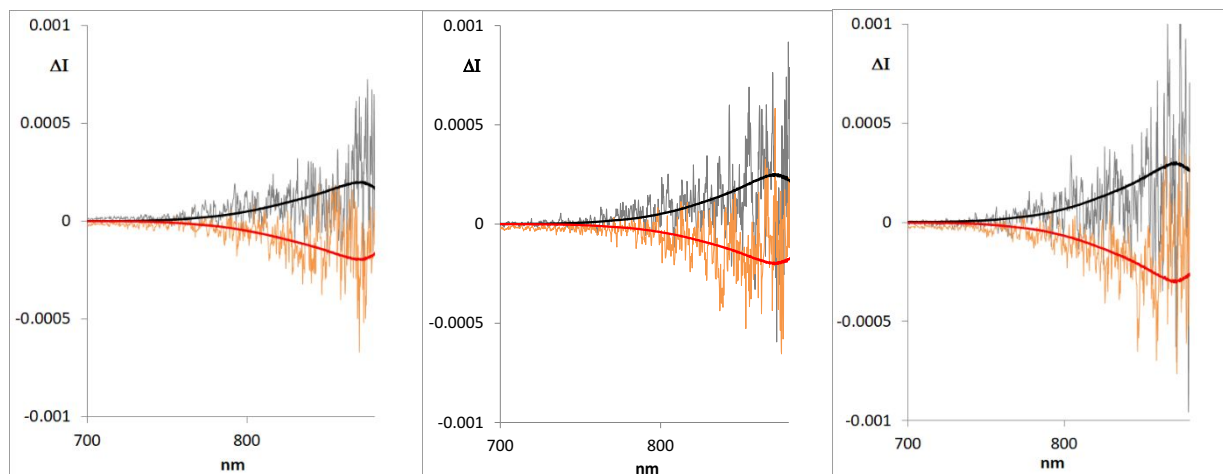


**Figure S29.** Original CPL spectra of  $\text{Ag}_{24}\text{Au}_1(\text{R/S-BINAS})_x(\text{DMBT})_{18-2x}$  group of clusters **I** (left), **II** (middle) and **III** (right). The superimposed black and red traces correspond to the fluorescence spectra recorded on the same instrument: (*R*) black trace, (*S*) red trace.  $\Delta I$  values are obtained after normalization of the corresponding fluorescence spectra and corrected for instrumental response, see also the following note.

#### Supplementary Note 1

The group **IV** seemed to be much less fluorescent (and hence, much more gain had to be used during measurement) and for this reason, the CPL is even more noisy than the other three clusters. With such a noise, it is difficult to confirm if the signal is null or not and hence, the CPL spectra of group **IV** is not presented. However, the other three clusters show a weak but distinct CPL activity compared to the achiral cluster, when measured in similar conditions.

The spectra recorded on the CPL apparatus (Figures S28 and S29) are slightly blue shifted with respect to the one reported in Figure 10. This is due to the limitations of the apparatus whose optical response is limited to 900 nm, but also falls dramatically above 860 nm. For this reason, the real CPL (and fluorescence) maximum cannot be reached; we may just be content that the couples of enantiomers give a trend with opposite sign, confirming emission with circularly polarized components.

The presented CPL signals have all been corrected taking into account a reference lamp with known emission spectrum.

### Supporting Information 31

**Table S2.** Analysis of the TDDFT/LB94/TZP excitation of  $[\text{Ag}_{24}\text{Au}_1(\text{DMBT})_{18}]^-$  at 1.62 eV (765 nm) and at 2.10 eV (590 nm) for the “best1” geometry.

$E_{\text{exc}}$ (eV / nm)	$f$	excited state composition
1.62 / 765	0.063	36% HOMO-2 → LUMO 30% HOMO-1 → LUMO+1 14% HOMO-2 → LUMO+1
2.10/ 590	0.102	17% HOMO-2 → LUMO+2 16% HOMO-1 → LUMO+2 14% HOMO-7 → LUMO+1 12% HOMO-1 → LUMO+3 10% HOMO → LUMO+3
Molecular Orbital energies (eV)	Molecular Orbital composition	
-8.255	HOMO-7 = 47% 3p S	
-7.787	HOMO-2 = 37% 3p S, 27% 5s Ag, 4% 6p Au	
-7.706	HOMO-1 = 29% 3p S, 26% 5s Ag, 5% 6p Au, 3% 5p Ag	
-7.600	HOMO = 34% 3p S, 30% 5s Ag, 6% 6p Au, 5% 5p Ag	
-6.326	LUMO = 31% 5s Ag, 12% 3p S, 10% 5p Ag, 2% 6d Au	
-6.275	LUMO+1 = 34% 5s Ag, 13% 3p S, 7% 5p Ag, 1% 6d Au	
-5.840	LUMO+2 = 23% 3p Ag, 23% 5s Ag, 9% 3p S, 1% 6d Au	
-5.670	LUMO+3 = 25% 5s Ag, 20% 3p Ag, 13% 3p S, 2% 7s Au	

## Supporting Information 32

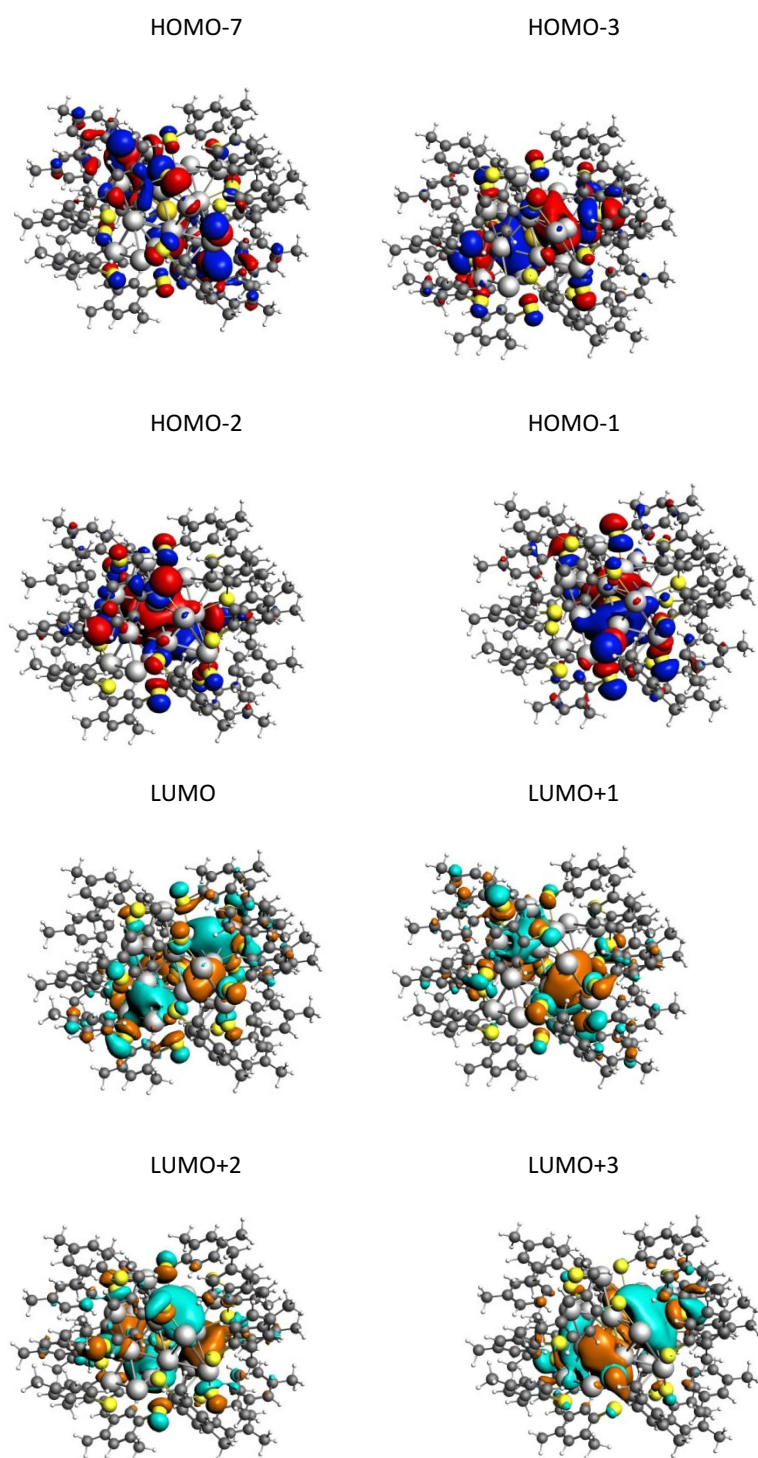


**Figure S30.** Plots of the Molecular orbitals mostly involved in the excited state at 1.62 eV (765 nm) and 2.10 eV (590 nm) of the  $[\text{Ag}_{24}\text{Au}_1(\text{DMBT})_{18}]^-$  cluster anion, see Table S2 and text for details. Isosurfaces are drawn at  $0.015 \text{ e}/\text{\AA}^{3/2}$ .

*ATTENTION: this is incomplete supporting information, please visit the article online*

# Crystal Structure of $\text{Au}_{36-x}\text{Ag}_x(\text{SPh-}t\text{Bu})_{24}$ Nanoalloy and the Role of Ag Doping in Excited State Coupling

Naga Arjun Sakthivel,<sup>†</sup> Mauro Stener,<sup>‡</sup> Luca Sementa,<sup>§</sup> Marco Medves,<sup>⊥</sup> Guda Ramakrishna,<sup>||</sup> Alessandro Fortunelli,<sup>§</sup> Allen G. Oliver,<sup>‡</sup> and Amala Dass<sup>\*,†</sup>

<sup>†</sup>Department of Chemistry and Biochemistry, University of Mississippi, Oxford, Mississippi 38677, United States

<sup>‡</sup>Department of Chemistry, University of Notre Dame, Notre Dame, Indiana 46556, United States

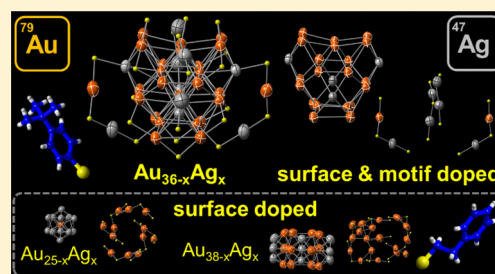
<sup>§</sup>CNR-ICCOM & IPCF, Consiglio Nazionale delle Ricerche, Pisa I-56124, Italy

<sup>⊥</sup>Department of Chemistry, Western Michigan University, Kalamazoo, Michigan 49008, United States

<sup>||</sup>Dipartimento di Scienze Chimiche e Farmaceutiche, Università di Trieste, Trieste I-34127, Italy

## Supporting Information

**ABSTRACT:** We report the X-ray crystal structure of  $\text{Au}_{36-x}\text{Ag}_x(\text{SPh-}t\text{Bu})_{24}$  alloy nanomolecules, optical properties, and the substitutional disorder refinement protocol to obtain a reliable structural model. Single crystal X-ray crystallography (SC-XRD) revealed a composition of  $\text{Au}_{33.17}\text{Ag}_{2.83}(\text{SPh-}t\text{Bu})_{24}$  with 2 Ag doped on the 28-atom face centered cubic core surface and 0.83 Ag distributed over metal atoms on dimeric staple motifs. Electrospray ionization mass spectrometry revealed a composition of  $\text{Au}_{32.5}\text{Ag}_{3.5}(\text{SPh-}t\text{Bu})_{24}$  complementing the SC-XRD data. Optical properties were investigated by steady-state and transient absorption spectroscopies and computational studies, showing faster excited-state decay for Ag-doped clusters due to enhanced electronic coupling. A previously published SC-XRD based  $\text{Au}_{36-x}\text{Ag}_x(\text{SPh-}t\text{Bu})_{24}$  structure used positional disorder refinement and concluded that the structure is "solely motif-doped". But the structure has unusually large and small thermal ellipsoids indicating potential problems with the atom assignment. Here, we have modeled our SC-XRD data using both positional disorder and substitutional disorder. Substitutional disorder modeling gave better  $R_1$  and other refinement indicators, and similarly sized thermal ellipsoids. The resulting substitutional disorder model structure has Ag atoms *not* as "solely motif-doped" but is found *both in the staple motifs and in the core*. The substitutional disorder refinement for alloy nanomolecules must be performed at each metal site with independent free variables to determine the partial occupancy of hetero atoms. The positional disorder refinement should be performed for atoms or groups disordered over different positions typically found in disordered *t*Bu group ligands.



## INTRODUCTION

Alloy nanomolecules (NM) exhibit new or enhanced properties compared to that of the parent compound.<sup>1–6</sup> Alloying or doping of a heterometal atom compound can be achieved by co-reduction of different metal salts and thiolate ligand mixture, by reacting a homometallic NMs with a heterometal salt, and by reacting nanomolecules of different metals.<sup>6–12</sup> Other types of ligands such as alkynyl, selenophenol, and triphenylphosphines are also being employed as protecting groups instead of thiolate ligands.<sup>13–16</sup> Each of these methods have opened new avenues for making nanoalloys with interesting properties.<sup>5,7,8,17–20</sup>

A wide array of Au and Ag based alloy nanomolecules have been reported and several have also been crystallographically studied.<sup>9,21–27</sup> Single crystal X-ray crystallography (SC-XRD) of the alloy NMs is crucial because it enables us to understand how the properties are tuned by doping heteroatoms at the atomic level.<sup>2,28–34</sup> The structural model refinement of the homometallic NMs are straightforward. However, alloy NMs structural model must be performed by substitutional disorder

refinement with individual free variables for each of the metal sites to achieve a reliable model.

$\text{Au}_{36}$  with 28 core Au atom with four interpenetrating cuboctahedra in a FCC arrangement is one of the stable nanomolecules and it has been prepared with different types of ligands: thiolates, selenolates, and alkynes.<sup>14,35–41</sup>  $\text{Au}_{36}$  protected by TBBT can be synthesized in high yields and can be stored for several years.<sup>42,43</sup> Aromatic thiolate protected  $\text{Au}_{36}$  NMs have two optical absorption bands  $\sim 370$  nm and  $\sim 575$  nm with an optical band gap of  $\sim 1.7$  eV and an electrochemical gap of  $\sim 2$  V.<sup>39,44</sup> It has been shown to be an electrocatalyst for oxygen reduction reaction with relatively low overpotential and a  $4e^-$  process yielding water.<sup>45</sup>  $\text{Au}_{36}$  also reversibly interconverts to  $\text{Au}_{30}$  upon ligand exchange with the *t*BuSH.<sup>46</sup>  $\text{Au}_{36}(\text{TBBT})_{24}$  has been studied with Ag doping at various Au:Ag ratios and a unique evolution of absorption

Received: September 24, 2019

Revised: November 6, 2019

Published: November 22, 2019

enhancement with doping levels was observed.<sup>47</sup> Au<sub>36</sub> have so far been alloyed with Ag and Cu, but both of these crystal structures have not used individual free variables for substitutional disorder modeling, leading to mis-assignment of locations of heteroatoms (Ag/Cu), namely, the “solely motif-doped” (vide infra).<sup>48,49</sup> Au<sub>36</sub> with a different type of kernel capped by chloride and 4-*tert*-butylbenzyl thiolate ligands has been reported.<sup>50</sup>

Although the crystal structure models hold valuable and rich structure-bonding information to understand the properties of nanomolecules and their alloy counterparts, care must be taken in modeling the structure to provide a model which would best represent the experimental diffraction data. In particular, the substitutional disorder refinement of partial occupancies of alloys must be done correctly using individual free variables. In the literature, some alloy crystal structures have been incorrectly refined using positional disorder (special position) modeling with EXYZ and EADP cards, leading to mis-assignments, and specifically assignments of heteroatoms to locations, where there is none.

Here, we report the following: (1) X-ray crystal structure of Au<sub>36-x</sub>Ag<sub>x</sub>(TBBT)<sub>24</sub>, (2) mass spectrometric analysis of the nanoalloy to determine the Ag composition, (3) a detailed substitutional disorder refinement protocol for alloy NMs, and a comparison with previous crystal structure that incorrectly used positional disorder modeling, (4) optical properties, studied both in absorption and via (4a) electron dynamics and (4b) computational studies.

## ■ EXPERIMENTAL SECTION

**Materials.** Hydrogen tetrachloroaurate(III) (HAuCl<sub>4</sub>·3H<sub>2</sub>O; Alfa Aesar ACS grade), silver nitrate (AgNO<sub>3</sub>; Alfa Aesar ACS grade), sodium borohydride (NaBH<sub>4</sub>; Acros, 99%), 4-*tert*-butylbenzene thiol (TBBT; TCI America, >97%), cesium acetate (Acros, 99%), and anhydrous ethyl alcohol (Acros, 99.5%) were used as received. HPLC grade solvents methylene chloride (DCM), tetrahydrofuran (THF), toluene, methanol, and ethanol were purchased from Fisher Scientific. All materials were used as received.

**Synthesis.** The Au<sub>36-x</sub>Ag<sub>x</sub>(SPh-*t*Bu)<sub>24</sub> nanomolecule was synthesized in two steps, first a polydisperse crude mixture of (AuAg)<sub>x</sub>(TBBT)<sub>y</sub> was obtained and thermochemically etched to obtain the product containing Au<sub>36-x</sub>Ag<sub>x</sub> as a major product.

**Step 1.** HAuCl<sub>4</sub>·3H<sub>2</sub>O (50 mg) and AgNO<sub>3</sub> (Au:Ag = 1:0.33) were dissolved in THF (10 mL) and stirred (1200 rpm) for 10–15 min. Subsequently, TBBT ligand (AuAg:HSR = 1:5) was added to the solution and stirred for 30 min. This reaction mixture was reduced with NaBH<sub>4</sub> (AuAg:NaBH<sub>4</sub> = 1:10) dissolved in ice cold water (5 mL). The reaction was stopped after 5 min and the solvent removed under reduced pressure, yielding an oily crude product. The crude product was washed with excess water and methanol to remove the byproducts and excess thiols.

**Step 2.** The crude product was then thermochemically etched<sup>51</sup> with excess TBBT ligand at 65 °C for 2 d. The etched product was washed with excess methanol to remove the byproducts and excess thiols. Final extraction was from DCM or toluene.

**Crystallization.** The single crystals of Au<sub>36-x</sub>Ag<sub>x</sub>(SPh-*t*Bu)<sub>24</sub> alloy nanomolecules were grown by dissolving 5 mg of the as obtained etched product in DCM (1.5 mL) and layered with ethanol (1 mL) at 4 °C for ~2 months. The block-like black single crystals were used for SC-XRD study.

**Crystal Structure.** Crystal structure for C<sub>240</sub>H<sub>312</sub>Ag<sub>2.83</sub>·Au<sub>33.17</sub>S<sub>24</sub>; formula weight 10805.42; orthorhombic; space group P2<sub>1</sub>2<sub>1</sub>2<sub>1</sub>; *a* = 24.016(5) Å; *b* = 28.775(6) Å; *c* = 22.090(4) Å; α = 90°; β = 90°; γ = 90°; volume = 15 266(5) Å<sup>3</sup>; *Z* = 2; ρ<sub>calc</sub> = 2.351 g/cm<sup>3</sup>; μ = 16.246 mm<sup>-1</sup>; F(000) = 9779.0; 2θ range = 2.83° to 46.234°; 225984 reflections collected; 21503 unique (R<sub>int</sub> = 0.0722); giving R<sub>1</sub> = 0.0331, wR<sub>2</sub> = 0.0742 for 21503 with [I > 2σ(I)] and R<sub>1</sub> = 0.0385, wR<sub>2</sub> = 0.0768 for all 225 984 data. Residual electron density (e<sup>-</sup>·Å<sup>-3</sup>) max/min: 3.14/-1.30.

SC-XRD data collection was performed at 273 K on a Bruker Apex II diffractometer with Mo Kα (λ = 0.71073 Å) radiation source. The reflections were indexed by using the APEX II program suite. Data were corrected for absorption effects with SADABS using multiscan methods.<sup>52</sup> The structure was solved with SHELXT<sup>53</sup> and subsequent structure refinements were performed with SHELXL<sup>54</sup> using Olex2 program.<sup>55</sup> All non C and H atoms were refined anisotropically and the H atoms were added as riding atoms.

**Alloy Crystal Structure Substitutional Disorder Refinement.** The structure solution from the experimental diffraction was obtained by assigning all the metal atoms as Au, i.e., a formula of C<sub>240</sub>S<sub>24</sub>Au<sub>36</sub> was used. The solution was then refined by SHELXL<sup>54</sup> least-squares method. One by one, all metal atom sites are assigned individual free variables in two PART instructions for Au and Ag partial occupancy along with EXYZ and EADP cards and refined (Figure S1). For a two component substitutional disorder refinement, the site occupancy factor (sof) for each metal site has to be modified from 11.0000 to 21.0000 (in PART 1), -21.0000 (in PART 2), and 31.0000 (in PART 1), -31.0000 (in PART 2) and so forth for all the metal sites (Figure S1). Accordingly, the element symbol in atom name and positional number in the SFAC line to indicate atom type for PART 2 instruction should be modified (Figure S1). After several cycles of refinement, sites with ≥10% Ag occupancy are retained for partial occupancy and the remaining are reverted to Au only. Then, followed by the several cycles of refinement, sites with ≥10% Ag occupancy are retained for partial occupancy, and the remaining are reverted to Au only. After repeating this procedure, sites that possess significant Ag occupancies can be reliably modeled for the nanoalloy molecule. The detailed ellipsoidal models, anisotropic displacement parameter (ADP) values, and partial occupancies during the various steps of substitutional disorder refinement are shown in Figures S2–S5.

**Transient Absorption Measurements.** Femtosecond transient absorption measurements were carried out at the Center for Nanoscale Materials, Argonne National Laboratory on Au<sub>36</sub> and Ag-doped Au<sub>36</sub>.<sup>56</sup> Briefly, a Spectra Physics Tsunami Ti:sapphire, 75 MHz oscillator was used to seed a 5 kHz Spectraphysics Spitfire Pro regenerative amplifier. 95% of the output from the amplifier is used to pump a TOPAS optical parametric amplifier, which is used to provide the pump beam in a Helios transient absorption setup (Ultrafast Systems Inc.). A pump beam of 370 nm was used for the measurements. The remaining 5% of the amplified output is focused onto a sapphire crystal to create a white light continuum that serves as the probe beam in our measurements (450 to 750 nm). The pump beam was depolarized and chopped at 2.5 kHz and both pump and probe beams were overlapped in the sample for magic angle transient measurements. Optical absorption measurements were carried out to monitor the stability of the clusters with laser excitation.

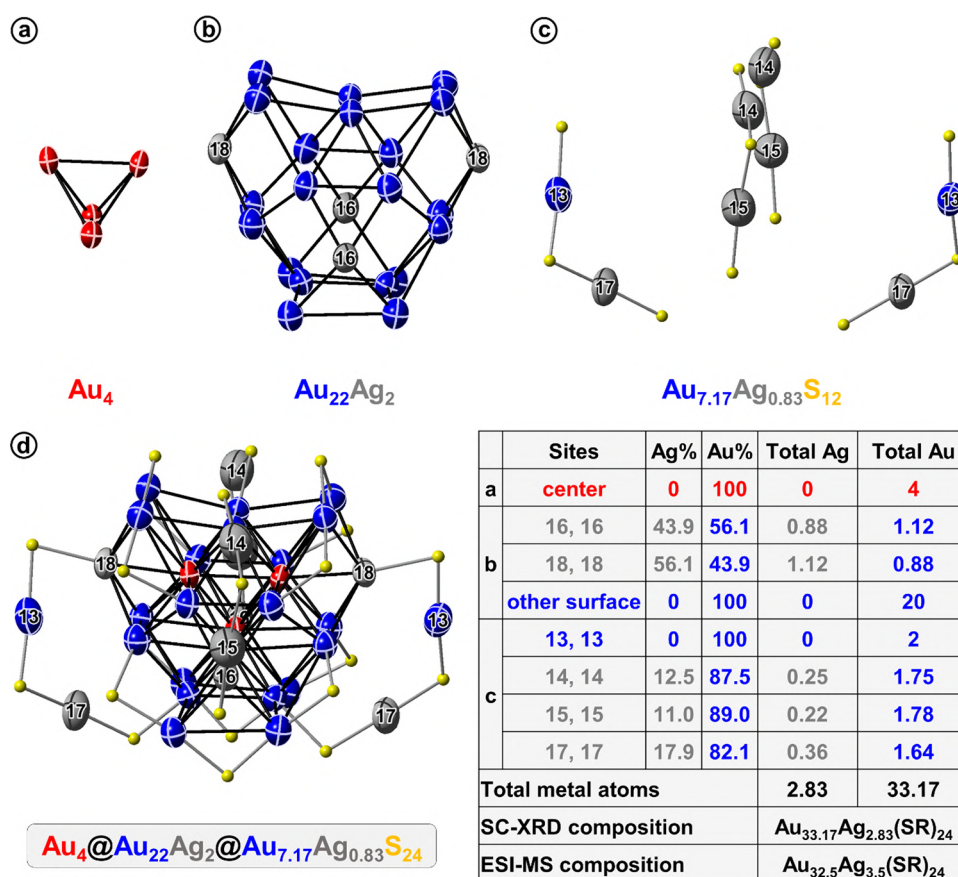


**Figure 1.** X-ray crystal structure of  $\text{Au}_{36-x}\text{Ag}_x(\text{SPh-}t\text{Bu})_{24}$  NMs. (a) 4 tetrahedral central Au atoms (red). (b) 24 metal atom sites following the central atoms, where 4 tetrahedrally symmetrical vertices sites are doped with Ag (16, 16, 18 and 18), contributing 2 Ag to the total composition. (blue, Au and gray, Ag partial occupancy sites) (c) 4 dimeric staples with 8 metal sites of which two metal sites (13, 13) has no Ag occupancy and rest of the sites contribute 7.17 Au and 0.83 Ag to the total composition. (d) 28 metal atom core protected by 4 dimeric staples and 12 bridging ligands. The anisotropic displacement parameter (ADP) is a key indicator to identify sites occupied by hetero metal atoms. Thermal ellipsoids' size and shape are visual indicators which reflects the ADP value and it is not revealed by typical ball and stick models. Therefore, metal sites are intentionally displayed as thermal ellipsoids to reveal the equally sized ellipsoids after modeling for substitutional disorder refinement (vide infra). Black bonds are bonds between metal atoms in core, gray bonds are S bonds to the metal sites. C and H groups of the ligand shell are excluded for clarity. Site-wise composition for the 36 metal sites is listed on the right-hand side table. SC-XRD and ESI-MS based (Au,Ag) composition are (33.17,2.83) and (32.5,3.5), respectively. The site numbers were assigned as in the crystallographic information file (CIF). Two sites have same site number (e.g., 16, 16) as the asymmetric unit in the crystal structure is half a molecule. Refer Figures S6 and S7 for ball and stick model view and the 24 surface atom site numbers, respectively. In the discussion below, some metal sites are described with a prime (') for clarity, they are symmetric sites generated from the asymmetric unit (for example, Ag16/Ag16').

**Instrumentation.** Electrospray Ionization mass spectrum (ESI-MS) was collected using a Waters Synapt HDMS instrument with THF as the solvent. Cesium acetate dissolved in anhydrous ethanol was used to facilitate the ionization. UV-vis absorption spectrum was collected using a Shimadzu UV-1601 spectrophotometer with toluene as the solvent.

## RESULTS AND DISCUSSION

**Crystallography.** The  $\text{Au}_{36-x}\text{Ag}_x(\text{SPh-}t\text{Bu})_{24}$  NMs crystallized in an orthorhombic unit cell in the  $P2_12_12$  space group with 2 molecular units per unit cell. The final  $\text{Au}_{33.12}\text{Ag}_{2.88}(\text{SPh-}t\text{Bu})_{24}$  structural model has a  $R_1$  value of 3.31%. The crystal structure of  $\text{Au}_{33.17}\text{Ag}_{2.83}$  nanoalloy is presented in Figure 1. The structural framework of the  $\text{Au}_{33.17}\text{Ag}_{2.83}(\text{SPh-}t\text{Bu})_{24}$  nanoalloy is identical to that of the parent compound  $\text{Au}_{36}(\text{SR})_{24}$ . This framework can be described in two different way; here we adopt the original description based on 28 metal atom FCC core protected by 12 bridging thiolate ligands ( $-\text{Au-S(R)-Au-}$ ) and 4 dimeric staple

motifs ( $-(\text{R})\text{S}-\text{Au}-\text{S(R)}-\text{Au-S(R)}-$ )<sup>37,39</sup> (for an alternative one see Theivendran et al.<sup>47</sup>). The truncated tetrahedral 28 metal atom core is made up of 4 interpenetrating cuboctahedra consisting of 4 atom tetrahedron in the center and 24 atoms on the surface (Figure 1). On the core-surface, four dimeric staple motifs protect 8 metal atoms and the remaining 16 metal atoms are protected by 12 bridging ligands. In the Ag-doped  $\text{Au}_{36}$ , the 4 sites on the surface of the core are heavily doped ( $\sim 50\%$ ) by Ag while the remaining 20 surface atoms and 4 center atoms are Au only (Figure 1a and 1b). The four Ag atoms (Ag16, Ag16', Ag18, and Ag18', designated ExTd by Theivendran.<sup>47</sup>) on the core-surface are doped in a tetrahedrally symmetrical fashion on the vertices of interpenetrating cuboctahedron protected by dimeric staple motifs (Figure 1b, only Ag containing sites are labeled for clarity, site numbers were assigned as in the crystallographic information file (CIF)). The partial occupancies at Ag16/Ag16' and Ag18/Ag18' are 44% and 56%, respectively. These 4 heavily doped sites on the core contribute to 2 Ag in the overall composition (accounting for  $\sim 71\%$  of Ag in the overall composition). The

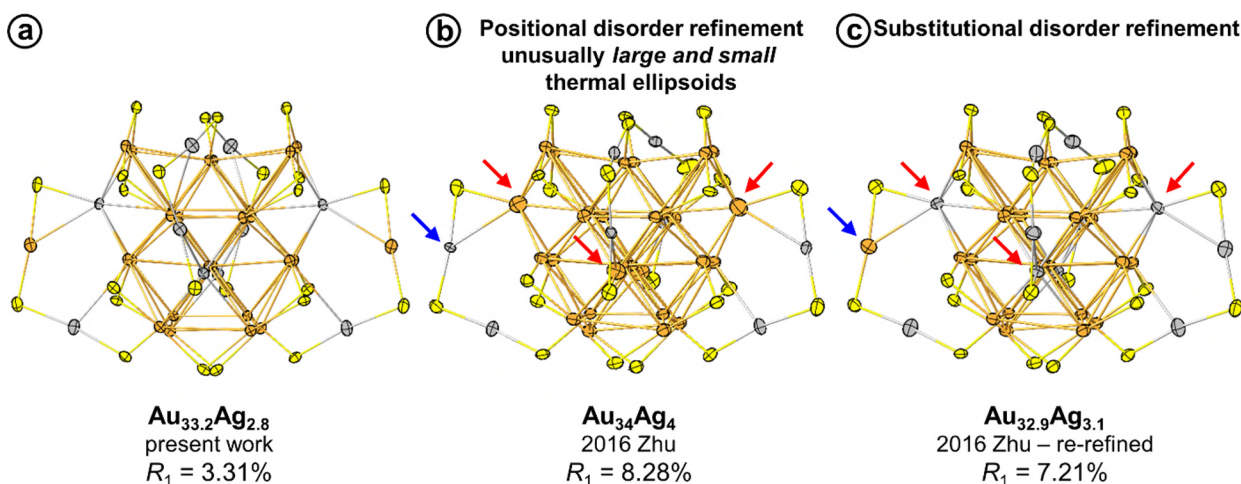


**Figure 2.** Comparison of X-ray crystal structure models refined for substitutional disorder by Ag doping in  $\text{Au}_{36}(\text{SPh-}t\text{Bu})_{24}$  nanomolecules.  $\text{Au}_{36-x}\text{Ag}_x(\text{SPh-}t\text{Bu})_{24}$  alloy structure model (a) from this present work, (b) from 2016 report with one free variable fixing 50% occupancy for 8 metal atom sites on dimeric staple motifs, and (c) structural model from 2016 report re-refined with independent free variables for each metal sites. Three of the thermal ellipsoids in (b) are indicated by red arrows revealing relatively higher ADP value than other Au atoms and in (c) ADP for the same site drops upon refinement for Ag partial occupancy leading to ~40–50% Ag occupancy on those sites. Blue arrow in (b) indicates a staple motif metal site (shrunk) with low ADP value whereas after refining for substitutional disorder, in (c) that site has only Au and the thermal ellipsoid is of similar size as neighboring sites. Totally in frame 2c, there are four Ag occupancy sites on the 28 atom FCC core surface, same as the structure obtained in the present work (Figure 1). Refer to the Experimental Section and Figures S2–S5 for detailed explanation on the substitutional disorder refinement. The work by Zhu et al.<sup>48</sup> is referred to as 2016 Zhu in (b) and (c).

remaining 0.83 Ag is spread out on the 6 dimeric staple motif sites (Ag14/Ag14', named ExSt-Near and Ag15/Ag15' and Ag17/Ag17', named ExSt-Far in Theivendran et al.<sup>47</sup>) with partial occupancies of 12.5%, 11%, and 18%, respectively (Figure 1C). The remaining two dimeric staple sites (Au13/Au13') are exclusively Au only (Figure 1C). Clearly, the level of Ag doping here achieved is smaller than that investigated previously,<sup>47</sup> so that we do not observe here phenomena such as the nonmonotonic behavior of optical properties as a function of doping content, as reported in our previous work.

In the case of phenylethanethiolate protected  $\text{Au}_{25-x}\text{Ag}_x$  and  $\text{Au}_{38-x}\text{Ag}_x$ , Au atoms were doped exclusively on the core surface. In the case of aromatic TBBT ligand protected  $\text{Au}_{36-x}\text{Ag}_x$ , it was reported that the Ag atoms are exclusively doped on the 8 Au atoms in dimeric staple motifs with 50% Ag occupancy at each of those sites (using positional disorder) contributing to 4 Ag atoms in the overall composition.<sup>48</sup> However, here we show that better modeling with improved  $R_1$  values is obtained allowing for partial Ag occupancy by refining for substitutional disorder,<sup>57</sup> leading to a significant population of the core surface sites (Figure 2), similar to the results discussed in Figure 1. This directly contradicts with the “solely motif-doped” conclusion from the earlier report.<sup>48</sup> This finding is more consistent with computational results indicating that Ag doping on the core surface is energetically preferred.<sup>47</sup>

**Substitutional Disorder vs Positional Disorder Refinement of  $\text{Au}_{36-x}\text{Ag}_x$ .** One of the key indicators for substitutional disorder in metal sites is the presence of large or small atomic displacement parameter (ADP) values compared to other sites which are occupied by only one element. The ADP values of the sites occupied with multiple elements, vary significantly after refining for substitutional disorder with individual free variables (Figure 2) and is reflected in the size of the ellipsoids. Figure 2 shows the comparison between ellipsoidal models for SC-XRD data from this work, 2016 report<sup>48</sup> and 2016 model re-refined following the protocol

described above (detailed protocol is provided in the Experimental Section).

The erroneous use of positional disorder modeling (instead of substitutional disorder modeling) resulted in the conclusion that the Ag atoms are “solely motif-doped”. For the 2016 Zhu paper, we extracted the data from the published crystallographic information file (CIF) embedded with hkl data, we hypothesized that the small and large thermal ellipsoids arise from substitutional disorder. We modeled it for substitutional disorder (instead of positional disorder as in 2016 Zhu paper) and the resulting model after refinement resulted in equally sized thermal ellipsoids and improved  $R_1$  values. The Ag occupancy sites and percentage Ag partial occupancies in the re-refined model of 2016 Zhu paper (Figures 2b, S4, and S5) are very similar to the findings in this work (Figures 1, 2a, S2, and S3).

To describe this in crystallographic terminology, Figure 2b was modeled by using positional disorder modeling for Au/Ag partial occupancy of the 8 staple motif metal sites with a special position, site occupancy factor (sof) of 10.5000 for Au and Ag sites in PART instructions coupled with EXYZ and EADP cards. (EXYZ assigns same x, y and z parameters to the named atoms, for example, EXYZ Au18 Ag18, instructs two elements to occupy the same position (coordinates). EADP assigns same isotropic or anisotropic displacement parameters for the named atoms.) This led to fixed 50% Ag occupancy on staple motifs metal sites and unusually large and small thermal ellipsoid sizes, as indicated by the red and blue arrows in Figure 2b, respectively. The sof value of 10.5000 for an atom in an ordered structure conveys that the site is at a special position located on a 2-fold axis or on an inversion center.<sup>57</sup> In the 2016 report, using the special position sof for substitutional disorder refinement lead to the “solely motif-doped” structure with 50% Ag occupancy on staple metal sites. In Figure 2c, after substitutional disorder modeling (Figures S4 and S5), the thermal ellipsoids were equally sized and Ag occupancy sites are similar to Figure 2a result from our work. We also refined

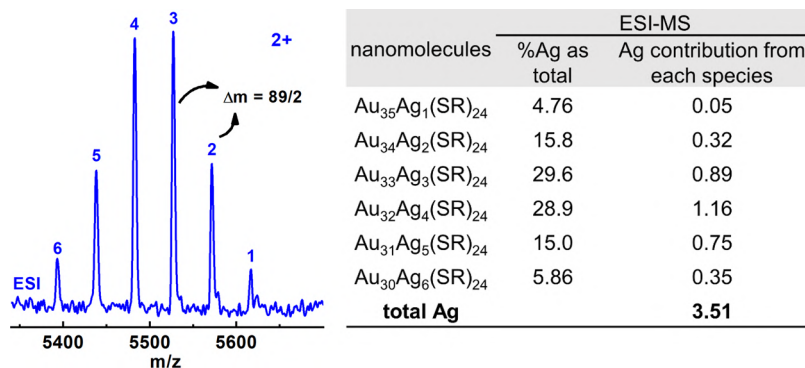


**Figure 3.** ESI mass spectra of Au<sub>36-x</sub>Ag<sub>x</sub>(SPh-tBu)<sub>24</sub> alloy NMs with  $x = 1-6$ . Au<sub>36-x</sub>Ag<sub>x</sub>(SPh-tBu)<sub>24</sub>Cs<sub>2</sub><sup>2+</sup> peaks of the alloy NMs. Each peak has a  $m/z$  difference of 89/2 Da corresponding to the 2+ charge state and mass difference between Au and Ag. The total Ag contributed to overall composition based on mass spectrometry is determined based on the peak intensity and are listed in the table.

our SC-XRD data similar to 2016 Zhu paper instead of substitutional disorder to illustrate how that affects the structure model (Figure S8). The staple motif metal sites were modeled for 50% partial occupancy by positional disorder refinement. It led to an increase in  $R_1$  value from 3.31% to 4.73%, unusually large and small thermal ellipsoids, and site 13 which has no significant Ag occupancy showed a non-positive definite.

In the Au<sub>36-x</sub>Cu<sub>x</sub> structure report, the model has several metal sites linked by only two free variables for Au/Cu partial occupancy with sof values of 21.0000,-21.0000 (4 sites) and 31.0000,-31.0000 (10 sites) instead of 14 independent free variables.<sup>49</sup> This led to a Cu partial occupancy of 21.5% and 13.3% in 4 sites and 10 sites, respectively (Figure S8).<sup>49</sup> Figure S9 reveals the unusually elongated thermal ellipsoids on 4 staple motif sites with 21.5% Cu occupancy linked by one free variable, instead of four independent free variables.

**Mass Spectrometry.** The composition of Au<sub>36-x</sub>Ag<sub>x</sub>(SPh-tBu)<sub>24</sub> alloy NMs was determined by ESI-MS to independently verify the composition determined by SC-XRD. Au<sub>36-x</sub>Ag<sub>x</sub>(SR)<sub>24</sub> alloy NMs ionized in its +2 charge state with two Cs<sup>+</sup> adducts facilitating the ionization of the neutral compound. The  $m/z$  peaks were observed at 5617, 5572, 5527, 5482, 5438, and 5393 Da with a difference of ~45 Da corresponding to half the mass difference between an Au and Ag atom (89 Da/2; Figure 3). The Ag<sub>x</sub> ranges from 1 to 6 and the average Ag contribution to the total composition was determined by considering the peak intensities, yielding an average composition of Au<sub>32.49</sub>Ag<sub>3.51</sub>(SPh-tBu)<sub>24</sub> (Figure 3). The relative contribution from each Au<sub>36-x</sub>Ag<sub>x</sub>(SR)<sub>24</sub> species (Au<sub>35</sub>Ag<sub>1</sub>, Au<sub>34</sub>Ag<sub>2</sub>, Au<sub>33</sub>Ag<sub>3</sub>, Au<sub>32</sub>Ag<sub>4</sub>, Au<sub>31</sub>Ag<sub>5</sub>, and Au<sub>30</sub>Ag<sub>6</sub>) are 4.96, 15.8, 29.6, 28.9, 15.0, and 5.86%, respectively (Figure 3 table). The average Ag composition determined by mass spectrometry is in reasonable agreement with the crystallographically determined formula of Au<sub>33.17</sub>Ag<sub>2.83</sub>(SPh-tBu)<sub>24</sub>. The difference in AuAg composition between mass spectrometry and SC-XRD could stem from the fact that the crystallographic model accounts only for significant Ag partial occupancies ( $\geq 10\%$ ) over several cycles of refinement and/or difference in ionization efficiency. The SC-XRD re-refined model of the previous report<sup>48</sup> has a composition of Au<sub>32.88</sub>Ag<sub>3.12</sub>(SPh-tBu)<sub>24</sub> and it is also in close agreement with our results and similar site occupancies.

**Optical Studies.** The Au<sub>36-x</sub>Ag<sub>x</sub>(TBBT)<sub>24</sub> alloy nanomolecule exhibits absorption features at ~373 and ~565 nm and a prominent shoulder at ~425 nm whereas the

homometallic Au<sub>36</sub>(TBBT)<sub>24</sub> nanomolecule has two prominent absorption bands at ~376 nm and ~575 nm and a broad shoulder at ~412 nm (Figure 4). The 373 and 376 nm features

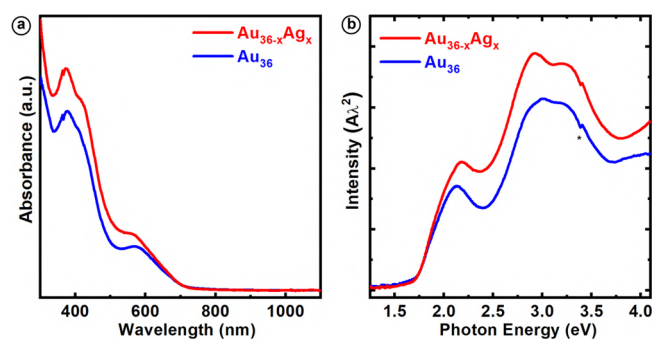


**Figure 4.** (a) UV-vis absorption spectra and (b) photon energy plot of Au<sub>36-x</sub>Ag<sub>x</sub>(SPh-tBu)<sub>24</sub> alloy compared with the parent compound Au<sub>36</sub>(SPh-tBu)<sub>24</sub>. red is Au<sub>36-x</sub>Ag<sub>x</sub> alloy and blue is Au<sub>36</sub>. \* instrumental artifact.

are almost similar in both the systems whereas there is a red shift in the shoulder at ~412 to ~425 nm and a blue shift in the ~575 nm peak to ~565 nm. Apart from these details, one can observe that at this low level of Ag doping the overall appearance of the optical absorption spectra is similar for both pure Au and Ag-doped species. The optical band gap of the Au<sub>36-x</sub>Ag<sub>x</sub>(TBBT)<sub>24</sub> alloy is not altered, and it is ~1.7 eV. The static optical response of the Au<sub>36-x</sub>Ag<sub>x</sub>(TBBT)<sub>24</sub> alloy nanomolecule is similar to the previous report by Zhu et al.<sup>48</sup> This indicates that independent of the synthetic route the doping pattern and property of Au<sub>36</sub> system is constant. However, we will see that Ag doping brings about significant differences in the dynamical optical response of Au<sub>36-x</sub>Ag<sub>x</sub>(TBBT)<sub>24</sub> alloy nanomolecules.

**Transient Absorption Analysis.** Metal doping of gold clusters can affect both ground and excited state optical properties. However, the optical absorption measurements of Au<sub>36</sub> and AgAu<sub>36</sub> reported above show no striking differences, suggesting that Ag-doping at this low level has little effect on the ground state optical properties. It is however still interesting to see the influence of Ag-doping on the excited state optical properties. Shown in Figure 5a are the excited state absorption (ESA) spectra at different time delays for Au<sub>36</sub> after excitation at 370 nm. Immediately after photoexcitation, a transient with a maxima around 480 and 660 nm is observed.

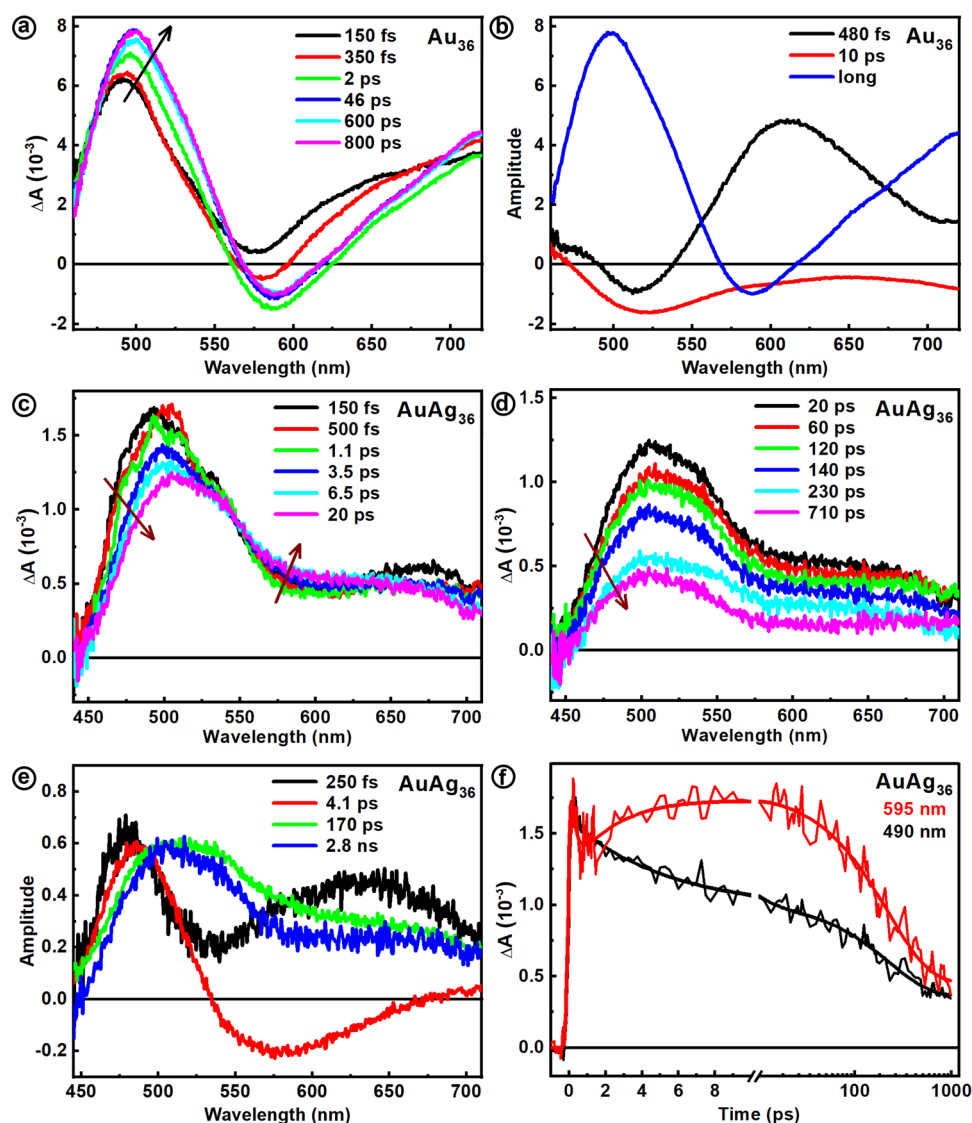


**Figure 5.** (a) Excited state absorption spectra at different time delays for  $\text{Au}_{36}$  and (b) species-associated spectra obtained from global fit analysis. Excited state absorption spectra at different time delays for  $\text{Au}_{36-x}\text{Ag}_x$  (noted as  $\text{AuAg}_{36}$ ) after excitation at 370 nm: (c) 150 fs to 20 ps and (d) 20 to 700 ps. (e) Species associated spectra obtained from global fit analysis. (f) Kinetic decay comparison at 490 nm (black) and 595 nm (red) showing the early relaxation and long-lived at two different wavelengths for  $\text{AuAg}_{36}$ .

This transient grows and decays, giving rise to a bleach with a maximum around 570 nm. Species-associated spectra obtained from global fit analysis (Figure 5b) show three main components: the first one with a time scale of 480 fs, a second one with 10 ps and a long-lived transient. Subpicosecond relaxation of the 480 fs transient is assigned to intracore state relaxation, while the 10s of picosecond relaxation is related to the growth of the transient and is assigned to the thermalization that was observed only for  $\text{Au}_{36}$  with aromatic ligands. The long-lived transient has a lifetime of 160 ns as determined from time-resolved luminescence measurements. The observed excited state relaxation is typical of most ligand-protected gold clusters. Let us now examine how the metal-doping altered the excited state relaxation dynamics.

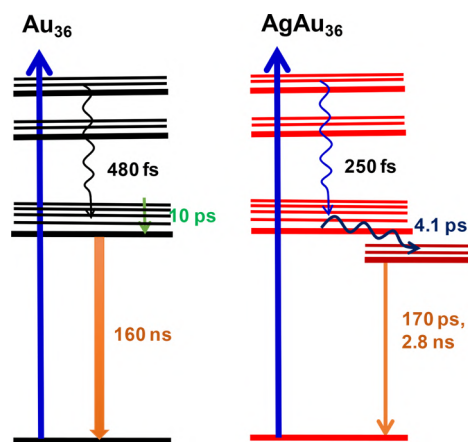
Contrary to what is observed in steady-state measurements, the excited state absorption measurements show that Ag-doping has a significant effect on the excited state relaxation dynamics. Shown in parts c and d of Figure 5 are the excited state absorption at short and long-time delays for  $\text{AgAu}_{36}$  after

excitation at 370 nm. A decay of ESA from 150 fs to 20 ps at 490 nm followed by an increase between 550 to 630 nm is observed (Figure 5c). However, a consistent decay is observed at all wavelengths from 20 to 700 ps (Figure 5d) suggesting that the excited state relaxation became faster with Ag-doping with respect to pure  $\text{Au}_{36}$ . For a better understanding, species-associated spectra were obtained from global fit analysis and are shown in Figure 5e. Interestingly, 4 components can be derived from this global fit analysis. The first component has a time scale of 250 fs that can be assigned to ultrafast intra-core state relaxation for  $\text{AuAg}_{36}$ . It appears that the intra-core state relaxation becomes faster with Ag-doping. The 4.1 ps component spectral properties matched well with long-lived excited state of  $\text{Au}_{36}$  indicating that the faster intra-core state relaxation populates the lowest excited state of  $\text{Au}_{36}$  but that decays to give rise to another state which decays with 170 ps and 2.8 ns. A comparison of kinetic traces at 490 and 595 nm (Figure 5f) shows the 250 fs and 4.1 ps decay components followed by faster charge recombination back to ground state

when compared to  $\text{Au}_{36}$ . A comparison of long-lived states (Figure S10) of  $\text{Au}_{36}$  and  $\text{AuAg}_{36}$  shows that overall lifetime of  $\text{Au}_{36}$  has decreased to around 2 ns from 160 ns of  $\text{Au}_{36}$ .

Overall, the excited state relaxation of Ag-doped  $\text{Au}_{36}$  can be summarized as shown in Scheme 1. Intra-core state relaxation

**Scheme 1. Cartoon Diagram Depicting the Excited-State Relaxation in  $\text{Au}_{36}$  and  $\text{AgAu}_{36}$  Clusters**



and thermalization followed by 160 ns decay with photoluminescence is observed for  $\text{Au}_{36}$ . Upon Ag-doping, the intra-core state relaxation became faster ending with the lowest excited state of  $(\text{AuAg})_{36}$  which decays to give rise to dark states with probable contributions from the shell-gold comprising of Ag. These shell-gold states decay nonradiatively with lifetimes of 170 ps and 2.8 ns, which are much faster than those observed in  $\text{Au}_{36}$ .

**Theoretical Analysis of the Optical Response.** The structural and static optical properties of  $\text{Ag}_x\text{Au}_{36-x}(\text{TBBT})_{24}$  nanomolecules were investigated using first-principles density-functional theory (DFT) and time-dependent DFT (TDDFT) modeling, along the lines of our previous work.<sup>47</sup> Within our computational method, we cannot achieve a statistical occupation of sites by Ag, therefore we have taken the experimental X-ray structure and produced a few isomers (homotops) by replacing selected Au atoms with Ag. In particular, in the following we will focus on two models with composition  $\text{Ag}_4\text{Au}_{32}(\text{TBBT})_{24}$ , in which we replaced either the [17,17',18,18'] Au atoms ( $\text{Ag}_4\text{Au}_{32}\text{-ExTd-ExStFar}$  in the nomenclature of Theivendran et al.<sup>47</sup>) or the [15,15',16,16'] Au atoms ( $\text{Ag}_4\text{Au}_{32}\text{-ExTd-ExStNear}$  in the nomenclature of Theivendran et al.<sup>47</sup>). The coordinates of the (Ag/Au,S) atoms were frozen to those of the  $\text{Ag}_x\text{Au}_{36-x}(\text{TBBT})_{24}$  crystallographic structure, while the organic part (CH atoms) were

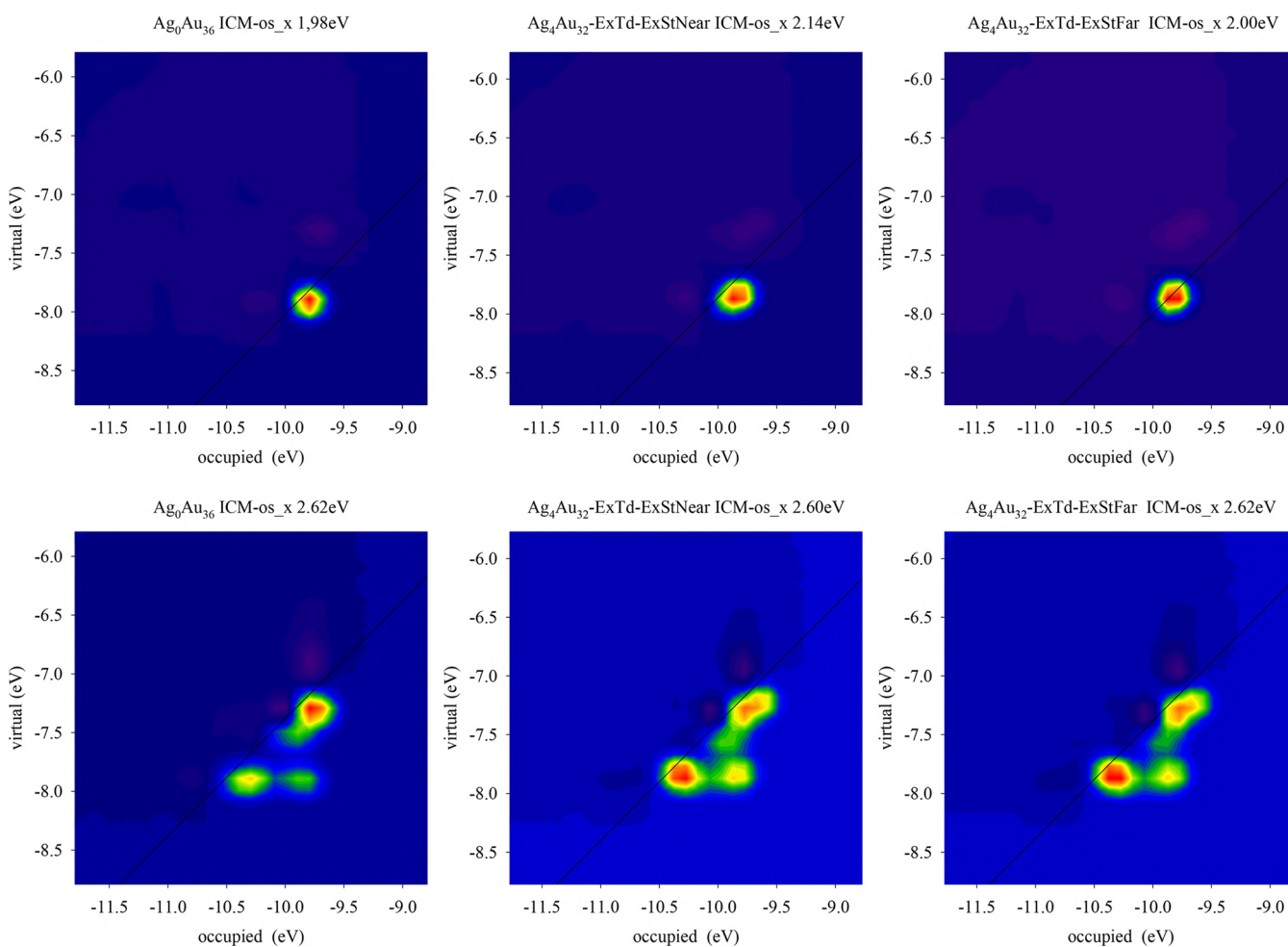


**Figure 6.** ICM-OS plots ( $x$  Cartesian component) for  $\text{Au}_{36}(\text{SPh-tBu})_{24}$  and the two homotop  $\text{Ag}_4\text{Au}_{32}(\text{SPh-tBu})_{24}$  model clusters considered in this work in the energy region corresponding to the 580 nm (upper boxes) and 500 nm (lower boxes), see text for details.

relaxed at DFT level. DFT calculations were performed by employing the CP2K code<sup>58</sup> within the hybrid Gaussian/Plane-Wave scheme (GPW). Core electrons were described with pseudopotentials derived by Goedecker, Teter, and Hutter<sup>59</sup> whereas DZVP basis sets<sup>60</sup> were used for representing the DFT Kohn–Sham valence orbitals. The cutoff for the auxiliary plane wave representation of the density was 400 Ry. Calculations were performed spin-unrestricted. The semi-empirical Grimme-D3 correction<sup>61</sup> was added to Perdew–Burke–Ernzerhof (PBE)<sup>62</sup> exchange and correlation (xc-) functional to take into account dispersion interactions. It can be noted that the  $\text{Ag}_4\text{Au}_{32}\text{-ExTd-ExStFar}$  homotop is more stable than the  $\text{Ag}_4\text{Au}_{32}\text{-ExTd-ExStNear}$  homotop by 0.19 eV, in contrast with the findings of Theivendran et al.,<sup>47</sup> Table S1, suggesting that the use of experimental geometries can tune the theoretical predictions, as previously observed.<sup>63</sup>

On the so-derived geometries, optical spectra were simulated using TDDFT via a complex polarizability algorithm,<sup>64,65</sup> the ADF package,<sup>66</sup> and the LB94 exchange-correlation potential,<sup>67</sup> while the exchange-correlation kernel in the TDDFT part was approximated according to the Adiabatic LDA (ALDA).<sup>68</sup> A STO basis set of TZP quality was employed, which has proven to provide accurate results.<sup>69</sup> The Zero Order Regular Approximation (ZORA)<sup>70</sup> was employed to include relativistic effects. The imaginary frequency employed to introduce finite lifetime of the excited state was fixed to 0.075 eV. Calculations were performed spin-restricted for predicting TDDFT response.

TDDFT/LB94 spectra were also analyzed in terms of Individual Component Maps of Oscillator Strength (ICM-OS) plots, as proposed in Theivendran et al.<sup>47</sup> These plots visualize the contribution to the Oscillator Strength from single-particle excitations in the (virtual/occupied) molecular orbital plane for an excited state at a given energy and in a given Cartesian direction of the exciting electric field.

The calculated photoabsorption profiles of  $\text{Au}_{36}(\text{SPh-}t\text{Bu})_{24}$  and the two homotop  $\text{Ag}_4\text{Au}_{32}(\text{SPh-}t\text{Bu})_{24}$  model nanomolecules are reported in Figures S11 and S12. A qualitatively similar profile was obtained for the pure and doped clusters in agreement with the experimental data. It is reasonable considering the low level of doping and the fact that most of Ag atoms occupy the ExTd sites which are energetically favorable (and should thus be preferably occupied when doping achieves thermodynamic equilibrium) but induce a smaller effect on optical absorption<sup>47</sup> (a more detailed discussion is provided in the SI). Although the absorption spectrum is not strongly affected by silver alloying, the transient absorption analysis has identified, for the silver doped clusters, two-state dynamics. This indicates that the decay mechanism passes through a higher excited state (at 500 nm) whose population constantly decreases, followed by a low-lying excited state (at 580 nm) whose population increases before eventually decaying to the ground state. To shed light on this mechanism however being unable to model long-time excited-state dynamics, we investigated the nature of the excited states at the ICM-OS level, which corresponds to the experimental features at 500 and 580 nm. ICM-OS plots are reported in Figure 6. The nature of the low-lying excited state (upper panels) is similar for the pure gold clusters and the two alloy homotops containing 4 silver atoms: the presence of only one spot on the straight line corresponding to orbital energy differences equal to the excitation energy suggests a “molecular” behavior without coupling. In contrast, the nature

of the higher-energy excited state (lower panel) is more complex: two spots on the straight line are supplemented by a third spot which is off-diagonal and suggests a strong coupling with lower-energy configurations. The third off-line spot corresponds to the low-energy excited state, so that a coupling between higher- and lower-energy excited states is disclosed from this analysis. Even more interestingly, such off-diagonal spot is much more pronounced in the silver alloys than in the pure gold cluster, suggesting that such coupling is much more effective in the presence of silver. This helps rationalize the dynamics observed in the transient absorption experiment: while in pure gold cluster the decay to the ground state is direct, since there is weak coupling with the low-lying state, in silver alloys such coupling is stronger and the decay to this intermediate low-lying excited state is favored. To give a more complete description of the different excited states, in Figures S13, S14, and S15 of the SI we report plots of the molecular orbitals involved. These plots show that all occupied and virtual orbitals mostly contributing to the single-particles excitations here involved are localized on the cluster ligand shell and outer metal core, with strong S contribution as well as significant contributions from metal staple atoms and atoms on the cluster surface, while the contribution of the organic residues are smaller although not negligible. The present analysis demonstrates the usefulness of the ICM-OS analysis to reveal coupling between excited states. Finally, the ICM-OS plots in Figure 6 also reveal that the similar absorption intensity between pure and Ag-doped systems actually results from a compensation (negative interference) between single-particle contributions giving rise to increasing and decreasing intensity: as discussed in Theivendran et al.,<sup>47</sup> absorption intensity corresponds to an absolute value and can therefore mask subtle quantum effects which are revealed in dynamics.

## CONCLUSIONS

In summary, the crystal structure of TBBT protected  $\text{Au}_{36-x}\text{Ag}_x$  nanomolecules has revealed that the core-centered metal sites are occupied by Au atoms only ( $\text{Au}_4$ ), Ag hetero atoms significantly populates 4 sites on the core-surface ( $\text{Au}_{22}\text{Ag}_2$ ), and Ag occupies 10–20% on 6 metal sites in the dimeric staple motifs while 2 sites are occupied by Au only. The doping pattern observed here is more consistent with computational results indicating that Ag doping on the core surface is energetically preferred.<sup>47</sup> The composition of the  $\text{Au}_{36-x}\text{Ag}_x$  nanomolecules determined by mass spectrometry agrees reasonably well with the SC-XRD structure. The optical absorption spectrum of the nanoalloy has absorption features at  $\sim 373$ ,  $\sim 425$ , and  $\sim 565$  nm. It is similar to the previous report by Zhu et al.<sup>48</sup> and the re-refined structural model of their data also exhibits a similar doping pattern as determined in this work. It indicates that care must be taken in performing the substitutional disorder refinement to obtain a reliable structural model.

We also studied the excited state optical properties of the  $\text{Au}_{36}$  and  $\text{Au}_{36-x}\text{Ag}_x$  alloy nanomolecules and ICM-OS analyses to provide insights into the experimental results. Transient absorption studies revealed that, Ag doping leads to faster excited state decay lifetimes compared to the  $\text{Au}_{36}$  nanomolecules. ICM-OS analyses revealed that Ag doping in  $\text{Au}_{36}$  leads to a stronger coupling between higher- and lower-energy excited states complementing the results from transient absorption measurements.

## ■ ASSOCIATED CONTENT

## S Supporting Information

The Supporting Information is available free of charge at <https://pubs.acs.org/doi/10.1021/acs.jpcc.9b09060>.

CCDC deposition number 1955713 (CIF)

Detailed figures, crystal structure tables, TDDFT details, transient decay kinetics, TDDFT spectra, molecular orbitals, substitutional disorder refinement (PDF)

## ■ AUTHOR INFORMATION

## Corresponding Author

\*E-mail: [amal@olemiss.edu](mailto:amal@olemiss.edu).

ORCID 

Naga Arjun Sakthivel: 0000-0001-8134-905X

Mauro Stener: 0000-0003-3700-7903

Guda Ramakrishna: 0000-0002-5288-8780

Alessandro Fortunelli: 0000-0001-5337-4450

Amala Dass: 0000-0001-6942-5451

## Notes

The authors declare no competing financial interest.

## ■ ACKNOWLEDGMENTS

NSF-CHE-1808138 and NSF-CHE-1255519 supported the work performed by N.S. and A. D. We gratefully acknowledge the support by Vignesh Raja Ganesh Raj in SC-XRD data collection and 2019 American Crystallographic Association Summer course. G.R. acknowledges the support of Western Michigan University-FRACAA and Dr. Gary Wiederrecht, Argonne national laboratory for help with transient absorption measurements. Use of the Center for Nanoscale Materials, an Office of Science user facility, was supported by the U.S. Department of Energy, Office of Science, Office of Basic Energy Sciences, under Contract No. DE-AC02-06CH11357. A.F. and L.S. gratefully acknowledge the computational support at CINECA supercomputing center (ISCRA awards HP10B89V25 and HP10BSR1VZ).

## ■ REFERENCES

- (1) Kumara, C.; Dass, A. AuAg<sub>144</sub>(SR)<sub>60</sub> Alloy Nanomolecules. *Nanoscale* **2011**, *3*, 3064–3067.
- (2) Kumara, C.; Aikens, C. M.; Dass, A. X-ray Crystal Structure and Theoretical Analysis of Au<sub>25</sub>-Ag<sub>x</sub>(SCH<sub>2</sub>CH<sub>2</sub>Ph)<sub>18</sub><sup>-</sup> Alloy. *J. Phys. Chem. Lett.* **2014**, *5*, 461–466.
- (3) Kumara, C.; Zuo, X.; Cullen, D. A.; Dass, A. Au<sub>329</sub>-Ag<sub>x</sub>(SR)<sub>84</sub> Nanomolecules: Plasmonic Alloy Faradaurate-329. *J. Phys. Chem. Lett.* **2015**, *6*, 3320–3326.
- (4) Kumara, C.; Gagnon, K. J.; Dass, A. X-ray Crystal Structure of Au<sub>38</sub>-Ag<sub>x</sub>(SCH<sub>2</sub>CH<sub>2</sub>Ph)<sub>24</sub> Alloy Nanomolecules. *J. Phys. Chem. Lett.* **2015**, *6*, 1223–1228.
- (5) Kwak, K.; Choi, W.; Tang, Q.; Kim, M.; Lee, Y.; Jiang, D.-e.; Lee, D. A Molecule-like PtAu<sub>24</sub>(SC<sub>6</sub>H<sub>13</sub>)<sub>18</sub> Nanocluster as an Electrocatalyst for Hydrogen Production. *Nat. Commun.* **2017**, *8*, 14723.
- (6) Hossain, S.; Ono, T.; Yoshioka, M.; Hu, G.; Hosoi, M.; Chen, Z.; Nair, L. V.; Niihori, Y.; Kurashige, W.; Jiang, D.-e.; et al. Thiolate-Protected Trimetallic Au<sub>20</sub>Ag<sub>4</sub>Pd and Au<sub>20</sub>Ag<sub>4</sub>Pt Alloy Clusters with Controlled Chemical Composition and Metal Positions. *J. Phys. Chem. Lett.* **2018**, *9*, 2590–2594.
- (7) Hossain, S.; Niihori, Y.; Nair, L. V.; Kumar, B.; Kurashige, W.; Negishi, Y. Alloy Clusters: Precise Synthesis and Mixing Effects. *Acc. Chem. Res.* **2018**, *51*, 3114–3124.
- (8) Wang, S.; Li, Q.; Kang, X.; Zhu, M. Customizing the Structure, Composition, and Properties of Alloy Nanoclusters by Metal Exchange. *Acc. Chem. Res.* **2018**, *51*, 2784–2792.

(9) Yan, J.; Teo, B. K.; Zheng, N. Surface Chemistry of Atomically Precise Coinage–Metal Nanoclusters: From Structural Control to Surface Reactivity and Catalysis. *Acc. Chem. Res.* **2018**, *51*, 3084–3093.

(10) Gan, Z.; Xia, N.; Wu, Z. Discovery, Mechanism, and Application of Antialgal Reaction. *Acc. Chem. Res.* **2018**, *51*, 2774–2783.

(11) Chakraborty, I.; Pradeep, T. Atomically Precise Clusters of Noble Metals: Emerging Link between Atoms and Nanoparticles. *Chem. Rev.* **2017**, *117*, 8208–8271.

(12) Krishnadas, K. R.; Baksi, A.; Ghosh, A.; Natarajan, G.; Som, A.; Pradeep, T. Interparticle Reactions: An Emerging Direction in Nanomaterials Chemistry. *Acc. Chem. Res.* **2017**, *50*, 1988–1996.

(13) Wang, Y.; Wan, X.-K.; Ren, L.; Su, H.; Li, G.; Malola, S.; Lin, S.; Tang, Z.; Häkkinen, H.; Teo, B. K.; et al. Atomically Precise Alkynyl-Protected Metal Nanoclusters as a Model Catalyst: Observation of Promoting Effect of Surface Ligands on Catalysis by Metal Nanoparticles. *J. Am. Chem. Soc.* **2016**, *138*, 3278–3281.

(14) Rambukwella, M.; Chang, L.; Ravishanker, A.; Fortunelli, A.; Stener, M.; Dass, A. Au<sub>36</sub>(SePh)<sub>24</sub> Nanomolecules: Synthesis, Optical Spectroscopy and Theoretical Analysis. *Phys. Chem. Chem. Phys.* **2018**, *20*, 13255–13262.

(15) Bootharaju, M. S.; Chang, H.; Deng, G.; Malola, S.; Baek, W.; Häkkinen, H.; Zheng, N.; Hyeon, T. Cd<sub>12</sub>Ag<sub>32</sub>(SePh)<sub>36</sub>: Non-Noble Metal Doped Silver Nanoclusters. *J. Am. Chem. Soc.* **2019**, *141*, 8422–8425.

(16) Shichibu, Y.; Negishi, Y.; Watanabe, T.; Chaki, N. K.; Kawaguchi, H.; Tsukuda, T. Bicosahedral Gold Clusters [Au<sub>25</sub>(PPh<sub>3</sub>)<sub>10</sub>(SC<sub>n</sub>H<sub>2n+1</sub>)<sub>5</sub>Cl<sub>2</sub>]<sup>2+</sup> (n = 2–18): A Stepping Stone to Cluster-Assembled Materials. *J. Phys. Chem. C* **2007**, *111*, 7845–7847.

(17) Jiang, D.-e.; Whetten, R. L. Magnetic Doping of a Thiolated-Gold Superatom: First-Principles Density Functional Theory Calculations. *Phys. Rev. B: Condens. Matter Mater. Phys.* **2009**, *80*, 115402.

(18) Choi, W.; Hu, G.; Kwak, K.; Kim, M.; Jiang, D.-e.; Choi, J.-P.; Lee, D. Effects of Metal-Doping on Hydrogen Evolution Reaction Catalyzed by MAu<sub>24</sub> and M<sub>2</sub>Au<sub>36</sub> Nanoclusters (M = Pt, Pd). *ACS Appl. Mater. Interfaces* **2018**, *10*, 44645–44653.

(19) Pelton, M.; Tang, Y.; Bakr, O. M.; Stellacci, F. Long-Lived Charge-Separated States in Ligand-Stabilized Silver Clusters. *J. Am. Chem. Soc.* **2012**, *134*, 11856–11859.

(20) Soldan, G.; Aljuhani, M. A.; Bootharaju, M. S.; AbdulHalim, L. G.; Parida, M. R.; Emwas, A.-H.; Mohammed, O. F.; Bakr, O. M. Gold Doping of Silver Nanoclusters: A 26-Fold Enhancement in the Luminescence Quantum Yield. *Angew. Chem., Int. Ed.* **2016**, *55*, 5749–5753.

(21) Desireddy, A.; Conn, B. E.; Guo, J.; Yoon, B.; Barnett, R. N.; Monahan, B. M.; Kirschbaum, K.; Griffith, W. P.; Whetten, R. L.; Landman, U.; et al. Ultrastable Silver Nanoparticles. *Nature* **2013**, *501*, 399–402.

(22) Yoon, B.; Luedtke, W. D.; Barnett, R. N.; Gao, J.; Desireddy, A.; Conn, B. E.; Bigioni, T.; Landman, U. Hydrogen-Bonded Structure and Mechanical Chiral Response of a Silver Nanoparticle Superlattice. *Nat. Mater.* **2014**, *13*, 807–811.

(23) Yang, H.; Wang, Y.; Huang, H.; Gell, L.; Lehtovaara, L.; Malola, S.; Häkkinen, H.; Zheng, N. All-Thiol-Stabilized Ag<sub>44</sub> and Au<sub>12</sub>Ag<sub>32</sub> Nanoparticles with Single-Crystal Structures. *Nat. Commun.* **2013**, *4*, 2422.

(24) Yang, H.; Wang, Y.; Edwards, A. J.; Yan, J.; Zheng, N. High-Yield Synthesis and Crystal Structure of a Green Au<sub>30</sub> Cluster Capped by Thiolate and Sulfide. *Chem. Commun.* **2014**, *50*, 14325–14327.

(25) Yang, H.; Wang, Y.; Chen, X.; Zhao, X.; Gu, L.; Huang, H.; Yan, J.; Xu, C.; Li, G.; Wu, J.; et al. Plasmonic Twinned Silver Nanoparticles with Molecular Precision. *Nat. Commun.* **2016**, *7*, 12809.

(26) Sels, A.; Salassa, G.; Pollitt, S.; Guglieri, C.; Ruppel, G.; Barrabés, N.; Bürgi, T. Structural Investigation of the Ligand

Exchange Reaction with Rigid Dithiol on Doped (Pt, Pd) Au<sub>25</sub> Clusters. *J. Phys. Chem. C* **2017**, *121*, 10919–10926.

(27) Kazan, R.; Zhang, B.; Bürgi, T. Au<sub>38</sub>Cu<sub>1</sub>(2-PET)<sub>24</sub> Nanocluster: Synthesis, Enantioseparation and Luminescence. *Dalton Trans* **2017**, *46*, 7708–7713.

(28) Weerawardene, K. L. D. M.; Häkkinen, H.; Aikens, C. M. Connections Between Theory and Experiment for Gold and Silver Nanoclusters. *Annu. Rev. Phys. Chem.* **2018**, *69*, 205–229.

(29) Weerawardene, K. L. D. M.; Aikens, C. M. Origin of Photoluminescence of Ag<sub>25</sub>(SR)<sub>18</sub><sup>−</sup> Nanoparticles: Ligand and Doping Effect. *J. Phys. Chem. C* **2018**, *122*, 2440–2447.

(30) Alkan, F.; Pandeya, P.; Aikens, C. M. Understanding the Effect of Doping on Energetics and Electronic Structure for Au<sub>25</sub>, Ag<sub>25</sub>, and Au<sub>38</sub> Clusters. *J. Phys. Chem. C* **2019**, *123*, 9516–9527.

(31) Xu, W. W.; Zeng, X. C.; Gao, Y. Application of Electronic Counting Rules for Ligand-Protected Gold Nanoclusters. *Acc. Chem. Res.* **2018**, *51*, 2739–2747.

(32) Conn, B. E.; Atnagulov, A.; Yoon, B.; Barnett, R. N.; Landman, U.; Bigioni, T. P. Confirmation of a De novo Structure Prediction for an Atomically Precise Monolayer-Coated Silver Nanoparticle. *Sci. Adv.* **2016**, *2*, No. e1601609.

(33) Conn, B. E.; Atnagulov, A.; Bhattarai, B.; Yoon, B.; Landman, U.; Bigioni, T. P. Synthetic and Postsynthetic Chemistry of M<sub>4</sub>Au<sub>x</sub>Ag<sub>44-x</sub>(p-MBA)<sub>30</sub> Alloy Nanoparticles. *J. Phys. Chem. C* **2018**, *122*, 13166–13174.

(34) Suyama, M.; Takano, S.; Nakamura, T.; Tsukuda, T. Stoichiometric Formation of Open-Shell [PtAu<sub>24</sub>(SC<sub>2</sub>H<sub>4</sub>Ph)<sub>18</sub>]<sup>−</sup> via Spontaneous Electron Proportionation between [PtAu<sub>24</sub>(SC<sub>2</sub>H<sub>4</sub>Ph)<sub>18</sub>]<sup>2−</sup> and [PtAu<sub>24</sub>(SC<sub>2</sub>H<sub>4</sub>Ph)<sub>18</sub>]<sup>0</sup>. *J. Am. Chem. Soc.* **2019**, *141*, 14048–14051.

(35) Price, R. C.; Whetten, R. L. All-Aromatic, Nanometer-Scale, Gold-Cluster Thiolate Complexes. *J. Am. Chem. Soc.* **2005**, *127*, 13750–13751.

(36) Nimmala, P. R.; Dass, A. Au<sub>36</sub>(SPh)<sub>23</sub> Nanomolecules. *J. Am. Chem. Soc.* **2011**, *133*, 9175–9177.

(37) Zeng, C.; Qian, H.; Li, T.; Li, G.; Rosi, N. L.; Yoon, B.; Barnett, R. N.; Whetten, R. L.; Landman, U.; Jin, R. Total Structure and Electronic Properties of the Gold Nanocrystal Au<sub>36</sub>(SR)<sub>24</sub>. *Angew. Chem., Int. Ed.* **2012**, *51*, 13114–13118.

(38) Das, A.; Liu, C.; Zeng, C.; Li, G.; Li, T.; Rosi, N. L.; Jin, R. Cyclopentanethiolato-Protected Au<sub>36</sub>(SC<sub>5</sub>H<sub>9</sub>)<sub>24</sub> Nanocluster: Crystal Structure and Implications for the Steric and Electronic Effects of Ligand. *J. Phys. Chem. A* **2014**, *118*, 8264–8269.

(39) Nimmala, P. R.; Knoppe, S.; Jupally, V. R.; Delcamp, J. H.; Aikens, C. M.; Dass, A. Au<sub>36</sub>(SPh)<sub>24</sub> Nanomolecules: X-ray Crystal Structure, Optical Spectroscopy, Electrochemistry, and Theoretical Analysis. *J. Phys. Chem. B* **2014**, *118*, 14157–14167.

(40) Wan, X.-K.; Guan, Z.-J.; Wang, Q.-M. Homoleptic Alkynyl-Protected Gold Nanoclusters: Au<sub>44</sub>(PhC≡C)<sub>28</sub> and Au<sub>36</sub>(PhC≡C)<sub>24</sub>. *Angew. Chem., Int. Ed.* **2017**, *56*, 11494–11497.

(41) Yang, Z.; Zhimin, L.; Kai, Z.; Gao, L. Controlled Synthesis of Au<sub>36</sub>(SR)<sub>24</sub> (SR = SPh, SC<sub>6</sub>H<sub>4</sub>CH<sub>3</sub>, SCH(CH<sub>3</sub>)Ph, and SC<sub>10</sub>H<sub>7</sub>) Nanoclusters. *Acta Phys.-Chim. Sin.* **2018**, *34*, 786–791.

(42) Theivendran, S.; Dass, A. Synthesis of Aromatic Thiolate-Protected Gold Nanomolecules by Core Conversion: The Case of Au<sub>36</sub>(SPh-tBu)<sub>24</sub>. *Langmuir* **2017**, *33*, 7446–7451.

(43) Rambukwella, M.; Dass, A. Synthesis of Au<sub>38</sub>(SCH<sub>2</sub>CH<sub>2</sub>Ph)<sub>24</sub>, Au<sub>36</sub>(SPh-tBu)<sub>24</sub> and Au<sub>30</sub>(S-tBu)<sub>18</sub> Nanomolecules from a Common Precursor Mixture. *Langmuir* **2017**, *33*, 10958–10964.

(44) Liao, L.; Zhuang, S.; Wang, P.; Xu, Y.; Yan, N.; Dong, H.; Wang, C.; Zhao, Y.; Xia, N.; Li, J.; et al. Quasi-Dual-Packed-Kernelled Au<sub>49</sub>(2,4-DMBT)<sub>27</sub> Nanoclusters and the Influence of Kernel Packing on the Electrochemical Gap. *Angew. Chem., Int. Ed.* **2017**, *56*, 12644–12648.

(45) Sumner, L.; Sakthivel, N. A.; Schrock, H.; Artyushkova, K.; Dass, A.; Chakraborty, S. Electrocatalytic Oxygen Reduction Activities of Thiol-Protected Nanomolecules Ranging in Size from Au<sub>28</sub>(SR)<sub>20</sub> to Au<sub>279</sub>(SR)<sub>84</sub>. *J. Phys. Chem. C* **2018**, *122*, 24809–24817.

(46) Dass, A.; Jones, T. C.; Theivendran, S.; Sementa, L.; Fortunelli, A. Core Size Interconversions of Au<sub>30</sub>(S-tBu)<sub>18</sub> and Au<sub>36</sub>(SPhX)<sub>24</sub>. *J. Phys. Chem. C* **2017**, *121*, 14914–14919.

(47) Theivendran, S.; Chang, L.; Mukherjee, A.; Sementa, L.; Stener, M.; Fortunelli, A.; Dass, A. Principles of Optical Spectroscopy of Aromatic Alloy Nanomolecules: Au<sub>36-x</sub>Ag<sub>x</sub>(SPh-tBu)<sub>24</sub>. *J. Phys. Chem. C* **2018**, *122*, 4524–4531.

(48) Fan, J.; Song, Y.; Chai, J.; Yang, S.; Chen, T.; Rao, B.; Yu, H.; Zhu, M. The Solely Motif-Doped Au<sub>36-x</sub>Ag<sub>x</sub>(SPh-tBu)<sub>24</sub> (x = 1–8) Nanoclusters: X-Ray Crystal Structure and Optical Properties. *Nanoscale* **2016**, *8*, 15317–15322.

(49) Rao, B.; Zhao, T.; Yang, S.; Chai, J.; Pan, Y.; Weng, S.; Yu, H.; Li, X.; Zhu, M. X-Ray Crystal Structure and Doping Mechanism of Bimetallic Nanocluster Au<sub>36-x</sub>Cu<sub>x</sub>(m-MBT)<sub>24</sub> (x = 1–3). *Dalton Trans* **2018**, *47*, 475–480.

(50) Yang, S.; Chai, J.; Song, Y.; Kang, X.; Sheng, H.; Chong, H.; Zhu, M. A New Crystal Structure of Au<sub>36</sub> with a Au<sub>14</sub> Kernel Capped by Thiolate and Chloride. *J. Am. Chem. Soc.* **2015**, *137*, 10033–10035.

(51) Schaaff, T. G.; Whetten, R. L. Controlled Etching of Au:SR Cluster Compounds. *J. Phys. Chem. B* **1999**, *103*, 9394–9396.

(52) Krause, L.; Herbst-Irmer, R.; Sheldrick, G. M.; Stalke, D. Comparison of Silver and Molybdenum Microfocus X-Ray Sources for Single-Crystal Structure Determination. *J. Appl. Crystallogr.* **2015**, *48*, 3–10.

(53) Sheldrick, G. SHELXT - Integrated Space-Group and Crystal-Structure Determination. *Acta Crystallogr., Sect. A: Found. Adv.* **2015**, *A71*, 3–8.

(54) Sheldrick, G. Crystal Structure Refinement with SHELXL. *Acta Crystallogr., Sect. C: Struct. Chem.* **2015**, *C71*, 3–8.

(55) Dolomanov, O. V.; Bourhis, L. J.; Gildea, R. J.; Howard, J. A. K.; Puschmann, H. OLEX2: A Complete Structure Solution, Refinement and Analysis Program. *J. Appl. Crystallogr.* **2009**, *42*, 339–341.

(56) Thanthirige, V. D.; Kim, M.; Choi, W.; Kwak, K.; Lee, D.; Ramakrishna, G. Temperature-Dependent Absorption and Ultrafast Exciton Relaxation Dynamics in MAu<sub>24</sub>(SR)<sub>18</sub> Clusters (M = Pt, Hg): Role of the Central Metal Atom. *J. Phys. Chem. C* **2016**, *120*, 23180–23188.

(57) Müller, P.; Herbst-Irmer, R.; Spek, A.; Schneider, T.; Sawaya, M. *Crystal Structure Refinement: A Crystallographer's Guide to SHELXL (IUCr Texts on Crystallography, 8)*; Oxford University Press: New York, 2006.

(58) Hutter, J.; Iannuzzi, M.; Schiffmann, F.; VandeVondele, J. CP2K: Atomistic Simulations of Condensed Matter Systems. *Wiley Interdiscip. Rev. Comput. Mol. Sci.* **2014**, *4*, 15–25.

(59) Goedecker, S.; Teter, M.; Hutter, J. Separable Dual-space Gaussian Pseudopotentials. *Phys. Rev. B: Condens. Matter Mater. Phys.* **1996**, *54*, 1703–1710.

(60) VandeVondele, J.; Hutter, J. Gaussian Basis Sets for Accurate Calculations on Molecular Systems in Gas and Condensed Phases. *J. Chem. Phys.* **2007**, *127*, 114105.

(61) Grimme, S.; Antony, J.; Ehrlich, S.; Krieg, H. A Consistent and Accurate Ab Initio Parametrization of Density Functional Dispersion Correction (DFT-D) for the 94 Elements H-Pu. *J. Chem. Phys.* **2010**, *132*, 154104.

(62) Perdew, J. P.; Burke, K.; Ernzerhof, M. Generalized Gradient Approximation Made Simple. *Phys. Rev. Lett.* **1996**, *77*, 3865–3868.

(63) Baseggio, O.; De Vetta, M.; Fronzoni, G.; Toffoli, D.; Stener, M.; Sementa, L.; Fortunelli, A. Time-Dependent Density-Functional Study of the Photoabsorption Spectrum of Au<sub>25</sub>(SC<sub>2</sub>H<sub>4</sub>C<sub>6</sub>H<sub>5</sub>)<sub>18</sub> Anion: Validation of the Computational Protocol. *Int. J. Quantum Chem.* **2018**, *118*, No. e25769.

(64) Baseggio, O.; Fronzoni, G.; Stener, M. A New Time Dependent Density Functional Algorithm for Large Systems and Plasmons in Metal Clusters. *J. Chem. Phys.* **2015**, *143*, 024106.

(65) Baseggio, O.; De Vetta, M.; Fronzoni, G.; Stener, M.; Fortunelli, A. A New Time-Dependent Density-Functional Method for Molecular Plasmonics: Formalism, Implementation, and the

Au<sub>144</sub>(SH)<sub>60</sub> Case Study. *Int. J. Quantum Chem.* **2016**, *116*, 1603–1611.

(66) Baerends, E. J.; Ellis, D. E.; Ros, P. Self-consistent Molecular Hartree—Fock—Slater Calculations I. The Computational Procedure. *Chem. Phys.* **1973**, *2*, 41–51.

(67) van Leeuwen, R.; Baerends, E. J. Exchange-Correlation Potential with Correct Asymptotic Behavior. *Phys. Rev. A: At, Mol, Opt. Phys.* **1994**, *49*, 2421–2431.

(68) Gross, E. K. U.; Kohn, W. Time-Dependent Density-Functional Theory. In *Adv. Quantum Chem.*; Löwdin, P.-O., Ed.; Academic Press: San Diego, CA, 1990; Vol. 21, pp 255–291.

(69) Baseggio, O.; De Vetta, M.; Fronzoni, G.; Stener, M.; Sementa, L.; Fortunelli, A.; Calzolari, A. Photoabsorption of Icosahedral Noble Metal Clusters: An Efficient TDDFT Approach to Large-Scale Systems. *J. Phys. Chem. C* **2016**, *120*, 12773–12782.

(70) Lenthe, E. v.; Baerends, E. J.; Snijders, J. G. Relativistic Regular Two-Component Hamiltonians. *J. Chem. Phys.* **1993**, *99*, 4597–4610.

## Supporting Information

### Crystal Structure of $\text{Au}_{36-x}\text{Ag}_x(\text{SPh-tBu})_{24}$ Nanoalloy and the Role of Ag Doping in Excited State Coupling

Naga Arjun Sakthivel,<sup>†</sup> Mauro Stener,<sup>‡</sup> Luca Sementa,<sup>§</sup> Marco Medves,<sup>±</sup> Guda Ramakrishna,<sup>||</sup> Alessandro Fortunelli,<sup>§</sup> Allen G. Oliver,<sup>‡</sup> and Amala Dass,<sup>†,\*</sup>

<sup>†</sup> Department of Chemistry and Biochemistry, University of Mississippi, Oxford, MS 38677, United States

<sup>‡</sup> Department of Chemistry, University of Notre Dame, Notre Dame, IN 46556, United States

<sup>§</sup> CNR-ICCOM & IPCF, Consiglio Nazionale delle Ricerche, Pisa, I-56124, Italy

<sup>||</sup> Department of Chemistry, Western Michigan University, Kalamazoo, Michigan 49008, United States

<sup>±</sup> Dipartimento di Scienze Chimiche e Farmaceutiche, Università di Trieste, Trieste I-34127, Italy

\*corresponding author(s): amal@olemiss.edu

---

### Table of contents

1. Table S1. Crystal data and structure refinement
  2. TDDFT study details
  3. Figure S1. Terminologies and the corresponding numbers in the result (.res) file for substitutional disorder refinement
  4. Figure S2. Thermal ellipsoid model of  $\text{Au}_{36-x}\text{Ag}_x\text{S}_{24}$  NMs during various stages of substitutional disorder modelling (this work SC-XRD data)
  5. Figure S3. Changes in (a) ADP values and (b) Au/Ag partial occupancy during various stages of substitutional disorder modelling (this work SC-XRD data)
  6. Figure S4. Thermal ellipsoid model of  $\text{Au}_{36-x}\text{Ag}_x\text{S}_{24}$  NMs during various stages of substitutional disorder modelling (2016 data – re-refined)
  7. Figure S5. Changes in (a) ADP values and (b) Au/Ag partial occupancy during various stages of substitutional disorder modelling (2016 data – re-refined)
  8. Figure S6. Ball and stick model of  $\text{Au}_{36-x}\text{Ag}_x(\text{SPh-tBu})_{24}$  NMs
  9. Figure S7. Surface 22 metal atom site numbers as in the CIF file
  10. Figure S8. Substitutional and positional disorder refinement of SC-XRD data in this work.
  11. Figure S9. Thermal ellipsoidal view of  $\text{Au}_{36-x}\text{Cu}_x(m\text{-MBT})_{24}$  crystal structure
  12. Figure S10. Comparison of kinetic decay traces of  $\text{Au}_{36}$  and  $(\text{AgAu})_{36}$
  13. Figure S11. Absorption of  $\text{Au}_{36-x}\text{Ag}_x(\text{SPh-tBu})_{24}$  nanoalloys with different homotops
  14. Figure S12. Absorption of  $\text{Au}_{36-x}\text{Ag}_x(\text{SPh-tBu})_{24}$  nanoalloys with different homotops
  15. Figure S13. Molecular orbitals of  $\text{Au}_{36}(\text{SPh-tBu})_{24}$  involved in the excited states calculated at 1.98 eV and 2.62 eV
  16. Figure S14. Molecular orbitals of  $\text{Ag}_4\text{Au}_{32}(\text{SPh-tBu})_{24}$  (Near) involved in the excited states calculated at 2.14 eV and 2.60 eV
  17. Figure S15. Molecular orbitals of  $\text{Ag}_4\text{Au}_{32}(\text{SPh-tBu})_{24}$  (Far) involved in the excited states calculated at 2.00 eV and 2.62 eV
  18. Table S2 Fractional Atomic Coordinates and Equivalent Isotropic Displacement Parameters
  19. Table S3 Anisotropic Displacement Parameters
  20. Table S4 Bond Lengths
  21. Table S5 Bond Angles
  22. Table S6 Hydrogen Atom Coordinates and Isotropic Displacement Parameters
  23. Table S7 Atomic Occupancy
  24. Table S8 Solvent masks information
-

**Table S1. Crystal data and structure refinement for auag2\_a**

Identification code	auag2_a
Empirical formula	C <sub>240</sub> H <sub>312</sub> Ag <sub>2.83</sub> Au <sub>33.17</sub> S <sub>24</sub>
Formula weight	10805.42
Temperature/K	273
Crystal system	orthorhombic
Space group	P2 <sub>1</sub> 2 <sub>1</sub> 2
a/Å	24.016(5)
b/Å	28.775(6)
c/Å	22.090(4)
α/°	90
β/°	90
γ/°	90
Volume/Å <sup>3</sup>	15266(5)
Z	2
ρ <sub>calc</sub> /cm <sup>3</sup>	2.351
μ/mm <sup>-1</sup>	16.246
F(000)	9779.0
Crystal size/mm <sup>3</sup>	0.15 × 0.1 × 0.05
Radiation	MoKα (λ = 0.71073)
2θ range for data collection/°	2.83 to 46.234
Index ranges	-26 ≤ h ≤ 26, -31 ≤ k ≤ 31, -24 ≤ l ≤ 24
Reflections collected	225984
Independent reflections	21503 [R <sub>int</sub> = 0.0722, R <sub>sigma</sub> = 0.0368]
Data/restraints/parameters	21503/70/747
Goodness-of-fit on F <sup>2</sup>	1.020
Final R indexes [I >= 2σ (I)]	R <sub>1</sub> = 0.0331, wR <sub>2</sub> = 0.0742
Final R indexes [all data]	R <sub>1</sub> = 0.0385, wR <sub>2</sub> = 0.0768
Largest diff. peak/hole / e Å <sup>-3</sup>	3.14/-1.30
Flack parameter	0.032(3)

**TDDFT study.** In Figure S10 and S11 we report the photoabsorption profiles of  $\text{Au}_{36}(\text{SPh-}t\text{Bu})_{24}$  and two homotop  $\text{Ag}_4\text{Au}_{32}(\text{SPh-}t\text{Bu})_{24}$  model clusters as simulated by our TDDFT approach (see main text for details). As discussed in the main text, the overall appearance of the spectra, is similar, with tiny differences rather sensitive to the chemical ordering of Ag doping. In general we observe that TDDFT-simulated features are shifted towards higher wavelength (lower energy) with respect to the experiment, which can be attributed to the deficiencies of the employed exchange-correlation potential. In order to discuss the intricate set of results, it is useful to identify in the simulated spectrum three different region: the first one around 600 nm to be compared with the experimental features at 575 – 565 nm, the second one around 500 nm to be compared with the experimental shoulder at 412-425 nm and the third one just above 400 nm to be compared with the experimental peak at 373-376 nm. Starting the discussion from lower wavelengths, the calculated feature in the third region is in agreement with the experiment: the pure gold cluster shows the lowest absorption with respect to the alloy homotops considered. Considering then the second region from 500 to 550 nm, we notice that the alloys spectral features lie at higher wavelengths with respect to the pure gold cluster, which is consistent with the observed red shift in the experimental shoulder at 412-425 nm. Finally in the region around 600 nm the comparison of the intensity trend is not in agreement with the experiment, as the calculated pure-gold cluster exhibits the largest absorption, whereas a slight increase is actually measured in the experiment as an effect of Ag doping. However, it is worth noting that in this energy region the calculated profiles of the alloys are in general blue-shifted with respect to the pure gold cluster, an effect which is in agreement with the experiment. In general we can conclude that theory is able to correctly reproduce the energy shift of the bands although the experimental intensity distribution is not always reproduced. This is not surprising, since intensity is in general very sensitive to small differences in the electronic structure description, and is therefore more sensitive to the deficiencies of the exchange-correlation potential than the energy positions of the spectral features.

```

.
.
SYMM 0.5+X,0.5-Y,-Z
SFAC C H Ag Au S
UNIT 480 624 5.65 66.35 48
.
.
EADP Au18 Ag18
.
.
EXYZ Au18 Ag18
.
.
atomname sfac x y z sof [11] U [0.05] or U11 U22 U33 U23 U13 U12
AU1 4 0.557309 0.482985 0.234701 11.00000 0.00874 0.01296 =
0.01723 0.00022 -0.00184 0.00093
.
.
PART 1
.
.
AU18 4 0.336734 0.549469 0.221747 61.00000 0.01489 0.01836 =
0.02071 0.00297 -0.00110 0.00359
PART 0
PART 2
.
.
AG18 3 0.336734 0.549469 0.221747 -61.00000 0.01489 0.01836 =
0.02071 0.00297 -0.00110 0.00359
PART 0
.
.

```

**SFAC line**  
**positional number for elements in the SFAC line**  

C	H	Ag	Au	S
1	2	3	4	5

**Site occupancy factor (sof)**

**Figure S1.** Terminologies and the corresponding numbers in the result (.res) file for substitutional disorder refinement.

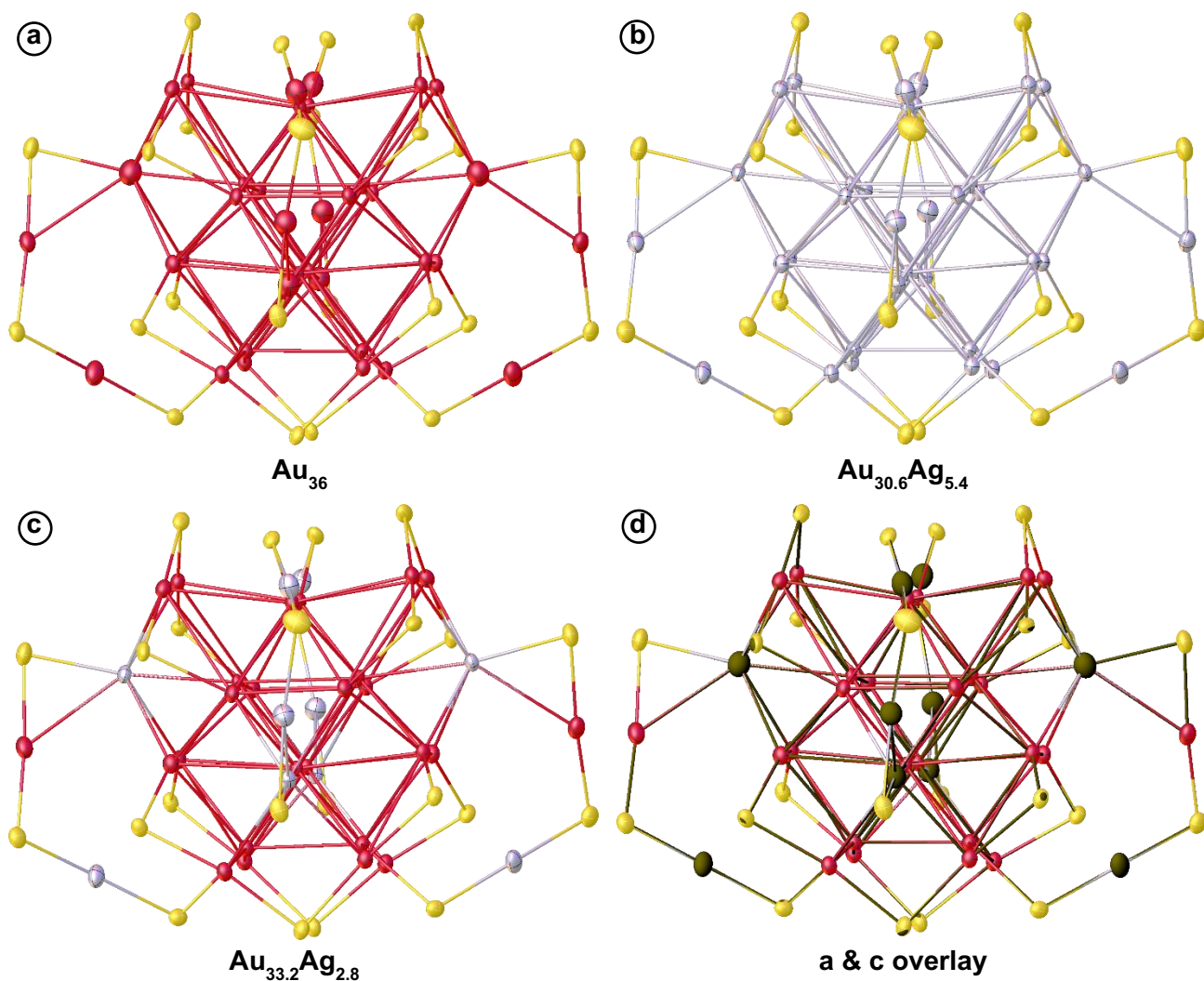


**Figure S2.** Thermal ellipsoid model of  $\text{Au}_{36-x}\text{Ag}_x\text{S}_{24}$  NMs during various stages of substitutional disorder modelling. (this work SC-XRD data) (a) Structure solution obtained with 36 metal sites as Au only. (b) All the 36 metal sites have been modelled for Au/Ag partial occupancy. (c) Reliable model obtained after several cycles of refinement after reverting sites with less than 10% Ag to Au only. (d) An overlay of the frame (a) and (c), frame (a) has been grouped as one entity in black color to illustrate how the ADP values vary at Au/Ag occupancy sites and Au only sites. Au – red, Ag – silver, and S – yellow.

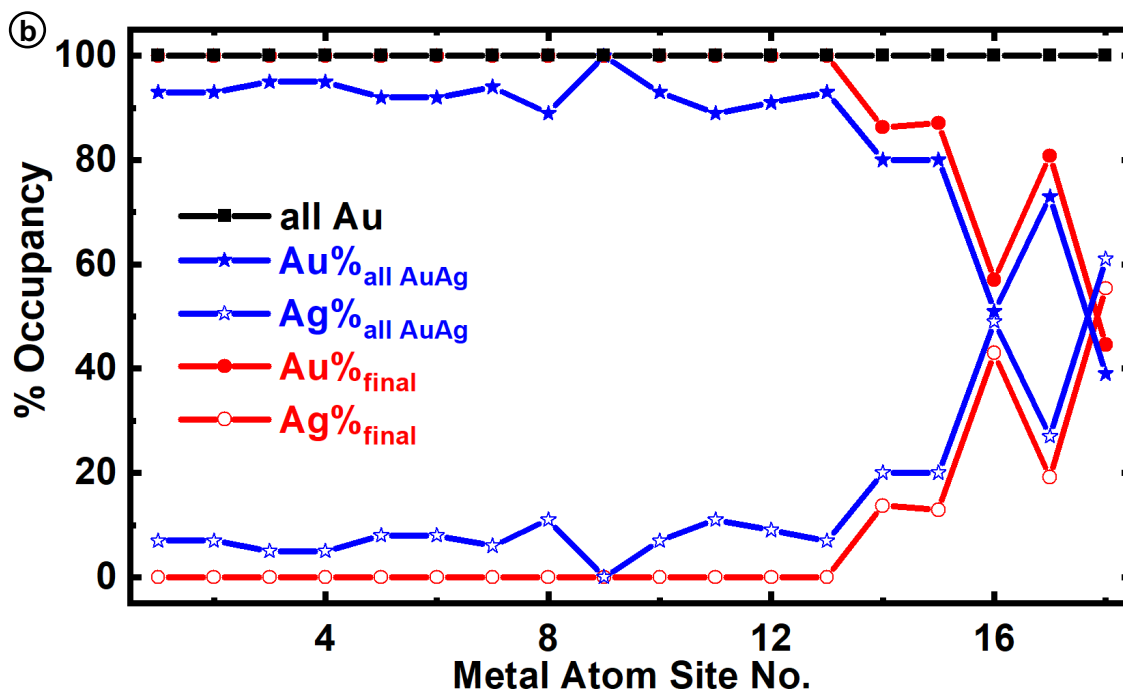
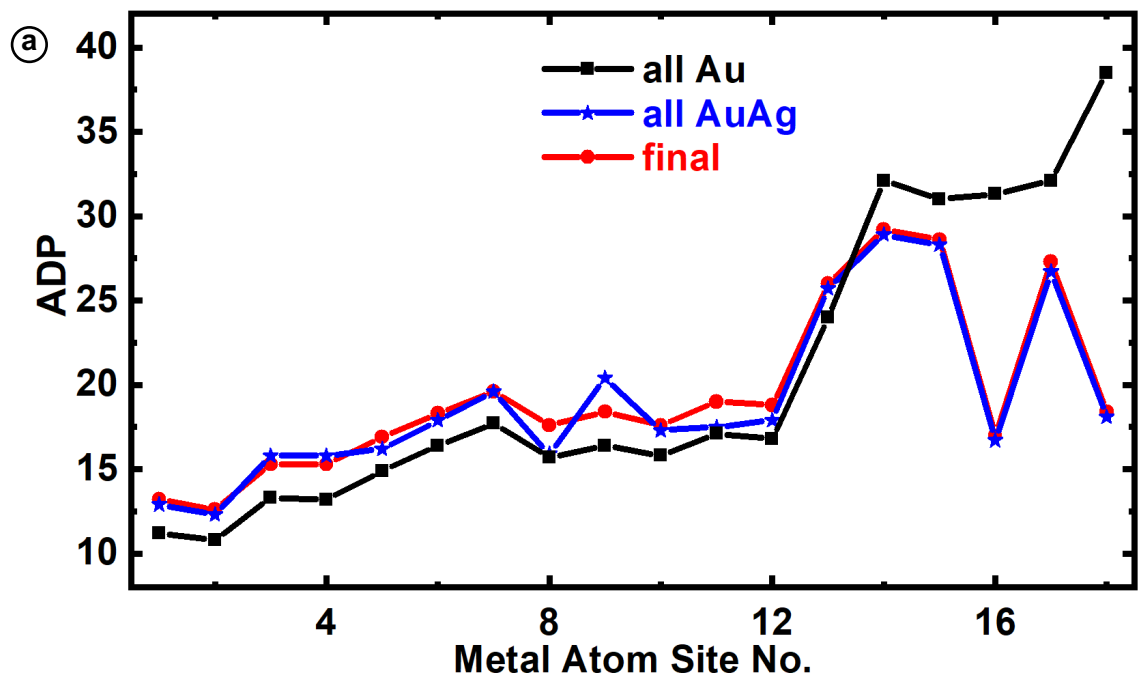


**Figure S3.** Changes in (a) ADP values and (b) Au/Ag partial occupancy during various stages of substitutional disorder modelling. (this work SC-XRD data) Solid black, square – all Au, solid blue, stars – all sites modelled for Au/Ag partial occupancy and solid red, spheres – final reliable model with 2.83 Ag. stars and spheres; filled - %Au and hollow - %Ag.

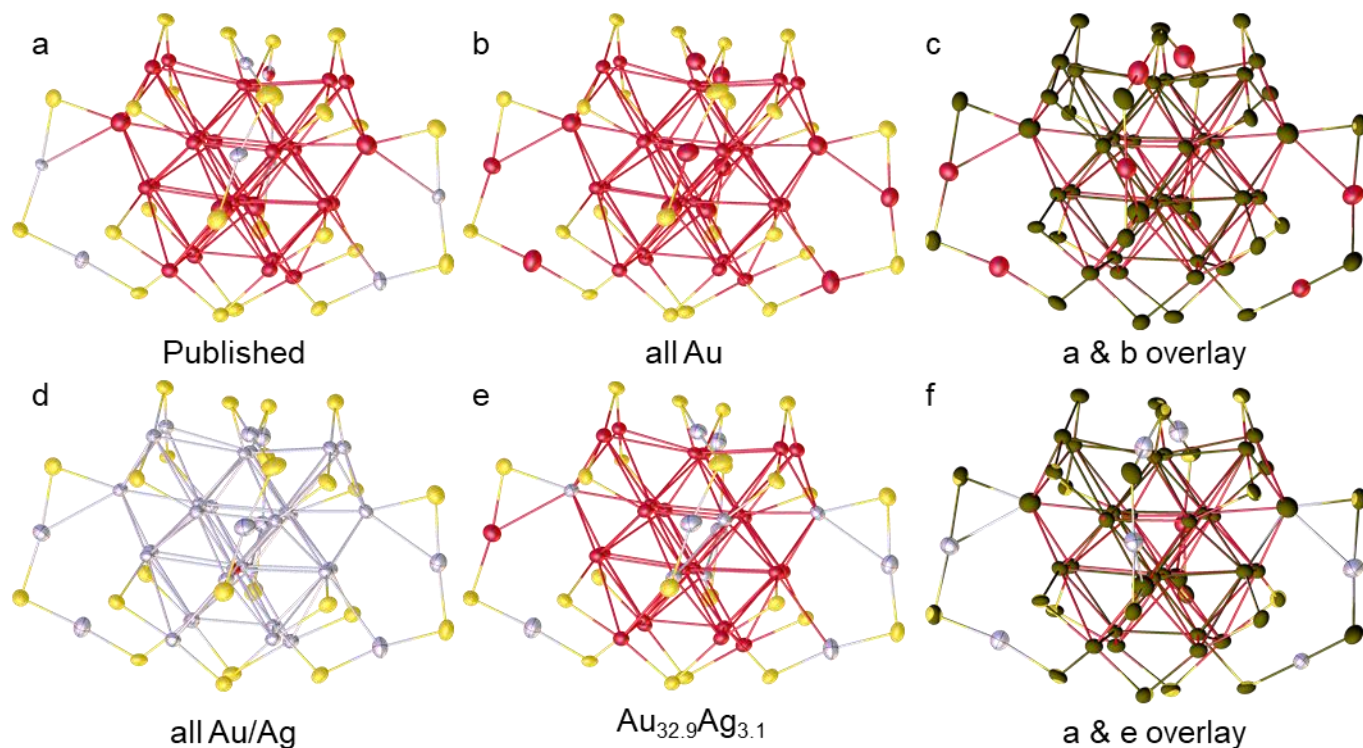


**Figure S4.** Thermal ellipsoid model of  $\text{Au}_{36-x}\text{Ag}_x\text{S}_{24}$  NMs during various stages of substitutional disorder modelling. (2016 data – re-refined) (a) published  $\text{Au}_{36-x}\text{Ag}_x\text{S}_{24}$  structure (2016), (b) 36 metal sites as Au only. (c) An overlay of the frame (a) and (b), frame (b) has been grouped as one entity in black color to illustrate how the ADP values vary at Au/Ag occupancy sites and Au only sites. (d) All the 36 metal sites have been modelled for Au/Ag partial occupancy. (e) Reliable model obtained after several cycles of refinement after reverting sites with less than 10% Ag to Au only. (f) An overlay of the frame (a) and (e), frame (a) has been grouped as one entity in black color to illustrate how the ADP values vary at Au/Ag occupancy sites and Au only sites. Au – red, Ag – silver, and S – yellow.

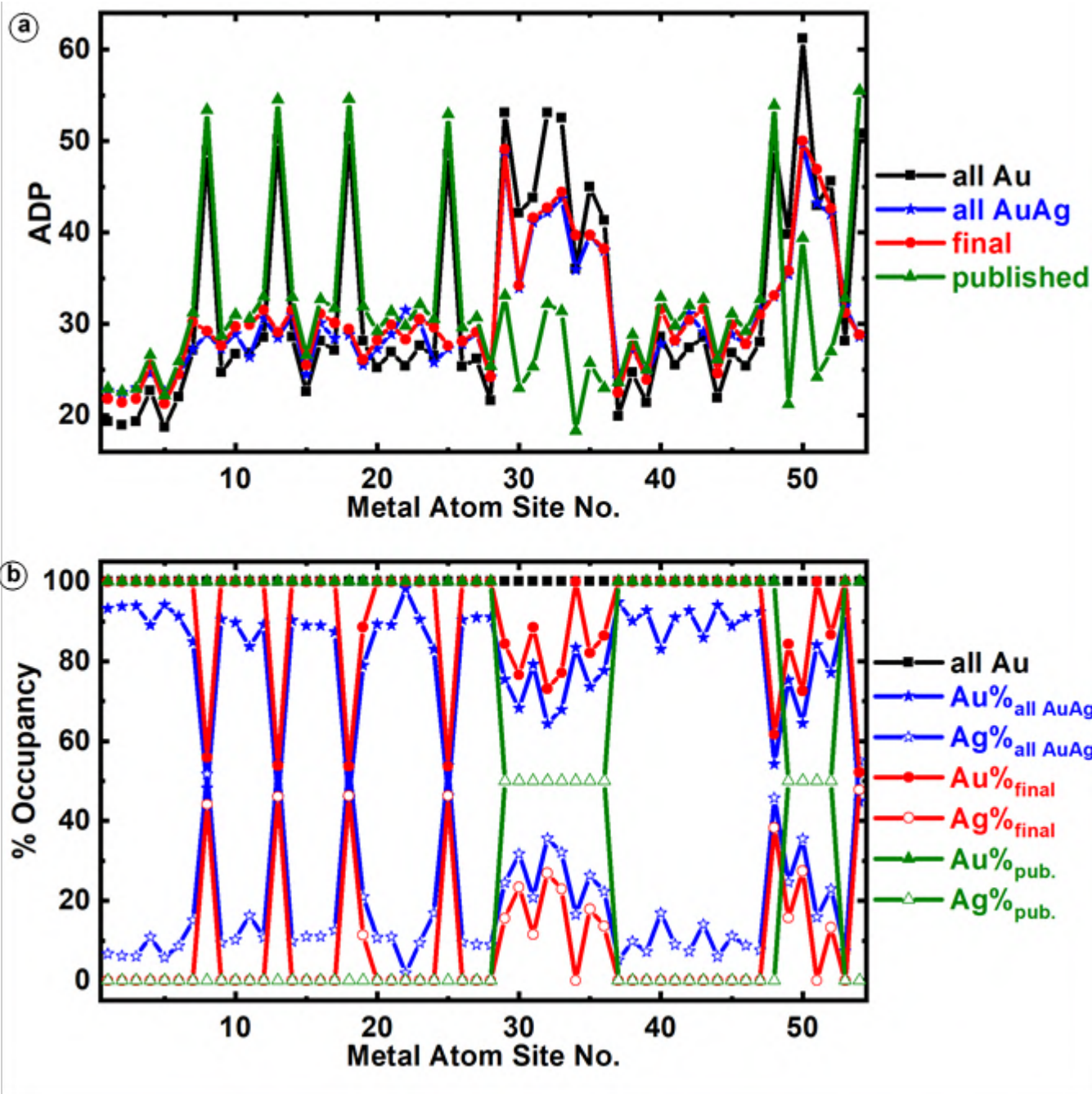


**Figure S5.** Changes in (a) ADP values and (b) Au/Ag partial occupancy during various stages of substitutional disorder modelling. (2016 data – re-refined) Solid black, square – all Au, solid blue, stars – all sites modelled for Au/Ag partial occupancy, solid red, spheres – final reliable model with 3.1 Ag and solid green, triangles published AuAg<sub>36</sub> structure from 2016 Nanoscale. Stars, spheres, and triangles; filled - %Au and hollow - %Ag.

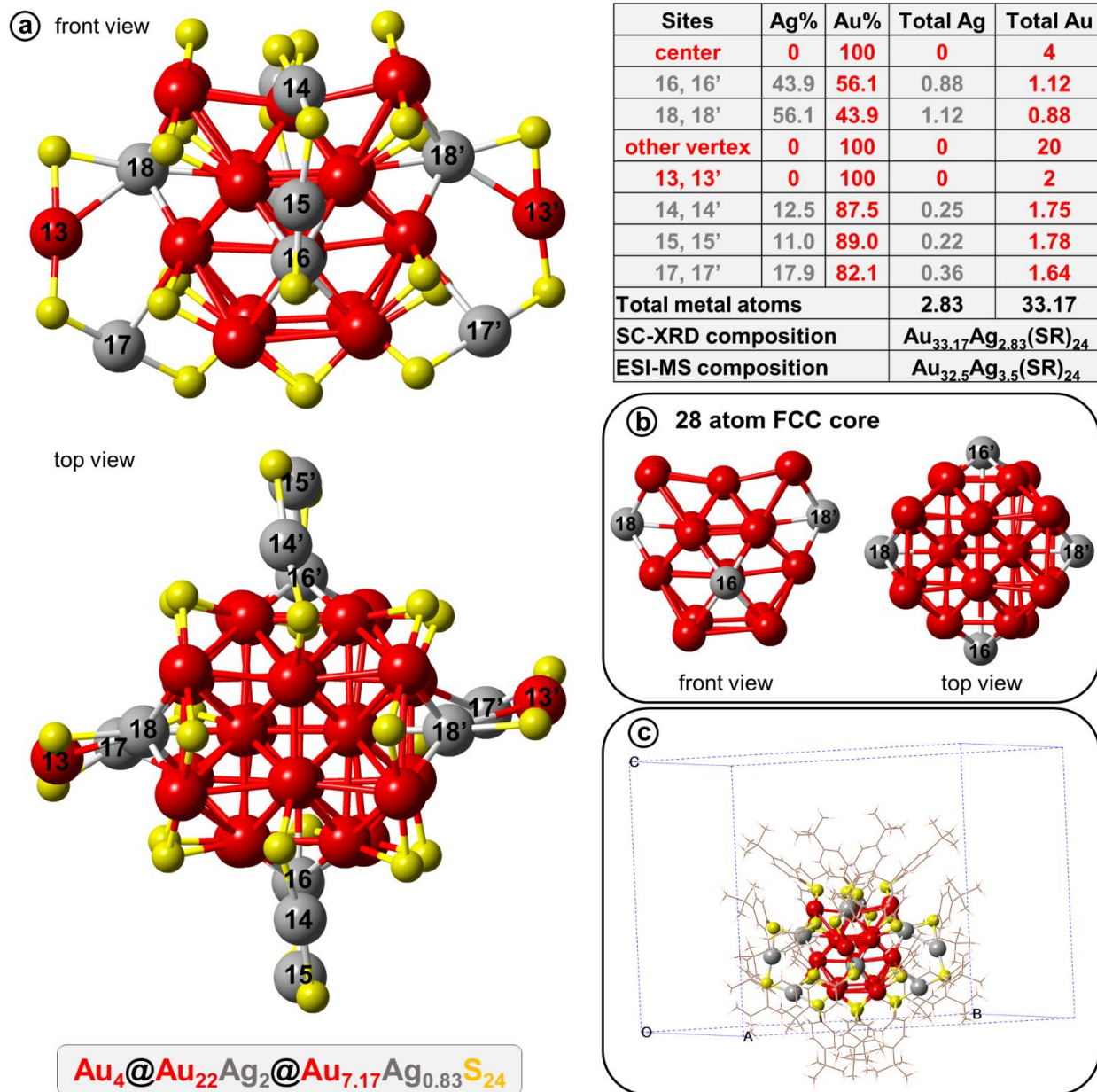


**Figure S6.** Ball and stick model of Au<sub>36-x</sub>Ag<sub>x</sub>(SPh-*t*Bu)<sub>24</sub> NMs. (a) 28 metal atom core protected by 4 dimeric staples with 8 metal sites of which two metal sites (13, 13') has no Ag doping and rest of the sites contribute 0.83 Ag to the total composition. (b) 28 metal atom core sites where 4 tetrahedrally symmetrical vertices sites are doped with Ag (16, 16', 18 and 18'), contributing 2 Ag to the total composition. C and H groups of the ligand shell are excluded for clarity. Site-wise composition for the 36 metal sites is listed on the right-hand side table. SC-XRD and ESI-MS based (Au,Ag) composition are (33.17,2.83) and (32.5,3.5), respectively. (c) Au<sub>36-x</sub>Ag<sub>x</sub>(SPh-*t*Bu)<sub>24</sub> alloy NMs in the orthorhombic unit cell. The site numbers were assigned as in the crystallographic information file (CIF). Sites with " ' " are symmetric sites generated from the asymmetric unit.

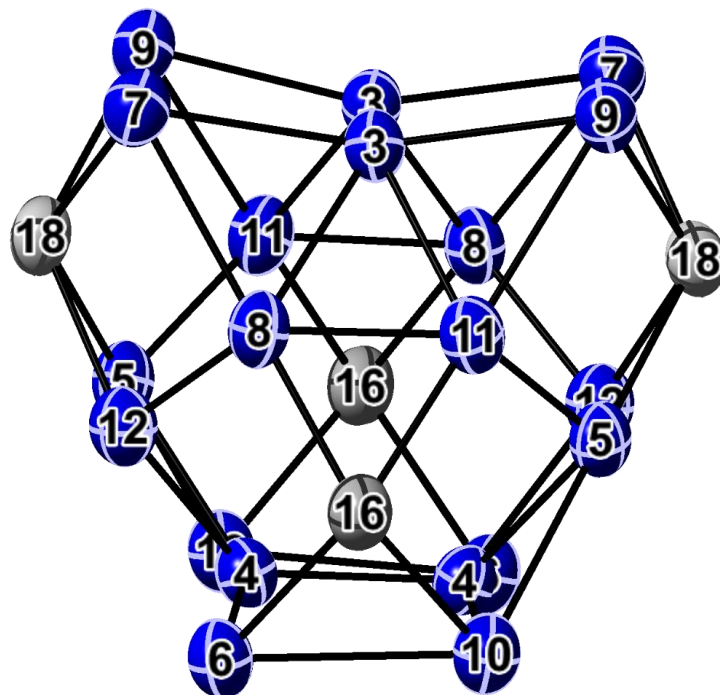


**Figure S7.** Surface 22 metal atom site numbers as in the CIF file.

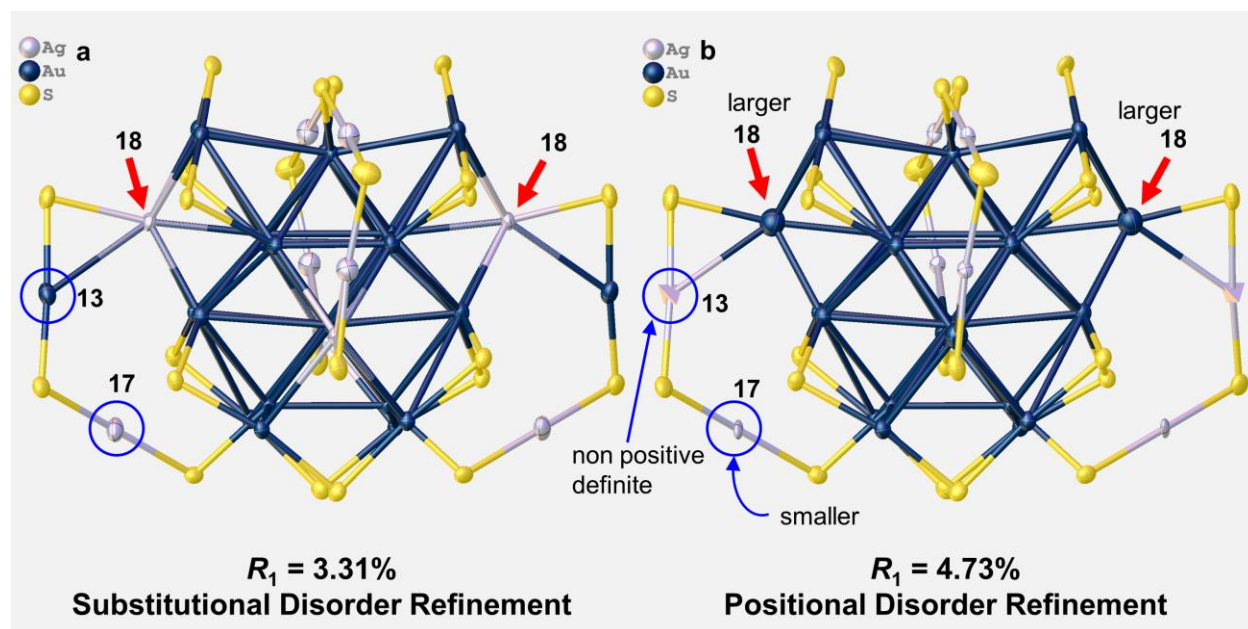


**Figure S8.** (a) Substitutional and (b) positional disorder refinement of our SC-XRD data in this work. The orientation of the structure is similar to that of Figure 1 and 2 in the main text. In panel (b), we performed positional disorder refinement of our data similar to 2016 Zhu paper (by using a *sof* value of 10.50000) and the structure model resulted with higher  $R_1$  value and unusually larger and smaller thermal ellipsoids. In the site 13 where there is no significant Ag occupancy, upon modeling for 50% occupancy, the model shows a non-positive definite.

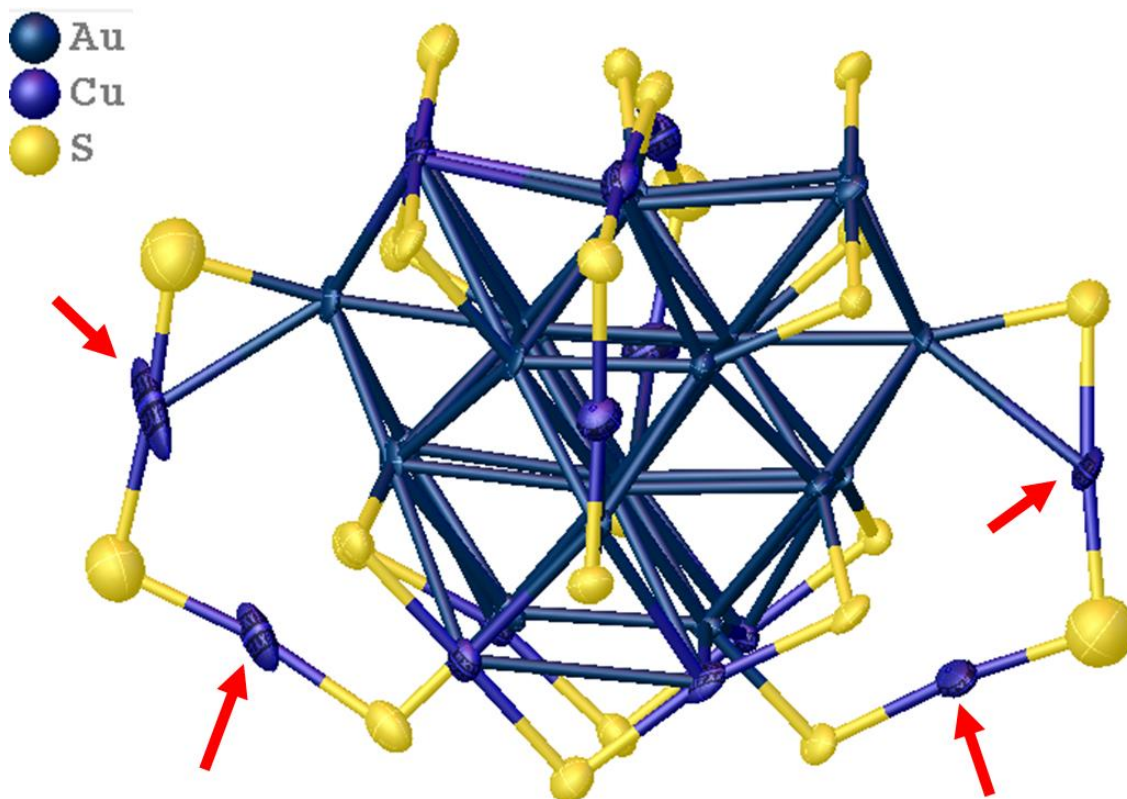


**Figure S9.** Thermal ellipsoidal view of  $\text{Au}_{36-x}\text{Cu}_x(m\text{-MBT})_{24}$  crystal structure. Red arrows indicate 4 sites linked by one free variable leading to 21.5% Cu occupancy at all 4 sites. All those 4 sites have elongated ellipsoids with higher ADP values. [Zhu et al. *Dalton Trans.*, 2018, 47, 475.]

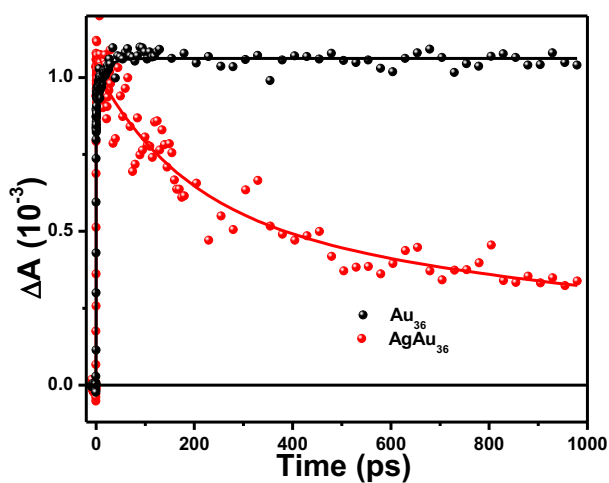


**Figure S10.** Comparison of kinetic decay traces of  $\text{Au}_{36}$  at 495 nm and  $(\text{AgAu})_{36}$  at 540 nm both depicting the long-lived decays. The solid lines are fitted lines.

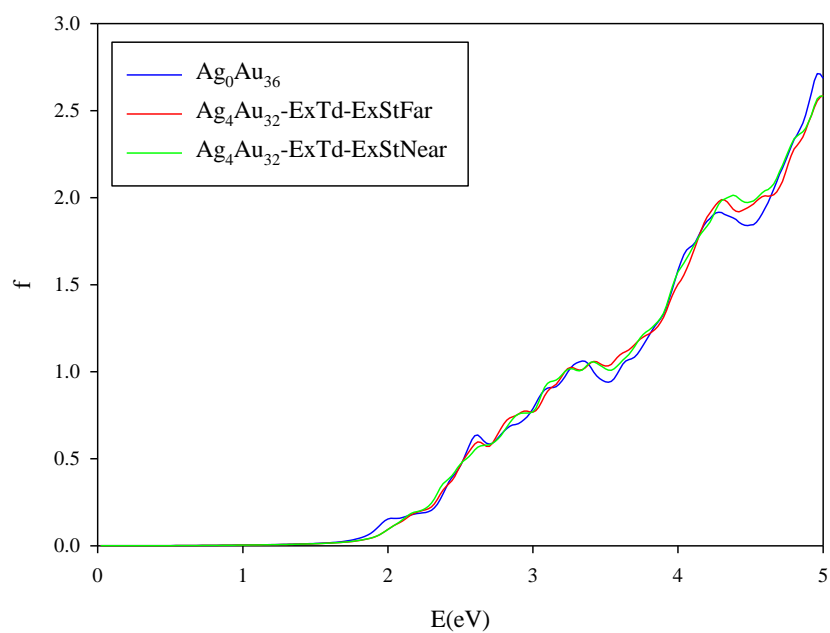


**Figure S11.** Absorption of  $\text{Au}_{36-x}\text{Ag}_x(\text{SPh-}t\text{Bu})_{24}$  nanoalloys with different homotops. Energy scale in eV.

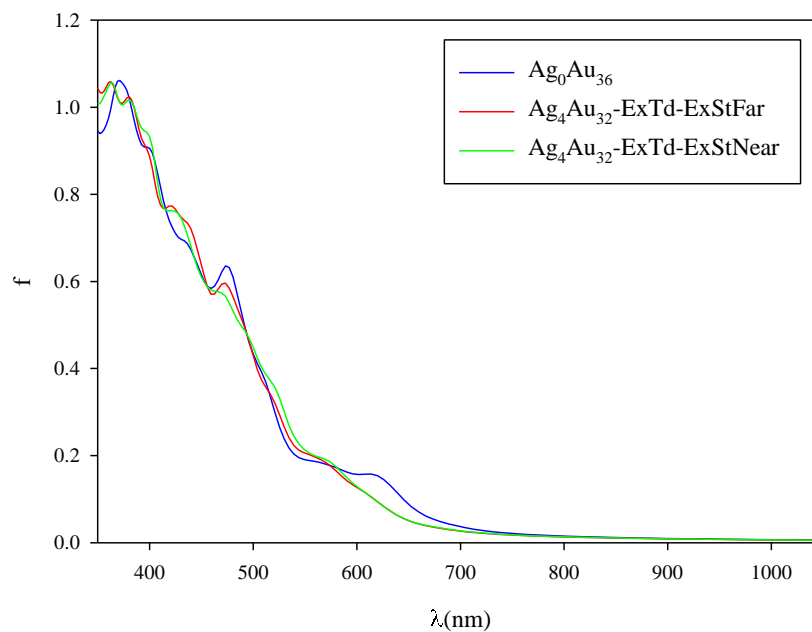
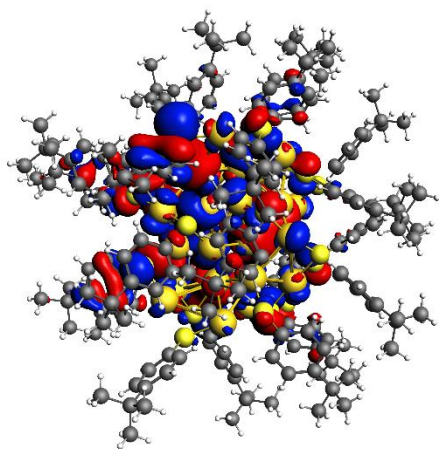
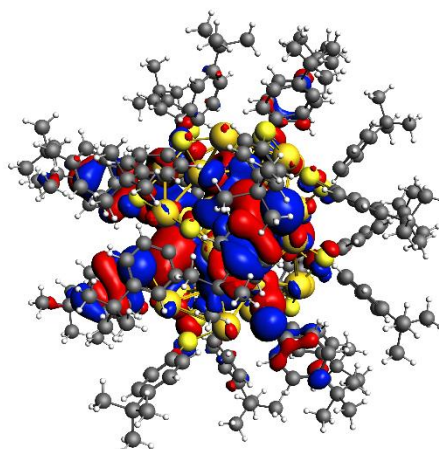


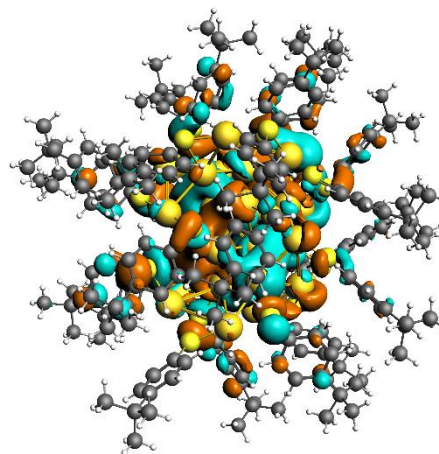
**Figure S12.** Absorption of  $\text{Au}_{36-x}\text{Ag}_x(\text{SPh-}t\text{Bu})_{24}$  nanoalloys with different homotops. Wavelength scale in nm.



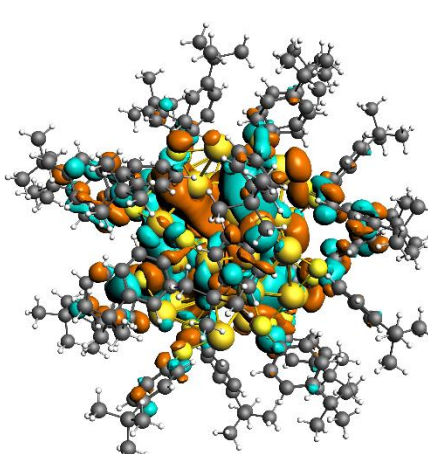
1046



1047



1051



1058

**Figure S13.** Molecular orbitals of  $\text{Au}_{36}(\text{SPh-tBu})_{24}$  involved in the excited states calculated at 1.98 eV and 2.62 eV. Isovalues  $0.01 \text{ bohr}^{-3/2}$ .

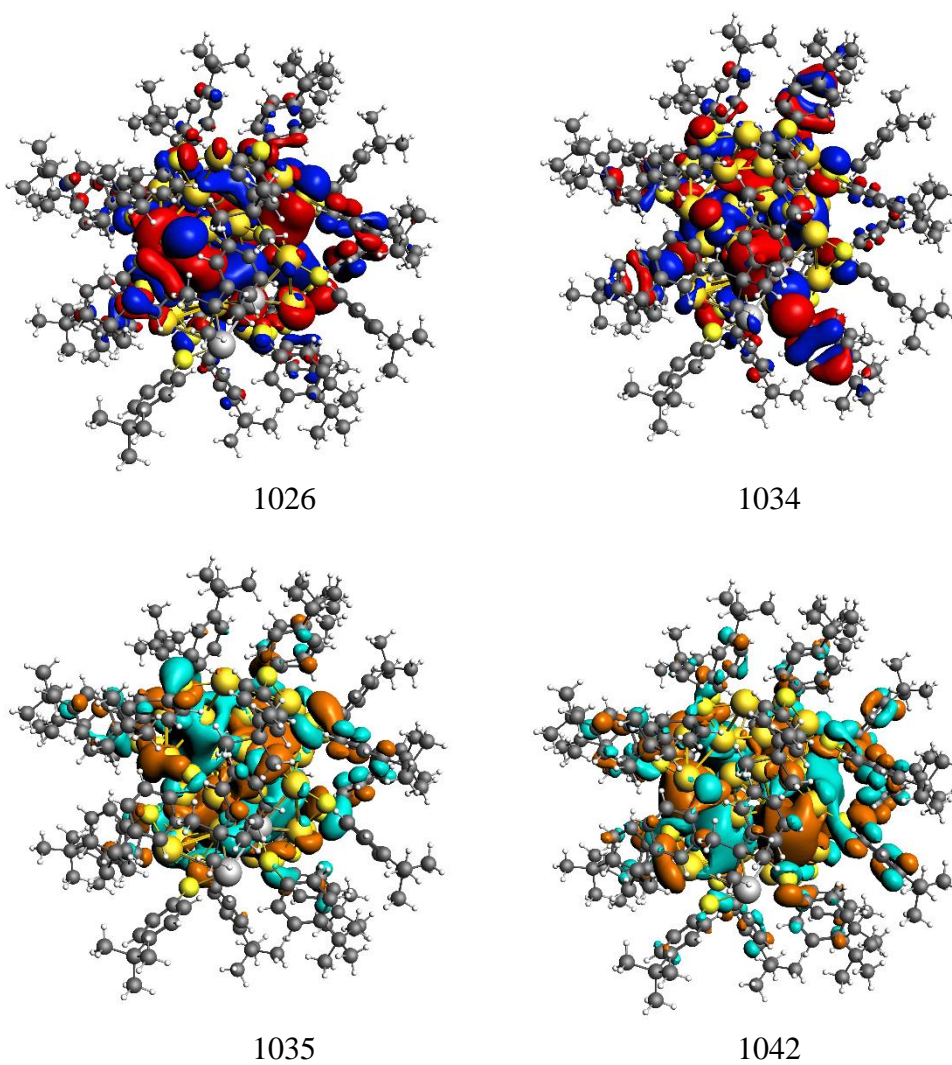
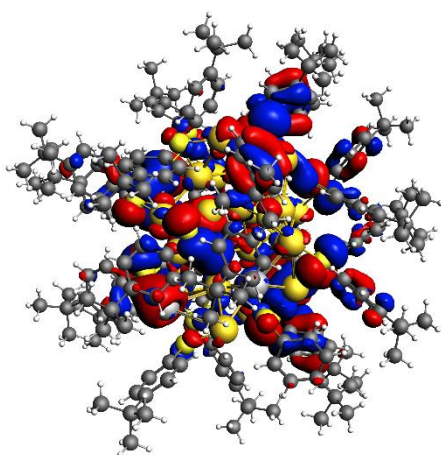
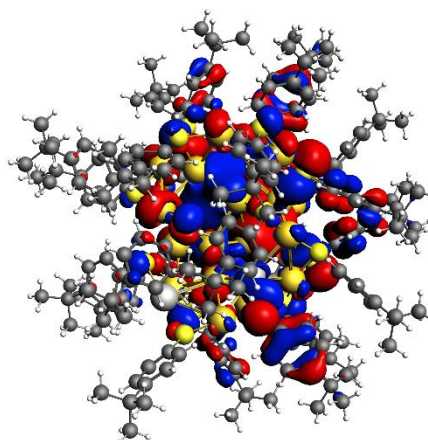


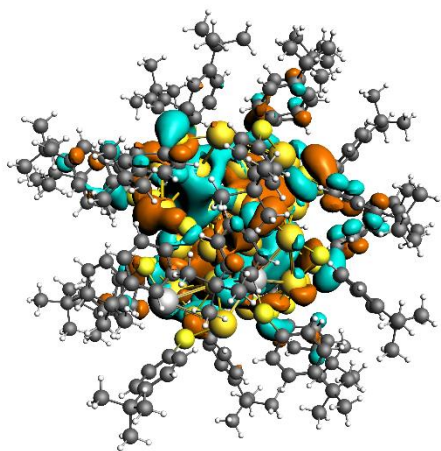
**Figure S14.** Molecular orbitals of  $\text{Ag}_4\text{Au}_{32}(\text{SPh-tBu})_{24}$  (Near) involved in the excited states calculated at 2.14 eV and 2.60 eV. Isovalues  $0.01 \text{ bohr}^{-3/2}$ .



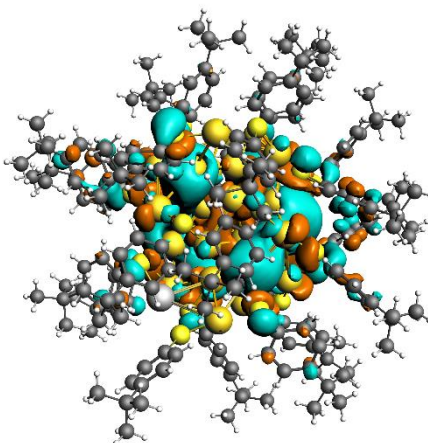
1014



1029



1035



1037

**Figure S15.** Molecular orbitals of  $\text{Ag}_4\text{Au}_{32}(\text{SPh-tBu})_{24}$  (Far) involved in the excited states calculated at 2.00 eV and 2.62 eV. Isovalues  $0.01 \text{ bohr}^{-3/2}$ .

*ATTENTION: this is incomplete supporting information, please visit the article online*

# An efficient hybrid scheme for time dependent density functional theory

Cite as: J. Chem. Phys. **152**, 184104 (2020); <https://doi.org/10.1063/5.0005954>

Submitted: 26 February 2020 . Accepted: 16 April 2020 . Published Online: 12 May 2020

Marco Medves,  Luca Sementa,  Daniele Toffoli,  Giovanna Fronzoni,  Alessandro Fortunelli, and  Mauro Stener



View Online



Export Citation



CrossMark

## ARTICLES YOU MAY BE INTERESTED IN

### NWChem: Past, present, and future

The Journal of Chemical Physics **152**, 184102 (2020); <https://doi.org/10.1063/5.0004997>

### Essentials of relativistic quantum chemistry

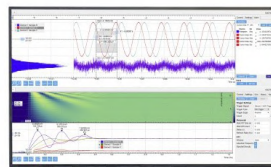
The Journal of Chemical Physics **152**, 180901 (2020); <https://doi.org/10.1063/5.0008432>

### TURBOMOLE: Modular program suite for ab initio quantum-chemical and condensed-matter simulations

The Journal of Chemical Physics **152**, 184107 (2020); <https://doi.org/10.1063/5.0004635>

Challenge us.

What are your needs for  
periodic signal detection?



Zurich  
Instruments



# An efficient hybrid scheme for time dependent density functional theory

Cite as: J. Chem. Phys. 152, 184104 (2020); doi: 10.1063/5.0005954

Submitted: 26 February 2020 • Accepted: 16 April 2020 •

Published Online: 12 May 2020



View Online



Export Citation



CrossMark

Marco Medves,<sup>1</sup> Luca Sementa,<sup>2</sup>  Daniele Toffoli,<sup>1</sup>  Giovanna Fronzoni,<sup>1</sup>  Alessandro Fortunelli,<sup>2,a)</sup>   
and Mauro Stener<sup>1,b)</sup> 

## AFFILIATIONS

<sup>1</sup>Dipartimento di Scienze Chimiche e Farmaceutiche, Università di Trieste, Via Giorgieri 1, 34127 Trieste, Italy

<sup>2</sup>CNR-ICCOM & IPCF, Consiglio Nazionale delle Ricerche, Via Giuseppe Moruzzi 1, 56124 Pisa, Italy

<sup>a)</sup>E-mail: [alessandro.fortunelli@cnr.it](mailto:alessandro.fortunelli@cnr.it)

<sup>b)</sup>Author to whom correspondence should be addressed: [stener@units.it](mailto:stener@units.it)

## ABSTRACT

A hybrid approach able to perform Time Dependent Density Functional Theory (TDDFT) simulations with the same accuracy as that of hybrid exchange-correlation (xc-) functionals but at a fraction of the computational cost is developed, implemented, and validated. The scheme, which we name Hybrid Diagonal Approximation (HDA), consists in employing in the response function a hybrid xc-functional (containing a fraction of the non-local Hartree–Fock exchange) only for the diagonal elements of the omega matrix, while the adiabatic local density approximation is employed for the off-diagonal terms. HDA is especially (but not exclusively) advantageous when using Slater type orbital basis sets and allows one to employ them in a uniquely efficient way, as we demonstrate here by implementing HDA in a local version of the Amsterdam Density Functional code. The new protocol is tested on NH<sub>3</sub>, C<sub>6</sub>H<sub>6</sub>, and the [Au<sub>25</sub>(SCH<sub>3</sub>)<sub>18</sub>]<sup>−</sup> cluster as prototypical cases ranging from small molecules to ligand-protected metal clusters, finding excellent agreement with respect to both full kernel TDDFT simulations and experimental data. Additionally, a specific comparison test between full kernel and HDA is considered at the Casida level on seven other molecular species, which further confirm the accuracy of the approach for all investigated systems. For the [Au<sub>25</sub>(SCH<sub>3</sub>)<sub>18</sub>]<sup>−</sup> cluster, a speedup by a factor of seven is obtained with respect to the full kernel. The HDA, therefore, promises to provide a quantitative description of the optical properties of medium-sized systems (nanoclusters) at an affordable cost, thanks to its computational efficiency, especially in combination with a complex polarization algorithm version of TDDFT.

Published under license by AIP Publishing. <https://doi.org/10.1063/5.0005954>

## I. INTRODUCTION

Chiro-optical absorption spectra represent one of the most direct, routine, and cheap experimental probes in chemistry, providing important information on the electronic structure of the system under study. For complex systems, however, a reliable assignment of the observed spectral features, leading to their rationalization and, eventually, design, is not straightforward. In this context, theory and computational simulations play an increasingly crucial role in arriving at an in-depth understanding of experimental observations.<sup>1</sup> The development and implementation of efficient computational schemes for the calculation of molecular photoabsorption spectra that can enable predictive simulations of complex systems is, thus, a very active area of current research.<sup>1</sup> Time Dependent Density Functional Theory (TDDFT) has gained a leader role in this race,

due to its optimal compromise between accuracy and computational economy. The most popular TDDFT implementation in quantum chemistry has been proposed by Casida,<sup>2</sup> which corresponds to a density-matrix approach according to the classification by Görling *et al.*<sup>3</sup> and consists in setting up and solving an eigenvalue problem over a basis of single-particle excitations. In addition to the Casida one, other TDDFT formulations have been developed and successfully implemented, which are briefly summarized as follows. One is based on an explicit time-propagation technique. This scheme was introduced in the pioneering work of Yabana and Bertsch<sup>4</sup> and is typically implemented over real space grids, like in the OCTOPUS code.<sup>5</sup> Another possibility is based on a super-operator formulation of TDDFT and has been implemented employing a Lanczos method and plane wave basis set.<sup>6</sup> The third, a more recent scheme, has been introduced by Grimme, and it consists in a simplified

Tamm–Dancoff Approximation (TDA)<sup>7</sup> and TDDFT.<sup>8</sup> A linear-scaling TDDFT has been developed by Zuehlsdorff *et al.*<sup>9</sup> An efficient method for large systems is the TDDFT time-propagation by Malola *et al.*<sup>10</sup> Recently, Noda *et al.* have developed a massively parallel implementation of TDDFT based on real time and real space,<sup>11</sup> which allowed them to study clusters containing up to 1414 gold atoms.<sup>12</sup> Finally, a complex polarizability algorithm for TDDFT<sup>13–15</sup> (called polTDDFT in the following) is particularly suitable for application to very large systems and will also be employed in the present work.<sup>16</sup>

These methods, especially the more recent ones, have achieved a high level of computational efficiency, allowing, nowadays, the treatment of molecules containing several hundreds of atoms at the TDDFT level.<sup>12,16</sup> Accuracy is, however, a more complicated issue at both DFT and TDDFT levels since it depends crucially on the choice of the exchange–correlation (xc-) functional employed to derive DFT Kohn–Sham (KS) orbitals and energies and in the response kernel of TDDFT. Although the search for increasingly more accurate xc-functionals and kernels is still active and new proposals appear continuously in the literature,<sup>17,18</sup> at the moment, the most accurate and popular choices correspond to hybrid xc-functionals for both DFT and TDDFT kernels, i.e., functionals containing a variable fraction of the exact [Hartree–Fock (HF)] non-local exchange. Among hybrid xc-functionals, B3LYP<sup>19,20</sup> is the most widely utilized one. B3LYP has the advantage of being rather versatile, that is, of performing reasonably well for both ground state (geometry optimization, bonding energy, and vibrational frequencies) and excited state (photoabsorption spectra) properties. Moreover, B3LYP has recently proven to be able to successfully describe vibronic effects in core electron excitations (NEXAFS) at the TDDFT level<sup>21</sup> and core electron ionization (XPS) at the DFT level within the  $\Delta$ SCF scheme.<sup>22</sup> Some limitations have, however, shown up in special instances, such as, for example, the absence of Rydberg states due to the lack of a correct asymptotic Coulombic behavior or the prediction of core-excited spectra shifted by several eV with respect to the experiment. Both deficiencies can be solved: the former, by adding Long-range Correction (LC),<sup>23</sup> and the latter, by adding Short-range Correction (SC)<sup>24</sup> to B3LYP. In this work, we will, therefore, implement and test our approach using the B3LYP functional although the scheme we propose here is quite general and can hold for any hybrid functionals.

It should be recalled that the use of hybrid functionals may present severe numerical issues connected with the HF non-local exchange, whose evaluation over basis sets involves matrix elements that can be treated efficiently when basis sets of Gaussian Type Orbitals (GTOs) are employed, but becomes problematic with other basis sets, such as Slater Type Orbitals (STOs) or Plane Waves (PWs). It should be observed that when using STO basis sets and hybrid xc-functionals, the SCF procedure becomes less efficient but is still computationally affordable even for large systems, whereas the TDDFT problem becomes soon intractable due to the extremely heavy computational cost of the HF non-local part of the kernel.

To solve these issues and arrive at an operational and efficient TDDFT approach employing hybrid xc-functionals, in the present work, we propose, develop, and validate an approximate treatment of the TDDFT kernel, which we call Hybrid Diagonal Approximation (HDA), and justify it by simple theoretical arguments.

The HDA is based on utilizing the hybrid exchange only for the diagonal terms in the response equations: this allows one to limit the computational cost of the TDDFT simulation while keeping basically the same accuracy as in the full TDDFT scheme using hybrid xc-functionals, as we will demonstrate hereafter. We implement our HDA approach both in the conventional Casida TDDFT scheme and in the more recent polTDDFT complex polarizability algorithm,<sup>13</sup> within a local version of the Amsterdam Density Functional (ADF) package, which will be distributed in a forthcoming release. Although the present work focuses on the implementation of HDA using STO basis sets, the fundamental idea behind the HDA approach is completely general and can be profitably extended to other basis sets as well, such as plane waves.

The article is organized as follows: we first provide a theoretical justification of the HDA. We then describe its implementation for both Casida and polTDDFT complex polarizability algorithms. Third, we validate and benchmark the method by comparing its results with respect to a standard Casida approach employing B3LYP in both DFT and in the TDDFT kernel, as well as with accurate experimental data for small systems (NH<sub>3</sub> and C<sub>6</sub>H<sub>6</sub>). We also validate our approach on a larger system, a medium-sized metal cluster [Au<sub>25</sub>(SR)<sub>18</sub>]<sup>−</sup>, for which both the x-ray crystal structure and the experimental optical absorption spectrum are available, in order to demonstrate the computational efficiency and economy of the HDA. Finally, we test the HDA with respect to the full kernel at the Casida level for seven other systems, in order to corroborate the general validity of the suggested approximation and provide information regarding the errors introduced by this scheme.

## II. THEORETICAL METHOD AND IMPLEMENTATION

### A. Casida TDDFT formulation

The standard (and most widely employed) TDDFT formulation in quantum chemistry consists in expanding the molecular Kohn–Sham (KS) orbitals as a linear combination of atomic functions and recast the TDDFT equations in terms of a diagonalization of a matrix omega ( $\Omega$ ) according to the density-matrix formulation of Casida.<sup>2</sup> In practice, the KS equations are first solved,

$$H_{KS}\varphi_i = \varepsilon_i\varphi_i. \quad (1)$$

Then, the  $\Omega$  matrix is diagonalized,

$$\Omega\mathbf{F}_I = \omega_I^2\mathbf{F}_I, \quad (2)$$

where the matrix elements of the  $\Omega$  matrix can be calculated from the solution of KS equation (1):

$$\Omega_{ia,jb} = \delta_{ij}\delta_{ab}(\varepsilon_a - \varepsilon_i)^2 + 2\sqrt{\varepsilon_a - \varepsilon_i}K_{ia,jb}\sqrt{\varepsilon_b - \varepsilon_j}, \quad (3)$$

and in expression (3), the coupling matrix  $K_{ia,jb}$  is defined as

$$K_{ia,jb} = \langle a|j|ib\rangle + \langle a|j|f_{\sigma\tau}^{xc}|ib\rangle. \quad (4)$$

In Eq. (4),  $f_{\sigma\tau}^{xc}$  is the xc-kernel, with  $\sigma$  and  $\tau$  being spin variables. The Casida problem consists in finding eigenvalues and eigenvectors of  $\Omega$ , Eq. (2). The eigenvalues of (2) correspond to the squared excitation energies, while from the eigenvectors, the intensities (absolute oscillator strengths) can be extracted.<sup>2</sup> It is worth noting that the  $\Omega$  matrix elements span the first-order density matrix,

which corresponds to all the products between occupied and virtual KS orbitals, so that the dimension of the  $\Omega$  matrix is  $N_{\text{occ}} \times N_{\text{virt}}$  and can be quite large ( $\approx 10^5$ ) for a cluster containing more than 100 metal atoms. The Casida approach is efficiently implemented in many quantum chemistry codes, such as, for example, ADF code,<sup>25–27</sup> which takes advantages of the molecular symmetry (employing the Wigner–Eckart theorem for the TDDFT part), of the Davidson diagonalization algorithm, of efficient fitting techniques of the first-order density through the use of auxiliary basis functions to improve matrix-vector multiplication within the Davidson algorithm, and finally of the parallelization of the code which can exploit modern supercomputer architectures. Although the formalism is quite general, issues can arise when hybrid xc-functionals and xc-kernels are chosen. When GTO are utilized, hybrid functionals and kernels can be implemented without hampering numerical efficiency, due to the availability of analytic formulas for non-local exchange integrals (although for large molecules, density fitting techniques<sup>28,29</sup> must be used, which can be problematic with large basis sets). On the contrary, many problems arise when using non-GTO basis sets, such as STO or PW. When STO are employed, non-local exchange integrals can be calculated in practice by means of density fitting techniques,<sup>28,29</sup> which allow one to approximate a product of STO centered on different atoms as a linear combination of auxiliary functions, employed to fit the electron density. This allows one to solve the DFT KS equations with a reasonable effort also for large systems, but in TDDFT, the non-local kernel becomes soon impracticable. For example, for a moderate-size metal cluster such as  $\text{Au}_{25}(\text{SR})_{18}$ , the TDDFT part calculated with hybrid B3LYP kernel needs 60 times more central processing unit (CPU)-time than a conventional generalized gradient approximation (GGA), i.e., non-hybrid calculation. It would then be appealing to reduce the computational effort of the hybrid xc-kernel without giving up to the high accuracy afforded by the use of hybrid xc-functionals for the description of the electronic structure of the systems under study.

A first possibility would be to employ the hybrid functional only for the DFT KS part and use the Adiabatic Local Density Approximation (ALDA)<sup>30</sup> for the TDDFT kernel. However, the presence of the non-local HF exchange in the KS equations causes a relevant shift (up to several eV) of the virtual orbital eigenvalues to higher energies rendering the calculated spectrum inaccurate. It is worth noting at this point that when a hybrid kernel is used, this effect is compensated by a shift in the opposite direction of the diagonal elements of the matrix, caused by the non-local HF exchange of the xc-kernel. This is best seen by casting the TDDFT equations in the Random Phase Approximation (RPA) structure,

$$\begin{pmatrix} A & B \\ B^* & A^* \end{pmatrix} \begin{pmatrix} X \\ Y \end{pmatrix} = \omega \begin{pmatrix} 1 & 0 \\ 0 & -1 \end{pmatrix} \begin{pmatrix} X \\ Y \end{pmatrix}, \quad (5)$$

where the submatrices A and B take the following general form for hybrid kernels:

$$A_{ia,jb} = \delta_{ij} \delta_{ab} (\varepsilon_a - \varepsilon_i) + \langle aj | ib \rangle - \alpha \langle aj | bi \rangle + (1 - \alpha) \langle a | \frac{\partial V_{XC}}{\partial \rho} j^* b | i \rangle, \quad (6)$$

$$B_{ia,jb} = \langle ab | ij \rangle - \alpha \langle ab | ji \rangle + (1 - \alpha) \langle a | \frac{\partial V_{XC}}{\partial \rho} b^* j | i \rangle, \quad (7)$$

where in expressions (6) and (7)  $\alpha$  represents the fraction of the non-local HF exchange in the xc-kernel and ALDA is assumed in the last terms of both equations.

Now, let us consider the diagonal elements of the RPA matrix, which corresponds to the diagonal elements of the matrix A,

$$A_{ia,ia} = (\varepsilon_a - \varepsilon_i) + \langle ai | ia \rangle - \alpha \langle ai | ai \rangle + (1 - \alpha) \langle a | \frac{\partial V_{XC}}{\partial \rho} i^* a | i \rangle. \quad (8)$$

The third element in the right-hand side of expression (8) is responsible for recovering the too high occupied-virtual energy difference obtained in the KS equation when a hybrid xc-functional, containing a fraction of the HF exchange, is used. This simple observation suggests that a possible strategy is to employ the non-local HF exchange of the kernel only for the diagonal elements of the A matrix, while treating at the simpler ALDA level (no HF exchange) all the off-diagonal elements of the A matrix and the full B matrix. With this choice, which we call Hybrid Diagonal Approximation (HDA), the matrices A and B take the following expressions:

$$A_{ia,jb} = \delta_{ij} \delta_{ab} (\varepsilon_a - \varepsilon_i - \Delta_{ia}) + \langle aj | ib \rangle + \langle a | \frac{\partial V_{XC}}{\partial \rho} j^* b | i \rangle, \quad (9)$$

$$B_{ia,jb} = \langle ab | ij \rangle + \langle a | \frac{\partial V_{XC}}{\partial \rho} b^* j | i \rangle, \quad (10)$$

where in expression (9), we have introduced a diagonal corrective term,

$$\Delta_{ia} = \alpha \langle ai | ai \rangle + \alpha \langle a | \frac{\partial V_{XC}}{\partial \rho} i^* a | i \rangle. \quad (11)$$

In expression (11), the second term is much smaller than the first one and can be safely neglected. With the expressions (9) and (10) for the A and B matrix, the difference A-B is still diagonal as it is customary in TDDFT with local kernels, so it is possible to solve the RPA-like equation with respect to Y and obtain again conventional Casida equation (3) for the  $\Omega$  matrix, with the only difference being limited to the eigenvalue differences, which must be corrected by term (11).

Importantly, following this approach, the number of needed exchange integrals is only  $(N_{\text{occ}} \times N_{\text{virt}})$  instead of  $(N_{\text{occ}} \times N_{\text{virt}})^2$ , i.e., it is greatly reduced. The implementation of such a scheme starting from a Casida code is straightforward: the elements of the  $\Omega$  matrix are calculated according to the conventional ALDA expressions with the exception of the diagonal elements, while the orbital energy differences are corrected according to Eqs. (9) and (11). In correction (11), the first term is calculated numerically, while the second term is neglected. Since the Davidson method is usually employed to diagonalize the  $\Omega$  matrix, only the lowest part of the excitation spectrum is obtained. Therefore, it is not necessary to correct all the diagonal elements of the A matrix, but only those which correspond to excitation energies not too far from the energy range of the spectrum extracted by the Davidson procedure. To this purpose, we have introduced a cutoff parameter that can be chosen in input.

## B. Complex polarizability TDDFT formulation

Despite the efficiency of numerical diagonalization techniques such as the Davidson one, it becomes hard to calculate valence

photoabsorption spectra over a wide excitation energy range when large systems are considered. The Davidson iterative algorithm, generally employed in all the TDDFT codes, which use the Casida method, is efficient on large  $\Omega$  matrices, but is limited to extracting a relatively small number of lowest eigenvalues and eigenvectors. Therefore, the Casida TDDFT algorithm remains efficient for large systems only when attention is focused on few low-energy transitions, but cannot be employed in practice to calculate a photoabsorption spectrum over a wide energy range, often necessary for a thorough simulation of and comparison with an experiment. As the molecule/cluster size increases, the diagonalization problem becomes more and more pathological, eventually rendering the approach unfeasible. In order to overcome this problem, we have recently proposed the complex polarizability TDDFT (polTDDFT) algorithm.<sup>13</sup> This approach is able to treat very large systems and avoid the bottleneck of the diagonalization via a direct solution of the response equations. The reader is referred to the original work for a detailed description of the algorithm,<sup>13</sup> together with its implementation in the ADF program.<sup>14</sup>

In practice, the photoabsorption spectrum  $\sigma(\omega)$  is calculated point by point, from the imaginary part of the dynamical polarizability  $\alpha(\omega)$ ,

$$\sigma(\omega) = \frac{4\pi\omega}{c} \text{Im}[\alpha(\omega)]. \quad (12)$$

This expression is of practical interest when the polarizability is calculated for complex frequency, i.e.,  $\omega = \omega_r + i\omega_i$ , where the real part  $\omega_r$  is the scanned photon frequency (energy) and  $\omega_i$  is the imaginary part, which corresponds to a broadening of the discrete lines and can be interpreted as a pragmatic inclusion of the excited states finite lifetime. The complex dynamical polarizability is calculated by solving the following non-homogeneous linear system:

$$[\mathbf{S} - \mathbf{M}(\omega)]\mathbf{b} = \mathbf{d}. \quad (13)$$

In Eq. (9),  $\mathbf{S}$  is the overlap matrix between fitting functions,  $\mathbf{b}$  is the unknown vector with the expansion coefficients  $b_\mu(\omega)$  of  $\rho_z^{(1)}$ ,  $\mathbf{d}$  is the frequency-dependent vector corresponding to the known non-homogeneous term, and finally the elements of the frequency-dependent matrix  $\mathbf{M}$  are

$$M_{\mu\nu} = \langle f_\mu | \chi_{KS}(\omega) K | f_\nu \rangle. \quad (14)$$

In Eq. (14),  $\chi_{KS}$  refers to the Kohn–Sham frequency-dependent dielectric function and  $K$  to the kernel. Notice that the matrix element is between density fitting functions, so the present implementation of the algorithm allows one to employ only density dependent kernels. For this reason, the density matrix dependent HF exchange kernel, which is an ingredient of hybrid functionals, is ruled out. The original characteristic of the polTDDFT method is the introduction of a simple approximation, which enables the construction of  $\mathbf{M}(\omega)$  as a linear combination of *frequency independent* matrices  $\mathbf{G}^k$  with *frequency-dependent* coefficients  $s_k(\omega)$ , with the following expression:

$$\mathbf{M}(\omega) = \sum_k s_k(\omega) \mathbf{G}^k. \quad (15)$$

With this idea, a set of matrices  $\{\mathbf{G}^k\}$  is calculated and stored only once at the beginning, and then the matrix  $\mathbf{M}(\omega)$  is calculated

very rapidly at each photon energy  $\omega$ , as a linear combination of the  $\{\mathbf{G}^k\}$  matrices with the following coefficients:

$$s_k(\omega) = \frac{4\bar{E}_k}{\omega^2 - \bar{E}_k^2}, \quad (16)$$

where in expression (16)  $\bar{E}_k$  refers to the center of the interval which discretizes the excitation energy variable and in the original formulation, corresponds to the difference between virtual and occupied orbital energies:  $\epsilon_a - \epsilon_i$ .

The discrepancies observed between the polTDDFT-HDA and the Casida TDDFT HDA results must be ascribed to the approximations inherent with the polTDDFT algorithm, namely, the choice of the fitting functions to represent the matrix of Eq. (13) and the energy discretization of Eq. (15).

Coming now to the present proposal, in order to apply within the polTDDFT algorithm the HDA approach already discussed for the Casida procedure, it is enough to correct the orbital energy differences with same corrective term (11) as already carried out for expression (9):  $\epsilon_a - \epsilon_i - \Delta_{ia}$ . With this “rescaling” of the excitation energies, the occupied-virtual pairs will change their position along the excitation energy axis, and expression (16) can be employed to calculate the coefficients  $s_k(\omega)$  to build matrix (15) at any given photon energy. Also, in this case, in correction (11), the first term is calculated numerically, while the second term is neglected and a cutoff parameter is introduced in order to avoid corrections of terms so high in energy that do not play a significant role in the calculation.

### III. COMPUTATIONAL DETAILS

All the DFT KS calculations reported in this work were performed employing a TZP basis of STO functions (included in the ADF database) and the B3LYP hybrid xc-functional. The TDDFT calculations were carried out after the KS section and were performed with the Casida or the polTDDFT algorithms. For the Casida procedure, both the full B3LYP kernel and the simplified HDA scheme have been employed and compared, whereas the polHDA-B3LYP level is the only available scheme for the hybrid functional within polTDDFT. For both Casida and polTDDFT, the HDA has been implemented by exploiting the parallelization at the general Message Passing Interface (MPI) level. The Casida scheme furnishes the spectra in terms of discrete lines, which have been broadened with Lorentzian functions of HWHM = 0.075 eV in the figures. The polTDDFT furnishes spectra which are already broadened, and in order to be consistent with the Casida broadened profiles, the imaginary part of the photon energy [see  $\omega_i$  after Eq. (12)] has been set to 0.075 eV as well. When comparing with experimental data, we employed a broadening equal to the experimental resolution (HWHM = 0.5 eV). All the calculations were performed with a local version of the ADF code, while the HDA implementation for both Casida and polTDDFT algorithms will be distributed in a forthcoming ADF release. The calculations for the gold cluster in Sec. IV C were performed employing the Zero Order Regular Approximation (ZORA) in order to include relativistic effects at the scalar level.

### IV. RESULTS AND DISCUSSION

We have fully tested the performances of the HDA scheme implemented in this work on two small systems ( $\text{NH}_3$ ,  $\text{C}_6\text{H}_6$ ) and

a medium-sized ligand-protected metal cluster  $\text{Au}_{25}(\text{SR})_{18}$ . The goal is to achieve a firm assessment of the accuracy of the HDA at both Casida and complex polarization algorithms using the hybrid B3LYP functional with respect to the full B3LYP kernel at the Casida level as well as to the experiment. For the metal cluster, also an analysis of the performances in terms of computational saving will be provided. Moreover, we have also tested the HDA with respect to the full kernel only at the Casida level for an additional set of seven systems, in order to show the effect of HDA on the excitation energies and the oscillator strengths, to corroborate the HDA validity and provide at least an estimate of the expected errors.

At the moment, the program is installed on a HP ProLiant DL580 Gen10 server (with four processors each with 18 cores Intel® Xeon® Gold 6140 CPU @ 2.30 GHz, in total, 72 cores and 728 GB of RAM), on which the present calculations were run using 24 cores at most. The implementation is general MPI.

### A. $\text{NH}_3$

In the upper panel of Fig. 1, we have reported three calculated spectra for  $\text{NH}_3$ : (1) the Casida profile at the B3LYP level with the full kernel (blue line), (2) the Casida profile at the B3LYP level with the HDA kernel (red line), and (3) the polTDDFT profile at

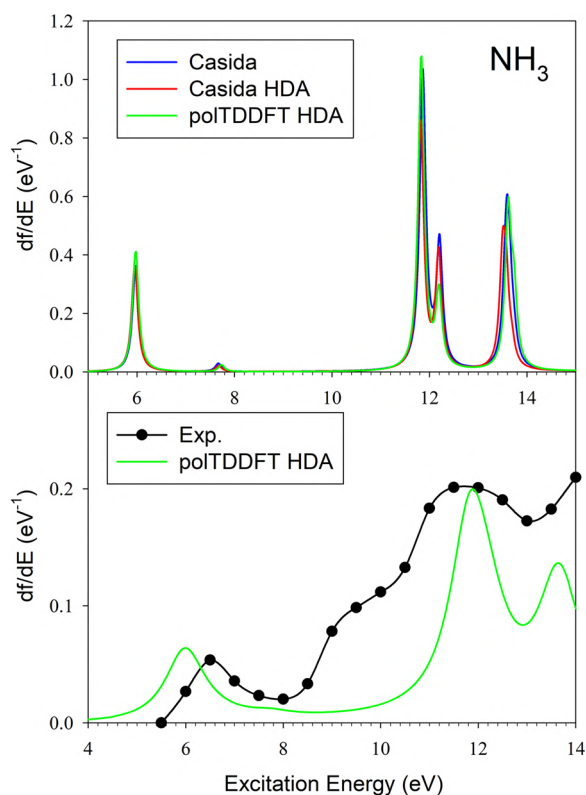


**FIG. 1.** Valence excitation spectra of  $\text{NH}_3$ . Upper panel: calculated profile with the Casida approach (blue line), Casida HDA (red line), and polTDDFT (green line), broadened with  $\text{HWHM} = 0.075$  eV. Lower panel: low-resolution experimental data<sup>31</sup> (black line and circles) and calculated profile with polTDDFT (green line), broadened with  $\text{HWHM} = 0.5$  eV.

the B3LYP level with the HDA kernel (green line), which we call hereafter pol-HDA. To validate the HDA approach, we compare the Casida full kernel with respect to HDA. As apparent from Fig. 1, the two profiles are almost superimposed: a very modest discrepancy is seen for the feature around 13.6 eV, but the difference is modest, the energy difference in peak positions is below 0.1 eV, and the intensity is also only slightly affected. This observation demonstrates the accuracy of the HDA scheme. It is worth noting that if a pure ALDA kernel would have been chosen in the TDDFT procedure after a B3LYP KS calculation, the first peak around 6 eV would have been shifted by about 0.7 eV to higher energy. This demonstrates our working hypothesis that the role of the non-local HF exchange in the kernel is limited to the diagonal elements, providing a robust argument to justify the HDA scheme. Also, the pol-HDA profile is in excellent agreement with the Casida HDA one, suggesting that the approximations introduced by polTDDFT are adequate for a proper description of the excitation process.

Although the goal of the present work is to assess the validity of the HDA with respect to the full kernel for B3LYP, it is also interesting to compare the theoretical excitation spectrum with respect to the experiment, to have an indication of the adequacy of the B3LYP xc-functional to describe valence excitation spectra. For this reason, the low-resolution total photoabsorption experimental measurement from the work of Brion *et al.*<sup>31</sup> has been shown (black line) in the lower box of Fig. 1, where in the reported calculated profile, the same broadening as the experimental resolution has been employed ( $\text{HWHM} = 0.5$  eV). Note that we have preferred to employ a much lower broadening ( $\text{HWHM} = 0.075$  eV) for comparison among different computational schemes (upper panel) to amplify possible differences.

The first band with a maximum at 6.5 eV is assigned by present calculations to the  $3a_1$  (HOMO)  $\rightarrow 4a_1$  (mixed valence -Rydberg 3s), in line with previous assignments. The energy position is properly described by theory, with few tenths of eV of error if we take the vertical values, and the absolute intensity is in fairly good agreement with the experiment as well. The next experimental feature is a very weak vibrational progression (visible in the high-resolution experiment reported in Ref. 31) encompassing the region between 7.5 eV and 8.5 eV, which is properly described by theory as a very weak peak; also, in this case, the transition corresponds to the excitation of the HOMO  $3a_1$  to the  $2e$  virtual orbital, with mixed valence, Rydberg nature, but this time of  $3p$  instead of  $3s$  nature. From 8.8 eV up to 11 eV, at least four different vibrational progressions have been identified in the experimental data,<sup>31</sup> which are not present in the calculated profiles. This is not surprising since these correspond to high Rydberg states  $ns$  with  $n > 3$ , which are not supported by the present theoretical approach for two reasons: (1) the B3LYP xc-functional does not have the correct asymptotic Coulomb behavior and, therefore, cannot support high-lying Rydberg states; (2) even using xc-functionals with the correct asymptotic behavior, for example Long-range Corrected (LC) ones<sup>32</sup> or more simple models such as LB94<sup>33</sup> or SAOP,<sup>34</sup> the description of high-lying Rydberg states requires improved basis set, augmented with very diffuse functions. Since the present HDA scheme has been proposed in order to save computational efforts when B3LYP is used in TDDFT calculations of large systems where Rydberg state does not play a relevant role, we did not try to improve the description of this spectral region. The ionization limit of  $\text{NH}_3$  is around

10.85 eV;<sup>31</sup> therefore, beyond this energy, the comparison with the experiment should include photoionization channels which are not considered in the present TDDFT formalism. Anyway, the “shape resonance” around 12 eV is properly described by two discrete bands in the calculated spectrum, and also, the following intensity increase around 14 eV is consistent with the discrete transition calculated at 13.7 eV. Therefore, we can conclude the analysis of NH<sub>3</sub> saying that B3LYP is adequate for a quantitative description of the valence excitation spectrum, with errors of few tenths of eV, and that HDA and polHDA exhibit similar accuracy as the full kernel simulations. Known limitations regarding Rydberg states are not expected to be important for applications to large systems. In any case, the possibility to use LC functionals and the basis set supplemented by diffuse functions is possible also in connection with the HDA approach, so this limitation is not intrinsic to the methodology.

## B. C<sub>6</sub>H<sub>6</sub>

The same analysis pursued for NH<sub>3</sub> has been applied to C<sub>6</sub>H<sub>6</sub>, and the results are shown in Fig. 2: in the upper panel, the three calculated profiles broadened with HWHM = 0.075 eV are reported, while in the lower panel, the polTDDFT calculation broadened with

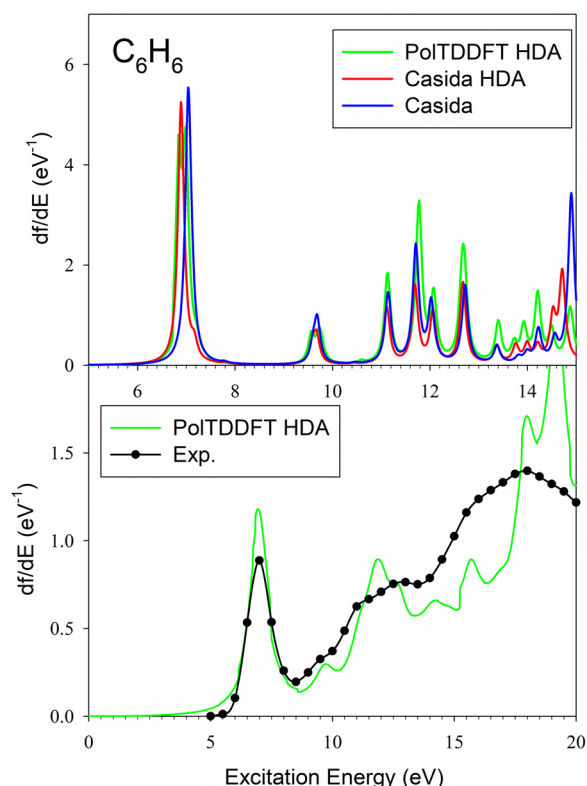


**FIG. 2.** Valence excitation spectra of C<sub>6</sub>H<sub>6</sub>. Upper panel: calculated profile with the Casida approach (blue line), Casida HDA (red line), and polTDDFT (green line), broadened with HWHM = 0.075 eV. Lower panel: low-resolution experimental data<sup>35</sup> (black line and circles) and calculated profile with polTDDFT (green line), broadened with HWHM = 0.5 eV.

the experimental resolution corresponding to an HWHM of 0.5 eV is reported together with the low-resolution total photoabsorption experimental data from Feng *et al.*<sup>35</sup> (black line). This time, the results of the Casida scheme using the HDA are in good agreement with the full kernel results, with differences in excitation energies below 0.3 eV in the worst cases. Intensities are properly reproduced as well, with modest discrepancies, the largest being an underestimate of 30% of the transition at 9.7 eV, but notice that the intensity of first strong  $\pi$ - $\pi^*$  transition at 7 eV is underestimated by only 5%. When the pol-HDA is considered, some discrepancies are apparent above 11 eV, but limited to the intensity of the transitions, whereas their energy positions remain in excellent agreement with the Casida results. Anyway, these discrepancies are inherent to the polTDDFT scheme and not to the HDA approach.

Also, for C<sub>6</sub>H<sub>6</sub>, it is interesting to compare the calculated results with respect to low-resolution measurement, in order to assess the quality of the B3LYP xc-functional. The first intense experimental band with a maximum at 6.94 eV has been ascribed<sup>35</sup> to the valence  $\pi$ - $\pi^*$  transition  ${}^1E_{1u} \leftarrow {}^1A_{1g}$ , confirmed by present calculations at 6.89 eV in excellent quantitative agreement. Also, the absolute normalization of the first peak is satisfactory, considering the arbitrariness of the broadening and the irregular shape of the experimental band.

For C<sub>6</sub>H<sub>6</sub>, the first vertical ionization energy falls at 9.45 eV, and the tiny structures in the range 8–9.5 eV have been ascribed to vibrational progressions of Rydberg transitions,<sup>35</sup> not supported by the present formalism. Beyond the first ionization limit, the photoionization continuum should be included for comparison with the experiment; however, the simple discrete spectrum here calculated is nevertheless able to describe with semi-quantitative accuracy the weak spectral features measured above 9.45 eV. In summary, also for C<sub>6</sub>H<sub>6</sub>, the HDA approximation is proven to be accurate, and B3LYP is confirmed to be able to describe properly the valence excitation spectrum, with quantitative agreement for the first  $\pi$ - $\pi^*$  transition.

## C. [Au<sub>25</sub>(SCH<sub>3</sub>)<sub>18</sub>]<sup>-</sup>

Finally, we tested the performance of the HDA approach on a much more complex system, in particular, on a medium-sized gold cluster protected by thiolate ligands. We choose the [Au<sub>25</sub>(SCH<sub>3</sub>)<sub>18</sub>]<sup>-</sup> system for several reasons: first, the structure of this system has been completely characterized by x-ray diffraction;<sup>36</sup> second, experimental photoabsorption data are available for comparison;<sup>37</sup> and third, this system has been already employed in our previous work to validate and assess the performances of computational protocols<sup>38</sup> such as xc-functional and basis set choice, ligand simplification, and geometry optimization protocols for ligands.

In Fig. 3, we report the results of the Casida full kernel and HDA, as well as the pol-HDA calculated profiles, together with experimental data.<sup>37</sup> Note that in this case, we did not consider absolute intensity, so we adopt an arbitrary unit intensity scale. Note also that the calculations have been performed for SR ligands with R = CH<sub>3</sub>, to allow us to perform full kernel B3LYP TDDFT calculations with our computational resources, while the experiment has been performed with SR' ligands with R' = CH<sub>2</sub>CH<sub>2</sub>C<sub>6</sub>H<sub>5</sub> (this simplification will be further discussed below). Figure 3 shows an

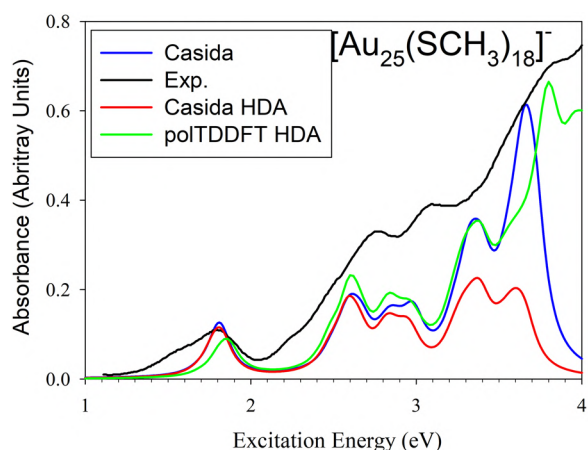


**FIG. 3.** Valence excitation spectra of  $[\text{Au}_{25}(\text{SCH}_3)_{18}]^-$ . Calculated profile with the Casida approach (blue line), Casida HDA (red line), and polTDDFT (green line), broadened with HWHM = 0.075 eV and experimental data<sup>37</sup> (black line).

excellent match between full kernel and HDA TDDFT Casida profiles apart from a minor deviation around 3.4 eV. Regarding the pol-HDA profile, it follows very well the Casida ones up to 2.6 eV, with a minor deterioration (less than 0.1 eV) for the first peak at 1.8 eV. Beyond 2.6 eV, the polTDDFT-HDA is in better agreement with the full kernel Casida than with the HDA one. The comparison with respect to the experiment is fairly good: for the first peak at 1.8 eV, the agreement between the Casida results and the experiment is quantitative, with pol-HDA worsening the agreement by less than 0.1 eV. We can recall that this first peak is quite hard to be properly reproduced, despite the previous studies<sup>38</sup> improving the basis set, changing the xc-functional, including full ligands (not simplified

methyl residues) in the calculation, and fully or partially optimizing the geometry. At the moment, the B3LYP seems to be the best xc-functional to reproduce quantitatively the experimental data. Additional spectral features appear in the experiment at higher energies, namely, at 2.75 eV, 3.1 eV, and 3.9 eV, and all of them are properly reproduced by theory, with deviations of few tenths of eV. It must be considered that, in the region around 3 eV, the nature of the ligand is important to properly assess the spectrum, so the simplification of  $\text{R}' = \text{CH}_2\text{CH}_2\text{C}_6\text{H}_5$  with the smaller  $\text{R} = \text{CH}_3$  can be the cause of this deterioration. In fact, it has been shown that, at the SAOP-TZP level, the substitution of  $\text{R}'$  with  $\text{R}$  induces an energy widening between the two peaks at 2.47 eV and 3.0 eV, see Fig. 3 and Table I in Ref. 38.

Finally, it is worth mentioning the CPU time of the calculations on this cluster. The calculations ran on the hardware described in the computational details, employing 24 cores for each run. In terms of elapsed time, the Casida with a full kernel spent 60.6 h, Casida with an HDA 8.75 h, and polTDDFT 16.4 h. The HDA allows us to get a factor of seven in the speedup of Casida procedure, and polTDDFT is four times faster than Casida with full kernel but allows one to calculate the spectrum to much higher energies.

#### D. Specific tests with the Casida method

In order to assess the effect of the HDA approximation, we decided to compare the B3LYP full kernel results with respect to the HDA at the Casida level for a set of seven additional molecules. In order to span different chemical situations, we considered five paradigmatic organic molecules (taken from Refs. 39 and 40): all-E-hexatriene ( $\text{C}_6\text{H}_8$ ), pyridine ( $\text{C}_5\text{H}_5\text{N}$ ), cytosine, 6,6'-difluoro-indigo, *p*-benzoquinone ( $\text{C}_6\text{H}_4\text{O}_2$ ), together with a metal-organic complex ferrocene  $\text{Fe}(\text{C}_5\text{H}_5)_2$ , and finally a chiral model metal cluster, Ag<sub>8</sub>.<sup>15,41</sup> In Figs. 4–6, we have reported the calculated

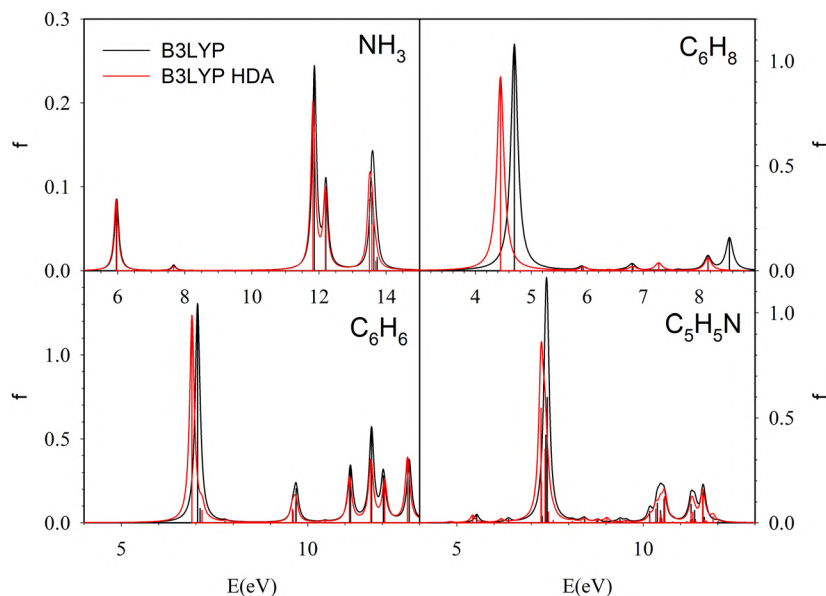


**FIG. 4.** Valence excitation spectra of  $\text{NH}_3$ ,  $\text{C}_6\text{H}_8$  (all-E-Hexatriene),  $\text{C}_6\text{H}_6$ , and  $\text{C}_5\text{H}_5\text{N}$  (pyridine). Calculated profiles with the Casida full kernel approach (black lines) and Casida HDA (red lines); discrete excitations are reported, together with broadened Lorentzian profiles by HWHM = 0.075 eV.

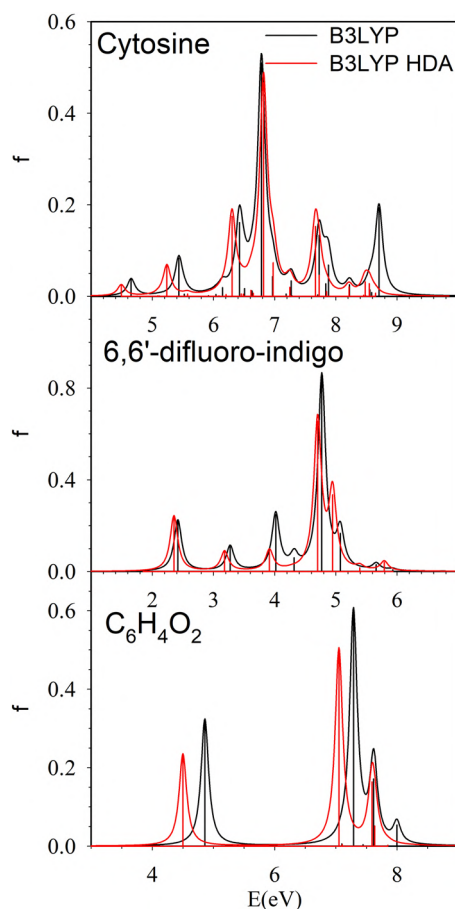


**FIG. 5.** Valence excitation spectra of cytosine, 6,6'-difluoro-indigo, and  $C_6H_4O_2$  (*p*-benzoquinone). Calculated profiles with the Casida full kernel approach (black lines) and Casida HDA (red lines); discrete excitations are reported, together with broadened Lorentzian profiles by HWHM = 0.075 eV.

spectra both as discrete lines and as broadened profiles with Lorentzian functions of HWHM = 0.075 eV by using black lines for the full kernel and red lines for HDA. Since we add discrete lines in the chiro-optical spectra, in our analysis, we included also the three systems considered in Secs. IV A–IV C in order to see the HDA effects on the individual discrete lines of these systems as well.

In Fig. 4,  $NH_3$  together three small organic molecules ( $C_6H_6$ ,  $C_6H_8$ , and  $C_5H_5N$ ) is considered: as a general statement, the difference between the calculated spectra are modest, although one should consider that different energy scales have been employed in the figures since the spectra are quite different from each other. Only for benzene and pyridine, we have employed the same energy scale due to their chemical similarity. In general, the errors in excitation energies are of the order of few tenths of eV, not exceeding 0.3 eV. All-*E*-hexatriene ( $C_6H_8$ ) gives the worst agreement; in this case, the spectrum is dominated by only one transition around 4.7 eV. It is important to underline that we do not advocate employing HDA for small systems like the present ones, for

which superior methods are available and practicable. We consider here small systems simply to assess HDA performance and have an idea of its accuracy when it is applied to large systems, where the B3LYP TDDFT full kernel scheme would be not practicable at all.

In Fig. 5, larger organic molecules are considered. Apart from *p*-benzoquinone, whose spectra appear much more complex and richer of spectral features, also in this case, all the spectra calculated at the HDA level show only modest differences with respect to the full kernel results, and in general, the excitation energy discrepancies remain below 0.2 eV. In occasional circumstances, more pronounced deterioration is apparent, such as, for example, the feature around 4 eV in 6,6'-difluoro-indigo and the first strong peak of *p*-benzoquinone, the latter corresponding to the largest found disagreement in present study which is 0.4 eV. In general, the HDA performs better when the molecule is larger and the spectrum is rich of features, and this is probably due to the fact that when many transitions are close together in a narrow energy interval, their mutual coupling tends to reduce the effect of the non-local xc-kernel. Such an effect is particularly evident from Fig. 6, where the largest systems are compared with each other.

We start the discussion of Fig. 6 noting that the discrete excitation spectrum of the  $[Au_{25}(SCH_3)_{18}]^-$  cluster is characterized by groups of discrete excitation, well separated by gaps, for example, there is a large gap between 1.8 eV and 2.4 eV and two narrow ones between 2.6 eV and 2.8 eV and between 3.0 eV and 3.2 eV. The HDA simulates nicely such feature of the excitation energies, but also the intensity distributions is very well reproduced, as demonstrated by the mutual agreement of the broadened profiles as well. The only appreciable yet modest deterioration is around 3.3 eV, where HDA slightly underestimates the intensity.

For  $Fe(C_5H_5)_2$ , the spectrum is dominated by the intense transition at 6.9 eV, which is shifted by only 0.1 eV and slightly reduced in intensity when HDA is employed. The remaining spectral features are less prominent and are satisfactorily reproduced by HDA.

Finally, we have included in the present analysis the bare cluster  $Ag_8$ , which was already employed previously as a model system to study the Circular Dichroism (CD) in chiral metal clusters.<sup>15,41</sup> Also, in this case, the photoabsorption oscillator strengths (left lower panel of Fig. 6) calculated by HDA are in good agreement with the full kernel B3LYP results, and the first strong transition at 1.3 eV is underestimated by only 0.1 eV and slightly reduced in intensity when HDA is introduced. In the right lower panel of Fig. 6, the  $Ag_8$  CD expressed as Rotatory strength (R) is reported. It is worth noting that the HDA is suitable to reproduce quantitatively the peak positions, their sign, and also the R values. For the HDA scheme, the usual gauge-dependence of the CD spectrum is expected, so the employment of a good quality basis set is necessary. The present basis set of TZP size has proven to be suitable in a previous study.<sup>15</sup>

We conclude from this section that the HDA scheme has proven suitable to reproduce nicely the photoabsorption and CD spectra of molecular systems, ranging from small organic molecules to metallorganic complexes and large metal clusters.

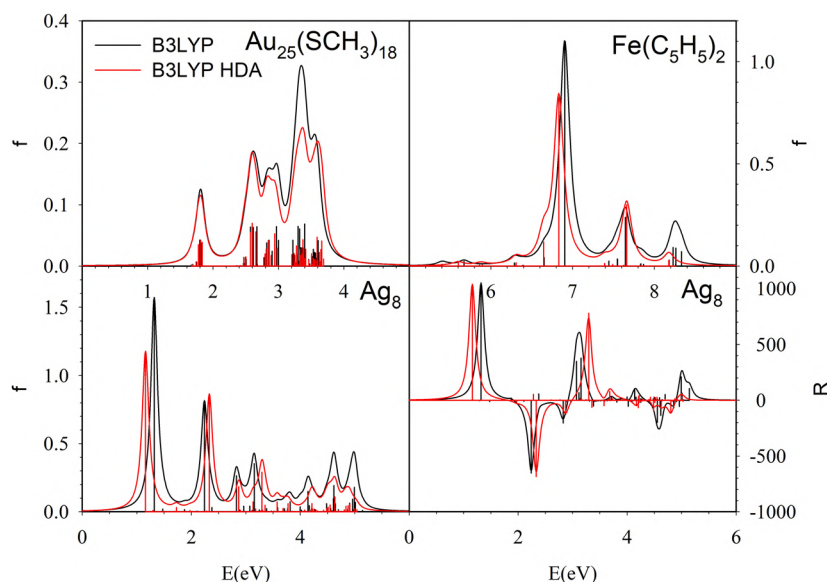


**FIG. 6.** Valence excitation spectra of  $[\text{Au}_{25}(\text{SCH}_3)_{18}]^-$ ,  $\text{Fe}(\text{C}_5\text{H}_5)_2$ , and  $\text{Ag}_8$ . Calculated profiles with the Casida full kernel approach (black lines) and Casida HDA (red lines); discrete excitations are reported, together with broadened Lorentzian profiles by  $\text{HWHM} = 0.075$  eV. For  $\text{Ag}_8$ , also the Rotatory strengths ( $R$ ) are reported (right lower panel) in units of  $10^{-40}$  esu<sup>2</sup> cm<sup>2</sup>.

## V. CONCLUSIONS

We propose and develop an approximate but physically grounded and accurate approach to greatly accelerate TDDFT simulations using hybrid xc-functionals, which we name Hybrid Diagonal Approximation (HDA). It is known that when hybrid xc-functionals are employed to solve the TDDFT equations, the kernel is called to recover the too wide energy gap introduced in the occupied-virtual orbital energy differences by the HF exchange. In this work, we show that this correction is essentially given by the diagonal part of the kernel, thus justifying the present simplified HDA scheme, in which the fraction of the HF exchange is employed only for the diagonal matrix elements, while for off-diagonal matrix elements, the simple ALDA is assumed. HDA is especially convenient in connection with Slater Type Orbitals (STO) basis sets as in the present work. In fact, the current TDDFT codes using STO basis sets are not efficient because the non-local HF exchange contribution of the kernel needs a CPU-demanding density fitting procedure to calculate two-electron integrals. Additionally, although the Gaussian Type Orbital (GTO) basis set does not suffer this problem due to its analytical product expansions,<sup>28,29</sup> significant speedups by a factor larger than four have still been achieved in explorative tests using GTO and the NWChem suite of codes.<sup>42</sup> In fact, HDA is a general approach and, therefore, can also help accelerate hybrid calculations on large molecules that use density fitting techniques for GTOs since density fitting for the exchange terms is known to be problematic for large basis sets. Moreover, the implementation of HDA is rather straightforward since it consists in disabling the calculation of the non-local kernel for the extradiagonal elements of the omega matrix rescaling the ALDA contribution to 100%, a procedure which should be easily implementable in any TDDFT code.

We applied the HDA approach to ten different systems, conducting a full comparison with experiment in particular for  $\text{NH}_3$ ,  $\text{C}_6\text{H}_6$ , and  $[\text{Au}_{25}(\text{SCH}_3)_{18}]^-$  as test cases, finding excellent

agreement with respect to both the full kernel and experimental data. For the metal cluster, a speedup of a factor of 7 has been obtained with respect to the full kernel implementation. The TDDFT-HDA/B3LYP protocol, therefore, promises to greatly facilitate achieving a quantitative description of the optical properties of medium-sized and complex systems, thanks to its computational efficiency, especially in the field of nanoclusters. Here, we have also developed and tested the implementation of the HDA within the complex polarization algorithm (polTDDFT) and proved that the approach is equally accurate and efficient, while allowing for the prediction of the high-energy part of the spectrum.

In addition to the three systems which we have analyzed in detail, we have also tested the validity of the HDA within the Casida approach by comparison with full kernel results for seven additional systems, ranging from simple to larger organic molecules, one metallorganic complex, and one chiral bare metal cluster. In all cases, the HDA has proven to be a good approximation of the full kernel results, with deviations with respect to excitation energies usually well below 0.3 eV and a slight reduction in the calculated intensity. For the metal cluster, the HDA has given an excellent quantitative reproduction of the CD spectrum.

As an overall conclusion of this work, we believe that the HDA is very promising to extend the range of applicability of TDDFT/B3LYP and in general, TDDFT using hybrid functionals, to very large systems, when the non-local Fock exchange kernel becomes prohibitive, a problem that plagues primarily non-GTO basis set, such as STO and plane waves (PWs), and also GTO basis sets.

Future extensions of the present methodology will include xc-functionals with Long-range Correction (LC), which should improve the description of virtual orbitals or with Short-range Correction (SC), for example, for applications in core excitation spectra,<sup>24</sup> as well as the implementation in codes using GTO and plane wave basis sets.

## ACKNOWLEDGMENTS

The authors are grateful to Edoardo Aprà for fruitful discussions and explorative tests using the NWChem suite of codes. A.F. acknowledges stimulating discussions with Nicola Durante. MS is grateful to Erik van Lenthe and Stan van Gisbergen of SCM (Amsterdam) for fruitful discussions and technical assistance during the implementation within the ADF program. Computational support from the CINECA supercomputing center within the ISCRA program is gratefully acknowledged. The authors are grateful to the Stiftung Beneficentia for a generous grant employed to set up a computational server. Support from Trieste University within the FRA program is gratefully acknowledged.

## DATA AVAILABILITY

The data that support the findings of this study are available from the corresponding author upon reasonable request.

## REFERENCES

- <sup>1</sup>V. Barone, *WIREs Comput. Mol. Sci.* **6**, 86 (2016).
- <sup>2</sup>M. E. Casida, *Recent Advances in Density-Functional Methods*, edited by D. P. Chong (World Scientific, Singapore, 1995), p. 155.
- <sup>3</sup>A. Görling, H. H. Heinze, S. Ph. Ruzankin, M. Staufer, and N. Rösch, *J. Chem. Phys.* **110**, 2785 (1999).
- <sup>4</sup>K. Yabana and G. F. Bertsch, *Phys. Rev. B* **54**, 4484 (1996).
- <sup>5</sup>M. A. L. Marques, A. Castro, G. F. Bertsch, and A. Rubio, *Comput. Phys. Commun.* **151**, 60 (2003).
- <sup>6</sup>B. Walker, A. M. Saitta, R. Gebauer, and S. Baroni, *Phys. Rev. Lett.* **96**, 113001 (2006).
- <sup>7</sup>S. Grimme, *J. Chem. Phys.* **138**, 244104 (2013).
- <sup>8</sup>C. Bannwarth and S. Grimme, *Comput. Theoret. Chem.* **1040-1041**, 45 (2014).
- <sup>9</sup>T. J. Zuehlsdorff, N. D. M. Hine, J. S. Spencer, N. M. Harrison, D. J. Riley, and P. D. Haynes, *Chem. Phys.* **139**, 064104 (2013).
- <sup>10</sup>S. Malola, L. Lehtovaara, J. Enkovaara, and H. Häkkinen, *ACS Nano* **7**, 10263 (2013).
- <sup>11</sup>M. Noda, K. Ishimura, K. Nobusada, K. Yabana, and T. Boku, *J. Comput. Phys.* **265**, 145 (2014).
- <sup>12</sup>K. Iida, M. Noda, K. Ishimura, and K. Nobusada, *Phys. Chem. A* **118**, 11317 (2014).
- <sup>13</sup>O. Baseggio, G. Fronzoni, and M. Stener, *J. Chem. Phys.* **143**, 024106 (2015).
- <sup>14</sup>O. Baseggio, M. De Vetta, G. Fronzoni, M. Stener, and A. Fortunelli, *Int. J. Quantum Chem.* **116**, 1603 (2016).
- <sup>15</sup>O. Baseggio, D. Toffoli, G. Fronzoni, M. Stener, L. Sementa, and A. Fortunelli, *J. Phys. Chem. C* **120**, 24335 (2016).
- <sup>16</sup>O. Baseggio, M. De Vetta, G. Fronzoni, M. Stener, L. Sementa, A. Fortunelli, and A. Calzolari, *J. Phys. Chem. C* **120**, 12773 (2016).
- <sup>17</sup>A. D. Becke, *J. Chem. Phys.* **140**, 18A301 (2014).
- <sup>18</sup>N. Mardirossian and M. Head-Gordon, *Mol. Phys.* **115**, 2315 (2017).
- <sup>19</sup>A. D. Becke, *J. Chem. Phys.* **98**, 5648 (1993).
- <sup>20</sup>P. J. Stephens, F. J. Devlin, C. F. Chabalowski, and M. J. Frisch, *Phys. Chem.* **98**, 11623 (1994).
- <sup>21</sup>A. Baiardi, M. Mendolicchio, V. Barone, G. Fronzoni, G. A. Cardenas Jimenez, M. Stener, C. Grazioli, M. de Simone, and M. Coreno, *J. Chem. Phys.* **143**, 204102 (2015).
- <sup>22</sup>M. Mendolicchio, A. Baiardi, G. Fronzoni, M. Stener, C. Grazioli, M. de Simone, and V. Barone, *J. Chem. Phys.* **151**, 124105 (2019).
- <sup>23</sup>A. Savin, in *Recent Developments and Applications of Modern Density Functional Theory*, edited by J. M. Seminario (Elsevier, Amsterdam, 1996), p. 327.
- <sup>24</sup>N. A. Besley, M. J. G. Peach, and D. J. Tozer, *Phys. Chem. Chem. Phys.* **11**, 10350 (2009).
- <sup>25</sup>E. J. Baerends, D. E. Ellis, and P. Ros, *Chem. Phys.* **2**, 41 (1973).
- <sup>26</sup>C. Fonseca Guerra, J. G. Snijders, G. te Velde, and E. J. Baerends, *Theor. Chem. Acc.* **99**, 391 (1998).
- <sup>27</sup>S. J. A. van Gisbergen, J. G. Snijders, and E. J. Baerends, *Comput. Phys. Commun.* **118**, 119 (1999).
- <sup>28</sup>A. Fortunelli and O. Salvetti, *J. Comput. Chem.* **12**, 36 (1991).
- <sup>29</sup>A. Fortunelli and O. Salvetti, *Chem. Phys. Lett.* **186**, 372 (1991).
- <sup>30</sup>E. K. U. Gross and W. Kohn, *Adv. Quantum Chem.* **21**, 255 (1990).
- <sup>31</sup>G. R. Burton, W. F. Chan, G. Cooper, and C. E. Brion, *Chem. Phys.* **177**, 217 (1993).
- <sup>32</sup>H. Iikura, T. Tsuneda, T. Yanai, and K. Hirao, *J. Chem. Phys.* **115**, 3540 (2001).
- <sup>33</sup>R. van Leeuwen and E. J. Baerends, *Phys. Rev. A* **49**, 2421 (1994).
- <sup>34</sup>O. V. Gritsenko, P. R. T. Schipper, and E. J. Baerends, *Chem. Phys. Lett.* **302**, 199 (1999).
- <sup>35</sup>R. Feng, G. Cooper, and C. E. Brion, *J. Electr. Spectrosc., Relat. Phenom.* **123**, 199 (2002).
- <sup>36</sup>M. W. Heaven, A. Dass, P. S. White, K. M. Holt, and R. W. Murray, *J. Am. Chem. Soc.* **130**, 3754 (2008).
- <sup>37</sup>M. Zhu, C. M. Aikens, F. J. Hollander, G. C. Schatz, and R. Jin, *J. Am. Chem. Soc.* **130**, 5883 (2008).
- <sup>38</sup>O. Baseggio, M. De Vetta, G. Fronzoni, D. Toffoli, M. Stener, L. Sementa, and A. Fortunelli, *Int. J. Quantum Chem.* **118**, e25769 (2018).
- <sup>39</sup>L. Goerigk, J. Moellmann, and S. Grimme, *Phys. Chem. Chem. Phys.* **11**, 4611 (2009).
- <sup>40</sup>M. Schreiber, M. R. Silva-Junior, S. P. A. Sauer, and W. Thiel, *J. Chem. Phys.* **128**, 134110 (2008).
- <sup>41</sup>N. V. Karimova and C. M. Aikens, *J. Phys. Chem. A* **119**, 8163 (2015).
- <sup>42</sup>M. Valiev, E. J. Bylaska, N. Govind, K. Kowalski, T. P. Straatsma, H. J. J. van Dam, D. Wang, J. Nieplocha, E. Apra, T. L. Windus, and W. A. de Jong, *Comput. Phys. Commun.* **181**, 1477 (2010).

# Predictive optical photoabsorption of $\text{Ag}_{24}\text{Au}(\text{DMBT})_{18}^-$ via efficient TDDFT simulations

Cite as: J. Chem. Phys. 155, 084103 (2021); doi: 10.1063/5.0056869

Submitted: 15 May 2021 • Accepted: 10 August 2021 •

Published Online: 27 August 2021



View Online



Export Citation



CrossMark

Marco Medves,<sup>1</sup> Luca Sementa,<sup>2</sup>  Daniele Toffoli,<sup>1</sup>  Giovanna Fronzoni,<sup>1</sup>  Kumaranchira Ramankutty Krishnadas,<sup>3</sup> Thomas Bürgi,<sup>3</sup>  Sara Bonacchi,<sup>4</sup>  Tiziano Dainese,<sup>4</sup>  Flavio Maran,<sup>4</sup>  Alessandro Fortunelli,<sup>2,a)</sup>  and Mauro Stener<sup>1,a)</sup> 

## AFFILIATIONS

<sup>1</sup>Dipartimento di Scienze Chimiche e Farmaceutiche, Università di Trieste, Via Giorgieri 1, I-34127 Trieste, Italy

<sup>2</sup>CNR-ICCOM & IPCF, Consiglio Nazionale delle Ricerche, via Giuseppe Moruzzi 1, I-56124 Pisa, Italy

<sup>3</sup>Département de Chimie Physique, Université de Genève, 1211 Geneva 4, Switzerland

<sup>4</sup>University of Padova, Department of Chemistry, Via Marzolo 1, I-35131 Padova, Italy

**Note:** This paper is part of the JCP Special Topic on From Atom-Precise Nanoclusters to Superatom Materials.

<sup>a)</sup>Authors to whom correspondence should be addressed: [alessandro.fortunelli@cnr.it](mailto:alessandro.fortunelli@cnr.it) and [stener@units.it](mailto:stener@units.it)

## ABSTRACT

We report a computational study via time-dependent density-functional theory (TDDFT) methods of the photo-absorption spectrum of an atomically precise monolayer-protected cluster (MPC), the  $\text{Ag}_{24}\text{Au}(\text{DMBT})_{18}$  single negative anion, where DMBT is the 2,4-dimethylbenzenethiolate ligand. The use of efficient simulation algorithms, i.e., the complex polarizability polTDDFT approach and the hybrid-diagonal approximation, allows us to employ a variety of exchange-correlation (xc-) functionals at an affordable computational cost. We are thus able to show, first, how the optical response of this prototypical compound, especially but not exclusively in the absorption threshold (low-energy) region, is sensitive to (1) the choice of the xc-functionals employed in the Kohn–Sham equations and the TDDFT kernel and (2) the choice of the MPC geometry. By comparing simulated spectra with precise experimental photoabsorption data obtained from room temperature down to low temperatures, we then demonstrate how a hybrid xc-functional in both the Kohn–Sham equations and the diagonal TDDFT kernel at the crystallographically determined experimental geometry is able to provide a consistent agreement between simulated and measured spectra across the entire optical region. Single-particle decomposition analysis tools finally allow us to understand the physical reason for the failure of non-hybrid approaches.

Published under an exclusive license by AIP Publishing. <https://doi.org/10.1063/5.0056869>

## I. INTRODUCTION

Atomically precise nanoclusters, also called nanomolecules or monolayer-protected clusters (MPCs), i.e., metal nanoclusters protected by a layer of coating ligands with a well-defined stoichiometry and chemical structure, constitute a class of materials of great interest in fundamental science and applications<sup>1–27</sup> and are also ideal systems to test and validate our physicochemical understanding of the phenomena exhibited by metal nanostructures at work.<sup>28–31</sup> Knowledge of the MPC precise chemical entity allows researchers to apply multiple characterization schemes, both experimental and theoretical, to these systems, thus cross-validating methods and results

in a rigorous framework. This possibility is especially important in the field of the computational prediction of the structure and properties of materials. Given the availability of widely different computational methods and schemes employing different approximations and techniques, it is crucial to assess precisely the performances and also the pitfalls of these different choices, so as to identify the computational protocols best reproducing experimental results and properties. These protocols can then be employed to obtain accurate information also in those cases in which theory is called to provide missing information that would be difficult or even impossible to obtain experimentally. In other words, once validation is successfully achieved, the computational protocol can be trusted within

well-understood limits and can be applied with grounded confidence in a predictive way to design new materials with desired optical properties.

The experimental photo-absorption spectrum of MPC compounds is one of the properties in strong need of validation studies.<sup>32,33</sup> Although qualitative agreement between experimentally observed and theoretically simulated spectra has been established,<sup>34–36</sup> quantitative agreement has been achieved only in few cases.<sup>37–39</sup> For example, to the best of our knowledge, the first response calculations using a hybrid exchange-correlation (xc-)functional both in the Kohn–Sham part and in the time-dependent density-functional theory (TDDFT) kernel were reported in Ref. 37, where real-time TDDFT/B3LYP simulations were conducted on the “green gold” Au<sub>30</sub>(S-tBu)<sub>18</sub> nanomolecule. In that work, via a detailed comparison with low-temperature experimental spectra, it was clearly demonstrated that a sophisticated and computationally expensive level of theory (hybrid xc-functionals in both Kohn–Sham orbitals and TDDFT kernel and experimentally validated geometry) is mandatory to predict, with good accuracy, both the position of the low-energy peak and especially the ratio of oscillator strengths between the low-energy peak and the higher energy excitations of Au<sub>30</sub>(S-tBu)<sub>18</sub>, where both the position of the low-energy peak and the intensity ratio give this aliphatic MPC its unique green color.

The challenge in achieving quantitative accuracy in theoretical predictions is due to the difficulties brought about by the coexistence in these species of three components with very different electronic properties: (1) the metal core where the metallic bond is dominant, (2) the cationic-like metal species in the “staple” motifs interacting simultaneously with the metal core and the ligands, and (3) the anionic-like dichalcogenide atoms in the ligands, again simultaneously interacting with the metal core surface and the cationic-like metal species. The simultaneous presence of these different M–M<sup>δ+</sup>, X<sup>δ–</sup>–M<sup>δ+</sup>, and X<sup>δ–</sup>–M interactions with partial ionic and partial covalent character (where M stands for a metal atom and X for a dichalcogenide atom) and the sensitivity of the property of interest (here, the photo-absorption spectrum) to fine details of the atomistic structure make the choice of a theoretical approach able to predict accurately both the structure and the chiroptical response of these compounds very difficult.<sup>37,38</sup> For example, it has been shown that, at the time-dependent density-functional theory (TDDFT) level, simulations using non-hybrid xc-functionals, such as gradient-corrected ones (GGA), in their kernel tend to underestimate the absorption threshold of MPCs.<sup>34</sup> This in turn poses serious questions on the reliability or at least the accuracy of these approaches in the prediction of more complex, photo-absorption-derived phenomena, such as optical photoluminescence, in which the low-energy excitations close to the absorption threshold play an essential role.<sup>40–43</sup>

To make progress in this field, here we focus on the photo-absorption spectrum of the Ag<sub>24</sub>Au(DMBT)<sub>18</sub> singly negative anion, where DMBT is the 2,4-dimethylbenzenethiolate ligand. This is a complex and realistic case exhibiting many of the prototypical features and physicochemical phenomena of the MPC class of materials. Indeed, the Ag<sub>24</sub>Au(DMBT)<sub>18</sub><sup>–</sup> compound has the characteristics of presenting: (1) both Ag and Au atoms, (2) aromatic thiolate ligands directly attached to the sulfur atoms, and (3) a well-defined and robust structure. These characteristics are advantageous for a

validation study because they allow one to test: (1) an alloyed system, (2) ligands electronically conjugated with the metal core, and (3) an unequivocal configurational framework. The present study thus significantly extends our previous study on the Ag<sub>25</sub>(CH<sub>3</sub>)<sub>18</sub><sup>–</sup> anion, in which we considered an MPC exhibiting a single metal element (Au) and aliphatic (non-aromatic and non-sulfur-conjugated) ligands<sup>38</sup> and our previous work on the aliphatic Au<sub>30</sub>(S-tBu)<sub>18</sub> nanomolecule.<sup>37</sup> To study the more complex Ag<sub>24</sub>Au(DMBT)<sub>18</sub><sup>–</sup> compound, we apply advanced, recently developed simulation and analysis tools<sup>44,45</sup> that allow us to predict the chiro-optical spectrum of this medium-sized cluster at the TDDFT level using a hybrid xc-functional in the kernel, to analyze it in terms of single-particle excitations, and to compare the results with those obtained using a non-hybrid xc-functional. Additionally, we also compare and validate theoretical predictions with experimental photoabsorption spectra obtained in the range from room to low (77 K) temperatures. Clearly, MPCs with conjugated ligands, as considered here, are more challenging than MPCs with aliphatic ligands, as previous literature regarding the accuracy of density-functional theory (DFT) and TDDFT in the prediction of geometries<sup>46</sup> and optical spectra<sup>47</sup> of conjugated organic molecules has shown that a high-level of theory is needed for these components, and thus, in turn, it is also necessary to make predictions for MPCs with conjugated ligands in which the conjugated organic ligands resonating with the metal–sulfur core must be described accurately to achieve a comparable level of accuracy for the composite system. However, we stress that qualitatively analogous conclusions hold also for MPCs with aliphatic ligands,<sup>37,38</sup> as we discuss at the end of Sec. IV.

As an outcome of this study, (i) we first demonstrate that the combination of hybrid xc-functionals in the kernel and experimental geometry is validated as a quantitatively predictive tool and that we can (ii) identify the reasons for the failure of non-hybrid TDDFT in achieving accurate simulations of the optical response of MPC compounds and (iii) single out which type of excitation is not correctly modeled by the use of non-hybrid approaches, thus providing insights into the nature of electronic excitations in these materials. The so-derived information should be useful in future studies, both computational and experimental, as it provides progress in methodological tools and physical understanding.

## II. THEORETICAL METHOD

Density-functional theory (DFT) is nowadays the most popular approach in quantum chemistry (QC) due to the optimal balance of accuracy and computational effort.<sup>48</sup> Although in principle an exact theory, in practice its accuracy depends significantly on the approximation of the xc-functional employed in any given case and is also system-dependent.<sup>49</sup> The most basic and also the most computationally efficient of these approximations is the Local Density Approximation (LDA).<sup>48</sup> At a higher level, but still typically requiring a comparable computational effort, lie the gradient-corrected xc-functionals, among which the generalized gradient approximation, GGA, and in particular the Perdew–Burke–Ernzerhof (PBE) flavor, is the most used.<sup>50</sup> A substantial increase in computational complexity is instead entailed by so-called hybrid xc-functionals, i.e., xc-functionals including a component of the Hartree–Fock exchange, among which B3LYP is one among the most used variants.<sup>51,52</sup>

Since the Hartree–Fock exchange is non-local, the evaluation of its matrix elements within hybrid xc-functionals represents a significant challenge for all QC codes based on periodic basis sets, such as plane waves, as well as localized but non-transferable basis sets, such as Slater-type orbitals (STOs). A compromise between GGA and hybrid xc-functionals is provided by mixed schemes, such as the LB94 one,<sup>53</sup> in which a correction term exhibiting an asymptotic Coulombic tail is added to the KS Hamiltonian and corrects one (however, not all) of the issues of semi-local xc-functionals.

DFT is a ground-state theory. Its response analogue is the Time-Dependent DFT (TDDFT) approach.<sup>54</sup> The most common implementation of the TDDFT approach consists in expanding the molecular Kohn–Sham (KS) orbitals as linear combinations of atomic functions and recast the TDDFT problem in terms of diagonalizing a matrix  $\Omega$  along the density-matrix formulation of Casida.<sup>55</sup> In practice, the KS equations are solved first,

$$H_{KS}\phi_i = \varepsilon_i\phi_i. \quad (1)$$

Then, the  $\Omega$  matrix is diagonalized,

$$\Omega F_I = \omega_I^2 F_I, \quad (2)$$

where the matrix elements of the  $\Omega$  matrix can be calculated from the KS orbitals and eigenvalues (1),

$$\Omega_{ia,jb} = \delta_{ij}\delta_{ab}(\varepsilon_a - \varepsilon_i)^2 + 2\sqrt{\varepsilon_a - \varepsilon_i}K_{ia,jb}\sqrt{\varepsilon_b - \varepsilon_j}, \quad (3)$$

and in Eq. (3) the coupling matrix elements  $K_{ia,jb}$  are defined as

$$K_{ia,jb} = \langle aj|ib\rangle + \langle aj|f_{\sigma\tau}^{XC}|ib\rangle. \quad (4)$$

In Eq. (4),  $f_{\sigma\tau}^{XC}$  is the XC kernel, with  $\sigma$  and  $\tau$  being spin variables. The Casida problem consists in finding eigenvalues and eigenvectors of the matrix  $\Omega$  [Eq. (2)]. The eigenvalues of Eq. (2) correspond to squared excitation energies, while from the eigenvectors the intensities (absolute oscillator strengths) can be extracted.<sup>55</sup> Note, importantly, that the choice of the xc-functional translates within TDDFT into a double choice of: (1) which xc-functional to use to derive KS orbitals and (2) which xc-functional to use in the XC kernel  $f_{\sigma\tau}^{XC}$  in Eq. (4).

Even using efficient diagonalization algorithms, such as Davidson's, it becomes very difficult to calculate photoabsorption spectra over a wide excitation energy range when big systems are considered. The Davidson algorithm is efficient on large  $\Omega$  matrices, but only for the extraction of a relatively small number of lowest eigenvalues and eigenvectors. Therefore, the Casida TDDFT algorithm cannot be employed in practice to calculate photoabsorption spectra over a wide energy range. To overcome this problem, we have proposed the complex polarizability TDDFT (polTDDFT) algorithm.<sup>56</sup> This approach is able to treat very large systems and avoid the bottleneck of the diagonalization via a direct solution of the response equations and provides very good accuracy when contrasted with the exact Casida solution.<sup>38,57</sup> The reader is referred to the original work for a detailed description of the algorithm<sup>56</sup> and its implementation in the ADF program.<sup>58</sup>

In practice, the photoabsorption spectrum  $\sigma(\omega)$  is calculated point by point, from the imaginary part of the dynamical polarizability  $\alpha(\omega)$ ,

$$\sigma(\omega) = \frac{4\pi\omega}{c} \text{Im}[\alpha(\omega)]. \quad (5)$$

This expression is of practical interest when the polarizability is calculated for complex frequency, i.e.,  $\omega = \omega_r + i\omega_i$ , where the real part  $\omega_r$  is the scanned photon frequency (energy) and  $\omega_i$  is the imaginary part, which corresponds to a broadening of the discrete lines and can be interpreted as a pragmatic inclusion of the excited state finite lifetime. The complex dynamical polarizability is calculated by solving the following non-homogeneous linear system, working with a basis set of density-fitting functions,

$$[\mathbf{S} - \mathbf{M}(\omega)]\mathbf{b} = \mathbf{d}. \quad (6)$$

In Eq. (6),  $\mathbf{S}$  is the overlap matrix between fitting functions,  $\mathbf{b}$  is the unknown vector with the expansion coefficients  $b_\mu(\omega)$  of  $\rho_z^{(1)}$ , and  $\mathbf{d}$  is the frequency-dependent vector corresponding to the known non-homogeneous term, and finally, the elements of the frequency-dependent matrix  $\mathbf{M}$  are

$$M_{\mu\nu} = \langle f_\mu|\chi_{KS}(\omega)K|f_\nu\rangle. \quad (7)$$

In Eq. (7),  $\chi_{KS}$  refers to the Kohn–Sham frequency-dependent dielectric function and  $K$  to the kernel. Note that the matrix element in Eq. (7) is between density fitting functions, and therefore, the present implementation of the algorithm allows one to employ only density-dependent kernels. For this reason, the density-matrix-dependent Hartree–Fock exchange kernel, which is an ingredient of hybrid xc-functionals, cannot directly be employed in polTDDFT. However, it is still possible to employ hybrid kernels with non-local Hartree–Fock exchange components in polTDDFT, if the Hybrid Diagonal Approximation (HDA) is employed. The HDA that we have recently proposed (see Ref. 44 to which we refer for further details) is a very efficient and robust approximation to TDDFT: by correcting only the diagonal matrix elements of the Casida  $\Omega$  matrix in Eq. (2) with non-local exchange terms, while including local-density (Coulomb-type) terms of the kernel in the off-diagonal elements, the computational complexity is drastically reduced while keeping an excellent accuracy.<sup>44</sup> The HDA has been implemented in both Casida and polTDDFT methods within the AMS suite of codes [<https://www.scm.com/product/ams/>] and allows users an important saving in the computational effort as well as, crucially, the possibility of using hybrid xc-functionals, such as B3LYP in polTDDFT, thereby achieving an accuracy otherwise impossible using LDA or GGA xc-functionals, as we will report below.

### III. COMPUTATIONAL DETAILS

The cluster geometry has been taken from the experiment,<sup>59</sup> then it has been fully or partially optimized in the staple units (both cases have been considered), where in the partial optimizations, the metal core and the staple units (i.e., the metal and sulfur atoms) have been kept fixed at their experimental geometry, whereas only the metal core has been frozen in the fully relaxed staple geometries. Geometry relaxations were performed using the

CP2K package<sup>60</sup> at the DFT/PBE level<sup>50</sup> with the addition of the Grimme-D3 dispersion terms.<sup>61</sup> DFT simulations, based on the hybrid Gaussian/Plane-Wave scheme (GPW),<sup>62</sup> employed Double-Zeta-Valence-plus Polarization (DZVP) basis sets<sup>63</sup> to represent the DFT Kohn–Sham orbitals, GTH pseudopotentials for describing the core-electrons of all the atomic species,<sup>64</sup> and an auxiliary set of plane-waves whose cutoff was set to 300 Ry.

Once geometries were thus derived as described above, optical response calculations were performed with the Amsterdam Modeling Suite (AMS) [<https://www.scm.com/product/ams/>] set of programs,<sup>65,66</sup> employing a basis set of Slater-type orbital (STO) functions of Triple Zeta plus Polarization (TZP) quality. Scalar relativistic effects have been included via the Zero Order Regular Approximation<sup>67</sup> (ZORA). Three different xc-functionals have been considered: (1) the standard GGA PBE,<sup>50</sup> (2) LB94 that carries the correct asymptotic Coulombic tail,<sup>53</sup> which is an important feature to obtain more accurate TDDFT results but is not supported by standard GGA functionals, and (3) the hybrid B3LYP that includes a portion of Hartree–Fock non-local exchange and provides consistently the most accurate predictions. As recalled in Sec. II, the use of hybrid xc-functionals is computational demanding because of the non-local nature of the Hartree–Fock exchange especially in the TDDFT kernel, which can be efficiently managed when Gaussian basis functions are used, but becomes dramatically inefficient when using an STO basis. We can, however, include hybrid xc-functionals via the Hybrid Diagonal Approximation (HDA).<sup>44</sup> The HDA scheme can be employed in both the traditional Casida approach and the polTDDFT approach, in the latter case by simply correcting the differences between KS orbital energies by the non-local exchange term. In short, HDA allows one to run B3LYP calculations with STO basis sets with a standard CPU usage using both Casida and polTDDFT algorithms. In order to facilitate the comparison with respect to the experiment, the Casida discrete spectra have been broadened with Lorentzian functions of 0.150 eV of Full Width at Half Maximum (FWHM). The polTDDFT results are intrinsically broadened by a Lorentzian function, and in order to have the same 0.150 eV FWHM, we employed in Eq. (5) an imaginary frequency  $\omega_i$  of 0.075 eV.

#### IV. RESULTS AND DISCUSSION

Figure 1 shows the photoabsorption spectra of  $[\text{Ag}_{24}\text{Au}(\text{DMBT})_{18}]^-$  anion, simulated via TDDFT using the Casida formalism<sup>55</sup> and the LB94<sup>53</sup> and B3LYP<sup>51,52</sup> xc-functionals in both the Kohn–Sham equations and the TDDFT kernel, together with the experimental spectrum taken at room temperature.<sup>42</sup> In panels (a) and (b), discrete bars are shown together with the continuous spectrum obtained by broadening these peaks (with a FWHM of 0.15 eV), while in box (c) the continuous spectra simulated using both xc-functionals are compared with the experimental profile. Note that the theoretical spectra are simulated using a fully DFT-relaxed geometry of the MPC anion. The LB94 spectrum in panel (a) was extracted including the 500 lowest eigenvalues of the Casida matrix, thus spanning an excitation energy interval up to 3.52 eV (wavelengths >352 nm). In this case, it is not numerically safe to extract more than 500 eigenvalues of the Casida matrix because numerical instabilities start to appear. The B3LYP spectrum in panel (b) was obtained including only the 20 lowest

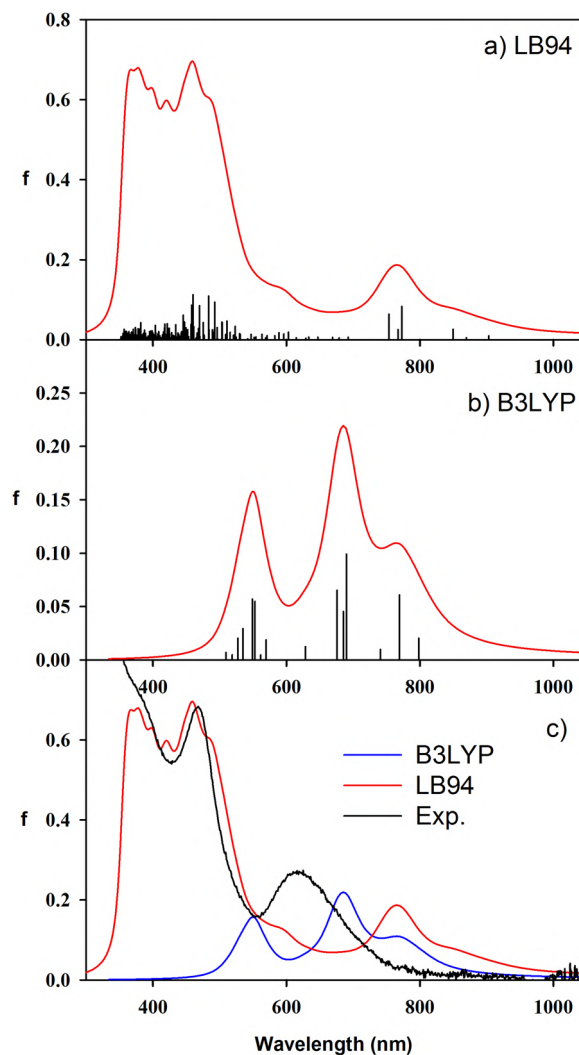
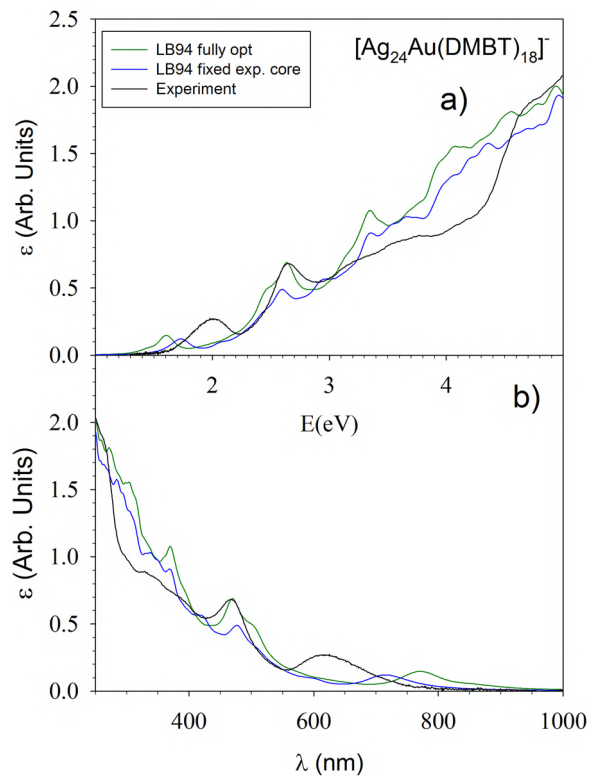


FIG. 1. Photoabsorption spectrum of  $[\text{Ag}_{24}\text{Au}(\text{DMBT})_{18}]^-$  (discrete lines and broadened with Lorentzian functions with a FWHM of 0.150 eV) calculated with the TZP basis set with the Casida method with different functionals: (a) LB94 and (b) B3LYP. In (c), a comparison between broadened LB94 and B3LYP is reported together with experimental data.<sup>42</sup>

eigenvalues of the Casida matrix, thus reaching an excitation energy of 2.46 eV (504 nm), before incurring into excessively long calculations. The reason for such a drastic reduction of the spectral energy interval accessible using B3LYP with respect to LB94 is connected with issues when using a hybrid xc-functional in our codes. When using a hybrid xc-functional, in fact, the efficiency of the ADF code is strongly hampered by the use of Slater-type orbital (STO) basis functions, which require a computationally heavy fitting procedure to calculate the non-local exchange in the response kernel. Fortunately, we have recently shown that this limitation can be overcome by employing the Hybrid Diagonal Approximation,<sup>44</sup> as we will see hereafter. In panel (c), the simulated broadened photoabsorption

profiles are compared with experiment.<sup>42</sup> Although the energy span of the B3LYP spectrum is quite limited, we are nevertheless able to assess the accuracy of TDDFT using two different xc-functionals on the lowest-energy peak, which in experiment falls at 619 nm (2.00 eV), while theory predicts it at 765 nm (1.62 eV) at the LB94 level and at 685 nm (1.81 eV) at the B3LYP level, respectively. It is clear that for this spectral feature, B3LYP performs much better than LB94 when compared with experiment, yielding an error of  $\sim 0.2$  eV, which is half the error given by LB94. Quite interestingly, the prominent experimental feature at 468 nm (2.65 eV) is very nicely reproduced by LB94, which predicts it at 459 nm (2.70 eV). The B3LYP simulations unfortunately do not reach this value of excitation energy, and therefore, it is not possible to compare B3LYP predictions for this peak. From this preliminary analysis, we conclude that the low energy features are reproduced reasonably well by the hybrid B3LYP xc-functional but not by the local density approximation nor even Coulomb-tail-corrected, the LB94 xc-functional. LB94, however, appears to perform well for the features at higher energy, as noted in previous studies (see Ref. 38 and references quoted therein). What, to the best of our knowledge, cannot be found in previous literature and is still missing is: (1) to extend this analysis to higher excitation energies; (2) to analyze the different nature of the transitions involved to understand why the low energy spectral feature is not well described at the non-hybrid level. Hereafter, we will try to give an answer to these open questions.

As a next step, we investigated the effect of the choice of the cluster geometry on the photo-absorption spectrum. Our previous analysis<sup>38</sup> showed that, in the case of atomically precise nanoclusters made of Au and aliphatic ligands, in order to obtain a good agreement between simulations and experiment in the calculation of photoabsorption spectra, it is important to employ the experimental geometry in the calculations (at least for the cluster core, i.e., the metal atoms and the sulfur atoms in the ‘staple’ fragments), rather than a fully DFT-relaxed geometry. Indeed, a worse agreement between theoretical and experimental spectra was obtained when fully optimized geometries were employed in the simulations in Ref. 38. Figure 2(a) shows the photo-absorption spectra, simulated using the LB94 xc-functional on the fully optimized geometry and on a partially optimized geometry, in which the cluster core (Ag, Au, and S atoms) is kept fixed and only the organic residues are optimized, together with the experimental spectrum taken at room temperature. To avoid the limitations connected with the diagonalization of large Casida matrices, whose difficulties hamper the calculation of the spectrum beyond 500 eigenvalues for LB94, and thus prevent access to features above 3.52 eV, in Fig. 2 and hereafter, we calculated all the spectra using the polTDDFT method, which does not have energy limitations and whose accuracy has been validated to be within  $\sim 0.1$  eV in the peak position with respect to the Casida approach.<sup>57</sup> In this connection, it must be noted that the accuracy of polTDDFT is now improved with respect to the original tests of the approach because it benefits from the use of the new auxiliary basis sets (here employed in Figs. 4, 9, and 10). To illustrate this point, we underline that polTDDFT using the new auxiliary basis set now provides an essentially quantitative agreement with respect to the Casida results even for very small gold clusters, such as, for example, Au<sub>6</sub> (as shown in Fig. S3 of the supplementary material), whereas the polTDDFT error in peak positions was up to 0.5 eV for the Au<sub>2</sub> system when using the original auxiliary basis set.<sup>56</sup> As apparent in



**FIG. 2.** Photoabsorption spectrum of  $[\text{Ag}_{24}\text{Au}(\text{DMBT})_{18}]^-$  calculated with the TZP basis set with the polTDDFT method and LB94 functional with different geometries. Experimental data from Ref. 42. In (a), the energy scale is in eV; in (b), the wavelength scale is in nm.

Fig. 2, the agreement between the calculated and measured spectra improves when using the experimental geometry in simulations. We thus conclude that, also in the present case of an alloyed MPC and conjugated ligands analogously to what has been observed previously for pure Au MPCs and aliphatic ligands,<sup>38</sup> a fixed-core partially optimized geometry gives a better agreement with experiment, especially for the lowest-energy spectral feature, which is very sensitive to the choice of the geometry and is also the most difficult to describe by theory. In detail, using polTDDFT/LB94, the position of this low-energy peak is 1.60 eV for the fully optimized geometry, 1.73 eV for the fixed-core partially optimized and 2.00 eV at the experimental level. Note that for the prominent feature at higher energy (around 2.65 eV), we still find a very good agreement between theory and experiment, so this agreement is not sensitive to the choice of geometry, the differences being all below 0.1 eV. Regarding even higher excitation energies, we find that the smooth experimental structure around 3.75 eV has counterparts in the calculated profiles (in the range between 3.30 and 3.70 eV), whereas the sudden experimental increase with a steep slope above 4.2 eV is not properly reproduced by theory. In Fig. 2(b), we show the spectrum also in the wavelength scale, and in this format, the discrepancy between LB94 predictions and experiment for the low-energy (high-wavelength) feature

is even more evident. We have also checked if the same conclusion, i.e., a better agreement between theory and experiment is obtained when using the experimental vs the DFT-optimized geometry, holds for TDDFT/B3LYP simulations as it does for TDDFT/LB94 simulations. The comparison of TDDFT/B3LYP results using the original and the new auxiliary basis set is reported in Fig. S1 of the [supplementary material](#) and fully supports the conclusion drawn from the LB94 analysis.

Having assessed that the experimentally constrained geometry gives a better agreement with experiment, in Fig. 3 we then investigate the effects of the choice of the xc-functional, while keeping frozen the experimental geometry of the cluster core and optimizing only the organic residues as described in Sec. III—panel (a) refers to the energy plot, and panel (b) refers to the wavelength plot. Besides the LB94 xc-functional, we considered the standard GGA PBE functional<sup>50</sup> as well as the hybrid B3LYP<sup>51,52</sup> within the HDA:<sup>44</sup> as noted at the beginning of this section, employing the HDA together with the polTDDFT scheme allows us to study the complete energy range of interest, overcoming the severe limitations of the standard Casida B3LYP scheme in the accessible excitation energy range. From Fig. 3, it is apparent that LB94 and PBE profiles are very similar, with a large error for the low energy feature with respect to experiment. On the contrary, the polTDDFT/B3LYP-HDA profile performs quite nicely

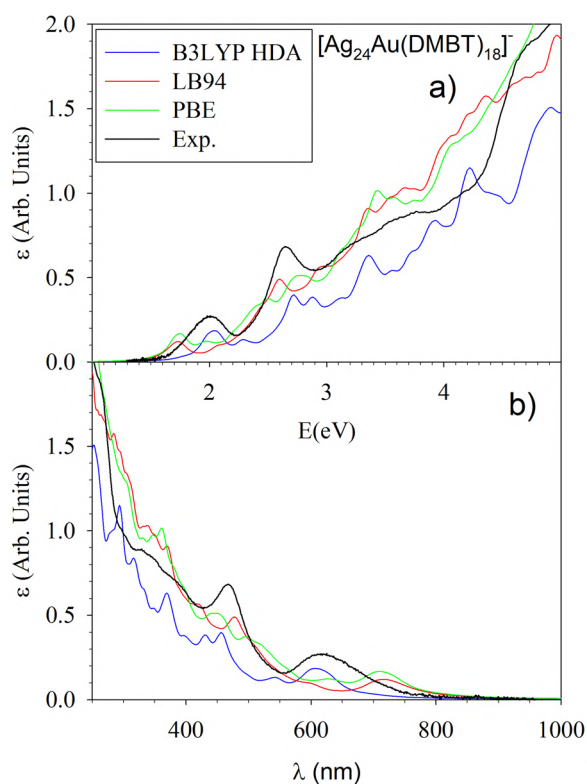


**FIG. 3.** Photoabsorption spectrum of  $[\text{Ag}_{24}\text{Au}(\text{DMBT})_{18}]^-$  calculated with the TZP basis set with the polTDDFT method and different functionals (B3LYP-HDA, LB94, and PBE). Experimental data from Ref. 42. In (a), the energy scale is in eV; in (b), the wavelength scale is in nm.

with respect to experiment on the complete energy range. The low energy structure is calculated at 2.04 eV by B3LYP-HDA, in excellent agreement with experiment (2.00 eV). Moreover, not only the other features at higher energy remain in nice agreement with the experiment, but one can also see an increase in the oscillator strength intensity at 4.5 eV that parallels the sudden slope increase above 4.2 eV in experiment, although with a blue shift of about 0.3 eV to higher energy. The excellent result obtained with the B3LYP-HDA scheme is particularly evident when photo-absorption is plotted against wavelength, as shown in the lower panel of Fig. 3(b).

For completeness, in Fig. 4, we investigate the role of the different approximations to TDDFT/B3LYP, and specifically of B3LYP-HDA, within the ADF code, to identify precisely which scheme affords the best compromise between accuracy and efficiency. First, we considered the pure effect of using the HDA, i.e., still within a Casida scheme (not polTDDFT): this scheme predicts the lowest-energy spectral feature at 1.96 eV (632 nm) vs 1.81 eV (685 nm) at the full B3LYP Casida (without HDA, see Fig. 1). The HDA *per se* thus introduces an error of only 0.15 eV, in line with previous work.<sup>44</sup> Keeping now the HDA but employing the polTDDFT scheme instead of the Casida one, the low energy feature is calculated at 2.04 eV (608 nm), so the polTDDFT approximation introduces a discrepancy of only 0.08 eV with respect to the

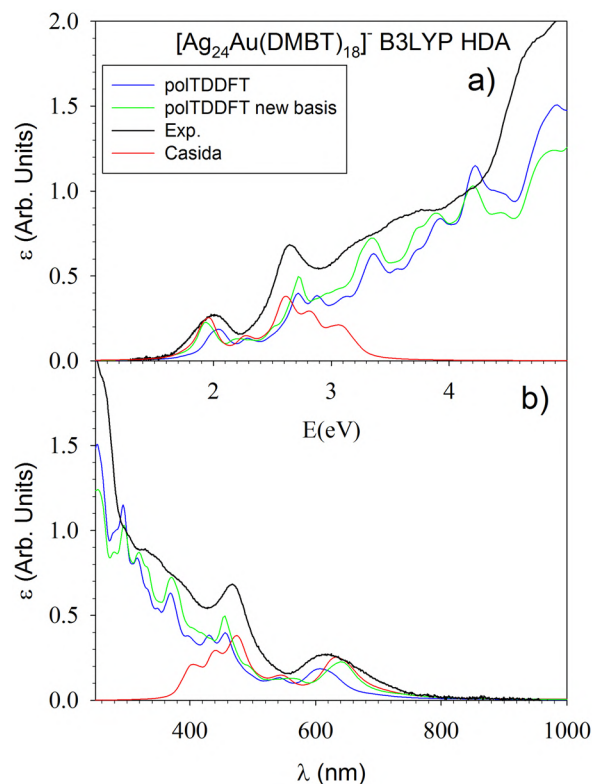


**FIG. 4.** Photoabsorption spectrum of  $[\text{Ag}_{24}\text{Au}(\text{DMBT})_{18}]^-$  calculated with the TZP basis set with the B3LYP-HDA functional. Casida and polTDDFT results are reported. PolTDDFT calculated with a new basis of fitting functions is also reported. Experimental data from Ref. 42. In (a), the energy scale is in eV; in (b), the wavelength scale is in nm.

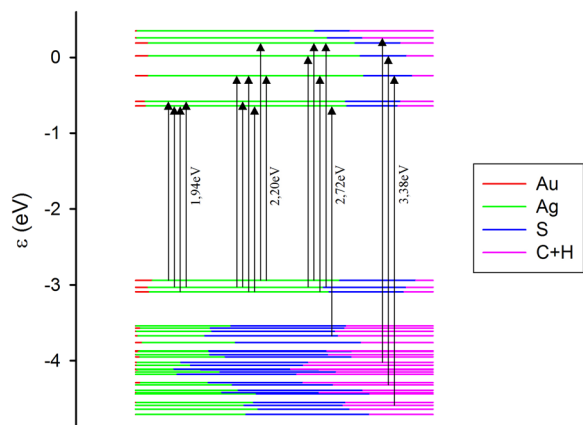


**FIG. 5.** Molecular orbital (energy levels) diagram showing the contributions to the four lowest leading transitions at 1.94, 2.20, 2.72, and 3.38 eV for the  $[\text{Ag}_{24}\text{Au}(\text{DMBT})_{18}]^{-}$  cluster anion, calculated at the TZP and B3LYP-HDA level of theory. Orbital character in terms of Mulliken analysis of Ag, Au, S, and C + H contributions is given in terms of colors of the level, according to the inset legend. HOMO and LUMO are at  $-2.94$  and  $-0.65$  eV, respectively.

Casida HDA scheme. This result was obtained using the original fitting basis functions derived in Ref. 44. We have recently derived a new set of density fitting basis functions purposely optimized for polTDDFT/B3LYP-HDA calculations, a brief description of this set can be found in the [supplementary material](#). Further discussion of these new fitting functions will be the subject of a future publication but details can also be found in the code documentation as they have been included in the 2021 version of the AMS [<https://www.scm.com/product/ams/>] suite of programs.<sup>65,66</sup> The polTDDFT/B3LYP-HDA profile obtained using this new set of density-fitting auxiliary functions (green curve in Fig. 4) is improved with respect to the old set and is in excellent agreement with the TDDFT/B3LYP-HDA Casida profile, giving a low-energy feature at 1.94 eV (639 nm) with an error of only 0.02 eV with respect to experiment together with a significant improvement in the prediction of the absolute intensity of this and other peaks.

Having so derived a very robust computational protocol, it remains as a scientifically important question to identify the nature

of the most relevant spectral features in the photoabsorption spectrum. Moreover, it is also very important to understand *why* the low energy feature is the most difficult to predict via theory. A summary of the transition assignments, from the polTDDFT/B3LYP/HDA calculations with the new density fitting basis set, are gathered in Fig. 5. The details of the transitions are provided in Table I. The transition at 1.94 eV is ascribed to a mixed character HOMO  $\rightarrow$  LUMO + 1, HOMO - 1  $\rightarrow$  LUMO, HOMO - 2  $\rightarrow$  LUMO, and HOMO - 1  $\rightarrow$  LUMO + 1. The B3LYP orbitals involved in this and the following transitions are depicted in Fig. 6 (occupied ones) and Fig. 7 (virtual ones), respectively. They can be characterized as follows: the occupied orbitals are strongly mixed with high Ag and S contributions and can be classified as Ag-S bonds at the staple units with the involvement of Ag atoms belonging to the cluster. The involved unoccupied levels are localized in the same spatial region of the occupied ones. The transition at 2.20 eV is weak and is not detected in the experiment. The next transition at 2.71 eV can be ascribed to HOMO - 1  $\rightarrow$  LUMO + 3 and HOMO  $\rightarrow$  LUMO + 4. Interestingly, the involved occupied orbitals are the same as in the low-energy peak, whereas the virtual orbitals are completely different. Note that the LUMO and LUMO + 1 are almost degenerate, whereas the LUMOs at higher energy are well separated. From the plot of the virtual orbitals, it is apparent that the LUMO + 3 and LUMO + 4 still have strong Ag and S contribution, but they are shifted toward the cluster core with respect to the staple units. The next transition at 3.38 eV is instead ascribed to  $\pi \rightarrow \pi^*$  ligand transitions, with the virtual  $\pi^*$  strongly mixed with S-C bonds and Ag atoms, so that for such transition some ‘charge transfer’ character from ligands to metal is found. As in the first three absorption bands the same occupied orbitals are involved in the transitions, we can conceivably ascribe the difficulty in describing the low energy bands via TDDFT/LB94 to an error in the energy positions of the virtual orbitals. LB94 is indeed known to excessively stabilize the lowest virtual orbitals (LUMO and LUMO + 1) and to place them at too low energies, whereas B3LYP, containing a Hartree-Fock non-local exchange component, raises the energy of virtual orbitals thus yielding more accurate results. We can further conjecture that such effects must compensate each other for the orbitals beyond LUMO + 2 since the higher experimental features are properly described by both LB94 and B3LYP. However, to identify, with precision, the reasons for the better performances of B3LYP in comparison with standard or tail-corrected GGA approaches (such as PBE and LB94),

**TABLE I.** Analysis of the most salient photoabsorption excitations of  $[\text{Ag}_{24}\text{Au}(\text{DMBT})_{18}]^{-}$  in terms of excited configurations obtained at the B3LYP-HDA polTDDFT level. Mulliken population analysis of the molecular orbitals involved is also reported.

Transition energy (eV)	f	Assignment (only contribution >10%)
1.94	0.23	21.7% HOMO (28% Ag 4s, 18% S 3p, 10% Ag 4p) $\rightarrow$ LUMO + 1 (34% Ag 4s, 18% Ag 4p, 11% S 3p)
		17.9% HOMO - 1 (27% Ag 4s, 20% S 3p) $\rightarrow$ LUMO (31% Ag 4s, 19% Ag 4p)
		17.3% HOMO - 2 (28% Ag 4s, 19% S 3p) $\rightarrow$ LUMO
		16.7% HOMO - 1 $\rightarrow$ LUMO + 1
2.20	0.13	34.7% HOMO - 1 $\rightarrow$ LUMO + 2 (28% Ag 4p, 26% Ag 4s)
2.72	0.50	19.9% HOMO - 1 $\rightarrow$ LUMO + 3 (27% Ag 4s, 24% Ag 4p, 10% S 3p)
3.38	0.72	16.3% HOMO $\rightarrow$ LUMO + 4 (25% Ag 4s, 24% Ag 4p)
		11.5% HOMO - 12 (37% S 3p, 18% C 2p) $\rightarrow$ LUMO + 5 (31% Ag 4p)

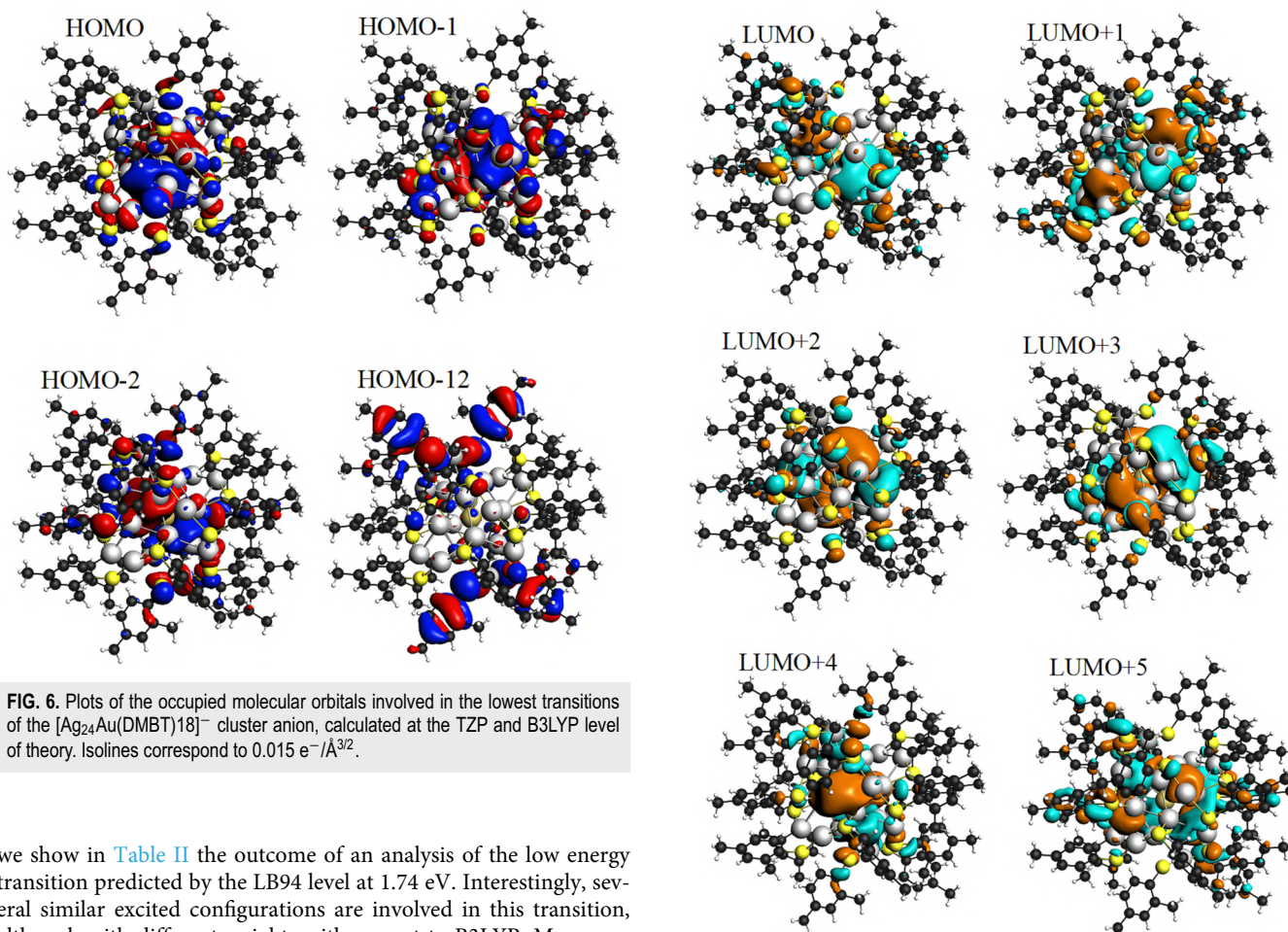


**FIG. 6.** Plots of the occupied molecular orbitals involved in the lowest transitions of the  $[\text{Ag}_{24}\text{Au}(\text{DMBT})_{18}]^-$  cluster anion, calculated at the TZP and B3LYP level of theory. Isolines correspond to  $0.015 \text{ e}^-/\text{\AA}^{3/2}$ .

we show in Table II the outcome of an analysis of the low energy transition predicted by the LB94 level at 1.74 eV. Interestingly, several similar excited configurations are involved in this transition, although with different weights with respect to B3LYP. More surprisingly, a comparison between Figs. 6 and 7 with Fig. 8 (where we show the orbitals calculated at the LB94 level) shows that the virtual orbitals are almost identical from the two methods, whereas the occupied ones (HOMO, HOMO – 1, and HOMO – 2) are mainly S 3p in LB94 and Ag 4s in B3LYP. Our conclusion is that the B3LYP functional is more accurate in describing the electronic structure of these clusters, with a more balanced contribution from Ag and S, while LB94 tends to overestimate the role of S 3p in the HOMO and HOMO – 1 orbitals by putting them at too low energies. This is the origin of the too low energy of the LB94 excitations at the absorption threshold, which are instead correctly placed by B3LYP in the proper

**FIG. 7.** Plots of the virtual molecular orbitals involved in the lowest transitions of the  $[\text{Ag}_{24}\text{Au}(\text{DMBT})_{18}]^-$  cluster anion, calculated at the TZP and B3LYP level of theory. Isolines correspond to  $0.015 \text{ e}^-/\text{\AA}^{3/2}$ .

(higher) energy region, overlapping with other excitations involving the same sets of occupied and virtual orbitals. Clearly, this difference has consequences also on the coupling between the orbitals, which takes place at the TDDFT level, and indeed the composition of the transition in terms of one-electron excited configurations is also

**TABLE II.** Analysis of the lowest photoabsorption excitation of  $[\text{Ag}_{24}\text{Au}(\text{DMBT})_{18}]^-$  in terms of excited configurations obtained at the LB94 polTDDFT level. Mulliken population analysis of the molecular orbitals involved is also reported.

Transition energy (eV)	f	Assignment (only contribution >10%)
1.74	0.12	24.0% HOMO – 2 (31% S 3p, 28% Ag 4s, 6% Ag 4p) → LUMO (32% Ag 4s, 11% Ag 4p, 10% S 3p)
		19.2% HOMO – 1 (32% S 3p, 30% Ag 4s) → LUMO + 1 (34% Ag 4s, 12% S 3p, 11% Ag 4p)
		16.7% HOMO – 2 → LUMO + 1
		12.7% HOMO (35% S 3p, 33% Ag 3s) → LUMO + 1
		10.0% HOMO – 1 → LUMO

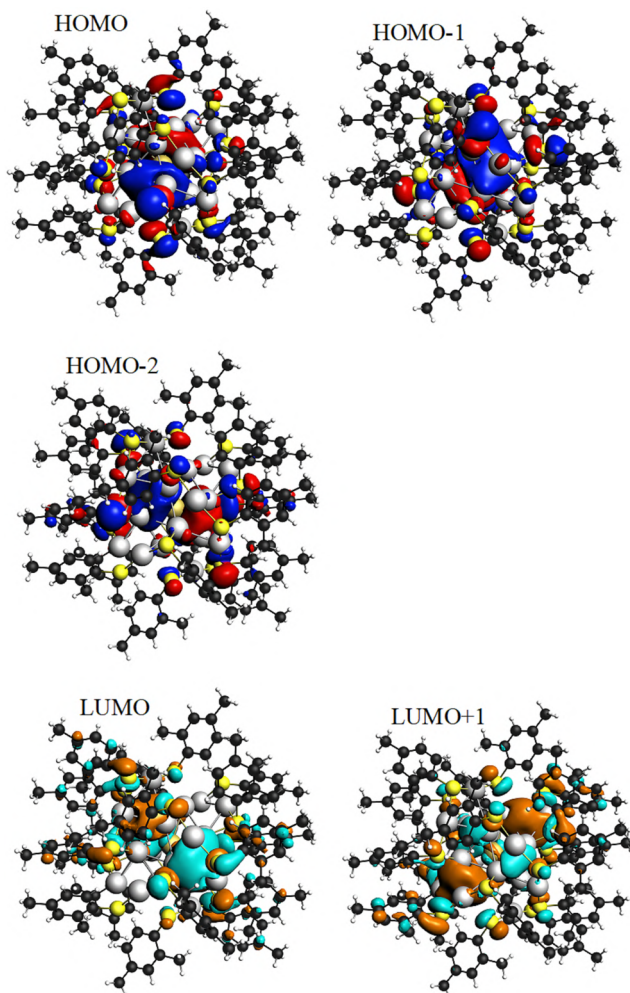


**FIG. 8.** Plots of the occupied and virtual molecular orbitals involved in the lowest transition of the  $[\text{Ag}_{24}\text{Au}(\text{DMBT})_{18}]^{-}$  cluster anion, calculated at the TZP and LB94 level of theory. Isolines correspond to  $0.015 \text{ e}^{-}/\text{\AA}^{3/2}$ .

somewhat changed in going from LB94 to B3LYP (Hartree–Fock exchange terms in the diagonal matrix elements of the TDDFT kernel change linear response both affecting directly excitation energies and indirectly by changing the composition of the excited states<sup>44</sup>). Therefore, we are led to ascribe the better performances of B3LYP to its more accurate capacity to describe the electronic structure of the clusters, in particular the balance between metal and ligand contributions.

To complete our validation study, since the TDDFT-HDA/B3LYP scheme has proven the best choice for the present mixed and conjugated MPC compounds, we decided to check its performances also for the  $[\text{Au}_{25}(\text{SR})_{18}]^{-}$  system, a non-conjugated and pure Au case that was investigated in our previous work.<sup>38</sup> In Fig. 9, the experimental data obtained for the  $[\text{Au}_{25}(\text{SCH}_2\text{CH}_2\text{C}_6\text{H}_5)_{18}]^{-}$  TOB<sup>+</sup> system in the present work are compared with the simulated spectrum of the simpler

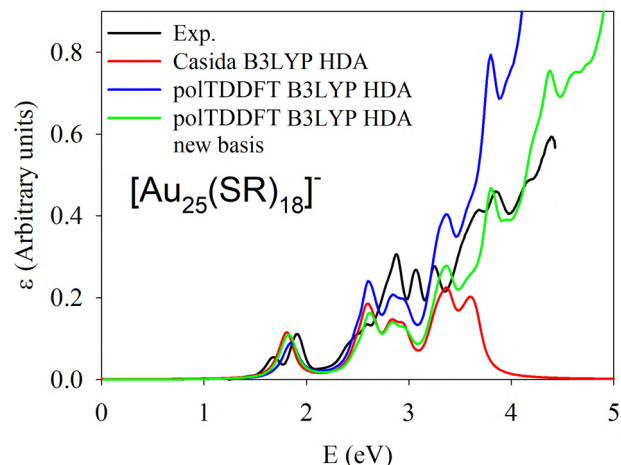


**FIG. 9.** Photoabsorption spectrum of  $[\text{Au}_{25}(\text{SCH}_3)_{18}]^{-}$  calculated with the TZP basis set with the B3LYP-HDA functional. Casida and polTDDFT results are reported. PolTDDFT calculated with the new basis of fitting functions is also reported. Experimental data: this work.

$[\text{Au}_{25}(\text{SCH}_3)_{18}]^{-}$  anion, using an experimental geometry for the AuSC core<sup>68</sup> and optimizing only the positions of the hydrogen atoms. In fact, in our previous work,<sup>38</sup> we have shown that for this aliphatic ligand (the phenyl ring is not directly bonded to the sulfur atom, but is tethered through an ethylene bridge), it is reasonably accurate to model the ligand by keeping the experimental geometry but simplifying it with the smaller  $\text{SCH}_3$  fragment. This does not drastically deteriorate the appearance of the spectrum at low energy. From Fig. 9, it is apparent that the polTDDFT B3LYP HDA results with the new basis follow very accurately the Casida profile (more accurately than the old basis). The comparison with the experiment is also fairly nice, with the first two experimental features detected at 1.80 and 2.75 eV well reproduced by theory at 1.82 and 2.62 eV, respectively. The next experimental feature at 3.1 eV can be ascribed to the calculated structure in the range between 2.84 and 2.94 eV, obtaining quantitative match at low energy and a discrepancy about 0.2 eV at this higher energy.

As a final remark, it is important to note that calculations give spectral features that are more resolved with respect to the experiment. This is due to the fact that simulations correspond to frozen geometries or formally a temperature of 0 K, whereas experiments are conducted at room temperature and are therefore affected by thermal broadening of spectral features. For a more accurate comparison and validation of theory vs experiment, it is important to perform photo-absorption experiments at low temperatures.

We have therefore performed a series of experiments aimed at measuring low-temperature photoabsorption spectra of the  $\text{Ag}_{24}\text{Au}(\text{DMBT})_{18}$  single negative anion (experimental details are provided in the [supplementary material](#)). We collected spectra down to 77 K, and a series of representative spectra obtained at different temperatures is shown in Fig. S2. The comparison between the absorption spectrum experimentally measured at 77 K and simulated via polTDDFT/B3LYP using the new auxiliary basis set at the core-frozen geometry is reported in Fig. 10. This comparison shows an excellent accuracy, which is extremely encouraging because the

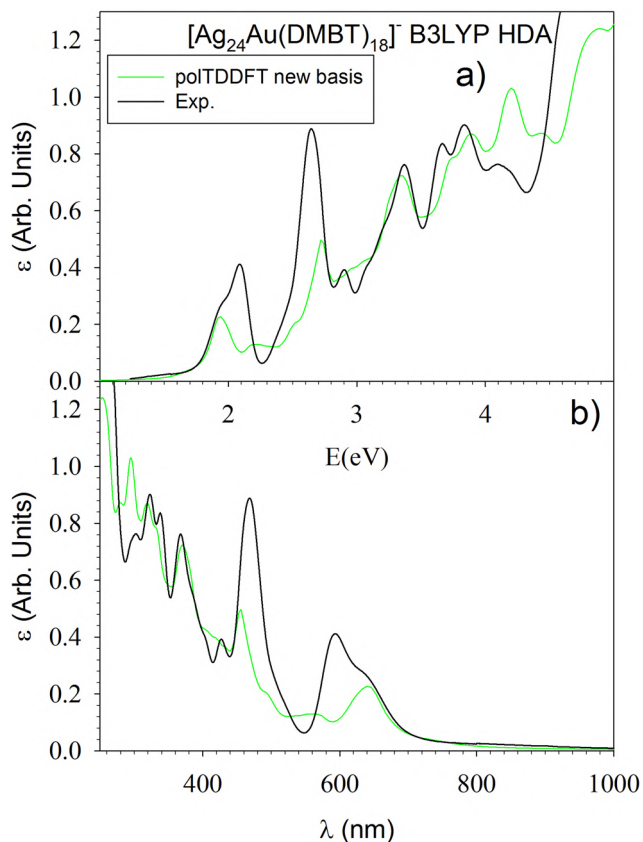


**FIG. 10.** Photoabsorption spectrum of  $[\text{Ag}_{24}\text{Au}(\text{SCH}_3)_{18}]^-$  calculated with the TZP basis set with the B3LYP-HDA functional and polTDDFT with the new basis of fitting functions. Experimental data taken at 77 K (this work).

much better resolved spectral features observed in the experimental spectrum compare even better with the features of the simulated spectrum. As the only discrepancy, a composite feature of the low-energy peak may be noted, exhibiting a small feature at around 740 nm, which is not present in the simulated spectrum. This discrepancy may be due to three main reasons: first, geometry effects connected with the difference between the solid-state and the solution environment. Indeed, the experimental spectra in Fig. S2 clearly show how sensitive is the lowest-energy peak with respect to vibronic coupling. Second, our predictions are based on a Lorentzian broadening of the theoretical spectra with a constant energy value throughout the excitation interval: especially at low energies, this may hide fine details and features when the energy splitting is below the broadening. Finally, Spin–Orbit Coupling (SOC) effects could also cause split peaks especially in the low-energy region.<sup>68</sup> At present, we cannot include SOC effects into our modeling, but we are currently working to solve this issue.

## V. CONCLUSIONS

Atomically precise nanoclusters, or monolayer-protected clusters (MPCs), represent an ideal playground to assess and validate

the performance of computational methods via a stringent comparison with chemical–physical experimental data, enabling singling out accurate simulation protocols that can then be applied with predictive confidence in the rational design of the optical properties of new metal-cluster-based materials.<sup>1–39</sup> Here, we focus on the prediction of the optical response (the photo-absorption spectrum) of these systems, we consider a prototypical compound, the  $\text{Ag}_{24}\text{Au}(\text{DMBT})_{18}$  single negative anion (DMBT = 2,4-dimethylbenzenethiolate ligand) as an alloyed and ligand-conjugated MPC, and we conduct a validation study to investigate which DFT/TDDFT simulation tools provide the best agreement between predicted and measured spectra.

For this purpose, we use efficient simulation algorithms, i.e., the complex polarizability polTDDFT approach and the Hybrid-Diagonal Approximation (HDA), that allow us to employ a variety of exchange–correlation (xc-) functionals with the needed accuracy and an affordable computational cost. We are so able to demonstrate that the spectrum of this prototypical compound, especially but not exclusively in the absorption threshold (low-energy) region, is sensitive to the choice of both the xc-functional and the MPC geometry. Technically, we confirm that the polTDDFT and HDA approaches achieve an accuracy within  $\approx 0.1$ – $0.2$  eV in the position of the main photo-absorption peaks that are accessible to an exact TDDFT prediction.

Moreover and importantly, the comparison of simulated and experimentally determined spectra recorded from room temperature down to 77 K allows us to validate that a hybrid xc-functional employed in both the Kohn–Sham equations and the diagonal TDDFT kernel at the crystallographically determined experimental geometry (as proposed in Refs. 37 and 38) is able to provide a consistent agreement ( $\sim 0.1$  eV accuracy) between simulated and measured spectra across the entire optical region. This level of accuracy is also obtained for a  $\text{Au}_{25}(\text{CH}_3)_{18}$  single negative anion, also included in this work as an example of a pure Au and non-ligand-conjugated MPC.

Finally, we conduct a single-particle decomposition analysis of the results and are so able to trace the physical reasons for the failure of non-hybrid xc-functionals in predicting the optical response of these systems. These are found to be due to the inability of non-hybrid xc-functionals to correctly describe the balance between metal and sulfur contributions to the electronic structure of these systems, and in particular to their tendency to put S 3p orbital contributions to bands around the HOMO–LUMO gap at too low energies, thus underestimating the position of the corresponding excitations that are instead correctly blue-shifted and merged with higher-energy peaks when hybrid xc-functionals are employed.

## SUPPLEMENTARY MATERIAL

See the [supplementary material](#) for tests using the B3LYP xc-functional with fully optimized geometry, Cartesian coordinates of the structures used in the TDDFT simulations, numerical raw data for Figs. 1–4 and 9, and brief description of the new fitting set.

## ACKNOWLEDGMENTS

Computational support from the CINECA supercomputing center within the ISCR program is gratefully acknowledged.

The authors are grateful to the Stiftung Beneficentia for a generous grant employed to set up a computational server. Support from the University of Trieste within the FRA program is gratefully acknowledged.

## DATA AVAILABILITY

The data that support the findings of this study are available from the corresponding authors upon reasonable request.

## REFERENCES

- 1 R. L. Whetten, J. T. Khoury, M. M. Alvarez, S. Murthy, I. Vezmar, Z. L. Wang, P. W. Stephens, C. L. Cleveland, W. D. Luedtke, and U. Landman, *Adv. Mater.* **8**, 428 (1996).
- 2 P. D. Jadzinsky, G. Calero, C. J. Ackerson, D. A. Bushnell, and R. D. Kornberg, *Science* **318**, 430 (2007).
- 3 J. Akola, M. Walter, R. L. Whetten, H. Häkkinen, and H. Grönbeck, *J. Am. Chem. Soc.* **130**, 3756 (2008).
- 4 M. W. Heaven, A. Dass, P. S. White, K. M. Holt, and R. W. Murray, *J. Am. Chem. Soc.* **130**, 3754 (2008).
- 5 H. Qian, W. T. Eckenhoff, Y. Zhu, T. Pintauer, and R. Jin, *J. Am. Chem. Soc.* **132**, 8280 (2010).
- 6 O. Lopez-Acevedo, H. Tsunoyama, T. Tsukuda, H. Häkkinen, and C. M. Aikens, *J. Am. Chem. Soc.* **132**, 8210 (2010).
- 7 C. Zeng, H. Qian, T. Li, G. Li, N. L. Rosi, B. Yoon, R. N. Barnett, R. L. Whetten, U. Landman, and R. Jin, *Angew. Chem.* **51**, 13114 (2012).
- 8 I. Dolamic, S. Knoppe, A. Dass, and T. Bürgi, *Nat. Commun.* **3**, 798 (2012).
- 9 Y. Negishi, C. Sakamoto, T. Ohyama, and T. Tsukuda, *J. Phys. Chem. Lett.* **3**, 1624 (2012).
- 10 A. Desireddy, B. E. Conn, J. Guo, B. Yoon, R. N. Barnett, B. M. Monahan, K. Kirschbaum, W. P. Griffith, R. L. Whetten, U. Landman, and T. P. Bigioni, *Nature* **501**, 399 (2013).
- 11 S. Mustalahti, P. Myllyperkiö, T. Lahtinen, K. Salorinne, S. Malola, J. Koivisto, H. Häkkinen, and M. Pettersson, *J. Phys. Chem. C* **118**, 18233 (2014).
- 12 A. Dass, S. Theivendran, P. R. Nimmala, C. Kumara, V. R. Jupally, A. Fortunelli, L. Sementa, G. Barcaro, X. Zuo, and B. C. Noll, *J. Am. Chem. Soc.* **137**, 4610 (2015).
- 13 A. Fernando, K. L. D. M. Weerawardene, N. V. Karimova, and C. M. Aikens, *Chem. Rev.* **115**, 6112 (2015).
- 14 W. Kurashige, Y. Niihori, S. Sharma, and Y. Negishi, *Coord. Chem. Rev.* **320–321**, 238 (2016).
- 15 R. Jin, C. Zeng, M. Zhou, and Y. Chen, *Chem. Rev.* **116**, 10346 (2016).
- 16 N. A. Sakthivel, S. Theivendran, V. Ganeshraj, A. G. Oliver, and A. Dass, *J. Am. Chem. Soc.* **139**, 15450 (2017).
- 17 M. Rambukwella, N. A. Sakthivel, J. H. Delcamp, L. Sementa, A. Fortunelli, and A. Dass, *Front. Chem.* **6**, 330 (2018).
- 18 T. Dainese, S. Antonello, S. Bogialli, W. Fei, A. Venzo, and F. Maran, *ACS Nano* **12**, 7057 (2018).
- 19 Z. Lei, J. J. Li, X. K. Wan, W. H. Zhang, and Q. M. Wang, *Angew. Chem.* **57**, 8639 (2018).
- 20 M. A. Abbas, P. V. Kamat, and J. H. Bang, *ACS Energy Lett.* **3**, 840 (2018).
- 21 N. A. Sakthivel, M. Shabaninezhad, L. Sementa, B. Yoon, M. Stener, R. L. Whetten, G. Ramakrishna, A. Fortunelli, U. Landman, and A. Dass, *J. Am. Chem. Soc.* **142**, 15799 (2020).
- 22 C. A. Hosier, I. D. Anderson, and C. J. Ackerson, *Nanoscale* **12**, 6239 (2020).
- 23 T. Kawawaki, A. Ebina, Y. Hosokawa, S. Ozaki, D. Suzuki, S. Hossain, and Y. Negishi, *Small* **17**, 2005328 (2021).
- 24 J. V. Rival, P. Mymoona, K. M. Lakshmi, Nonappa, T. Pradeep, and E. S. Shibui, *Small* **17**, 2005718 (2021).
- 25 T. Dainese, M. Agrachev, S. Antonello, D. Badocco, D. M. Black, A. Fortunelli, J. A. Gascón, M. Stener, A. Venzo, R. L. Whetten, and F. Maran, *Chem. Sci.* **9**, 8796–8805 (2018).
- 26 M. Agrachev, M. Ruzzi, A. Venzo, F. Maran, *Acc. Chem. Res.*, 2019, **52**, 44–52.
- 27 M. Agrachev, W. Fei, S. Antonello, S. Bonacchi, T. Dainese, A. Zoleo, M. Ruzzi, and F. Maran, *Chem. Sci.* **11**, 3427–3440 (2020).
- 28 E. Boisselier and D. Astruc, *Chem. Soc. Rev.* **38**, 1759 (2009).
- 29 U. H. F. Bunz and V. M. Rotello, *Angew. Chem.* **49**, 3268 (2010).
- 30 Y. Du, H. Sheng, D. Astruc, and M. Zhu, *Chem. Rev.* **120**, 526 (2020).
- 31 R. Jin, G. Li, S. Sharma, Y. Li, and X. Du, *Chem. Rev.* **121**, 567 (2021).
- 32 A. Tlahuice-Flores, *Phys. Chem. Chem. Phys.* **18**, 27738 (2016).
- 33 C. M. Aikens, *Acc. Chem. Res.* 2018, **51**, 3065 (2018).
- 34 K. L. D. M. Weerawardene and C. M. Aikens, *Phys. Chem. C* **122**, 2440 (2018).
- 35 K. L. D. M. Weerawardene and C. M. Aikens, *J. Am. Chem. Soc.* **138**, 11202 (2016).
- 36 G. Barcaro, L. Sementa, A. Fortunelli, and M. Stener, *Phys. Chem. Chem. Phys.* **17**, 27952 (2015).
- 37 A. Dass, T. Jones, M. Rambukwella, D. Crasto, K. J. Gagnon, L. Sementa, M. De Vetta, O. Baseggio, E. Aprà, M. Stener, and A. Fortunelli, *J. Phys. Chem. C* **120**, 6256 (2016).
- 38 O. Baseggio, M. De Vetta, G. Fronzoni, D. Toffoli, M. Stener, L. Sementa, and A. Fortunelli, *Int. J. Quantum Chem.* **118**, e25769 (2018).
- 39 H.-C. Weissker, H. B. Escobar, V. D. Thanthirige, K. Kwak, D. Lee, G. Ramakrishna, R. L. Whetten, and X. López-Lozano, *Nat. Commun.* **5**, 3785 (2014).
- 40 C. M. Aikens, *J. Phys. Chem. Lett.* **2**, 99 (2011).
- 41 C. Yu, W. Harbich, L. Sementa, L. Ghiringhelli, E. Aprà, M. Stener, A. Fortunelli, and H. Brune, *J. Chem. Phys.* **147**, 074301 (2017).
- 42 K. R. Krishnadas, L. Sementa, M. Medves, A. Fortunelli, M. Stener, A. Fürstenberg, G. Longhi, and T. Bürgi, *ACS Nano* **14**, 9687 (2020).
- 43 A. Fortunelli and M. Stener, *Encyclopedia of Interfacial Chemistry, Surface Science and Electrochemistry* (Elsevier, 2018), pp. 534–545.
- 44 M. Medves, L. Sementa, D. Toffoli, G. Fronzoni, A. Fortunelli, and M. Stener, *J. Chem. Phys.* **152**, 184102 (2020).
- 45 S. Theivendran, L. Chang, A. Mukherjee, L. Sementa, M. Stener, A. Fortunelli, and A. Dass, *J. Phys. Chem. C* **122**, 4524 (2018).
- 46 E. Brémond, M. Savarese, C. Adamo, and D. Jacquemin, *J. Chem. Theory Comput.* **14**, 3715 (2018).
- 47 D. Jacquemin, V. Wathelet, E. A. Perpète, and C. Adamo, *J. Chem. Theory Comput.* **5**, 2420 (2009).
- 48 R. G. Parr and W. Yang, *Density-Functional Theory of Atoms and Molecules* (Oxford University Press, New York, 1989), ISBN: 978-0-19-504279-5.
- 49 J. P. Perdew and K. Schmidt, *AIP Conf. Proc.* **577**, 1 (2001).
- 50 J. P. Perdew, K. Burke, and M. Ernzerhof, *Phys. Rev. Lett.* **77**, 3865 (1996); Erratum *Phys. Rev. Lett.* **78**, 1396 (1997).
- 51 A. D. Becke, *J. Chem. Phys.* **98**, 5648 (1993).
- 52 P. J. Stephens, F. J. Devlin, C. F. Chabalowski, and M. J. Frisch, *J. Phys. Chem.* **98**, 11623 (1994).
- 53 R. Van Leeuwen and E. J. Baerends, *Phys. Rev. A: At., Mol., Opt. Phys.* **49**, 2421 (1994).
- 54 C. Ullrich, *Time-Dependent Density-Functional Theory: Concepts and Applications* (Oxford University Press, 2012).
- 55 M. E. Casida, *Recent Advances in Density-Functional Methods*, edited by D. P. Chong (World Scientific, Singapore, 1995), p. 155.
- 56 O. Baseggio, G. Fronzoni, and M. Stener, *J. Chem. Phys.* **143**, 024106 (2015).
- 57 O. Baseggio, M. De Vetta, G. Fronzoni, M. Stener, L. Sementa, A. Fortunelli, and A. Calzolari, *J. Phys. Chem. C* **120**, 12773 (2016).
- 58 O. Baseggio, M. De Vetta, G. Fronzoni, M. Stener, and A. Fortunelli, *Int. J. Quantum Chem.* **116**, 1603 (2016).
- 59 M. S. Bootharaju, C. P. Joshi, M. R. Parida, O. F. Mohammed, and O. M. Bakr, *Angew. Chem.* **128**, 934 (2016).
- 60 J. Hutter, M. Iannuzzi, F. Schiffmann, and J. VandeVondele, *Wiley Interdiscip. Rev.: Comput. Mol. Sci.* **4**, 15 (2014).
- 61 S. Grimme, J. Antony, S. Ehrlich, and H. Krieg, *J. Chem. Phys.* **132**, 154104 (2010).

<sup>62</sup>G. Lippert, J. X. R. Hutter, and M. Parrinello, *Theor. Chem. Acc.* **103**, 124 (1999).

<sup>63</sup>J. VandeVondele and J. Hutter, *J. Chem. Phys.* **127**, 114105 (2007).

<sup>64</sup>S. Goedecker, M. Teter, and J. Hutter, *Phys. Rev. B* **54**, 1703 (1996).

<sup>65</sup>E. J. Baerends, D. E. Ellis, and P. Ros, *Chem. Phys.* **2**, 41 (1973).

<sup>66</sup>C. Fonseca Guerra, J. G. Snijders, G. Te Velde, and E. J. Baerends, *Theor. Chem. Acc.* **99**, 391 (1998).

<sup>67</sup>E. van Lenthe, E. J. Baerends, and J. G. Snijders, *J. Chem. Phys.* **99**, 4597 (1993).

<sup>68</sup>D.-E. Jiang, M. Kühn, Q. Tang, and F. Weigend, *J. Phys. Chem. Lett.* **5**, 3286 (2014).

Supporting Information for:

# Predictive optical photoabsorption of $\text{Ag}_{24}\text{Au}(\text{DMBT})_{18}^-$ via efficient TDDFT simulations

Marco Medves<sup>1</sup>, Luca Sementa<sup>2</sup>, Daniele Toffoli<sup>1</sup>, Giovanna Fronzoni<sup>1</sup>, Kumaranchira Ramankutty Krishnadas<sup>3</sup>, Thomas Bürgi<sup>3</sup>, Sara Bonacchi<sup>4</sup>, Tiziano Dainese<sup>4</sup>, Flavio Maran<sup>4</sup>, Alessandro Fortunelli<sup>2\*</sup>, and Mauro Stener<sup>1\*</sup>

<sup>1</sup>*Dipartimento di Scienze Chimiche e Farmaceutiche, Università di Trieste, Via Giorgieri 1, I-34127 Trieste, Italy*

<sup>2</sup>*CNR-ICCOM & IPCF, Consiglio Nazionale delle Ricerche, via Giuseppe Moruzzi 1, I-56124 Pisa, Italy*

<sup>3</sup>*Département de Chimie Physique, Université de Genève, 1211 Geneva 4, Switzerland*

<sup>4</sup>*University of Padova, Department of Chemistry, Via Marzolo 1, I-35131 Padova, Italy*

Hereafter we report the details of the experiments in which we recorded the photo-absorption spectrum of  $\text{Ag}_{24}\text{Au}(\text{DMBT})_{18}^-$ , down to liquid nitrogen temperature, in addition to further computational details and tests, the Cartesian coordinates of the structures used in the TDDFT simulations, and the numerical raw data for Figures 1,2,3,4,9 of the main text.

**Chemicals.** Silver nitrate (Sigma-Aldrich,  $\geq 99.0\%$ ), hydrogen tetrachloroaurate trihydrate (Sigma-Aldrich, 99.9%), tetra-*n*-octylammonium bromide (Sigma-Aldrich, 98%),  $\text{NaBH}_4$  (Sigma-Aldrich, 99%), triphenylphosphine (Sigma-Aldrich, 99%), 2,4-dimethylbenzenethiol (Sigma-Aldrich, 95%), dichloromethane (DCM, Sigma-Aldrich,  $\geq 99.9\%$ ), tetrahydrofuran (THF, Sigma-Aldrich, 99.9%), toluene (Sigma-Aldrich, 99.7%), methanol (Sigma-Aldrich, 99.8%), acetonitrile (Carlo Erba RS), hexane (Aldrich,  $\geq 99\%$ ), pentane (Sigma-Aldrich, 99.8%), butyronitrile (Sigma-Aldrich,  $\geq 99.0\%$ ), propionitrile (Sigma-Aldrich, 99%) were used as received.

$\text{Ag}_{24}\text{Au}(\text{SPhMe}_2)_{18}^-$  was synthesized according to a known procedure,<sup>1</sup> with minor modifications.

$[\text{n-Oct}_4\text{N}^+][\text{Ag}_{25}(\text{SPhMe}_2)_{18}^-]$ . 0.478 mL of 2,4-dimethylbenzenethiol (3.54 mmol, 3 equiv) was slowly added to a solution of 200 mg (1.18 mmol)  $\text{AgNO}_3$  dissolved in 10 mL of methanol. To the resulting opaque yellow mixture, 90 mL of DCM was added, and the mixture stirred for 30 min at 0 °C. A solution of tetra-*n*-octylammonium bromide ( $\text{n-Oct}_4\text{N}^+$ , 64.4 mg, 0.118 mmol, 0.1 equiv) in 3 mL methanol was added, and then 3 mL of an ice-cold  $\text{NaBH}_4$  aqueous solution (89.1 mg, 2.35 mmol, 2 equiv) was added dropwisely. The resulting dark-brown mixture was stirred for 4 h at 0 °C. The product was filtered on paper to remove black/dark grey residues. The brown/dark orange solution was concentrated and the product was precipitated with methanol and then dried.  $[\text{n-Oct}_4\text{N}^+][\text{Ag}_{25}(\text{SPhMe}_2)_{18}^-]$  is obtained as a dark-brown orange powder, which was stored at 4 °C in the dark.

*AuCIPPh*<sub>3</sub>. To a solution of 50 mg (0.127 mmol)  $\text{HAuCl}_4 \cdot 3\text{H}_2\text{O}$  in 5 ml THF, 100 mg (0.381 mmol, 3 equiv) triphenylphosphine in 5 ml THF was added dropwise. The yellow solution quickly became colorless, and was then concentrated to 2 mL. The white product was precipitated with pentane and washed with methanol (4 x 10 mL).

$[\text{n-Oct}_4\text{N}^+][\text{Ag}_{24}\text{Au}(\text{SPhMe}_2)_{18}^-]$ . *AuCIPPh*<sub>3</sub> (1 mg in 1 mL DCM) was added to 5 mL DCM containing 20 mg of  $[\text{n-Oct}_4\text{N}^+][\text{Ag}_{25}(\text{SPhMe}_2)_{18}^-]$ . The solution was stirred for 4 h during which the color of the solution changed from brown/orange to green. Then, the solution was concentrated and the product was precipitated with pentane and washed with methanol (4 x 10 mL). The solid was extracted with acetonitrile, concentrated, precipitated with a mixture toluene:hexane 1:1, and

finally washed with pentane.  $[\text{n-Oct}_4\text{N}^+][\text{Ag}_{24}\text{Au}(\text{SPhMe}_2)_{18}^-]$  was obtained as a black/dark green powder, which was stored at 4 °C in the dark.

### UV-vis Absorption Spectroscopy

Photoabsorption measurements were carried out with a near-infrared VARIAN Cary 5000 spectrophotometer with a spectral resolution of 0.5 nm. The spectra were collected over a range of 250–1200 nm.  $[\text{n-Oct}_4\text{N}^+][\text{Ag}_{24}\text{Au}(\text{DMBT})_{18}^-]$  was dissolved in a 5:4:2 vol butyronitrile/propionitrile/dichloromethane solution, which we found to form a clear glass at low temperatures. The solution was adjusted to obtain an absorbance of 0.5 at 460 nm, using a 1 mm optical-path quartz cuvette. The temperature was controlled with an OptistatDN cryostat equipped with a MercuryiTC temperature controller (Oxford Instrument). A HiCube 80 Eco, DN 63 ISO-K turbo pumping station (PFEIFFER Vacuum) was used to generate a high vacuum inside the outer vacuum chamber of the cryostat. Before experiment, the sample holder was purged with high-purity helium, which was used as the temperature-exchange gas. The temperature of the cryostat was lowered using liquid nitrogen. Spectra were obtained as a function of temperature (40 K intervals) after 10 min equilibration at each temperature. Figure S2 shows the spectra.

### New density fitting basis set.

When the polTDDFT method is employed within the ADF code, it is necessary to use a basis set of Slater Type Orbitals in order to expand the vector  $\mathbf{b}$  in equation (6). In the original work such basis was available only for a very limited number of elements of the periodic table. With the release of the 2021 version of AMS (<https://www.scm.com/product/ams>) such basis sets have been reoptimized and extended to the whole periodic table (with the exceptions of lanthanides and actinides). More precisely for each element considered we have considered at least three different molecules (in order to consider the same element in different chemical environments) for each molecule the spectrum has been calculated with the Casida method for reference, then several spectra (of the order of few thousands) have been calculated with the polTDDFT but with different density fitting functions sets. In practice we start from the almost complete density fitting STO set already used by ADF for the fitting of the SCF density, deleting gradually the fitting function reducing the size of the set. The quality of the set has been evaluated defining several descriptors. The ‘best’ basis set has been chosen as the best compromise between accuracy (best descriptor) and computational economy (lowest number of basis

elements). As an example in Figure S3 we have reported the comparison for the planar D<sub>3h</sub> cluster Au<sub>6</sub>, between the original basis, the new reoptimized basis and the Casida reference calculation. As can be seen the new basis gives quantitative match with respect to Casida, while original basis set was less accurate.

## References

1. M. S. Bootharaju, C. P. Joshi, M. R. Parida, O. F. Mohammed, and O. M. Bakr, "Templated Atom-Precise Galvanic Synthesis and Structure Elucidation of a [Ag<sub>24</sub>Au(SR)<sub>18</sub>]<sup>-</sup> Nanocluster," *Angew. Chem. Int. Ed.* **55**, 922–926 (2016).

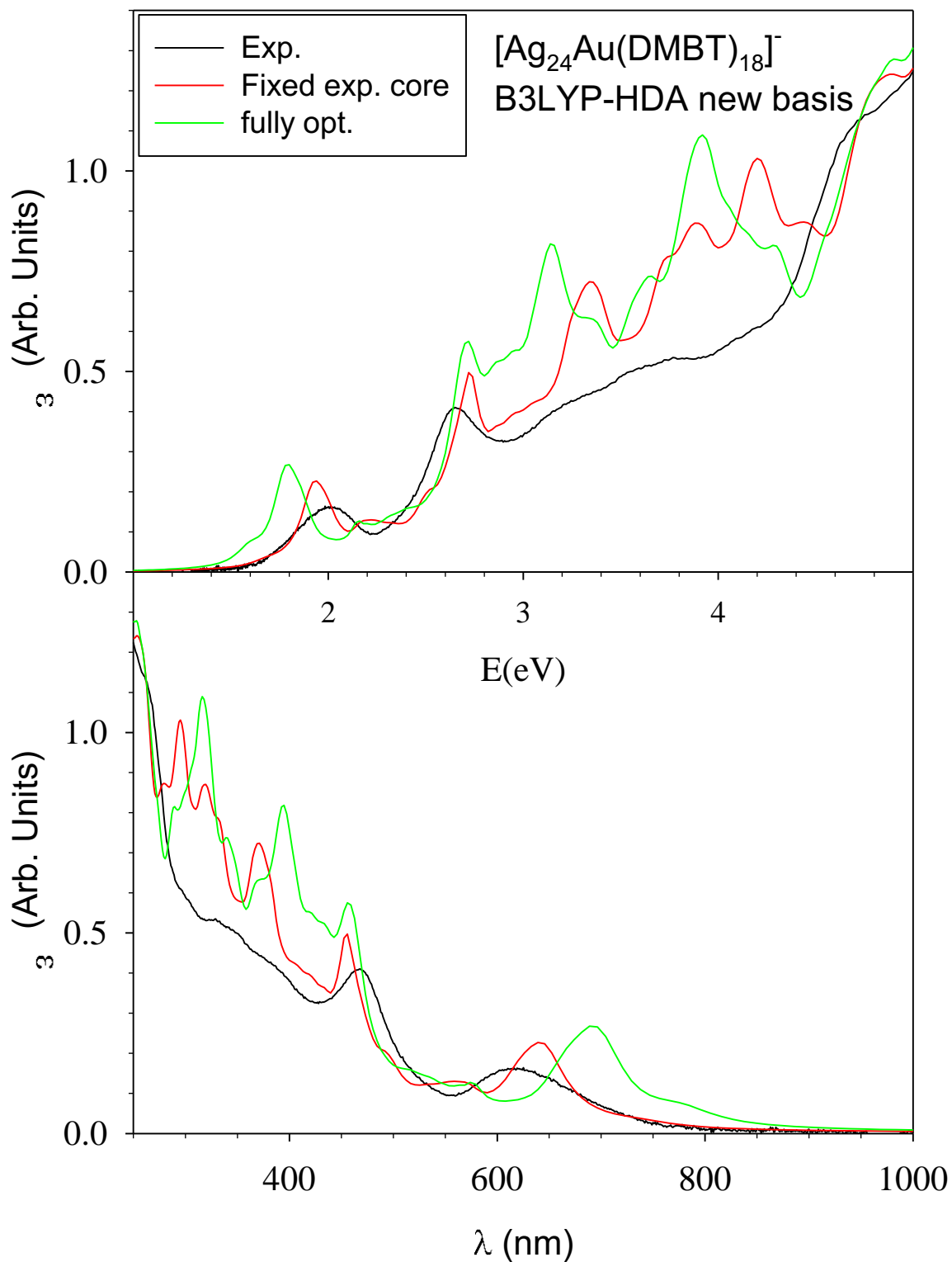


**Fig. S1.** Photoabsorption spectrum of  $[\text{Ag}_{24}\text{Au}(\text{DMBT})_{18}]^-$  calculated with the TZP basis set and the new basis set of fitting functions using the polTDDFT method and the B3LYP functional at two different geometries as described in the main text, in comparison with experimental data from Ref.[37]. In panel (a) the energy scale is in eV, while in panel (b) the wavelength scale is in nm.

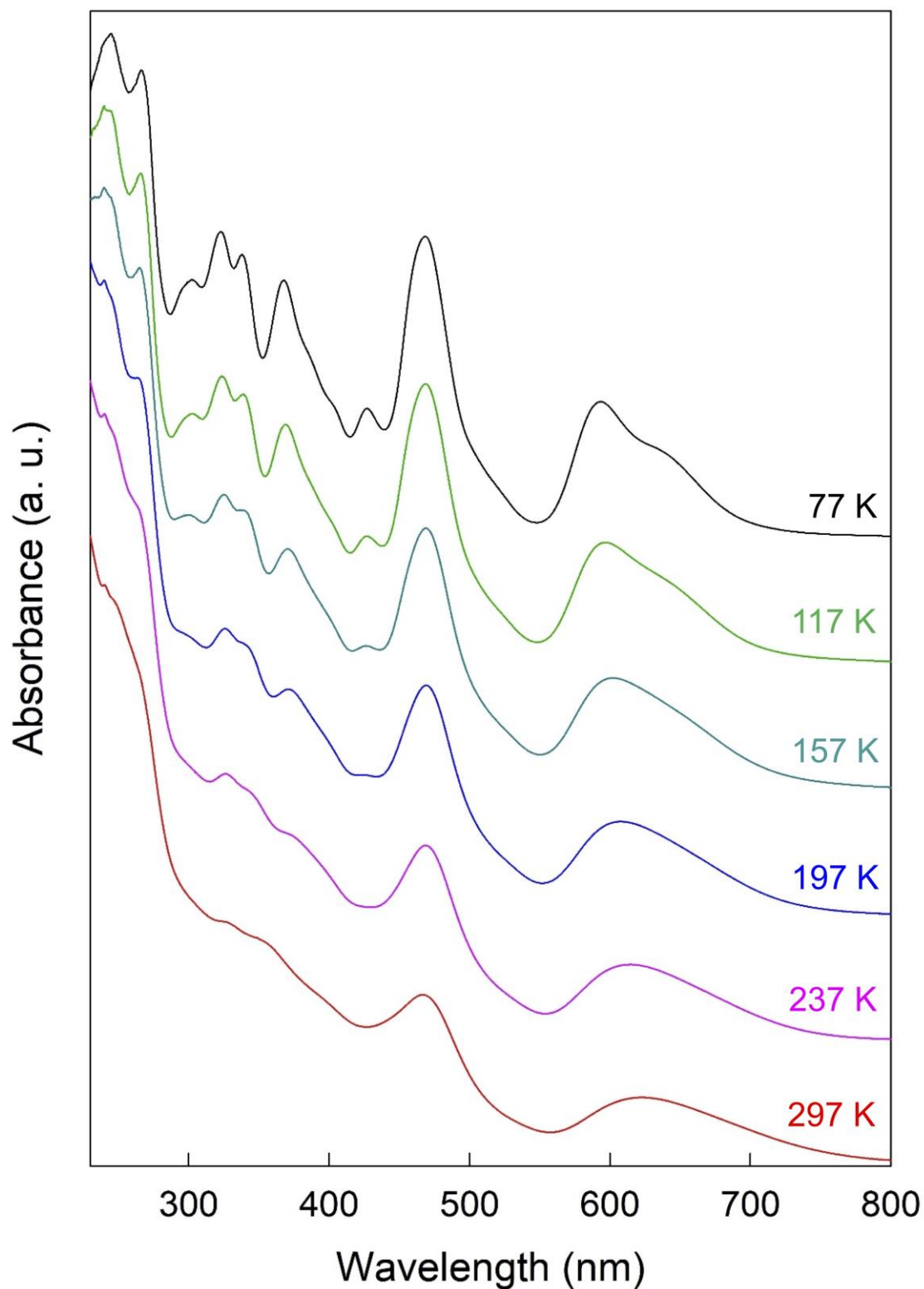


**Fig. S2.** Photoabsorption spectra of  $[Ag_{24}Au(DMBT)_{18}]$  obtained at temperatures from 297 to 77 K, as specified in the graph. For clarity, the spectra obtained at temperatures lower than 297 K have been vertically shifted.

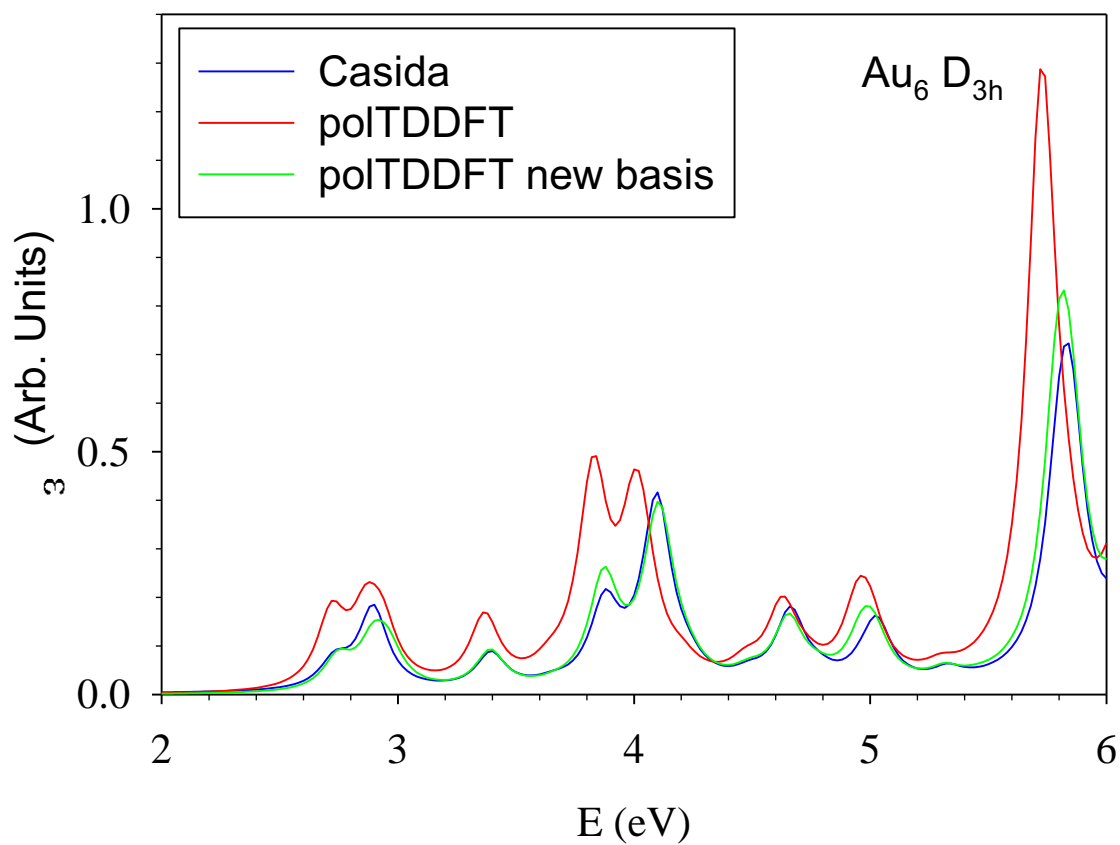


**Fig. S3.** Photoabsorption spectrum of  $Au_6$  calculated with TZP basis set with the Casida method and with the polTDDFT method (original and new density fitting basis). B3LYP-HDA functional.

*ATTENTION: this is incomplete supporting information, please visit the article online*

Article

# Plasmonic Circular Dichroism in Chiral Gold Nanowire Dimers

Daniele Toffoli <sup>1</sup>, Marco Medves <sup>1</sup>, Giovanna Fronzoni <sup>1</sup>, Emanuele Coccia <sup>1</sup>, Mauro Stener <sup>1,\*</sup>, Luca Sementa <sup>2</sup> and Alessandro Fortunelli <sup>2,\*</sup>

<sup>1</sup> Dipartimento di Scienze Chimiche e Farmaceutiche, Università di Trieste, Via Giorgieri 1, 34127 Trieste, Italy; toffoli@units.it (D.T.); marcomedves@virgilio.it (M.M.); fronzoni@units.it (G.F.); ecoccia@units.it (E.C.)

<sup>2</sup> CNR-ICCOM & IPCF, Consiglio Nazionale delle Ricerche, Via Giuseppe Moruzzi 1, 56124 Pisa, Italy; luca.daumann@gmail.com

\* Correspondence: stener@units.it (M.S.); alessandro.fortunelli@cnr.it (A.F.)

**Abstract:** We report a computational study at the time-dependent density functional theory (TDDFT) level of the chiro-optical spectra of chiral gold nanowires coupled in dimers. Our goal is to explore whether it is possible to overcome destructive interference in single nanowires that damp chiral response in these systems and to achieve intense plasmonic circular dichroism (CD) through a coupling between the nanostructures. We predict a huge enhancement of circular dichroism at the plasmon resonance when two chiral nanowires are intimately coupled in an achiral relative arrangement. Such an effect is even more pronounced when two chiral nanowires are coupled in a chiral relative arrangement. Individual component maps of rotator strength, partial contributions according to the magnetic dipole component, and induced densities allow us to fully rationalize these findings, thus opening the way to the field of plasmonic CD and its rational design.

**Keywords:** plasmon; circular dichroism; nanoplasmonics; metal clusters



**Citation:** Toffoli, D.; Medves, M.; Fronzoni, G.; Coccia, E.; Stener, M.; Sementa, L.; Fortunelli, A. Plasmonic Circular Dichroism in Chiral Gold Nanowire Dimers. *Molecules* **2022**, *27*, 93. <https://doi.org/10.3390/molecules27010093>

Academic Editors: Noelia Barrabés and Joanna Olesiak-Bańska

Received: 17 November 2021

Accepted: 18 December 2021

Published: 24 December 2021

**Publisher's Note:** MDPI stays neutral with regard to jurisdictional claims in published maps and institutional affiliations.



**Copyright:** © 2021 by the authors. Licensee MDPI, Basel, Switzerland. This article is an open access article distributed under the terms and conditions of the Creative Commons Attribution (CC BY) license (<https://creativecommons.org/licenses/by/4.0/>).

## 1. Introduction

Among the wide variety of phenomena which emerge at the nanoscale régime, the localized surface plasmon resonance (LSPR), typical of nanostructured metals, plays a major role in nanotechnology due to its ability of focusing the electromagnetic field with a high energy density in a small region of space [1–3]. This effect has direct application in enhanced spectroscopic techniques, such as surface enhanced Raman spectroscopy [4], and in single-molecule spectroscopy [5,6]. Additionally, the possibility of having LSPR exhibiting chiral features is extremely appealing, because it would allow one to enhance the specificity and selectivity of sensing devices, especially in the biological applications [7]. It is worth noting that, while conventional plasmons in extended systems are well understood as collective motions of conduction band electrons, for finite systems such as nanoclusters and nanowires, their nature is still debated [8–12]. The picture is even less clear in the field of chirality, as experiments are here much more difficult to conduct and interpret, and less conclusive. For all these reasons, contribution from theoretical insight and understanding is dramatically required.

Chiral systems generally give a non-zero circular dichroism (CD) signal. The CD response is routinely employed to study biomolecules, while frontier applications are in the emerging field of chiral sensing [13]. Managing the CD signal is challenging due to its intrinsic weakness, usually five orders of magnitude less intense than the corresponding absorption signal, as a consequence of the electric-dipole/magnetic-dipole scalar product that governs the CD intensity according to the Rosenfeld equation [14]. For this reason, the amplification of the CD signal in plasmonic systems is quite intriguing, and many attempts have been reported along this research direction [15–18]. It is convenient to classify plasmonic CD into structural and induced CD [18], according to its physical origin. A chiral plasmonic metal cluster or nanostructure gives rise to structural plasmonic CD [19], while a chiral arrangement of non-chiral systems promotes an induced plasmonic CD. Although

induced plasmonic CD is easier to obtain at the experimental level, [20] the field of structural chiral plasmonics, although still in its infancy, offers very promising possibilities, for example, chiral growth promoted by hot electron mechanisms in nanocrystals [21] or hot-electron transfer [22]. Despite the interest in these new developments, at present, at the experimental level, only modest plasmonic CD enhancements have been observed [18]. We believe that a rationalization of both structural and induced plasmonic CD in terms of quantum mechanics is needed to allow understanding the issues limiting experimental observations, the design of optimal systems, and the ensuing exploitation of this phenomenon. To this aim, some of us recently studied the CD of a series of chiral plasmonic gold nanowires by means of time dependent density functional theory (TDDFT) [23]. As a main outcome of this work, we found that chiral linear gold nanowires do not give rise to a plasmonic CD, notwithstanding the presence of a very strong and sharp plasmonic resonance in absorption. In contrast, a very strong plasmonic CD was predicted when the chiral nanowires were no longer linear, but assumed a helical shape winding around the external surface of a cylinder. An analysis based on the individual component mapping of the rotator strength (ICM-RS) [24] allowed us to ascertain that, for linear nanowires, the absence of CD in correspondence of the plasmon absorption is due to a destructive interference among huge contributions of opposite sign. This finding then triggered the present analysis, where we now try to overcome and bypass the destructive interference phenomenon and also recover a plasmonic CD in linear nanowires (that are much easier to synthesize) by coupling two chiral nanowires. As we will detail below, the ICM-RS analysis in fact suggested that the nanowire/nanowire interaction can perturb the interference between positive and negative contributions to CD, thus greatly decreasing its destructive character, and therefore leading to plasmonic circular dichroism.

In the present work, we considered various coupling modes between the chiral nanowires: we started with two chiral nanowires coupled via an achiral relative arrangement (pure structural CD); then we considered two chiral nanowires coupled in a chiral relative arrangement (structural and induced CD). In the latter case, in order to identify the effect of pure induced CD, we also considered two achiral nanowires coupled in a chiral relative arrangement. We then showed that the nanowire coupling indeed produced the expected effect of strongly diminishing the destructive interference phenomenon, such that we predicted to the best of our knowledge for the first time an intense plasmonic CD also in linear nanowire systems. ICM-RS, partial contributions according to the magnetic dipole components, and induced densities were then exploited to fully rationalize our finding. In general, gold nanowires are systems which, besides chirality, are interesting for their properties, e.g., their propensity to form hybrid structures such as encapsulation in single wall carbon nanowires (SWCN) [25].

## 2. Discussion

In our previous work [23], the structure of the (5,3)NT nanowire was inspired by experimental work on the synthesis of helical gold multi-shell nanowires [26]. The starting point is given by the helical linear structure (constructed according to the prescription of Senger et al. [27]) that is intrinsically chiral. The calculated plasmon was very intense in absorption, but no CD signal was found at the energy of the plasmon resonance [23].

Since we found that the plasmon CD was suppressed by destructive interference, we suggested that a perturbation of the system might remove, at least partially, such destructive interference. In this work, we explored this idea considering the interaction between pairs of nanowires.

The simplest interaction between two nanowires is obtained by keeping their axis parallel to each other and changing only their relative distance. In Figure 1a, the geometry actually employed in the calculations is reported, where the original structure of the (5,3)NT taken from ref. [23] has been repeated two times in order to keep the  $C_2$  symmetry z-axis: we will refer to this system in the following as the parallel geometry.

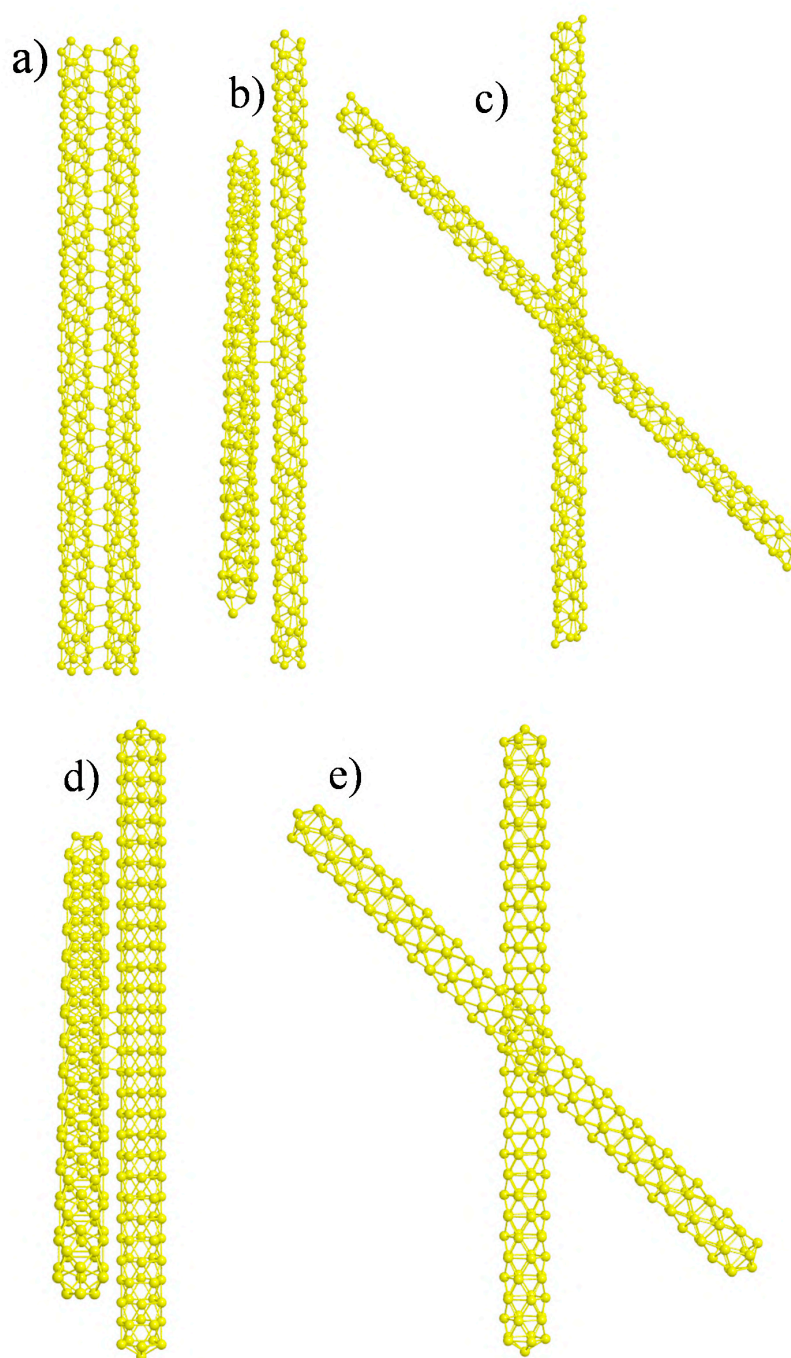


**Figure 1.** (a) Structure of a pair of interacting gold chiral nanowires with parallel axis so their arrangement is not chiral. (b) side view and (c) top view of a pair of interacting gold chiral nanowires with axis rotated by 45 degrees so their relative orientation is chiral. (d) side view and (e) top view of a pair of interacting gold achiral nanowires with axis rotated by 45 degrees so their relative orientation is chiral.

The distance between the two nanowires has been set to 2.88 Å, equal to the bulk gold–gold interatomic distance. Note that, in this case, the two nanowires were both chiral but their relative orientation was achiral. The chosen distance between Au atoms corresponds to the distance of physical systems not otherwise constrained (the nanowires will tend to touch each other to minimize energy). We have also tried a larger distance between nanowires equal to 5 Å; however, in that case the nanowires were non-interacting and we did not obtain an appreciable difference in absorption and CD spectra with respect

to a single nanowire. Distances between 2.88 Å and 5 Å were difficult to explore because the chemical bonds connecting the two nanowires were partially broken, making the SCF difficult to converge.

In Figure 1b,c another geometric configuration is reported, which is derived from the previous parallel geometry obtained via a rotation of only one of the two nanowires by 45 degrees around the  $C_2$  z-axis: we will refer to this system as the rotated geometry. In Figure 1 we have reported the same system viewed from two different perspectives: in the side view (b), the chemical bonds connecting the two nanowires are visible, while in top view (c) it is possible to appreciate the relative rotation of the two nanowires. In this case, the relative orientation itself is chiral; in fact, in the present relative orientation, we do not have any symmetry plane and a chiral system is obtained. We may therefore distinguish between structural chirality (of the single nanowire) and induced chirality (by the relative orientation between the two objects). In order to distinguish even more clearly the two effects we have also considered a chiral relative orientation of two achiral nanowires, like in Figure 1d,e. In this case we first built an achiral nanowire with the same size of the chiral one (152 gold atoms), whose structure has been generated starting from the  $Au_{12}$  icosahedral cluster with a gold–gold interatomic distance of 2.88 Å, adding 14 equatorial ribbons of  $Au_{10}$  units, obtaining finally the  $Au_{152}$  cluster with  $D_{5d}$  symmetry. Then two of such clusters were paired in the same way as the rotated geometry of the previous Figure 1b,c. This new configuration was reported in Figure 1d,e and will be referred to as *rotated achiral*; note that, in this case, only induced plasmonic CD is expected.

The photoabsorption (upper panel) and CD (lower panel) for the single chiral nanowire (red lines) and the pair of interacting gold chiral nanowires with parallel axis (blue line) are reported in Figure 2. The single chiral nanowire results have been taken from our previous work [23]. The effect of coupling on the photoabsorption is an intensity enhancement with the absorption approximately doubled in the two-nanowire systems, and a blue shift from 1.04 eV to 1.24 eV of the plasmon peak. These results can be rationalized in terms of plasmon coupling: the induced dipoles on the two nanowires are parallel; as a consequence, the coupled plasmon energy is increased due to their repulsive interaction. In contrast, the effect of nanowire coupling on the CD is striking: while the single nanowire gives negligible CD at the plasmon energy, the pair with parallel axis gives a huge positive contribution, with a peak value exceeding  $10,000 \times 10^{-40} \text{ esu}^2 \cdot \text{cm}^2$ , i.e., an increase of four orders of magnitude of the CD signal with respect to the single-nanowire system. This value is of the same order of magnitude as that obtained for the helical nanowires [23], which reached a maximum around  $40,000 \times 10^{-40} \text{ esu}^2 \cdot \text{cm}^2$ . In the Figure 3 we have reported the ICM-RS plots of both present pair of interacting nanowires (boxes (a) and (c)) as well as those of the single chiral nanowire (boxes (b) and (d)) taken from our previous work [23]. Moreover, we have generated both 2D (boxes (a) and (b)) as well as 3D plots (boxes (c) and (d)) in order to have a more direct visualization of the effects. All the details regarding the definition and calculation of the ICM-RS plots have been reported in Appendix A.2 of the Appendix A of the present work. Such plots consist of decomposing the rotator strength (R) of a given transition in its components in terms of occupied-virtual pairs; on the x and y axis, the occupied and virtual orbital energies are considered. The presence of a ‘spot’ indicates that the orbital pair that had the corresponding energy is involved in the transition. In 2D, the ‘intensity’ of the involvement is given by a colour scale; for 3D plots, the ‘intensity’ corresponds to the scale of the z axis. As observed previously and considering the present Figure 3b,d, the negligible CD of the single chiral nanowire is a consequence of a destructive interference of two opposite and large contributions. These opposite (positive and negative) contributions in the ICM-RS spectrum of the (5,3) nanowire are individually very large but are practically equal in absolute value. They thus cancel each other almost perfectly, producing a nearly zero CD spectrum. This suggested that by perturbing the system with a proper coupling, it should be possible to remove, at least partially, such a destructive interference, allowing the manifestation of a plasmonic CD. The present results fully confirm this hypothesis: here we have demonstrated that

the coupling between a pair of nanowires is sufficient to allow a partial suppression of the destructive interference phenomenon. Indeed, in Figure 3a,d, we report the ICM-RS plots of the parallel pair taken at the energy corresponding to the maximum dichroism. Only the y dipole component was considered (along the direction of maximum nanowire length), the other components being negligible. It is evident that there was still destructive interference, since there were regions with the opposite sign, but now the positive region was wider and more intense than the negative one, such that there was only a partial cancellation. However, this also shows that the destructive interference had been only partially removed, and that there was still wide room for further increasing the dichroism, suggesting a promising path for future work.

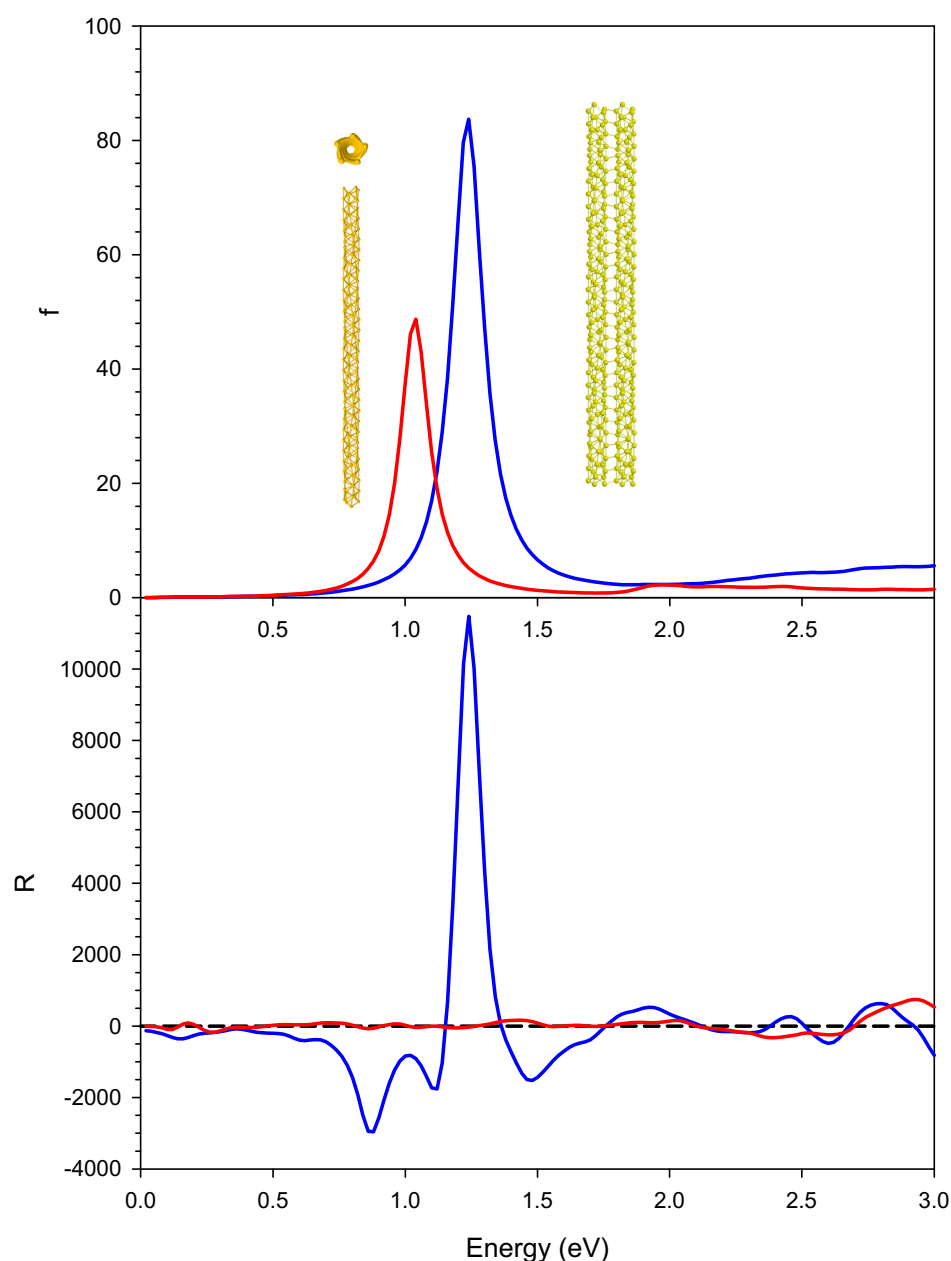


**Figure 2.** Photoabsorption (upper panel) and CD (lower panel) for the single chiral nanowire (red lines) and the pair of interacting gold chiral nanowires with parallel axis (blue line). Oscillator strengths are given in atomic units, while R is given in  $10^{-40}$  esu<sup>2</sup>·cm<sup>2</sup>.

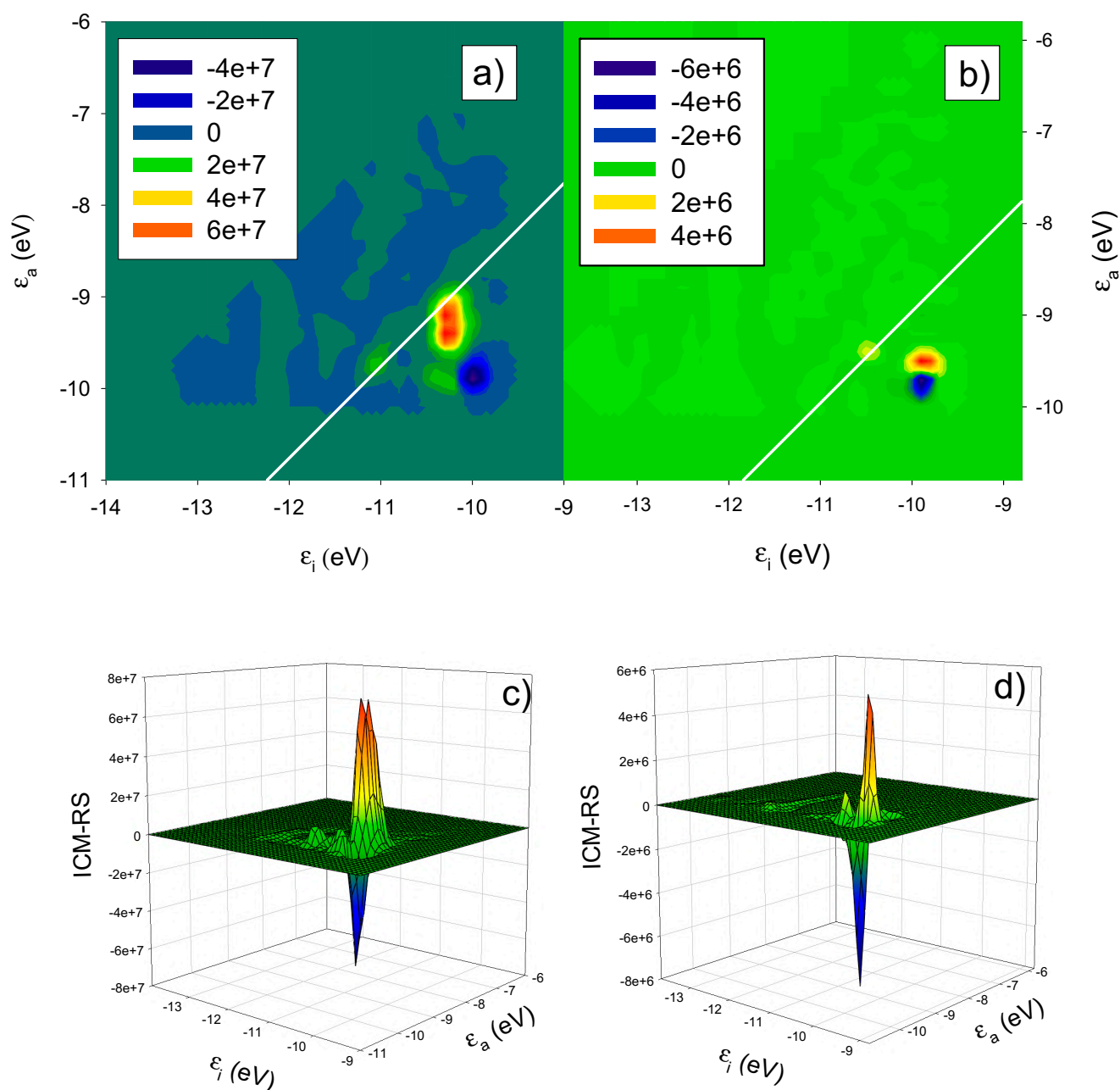


**Figure 3.** ICM-RS plots relative to the y component taken at the energy corresponding to the maximum CD: 1.04 eV for the single nanowire in panels (a,c); 1.24 eV for the pair of interacting gold chiral nanowires with parallel axis in panels (b,d) as in Figure 1.  $\epsilon_i$  and  $\epsilon_a$  are energies of occupied and virtual orbitals, respectively.

We then analyzed the rotated geometry described in Figure 1b,c, whose photoabsorption and dichroism are reported in Figure 4, together with the results of the parallel geometry for comparison. The plasmon in absorption of the rotated systems displayed a red shift with respect to the parallel one, going from 1.24 eV to 1.10 eV, while the oscillator strengths showed only a modest decrease. The red shift could be easily rationalized if we described the plasmon as the sum of the dipolar plasmons of the individual nanowires. The destabilizing interaction between the dipoles was reduced in the rotated systems, producing a red shift. We tried to study the effect of varying the angle between the nanowires on the spectral features. This was not a straightforward task, since the mutual orientation between the two nanowires had to allow a suitable formation of chemical bonds between them; if

such bonds were too deformed, the SCF procedure would not converge, hampering such analysis. The only angle we were able to consider was  $30^\circ$ ; we have reported in Figure 4 the corresponding plots as a red line. Such results (both in terms of photoabsorption and CD) were very similar to those obtained by a rotation of  $45^\circ$ , lying in between the  $45^\circ$  and the parallel ones. For this reason, we limit further discussion to the geometry rotated by  $45^\circ$ .

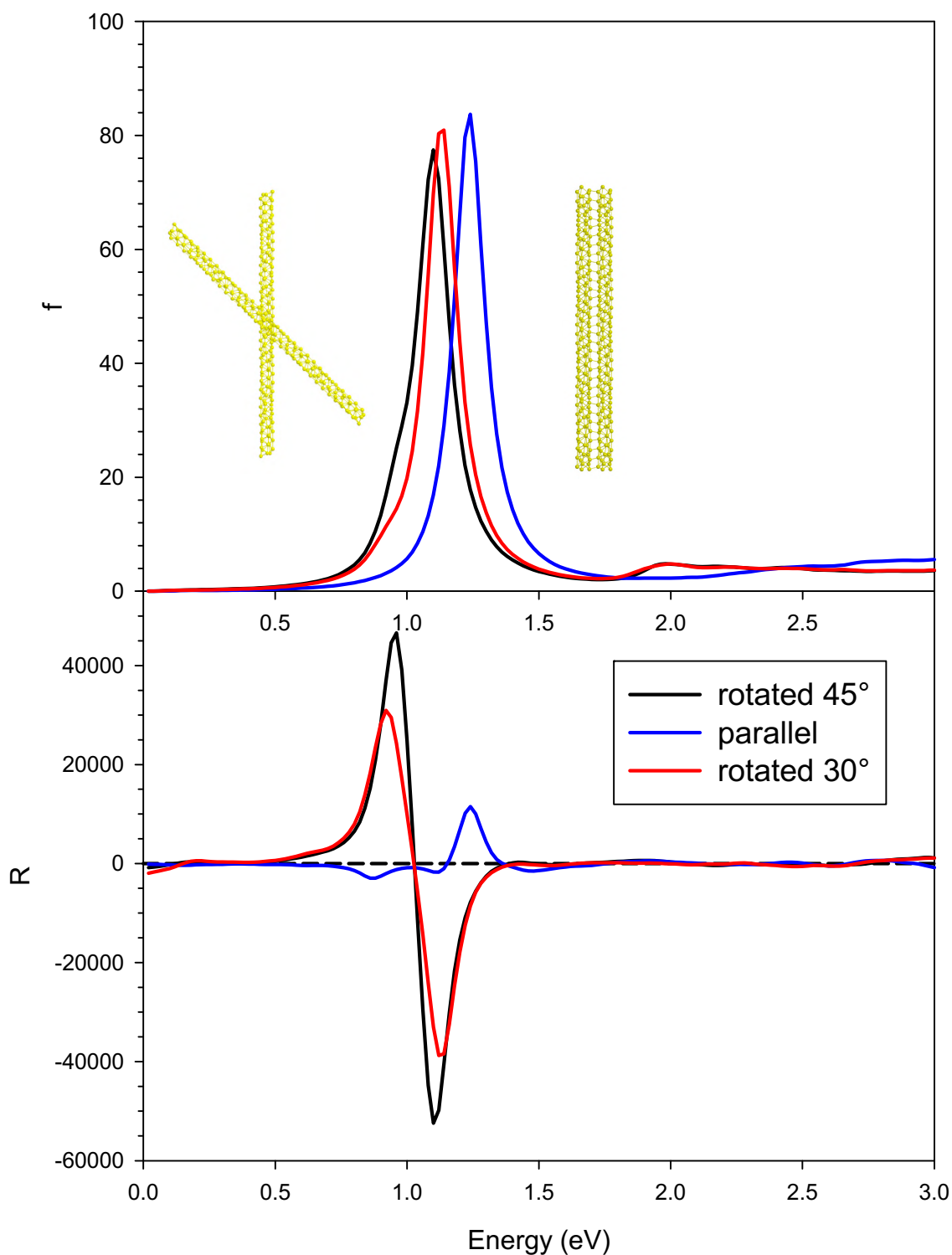


**Figure 4.** Photoabsorption (upper panel) and CD (lower panel) for the pair of interacting gold chiral nanowires with parallel axis (blue line) and rotated axis by  $45^\circ$  (black line) and  $30^\circ$  (red line). Oscillator strengths are given in atomic units, while R is given in  $10^{-40}$  esu $^2$ ·cm $^2$ .

In contrast, the difference between the CD profiles is dramatic: while the parallel system gives in practice only one very strong positive feature up to  $10,000 \times 10^{-40} \text{ esu}^2 \cdot \text{cm}^2$ , the one rotated by  $45^\circ$  gave a pair of strong peaks with opposite sign, separated by only 0.14 eV, with rotator strength up to  $\pm 50,000 \times 10^{-40} \text{ esu}^2 \cdot \text{cm}^2$ . This finding suggests that, in this case, induced plasmonic CD was stronger than structural plasmonic CD, analogously to what was reported in our previous work for the comparison between linear and helical nanowires [23]. It is hard to say if this is a general behavior or one specific to the present systems. In fact, it is worth noting that the structural plasmonic observed in the parallel situation kept a large amount of destructive interference; therefore, it is still possible that more effective coupling between nanowires may remove further the destructive character giving rise to much higher structural plasmonic CD. Induced densities of the rotated geometry at the two energies corresponding to the maximum and minimum CD, respectively 0.96 and 1.10 eV, are reported in Figure 5. In both cases, the induced density displays a clear dipolar shape for each individual nanowire, typical of a plasmon. However, at lower energy, the individual dipoles of the wires displayed opposite direction, corresponding to a negative scalar product; at higher energy, the dipoles had the same direction.

In order to have a better understanding of the phenomenon, we show in Figure 6 the ICM-RS of the two CD peaks at 0.96 eV (left boxes) and 1.10 eV (right boxes). Both x dipole component (upper boxes), as well y dipole component (lower boxes), are reported. Such ICM-RS plots are quite different from that of the parallel system (Figure 3). Indeed, we did not observe any destructive interference for the rotated geometry for x and y components of the dipole. In fact, for both energies, the x component was positive and the y component was negative for all of the spots on the 2D ICM-RS plot. More precisely, at 0.96 eV, the x component was more positive than the negative y component, a situation that was reversed at 1.10 eV; here, the order of magnitude of the x component did not change, while the negative y components increased by two orders of magnitude and became preponderant. Since the present ICM-RS analysis suggests that the mutual interplay between individual dipole components was fundamental to rationalize the specific CD behavior, in Figure 7 we have considered, for both parallel and rotated geometries, the photoabsorption and CD partial profiles from the dipole components. For the parallel geometry the situation was obviously quite simple: only the y component played a fundamental role for both photoabsorption and CD, the y axis being along the nanowires axis. For the rotated geometry, instead, the situation was more interesting: the total photoabsorption peak was contributed essentially by both x and y components; however, while the y component had a single maximum at 1.10 eV, the x component displayed two maxima at 0.98 and 1.10 eV. Consistently with what was already found in the ICM-RS analysis the x component had very similar values at the two energies, while the y component increased by a factor of four, going from 0.98 eV to 1.10 eV. In practice, the feature at 0.98 eV almost disappeared in the total profile; thus, only a sketched shoulder can be hardly seen in the left side of the peak. Passing to the CD, the partial profiles display similar shape (two maxima for the x dipole and one maximum for the y dipole); however, the y component was negative, which explains the observed behavior in the total profile.

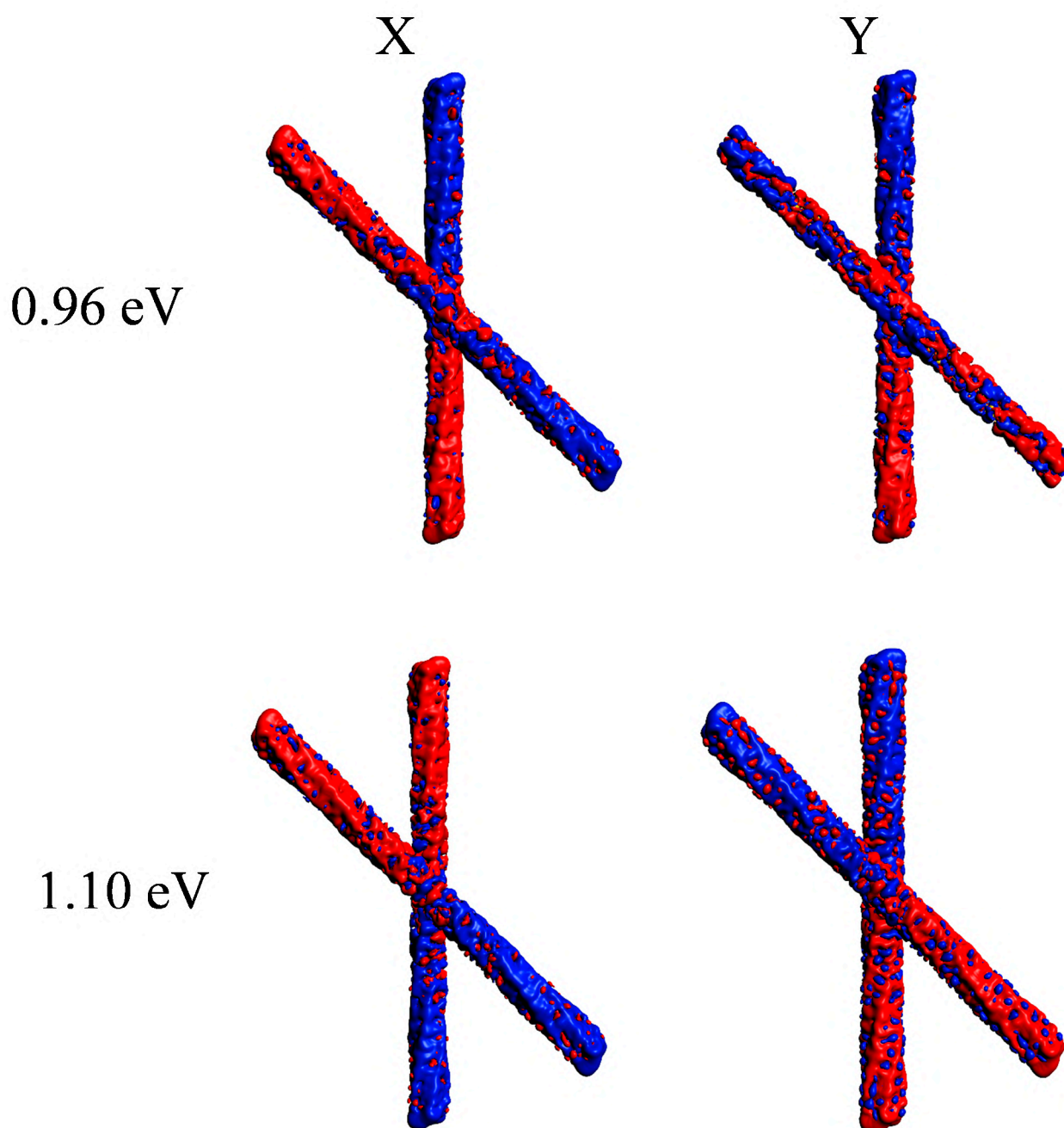


**Figure 5.** Induced density plots relative to the x and y components taken at the energy corresponding to the maximum CD (0.96 eV) and the minimum CD (1.10 eV) of a pair of interacting gold chiral nanowires with axis rotated by 45 degrees as in Figure 1.

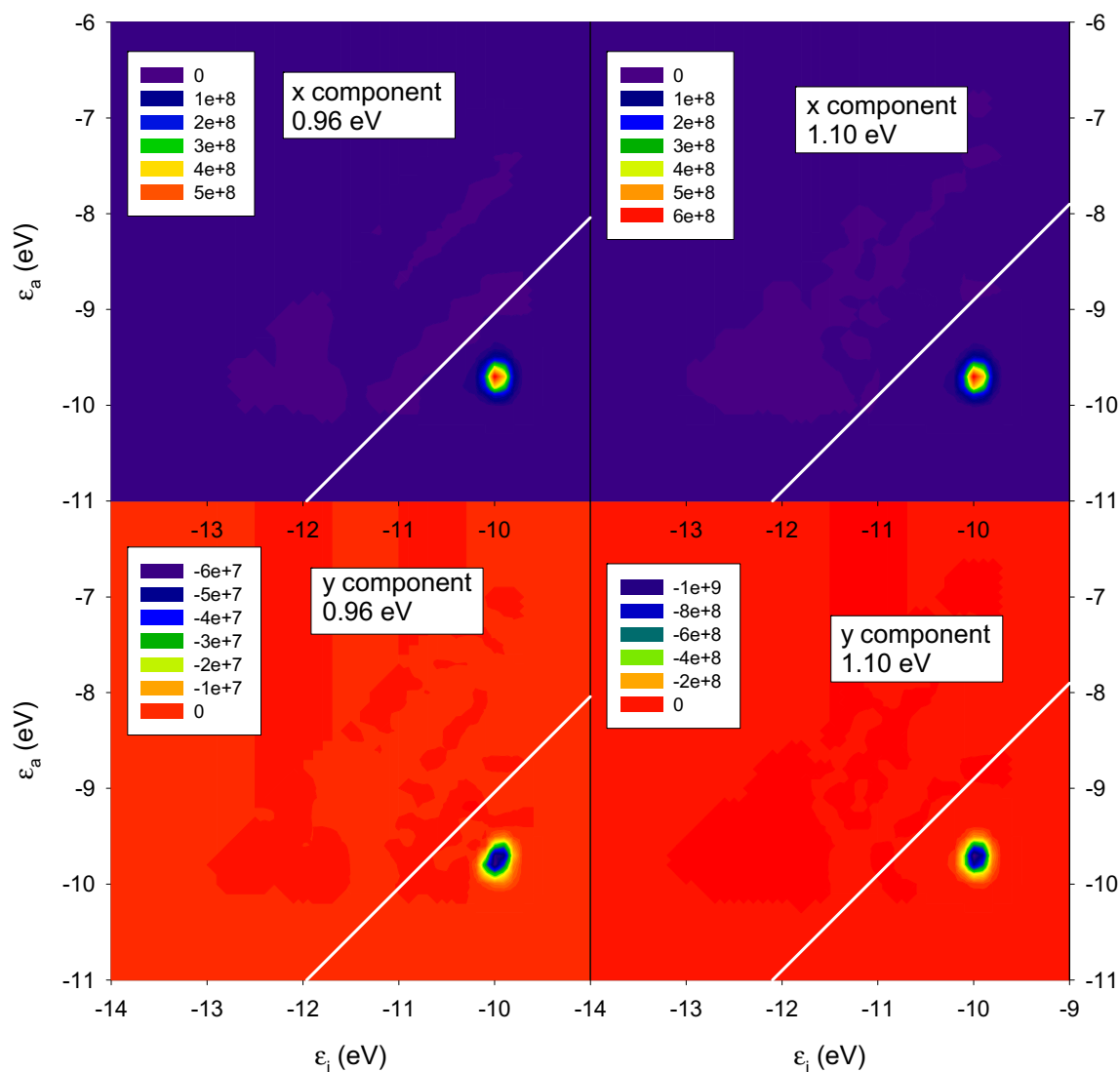


**Figure 6.** ICM-RS plot relative to the x and y components taken at the energy corresponding to the maximum CD (0.96 eV) and the minimum CD (1.10 eV) of a pair of interacting gold chiral nanowires with axis rotated by 45 degrees as in Figure 2.  $\epsilon_i$  and  $\epsilon_a$  are energies of occupied and virtual orbitals, respectively.

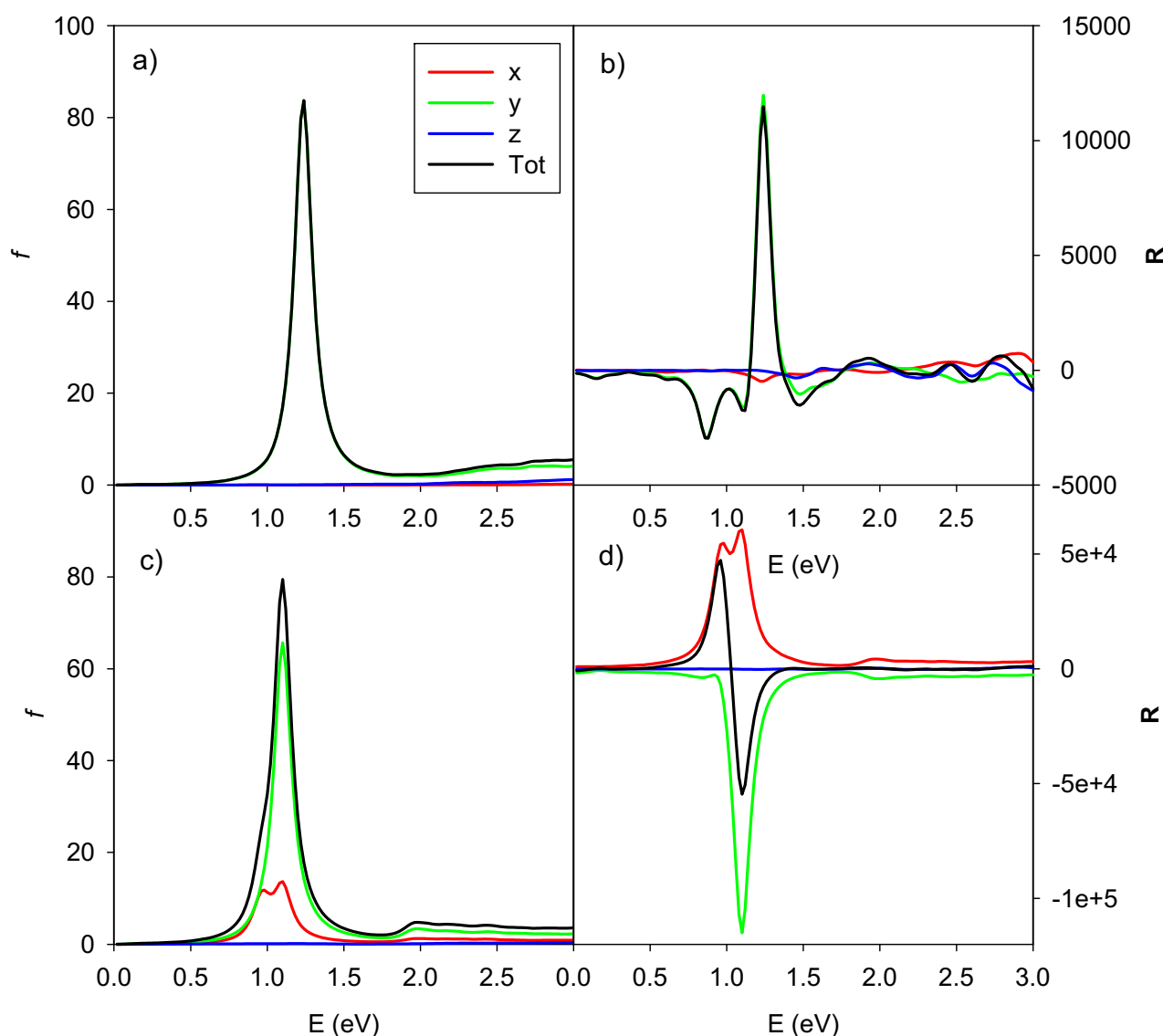


**Figure 7.** Dipole components partial contributions of photoabsorption (left panels (a,c)) and CD (right panels (b,d)) for the pair of interacting gold chiral nanowires with parallel axis (upper panels (a,b)) and rotated axis (lower panels (c,d)). Oscillator strengths are given in atomic units, while R is given in  $10^{-40}$  esu<sup>2</sup>·cm<sup>2</sup>, x, y, z and total contributions are in red, green, blue and black lines, respectively.

In order to better identify the role of the induced plasmonic CD, we report in Figure 8 the photoabsorption and the CD of the rotated achiral system, whose geometry is reported in Figure 1d,e, together with the profiles of the rotated chiral system for comparison. We observed a blue shift for both photoabsorption and CD profiles; the photoabsorption was slightly attenuated, while, for CD, the weakening seemed more pronounced. The nanowires that constitute this system are achiral, so the CD is purely an induced one: its maximum and minimum values of  $30,000 \times 10^{-40}$  and  $-40,000 \times 10^{-40}$  esu<sup>2</sup>·cm<sup>2</sup> are roughly a factor of three larger than the pure structural CD reported in the previous Figure 2 for the parallel geometry. We may conclude this analysis by saying that, at least for the system considered in the present study, the strength of the induced CD was roughly three times the structural one, and these effects sum up when both of them are present in the same system.

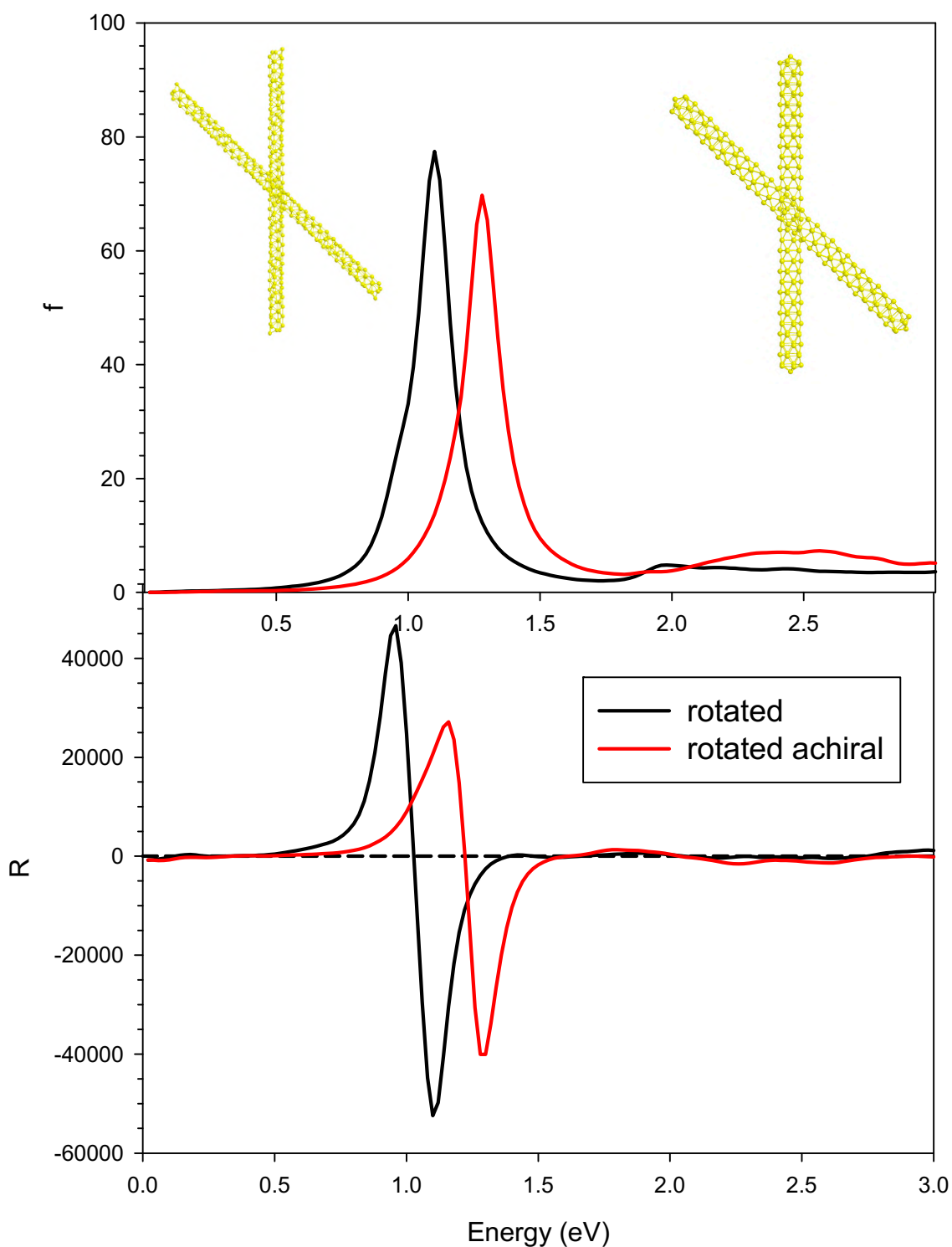


**Figure 8.** Photoabsorption (upper panel) and CD (lower panel) for the pair of interacting gold chiral nanowires with rotated axis (black line) and achiral nanowires with rotated axis (red line). Oscillator strengths are given in atomic units, while R is given in  $10^{-40}$  esu<sup>2</sup>·cm<sup>2</sup>.

### 3. Conclusions

In this work, TDDFT simulations were performed on a series of dimers (pairs) of chiral gold nanowires to explore whether an enhancement of circular dichroism at the plasmon resonance is possible through a coupling between nanostructures.

We find that, when two chiral nanowires are coupled in an achiral relative arrangement, a strong enhancement of the plasmonic CD is predicted by theory with respect to the separate nanowires, which individually did not give any appreciable plasmonic CD. This demonstrates that coupling between two ‘inactive because of destructive interference’ chiral plasmonic systems could still give strong structural CD. We fully rationalized this finding via an analysis of ICM-RS plots. The enhancement is even more pronounced when two chiral nanowires are coupled in a chiral relative arrangement, because, in this configuration, the structural and induced effects sum up to give the largest effect. In order to distinguish between structural CD and induced CD we also considered two achiral nanowires coupled in a chiral relative arrangement, in which case the plasmonic CD was purely induced. From such analysis, at least for the gold clusters and the configurations considered in this work, we found that the induced plasmonic CD is somewhat more intense than the structural one and the two effects sum up when they are simultaneously present. Further studies to demonstrate the generality of the present conclusions would be desirable, especially to identify which are the most effective coupling between chiral systems to produce the highest plasmonic CD phenomenon. In this respect we can, e.g., hypothesize that the addition of ligands adsorbed on the wires, thus locally perturbing their wave functions in a proper way, could be a possible (and technically easier to materialize) alternative to obtain a strong plasmonic CD with respect to coupling pairs of nanowires as in the present work.

**Author Contributions:** Writing—original draft preparation, M.S. and A.F.; Conceptualization: M.S., A.F., G.F. and L.S.; methodology M.S., D.T., M.M. and A.F.; software M.M.; writing—review and editing D.T., G.F., E.C. and L.S. All authors have read and agreed to the published version of the manuscript.

**Funding:** This research received no external funding.

**Institutional Review Board Statement:** Not applicable.

**Informed Consent Statement:** Not applicable.

**Data Availability Statement:** The data presented in this study are available on request from the corresponding author.

**Acknowledgments:** Computational support from CINECA supercomputing centre within the ISCRA programme is gratefully acknowledged. The authors are grateful to the Stiftung Beneficentia for the financial support to set up a computing server. Support from Trieste University within the FRA and MICROGRANTS2020 programmes is also acknowledged.

**Conflicts of Interest:** The authors declare no conflict of interest.

**Sample Availability:** Samples of the compounds are not available from the authors.

## Appendix A. Theoretical Method

The computational study of CD in plasmons is challenging due to the large size of the metal clusters involved and the chirality, which implies very low symmetry (if any), of the system. Therefore, very accurate (explicitly correlated) ab-initio methods are ruled out, while the density functional theory (DFT) and TDDFT represent reliable options. The first CD calculation at the TDDFT level has been done by Autschbach and Ziegler [28] using the Casida scheme [29], which consists of diagonalizing a large matrix, with dimensions corresponding to the number of occupied-virtual orbitals pairs. This method is very efficient to investigate the lowest part of the spectrum, a situation which is not effective for nanoclusters in which a large number of roots are needed to cover the optical region. For this reason, a TDDFT algorithm which avoids large matrix diagonalization has been implemented [30], named polTDDFT, and extended to the calculation of the CD spectrum [31].

### Appendix A.1. The Complex Polarizability Method

The reader is referred to the original work for a detailed description of the algorithm [30], together with its implementation in the ADF program [32].

In practice, the photoabsorption spectrum  $\sigma(\omega)$  is calculated point by point, from the imaginary part of the dynamical polarizability  $\alpha(\omega)$ :

$$\sigma(\omega) = \frac{4\pi\omega}{c} \text{Im}[\alpha(\omega)] \quad (\text{A1})$$

This expression is of practical interest when the polarizability is calculated for complex frequency, i.e.,  $\omega = \omega_r + i\omega_i$ , where the real part  $\omega_r$  is the scanned photon frequency (energy) and  $\omega_i$  is the imaginary part that corresponds to a broadening of the discrete lines and can be interpreted as a pragmatic inclusion of the excited states' finite lifetime. The complex dynamical polarizability is calculated by solving the following non-homogeneous linear system:

$$[\mathbf{S} - \mathbf{M}(\omega)]\mathbf{b} = \mathbf{d} \quad (\text{A2})$$

In Equation (A2)  $\mathbf{S}$  is the overlap matrix between fitting functions,  $\mathbf{b}$  is the unknown vector with the expansion coefficients  $b_\mu(\omega)$  of the induced density  $\rho^{(1)}_z$ ,  $\mathbf{d}$  is the frequency dependent vector corresponding to the known non-homogeneous term, and finally the elements of the frequency dependent matrix  $\mathbf{M}$  are:

$$M_{\mu\nu} = \langle f_\mu | \chi_{KS}(\omega) K | f_\nu \rangle \quad (\text{A3})$$

In Equation (A3),  $\chi_{KS}$  refers to the Kohn-Sham frequency-dependent dielectric function and  $K$  to the kernel.

The original characteristic of the polTDDFT method is the introduction of a simple approximation which enables the construction of  $\mathbf{M}(\omega)$  as a linear combination of frequency independent matrices  $\mathbf{G}^k$  with frequency dependent coefficients  $s_k(\omega)$ , with the following expression:

$$\mathbf{M}(\omega) = \sum_k s_k(\omega) \mathbf{G}^k \quad (\text{A4})$$

With this idea, a set of matrices  $\{\mathbf{G}^k\}$  was calculated and stored only once at the beginning. Then the matrix  $\mathbf{M}(\omega)$  was calculated very rapidly at each photon energy  $\omega$ , as a linear combination of the  $\{\mathbf{G}^k\}$  matrices with the following coefficients:

$$s_k(\omega) = \frac{4\bar{E}_k}{\omega^2 - \bar{E}_k^2} \quad (\text{A5})$$

where in Equation (A5)  $\bar{E}_k$  refers to the centre of the interval which discretizes the excitation energy variable and in the original formulation corresponds to the difference between virtual and occupied orbital energies:  $\varepsilon_a - \varepsilon_i$ .

In order to introduce the complex polarizability method to calculate the CD of large clusters, we briefly recall the basic theory of CD. For a molecule with fixed orientation, the CD of an electronic transition from the ground state  $|0\rangle$  to the  $n$ -th excited state  $|n\rangle$  corresponds to the difference between the absorbance of left and right circularly polarized light, which propagates along the X direction as follows [33]:

$$CD = A_L - A_R = 2\gamma \text{Im}(\langle 0 | \mu_Y | n \rangle \langle n | m_Z | 0 \rangle + \langle 0 | \mu_Z | n \rangle \langle n | m_Y | 0 \rangle) \quad (\text{A6})$$

where in (6)  $\mu$  and  $\mathbf{m}$  are the electric dipole and magnetic dipole moment operators and  $\gamma$  is a constant.

In solution or in the gas phase molecules are randomly oriented, thus Equation (A6) must be rotationally averaged, and the Rosenfeld equation is obtained:

$$CD = \frac{4}{3}\gamma \text{Im}(\langle 0|\boldsymbol{\mu}|n\rangle \cdot \langle n|\mathbf{m}|0\rangle) \quad (\text{A7})$$

The rotatory strength,  $R_{0n}$ , is therefore defined as follows:

$$R_{0n} = \text{Im}(\langle 0|\boldsymbol{\mu}|n\rangle \cdot \langle n|\mathbf{m}|0\rangle) \quad (\text{A8})$$

To calculate  $R_{0n}$  by the complex polarizability algorithm [30], it is convenient to consider the dipole moment induced by an electromagnetic field [34]:

$$\boldsymbol{\mu}'_u = \sum_v \alpha_{uv} E_v - \sum_v \frac{\beta_{uv}}{c} \frac{\partial B_v}{\partial t}. \quad (\text{A9})$$

In Equation (A9)  $E_v$  and  $B_v$  are the electric and magnetic field components,  $c$  is the speed of light,  $\alpha$  is the dynamical polarizability tensor and  $\beta$  is the optical rotation tensor, which is related to the rotatory strength by the following sum over states (SOS) expression:

$$\bar{\beta} = \frac{1}{3} \sum_u \beta_{uu} = \frac{2c}{3} \sum_n \frac{R_{0n}}{\omega_{0n}^2 - \omega^2} \quad (\text{A10})$$

In Equation (A10)  $\omega$  is the photon energy and  $\omega_{0n}$  corresponds to the  $|0\rangle \rightarrow |n\rangle$  excitation energy. Therefore, it is convenient to extract  $R_{0n}$  from the  $\beta$  imaginary part as in conventional photoabsorption. From Equation (A9),  $\beta$  consists in the electric dipole moment induced by a time-dependent (TD) magnetic field and can be calculated by the following expression:

$$\beta_{zz}(\omega) = \left(-\frac{ic}{\omega}\right) \sum_i^{occ} \sum_a^{virt} \langle \phi_i | m_z | \phi_a \rangle \bar{P}_i^a \quad (\text{A11})$$

with

$$\bar{P}_i^a = t_k(\omega) \left[ \langle \phi_a | \mu_z | \phi_i \rangle + \sum_{\mu\tau}^{fit} \left(A^k\right)_{ia,\mu}^+ L_{\mu\tau} b_\tau \right] \quad (\text{A12})$$

In Equations (A11) and (A12), the  $A_{\mu,ia}^k$  are integrals between the auxiliary fitting function  $f_\mu$  and the product between the  $i$ -th occupied and the  $a$ -th virtual orbitals,  $\phi_i | \mu_z | \phi_a$  and  $\phi_i | m_z | \phi_a$  are the electric and magnetic dipole moment matrix elements respectively, between the same occupied-virtual ( $ia$ ) orbitals pair, the matrix  $\mathbf{L}$  is defined by Equation (28) of Ref. [31],  $t_k$  is given by:

$$t_k(\omega) = \frac{1}{\omega - \omega_{0n} + i\varepsilon} + \frac{1}{\omega + \omega_{0n} + i\varepsilon} \quad (\text{A13})$$

and the vector  $\mathbf{b}$  is the solution of the linear system (2).

In practice, the resolution of the TDDFT equations is recast to the linear system (2) (see Ref. [30] for a detailed description), which was already solved to calculate the photoabsorption, so the CD calculation is computationally irrelevant. It is worth noting that the linear system (2) was solved by employing the auxiliary density fitting functions as a basis set to represent vectors and matrices. This means that the dimension of (2) was much smaller with respect to the Casida approach.

Equation (A2) was then solved point by point for each photon energy. Moreover, the real part of the photon energy was supplemented with a small imaginary part, thus generating a Lorentzian broadening of the discrete transition.

### Appendix A.2. Individual Component Maps of Rotatory Strength (ICM-RS) Analysis

Recently, an analysis tool of the absorption spectra derived from TDDFT simulation has been proposed [35], i.e., individual component maps of oscillatory strength (ICM-OS) plots, which allows one to investigate the connection between absorption and single-particle excitations (ICM-OS). This field is subject to intense research efforts, and there are currently many efforts to find a proper method to rationalize CD (or in general spectral features) obtained from response calculations [36].

The same approach has been extended from the oscillator strength to the rotator strength, so in an analogous way we defined individual component maps of rotatory strength (ICM-RS) plots [24] as analysis tools of chiro-optical linear response spectra derived from TDDFT simulations. Starting with the expression of rotator strength at each given frequency (z component) calculated as the imaginary part of the zz diagonal element of the circular dichroic tensor:

$$CD_z(\omega) = -\frac{3\varepsilon}{2} \operatorname{Re} \left( \sum_i^{\text{occ}} \sum_a^{\text{virt}} \langle \phi_i | m_z | \phi_a \rangle \bar{P}_i^a[z] \right) \quad (\text{A14})$$

where in Equation (A14)  $\varepsilon$  corresponds to the Lorentzian energy broadening,  $\bar{P}_i^a$  is the density-matrix element given by previous Equation (A12), due to the perturbation induced by the z-component of the electric dipole, and  $\phi_i | m_z | \phi_a$  is the matrix elements of the magnetic dipole over a pair of occupied/virtual single-particle molecular orbitals. Then the plot of the individual  $\phi_i | m_z | \phi_a \bar{P}_i^a[z]$  components as functions of the single-particle energies of occupied ( $\varepsilon_i$ ) and virtual ( $\varepsilon_a$ ) orbitals is generated. ICM-RS ( $\omega$ ) plots allow one to visualize the source of chiral response in momentum space, including signed contributions, therefore highlighting cancellation terms that are ubiquitous and critical in chiral phenomena.

### Appendix A.3. Computational Details

The geometry of the single gold nanowire (5,3)NT has been taken from our previous work, see Figure 1 in Ref. [23]. The DFT calculations have been performed with a Triple Zeta plus Polarization (TZP) basis set of Slater Type Orbitals (STO) functions. The LB94 [37] exchange-correlation (XC) potential with the correct asymptotic behaviour has been employed. All the systems considered in this work belong to the  $C_2$  point group, the z axis being the binary rotation axis, such symmetry has been exploited in the calculations. Core electrons have been kept frozen up to the Au 4f level. Relativistic effects have been considered at scalar level employing the zero order regular approximation (ZORA) level [38].

The TDDFT equations have been solved by means of the polTDDFT method [30,31] assuming adiabatic local density approximation for the response XC kernel.

In the polTDDFT scheme we have divided the excitation energy in intervals with a step of 0.025 eV and a cutoff of 2 eV above the excitation energy has proven accurate. An imaginary part of 0.060 eV has been employed in the photon energy, corresponding to an intrinsic Lorentzian broadening of the same HWHM value.

All the calculations have been performed with the AMS-ADF suite of programs [39].

## References

- Zhang, C.; Noguez, J.Z. Plasmonic Optical Properties and Applications of Metal Nanostructures. *Plasmonics* **2008**, *3*, 127–150. [CrossRef]
- Rycenga, M.; Cobley, C.M.; Zeng, J.; Li, W.; Moran, C.H.; Zhang, Q.; Qin, D.; Xia, Y. Controlling the Synthesis and Assembly of Silver Nanostructures for Plasmonic Applications. *Chem. Rev.* **2011**, *111*, 3669–3712. [CrossRef]
- Durante, N.; Fortunelli, A.; Broyer, M.; Stener, M. Optical properties of Au nanoclusters from TD-DFT calculations. *J. Phys. Chem. C* **2011**, *115*, 6277–6282. [CrossRef]
- Langer, J.; Jimenez de Aberasturi, D.; Aizpurua, J.; Alvarez-Puebla, R.A.; Auguie, B.; Baumberg, J.J.; Bazan, G.C.; Bell, S.E.J.; Boisen, A.; Brolo, A.G.; et al. Present and Future of Surface-Enhanced Raman Scattering. *ACS Nano* **2020**, *14*, 28–117. [CrossRef]

5. Barbry, M.; Koval, P.; Marchesin, F.; Esteban, R.; Borisov, A.G.; Aizpurua, J.; Sánchez-Portal, D. Atomistic Near-Field Nanoplasmonics: Reaching Atomic-Scale Resolution in Nanooptics. *Nano Lett.* **2015**, *15*, 3410–3419. [[CrossRef](#)]
6. Sementa, L.; Marini, A.; Negreiros, F.R.; Fortunelli, A. Atomistic Quantum Plasmonics of Gold Nanowire Arrays. *ACS Photonics* **2014**, *1*, 315–322. [[CrossRef](#)]
7. Phan, Q.-H.; Lo, Y.-L.; Huang, C. L Surface plasmon resonance prism coupler for enhanced circular dichroism sensing. *Opt. Exp.* **2016**, *24*, 12812–12824. [[CrossRef](#)]
8. Bernadotte, S.; Evers, F.; Jacob, C.R. Plasmons in molecules. *J. Phys. Chem. C* **2013**, *117*, 1863–1878. [[CrossRef](#)]
9. Zhang, R.; Bursi, L.; Cox, J.D.; Cui, Y.; Krauter, C.M.; Alabastri, A.; Manjavacas, A.; Calzolari, A.; Corni, S.; Molinari, E.; et al. How To Identify Plasmons from the Optical Response of Nanostructures. *ACS Nano* **2017**, *11*, 7321–7335. [[CrossRef](#)] [[PubMed](#)]
10. Sinha-Roy, R.; García-González, P.; Weissker, H.-C.; Rabilloud, F.; Fernández-Domínguez, A.I. Classical and ab Initio Plasmonics Meet at Sub-nanometric Noble Metal Rods. *ACS Photonics* **2017**, *4*, 1484–1493. [[CrossRef](#)]
11. Mokka, J.H.; Schwingschlögl, U. Optical properties of Al nanostructures from time dependent density functional theory. *J. Chem. Phys.* **2016**, *144*, 134305. [[CrossRef](#)] [[PubMed](#)]
12. Halas, N.J.; Lal, S.; Chang, W.-S.; Link, S.; Nordlander, P. Plasmons in Strongly Coupled Metallic Nanostructures. *Chem. Rev.* **2011**, *111*, 3913–3961. [[CrossRef](#)]
13. Kameta, N.; Masuda, M.; Shimizu, T. Qualitative/chiral sensing of amino acids by naked-eye fluorescence change based on morphological transformation and hierarchizing in supramolecular assemblies of pyrene-conjugated glycolipids. *Chem. Commun.* **2015**, *51*, 11104–11107. [[CrossRef](#)] [[PubMed](#)]
14. Pelayo, J.J.; Valencia, I.; García, A.P.; Chang, L.; López, M.; Toffoli, D.; Stener, M.; Fortunelli, A.; Garzón, I.L. Chirality in bare and ligand-protected metal nanoclusters. *Adv. Phys. X* **2018**, *3*, 1. [[CrossRef](#)]
15. Karimova, N.; Aikens, C.M. Time-Dependent Density Functional Theory Investigation of the Electronic Structure and Chiroptical Properties of Curved and Helical Silver Nanowires. *J. Phys. Chem. A* **2015**, *119*, 8163–8173. [[CrossRef](#)]
16. Nguyen, L.; Dass, M.; Ober, M.F.; Besteiro, L.V.; Wang, Z.M.; Nickel, B.; Govorov, A.O.; Liedl, T.; Heuer-Jungemann, A. Chiral Assembly of Gold–Silver Core–Shell Plasmonic Nanorods on DNA Origami with Strong Optical Activity. *ACS Nano* **2020**, *14*, 7454–7461. [[CrossRef](#)] [[PubMed](#)]
17. Slocik, J.M.; Dennis, P.B.; Govorov, A.O.; Bedford, N.M.; Ren, Y.; Naik, R.R. Chiral Restructuring of Peptide Enantiomers on Gold Nanomaterials. *ACS Biomater. Sci. Eng.* **2020**, *6*, 2612–2620. [[CrossRef](#)]
18. Hu, Z.; Meng, D.; Lin, F.; Zhu, X.; Fang, Z.; Wu, X. Plasmonic Circular Dichroism of Gold Nanoparticle Based Nanostructures. *Adv. Opt. Mater.* **2019**, *7*, 1801590. [[CrossRef](#)]
19. Fan, Z.; Govorov, A.O. Chiral Nanocrystals: Plasmonic Spectra and Circular Dichroism. *Nanoletters* **2012**, *12*, 3283–3289. [[CrossRef](#)]
20. Zeng, C.; Chen, Y.; Liu, C.; Nobusada, K.; Rosi, N.L.; Jin, R. Gold tetrahedra coil up: Kekulé-like and double helical superstructures. *Sci. Adv.* **2015**, *1*, e1500425. [[CrossRef](#)]
21. Khorashad, L.K.; Besteiro, L.V.; Correa-Duarte, M.A.; Burger, S.; Wang, Z.M.; Govorov, A.O. Hot Electrons Generated in Chiral Plasmonic Nanocrystals as a Mechanism for Surface Photochemistry and Chiral Growth. *J. Am. Chem. Soc.* **2020**, *142*, 4193–4205. [[CrossRef](#)] [[PubMed](#)]
22. Fang, Y.; Verre, R.; Shao, L.; Nordlander, P.; Käll, M. Hot Electron Generation and Cathodoluminescence Nanoscopy of Chiral Split Ring Resonators. *Nano Lett.* **2016**, *16*, 5183–5190. [[CrossRef](#)] [[PubMed](#)]
23. Toffoli, D.; Russi, A.; Fronzoni, G.; Coccia, E.; Stener, M.; Sementa, L.; Fortunelli, A. Circularly Polarized Plasmons in Chiral Gold Nanowires via Quantum Mechanical Design. *J. Phys. Chem. Lett.* **2021**, *12*, 5829–5835. [[CrossRef](#)]
24. Chang, L.; Baseggio, O.; Sementa, L.; Cheng, D.; Fronzoni, G.; Toffoli, D.; Aprà, E.; Stener, M.; Fortunelli, A. Individual Component Map of Rotatory Strength and Rotatory Strength Density plots as analysis tools of circular dichroism spectra of complex systems. *J. Chem. Theory Comput.* **2018**, *14*, 3703–3714. [[CrossRef](#)] [[PubMed](#)]
25. Ajori, S.; Parsapour, H.; Ansari, R. A molecular dynamics study on the buckling behavior of single-walled carbon nanotubes filled with gold nanowires. *J. Mol. Modeling* **2020**, *26*, 196. [[CrossRef](#)] [[PubMed](#)]
26. Oshima, Y.; Onga, A.; Takayanagi, K. Helical Gold Nanotube Synthesized at 150 K. *Phys. Rev. Lett.* **2003**, *91*, 205503. [[CrossRef](#)]
27. Senger, R.T.; Dag, S.; Ciraci, S. Chiral Single-Wall Gold Nanotubes. *Phys. Rev. Lett.* **2004**, *93*, 196807. [[CrossRef](#)]
28. Autschbach, J.; Ziegler, T. Calculating Molecular Electric and Magnetic Properties from Time-Dependent Density Functional Response Theory. *J. Chem. Phys.* **2002**, *116*, 891. [[CrossRef](#)]
29. Casida, M.E. *Recent Advances in Density-Functional Methods*; Chong, D.P., Ed.; World Scientific: Singapore, 1995; p. 155.
30. Baseggio, O.; Fronzoni, G.; Stener, M. A New Time Dependent Density Functional Algorithm for Large Systems and Plasmons in Metal Clusters. *J. Chem. Phys.* **2015**, *143*, 024106. [[CrossRef](#)]
31. Baseggio, O.; Toffoli, D.; Fronzoni, G.; Stener, M.; Sementa, L.; Fortunelli, A. Extension of the Time-Dependent Density Functional Complex Polarizability Algorithm to Circular Dichroism: Implementation and Applications to Ag<sub>8</sub> and Au<sub>38</sub>(SC<sub>2</sub>H<sub>4</sub>C<sub>6</sub>H<sub>5</sub>)<sub>24</sub>. *J. Phys. Chem. C* **2016**, *120*, 24335. [[CrossRef](#)]
32. Baseggio, O.; De Vetta, M.; Fronzoni, G.; Stener, M.; Fortunelli, A. A New Time-Dependent Density-Functional Method for Molecular Plasmonics: Formalism, Implementation, and the Au<sub>144</sub>(SH)<sub>60</sub> Case Study. *Int. J. Quantum Chem.* **2016**, *116*, 1603. [[CrossRef](#)]
33. Rodger, A.; Nordén, B. *Circular Dichroism & Linear Dichroism*; Oxford University Press: Oxford, UK, 1997.

34. Buckingham, A.D. Permanent and Induced Molecular Moments and Long-Range Intermolecular Forces. *Adv. Chem. Phys.* **1967**, *12*, 107.
35. Theivendran, S.; Chang, L.; Mukherjee, A.; Sementa, L.; Stener, M.; Fortunelli, A.; Dass, A. Principles of Optical Spectroscopy of Aromatic Alloy Nanomolecules:  $\text{Au}_{36-x}\text{Ag}_x(\text{SPh-tBu})_{24}$ . *J. Phys. Chem. C* **2018**, *122*, 4524. [[CrossRef](#)]
36. de Wergifosse, M.; Grimme, S. A Unified Strategy for the Chemically Intuitive Interpretation of Molecular Optical Response Properties. *J. Chem. Theory Comput.* **2020**, *16*, 7709. [[CrossRef](#)] [[PubMed](#)]
37. van Leeuwen, R.; Baerends, E.J. Exchange-correlation potential with correct asymptotic behavior. *Phys. Rev. A* **1994**, *49*, 2421. [[CrossRef](#)] [[PubMed](#)]
38. Wang, F.; Ziegler, T.; van Lenthe, E.; van Gisbergen, S.; Baerends, E.J. The calculation of excitation energies based on the relativistic two-component zeroth-order regular approximation and time-dependent density-functional with full use of symmetry. *J. Chem. Phys.* **2005**, *122*, 204103. [[CrossRef](#)] [[PubMed](#)]
39. Velde, G.t.; Bickelhaupt, F.M.; Baerends, E.J.; Guerra, C.F.; van Gisbergen, S.J.A.; Snijders, J.G.; Ziegler, T. Chemistry with ADF. *J. Comput. Chem.* **2001**, *22*, 931. [[CrossRef](#)]

This document is confidential and is proprietary to the American Chemical Society and its authors. Do not copy or disclose without written permission. If you have received this item in error, notify the sender and delete all copies.

**Coupling between Plasmonic and Molecular Excitations:  
TDDFT Investigation of an Ag-Nanorod/BODIPY-Dye  
Interaction**

Journal:	<i>The Journal of Physical Chemistry</i>
Manuscript ID	jp-2022-04168u
Manuscript Type:	Special Issue Article
Date Submitted by the Author:	16-Jun-2022
Complete List of Authors:	Medves, Marco; Universita degli Studi di Trieste Toffoli, Daniele; Universita degli Studi di Trieste, Stener, Mauro; Universita degli Studi di Trieste, Dipartimento di Scienze chimiche Sementa, Luca; CNR, IPCF Fortunelli, Alessandro; CNR, ICCOM

SCHOLARONE™  
Manuscripts

# Coupling between Plasmonic and Molecular Excitations: TDDFT Investigation of an Ag-Nanorod/BODIPY-Dye Interaction

Marco Medves<sup>1</sup>, Daniele Toffoli<sup>1</sup>, Mauro Stener<sup>1,\*</sup>, Luca Sementa<sup>2</sup>, and Alessandro Fortunelli<sup>2,\*</sup>

<sup>1</sup>Dipartimento di Scienze Chimiche, Università di Trieste, Via L. Giorgieri 1, 34127 Trieste, Italy.

<sup>2</sup>CNR-ICCOM & IPCF, Consiglio Nazionale delle Ricerche, via G. Moruzzi 1, Pisa, 56124, Italy.

## Abstract

A time-dependent density functional theory (TDDFT) computational approach is employed to study the optical coupling between a plasmonic system (a Ag<sub>50</sub> nanorod) and a fluorescent dye (BODIPY). It is found that the BODIPY dye can interact with a plasmonic systems in a rather different and selective way according to the mutual orientation of the fragments. Indeed, (i) the plasmon excitation turns out to be sensitive to the presence of the BODIPY transition and (ii) this can lead to amplify or suppress the resonance accordingly to the relative orientation of the corresponding transition dipoles. To understand the coupling mechanism, we analyse the shape of the induced density in real space and the Individual Component Map of the Oscillator Strength (ICM-OS) plots, and achieve a simple rationalization and insight on the origin and features of the coupling. The resulting possibility of understanding plasmon/fluorophore interactions by simple qualitative arguments opens the way to a rational design of hybrid (plasmon + dye) systems with the desired optical behaviour.

\*Corresponding authors' email: stener@units.it (MS) and alessandro.fortunelli@cnr.it (AF)

## 1. Introduction

Fluorescence of molecular dyes<sup>1</sup> is a phenomenon that has a wide range of applications in several diverse fields, ranging from biology and medicine (sensing, imaging)<sup>2,3</sup>, to food analysis<sup>4</sup> as well as optoelectronic devices<sup>5 - 7</sup>, etc. Among the class of fluorescent dyes, 4,4-difluoro-4-bora-3a,4a-diaza-s-indacene, commercially known as BODIPY, is one of the most robust and versatile compound, giving rise to a large and extensively employed family of derivative species<sup>8 - 10</sup>. Of great current interest in this field are the effects arising from the interaction between fluorescent molecules with semiconductor or metal nanoparticles<sup>11 - 14</sup>. The coupling of extended and sometimes collective resonant excitations in the nanostructures with the localized excited states of the fluorescent molecule can give rise to varied and subtle phenomena, such as energy transfer processes, that can e.g. enhance or in general finely tune (also anisotropically) the absorption cross-section of the system<sup>15 - 18</sup> or quench the fluorescence signal by surface energy transfer with the metal nanostructure<sup>19</sup>, thus greatly extending the scope of potential applications. Although the basic concepts and theoretical framework of these phenomena have been established<sup>20 - 22</sup>, the number of possible combinations of different systems and the need to understand the details of the nanostructure/fluorophore interaction to be able to properly control the final response together with new effects arising e.g. in the strong coupling régime, etc.<sup>23,24</sup> make that investigations in this field represent an active topic of current research<sup>2</sup>. An ideal tool to provide a rigorous ground to such investigations is via predictive simulations<sup>25,26</sup>, whose controlled accuracy can simultaneously cross-validate experimental results in complex systems thus helping their interpretation<sup>27</sup>, as well as suggest configurations and combinations<sup>28</sup> which would otherwise be difficult to single out even from high-throughput techniques<sup>29</sup>, or explore exotic confinement effects on the interaction between electromagnetic cavity fields and quantum emitters<sup>30</sup>. To this purpose, among the possible theoretical approaches time-dependent density functional theory (TDDFT)<sup>31 - 33</sup> currently represents the most convenient and effective compromise between accuracy and computational effort<sup>34</sup>. Although the exact prediction of the excitation spectrum of some fluorescent dyes, including BODIPY, presents accuracy issues at the TDDFT level and alternative post-Hartree-Fock methods have been proposed to overcome these issues,<sup>35</sup> in addition to including possible effects such as solvent<sup>36</sup>, the possibility of treating systems of realistic dimensions<sup>37</sup> that is offered by recent software and TDDFT algorithmic advances<sup>38 - 40</sup> makes of TDDFT the method of choice for shedding theoretical light on the coupling of plasmonic-nanostructure/fluorophore optical excitations.

Here we follow such line of research, and investigate at the TDDFT level system composed of BODIPY and a model of a plasmonic metal nanorod (Ag<sub>50</sub>). We have selected BODIPY as one

of the most common fluorophores, and a silver nanostructure (in particular a Ag<sub>50</sub> nanorod) because this element supports plasmons already at small cluster size, typically already with few tens of atoms. We investigate different configurations of the two fragments and try to analyze/understand the interaction mechanisms between the plasmon and the dye excitations. We find that the interaction is significant only when the transition dipole of the dye excitation is parallel to the plasmonic one. The interaction can be constructive or destructive, i.e., it can increase or decrease the intensity of the plasmon resonance, and which of these two opposite effects is predominant can be discriminated and predicted by inspecting the induced density plots at the excitation energy, where a parallel or antiparallel interaction among the corresponding dipoles corresponds to an increase or a decrease, respectively, in the absorption intensity.

The article is structured as follows. In Section 2 we describe briefly the theoretical methods employed in our calculations. In Section 3, the results are presented and discussed, as grouped in three sections: free BODIPY, free plasmonic Ag<sub>50</sub>, and the adduct BODIPY-Ag<sub>50</sub>. Finally the conclusions are given.

## 2. Theoretical methods and computational details

Initial atomistic configurations of the Ag<sub>50</sub> plasmonic cluster were taken from a previous work on Au nanowires<sup>41</sup>, simply by substituting the element Au with Ag in the Au<sub>50</sub> <110> nanowire. For BODIPY we employed the experimental geometry from Ref. <sup>42</sup>.

Photoabsorption spectra were evaluated using the Casida formalism<sup>31</sup> as well as the complex polarizability algorithm<sup>43</sup>, both available in the ADF program<sup>44</sup>. In the complex polarizability algorithm, the absorption spectrum is extracted from the imaginary part of the complex dynamical polarizability, solving the TDDFT equations over the space of the density instead of the occupied-virtual pairs of the density matrix. The induced time-dependent density is represented employing an auxiliary basis set of Slater Type Orbitals (STO).<sup>43,45</sup> Such method (referred to as complex polarizability TDDFT algorithm, or polTDDFT) has proven to be efficient to describe metal particles with many hundreds of atoms.<sup>46</sup>

It is worth noting that in the present work we consider two fragments at different distances, and this may represent a delicate issue in terms of accuracy due to the numerical integration employed in ADF. We carefully checked this point and found that the default integration scheme based on Becke Fuzzy Cells<sup>47</sup> is quite accurate and robust when the distance between the two fragments is varied. On the contrary, we noticed that the Voronoi grid<sup>48</sup> scheme is less robust, and the Voronoi integration technical parameters need a very careful fine-tuning in order to obtain accurate results.

1  
2  
3 We thus employed the default Becke Fuzzy Cells as numerical integration scheme. The numerical  
4 robustness of the simulation is further corroborated by the regular behavior of the transition  
5 intensity with distance, see the discussion below.  
6  
7

8 The BP86 exchange-correlation (xc-) functional<sup>49,50</sup> is chosen to solve the KS equations while  
9 the Adiabatic Local Density Approximation<sup>51</sup> (ALDA) is used in the TDDFT part for the exchange-  
10 correlation kernel. The basis set employed is included in the ADF code and consists in Slater Type  
11 Orbitals (STO) of Triple- $\zeta$  Polarized (TZP) quality for H atom and with Frozen Core (FC) of 1s  
12 shell for B, C, N and F atoms, while for Ag a DZ basis with FC up to 4p shell has been employed.  
13  
14  
15  
16

17 Although relativistic effects are rather weak for Ag, we have employed the Zero Order Regular  
18 Approximation (ZORA) to include relativistic effects at the scalar level in the calculations<sup>52</sup>.  
19

20 In terms of analysis tools, we have used two complementary ones.  
21

22 The Individual Component Map of the Oscillator Strength (ICM-OS)<sup>53</sup> tool has been employed  
23 to analyze and better understand the features of electronic transitions. This tool allows one to  
24 decompose a specific absorption peak in terms of electronic transitions labeled by the energy of the  
25 occupied (x-axis) and virtual (y-axis) orbitals involved. Briefly, the diagonal line formed by the  
26 most intense features in the ICM-OS plots corresponds to the energy of the exciting photon  
27 (indicated above each plot), which results from the energy difference between virtual and occupied  
28 molecular orbitals. Therefore, spots on the diagonal correspond to single-particle excitations,  
29 whereas the presence of off-diagonal features indicates a collective behaviour typical of plasmons.  
30 These collective plasmonic features are characterized by occupied and virtual orbitals with smaller  
31 energy differences than the analyzed excitation energy, indicating that the excitation involves more  
32 than one single-particle excitation. Importantly, in addition to the weight of each pair of orbitals in  
33 the oscillator strength, ICM-OS also accounts for the signs of the associated dipole contributions,  
34 which may result in constructive or destructive interferences among excited configurations.  
35  
36  
37  
38  
39  
40  
41  
42  
43

44 In this work we have also analyzed the induced density associated of selected excitations, which  
45 has proven to be very informative in order to discriminate between constructive and destructive  
46 interactions of the two interacting systems with a concomitant increase or decrease of the intensity,  
47 respectively. The induced density consists in the time-dependent first-order perturbation of the  
48 electron density as an effect of the external time-dependent electromagnetic field. This quantity is a  
49 fundamental ingredient of the complex polarizability algorithm and can be conveniently plotted for  
50 analysis as a 3D isosurface with a phase (positive and negative induced density means electron  
51 density accumulation or depletion respectively).  
52  
53  
54  
55  
56  
57  
58  
59  
60

### 3. Results and discussion

Our goal in the present study is assessing the mechanisms of interaction between a plasmon resonance and the molecular transitions of a fluorescent dye. For the dye, we have chosen BODIPY due to its major role in many photochemical processes<sup>8,9</sup>. As a model plasmonic system, we have chosen a silver nanorod (Ag<sub>50</sub>) because, as recalled in the introduction, silver supports plasmonic excitations already in structures of small size, typically few tens of atoms, at variance with gold which needs larger sizes<sup>54</sup>. As well known, this is due to the presence in gold of the quenching effect of the 5d band<sup>55</sup>, whereas in silver the 4d band is deeper and does not suppress the plasmon. The size and shape of Ag<sub>50</sub> has been chosen because for this nanocluster the plasmon resonance falls at the same energy as that of the lowest transition of the BODIPY, and this is expected to maximize their mutual interaction: we note however that, in general, it is easy to tune Ag nanorods to give the desired plasmon frequency to maximally interact with other transitions<sup>56-58</sup>. We start by briefly describing the excitation spectra of the isolated systems, then we couple them in a system which we shall designate as the adduct, and analyse and try to rationalize the changes occurred upon interaction. In the interaction system, the two fragments have been positioned in different mutual orientations, in order to have the dipole transition density of the BODIPY pointing towards or away from the nanorod, and at different distances.

#### 3.1. The BODIPY excitation spectrum

The three lowest TDDFT excitations of the BODIPY molecule calculated using the Casida approach<sup>31</sup> are reported in Table 1, while in Figure 1 we report the optical absorption spectrum calculated using two different methods: the Casida approach<sup>31</sup> and the polTDDFT method<sup>43</sup>, where the latter is an approximation of TDDFT that enables us to perform calculations on large systems such as those involving a nanorod. In Figure 1 we use the label of the  $C_{2V}$  point group symmetry to classify excitations and molecular orbitals, while the BODIPY structure is reported at the top of Figure 2, together with the main orbitals (the occupied  $3a_2$ ,  $4a_2$ , and  $6b_1$ , and the virtual  $7b_1$ ) involved in the low-energy excited states. Note that the  $C_2$  axis corresponds to the  $z$  direction, while the molecular plane lies in the  $yz$  plane (actually only the two F atoms do not belong to this plane). The lowest-energy  $1B_2$  transition corresponds to the  $y$  component of the electric dipole, and its assignment shows that it can be ascribed as a linear combination of two one-electron excited configurations: 55%  $3a_2(\text{HOMO}-1) \rightarrow 7b_1(\text{LUMO})$  and 44%  $4a_2(\text{HOMO}) \rightarrow 7b_1(\text{LUMO})$ . As apparent from Figure 2 where schematic depictions of these molecular orbitals are reported, they are all  $\pi$  orbitals, the molecular plane being nodal. The lowest-energy  $1B_2$  transition finds its counterpart in the third  $2B_2$  transition, that not only has the same symmetry, but also has a similar

percent composition in terms of the same two excited configurations. We can obtain a qualitative but very useful understanding of such configuration mixing by looking at the induced density plots reported at the bottom of Figure 1: while for the  $2B_2$  excitation a typical dipolar shape along the y direction is apparent, for the  $1B_1$  it seems that two dipoles with opposite direction are interpenetrating each other. This finding has a simple interpretation: when the dipoles have opposite direction their energy is lower due to the stabilizing effect between charges of opposite sign, but concomitantly the oscillator strength is lower due to the destructive interference between the dipoles. This clearly rationalizes why the interpenetrating induced density corresponds to a lower excitation energy and a lower intensity in Figure 1. The second  $1A_1$  transition (see Table 1) corresponds to the z component of the electric dipole transition moment, it has an almost pure (97%)  $6b_1(\text{HOMO}-2) \rightarrow 7b_1(\text{LUMO})$  nature, but has a negligible intensity due to the reduced extension of the molecule along the z direction. We also note that the energy of the TDDFT-calculated lowest vertical excitation energy (3.00 eV) is overestimated with respect to the experimental value (2.46 eV)<sup>42</sup>. As recalled in the introduction, such a discrepancy is well known: previous *ab-initio* studies on BODIPY and its derivatives<sup>59,60</sup> have shown that this shortcoming is not related to the choice of the exchange-correlation functional within TDDFT, but rather is intrinsic to the TDDFT single-particle excitation formalism (only one-electron excited configurations are used in the description of the excited state), and that two-electron excited configurations must be included in the calculation in order to obtain accurate excitation energies. We underline, however, that the goal of the present work is not an accurate description of an experiment, but rather a fundamental investigation of the nature of interaction between a plasmonic and molecular excitations. To this end we must employ the same approach to describe the excited states of both the plasmonic system and the dye, and at the moment it is not computationally feasible to employ highly correlated post-Hartree-Fock *ab-initio* methods to treat plasmonic systems, which typically consist of a metal nanostructure containing several tens of metal atoms. We expect that the neglect of two-electron excitations will deteriorate only the energy position of the transitions, but will not change the global description of the coupling mechanism between the plasmon and the dye.

### 3.2. The $Ag_{50}$ excitation spectrum

In Figure 3 we report the excitation spectrum of  $Ag_{50}$  calculated using the polTDDFT method, together with induced density plots of the two major excitations reported at the bottom of Figure 3. The shape and the structure of  $Ag_{50}$  were constructed by following a suggestion taken from a previous work on gold nanowires<sup>41</sup>: with respect to these previously derived nanorod atomistic

arrangements, we simply tuned the length of the present Ag nanorod so that its plasmon falls at the same energy as the lowest-energy BODIPY absorption transition. Indeed, as apparent from Figure 3, the first intense absorption peak of Ag<sub>50</sub> falls nearly exactly at 3.00 eV. The plasmonic nature of this absorption peak is confirmed by the ICM-OS analysis, which is reported in Figure 4 for the *z* Cartesian component as 2D plot (upper panel) and 3D plot (lower panel). In fact in the 2D plot we find two spots that are considerably far from the straight line connecting orbital energy differences equal to excitation energies, thus indicating strong coupling among different single-particle excitations, while the 3D plot shows in a clearer way the absolute scale of the ICM-OS components. Moreover it can be observed that the shape of the induced density of the peak at 3 eV, reported in the bottom of Figure 3, displays a characteristic dipolar shape, typical of plasmons. The higher-energy peak at 3.76 eV exhibits about half the intensity of the main peak, and quite interestingly its induced density plot shows the interpenetration and thus the coupling of two parallel dipoles, located at different locations along the longitudinal cluster direction. We may describe this situation as a pair of plasmons, each one belonging to one half of the cluster, coupled to give constructive interference (sum) of their dipoles.

### 3.3. The BODIPY-Ag<sub>50</sub> longitudinal and lateral adducts: excitation spectrum

The interaction between the nanorod and the BODIPY will depend on their distance and the mutual orientation. To have a systematic picture, we have explored all the possible relative configurations, but here we will report explicitly only those giving the most noticeable effects. In general we noticed that the interaction effects are much larger when the BODIPY dipole component *y* of the most intense transitions (both with B<sub>2</sub> symmetry, see Figure 1) is parallel to the Ag<sub>50</sub> longitudinal direction, which is also the dipole orientation of the plasmon. This can be achieved in two different configurations: the longitudinal one (shown in the inset of Figure 5) and the lateral one (shown in the inset of Figure 7).

Starting with the longitudinal geometrical configuration, first, in Figure 5 we report two calculated absorption profiles: the absorption profile of the adduct system at a distance in which BODIPY is ‘touching’ the cluster, with a Ag-H distance of 1.507 Å, and the absorption profile obtained by summing the spectra of the isolated Ag<sub>50</sub> + BODIPY fragments. This direct comparison allows us to appreciate even tiny effects on the optical features of the plasmon excitation following interaction with the BODIPY. From Figure 5 it is well apparent that both peaks at 3.00 eV and 3.75 eV gain intensity with respect to sum of the isolated systems. Since the changes are of the order of 10-30% of the peak themselves, it is necessary to check that they are not due to numerical artefacts. Thus, in order to check the numerical stability of our approach, we have calculated the spectra at

1  
2  
3 various BODIPY/nanorod distances, and we have integrated the oscillator strength as a function of  
4 this distance. The results of this exercise are reported in Figure S1 of the Supplementary  
5 Information (SI). As apparent from Figure S1, we obtain a smooth evolution of the spectrum, thus  
6 validating the numerical stability of our approach. Note in passing that in practice it is enough to  
7 increase the distance between the two fragments by 10 Å to recover a spectrum that is practically  
8 identical to that of the sum of the isolated species, pointing to a fast decrease of the coupling with  
9 inter-separation distance.

10  
11 To better analyse these findings, we have plotted the induced densities corresponding to the two  
12 main absorption peaks, also reported at the bottom of Figure 5. It is apparent from these plots that  
13 the dipolar-like main excitations of the silver cluster sum up constructively with the dipolar-like  
14 excitation of the BODIPY (note the opposite colours at the touching sides): this explains why we  
15 observe a gain in the absorption intensity for both bands. A similar conclusion can be drawn by  
16 inspecting the ICM-OS plot, reported in Figure 6 for the main, lowest-energy peak along the  $z$   
17 Cartesian coordinate. From the 2D plot (upper panel in Figure 6), we find that the plasmonic peaks  
18 in the ICM-OS appear in the same region of the peaks observed in the previous Figure 4, but with a  
19 different intensity: in particular, the peaks associated with the virtual orbitals at higher energies  
20 acquire intensity with respect to the separated-fragment case, which is the main reason of the  
21 increase in total absorption strength. Additionally, the contribution of the interaction of the nanorod  
22 with BODIPY is also apparent in a small spot in the region of the BODIPY excitations, that we  
23 have highlighted with a white circle in Figure 6 (upper panel) to help the reader to identify its  
24 position. The BODIPY contribution can be identified even more clearly in the ICM-OS 3D plot  
25 (lower panel of Figure 6), this time it is included in a yellow circle. It is noteworthy and quite  
26 interesting that the BODIPY spot is weak in terms of ICM-OS contribution, so it cannot be  
27 considered as directly responsible for the increase in the intensity of the 3 eV band, but that the  
28 nanorod plasmonic spots are nevertheless amplified by the presence of the dye. We are lead to  
29 conclude that the intensity gain of the plasmonic peak is not due to the fact that the BODIPY  
30 absorption is summed with that of the silver cluster, but rather that the presence of the fluorophore  
31 makes the silver plasmon more intense due to coupling matrix elements which increase the electric  
32 dipole transition moment.

33  
34 Second, we consider the lateral configuration, and report the spectra of the adduct system in  
35 Figure 7: one at a distance in which BODIPY is almost 'touching' the cluster before the formation  
36 of a chemical bond and one obtained by summing the spectra of the isolated  $\text{Ag}_{50}$  + BODIPY  
37 fragments. Interestingly, for this interaction configuration we find a behaviour opposite to that  
38 observed for the longitudinal one: the first plasmonic peak is now strongly quenched, while the  
39  
40  
41  
42  
43  
44  
45  
46  
47  
48  
49  
50  
51  
52  
53  
54  
55  
56  
57  
58  
59  
60

1  
2  
3 second peak is still slightly amplified by the fluorophore/nanorod mutual interaction. Also in this  
4 case the induced densities reported at the bottom of Figure 7 help to explain and fully rationalize the  
5 observed behaviour. In the lowest-energy peak the excitation dipole of the BODIPY is antiparallel  
6 with respect to the plasmonic one, so that the intensity is finally reduced by about 35%. At variance,  
7 in the induced density plot corresponding to the second peak the excitation dipoles of the two  
8 fragments are parallel, so that the final intensity is slightly larger than that for the isolated systems.  
9 To further analyse and understand, the ICM-OS plot for the first peak of the lateral geometry is  
10 reported in Figure 8: the corresponding 2D plot in the upper panel shows that the BODIPY  
11 contribution is so weak that it cannot be identified. The 3D plot in the lower panel of Figure 8  
12 allows us to identify a very weak negative BODIPY contribution, which has been included in a  
13 yellow circle for sake of clarity, suggesting a suppressing effect (destructive interference). Also in  
14 this case this tiny destructive effect cannot explain the significant amount of plasmon quenching:  
15 rather, this can be ascribed to the fact, apparent in Figures 6 and 8, that the plasmonic spots are less  
16 intense than in the longitudinal geometry.  
17  
18  
19  
20  
21  
22  
23  
24  
25  
26  
27  
28

#### 29 **4. Conclusions**

30  
31 The goal of the present work is to investigate via TDDFT simulations the optical coupling  
32 between a plasmonic system (a Ag<sub>50</sub> nanorod) and a fluorescent dye (BODIPY), a topic with several  
33 perspective applications<sup>2 - 7</sup> and on which rigorous information is strongly needed. As a major  
34 outcome of this study, we have found that the BODIPY dye can interact with a plasmonic systems  
35 in a very different and selective way according to the mutual orientation of the fragments.  
36  
37  
38  
39

40 The plasmon excitations of Ag<sub>50</sub> (two major plasmonic peaks are found in the optical spectra of  
41 this nanorod) turned out to be sensitive to the presence of the BODIPY transition and can be  
42 amplified or suppressed accordingly to the relative orientation of the corresponding transition  
43 dipoles. We found that the alignment of the transition dipoles in the longitudinal configuration gives  
44 rise to a constructive interference and therefore to an enhancement of absorption intensity for both  
45 major plasmonic peaks of the nanorod, whereas in the case of the lateral arrangement the lowest-  
46 energy peak is quenched by an unfavourable interaction with the BODIPY excitations (destructive  
47 interference).  
48  
49  
50  
51  
52

53 We have then shown that the coupling mechanism responsible for these effects can be clearly  
54 and easily singled out and understood via two analysis tools: (i) by inspecting the shape of the  
55 induced density in real space and (ii) by analysing the ICM-OS plots in the space of one-electron  
56 excited configurations. The possibility of understanding plasmon/fluorophore interactions by simple  
57 arguments and physical observables which can be easily represented in real space, such as the  
58  
59  
60

1  
2  
3 induced density plots, or in momentum space, such as the ICM-OS plots, opens the way to a  
4 rational design of hybrid (plasmon + dye) systems with a desired optical behaviour. Moreover, the  
5 fact that it is possible to rationalize qualitatively the changes in absorption intensity in terms of  
6 simple interactions between dipoles, suggests that simplified models, for example based on exciton  
7 models, can be effective and efficient for predicting and for such rational design activity, a fact that  
8 is especially convenient for studying large and complex systems. In perspective, the present  
9 simulations provide thus the basis for a multi-scale modeling of complex materials composed of  
10 several plasmonic and BODIPY units simultaneously interacting, i.e. of a TDDFT-informed  
11 excitonic models describing the response of these systems<sup>27,61,62</sup>.

12  
13 Finally, a further promising perspective of the present line of research is to combine BODIPY  
14 compounds<sup>63</sup> (possibly functionalized so as to be chiral) with chiral nanowires,<sup>64 - 66</sup> thus achieving  
15 Circularly Polarized Luminescence<sup>67 - 69</sup>.

### 26 **Supporting Information**

27 The Supporting Information is available free of charge at <http://pubs.acs.org>.

28  
29 Integral of Oscillator Strength as a function of fragments distance. Cartesian coordinates of the  
30 longitudinal and lateral adducts at minimum distance.

### 34 **Acknowledgements**

35  
36 This work was supported by Stiftung Beneficentia and by Finanziamento per la Ricerca di Ateneo,  
37 (FRA) of the Università degli Studi di Trieste, Italy.

## References

- <sup>1</sup> Joseph R. Lakowicz, "Principles of Fluorescence Spectroscopy" (Springer US, Boston, 2006)
- <sup>2</sup> Bossi, M.; Fölling, J.; Belov, V. N.; Boyarskiy, V. P.; Medda, R.; Egner, A.; Eggeling, C.; Schönle, A.; Hell, S.W. Multicolor Far-Field Fluorescence Nanoscopy through Isolated Detection of Distinct Molecular Species *Nano Letters* **2008**, *8*, 2463-2468.
- <sup>3</sup> Wu, Z.; Jin, R. On the Ligand's Role in the Fluorescence of Gold Nanoclusters, *Nano Letters* **2010**, *10*, 2568-2573.
- <sup>4</sup> Christensen, J.; Nørgaard, L.; Bro, R.; Engelsen, S. B. Multivariate Autofluorescence of Intact Food Systems *Chemical Reviews* **2006**, *106*, 1979-1994.
- <sup>5</sup> Katz, E.; Itamar Willner, I. Integrated Nanoparticle–Biomolecule Hybrid Systems: Synthesis, Properties, and Applications, *Angew. Chem. Int. Ed.* **2004**, *43*, 6042-6108.
- <sup>6</sup> Cai, X.; Su, S.-J. Marching Toward Highly Efficient, Pure-Blue, and Stable Thermally Activated Delayed Fluorescent Organic Light-Emitting Diodes *Adv. Funct. Mater.* **2018**, *28*, 1802558.
- <sup>7</sup> Lee, J.-H.; Chen, C.-H.; Lee, P.-H.; Lin, H.-Y.; Leung, M.; Chiu T.-L.; Lin, C.-F. Blue organic light-emitting diodes: current status, challenges, and future outlook, *J. Mater. Chem. C*, **2019**, *7*, 5874-5888.
- <sup>8</sup> Karolin, J.; Johansson, L. B.-A.; Strandberg, L.; Ny, T. Fluorescence and Absorption Spectroscopic Properties of Dipyrrometheneboron Difluoride (BODIPY) Derivatives in Liquids, Lipid Membranes, and Proteins, *J. Am. Chem. Soc.* **1994**, *116*, 7801-7806.
- <sup>9</sup> Boens, N.; Verbelen, B.; Ortiz, M. J.; Jiao, L.; Dehaen, W. Synthesis of BODIPY dyes through postfunctionalization of the boron dipyrromethene core, *Coord. Chem. Rev.* **2019**, *399*, 213024.
- <sup>10</sup> Niu, S. L.; Ulrich, G.; Ziessel, R.; Kiss, A.; Renard, P.-Y.; Romieu, A. Water-Soluble BODIPY Derivatives *Org. Lett.* **2009**, *11*, 2049-2052.
- <sup>11</sup> Kazan, R.; Zhang, B.; Bürgi, T. Au<sub>38</sub>Cu<sub>1</sub>(2-PET)<sub>24</sub> nanocluster: synthesis, enantioseparation and luminescence *Dalton Trans.*, **2017**, *46*, 7708-7713.
- <sup>12</sup> Yu, Y.; Luo, Z.; Chevrier, D. M.; Leong, D. T.; Zhang, P.; Jiang, D.; Xie, J. Identification of a Highly Luminescent Au<sub>22</sub>(SG)<sub>18</sub> Nanocluster, *J. Am. Chem. Soc.* **2014**, *136*, 1246-1249.
- <sup>13</sup> Goswami, N.; Yao, Q.; Luo, Z.; Li, J.; Chen, T.; Xie, J. Luminescent Metal Nanoclusters with Aggregation-Induced Emission, *J. Phys. Chem. Lett.* **2016**, *7*, 962-975.
- <sup>14</sup> Jin, R.; Zeng, C.; Zhou, M.; Chen, Y. Atomically Precise Colloidal Metal Nanoclusters and Nanoparticles: Fundamentals and Opportunities *Chem. Rev.* **2016**, *116*, 10346-10413.
- <sup>15</sup> Medintz, I. L.; Mattoussi, H. Quantum dot-based resonance energy transfer and its growing application in biology, *Phys. Chem. Chem. Phys.*, **2009**, *11*, 17-45.
- <sup>16</sup> Beljonne, D.; Curutchet, C.; Scholes, G. D.; Silbey, R. J. Beyond Förster Resonance Energy Transfer in Biological and Nanoscale Systems *J. Phys. Chem. B* **2009**, *113*, 6583-6599.
- <sup>17</sup> Efros, A. L.; Nesbitt, D. J. Origin and control of blinking in quantum dots *Nature Nanotech* **2016**, *11*, 661-671.
- <sup>18</sup> Medintz, I. L.; Pons, T.; Susumu, K.; Boeneman, K.; Dennis, A. M.; Farrell, D.; Deschamps, J. R.; Melinger, J. S.; Bao, G.; Mattoussi, H. Resonance Energy Transfer Between Luminescent Quantum Dots and Diverse Fluorescent Protein Acceptors *J. Phys. Chem. C* **2009**, *113*, 18552-18561.
- <sup>19</sup> Riccardi, L.; Gabrielli, L.; Sun, X.; De Biasi, F.; Rastrelli, F.; Mancin, F.; De Vivo M. Nanoparticle-Based Receptors Mimic Protein-Ligand Recognition, *Chem.* **2017**, *3*, 92-109.
- <sup>20</sup> Fermi, E. Quantum theory of radiation. *Reviews of modern physics*, **1932**, *4*, 87.
- <sup>21</sup> Förster, Th. Zwischenmolekulare Energiewanderung und Fluoreszenz, *Annalen der Physik*, **1948**, *437*, 55-75.
- <sup>22</sup> Yeung M. S.; Gustafson, T. K. Spontaneous emission near an absorbing dielectric surface *Phys. Rev. A* **1996**, *54*, 5227.

- 23 Thomas, R.; Kumar, J.; George, J.; Shanthil, M.; Naidu, G. N.; Swathi, R. S.; Thomas, K. G. Coupling of Elementary Electronic Excitations: Drawing Parallels Between Excitons and Plasmons *J. Phys. Chem. Lett.* **2018**, *9*, 919-932.
- 24 Thomas, R.; Thomas, A.; Pullanchery, S.; Joseph, L.; Somasundaran, S. M.; Swathi, R. S.; Gray, S. K.; Thomas, K. G. Plexcitons: The Role of Oscillator Strengths and Spectral Widths in Determining Strong Coupling *ACS Nano* **2018**, *12*, 402-415.
- 25 Improta, R. Toward effective and reliable fluorescence energies in solution by a new state specific polarizable continuum model time dependent density functional theory approach *J. Chem. Phys.* **2007**, *127*, 074504.
- 26 Scalmani, G.; Frisch, M. J.; Mennucci, B.; Tomasi, J. Geometries and properties of excited states in the gas phase and in solution: Theory and application of a time-dependent density functional theory polarizable continuum model *J. Chem. Phys.* **2006**, *124*, 094107.
- 27 Fortunelli, A.; Stener, M. Optical Properties of Metal Nanoclusters—Theory, *Encyclopedia of Interfacial Chemistry, Surface Science and Electrochemistry* **2018**, Pages 534-545 (Elsevier).
- 28 Peruffo, N.; Gil, G.; Corni, S.; Mancin, F.; Collini, E. Selective switching of multiple plexcitons in colloidal materials: directing the energy flow at the nanoscale *Nanoscale*, **2021**, *13*, 6005-6015
- 29 Yamankurt, G.; Berns, E. J.; Xue, A.; Lee, A.; Bagheri, N.; Mrksich M.; Mirkin, C. A. Exploration of the nanomedicine-design space with high-throughput screening and machine learning *Nat. Biomed. Eng.* **2019**, *3*, 318–327.
- 30 Ciraci, C.; Jurga, R.; Khalid, M.; Della Sala F. Plasmonic quantum effects on single-emitter strong coupling *Nanophotonics*, **2019**, *8*, 1821-1833.
- 31 Casida, M. E. In Recent Advances in Density-Functional Methods; Chong, D. P., Ed.; World Scientific: Singapore, 1995; p 155.
- 32 Zhang, C.; Noguez, J.Z. Plasmonic Optical Properties and Applications of Metal Nanostructures. *Plasmonics* **2008**, *3*, 127–150.
- 33 Adamo, C.; Barone, V. Inexpensive and accurate predictions of optical excitations in transition-metal complexes: the TDDFT/PBE0 route, *Theor. Chem. Acc.* **2000**, *105*, 169–172.
- 34 Guillemoles, J.-F.; Barone, V.; Joubert, L.; Adamo, C. A Theoretical Investigation of the Ground and Excited States of Selected Ru and Os Polypyridyl Molecular Dyes *J. Phys. Chem. A* **2002**, *106*, 11354-11360.
- 35 Jacquemin, D.; Planchat, A.; Adamo, C.; Mennucci, B. *J. Chem. Theory Comput.* **2012**, *8*, 2359-2372.
- 36 Egidi, F.; Trani, F.; Ballone, P. A.; Barone, V.; Andreoni, W. Low-lying electronic excitations of a water-soluble BODIPY: from the gas phase to the solvated molecule *Theoret. Chem. Acc.* **2016**, *135*, 264.
- 37 Trani, F.; Scalmani, G.; Zheng, G.; Carnimeo, I.; Frisch, M. J.; Barone, V. Time-Dependent Density Functional Tight Binding: New Formulation and Benchmark of Excited States *J. Chem. Theory Comput.* **2011**, *7*, 3304-3313.
- 38 Medves, M.; Sementa, L.; Toffoli, D.; Fronzoni, G.; Fortunelli, A.; Stener M. An efficient hybrid scheme for time dependent density functional theory *J. Chem. Phys.* **2020**, *152*, 184104.
- 39 Asadi-Aghbolaghi, N.; Rüger, R.; Jamshidi, Z.; Visscher, L. TD-DFT+TB: An Efficient and Fast Approach for Quantum Plasmonic Excitations *J. Phys. Chem. C* **2020**, *124*, 7946-7955.
- 40 Giannone, G.; Della Sala F. Minimal auxiliary basis set for time-dependent density functional theory and comparison with tight-binding approximations: Application to silver nanoparticles *J. Chem. Phys.* **2020**, *153*, 084110.
- 41 Piccini, G. M.; Havenith, R. W. A.; Broer, R.; Stener, M. Gold nanowires: a Time Dependent Density Functional assessment of plasmonic behaviour, *J. Phys. Chem. C*, **2013**, *117*, 17196 – 17204.
- 42 Arroyo, I. J.; Hu, R.; Merino, G.; Tang, B. Z.; Peña-Cabrera, E. The Smallest and One of the Brightest. Efficient Preparation and Optical Description of the Parent Borondipyrromethene System

1  
2  
3  
4  
5  
6 *J. Org. Chem.* **2009**, *74*, 5719-5722.

7 <sup>43</sup> Baseggio, O.; Fronzoni, G.; Stener, M. A new time dependent density functional algorithm for  
8 large systems and plasmons in metal clusters *J. Chem. Phys.* **2015**, *143*, 024106.

9 <sup>44</sup> te Velde, G.; Bickelhaupt, F. M.; Baerends, E. J.; Fonseca Guerra, C.; van Gisbergen, S. J. A.;  
10 Snijders, J. G.; Ziegler, T. Chemistry with ADF *J. Comput. Chem.* **2001**, *22*, 931-967.

11 <sup>45</sup> Baseggio, O.; De Vetta, M.; Fronzoni, G.; Stener, M.; Fortunelli, A. A new Time Dependent  
12 Density Functional Method for molecular plasmonics: formalism, implementation and the  
13 Au<sub>144</sub>(SH)<sub>60</sub> case study. *Int. J. Quantum Chem.* **2016**, *116*, 1603-1611

14 <sup>46</sup> Baseggio, O.; De Vetta, M.; Fronzoni, G.; Stener, M.; Sementa, L.; Fortunelli, A.; Calzolari, A.  
15 Photoabsorption of icosahedral noble metal clusters: an efficient TDDFT approach to large scale  
16 systems *J. Phys. Chem. C* **2016**, *120*, 12773-12782.

17 <sup>47</sup> Franchini, M.; Philippsen, P. H. T.; Visscher, L. The Becke Fuzzy Cells Integration Scheme in the  
18 Amsterdam Density Functional Program Suite, *J. Comput. Chem.* **2013**, *34*, 1819-1827.

19 <sup>48</sup> te Velde, G.; Baerends, E. J. Numerical Integration for Polyatomic Systems, *J. Comput. Phys.*  
20 **1992**, *99*, 84-98.

21 <sup>49</sup> Becke, A. D. Density-functional exchange-energy approximation with correct asymptotic  
22 behavior, *Physical Review A* **1988**, *38*, 3098-3100.

23 <sup>50</sup> Perdew, J. P. Density-functional approximation for the correlation energy of the inhomogeneous  
24 electron gas, *Phys. Rev. B* **1986**, *33*, 8822-8824.

25 <sup>51</sup> Gross, E. K. U.; Kohn, W. Time-Dependent Density-Functional Theory. *Adv. Quantum Chem.*  
26 **1990**, *21*, 255-291

27 <sup>52</sup> van Lenthe, E.; Baerends, E. J.; Snijders, J. G. Relativistic regular two-component Hamiltonians.  
28 *J. Chem. Phys.* **1993**, *99*, 4597-4610.

29 <sup>53</sup> Theivendran, S.; Chang, L.; Mukherjee, A.; Sementa, L.; Stener, M.; Fortunelli, A.; Dass, A.  
30 Principles of Optical Spectroscopy of Aromatic Alloy Nanomolecules: Au<sub>36-x</sub>Ag<sub>x</sub>(SPh-tBu)<sub>24</sub>. *J.*  
31 *Phys. Chem. C* **2018**, *122*, 4524-4531.

32 <sup>54</sup> Zheng, J.; Cheng, X.; Zhang, H.; Bai, X.; Ai, R.; Shao, L.; Wang, J. Gold Nanorods: The Most  
33 Versatile Plasmonic Nanoparticles *Chem. Rev.* **2021**, *121*, 13342-13453.

34 <sup>55</sup> Desclaux, J. P.; Pyykko, P. Dirac-Fock one-centre calculations. The molecules CuH, AgH and  
35 AuH including p-type symmetry functions *Chem. Phys. Lett.* **1976**, *39*, 300-303.

36 <sup>56</sup> Johnson, H. E.; Aikens, C. M.; *J. Phys. Chem. A* **2009**, *113*, 4445-4450.

37 <sup>57</sup> Giannone, G.; Śmiga, S.; D'Agostino, S.; Fabiano, E.; Della Sala, F. Plasmon Couplings from  
38 Subsystem Time-Dependent Density Functional Theory *J. Phys. Chem. A* **2021**, *125*, 7246-7259.

39 <sup>58</sup> Barcaro, G.; Sementa, L.; Fortunelli, A.; Stener, M. Optical Properties of Silver Nanoshells from  
40 Time-Dependent Density Functional Theory Calculations *J. Phys. Chem. C* **2014**, *118*, 12450-  
41 12458.

42 <sup>59</sup> Chibani, S.; Laurent, A. D.; Le Guennic, B.; Jacquemin, D. *J. Chem. Theory Comput.* **2014**, *10*,  
43 4574-4582.

44 <sup>60</sup> Momeni, M. R.; Brown, A. Why Do TD-DFT Excitation Energies of BODIPY/Aza-BODIPY  
45 Families Largely Deviate from Experiment? Answers from Electron Correlated and Multireference  
46 Methods. *J. Chem. Theory Comput.* **2015**, *11*, 2619-2632.

47 <sup>61</sup> Bonatti, L.; Gil, G.; Giovannini, T.; Corni, S.; Cappelli, C. Plasmonic Resonances of Metal  
48 Nanoparticles: Atomistic vs. Continuum Approaches *Front. Chem.* **2020**, *8*, 340.

49 <sup>62</sup> Mennucci, B.; Corni, S. Multiscale modelling of photoinduced processes in composite systems.  
50 *Nat Rev Chem* **2019**, *3*, 315-330.

51 <sup>63</sup> Yang, Q.; Fusè, M.; Bloino, J. Theoretical Investigation of the Circularly Polarized Luminescence  
52 of a Chiral Boron Dipyrromethene (BODIPY) Dye *Front. Chem.* **2020**, *8*, 801.

53 <sup>64</sup> Kumar, J.; Liz-Marzán, L. M. Recent Advances in Chiral Plasmonics — Towards Biomedical  
54 Applications *Bull. Chem. Soc. Jpn.* **2019**, *92*, 30-37.

- 1  
2  
3  
4  
5  
6  
7  
8  
9  
10  
11  
12  
13  
14  
15  
16  
17  
18  
19  
20  
21  
22  
23  
24  
25  
26  
27  
28  
29  
30  
31  
32  
33  
34  
35  
36  
37  
38  
39  
40  
41  
42  
43  
44  
45  
46  
47  
48  
49  
50  
51  
52  
53  
54  
55  
56  
57  
58  
59  
60
- 
- <sup>65</sup> Toffoli, D.; Russi, A.; Fronzoni, G.; Coccia, E.; Stener, M.; Sementa, L.; Fortunelli, A. Circularly Polarized Plasmons in Chiral Gold Nanowires via Quantum Mechanical Design. *J. Phys. Chem. Lett.* **2021**, *12*, 5829–5835.
- <sup>66</sup> Toffoli, D.; Medves, M.; Fronzoni, G.; Coccia, E.; Stener, M.; Sementa, L.; Fortunelli, A. Plasmonic Circular Dichroism in Chiral Gold Nanowire Dimers. *Molecules.* **2022**, *27*, 93.
- <sup>67</sup> Tanaka, H.; Inoue, Y.; Mori, T. Circularly Polarized Luminescence and Circular Dichroisms in Small Organic Molecules: Correlation between Excitation and Emission Dissymmetry Factors *ChemPhotoChem* **2018**, *2*, 386–402.
- <sup>68</sup> Han, J.; Guo, S.; Lu, H.; Liu, S.; Zhao, Q.; Huang, W. Recent Progress on Circularly Polarized Luminescent Materials for Organic Optoelectronic Devices *Adv. Optical Mater.* **2018**, *6*, 1800538.
- <sup>69</sup> Krishnadas, K. R.; Sementa, L.; Medves, M.; Fortunelli, A.; Stener, M.; Fürstenberg, A.; Longhi, G.; Bürgi, T. Chiral Functionalization of an Atomically Precise Noble Metal Cluster: Insights into the Origin of Chirality and Photoluminescence *ACS Nano* **2020**, *14*, 9687-9700.

**Table 1.** The three lowest BODIPY electronic excitations calculated at TDDFT level with BP86 XC functional and TZP basis set.

Excitation	Excitation E (eV)	f	assignment
1B <sub>2</sub>	3.00	0.131	55% 3a <sub>2</sub> → 7b <sub>1</sub> ; 44% 4a <sub>2</sub> → 7b <sub>1</sub>
1A <sub>1</sub>	3.33	0.0182	97% 6b <sub>1</sub> → 7b <sub>1</sub>
2B <sub>2</sub>	3.89	0.404	54% 4a <sub>2</sub> → 7b <sub>1</sub> 43% 3a <sub>2</sub> → 7b <sub>1</sub>

## Captions to Figures

**Figure 1.** The discrete and smoothed (by lorentzian function) Casida (black line) and polTDDFT (blue line) excitation spectrum of BODIPY up to 5 eV (upper panel). HWHM for lorentzian broadening and imaginary photon energy both equal to 0.075 eV. Lower panel: induced density of the two most intense transitions (isolines  $0.03 \text{ e}^-/\text{bohr}^3$ ).

**Figure 2.** Molecular orbitals of BODIPY involved in the three lowest excitations. Isolines  $0.03 \text{ (e}^-)^{1/2}(\text{bohr})^{-3/2}$ .

**Figure 3.** The polTDDFT excitation spectrum of  $\text{Ag}_{50}$  up to 5 eV (upper panel). Lower panel: induced density of the two most intense transitions (isolines  $0.10$  and  $0.03 \text{ e}^-/\text{bohr}^3$  for first and second peak respectively).

**Figure 4.** The ICM-OS analysis of the first peak of  $\text{Ag}_{50}$  at 3.00 eV. Upper and lower panels report the 2D and 3D representations respectively.

**Figure 5.** The polTDDFT excitation spectrum of the longitudinal  $\text{Ag}_{50}$ -BODIPY adduct up to 5 eV (upper panel). Lower panel: induced density of the two most intense transitions (isolines  $0.03 \text{ e}^-/\text{bohr}^3$ ).

**Figure 6.** The ICM-OS analysis of the first peak of the longitudinal  $\text{Ag}_{50}$ -BODIPY adduct at 2.98 eV. Upper and lower panels report the 2D and 3D representations respectively.

**Figure 7.** The polTDDFT excitation spectrum of the lateral  $\text{Ag}_{50}$ -BODIPY adduct up to 5 eV (upper panel). Lower panel: induced density of the two most intense transitions (isolines  $0.03 \text{ e}^-/\text{bohr}^3$ ).

**Figure 8.** The ICM-OS analysis of the first peak of the lateral  $\text{Ag}_{50}$ -BODIPY adduct at 2.98 eV. Upper and lower panels report the 2D and 3D representations respectively.

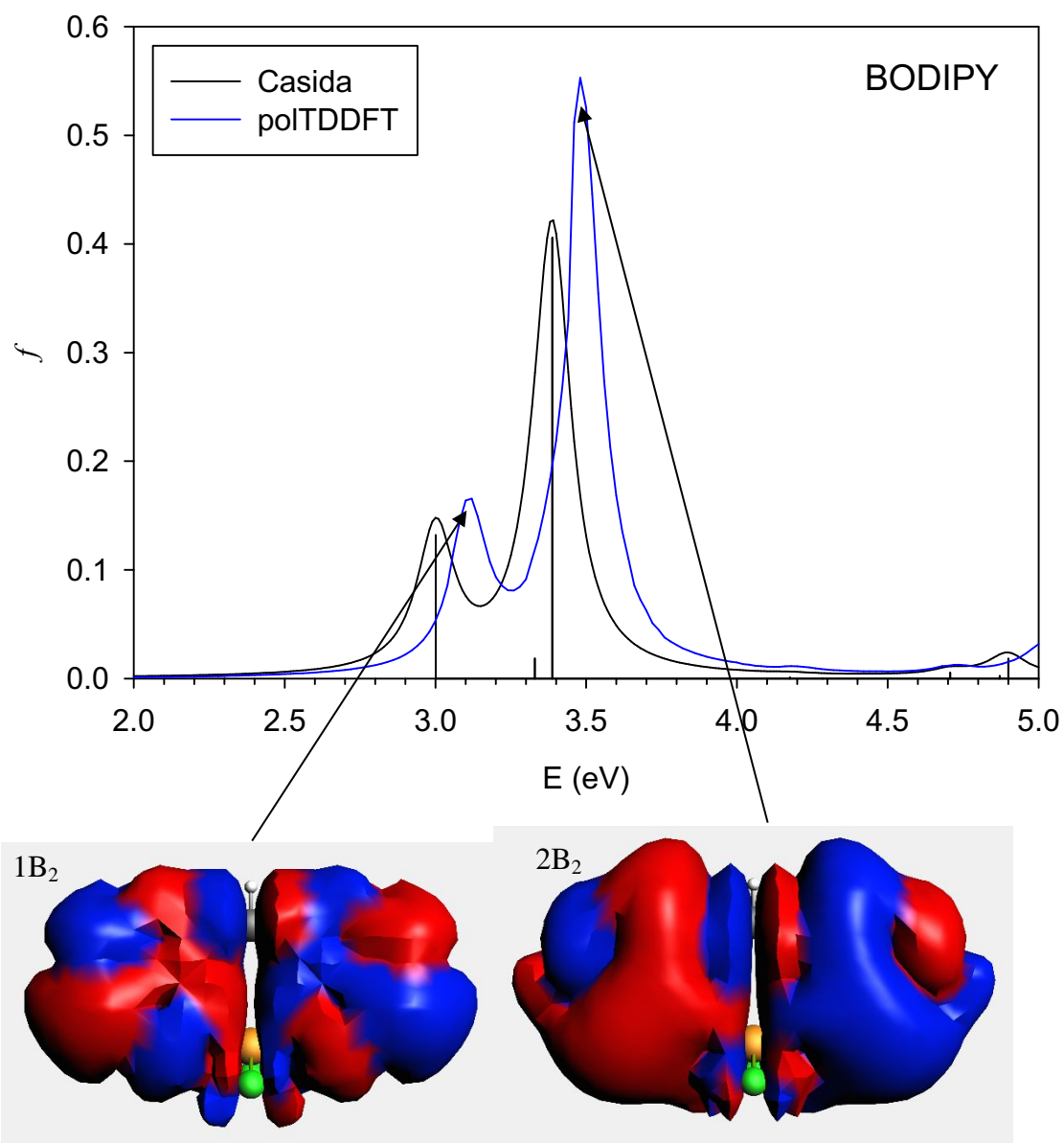


Fig. 1

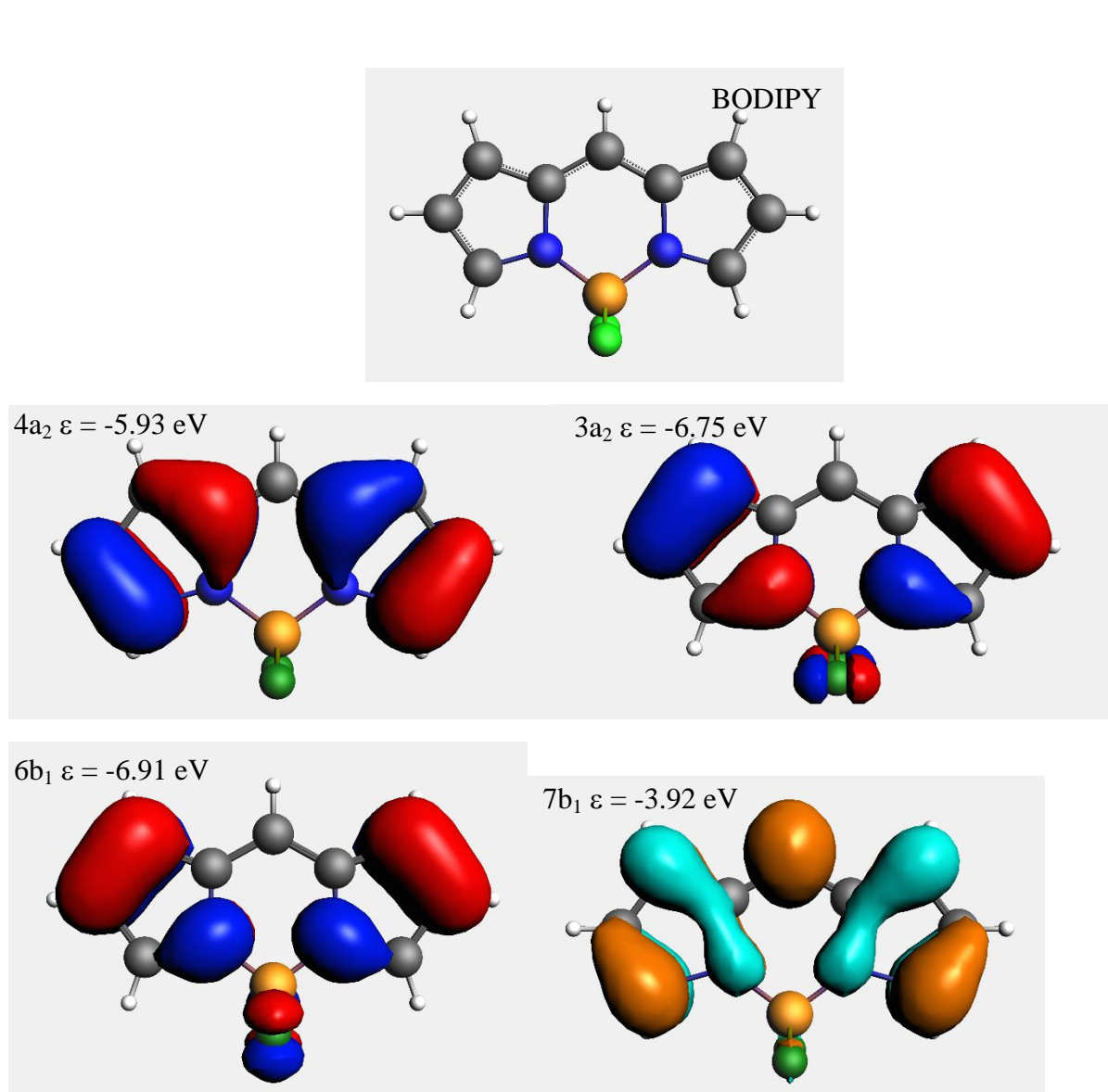


Fig. 2

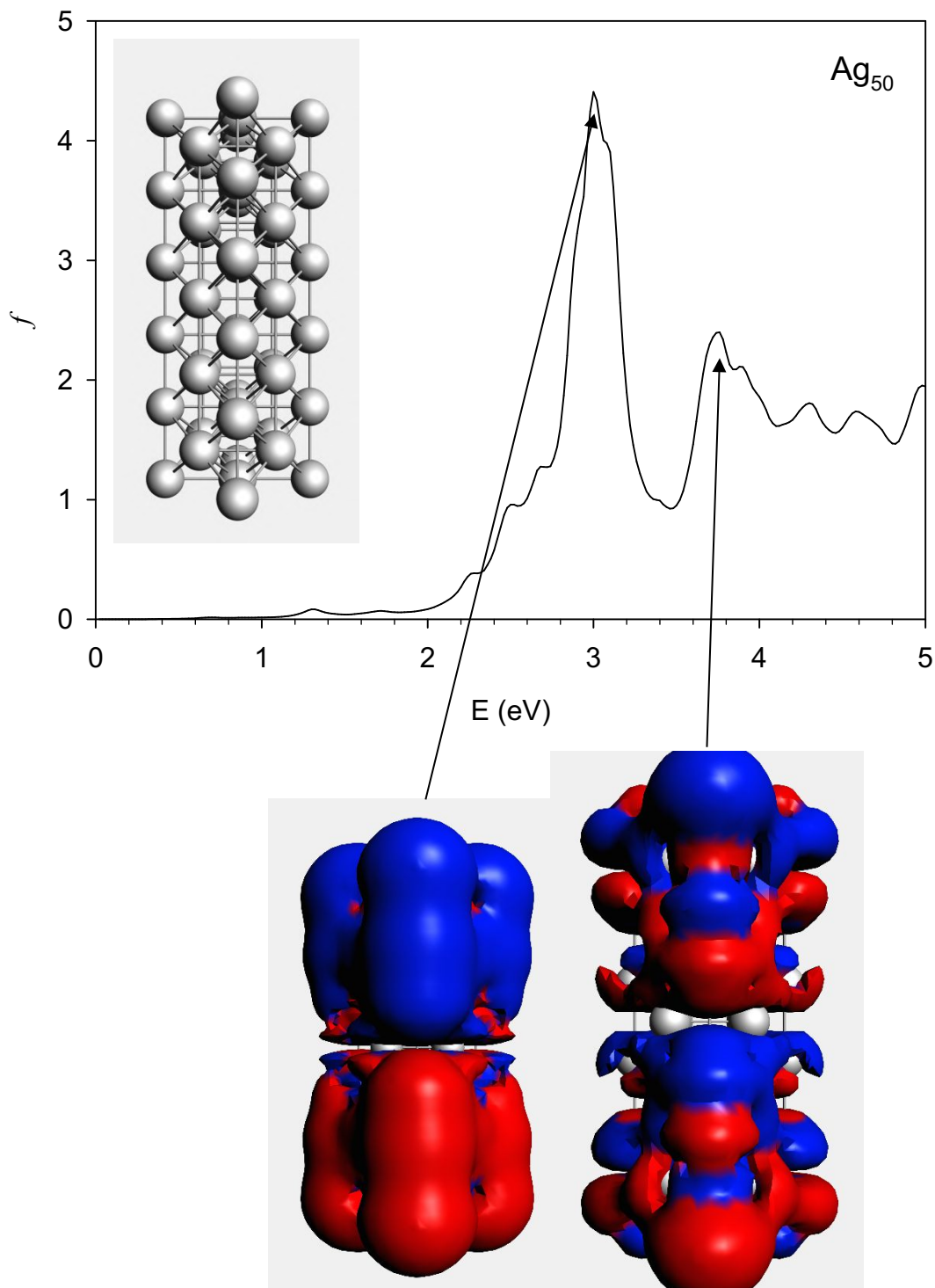


Fig. 3

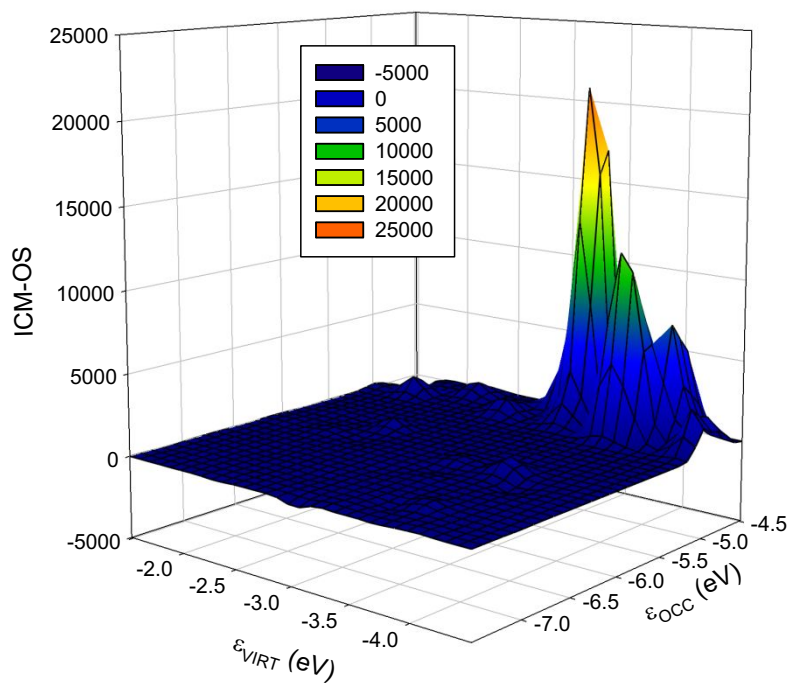
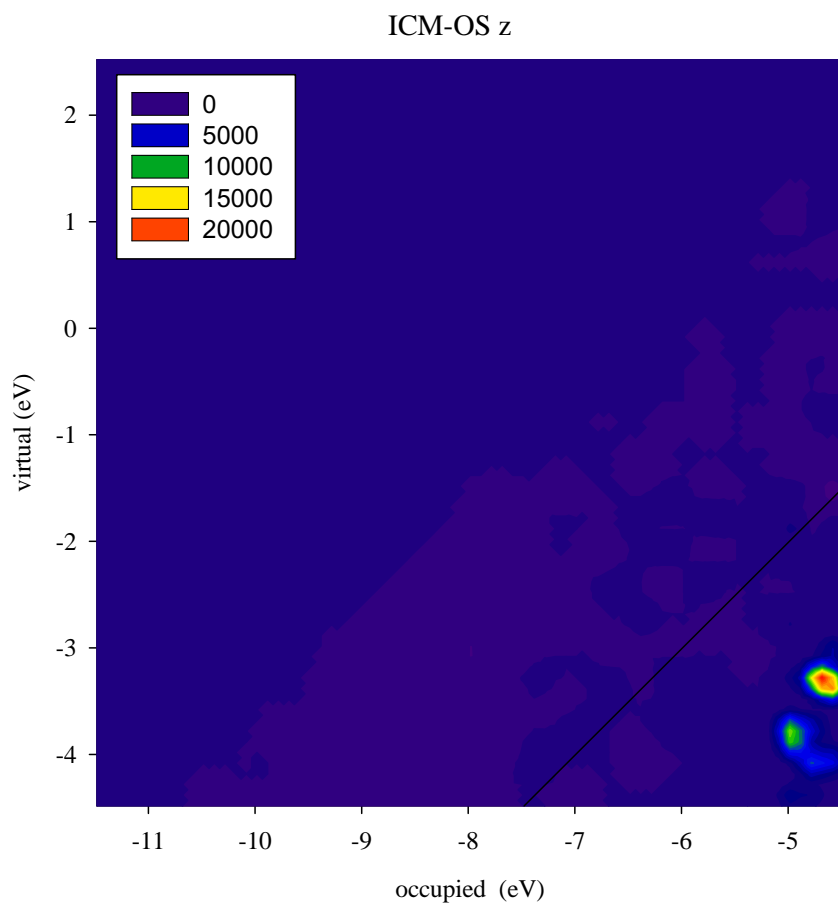


Fig. 4

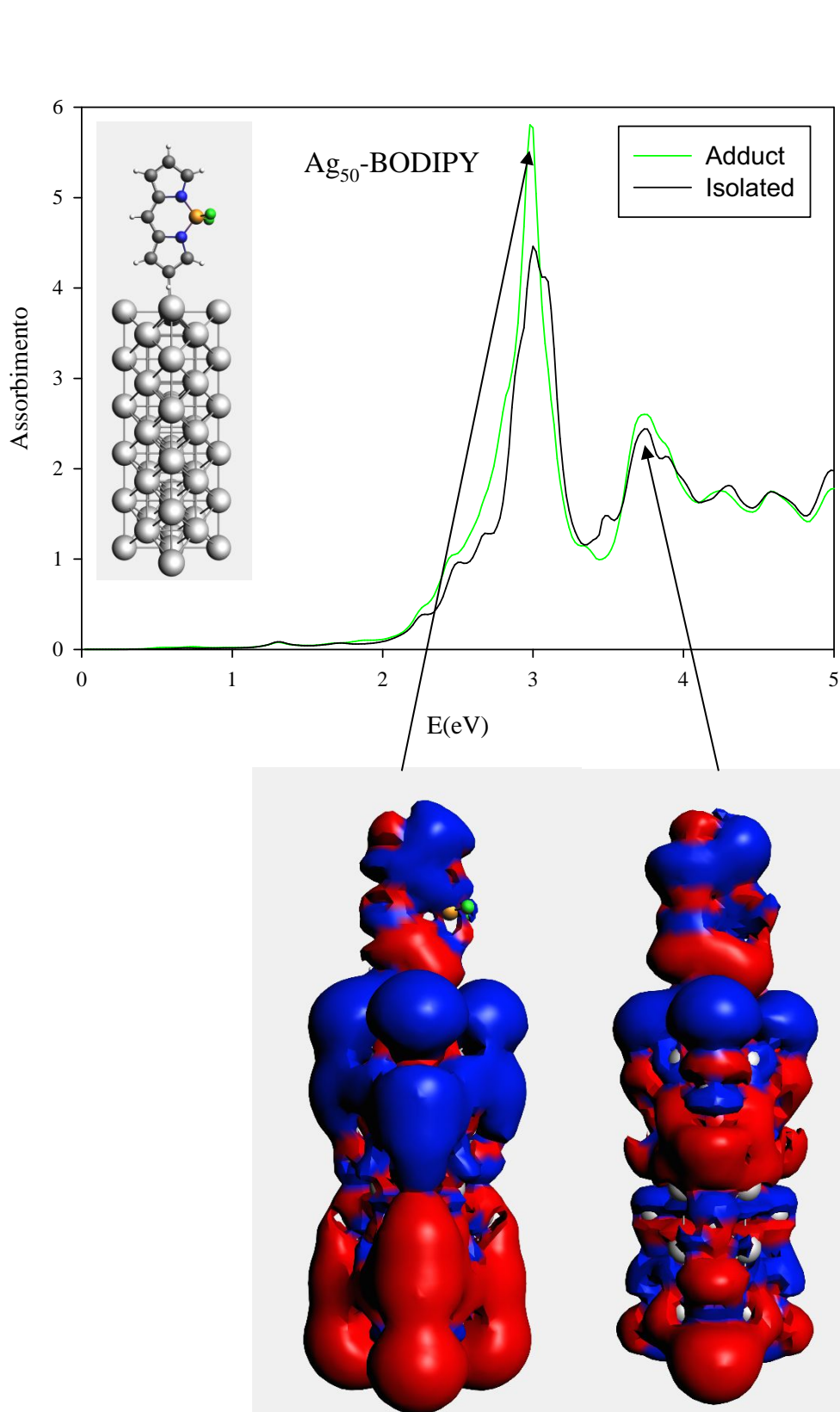


Fig. 5

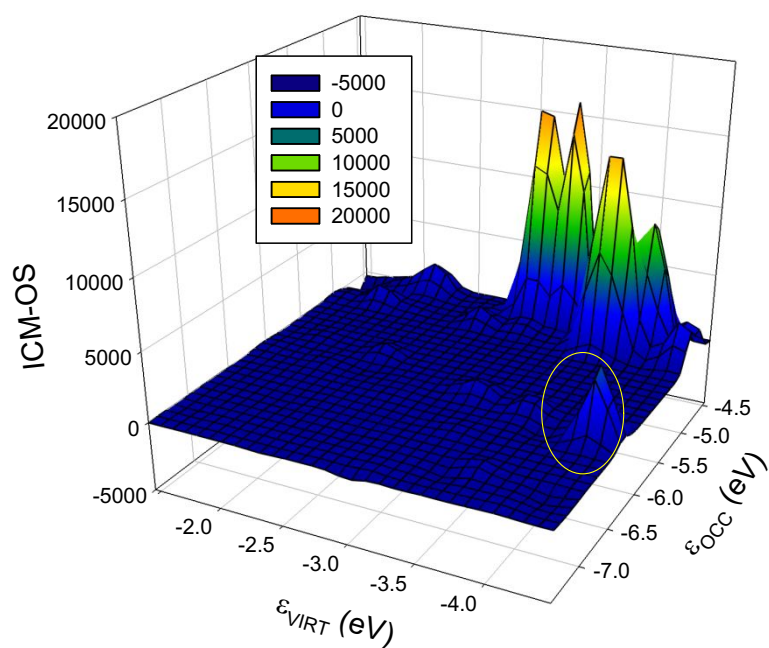
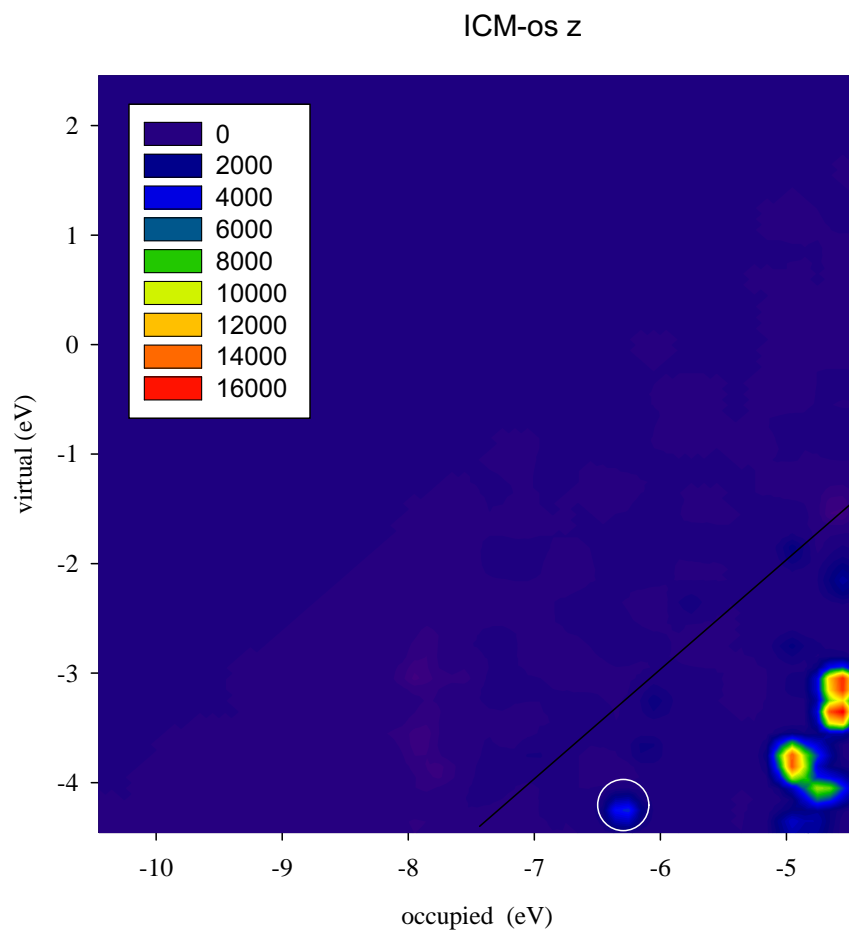


Fig. 6

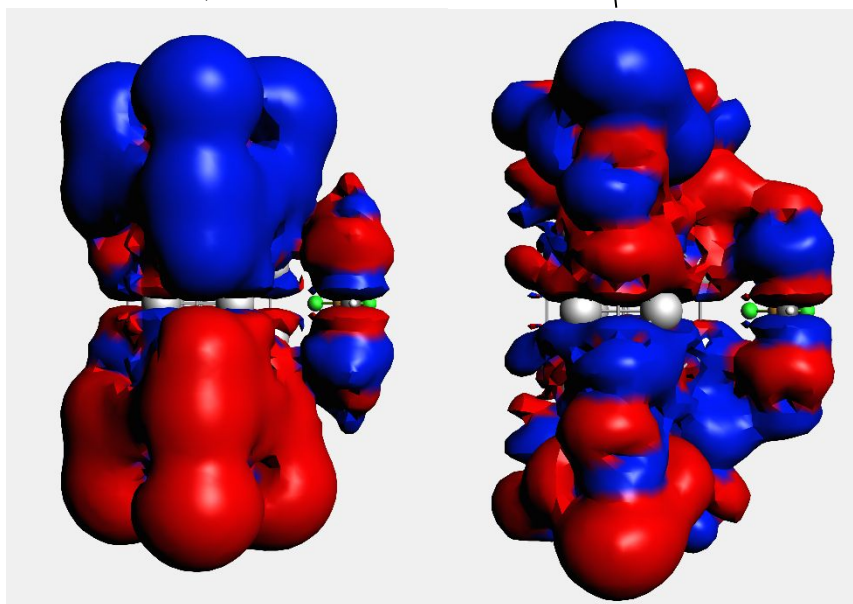
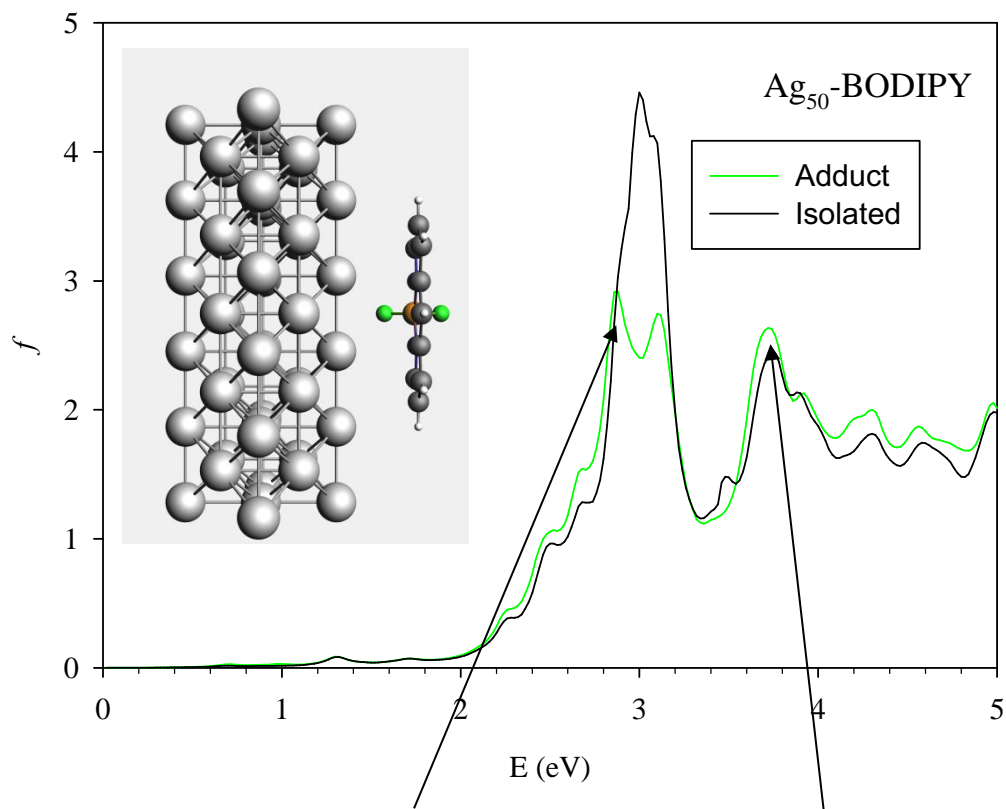


Fig. 7

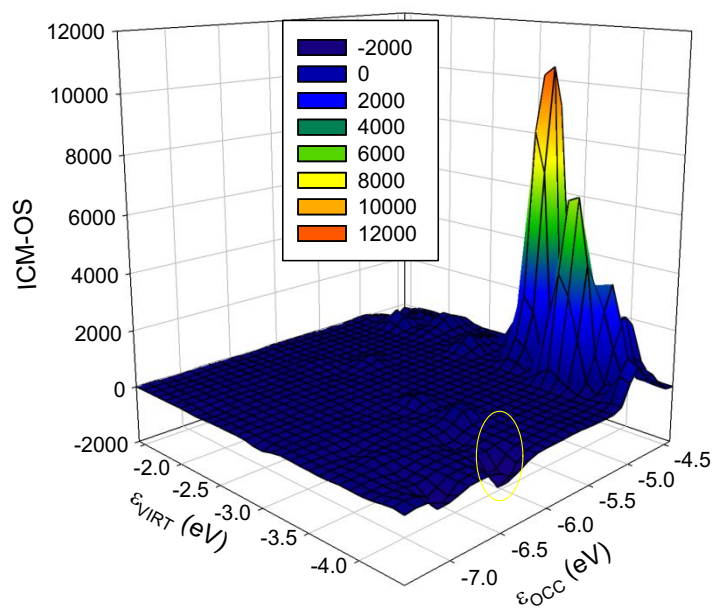
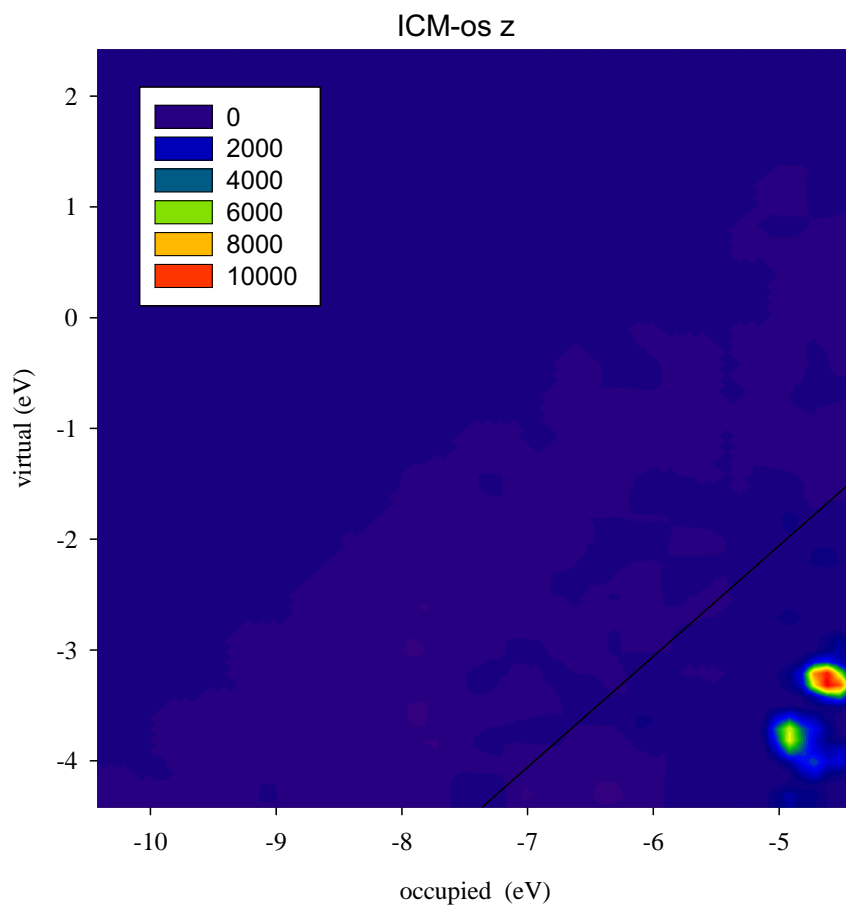


Fig. 8

**Supporting Information for:**

**Coupling between Plasmonic and Molecular Excitations: TDDFT Investigation of an Ag-Nanorod/BODIPY-Dye Interaction**

Marco Medves<sup>1</sup>, Daniele Toffoli<sup>1</sup>, Mauro Stener<sup>1,\*</sup>, Luca Sementa<sup>2</sup>, and Alessandro Fortunelli<sup>2,\*</sup>

<sup>1</sup>Dipartimento di Scienze Chimiche, Università di Trieste, Via L. Giorgieri 1, 34127 Trieste, Italy.

<sup>2</sup>CNR-ICCOM & IPCF, Consiglio Nazionale delle Ricerche, via G. Moruzzi 1, Pisa, 56124, Italy.

\*Corresponding authors' email: stener@units.it (MS) and alessandro.fortunelli@cnr.it (AF)

Content:

- Oscillator strength as a function of fragments distance (Figure S1)
- Cartesian coordinates of the longitudinal and lateral adducts.

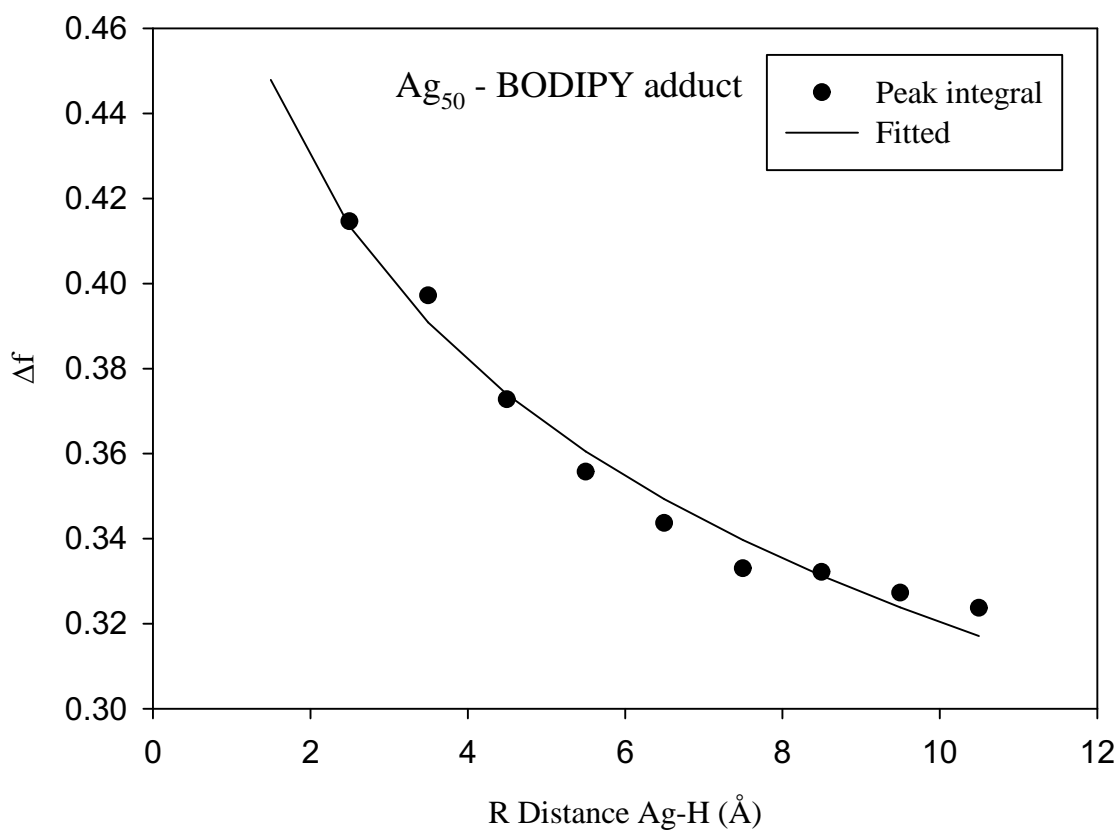


**Figure S1.** Integral of the oscillator strength of the excitation spectrum of the BODIPY/ $\text{Ag}_{50}$ nanorod adduct in the longitudinal configuration as a function of the distance of the fragments. Fitted curve:  $\Delta f = \frac{a}{R^b} + c$  with  $a = 43.1710016$ ,  $b = 0.001559305$ ,  $c = -42.695929$ .

*ATTENTION: this is incomplete supporting information, please visit the article online*



**Optimization of Density Fitting Auxiliary Slater Type Basis Functions for Time Dependent Density Functional Theory**

Journal:	<i>Journal of Computational Chemistry</i>
Manuscript ID	JCC-22-0344
Wiley - Manuscript type:	Research Article
Date Submitted by the Author:	29-Jun-2022
Complete List of Authors:	Medves, Marco; Università degli Studi di Trieste Dipartimento di Scienze Chimiche e Farmaceutiche Fronzoni, G.; Università degli Studi di Trieste Dipartimento di Scienze Chimiche e Farmaceutiche Stener, Mauro; Università' Trieste,
Key Words:	density fitting, TDDFT

SCHOLARONE™  
Manuscripts

# Optimization of Density Fitting Auxiliary Slater Type Basis Functions for Time Dependent Density Functional Theory

Marco Medves<sup>1</sup>, Giovanna Fronzoni<sup>1</sup>, and Mauro Stener<sup>1\*</sup>

<sup>1</sup> Dipartimento di Scienze Chimiche, Università di Trieste, Via L. Giorgieri 1, 34127 Trieste, Italy.

## Abstract

A new set of auxiliary basis function suitable to fit the induced electron density is presented. Such set has been optimized in order to furnish accurate absorption spectra using the complex polarizability algorithm of TDDFT. An automatic procedure has been set up, able, thanks to the definition of suitable descriptors, to evaluate the resemblance of the auxiliary basis dependent calculated spectra with respect to a reference. In this way it has been possible to reduce the size of the basis set maximizing the basis set accuracy. Thanks to the choice to employ a collections of molecules for each element, such basis has proven transferable to molecules outside the collection. The final sets are therefore much more accurate and smaller than the previously optimized ones and have been already included in the database of the last release of the AMS suite of programs. The availability of the present new set will allow to improve drastically the applicability range of the polTDDFT method with higher accuracy and less computational effort.

\*Corresponding author: [stener@units.it](mailto:stener@units.it)

## 1. Introduction

The present study has been promoted by the recent new Time Dependent Density Functional Theory (TDDFT) algorithm<sup>1</sup>, whose implementation within the ADF-AMS program using Slater Type Orbitals (STO) basis sets<sup>2</sup> has proven very efficient to treat very large systems<sup>3 - 6</sup>. Such algorithm, which consists to extract the photoabsorption spectrum from the imaginary part of the complex polarizability, will be referred as the polTDDFT algorithm in the following. The great advantage of polTDDFT consists to avoid the diagonalization (as in the typical Casida implementation of quantum chemistry<sup>7</sup>), in fact the spectrum is calculated point by point solving a linear system of equations at each photon energy. The unknown term of the linear system is the induced density, so it is quite natural to represent such an equation over a basis set of density fitting functions. In this way the matrix dimension remains much smaller than in Casida or in Random Phase Approximation (RPA) where the size of the matrix to be diagonalized has a dimension equal to the product between the number of occupied and virtual orbitals. On the other hand, in order to employ in practice the polTDDFT method, it is necessary to have available the auxiliary density fitting basis set, which must be optimized for polTDDFT calculation. In fact it has been found that the standard density fitting auxiliary STO basis set included in the ADF program, which is employed to fit the SCF electron density for the calculation of the coulomb term of the Kohn-Sham Hamiltonian matrix, is too large for polTDDFT<sup>1</sup>. It is too large because it was developed to fit the electron density from deep core to valence orbitals, while in polTDDFT usually we need only a limited energy interval, typically up to 10 eV at most. In fact one is usually interested in the optical region of photoabsorption, so it is not necessary to include in the density fitting set functions which describe core electron density. Up to now polTDDFT optimized fitting set were available only for few elements<sup>1</sup>, with present work we have generated a database to be employed for polTDDFT calculations of the whole periodic table of the elements, with the exception of lanthanides and actinides.

The optimization of basis functions is a well consolidated problem in quantum chemistry, although it has been recently found, especially for solid state applications, that the 'system-specific' basis can be much more accurate than the 'all-purposes' ones<sup>8</sup>. The optimization of the basis set is usually performed variationally and this ensures that the resulting basis set will be optimized for the total energy. Therefore other properties may have more stringent basis set requirements to obtain convergent results<sup>9,10</sup>. Similar situations happen for density fitting auxiliary basis set: they are usually employed to fit the SCF density for the efficient calculation of the coulomb term. For such task it is possible to employ a variational scheme<sup>11</sup> or a 'pair fitting' scheme as in ADF<sup>12</sup> or with a partitioning technique as in AMS<sup>13</sup>. Pair fitting is quite appealing since it consists in splitting the

1  
2  
3 exact density in two-center contributions and in fitting separately each pair: this is very efficient and  
4 numerically stable, since the problem is recast into a Cholesky decomposition. This allows to  
5 employ very large density fitting auxiliary basis functions without incurring in numerical  
6 instabilities and gaining high accuracy in coulomb integrals. Unfortunately, this density fitting set  
7 cannot be directly employed in polTDDFT algorithm: it is suitable for pair fitting but it is not  
8 suitable to fit the induced density for the whole molecules. In fact the polTDDFT algorithm is  
9 numerically less stable than Cholesky decomposition therefore the auxiliary basis must be in any  
10 case heavily reduced. It is worth noting that the optimization of the density fitting functions to gain  
11 accurate TDDFT spectra has been already considered, for example to realize efficient matrix-vector  
12 products avoiding the construction of the omega Casida matrix<sup>14</sup>. More recently it has been  
13 surprisingly found that for bare silver clusters a ‘minimal basis’ density fitting set consisting of only  
14 one *s* orbital per atom is enough accurate to give quantitative match with respect to reference  
15 TDDFT<sup>15</sup>.

16  
17 Another important issue concerns the optimization method: while it is natural to assume a  
18 variational criterion to fit the coulomb potential, it is much less natural to find a method to optimize  
19 the density fitting set in order to reproduce at best the photoabsorption polTDDFT spectrum.  
20 Several attempts in this direction can be found in the literature<sup>16</sup>. More recently new techniques  
21 based on Artificial Intelligence (AI), like Artificial Neural Networks (ANN), have proven very  
22 suitable for basis set optimization, in particular to identify a descriptor defining the resemblance of  
23 an approximate spectrum with respect to a reference one<sup>17</sup>.

24  
25 Also in the present work we have employed two different descriptors in order to define how  
26 much ‘resemblance’ there is between a calculated spectrum and a reference spectrum which we  
27 assume, by definition, correct. Therefore the quality of a given auxiliary basis set is simply given by  
28 the value of the adopted descriptor, and the optimization process consists to find the auxiliary basis  
29 set which maximizes such descriptor.

30  
31 The present work is organized as follows: first a short review of the polTDDFT and the Casida  
32 algorithms is given in order to stress the role of the density fitting auxiliary basis set, second an  
33 efficient method to reduce the size of the large density fitting set already available in the ADF-AMS  
34 database is described. Third, a procedure to optimize the exponents of the reduced fit is also  
35 proposed. The size reduction of the basis set is then applied to all the elements of the periodic table  
36 (except the *f*-blocks), while the optimization of the exponents has been applied only to a selected  
37 subset of elements. Finally a description of the database generate for the AMS program is  
38 presented.

## 2. Theoretical methods and procedures

### 2.1 The polTDDFT method

The polTDDFT algorithm consists in an alternative method to solve the TDDFT equations. It is convenient to start with standard first-order linear response TDDFT equations<sup>1</sup>:

$$(1) \begin{cases} \rho_z^{(1)}(\omega, \vec{r}) = \int \chi_{KS}(\omega, \vec{r}, \vec{r}') V_{SCF}^z(\omega, \vec{r}') d\vec{r}' \\ V_{SCF}^z(\omega, \vec{r}) = V_{EXT}^z(\omega, \vec{r}) + \int \frac{\rho_z^{(1)}(\omega, \vec{r}')}{|\vec{r} - \vec{r}'|} d\vec{r}' + \frac{\partial V_{XC}}{\partial \rho} | \rho_0 \rho_z^{(1)}(\omega, \vec{r}) \end{cases}$$

In equation (1)  $\rho_z^{(1)}(\omega, \vec{r})$  refers to the Fourier component of  $\omega$  frequency of the time-dependent first-order density induced by the external potential polarized along the z direction and  $\chi_{KS}(\omega, \vec{r}, \vec{r}')$  is the dielectric susceptibility of the Kohn-Sham non-interacting systems.  $V_{SCF}^z(\omega, \vec{r}')$  is the sum of three terms. The first one is the external potential (in present case only the dipole field is considered), the second one is the Coulomb response of the system to the induced density (i.e. the electrostatic field generated by the induced density) finally the third term is the XC response, already approximated at the Adiabatic Local Density Approximation (ALDA) level<sup>18</sup>.

It is formally possible to solve the above system with respect to the first order density:

$$(2) (1 - \chi_{KS}K)\rho_z^{(1)} = \chi_{KS}V_{EXT}^z$$

If we now represent equation (2) within a basis set to expand the induced density, the following non-homogeneous linear system is obtained:

$$(3) [S - M(\omega)]b = d$$

In practice by solving the linear system (3) we obtain the vector  $b$ , which contains the coefficients of expansion of the induced density:

$$(4) \rho_z^{(1)}(\omega, \vec{r}) = \sum_{\mu} f_{\mu}(\vec{r}) b_{\mu}(\omega)$$

In expression (4)  $f_{\mu}(\vec{r})$  are the auxiliary basis functions employed to represent the induced density. Once the linear system (3) is solved, it is possible to calculate the dynamical polarizability tensor:

$$(5) \alpha_{zz}(\omega) = \int \rho_z^{(1)}(\omega, \vec{r}) z d\vec{r}$$

as well as the photoabsorption spectrum:

$$(6) \sigma(\omega) = \frac{4\pi\omega}{c} \text{Im}[\alpha(\omega)]$$

The photoabsorption spectrum is therefore calculated point by point, with a scan on the excitation energy (step of 0.02 eV) and employing a small but still finite imaginary photon energy. Such imaginary energy corresponds to the reciprocal lifetime of the excited state and makes the calculated spectrum intrinsically broadened by a lorentzian function with Half-Width-Half-Maximum (HWHM) equal to the imaginary photon energy 0.075 eV.

Such spectrum can be also obtained in terms of oscillator strengths:

$$(7) f(\omega_r) = \frac{2\omega_i\omega_r}{3} \text{Im}[\alpha(\omega)]$$

Expression (7) is quite useful since it can be directly compared with photoabsorption spectra obtained as discrete lines, provided the last ones are broadened by lorentzian functions with HWHM equal to the imaginary frequency (reciprocal lifetime) employed in the polTDDFT<sup>1</sup>.

It is worth noting that in polTDDFT calculations we must specify two different basis sets: first the standard basis set employed to expand the KS orbitals, second the auxiliary basis set to expand the induced density. To avoid any confusion we will refer to former as the ‘standard basis’ and to the latter as the ‘auxiliary basis’. In fact to build the  $M$  matrix and the  $d$  vector in the linear system (3) we need the KS orbitals and their energies (eigenvalues) which are taken from a preliminary DFT KS calculation, employing a ‘standard basis’ of Slater Type Orbitals of TZP type and the B3LYP XC hybrid functional<sup>19,20</sup>. The practice goal of the present study is to generate an optimized set of ‘auxiliary basis’  $f_\mu(\vec{r})$ , and we require that such set would be a good compromise between accuracy and computational economy. This means that we try to minimize the number of elements of the ‘auxiliary basis’ but we must also maximize its goodness. In order to maximize the goodness we must select a standard reference spectrum which we assume to be error-free and then define (with some degree of arbitrariness) a degree of ‘resemblance’ between the polTDDFT spectrum and the standard one. Then the auxiliary basis set is changed in order to maximize the ‘resemblance’ and minimize the basis size.

## 2.2 The reference Casida TDDFT method

As we have pointed out in previous section, in order to optimize the auxiliary basis with polTDDFT, we must define a reference spectrum. It is quite natural to choose the Casida method<sup>7</sup> to obtain the reference spectrum, in fact in this case it is possible to employ exactly the same numerical choice such as the standard basis and the XC functional. The Casida TDDFT implementation consists in solving the following eigenvalue equation:

$$(8) \Omega F = \omega^2 F$$

It is worth noting that the dimension of the  $\Omega$  matrix corresponds to the product of the number of occupied orbitals times the number of virtual orbitals and becomes rapidly very large. Therefore the Davidson algorithm is usually employed to extract at least the lowest part of the excitation spectrum in terms of discrete lines with specific energy and intensity (oscillator strength). In order to obtain a spectrum that can be consistently compared with that obtained with the polTDDFT method, it is necessary to broaden the discrete lines with a lorentzian function, whose width has been discussed previously. In practice the following broadening is performed:

$$(9) f(\omega) = \sum_I^N \frac{\eta^2 f_I}{(\omega - \omega_I)^2 + \eta^2}$$

where in expression (9)  $\omega_I$  and  $f_I$  are the energies and the oscillator strengths of the I-th discrete line respectively, while  $\eta$  is the HWHM. With this representation of the spectrum, in presence of only one discrete line we obtain a lorentzian function centered at the excitation energy having the maximum corresponding to the oscillator strength<sup>1</sup>.

### 2.3 The quality descriptors

The choice of the descriptors is somehow arbitrary, in fact the deviations of a spectrum with respect to the reference one may weight different aspects, for example the energy of the spectral features, their intensity, the area under the absorption band and so on. In order to define the descriptors, it is convenient to arrange the polTDDFT spectrum, which consists in a set of N pairs  $(E_i, f_i)$  (energy and oscillator strength respectively), in a set of N two-dimensional vectors  $\bar{v}_i = (E_i, f_i) = (x_i, y_i)$ . The same can be done for the reference Casida spectrum, in this case we designate the vectors as  $\bar{v}'_i = (E'_i, f'_i) = (x'_i, y'_i)$ . The first descriptor considered (named 2D\_xy) has been inspired by the Cosine Similarity (CS)<sup>21</sup>, which is a typical measure of similarity in data analysis:

$$\text{cosine similarity} = \frac{\bar{v} \cdot \bar{v}'}{\|\bar{v}\| \|\bar{v}'\|}$$

$$2D_{xy} = \frac{1}{N} \sum_{i=1}^N \frac{\bar{v}_i \cdot \bar{v}'_i}{\|\bar{v}_i\| \|\bar{v}'_i\|}$$

The Euclidean norm  $\|\bar{v}_i\| = \sqrt{x_i^2 + y_i^2}$  is adopted in this work. Such 2D<sub>xy</sub> descriptor takes the value 1 for perfect match and 0 for absence of match (orthogonal vectors). This descriptor is defined for a single spectrum, if a collection of spectra is considered then the descriptor of the collection is defined as the arithmetic mean of the descriptors relative to the single spectra.

Since it is useful to consider more descriptors, in order to check that the results are robust enough, we introduce another descriptor designed as nD<sub>y</sub>:

$$nD_y = \frac{\bar{y} \cdot \bar{y}'}{\|\bar{y}\| \|\bar{y}'\|}$$

where the vector  $\bar{y} = (f_i) = (y_i)$  contains only the polTDDFT intensities and  $\bar{y}' = (f'_i) = (y'_i)$  contains only the Casida intensities.

This second descriptor is less stringent for the intensity: in fact in presence of a spectrum which has the same shape of the reference one but is just rescaled with respect to the intensity, a perfect match is obtained since nD<sub>y</sub>=1.

#### 2.4 Procedure to optimally reduce the auxiliary basis set

In the previous section we have defined the reference spectrum and two possible measures of the quality of the approximated polTDDFT spectrum (2D<sub>xy</sub> and nD<sub>y</sub> descriptors). The next step consists to assess a practical procedure to identify an auxiliary basis which is expected to be an optimal compromise between the auxiliary basis of minimum size and the descriptor being as close as possible to +1 (best quality). All the following steps are graphically considered in the flow chart Scheme 1. It is worth noting that a very large auxiliary basis set is already available within the database included in the AMS package, but such set is not useful for polTDDFT calculations since it is far too large. We designate such set as the Initial Almost Complete Auxiliary Set (IACAS) represented by the yellow box in Scheme 1. In fact such set was specifically designed to fit the electron density of each atom pairs (“pair fitting”) in order to obtain the electrostatic potential of the Hartree term of the Kohn Sham hamiltonian. This set must be very large, virtually complete, in order to get the required numerical accuracy, but it can be safely employed since a Cholesky decomposition is performed to fit the pair density, which is numerically very stable. On the other hand for polTDDFT a too large auxiliary basis might give rise to problems of numerical linear dependence. For these reasons our ‘target’

1  
2  
3 auxiliary basis set is required to be small not only to be computationally cheap but also to safely  
4 avoid numerical instabilities. Therefore we have considered first a procedure consisting to  
5 reduce systematically the number of auxiliary basis function starting from the IACAS which is  
6 already available. It is worth noting that the IACAS contains functions to fit the electron density  
7 from the compact deep core orbitals to the more diffuse outer valence, while for polTDDFT we  
8 need only to perturb the outer valence orbitals. To this purpose a pre-reduction is preliminary  
9 done on the IACAS just deleting all the STO having an exponent larger than 15. This simple  
10 procedure (green box in Scheme 1) has proven useful in order to start with a set containing a  
11 much lower number of auxiliary functions having cancelled all those needed to fit the core  
12 electron density. Moreover the so obtained auxiliary set, although still too large, does not  
13 usually suffer of the numerical instability problems so it can be employed to run polTDDFT  
14 calculations. In some circumstances, such set was still too rich and it was not possible to run the  
15 polTDDFT calculation due to numerical linear dependence problems. In that case we simply  
16 further reduced the set doing a diagonalization of the overlap matrix and then deleting the basis  
17 element with higher contribution in the eigenvector with minimum eigenvalue. This procedure  
18 can be repeated until the set is suitable for the polTDDFT calculation. At this point we have set  
19 up an automatic procedure which, starting with the pre-reduced IACAS consisting of  $n$  auxiliary  
20 basis function, calculates  $n$  polTDDFT spectra, one for each basis set consisting of  $n-1$   
21 elements, obtained deleting 1 basis function from the original set (blues boxes in Scheme 1). For  
22 every polTDDFT spectrum the 2D<sub>xy</sub> descriptor is calculated, and in this way the best set  
23 consisting of  $n-1$  auxiliary functions is chosen as the set giving the best 2D<sub>xy</sub> descriptor  
24 (closest to 1), as reported in the red box of Scheme 1. This step can be iterated  $n$  times, until the  
25 set is reduced to one single function. In this way we can associate a descriptor to each basis set  
26 of decreasing size. The evolution of the descriptor can be profitably described as reported in  
27 Figure 1. The T index reported on the x axis corresponds to each different set considered: the  
28 vertical straight lines corresponds to a jump to a basis set with one less function. Within the  
29 rectangles there are many blue dots which correspond to the different basis, the best basis (the  
30 highest) is designated in red. So when we jump to the next rectangle we start from the best basis  
31 of the previous one, and again all the basis consisting of  $n-1$  elements are tested (blue dots) and  
32 the best one (red dot) is kept for the next step. It is interesting to note that within a rectangle the  
33 blue dots are distributed over a rather wide descriptor range, indicating that some basis elements  
34 are crucial to obtain accurate spectra and their suppression introduces a strong deterioration in  
35 the calculated spectrum.

1  
2  
3 In order to better appreciate the evolution of the best set, in Figure 2 we have reported only the  
4 red dots which correspond to the best set of a give size. It is worth noting that up to  $T = 30$  we  
5 observe a very slight improvement reducing the basis size (as  $T$  increases) which at the  
6 beginning is regular, but for  $T$  beyond 20 the behaviour starts to be irregular although still  
7 increasing as average. Beyond  $T=30$  a sudden and fast regular deterioration is found. The  
8 observed behaviour indicates clearly that the reduction of the basis set up to  $T=30$  does not  
9 decrease the accuracy, but beyond this point a rapid loose of accuracy is evident. At this point  
10 the chosen optimal auxiliary basis is the one just before the sudden accuracy drop: this criterion  
11 allows to choose the basis having the smallest possible size but giving an accuracy comparable  
12 with that of larger sets. It is worth noting that the behaviour reported in Figures 1 and 2 refers to  
13 the Sn element, but it is completely general, in fact it has been found in all the elements of the  
14 periodic table considered in the present work. Another very important point consists in the  
15 choice of the descriptor employed to reduce the basis set. Although in general the descriptors  
16 are consistent each other (they usually identify the same function to be deleted) in cases where  
17 more than one function have very similar descriptors the outcome can be descriptor dependent.  
18 Since the 2D\_xy descriptor has proven more stringent, we have used this one for the reduction  
19 process. Instead, in order to choose the best auxiliary basis, both descriptors have been checked,  
20 in order to take the safer choice. In practice we have calculated both descriptors for the  
21 reduction series and the basis is selected so that both descriptors are maximized with the basis as  
22 small as possible.

23  
24  
25  
26  
27  
28  
29  
30  
31  
32  
33  
34  
35  
36  
37 A very important issue consists in the transferability of the obtained basis set: we must  
38 guarantee that the optimized basis for a given element using a specific molecule as a reference  
39 can be employed in other systems containing such element. This is not trivial at all, in fact from  
40 preliminary tests we found that if only one molecule is taken as reference the obtained set is not  
41 transferable in general. This problem can be solved taking a collection of  $k$  molecules  
42 containing the same element as reference: so a set of  $k$  reference spectra will be defined and a  
43 set of different  $k$  descriptors will be obtained for each auxiliary basis. Then a 'collection'  
44 descriptor can be defined taking the arithmetic mean of the  $k$  ones, and the same procedure can  
45 be applied to optimize the auxiliary basis over the collection. The so obtained auxiliary basis has  
46 proven transferable, in fact we always checked this by comparing a polTDDFT and a Casida  
47 spectrum on a molecule outside the collection and we always got an acceptable match. In order  
48 to obtain a transferable auxiliary basis set it is important that the collection contains the same  
49 elements in various chemical environment, but mainly as it concerns the oxidation state and the  
50 coordination number. From a computational point of view the procedure is quite cheap: taking a  
51  
52  
53  
54  
55  
56  
57  
58  
59  
60

1  
2  
3 collection of 4 molecules consisting of few tens of atoms, the optimal reduced basis takes a  
4 couple of days using around 20 cores on a HPE ProLiant ML350 Gen9 server with processor  
5 Intel® Xeon® CPU E5-2650 v3 @ 2.30GHz.  
6  
7

8 In summary, as an example, Table 1 reports the original IACAS auxiliary set, the pre-reduction  
9 operated by cutting the  $\alpha > 15$  exponents, and the final reduced set (bold functions and  
10 exponents) for the Sn atom. The effect on size is dramatic, going from 57 to 6 different  
11 functions. If we take into account the angular momentum multiplicity  $2L+1$ , the reduction is  
12 similar, going from 209 to 20 basis elements.  
13  
14  
15  
16  
17  
18

### 19 *2.5 Procedure to refine the auxiliary basis set*

20  
21 In the previous section we have described how to select the most important auxiliary basis  
22 elements starting from an initial very large set, the IACAS, so in the procedure the STO  
23 exponent were kept constant. Now we want to optimize the exponents in order to obtain an even  
24 better basis set, the procedure is described in the following and is graphically described in  
25 Scheme 2. The start is from the reduced set obtained in the previous section (upper yellow box  
26 in Scheme 2). Then, the exponent of each function is optimized separately: the exponent of the  
27 first function is varied over a set of values (blues boxes) , the potTDDFT spectra are calculated  
28 and the 2D\_xy descriptor is calculated. The exponent giving the best descriptor is then chosen  
29 (red box), and the next exponent is optimized (inner loop), using the optimized value of the  
30 previous exponent. This procedure is repeat until all the exponents are optimized. Since each  
31 exponent is optimized independently of the other ones, the cycle is repeated again on all the  
32 exponents until convergence is reached (outer loop), typically only 3 or 4 cycles are necessary.  
33 The procedure is performed on the same collection of molecules employed in the previous  
34 section. In order to increase the efficiency, the procedure is split in two successive steps: in the  
35 first step the basis is optimized only on the first decimal digit, in the second step also the second  
36 digit is optimized. So in the first step the exponent is varied on an interval which is wider but  
37 with steps of 0.1, then in the second step the interval is narrower but a step of 0.01 is employed.  
38 The interval wideness and step size are indicated by  $\Delta$  and  $\delta$  respectively in the blue boxes of  
39 Scheme 2. Such optimization procedure is much more demanding than the simpler reduction,  
40 requiring about one order of magnitude more of computer time, typically 2 or 3 weeks using 20  
41 cpu on the same server. However, we have found that for most of the elements the reduction is  
42 enough to get a basis of good accuracy, so we have applied the exponent optimization only for  
43 few elements which were less easy to optimize or for which we required a special accuracy.  
44  
45  
46  
47  
48  
49  
50  
51  
52  
53  
54  
55  
56  
57  
58  
59  
60

## 2.6 Computational details

In all calculations the basis set for the expansion of the molecular Kohn-Sham orbitals has been taken from the AMS database of STO functions. The accurate Triple Zeta plus Polarization (TZP) set has been chosen. For the geometry optimization of the molecules considered in the collection, the exchange correlation energy functional has been approximated at the Local Density Approximation (LDA) with the VWN parametrization<sup>22</sup>. In order to have accurate spectra calculations, we have considered in both Casida and polTDDFT calculations the B3LYP hybrid energy functional for both SCF and response part. In the response part the non-local exchange of the kernel has been approximated at the Hybrid Diagonal Approximation (HDA level) in order to save computer time without loss of accuracy<sup>23</sup>. Since we have considered also heavy elements we have included relativistic effects at the ZORA level<sup>24</sup>.

## 3. Results and discussion

### 3.1. Reduction of the auxiliary basis set

In order to describe how to realize the procedure previously described, we have selected one element of the period table (Sn) as a typical example. For the collection we chose the following 4 molecules: SnO<sub>2</sub>, SnCl<sub>2</sub>, SnF<sub>4</sub> and Sn(CH<sub>3</sub>)<sub>4</sub>, in order to have two oxidation states (+2 and +4) as well as two coordination numbers (2 and 4). The geometries have been optimized and are reported in the Supporting Information. In Table 1 we have reported the IACAS of Sn atom which initially consists of 57 STO, we have highlighted the 22 exponents  $\alpha > 15$  which have been deleted before to start the reduction procedure, so the pre-reduced set consists of 35 STO. In Figure 3 we have reported the polTDDFT spectrum of SnCl<sub>2</sub> employing the pre-reduced fit, compared with the Casida one. The match is excellent but the auxiliary set is by far too large with respect to the real necessity. In Figure 4 we have reported the 2D<sub>xy</sub> descriptor trends for each molecule of the collection, together with their arithmetic mean. It is apparent that at the beginning of the procedure the reduction does not deteriorate the quality, but around T=30 a sudden drop out is apparent for all the here considered systems. Quite interestingly in Figure 5 we have considered the nD<sub>y</sub> descriptor trend on the basis set selected by the 2D<sub>xy</sub> descriptor: not only the behaviour is the same but also the same 'best' basis set would have been identified by the nD<sub>y</sub> descriptor. This suggests that the selection procedure is quite robust and although intrinsically descriptor-dependent, in practice the descriptor choice does not seem to represent a critical issue. Actually this is not true in general: in some circumstances the selection would be different, in that case we checked both set (one selected by 2D<sub>xy</sub> and the other one selected by nD<sub>y</sub>) and we always found that the selection from nD<sub>y</sub> is more accurate. In summary the 2D<sub>xy</sub> descriptor has been employed to do the reduction but the

nD<sub>y</sub> descriptor has been chosen to select the final basis. We also tried to do the reduction by nD<sub>y</sub> descriptor, but this proven not accurate since the resulting spectra were less accurate in terms of intensity. This was not unexpected, due to the nature of the nD<sub>y</sub> descriptor which is not sensitive to errors due to a rescaling of the intensity. Finally, in Figure 6 we report the polTDDFT spectrum calculated for a system chosen outside the collection (Sn(CH<sub>2</sub>CH<sub>3</sub>)<sub>2</sub>Cl<sub>2</sub>), in order to verify the transferability of the so obtained auxiliary basis set. As we can see the agreement with the reference Casida results is very satisfactory confirming the transferability. In practice, this procedure has been applied to all the atoms of the periodic table, except the f-block elements, taking into account only closed shell molecules for the collection.

### 3.2. Exponent optimization of the auxiliary basis set

In most cases and for standard purposes, the basis set obtained by reduction as in the previous section does not need to be further optimized as concerns the exponents. However there are situations in which this is necessary. In particular at the beginning of the procedure we do not have any basis available at all. Therefore we started from hydrogen as the first element, which we take from a previous optimization<sup>1</sup>. Then we reduced and optimized in order the following elements: C, O, Cl, S, F, N, Se, Si, P, Br and I. In case the collection includes elements not yet available, we employed the previous optimized auxiliary basis set from<sup>1</sup>.

Carbon has demonstrated as one of the most tricky atoms to optimize, probably due to its very complex chemistry which makes it to be in very different chemical contexts.

As a typical example, we discuss the optimization results relative to the exponent refinement of the auxiliary basis set for the chlorine atom. The collection employed for optimization and previous reduction consists of three molecules: HCl, CCl<sub>4</sub> and Cl<sub>2</sub>O. The trend of the descriptor during the process of exponent optimization is considered in figure 7, where the value of the 2D<sub>xy</sub> descriptor is reported for each basis calculated accordingly to the procedure outlined in previous Section 2.5. It is well apparent that the optimization is quite smooth: at the beginning of the process the descriptor increases, but it assumes quickly a flat behaviour indicating that the optimization is in practice completed. In figure 8 we have reported the polTDDFT spectra of the three molecules belonging to the Cl collection, calculated with the optimized Cl basis set, in comparison with the reference Casida TDDFT spectra. The agreement is fairly nice for all molecules over the complete energy range here considered. In order to check the 'transferability' of the basis, we have repeated the same analysis for six molecules not belonging to the collection, namely: S<sub>2</sub>Cl<sub>2</sub>, SOCl<sub>2</sub>, SO<sub>2</sub>Cl<sub>2</sub>, VOCl<sub>3</sub>, AgCl and ArCl<sub>2</sub>, whose spectra are reported in Figure 9. ArCl<sub>2</sub> is just a model system we used to reduce the basis for argon, in which Cl is in an unconventional molecular context: nevertheless the

1  
2  
3 agreement between Casida and polTDDFT is excellent in this case as well. This finding suggests  
4 that the so-obtained auxiliary basis are transferable in different chemical context, keeping the good  
5 accuracy showed during the reduction or optimization processes.  
6  
7

8 As a final test we have considered that in a recent work from Della Sala group<sup>15</sup> it has been found  
9 that for silver clusters it is possible to obtain very accurate photoabsorption spectra by using a  
10 minimal auxiliary basis set to fit the transition density. So we have directly optimized the exponent  
11 of a single 1S STO function for a collection consisting of only the Ag<sub>20</sub> T<sub>d</sub> neutral cluster, obtaining  
12 a best exponent value equal to 0.40. The agreement with the reference Casida spectrum is fairly nice  
13 indeed (upper panel in Figure 10). Such basis allows to calculate huge systems, for example in the  
14 lower panel of Figure 10 we have reported the polTDDFT absorption spectrum of [Ag<sub>301</sub>]<sup>3+</sup>  
15 calculated with the optimized auxiliary minimal basis, a conventional DZ basis for the molecular  
16 orbital and the LB94 functional<sup>25</sup>, in order to be consistent with the spectrum already reported for  
17 the same systems<sup>3</sup>. Thanks to the minimal size of the basis set, such calculation is extremely cheap:  
18 using the hardware described in previous section 2.4. the whole calculation took only 64 hours  
19 using 24 cores. We optimized a minimal basis set for gold, but the spectrum obtained was very  
20 poor: gold atom is more demanding in terms of basis size. This is due to the more important role  
21 played by the 5d shell, while for Ag the 4d manifold is much deeper, and only 5s electrons are  
22 responsible for the optical properties.  
23  
24  
25  
26  
27  
28  
29  
30  
31  
32  
33  
34  
35

### 36 *3.3 Auxiliary basis set database organization*

37 The database covers all the periodic table of elements, except lanthanides and actinides. The  
38 auxiliary basis are all obtained by reduction, furthermore for the C, O, Cl, S, F, N, Se, Si, P, Br and  
39 I elements also the exponent optimization has been done. The set is already available in the last  
40 AMS2022 distributed release, in the \$AMSRESOURCES/POLTDDFT directory. The complete  
41 auxiliary basis sets have been reported in the Supporting Information.  
42  
43  
44  
45  
46  
47

## 48 **4. Conclusions**

49 In the present work a new procedure to generate a set of STO auxiliary basis function suitable to  
50 fit the induced electron density is proposed, implemented and applied. Such set has been  
51 optimized for each element of the periodic table (except the f-block elements) in order to furnish  
52 accurate absorption spectra using the complex polarizability algorithm of TDDFT, also known  
53 as polTDDFT. To obtain such result we have set up an automatic procedure which is able,  
54 thanks to the definition of suitable descriptors, to evaluate the resemblance of the auxiliary basis  
55 dependent calculated spectra with respect to a reference spectrum. In particular two different  
56  
57  
58  
59  
60

1  
2  
3 descriptors have been considered, which are very easy to calculate and have proven very  
4 efficient to quantify the resemblance of a calculated spectrum with respect to the reference  
5 spectrum. In this way it is possible to reduce the size of the basis set maximizing the basis set  
6 accuracy. Thanks to the choice to employ a collection of molecules for each element, such basis  
7 has proven transferable to molecules outside the collection. It has been found that for most  
8 elements the reduction of the auxiliary basis set size by deleting the unnecessary functions is  
9 enough to get accurate results and small auxiliary basis sets. For some elements a further  
10 exponent refinement has been found useful for a further improvement. The final sets are  
11 therefore much more accurate and smaller than the previous ones and have been already  
12 included in the database present in the last release of the AMS program. The availability of the  
13 present new set will allow to improve drastically the applicability range of the polTDDFT  
14 method with higher accuracy and less computational effort.  
15  
16  
17  
18  
19  
20  
21  
22  
23  
24

### 25 **Supporting Information**

26 Geometries of all the collections of molecules employed to obtain the auxiliary basis set and  
27 final optimized basis set.  
28  
29  
30  
31

### 32 **Acknowledgements**

33 This work was supported by Stiftung Beneficentia and by Finanziamento per la Ricerca di  
34 Ateneo, (FRA) of the Università degli Studi di Trieste, Italy.  
35  
36  
37  
38  
39  
40  
41  
42  
43  
44  
45  
46  
47  
48  
49  
50  
51  
52  
53  
54  
55  
56  
57  
58  
59  
60

## References

- <sup>1</sup> O. Baseggio, G. Fronzoni, M. Stener, *J. Chem. Phys.* **2015**, *143*, 024106.
- <sup>2</sup> O. Baseggio, M. De Vetta, G. Fronzoni, M. Stener and A. Fortunelli *Int. J. Quantum Chem.*, **2016**, *116*, 1603.
- <sup>3</sup> O. Baseggio, M. De Vetta, G. Fronzoni M. Stener, L. Sementa, A. Fortunelli and A. Calzolari *J. Phys. Chem. C* **2016**, *120*, 12773.
- <sup>4</sup> O. Baseggio, D. Toffoli, G. Fronzoni, M. Stener, L. Sementa, A. Fortunelli *J. Phys. Chem. C* **2016**, *120*, 24335.
- <sup>5</sup> D. Toffoli, A. Russi, G. Fronzoni, E. Coccia, M. Stener, L. Sementa and A. Fortunelli *J. Phys. Chem. Lett.* **2021**, *12*, 5829.
- <sup>6</sup> D. Toffoli, M. Medves, G. Fronzoni, E. Coccia, M. Stener, L. Sementa, A. Fortunelli, *Molecules* **2022**, *27*, 93.
- <sup>7</sup> Casida, M. E. In *Recent Advances in Density Functional Methods*; Chong, D. P., Ed.; World Scientific: Singapore, 1995; pp 155-193
- <sup>8</sup> L. E. Daga, B. Civalleri, and L. Maschio *J. Chem. Theory Comput.* **2020**, *16*, 2192.
- <sup>9</sup> D. Rappoport and F. Furche *J. Chem. Phys.* **2010**, *133*, 134105.
- <sup>10</sup> T. P. Rossi, S. Lehtola, A. Sakko, M. J. Puska, and R. M. Nieminen, *J. Chem. Phys.* **2015**, *142*, 094114.
- <sup>11</sup> B.I.Dunlap and N.Rosch *Advances in Quantum Chemistry* **1990**, *21*, 317.
- <sup>12</sup> E. J. Baerends, D.E. Ellis and P. Roos, *Chem. Phys.* **1973**, *2*, 41.
- <sup>13</sup> M. Franchini, P. H. T. Philipsen, E. van Lenthe and L. Visscher *J. Chem. Theory Comput.* **2014**, *10*, 1994.
- <sup>14</sup> J. Carmona-Espíndola and A. M. Köster, *Can. J. Chem.* **2013**, *91*, 795.
- <sup>15</sup> G. Giannone and F. Della Sala *J. Chem. Phys.* **2020**, *153*, 084110.
- <sup>16</sup> S. Lehtola *J. Comput. Chem.* **2015**, *36*, 335.
- <sup>17</sup> N. A. Seifert, K. Prozument, and M. J. Davis *J. Chem. Phys.* **2021**, *155*, 184101.
- <sup>18</sup> E. K. U. Gross and W. Kohn *Adv. Quantum Chem.* **1990**, *21*, 255.
- <sup>19</sup> A. D. Becke, *J. Chem. Phys.* 1993, *98*, 5648.
- <sup>20</sup> P. J. Stephens, F. J. Devlin, C. F. Chabalowski, and M. J. Frisch, *J. Phys. Chem.* **1994**, *98*, 11623.
- <sup>21</sup> John W. Foreman, *Data Smart: Using Data Science to Transform Information into Insight*, 1st Edition, Wiley, 2013.
- <sup>22</sup> S. H. Vosko, L. Wilk, M. Nusair *Can. J. Phys.* **1980**, *58*, 1200.
- <sup>23</sup> M. Medves, L. Sementa, D. Toffoli, G. Fronzoni, A. Fortunelli and M. Stener *J. Chem. Phys.* **2020**, *152*, 184102.
- <sup>24</sup> E. van Lenthe, E. J. Baerends and J. G. Snijders, *J. Chem. Phys.* **1993**, *99*, 4597.
- <sup>25</sup> R. van Leeuwen and E. J. Baerends *Physical Review A* **1994**, *49*, 2421.

## Captions to Figures

**Scheme 1.** Flow chart relative to the procedure to reduce the auxiliary basis set.

**Scheme 2.** Flow chart relative to the procedure to optimize the exponents of the auxiliary basis set.

**Figure 1.** Evolution of the 2D<sub>xy</sub> descriptor during the automated reduction of the auxiliary basis set for the Sn element.

**Figure 2.** Evolution of the best 2D<sub>xy</sub> descriptor along the reduction of the auxiliary basis set for the Sn element.

**Figure 3.** Comparison between reference (Casida) and polTDDFT spectra with reduced basis set for SnCl<sub>2</sub>, which belongs to the Sn collection.

**Figure 4.** Evolution of the best 2D<sub>xy</sub> descriptor along the reduction of the auxiliary basis set for the Sn element for each molecule of the collection. The arithmetic mean is reported as well.

**Figure 5.** Evolution of the nD<sub>y</sub> descriptor along the best 2D<sub>xy</sub> reduced series of the auxiliary basis set for the Sn element.

**Figure 6.** Comparison between reference (Casida) and polTDDFT spectra with reduced basis set for Sn(CH<sub>2</sub>CH<sub>3</sub>)<sub>2</sub>Cl<sub>2</sub>, which does not belong to the Sn collection.

**Figure 7.** Evolution of the 2D<sub>xy</sub> descriptor along the optimization procedure (exponent refinement) of the auxiliary basis set for the Cl element, calculated as arithmetic mean for HCl, CCl<sub>4</sub> and Cl<sub>2</sub>O, which belong to the Cl collection.

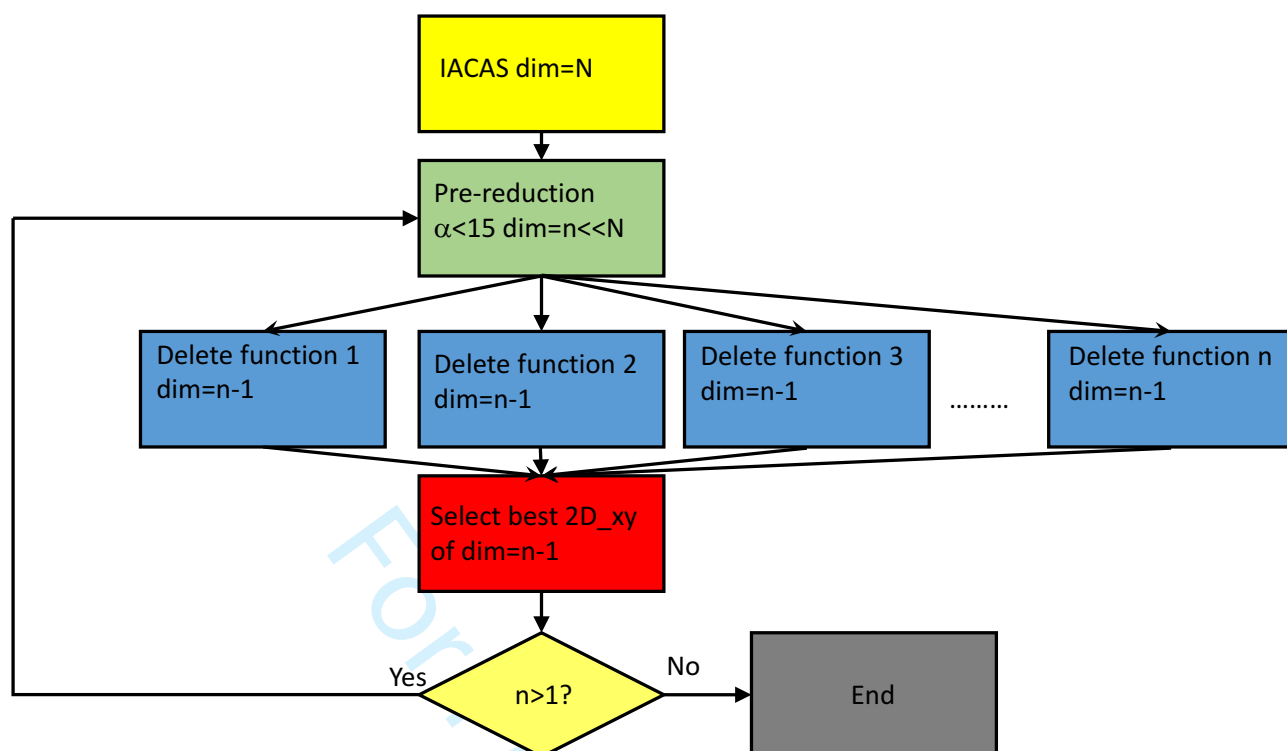
**Figure 8.** Comparison between reference (Casida) and polTDDFT spectra with optimized exponents basis set for HCl, CCl<sub>4</sub> and Cl<sub>2</sub>O, which belong to the Cl collection.

**Figure 9.** Comparison between reference (Casida) and polTDDFT spectra with Cl optimized exponents basis set for AgCl, Ar-Cl<sub>2</sub>, VOCl<sub>3</sub>, S<sub>2</sub>Cl<sub>2</sub>, SOCl<sub>2</sub> and SO<sub>2</sub>Cl<sub>2</sub>, which do not belong to the Cl collection.

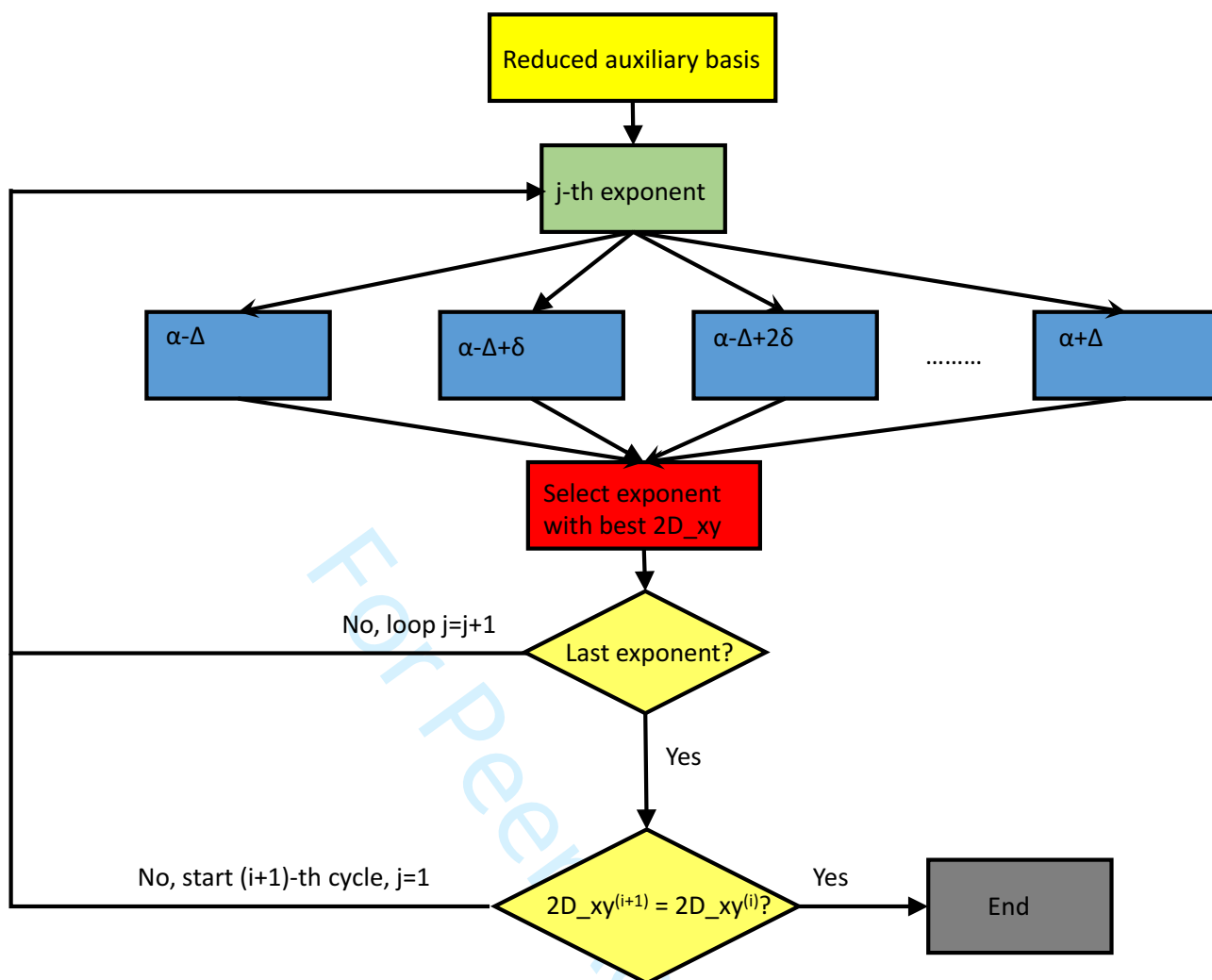
**Figure 10.** Upper panel: comparison between reference (Casida) and polTDDFT spectra with auxiliary minimal basis with optimized exponent ( $\alpha=0.40$ ) for Ag<sub>20</sub>. Lower panel: polTDDFT spectra calculated with auxiliary minimal basis with optimized exponent ( $\alpha=0.40$ ) and DZ conventional basis for the molecular orbitals and LB94 XC potential for [Ag<sub>301</sub>]<sup>3+</sup>.

**Table 1.** The original density fitting auxiliary basis set for Sn atom. The broken line refers to the pre-reduction of the exponents with  $\alpha > 15$ . The final optimally reduced basis elements are in bold.

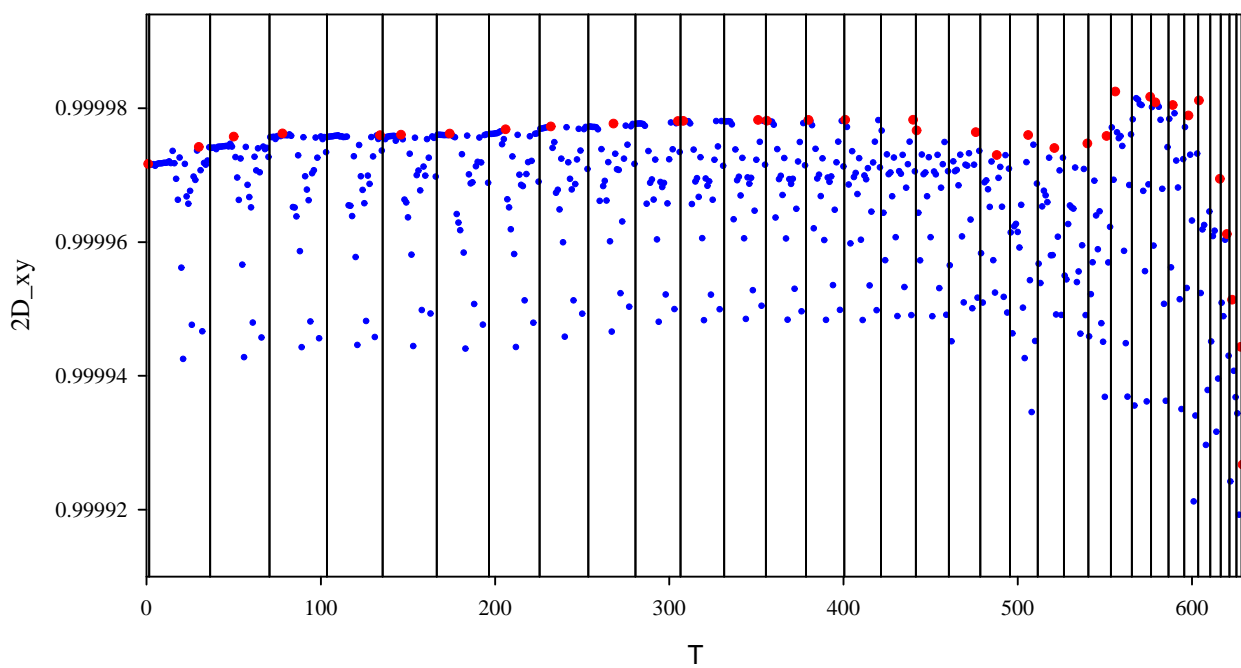
<i>ns</i>	$\alpha$	<i>np</i>	$\alpha$	<i>nd</i>	$\alpha$	<i>nf</i>	$\alpha$	<i>ng</i>	$\alpha$
1s	64.80	2p	55.70	3d	46.60	4f	35.80	5g	25.30
1s	39.22	3p	45.83	4d	34.44	5f	24.00	6g	14.59
2s	43.94	4p	37.10	5d	25.64	6f	16.38	7g	8.67
2s	29.81	5p	29.94	6d	19.26	7f	11.37	8g	5.28
3s	29.67	5p	20.10	6d	12.43	7f	6.95	8g	2.88
3s	21.38	6p	16.25	7d	9.43	8f	4.89		
4s	20.36	6p	11.26	7d	6.27	8f	3.08		
4s	15.25	7p	9.14	8d	4.80				
5s	14.23	7p	6.50	<b>8d</b>	<b>3.27</b>				
5s	10.96	8p	5.30	9d	2.53				
6s	10.11	<b>8p</b>	<b>3.85</b>	<b>9d</b>	<b>1.76</b>				
6s	7.95	<b>9p</b>	<b>3.15</b>						
7s	7.29	<b>9p</b>	<b>2.33</b>						
7s	5.83								
8s	5.33								
8s	4.32								
8s	3.50								
<b>9s</b>	<b>3.19</b>								
9s	2.62								
9s	2.15								
9s	1.76								



Scheme 1.



Scheme 2.

**Figure 1**

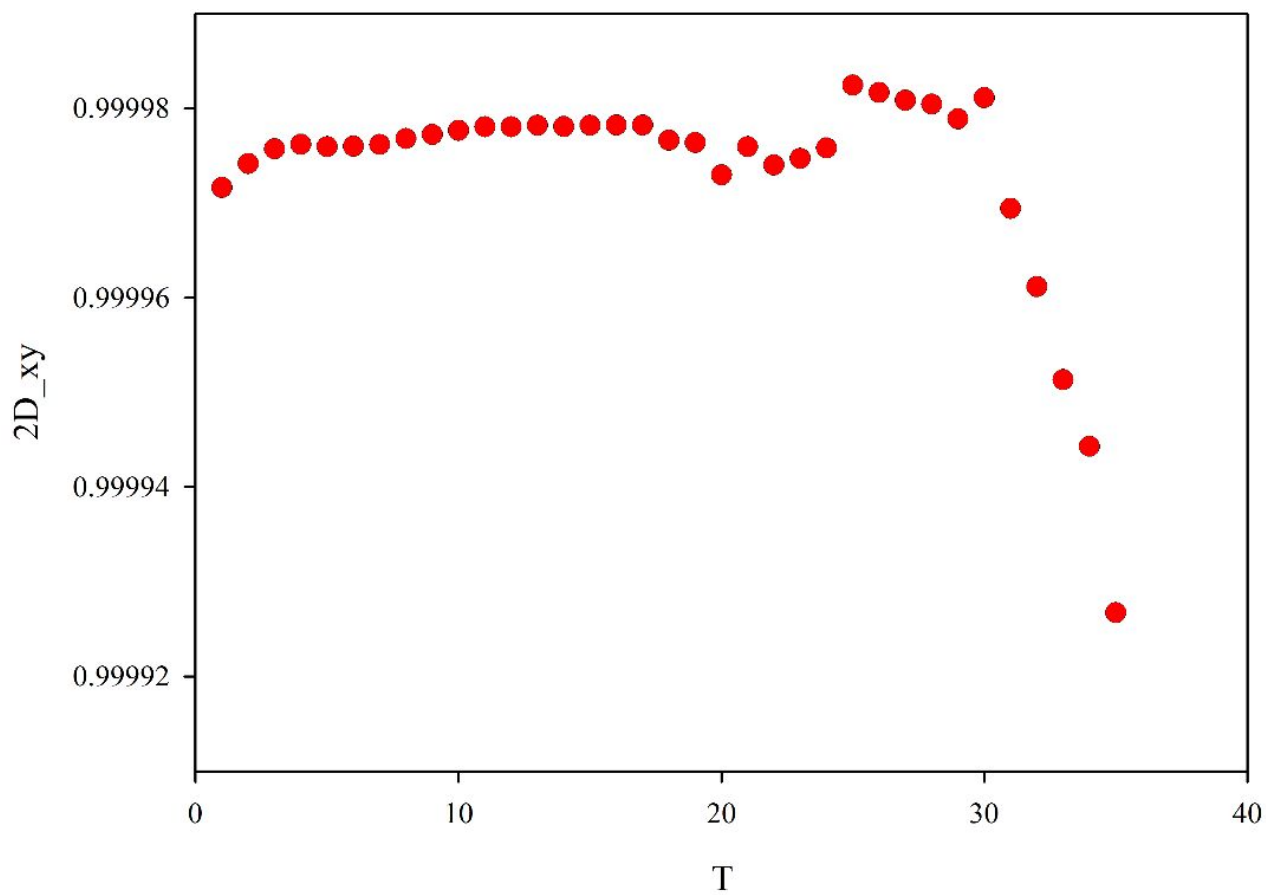


Figure 2

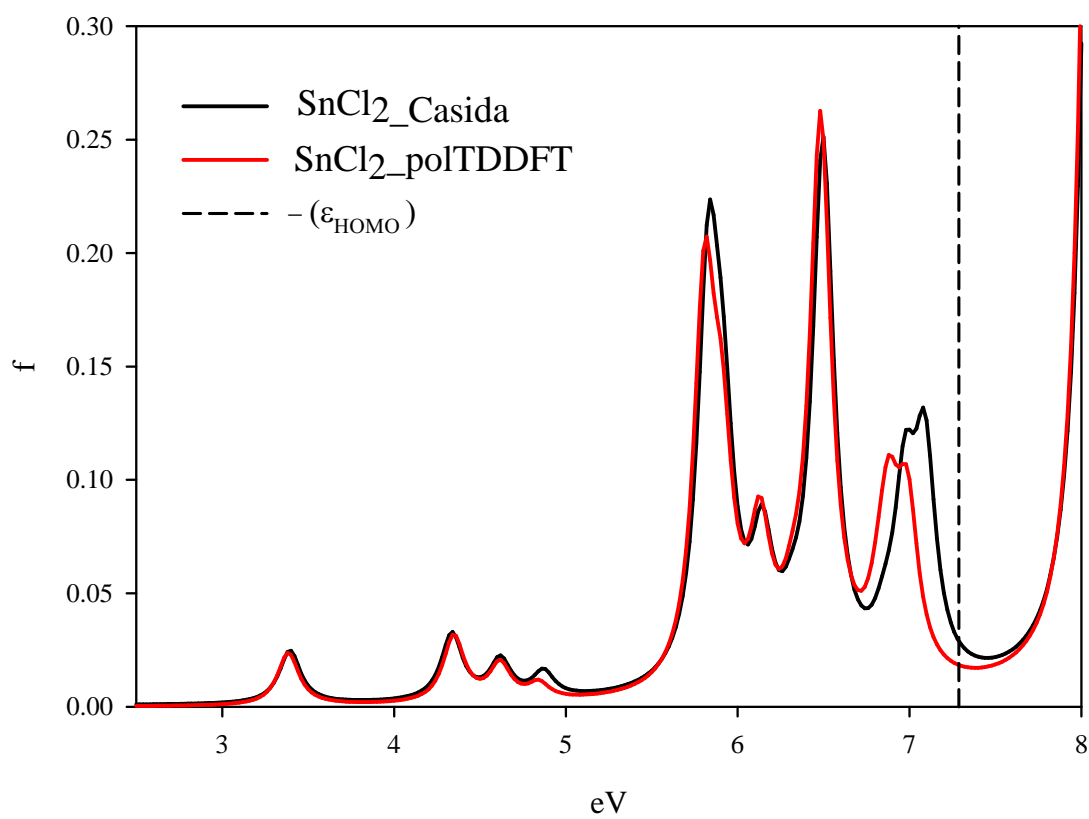


Fig.3

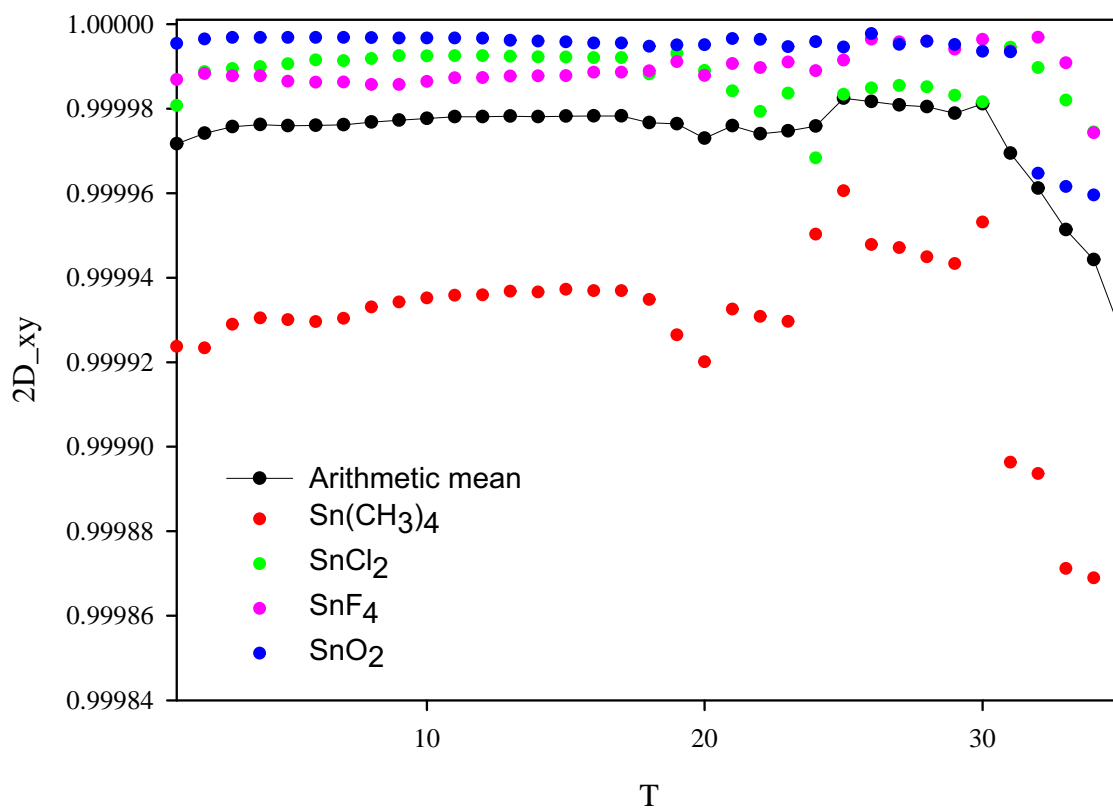


Fig 4

Review

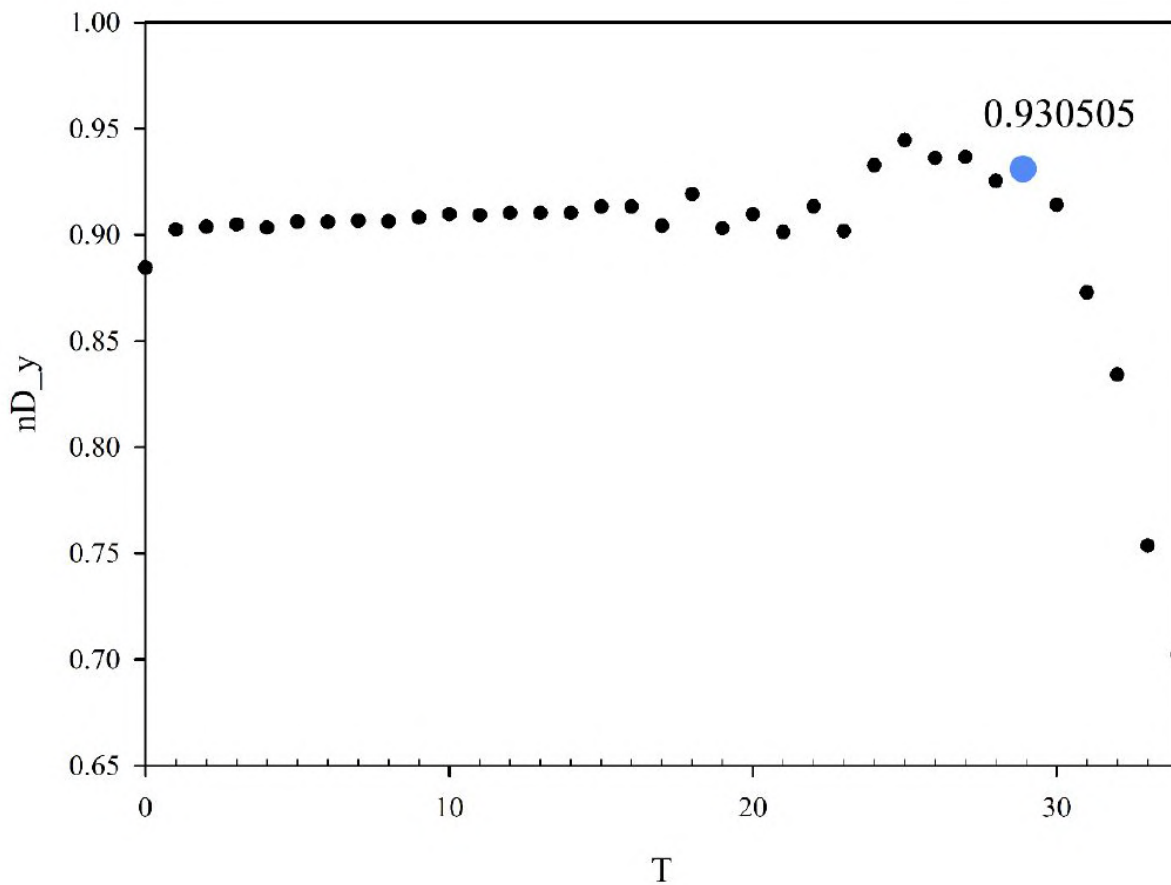


Fig 5

Review

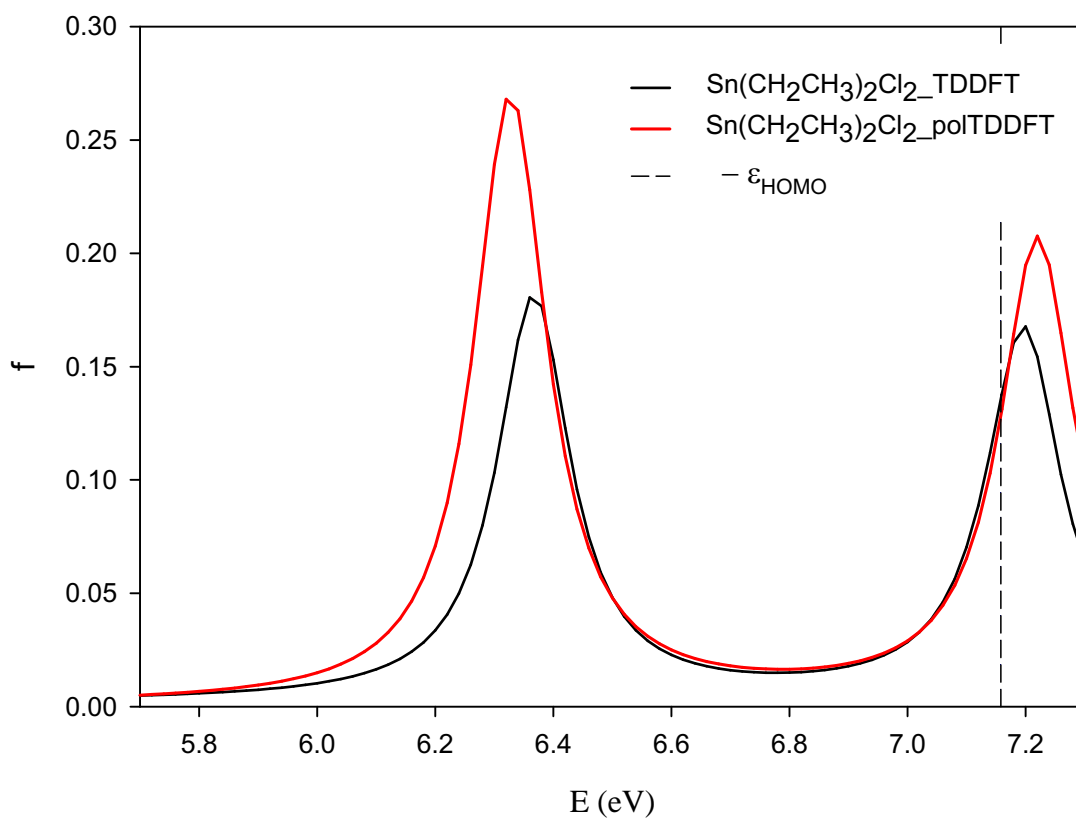


Fig 6

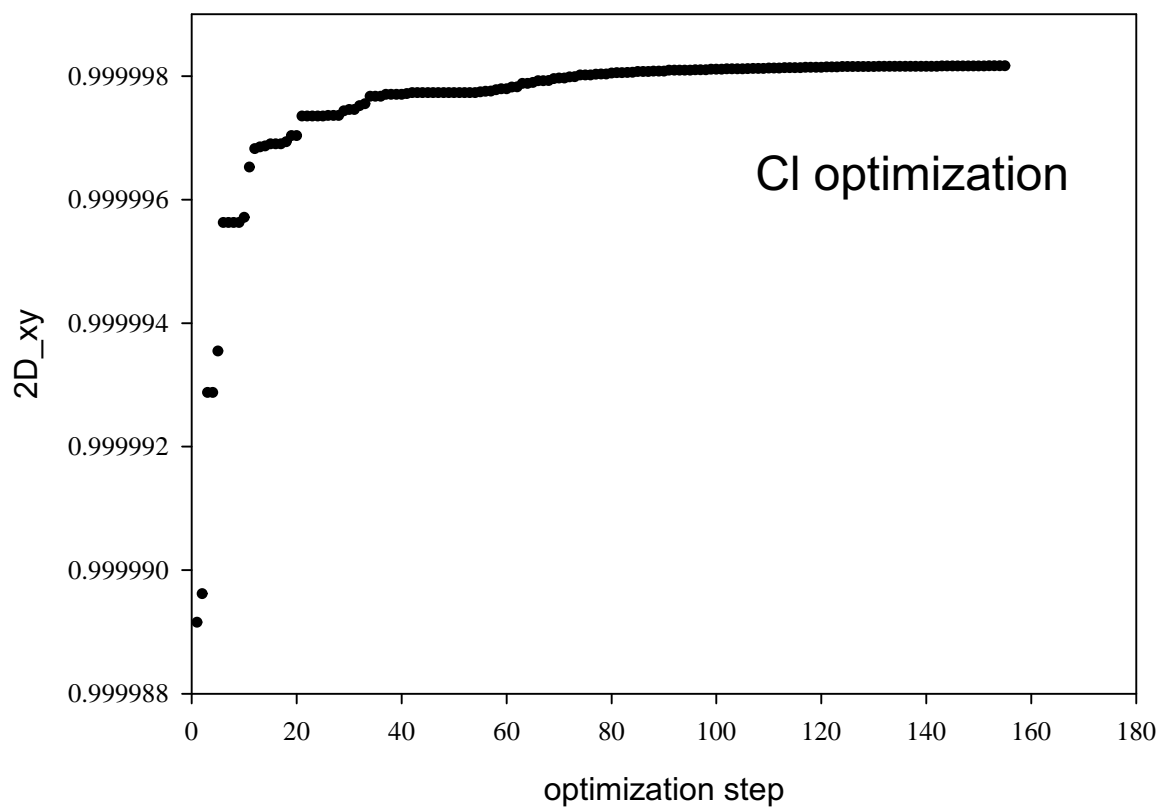


Fig. 7

Review

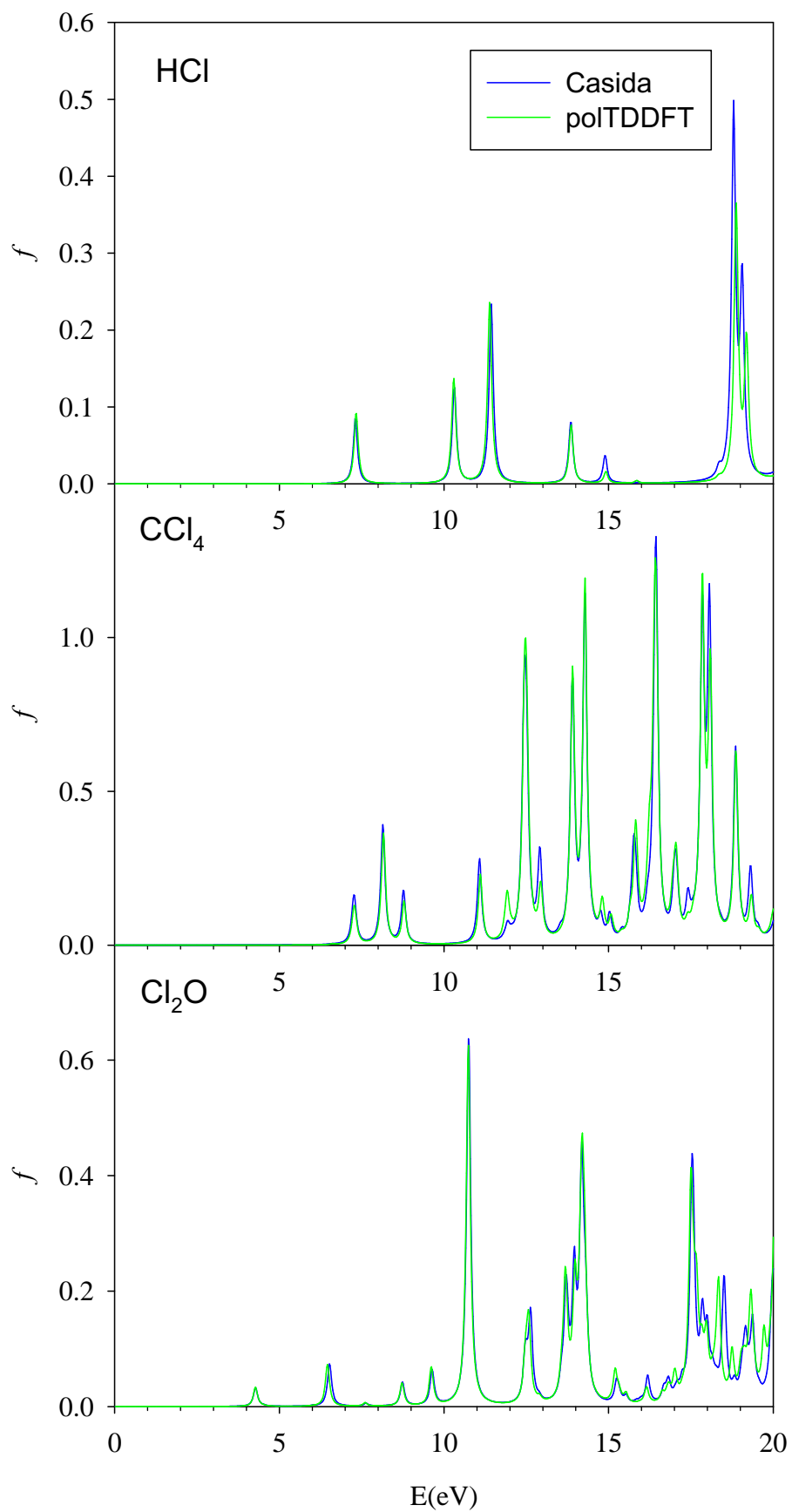


Fig. 8

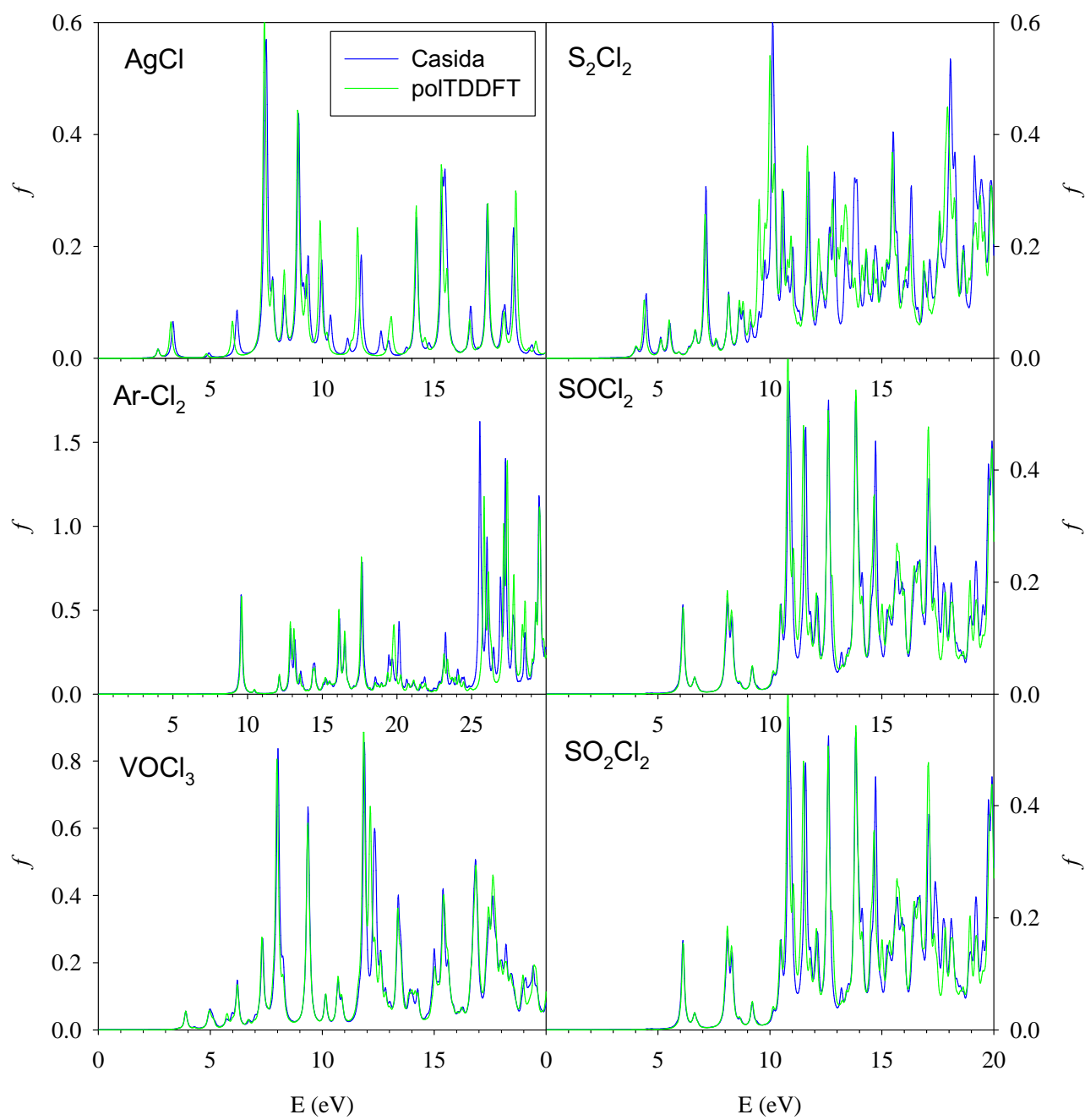


Fig. 9

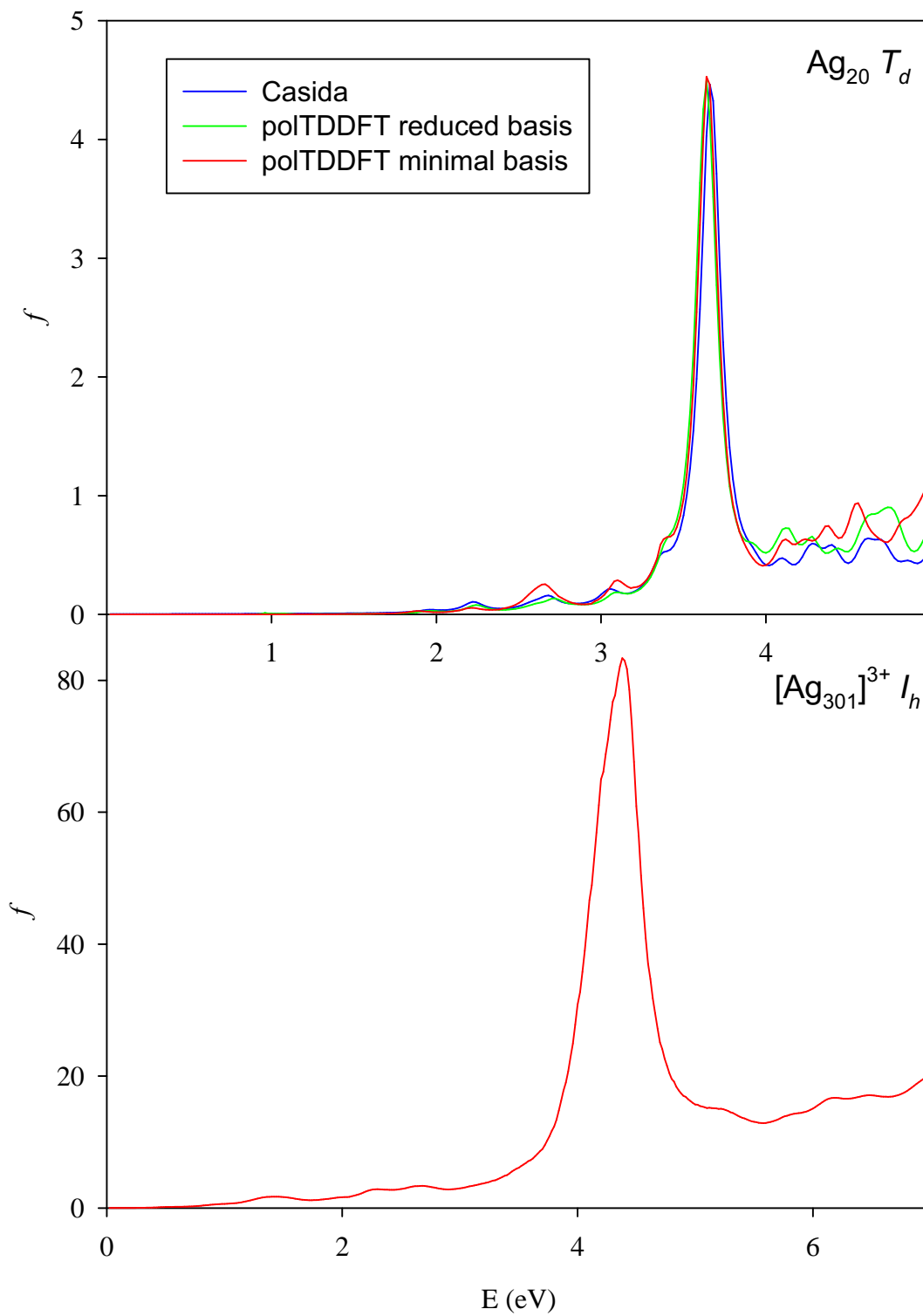


Fig. 10

ATTENTION: for supporting information visit the article online

## 5 CONCLUSION

The present thesis work has been devoted to the accurate computational description of the optical properties of metal clusters. Although the TDDFT is already a well consolidated technique to describe optical properties of large systems, when the systems become very large (many hundreds of atoms) specific issues must be considered. For this reason in the present Thesis we did not use the conventional Casida TDDFT formulation, but rather the complex polarizability algorithm (also known as polTDDFT) has been employed. This choice has been driven by the need to avoid the diagonalization of a large matrix which becomes prohibitive and numerically unstable as the systems size grows. In order to improve the accuracy with respect to the experiment, the first target of this thesis was to make the calculations with hybrid functional (like B3LYP) feasible for large systems as well. This task is not trivial, since the non-local exchange term of the hybrid TDDFT kernel makes the calculation extremely time-consuming. This problem is even worse when non-conventional basis are employed, like STO as in the ADF code since it is not possible to exploit the advantage offered by GTO for analytic integration. Therefore in this thesis the Hybrid Diagonal Approximation (HDA) has been introduced and implemented in the ADF code. This scheme, which consists to employ the full non-local kernel only in the diagonal matrix elements of the TDDFT equation, has proven very accurate and extremely efficient. This new feature allowed to obtain a quantitative match with respect to a low temperature experiment for the cluster  $\text{Ag}_{24}\text{Au}(\text{DMBT})_{18}]^-$ . In addition to the new HDA scheme, also a new density fitting basis set has been optimized for POLTDDFT, by means of an automatic procedure inspired by Artificial Intelligence (AI) techniques. Such procedure allowed to define a set of descriptors which can be considered as indexes of the ability of the fitting basis set to correctly reproduce the photoabsorption spectrum. Such procedure allowed to build a database of fitting functions for the atoms of whole the periodic table, with the exceptions of lanthanides and actinides. So the availability of a competitive scheme like HDA as well as a very efficient density fitting, allowed to apply the method to systems which were not tractable before and with an unprecedented accuracy. In the present thesis the method has been applied to study and rationalize the ECD of chiral clusters, the photoabsorption at low temperature and the coupling between plasmonic systems.

In summary, the joint efforts between method development as well as technical improvements, have allowed to improve the potential applications of the polTDDFT method. Since now the method has gained almost quantitative accuracy with respect to the experiment, it can be profitably employed, for example, also with predictive potential, for example for the *in-silico* design of new optical materials.

Future directions starting from the present work can be envisaged, for example with the inclusion of Range Separated (RS) functional in the HDA scheme, the extension of polTDDFT to open shell systems by means of an unrestricted formulation, the extension of some part of the codes to more efficient parallelization and the inclusion of the ligand conformational motion by means of molecular dynamics technique.

Regarding the HDA a further step forward concerns the use of STO fitting (the same optimized bases) rather than use of numerical integration, this was performed during a master's thesis work (of which I was co-supervisor), this upgrade makes possible a further speedup in the calculation from

one to two orders of magnitude, bringing HDA to be comparable with a GGA functional like LB94 with a very slight deviation from numerical calculations.

This thesis work is focused on providing new tools and methods rather than producing results in the form of simulations. In addition to the scientific interest in itself, the proposed simulations are to be considered as examples of the innumerable possible applications of polTDDFT and the AMS package. Various undergraduates and PhD students have and are using the code deriving from this thesis work, using it in very different sectors, for example: CD and ABS spectra of protein (where many structures of medium-large molecule are required), quantum dots and various doped carbon-based materials (that requires different element basis set and fast methods), nanoalloys, metal clusters (non only noble metal), organic shell protected clusters, surface doping, supramolecular compounds, and much more. Other interesting application are: photochemistry (synthesis, artificial CO<sub>2</sub> fixation, coupling reaction), sensor (fluorescence quenching or enhancement, chemiluminescence, colorimetric test, plasmon resonance devices such as immunoassay), LED (more efficient or more exotic, for example circular polarized light, far UV source), photodiode (as sensor or photovoltaic panels), photocatalysis (water splitting, waste destruction and autocleaning materials), fluorescent dye (paint, reagent, labelling), nanomotor, lighting technology, etc. Nowadays, all these applications require a preliminary theoretical study, as they are phenomena with a relevant quantum component and therefore not easy to interpret and rationalize, moreover this allows to save reagents and time by being able to limit the number of compounds to be synthesized.



# RINGRAZIAMENTI

*In questo ultimo capitolo intendo ringraziare tutte le persone che hanno dato un contributo scientifico e non al raggiungimento di questo traguardo.*

*Si ringrazia il gruppo del Dott. Alessandro Fortunelli per l'importante e proficua collaborazione che dura ormai da molti anni.*

*Si ringrazia il Prof. Thomas Bürgi per la sintesi e caratterizzazione di alcuni sistemi studiati in questa tesi.*

*Si ringrazia il Prof. Flavio Maran per la registrazione di preziosi spettri, in particolare quelli a bassa temperatura, di alcuni sistemi studiati in questa tesi.*

*Ringrazio tutti i professori che ho avuto il piacere di ascoltare in tutti questi anni di scuola/università, mi hanno insegnato molto e mi hanno fatto amare le scienze ogni giorno di più.*

*Un ringraziamento particolare va ai Prof. del gruppo di chimica teorica di Trieste, sia per la collaborazione durante questi anni di dottorato, sia per avermi avvicinato a questo interessante aspetto delle scienze.*

*Si ringraziano tutti i colleghi e studenti passati dall'ufficio 465, avete reso la mia permanenza davvero gioiosa, è stato un piacere stare insieme a voi!*

*Ringrazio tutte le persone con cui ho affrontato questi anni da studente: amici, coinquilini, compagni di corso e molti altri ancora, la lista è davvero lunga.*

*Per concludere riservo un ringraziamento davvero speciale al mio supervisore di tesi, il Prof. Mauro Stener; in tutti questi anni è stato fonte di ispirazione, un vero "uomo di scienza" e di grande umanità, tanto "teorico" quanto concreto nella realizzazione di progetti davvero ambiziosi, spero che possa a lungo continuare a diffondere pillole di scienza e serenità in coloro che hanno la fortuna di incontrarlo, grazie di tutto.*